THE PHYSICAL REVIEW

VOLUME 89 Second Series NUMBER 4

FEBRUARY 15, 1953

Published for the

AMERICAN PHYSICAL SOCIETY

by the

AMERICAN INSTITUTE OF PHYSICS

Incorporated

LANCASTER, PA., AND NEW YORK, N. Y.

THE PHYSICAL REVIEW

A journal of experimental and theoretical physics established by E. L. Nichols in 1893

Published by the American Institute of Physics
for the
AMERICAN PHYSICAL SOCIETY

Officers

President

J. H. Van Vleck
Harvard University
Cambridge, Massachusetts

Vice-President

Enrico Fermi
Institute for Nuclear Studies
University of Chicago
Chicago 37, Illinois

Secretary

K. K. Darrow
Bell Telephone Laboratories
Office
Columbia University
New York 27, New York

Treasurer

G. B. Pegram
Columbia University
New York 27, New York

Local Secretary
for the Pacific Coast

J. Ham
University of California at Los
Angeles
Los Angeles, California

Managing Editor

S. A. Goudsmit
Brookhaven National Laboratory
Upton, Long Island
New York

BOARD OF EDITORS

Associate Editors

M. Goldhaber
S. Hayward
L. W. Lawson
A. Pais
E. Rogers
C. H. Townes

W. P. Allis
F. G. Brickwedde
W. B. Fowler
Conyers Herring
H. W. Lewis
Arnold Nordsieck

Communications for publication should be addressed to S. A. Goudsmit, Brookhaven National Laboratory, Upton, Long Island, New York. The Board of Editors has authorized us to pay a publication charge of $12 per page. If desired, authors obtain up to 100 free reprints. Instructions will accompany galley proofs.

Requests for nonexclusive permission concerning papers in the process of publication should be addressed to the Publication Manager, American Institute of Physics, 57 East 55 Street, New York 22, New York.

Subscription Rates

United States and Canada.....$20.00
Foreign.....$21.00

Back Numbers

Orders for back numbers and volumes should be addressed to the American Institute of Physics, 57 East 55 Street, New York 22, New York.

Prices of volumes in the case of members of the American Physical Society will be furnished by the Treasurer; in the case of other subscribers by the American Institute of Physics.

Publication Office: 1 Northgate Plaza, Grand Concourse, Bronx, New York.

The Physical Review is published monthly by the American Physical Society at Easton, Pennsylvania.

Entered as second-class matter March 6, 1929, at the Post Office at Easton, Pennsylvania, under the Act of March 3, 1879.

Acceptance for mailing at special rate of postage provided for in paragraph (d-2), section 34.40, P. L. & R. of 1948, authorized January 27, 1950.

THE
PHYSICAL REVIEW

A journal of experimental and theoretical physics established by E. L. Nichols in 1893

SECOND SERIES, VOL. 89, NO. 4 FEBRUARY 15, 1953

The Theory of Electron Diffraction

ROY GLAUBER,* *Norman Bridge Laboratory of Physics, California Institute of Technology, Pasadena, California*
AND
VERNER SCHOMAKER, *Gates and Crellin Laboratories of Chemistry, California Institute of Technology,† Pasadena, California*
(Received October 14, 1952)

It is shown that the omission of an angle-dependent phase factor in the scattering amplitude constitutes a significant error of the Born approximation, as customarily applied to electron diffraction experiments. Some general properties of the scattering amplitude are discussed in relation to the Born approximation and used to derive a simple estimate of the required phase. The theory, thus corrected, is found to remove the need for assuming rather distorted structures in some molecules containing heavy atoms. The effect discussed is present quite generally in the interference of waves scattered by differing potentials and becomes more prominent as the particle energy is lowered. In the Appendix a semiclassical procedure is used to treat the analogous effect in proton diffraction.

THE Born approximation is well known to predict exactly, in the nonrelativistic region, the intensity of electrons scattered by a Coulomb field. Although still a perturbation method, it has seemed in this case nearly immune from the usually attendant inaccuracies and has been widely and successfully used in the analysis of electron diffraction patterns. Confidence in the approximation as ordinarily applied to molecular structure determinations has extended even to a number of cases which have seemed to reveal rather improbable structures. On re-examining several of these (which are briefly noted in Sec. I), we have found that a phase change, heretofore neglected, which takes place on scattering is the probable cause of the anomalies.[1] It may, in extreme cases, lead to strikingly altered conclusions about molecular structure. The error is one characteristic of the Born approximation and appears whenever it is applied to the interference of waves scattered by potentials of different strengths. The phase shift in question, which depends significantly on the effects of screening, is calculated approximately in Sec. II, and the results are then compared with experiment.

I. NATURE OF THE EFFECT

The diffraction patterns of electrons scattered by gases consist of weak concentric rings superposed on the intense forward maximum of Coulomb scattering (modified by screening). Fourier analysis of the ring structure gives the distances between the scattering centers of the molecule. In some molecules containing heavy atoms a curious effect involving these distances has been found. Uranium hexafluoride, in which the effect was first noted, might be expected to show octahedral symmetry about the uranium atom. The molecule has instead appeared rather puzzlingly asymmetric: the calculated curves showing the distribution of interatomic distances[2] have two distinctly separated peaks at 1.87A and 2.17A rather than a single one corresponding to a unique U−F bond length. Information from other sources, however, in no way confirms this picture. The data on infrared spectra, molecular entropy, and the dipole moment are all consistent with the symmetrical structure.[3] Similar apparent asymmetries have also been found to occur in a number of other molecules of the form MX_n, containing single heavy atoms. The distances between the heavy atom and its neighbors are apparently split into two equal groups differing by an amount roughly proportional to $Z_M - Z_X$. For equal atomic numbers as in the heavy molecule I_2, nothing unusual is observed.

We shall not dwell upon the valence-theoretical

* Present address: Lyman Laboratory of Physics, Harvard University, Cambridge 38, Massachusetts.
† Contribution No. 1743.
[1] V. Schomaker and R. Glauber, Nature **170**, 290 (1952).
[2] S. H. Bauer, J. Chem. Phys. **18**, 27 (1950).
[3] See especially Bigeleisen, Mayer, Stevenson, and Turkevich, J. Chem. Phys. **16**, 442 (1948); and Burke, Smith, and Nielsen, J. Chem. Phys. **20**, 447 (1952).

attempts which have been made to explain these results. The smoothness of the dependence on nuclear charges indicates an inadequacy of the scattering theory rather than any actual effects of chemical bonding. In demonstrating this we shall show that the molecules in question are in fact as accurately symmetrical as the present diffraction techniques may discern.

Of the various inaccuracies implicit in the conventional calculations, the most obvious, perhaps, is the use of the Born approximation for the atomic scattering amplitudes. Other points more specifically molecular in nature are the neglect of multiple scattering (by the different atoms) and of valence distortion of the charge distribution. A strong dependence on the difference of atomic numbers cannot, however, be produced by either of the latter two effects, whereas interference between corrections to the atomic scattering amplitudes may easily do so. For this reason we assume that the wave scattered by a molecule may still be represented by a superposition of waves $f_j(\mathbf{k}', \mathbf{k})e^{ikr}/r$ scattered by the individual atoms ($j=1, 2, 3, \cdots$) from the direction $\mathbf{k}$ to the direction $\mathbf{k}'$.

The amplitudes $f_j(\mathbf{k}', \mathbf{k})$ may be shown quite generally (see Sec. II) to be complex functions of the scattering angle. It is characteristic of the Born approximation, however, that these amplitudes, given by the familiar matrix element,

$$f_B(\mathbf{k}', \mathbf{k}) = -\frac{m}{2\pi\hbar^2}\int e^{i(\mathbf{k}-\mathbf{k}')\cdot\mathbf{r}}V(\mathbf{r})d\tau, \qquad (1)$$

are always real for atomic scattering potentials $V(\mathbf{r})$ (or more generally, for any potential unchanged by inversion in the origin). An example close at hand is scattering by a pure Coulomb field, for which the expression (1) predicts exactly the absolute value of the scattered amplitude but omits at the same time a phase factor sensitively dependent on the angle of scattering.[4] Abbreviating the amplitudes for the moment, as $f_j(\theta)$, we take explicit account of their phases by writing them as $|f_j(\theta)|\exp(i\eta_j(\theta))$. The intensity of the scattered electrons averaged over the random orientations of the gas molecules is then proportional to

$$\sum_{i,j} f_i^*(\theta)f_j(\theta)\frac{\sin sr_{ij}}{sr_{ij}} = \sum_{i,j}|f_i(\theta)||f_j(\theta)| \times\cos\{\eta_i(\theta)-\eta_j(\theta)\}\frac{\sin sr_{ij}}{sr_{ij}}, \qquad (2)$$

where $s=|\mathbf{k}-\mathbf{k}'|=(4\pi/\lambda)\sin(\theta/2)$, and r_{ij} is the distance between atoms i and j.

To see the way the phase $\eta(\theta)$ may explain the apparent asymmetry, let us suppose the amplitudes $f_j(\theta)$ are real. Then the sum of the terms contributed by a split pair of distances $r_{ij}=r_0-\delta$ and $r_{ij}=r_0+\delta$ with similar atoms j and j', would be approximately

$$2|f_i(\theta)||f_j(\theta)|\cos s\delta\,\sin sr_0/sr_0. \qquad (3)$$

(The amplitude difference, of order δ/r_0, is neglected.)

This expression is of just the form that would be given by (2) if the phase difference $|\eta_i(\theta)-\eta_j(\theta)|$ were proportional to s, and if no distance splittings at all existed. The scattering angle at which the amplitude of the wave corresponding to (3) first changes sign (and vanishes) is given by $|\eta_i(\theta)-\eta_j(\theta)|=\pi/2$. In practice it is the behavior of the diffraction pattern in the neighborhood of this critical angle that has been principally responsible for the interpretation in terms of beating sine waves and its implied molecular asymmetry. It is hoped that in future experiments the very faint outer fringes of the diffraction pattern may be observed at scattering angles sufficiently large to include the second critical angle $|\eta_i(\theta)-\eta_j(\theta)|=3\pi/2$. Since these data are lacking, the correct prediction of the scattering angle for which the phase difference is $\pi/2$ is the only quantitative test now available.

Moderate deviations of the phase shift from linearity in s on either side of the single critical angle observed will not very noticeably change the character of the predicted pattern. Indeed the desire that $|\eta_i(\theta)-n_j(\theta)|$ be linear in s comes from comparison with the asymmetric model, whose fit to the experimental diffraction pattern, although good, is not beyond improvement. The theoretically predicted phase differences (see Sec. II) which are monotonically increasing functions of s (but not proportional to s) appear in fact to fit the observed patterns more satisfactorily than the asymmetric model.[5]

II. THEORY

Before specializing to the atomic case, it will be useful to discuss several quite general properties of scattering amplitudes. Let us suppose $\psi_{\mathbf{k}}(\mathbf{r})$, $\psi_{\mathbf{k}'}(\mathbf{r})$ and $\psi_{-\mathbf{k}'}(\mathbf{r})$ are solutions of the Schrödinger equation for equal energies arising from initial plane waves in the directions $\mathbf{k}$, $\mathbf{k}'$, and $-\mathbf{k}'$, respectively. They then obey the relations

$$\psi_{-\mathbf{k}'}\nabla^2\psi_{\mathbf{k}}-\psi_{\mathbf{k}}\nabla^2\psi_{-\mathbf{k}'}=0, \qquad (4a)$$

$$\psi_{\mathbf{k}'}{}^*\nabla^2\psi_{\mathbf{k}}-\psi_{\mathbf{k}}\nabla^2\psi_{\mathbf{k}'}{}^*=0, \qquad (4b)$$

which, integrated over the volume of a sphere surrounding the scatterer, are immediately expressed as the surface integrals

$$\int_S\left(\psi_{-\mathbf{k}'}\frac{\partial}{\partial r}\psi_{\mathbf{k}}-\psi_{\mathbf{k}}\frac{\partial}{\partial r}\psi_{-\mathbf{k}'}\right)dS=0, \qquad (5a)$$

$$\int_S\left(\psi_{\mathbf{k}'}{}^*\frac{\partial}{\partial r}\psi_{\mathbf{k}}-\psi_{\mathbf{k}}\frac{\partial}{\partial r}\psi_{\mathbf{k}'}{}^*\right)dS=0, \qquad (5b)$$

[4] For the exact solution see N. F. Mott and H. S. W. Massey, *Theory of Atomic Collisions* (Oxford University Press, London, 1949), second edition, p. 48.

[5] G. Felsenfeld and J. Ibers, private communication.

with dS an element of surface. If the radius of the sphere is made sufficiently large, the wave functions assume their asymptotic values on the surface. We may then substitute

$$\psi_k(\mathbf{r}) = \exp(i\mathbf{k}\cdot\mathbf{r}) + f(\mathbf{k}_r, \mathbf{k}) \exp(ikr)/r$$

(where $\mathbf{k}_r$ is a propagation vector in the direction $\mathbf{r}$; $|\mathbf{k}_r| = k$) together with the analogous expressions for the other wave functions. The asymptotic values of the surface integrals for large sphere radii are then easily found and furnish two important relations involving the scattering amplitude. The first of these, coming from (5a), is

$$f(\mathbf{k}', \mathbf{k}) = f(-\mathbf{k}, -\mathbf{k}'), \tag{6}$$

which expresses the reversibility of the scattering between any pair of directions. From (5b) we find the relation

$$\frac{1}{2i}\{f(\mathbf{k}', \mathbf{k}) - f^*(\mathbf{k}, \mathbf{k}')\} = \frac{k}{4\pi}\int f^*(\mathbf{k}'', \mathbf{k}') f(\mathbf{k}'', \mathbf{k}) d\Omega_{\mathbf{k}''}, \tag{7}$$

in which the vector $\mathbf{k}''$ on the right is integrated over the sphere $|\mathbf{k}''| = k$. For the particular case $\mathbf{k}' = \mathbf{k}$, Eqs. (4b) and (5b) express the conservation of the particle current. Equation (7) then reduces to

$$\mathrm{Im} f(\mathbf{k}, \mathbf{k}) = (k/4\pi)\sigma \tag{8}$$

(where σ is the total scattering cross section), a relation which illustrates how fundamental is the requirement that the amplitude of the scattered wave be complex rather than real.

The more general form of Eq. (7) may be simplified by assuming that the scattering potential has inversion symmetry $V(\mathbf{r}) = V(-\mathbf{r})$. Nothing then is changed by inverting all vectors in the origin, and it follows, in particular, that $f(\mathbf{k}', \mathbf{k}) = f(-\mathbf{k}', -\mathbf{k})$. The latter relation together with the principle of reversibility (6) shows that the scattering amplitude is symmetric:

$$f(\mathbf{k}', \mathbf{k}) = f(\mathbf{k}, \mathbf{k}'). \tag{9}$$

Equation (7), under our assumption, then reduces to

$$\mathrm{Im} f(\mathbf{k}', \mathbf{k}) = \frac{k}{4\pi}\int f^*(\mathbf{k}', \mathbf{k}'') f(\mathbf{k}'', \mathbf{k}) d\Omega_{\mathbf{k}''}, \tag{10}$$

a relation we shall have frequent occasion to apply.

The reason for the inadequacy of the Born approximation (i.e., the first term of a power series expansion in $\alpha = -Ze^2/\hbar v$) in the present context is easily seen from (10). For $f(\mathbf{k}', \mathbf{k}) = O(\alpha)$ we have $\mathrm{Im} f(\mathbf{k}', \mathbf{k}) = O(\alpha^2)$, from which it follows that the phase increases with α, $\eta(\mathbf{k}', \mathbf{k}) = \arg f(\mathbf{k}', \mathbf{k}) = O(\alpha)$. Clearly then we must either go beyond the first term of the series or employ a fundamentally more accurate formulation of the scattering problem. In the present work we shall use some assumptions based on our experience with Coulomb scattering to simplify the higher terms of the Born series, thereby avoiding a good deal of numerical work but allowing still a reasonable comparison with experiment. We shall leave to a later treatment the refinements introduced by a basically different and more accurate procedure for approximating the scattering amplitude, calculations for which are now in progress.

At the energies at which diffraction experiments are performed ($\sim$40 kev), electron wavelengths are substantially smaller than the atomic radius a, ($ka \sim 10$ to 20). For all save small angles ($\theta \sim 1/ka$), therefore, the intensity of scattering is negligibly affected by the screening of atomic fields. For these angles the Rutherford formula and, hence, the Born approximation intensities are nearly exact. At smaller angles the effects of screening are partially accounted for by the structure factor implicit in (1). We shall assume for simplicity that the Born approximation (1) represents the absolute value of the scattering amplitude at all angles. The characteristic features of the simpler diffraction patterns are in any case quite insensitive to the over-all atomic scattering intensities.

The difference between screened and unscreened Coulomb fields becomes particularly important for the phase of the scattering amplitude. For the unscreened field the phase of the exact solution[4] contains principally the coordinate-dependent term $-\alpha \log\{kr(1-\cos\theta)\}$, which increases indefinitely with r, the distance from the scatterer. This is, of course, a property peculiar to the slow decrease of the Coulomb potential and is absent for screened fields. A simple estimate of the phase in the screened case may be obtained by substituting the Born approximation amplitude $f_B(\mathbf{k}', \mathbf{k})$ on the right side of (10) and equating both sides to order α^2. We obtain

$$\eta(\mathbf{k}', \mathbf{k}) = \frac{k}{4\pi f_B(\mathbf{k}', \mathbf{k})}\int f_B(\mathbf{k}', \mathbf{k}'') f_B(\mathbf{k}'', \mathbf{k}) d\Omega_{\mathbf{k}''}, \tag{11}$$

an expression which is equivalent to the second Born approximation.

To evaluate the phase, we chose as an analytically convenient model of the screened field the exponential form

$$V(r) = -Ze^2 e^{-r/a}/r, \tag{12}$$

for which the Born approximation amplitude is

$$f_B(\mathbf{k}', \mathbf{k}) = -2\alpha k a^2/(|\mathbf{k}' - \mathbf{k}|^2 a^2 + 1). \tag{13}$$

The angular integration of (11) is not difficult to perform, and the resulting phase, as a function of the scattering angle θ, is

$$\eta(\theta) = -2\alpha\left(1 + \frac{1}{4k^2a^2\sin^2(\theta/2)}\right) A \tanh^{-1} A, \tag{14}$$

with

$$A = \frac{\sin(\theta/2)}{[(1+(1/2k^2a^2))^2 - \cos^2\theta/2]^{\frac{1}{2}}}. \tag{15}$$

Since $2k^2a^2 \gg 1$ these expressions may be reduced to

$$\eta(\theta) = -2\alpha \frac{1+s^2a^2}{sa(4+s^2a^2)^{\frac{1}{2}}} \tanh^{-1} \frac{sa}{(4+s^2a^2)^{\frac{1}{2}}}, \quad (16)$$

in which we have once again used the notation

$$s = |\mathbf{k}' - \mathbf{k}| = 2k \sin(\vartheta/2).$$

A graph of $|\eta(\theta)/\alpha|$ according to Eq. (16) is given in Fig. 1. For the forward direction, the value $\eta(0) = -\alpha/2$ is quite insensitive to the screening radius. For large angles the phase is asymptotically

$$\eta(\theta) \sim -2\alpha \log(2ka \sin\theta/2), \quad (17)$$

the value of which may in practice be appreciable, even for the lighter elements.

The validity of the expression (16) for the phase, at least for large angles, is somewhat stronger than its derivation by the present perturbation procedure might imply. This may be seen by exploiting the similarity of the large angle scattering by screened and unscreened Coulomb fields.[6] In particular the dependence of the asymptotic phase (17) on θ is the same (apart from an additive constant) as that of the exact Coulomb phase, a fact which implies correctly that for angles $\theta \gg 1/ka$ the scattering amplitudes for the screened and unscreened fields differ only by a phase factor, independent of angle.[7]

In undertaking comparisons with experimental results we shall assume that the estimate of the phase given by (16) is sufficiently accurate to be used directly[8] in the formalism of Sec. I. The accuracy of this method is difficult to estimate without performing numerically more involved calculations. We may mention, however, that the preliminary results obtained using a more accurate method (based on the smallness of α/ka rather than α) are favorable. They indicate that the accuracy of (16) for $\alpha \sim 1$ is roughly commensurate with that of the screening model (12).

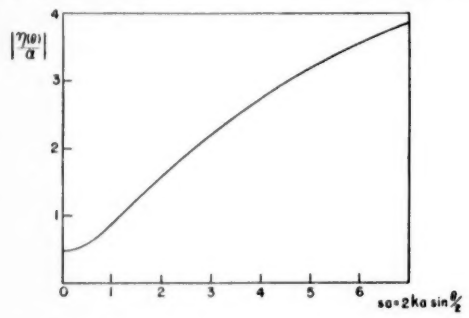

FIG. 1. Graph of the dependence of the phase on scattering angle: $|\eta(\theta)/\alpha|$ *vs* $2ka \sin(\theta/2)$, as given by Eq. (16).

III. COMPARISON WITH EXPERIMENT

While the phase shift we have discussed will modulate the intensities of the diffraction patterns of all heteratomic molecules, its effect is most strongly felt when large differences in the nuclear charges prevail. In such cases the attempt to account in the conventional way for the observed modulation has led, as we have already noted in Sec. I, to the assumption of curiously unsymmetrical molecular structures. For a proper interpretation in the light of the present work, the diffraction data for each of the molecules in question will eventually require detailed re-analysis. A simple way, however, of checking the corrected theory is to show the way in which the treatment based on symmetrical models with phase shifts is able to duplicate the numerical results previously arrived at for the apparent asymmetries. To do this we note by comparing (2) and (3) the approximate relation

$$2\delta = \pi/s_{\text{crit.}}, \quad (18)$$

in which s_{crit} is the value of $2k \sin(\theta/2)$ for which the phase difference is $\pi/2$. An approximate value of the screening distance, adequate for the calculation is $a = 0.528Z^{-\frac{1}{3}}$A. The predicted apparent "splits" (2δ) that result are listed in Table I along with the corresponding experimental values. Their agreement, it may be seen, is quite close. It follows that for these molecules the diffraction patterns predicted by the present formulation will be in good agreement with those observed. The intensity curve calculated for UF_6 at 40 kev seems to show even better agreement than the previous work for the central and outer parts of the pattern.[5] This is a consequence of the deviation of the phases from proportionality to s.

A large number of electron diffraction studies of molecules containing heavy atoms are on record in which nothing anomalous was observed, a circumstance which no doubt helped delay the recognition of the phase shifts. It is important, therefore, to remark that in all the adequately reported cases, the pattern was observed only at angles at which the phase difference is less than the critical value $\pi/2$.

The phase given by Eq. (16) is increased by lowering the electron energy, and its modulation of the diffraction pattern varies more rapidly with s. The resulting energy dependence of the pattern is a feature absent from any treatment based on the first Born approximation. Some photographs of UF_6, taken at 10 kev do indeed show changes in the direction predicted,[5] and will be analyzed

[6] It may also be seen from the work of R. Dalitz [Proc. Roy. Soc. (London) **A206**, 509 (1951)], who has derived the asymptotic form (17) and shown that its occurrence as a phase is consistent with the third Born approximation as well as the second.

[7] This behavior is implicitly made use of in computing the Coulomb scattering of identical particles when one of them is screened (e.g., p-p scattering). The constant phase factor by which the Coulomb and correctly screened solutions differ is not observed. For other potentials the interference effect involved in the scattering of similar particles will also require a knowledge of the angle-dependent part of the phase, omitted in the first Born approximation.

[8] Our procedure here actually goes beyond the second Born approximation, which, strictly speaking, would only consider the terms of (2) to order α^3, and would thereby eliminate the contribution of the phase entirely.

in forthcoming work. It should be noted, however, that the simple approximation we have here used for the phase becomes less reliable as the parameter $Ze^2/\hbar v$ is increased and requires improvement for the heavier elements at energies less than 40 kev. The computations for this are in progress.

In crystal diffraction an effect may be observable even for lighter atoms, for which the phase shift is small. This will happen, for example, if the contributions to the scattered amplitude by two classes of atoms are nearly equal in magnitude and opposite in phase, so that a small phase shift can give rise to a large relative change in the intensity. We have examined the published intensity anomalies of fluorite,[9] cuprous chloride[9] and zinc oxide.[10] The first two appear well explained in this way; zinc oxide is not. In conclusion we may note that it would be most interesting to observe the modulation of the diffraction pattern for a diatomic molecule. Little room would be left for belief in a structural anomaly.

APPENDIX

Note on Proton Diffraction

It may be of interest to consider the rather different situation which arises in the diffraction of proton beams. The energies of protons with wavelengths suitable for diffraction work are lower ($\sim$0.5 to 15 kev) than the corresponding electron energies. Their velocities, of course, are smaller still, and we must consequently deal with quite large values of the parameter $\alpha=Ze^2/\hbar v$. For 2-kev protons, for example, and $Z=30$ we have $\alpha\sim100$. It is clear that the approximation used in treating electron scattering will hardly avail us here. Since the proton wavelengths are furthermore substantially smaller than atomic dimensions ($ka\sim160$ in the above example), the scattering may instead be treated by a simple semiclassical procedure. We assume, in the spirit of the familiar optical analogy, that the phase of the wave function at any point is $1/\hbar$ times the classical action integral $\int\mathbf{p}\cdot d\mathbf{r}$ taken along the dynamical path leading to the point. Since the required integration unfortunately cannot be performed analytically for the exponentially screened field (12), we employ instead the somewhat simpler model in which all of the shielding charge is assumed localized on a sphere of radius a:

$$V(r)=Ze^2\left(\frac{1}{r}-\frac{1}{a}\right), \quad r<a,$$
$$=0, \quad r>a. \tag{A.1}$$

The integration along the trajectories then yields

$$\eta(\theta)=-\frac{2\alpha}{\sqrt{\gamma}}\log\left\{\frac{\sqrt{\gamma}}{2\alpha}\left[sa+(s^2a^2+4\alpha^2\gamma^{-1})^{\frac{1}{2}}\right]\right\}, \tag{A.2}$$

in which

$$\gamma=1+(2\alpha/ka), \quad \alpha>0,$$
$$s=2k\sin(\theta/2).$$

The phase (A.2) vanishes for forward scattering, as it must in a semiclassical treatment, since such particles are completely uninfluenced by the potential. Near the forward direction then ($sa\ll2\alpha\gamma^{-\frac{1}{2}}$) the phase assumes the simple form

$$\eta(\theta)=-2ka\sin(\theta/2). \tag{A.3}$$

Since this is independent of nuclear charge it will not affect the diffraction pattern [see Eq. (2)]. For larger scattering angles, however, the effect of the phase will once again be felt. The scattering in the region between the two extremes of α small and large will be treated in a forthcoming paper.

TABLE I. Comparison of apparent distance splittings observed with those predicted.

Molecule	Distance	Apparent split (A) Observed	Calculated[a]
UF_6	U−F	0.30[b,c]	0.28
OsO_4	Os−O	0.23[d]	0.24
$W(CO)_6$	W−C	0.24[d]	0.24
	W···O	0.23	0.23
WF_6	W−F	0.23[e]	0.22
WCl_6	W−Cl	~0.18[e]	0.18
IF_5	I−F	0.18[f]	0.15
$Mo(CO)_6$	Mo−C	0.13[d,g]	0.13
	Mo···O	0.13	0.12
MoF_6	Mo−F	0.14[e]	0.12

[a] For 40-kev electrons, employing the relativistic value of α.
[b] S. H. Bauer, reference 2.
[c] O. Bastiansen, unpublished work in these laboratories.
[d] W. F. Sheehan, Jr., thesis, California Institute of Technology, unpublished (1952).
[e] From re-examination of photographs described by R. A. Spurr, thesis, California Institute of Technology, unpublished (1942).
[f] Results of M. T. Rogers, thesis, California Institute of Technology (1941), adjusted to a symmetrical (2½ : 2½) split. The actual I–F distances may well not all be equal.
[g] Mo−C and Mo···O splits assumed equal.

[9] L. H. Germer, Phys. Rev. **56**, 58 (1939).
[10] H. J. Yearian, Phys. Rev. **48**, 631 (1935).

Experimental Energy and Angular Distributions of Inner Bremsstrahlung

T. B. Novey
Chemistry Division, Argonne National Laboratory, Lemont, Illinois
(Received September 29, 1952)

The spectra of the continuous radiation or inner bremsstrahlung emitted in the beta-decay of P^{32} and RaE have been measured in the region of 20–250 kev with a NaI scintillation spectrometer. Comparison of the spectra on an absolute basis with the prediction of the theory shows good agreement.

The angular correlation of the radiation with the emitting beta-particles was also measured. The results are in excellent agreement with theoretical predictions.

I. INTRODUCTION

THE continuous radiation known as inner bremsstrahlung emitted in the process of beta-decay has been studied experimentally over a period of twenty-five years. A series of measurements has been made using ionization chambers or G-M tube detectors where little or no energy resolution was possible. The most recent of these were by Wu[1] and by Stahel and Guillessen[2] in which the average radiation energy per emitted beta-particle in the decay of P^{32} and RaE was determined with integrating ionization chambers. The integral radiation intensity was found to agree with theory.

The theory of the process was developed independently by Knipp and Uhlenbeck[3] and by Bloch[4] for allowed beta-transitions assuming the polar vector interaction and recently was extended by Wang Chang and Falkoff[5] and Madansky *et al.*[6] for forbidden transitions and other interaction types. The cross section for radiative transition per beta-particle was shown to be insensitive to the degree of forbiddenness or type of interaction responsible for the birth of the beta-particle, so no information is needed concerning nuclear wave functions in order to calculate the radiation intensity and angular correlation to a good approximation.

The development in recent years of scintillation detectors and in particular of thallium-activated sodium iodide scintillators has made it possible to make measurements with good energy discrimination and high efficiency on this type of a low probability process involving the emission of low energy gamma-radiation. Measurements of this type have been undertaken independently by Madansky and Rasetti[7] and the author. Preliminary reports have been published on the measurements reported in this paper.[8]

In this work the inner bremsstrahlung spectra of P^{32} and RaE have been measured experimentally and compared on an absolute basis with the theory in the range of 20 to 250 kev. The angular correlation between the beta-particles and the radiations has also been measured in the angular range of 30° to 180°, and the shapes have been compared with those predicted theoretically. In both cases agreement with theory is obtained.

[1] C. S. Wu, Phys. Rev. **59**, 481 (1941); references to earlier papers are given here.
[2] E. Stahel and J. Guillessen, J. phys. et radium **1**, 12 (1940).
[3] J. K. Knipp and G. E. Uhlenbeck, Physica **3**, 425 (1936).
[4] F. Bloch, Phys. Rev. **50**, 272 (1936).
[5] C. S. Wang Chang and D. L. Falkoff, Phys. Rev. **76**, 365 (1949).
[6] Madansky, Lipps, Bolgiano, and Berlin, Phys. Rev. **84**, 596 (1951).
[7] L. Madansky and F. Rasetti, Phys. Rev. **83**, 187 (1951).
[8] T. B. Novey, Phys. Rev. **84**, 145 (1951); **86**, 619 (1952).

II. ENERGY SPECTRA

A. Apparatus

The apparatus used is shown schematically in Fig. 1. The source is evaporated from aqueous solution over an area of 0.3 cm^2 on a thin plastic film (50 $\mu g/cm^2$) which is located at a distance of 20 cm from a NaI(Tl) scintillator $1\frac{1}{4}$ in. in diameter and $\frac{1}{2}$ in. thick. A lead collimator is located halfway between the source and detector. Over the collimator is placed a 1.03 g/cm^2 beryllium absorber, which is thick enough to absorb completely the beta-radiations coming from the source. A rough estimate of the outer bremsstrahlung produced in the beryllium can be obtained by extrapolation of the measurements of Wu,[1] who found experimentally that the ratio of outer bremsstrahlung to inner bremsstrahlung produced when P^{32} radiations are absorbed in aluminum is about four to one, in agreement with theory.

Wu also showed that the total intensity of outer bremsstrahlung produced when electrons are completely absorbed is approximately proportional to the first power of the atomic number of the absorber and not to the square as is the case for single nuclear scattering. This decreased dependency on Z is due to the fact that the number of nuclei encountered by an electron in its range depends inversely upon the atomic number of the absorber.

For the case of absorption in beryllium the amount of outer bremsstrahlung produced is then about 4/13 of that produced in aluminum, and so the ratio of outer to inner bremsstrahlung is close to unity.

As the paths of the electrons in the beryllium are winding, the resultant outer bremsstrahlung distribution would be expected to be nearly isotropic.

The amount of inner bremsstrahlung passing through the collimator hole and into the detector is equal to the amount of outer bremsstrahlung produced in the

beryllium over the collimator hole. The latter, however, is emitted isotropically, and so only a small portion is detected as given by the geometrical efficiency of the detector for a source at the position of the collimator. This efficiency is 0.6 percent for ten centimeter spacing between collimator and detector, and so the percentage of outer to inner bremsstrahlung reaching the detector is about 0.6 percent.

All other parts of the apparatus are located at a distance of at least 20 cm from the source so that very little of the outer bremsstrahlung which is produced in the eventual absorption of the source radiations can be detected. The space between the collimator and the detector, and the detector itself is completely shielded by two inches of lead in order to prevent detection of scattered photons.

The sodium iodide detector is assembled in a moisture-proof container with a 0.013-inch thick aluminum window and is optically coupled through a short Lucite light pipe to a 5819 photomultiplier tube. The pulses are fed from a cathode follower preamplifier into a linear amplifier and sliding single-channel pulse-height analyzer designed by R. Swank of this laboratory. The spectrometer was calibrated with photon lines of known energies 22, 84, and 667 kev from Cd^{109}, Tm^{170}, and Cs^{137}. The energy resolution widths at half-height were 57 percent, 30 percent, and 11 percent, respectively.

The channel width on the analyzer was selected in the light of the above energy resolutions to be at least a factor of four smaller than the line resolution at any given energy.

B. Source Preparation

The P^{32} sources were prepared by evaporating high specific activity P^{32} solution newly obtained from Oak Ridge National Laboratory. One-millicurie sources were used. The sources were evaporated on 50 $\mu g/cm^2$ LC-600 films. The active solution was spread over an area of 0.3 cm^2 with the help of dilute insulin solution. The source weight was less than 25 μg. The films were supported on aluminum rings of outer diameter 2 in., inner diameter $1\frac{1}{2}$ in., and thickness 0.015 in.

The RaE was extracted from a RaDEF mixture on a semimicro scale using a separation based upon the precipitation of RaE (bismuth) with iron hydroxide in dilute sodium hydroxide solution, the RaD (lead) with added lead holdback carrier remaining in solution. The RaD is thoroughly removed by a few reprecipitations as indicated by the elimination of the 47-kev gamma-peak in the spectrum. The iron is ether-extracted, and the RaF plated out onto silver powder in 0.5N HCl until less than 1 percent remains. The RaE was carried on a few micrograms of aluminum hydroxide which was carefully washed, slurried up, transferred to the film, and evaporated to dryness.

Great care was taken to remove all of the lead in the final RaE separations. In the preparation of the source for the measurements described in the preliminary

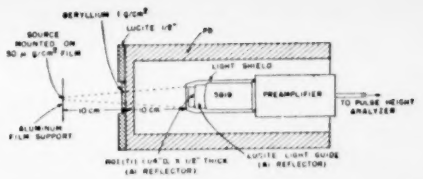

FIG. 1. Arrangement of apparatus for measurement of inner bremsstrahlung spectra.

communication[8] about twenty micrograms of lead were left in the source. This was sufficient to result in the production of twice as much outer bremsstrahlung as inner in the source and caused the high results reported.

The absence of outer bremsstrahlung production in the final sources was demonstrated by measuring the gamma-spectrum and then spreading the source over a twofold larger area, Fig. 8. As the intensity did not change appreciably, source thickness effects were not affecting the results.

C. Corrections to the Spectra

1. Background

Background was determined at the various energies by placing a 7.5 g/cm^2 lead absorber over the collimator hole.

2. Resolution

Correction for the finite energy resolution of the scintillation spectrometer was made using the expression given by Palmer and Laslett.[9] The corrected spectrum N_T is given by

$$N_T(E)=N_e(E)-KN_e'(E)-\tfrac{1}{2}KEN_e''(E), \qquad (1)$$

where

$$K=W^2(E)/(0.693\cdot 2E).$$

$W(E)$ is the half-width at half-height of a peak produced by photons of energy E. N_e, N_e', N_e'' are the experimental spectrum and its first and second derivatives, respectively.

3. Absorption

Corrections for absorption of the radiation in 1.03 g/cm^2 of beryllium (beta-absorber) and 90 mg/cm^2 of aluminum (NaI container cover) were made using absorption coefficients given by Compton and Allison.[10] A plot of the correction factors A_{Be} and A_{Al} is shown in Fig. 2. The absorption coefficient for the beryllium absorber was checked at 22 and 84 kev using monochromatic gamma-sources in order to make sure the beryllium did not contain any appreciable heavy element impurities. Agreement was obtained to a few percent.

[9] J. P. Palmer and L. J. Laslett, Atomic Energy Commission Report AECU-1220 (March 14, 1951), unpublished.

[10] A. H. Compton and S. K. Allison, *X-Rays in Theory and Experiment* (D. Van Nostrand Company, Inc., New York, 1935), Appendix IX.

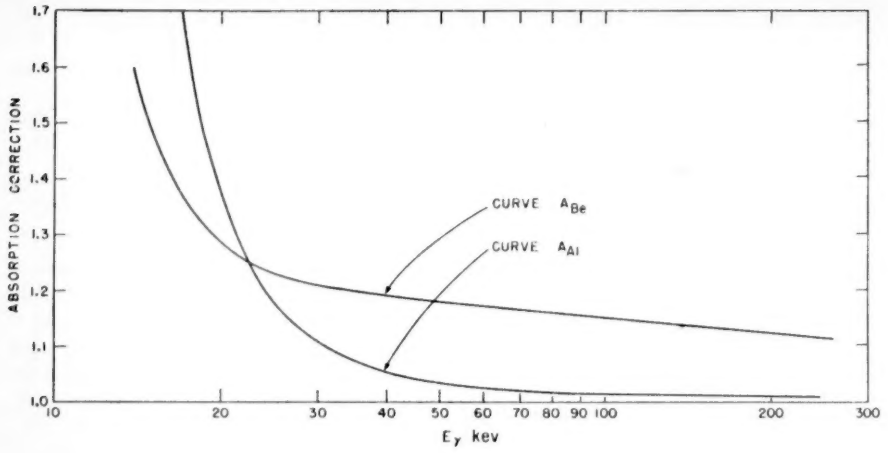

FIG. 2. Absorption factors for photons in 1.03 g/cm² Be (curve A_{Be}) and 0.090 mg/cm² Al (curve A_{Al}).

Absorption in the 20-cm air path was negligible in the energy range investigated.

4. *Gamma-Detection Efficiency*

In determining the spectral shape, it is important that all of the photons detected give their full energy to the scintillator as the presence of Compton continua will smear out the curve. For the ½-inch thick crystal used the former condition holds very well up to 250 kev although at this energy the Compton and photoelectric cross sections are equal. This is due to secondary reaction of the Compton scattered photons which result in the full energy being dissipated in the crystal. This effect is shown in Fig. 3. Curve *B* shows the fraction of the pulses falling in the photoelectric peak compared to the sum of the areas in the photoelectric peak and the Compton continuum as a function of the incident photon energy based on a series of unpublished measurements by D. Engelkemeir of this laboratory. Curve *A* shows the fraction of the total cross section that is derived from photoelectric absorption. The efficiency ϵ_γ calculated from the total cross section in NaI is shown in Fig. 4.

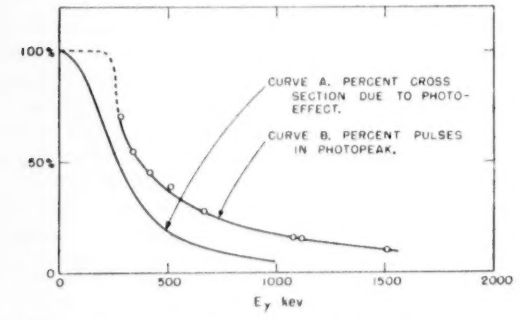

FIG. 3. Comparison of percentage of photoelectric to total absorption cross section (curve *A*) with percentage of scintillation pulses falling in the photoelectric peak (curve *B*) for photon absorption in a ½-inch thick NaI(Tl) crystal.

Thus although the gamma-efficiency is diminishing and the Compton cross section becomes comparable to the photoelectric cross section, in the region up to 250 kev the spectrum measured is almost entirely due to pulses arising from complete absorption of the photons. As the intensity of photons drops off very rapidly with energy, the contribution of the Compton continua from higher energy photons can be neglected in these measurements.

The accuracy of this calculated efficiency decreases in the region of 200–250 kev owing to the onset of edge effects.

5. *Iodine K X-Ray Escape*

The escape of iodine *K* x-rays from the detector following photoelectric absorption near the surface becomes important in the region just above the *K* edge of iodine at 34 kev and results in the shifting of photon pulses down in energy by the *K* x-ray energy 29 kev.

The magnitude of the escape was calculated on an infinite plane approximation which is satisfactory in the present case of a surface $1\frac{1}{4}$ in. in diameter. The edge effects are small owing to the high absorption coefficient of the iodine *K* x-rays in sodium iodide ($T_{\frac{1}{2}}=0.01$ in.). The photons are assumed to be normally incident, and the x-rays are emitted isotropically. The probability that a photon will undergo a photoelectric effect and the x-ray escape is then

$$P_e=\frac{\mu_\gamma}{2}\int_0^\infty\int_0^{\pi/2}\exp\{-[\mu_\gamma+(\mu_x/\cos\theta)]x\}\sin\theta d\theta dx, \quad (2)$$

where μ_γ is the incident photon absorption coefficient, μ_x is the iodine *K* x-ray absorption coefficient, x is the depth of penetration into the surface, and θ is the angle between the directions of the normal to the surface and the emitted x-ray. Upon integration this becomes

$$P_e=0.5\left[1-\frac{\mu_x}{\mu_\gamma}\ln\left(1+\frac{\mu_\gamma}{\mu_x}\right)\right]. \quad (3)$$

A graph of P_e is shown in Fig. 5 for the escape of iodine K x-rays (28.7 kev). The net correction p to the continuous spectra, taking into account the fact that loss of the x-ray shifts the pulses to lower apparent energy, is shown in Fig. 6.

This net correction was made assuming from the theory (Sec. E) that the probability spectrum varies approximately inversely with energy so that the number of photons per unit energy interval at energy $E_\gamma - 28.7$ kev is equal to $E_\gamma - 28.7/E_\gamma$ of the number at energy E_γ. If the loss of pulses at energy E_γ due to K x-ray escape is p_1 and that at $E_\gamma - 28.7$ kev is p_2, then the net fractional loss p at $E_\gamma - 28.7$ kev is $p_2 - p_1(E_\gamma - 28.7/E_\gamma)$. The net correction changes sign abruptly at the K edge because at this point p_2 suddenly becomes zero. A smoothed-out correction was used because the resolution correction could not completely reconstruct the sharp K edge effect.

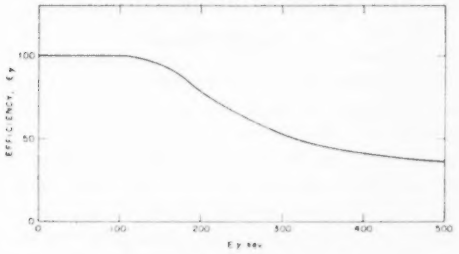

FIG. 4. Gamma-efficiency of $\frac{1}{2}$ inch thick NaI crystal calculated from total absorption cross section for normally incident photons.

6. *Geometrical Efficiency*

The geometry factor was calculated using the formula

$$G = a^2/4r^2 = 0.16 \text{ percent}, \tag{3}$$

where a, the crystal radius, is 1.6 cm and r, the distance to the edge of the crystal face, is 20 cm.

7. *Source Calibration*

The source disintegration rates R were determined by reference to lower activity sources which were calibrated using a 4π proportional counter and standard RaDEF[11] sources. The ratios of activities of the high and low activity sources were determined by counting on an end window flow type proportional counter through an absorber selected to bring the activities into the counting rate range of the counter.

8. *Normalization*

The spectra were normalized to unit mc^2 energy interval by dividing the data by the analyzer window width Δk in units of mc^2, converted to energy intensity by multiplication by the energy k in units of mc^2, and normalized to radiation per beta-decay.

[11] T. B. Novey, Rev. Sci. Instr. **21**, 280 (1950).

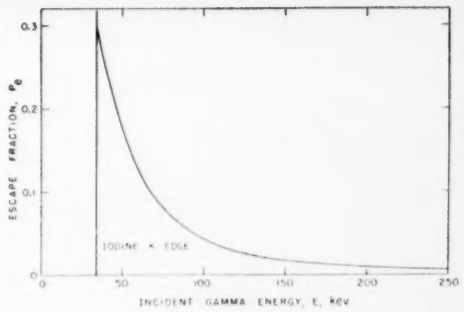

FIG. 5. Calculated fraction of iodine K x-rays escaping from a NaI crystal for normally incident photons.

D. Results

The final result of these corrections is the intensity spectrum $kS(k)$, the radiation intensity per unit energy interval per beta-decay,

$$kS(k) = A_{\mathrm{Be}} A_{\mathrm{Al}} k N_T / [\epsilon_\gamma (1-p) G R \Delta k]. \tag{4}$$

The results of two experiments on P^{32} are shown in Fig. 7. Run 2 was made with the apparatus as described in part **A** of this section. Run 1 was an earlier run made with somewhat less favorable geometrical conditions. The source to detector distance was 15 cm, the absorber was Lucite instead of beryllium, and the collimator opening was $1\frac{1}{4}$ in. in diameter. The estimated outer bremsstrahlung contribution was 5 percent as compared to 0.6 percent for Run 2.

Figure 8 shows the results for RaE for the source as originally prepared and the source spread over a twofold larger area. In the latter case it was necessary to use the larger $1\frac{1}{4}$ inch collimator.

E. Comparison with Theory

It has been shown by Wang Chang and Falkoff[5] that, in the low energy photon region in which most of the

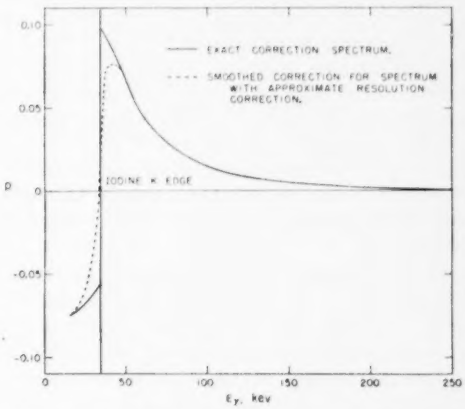

FIG. 6. Net correction to the spectrum resulting from escape of K x-rays.

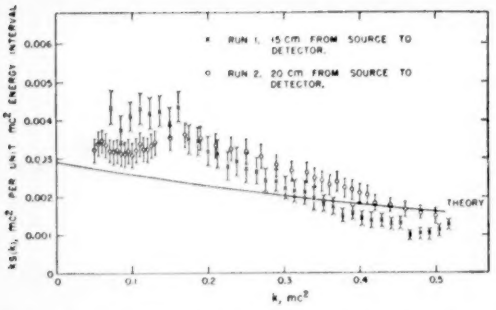

FIG. 7. P^{32} inner bremsstrahlung spectrum, $kS(k)$, mc^2 per unit mc^2 energy interval *vs* k in units of mc^2.

radiation occurs and in which these studies were made, the intensity per beta-particle is insensitive to the degree of forbiddenness or the nature of the interaction involved in the beta-decay process and that, to an accuracy well within limits set by these measurements, the emission probability $S(k)$ can be factored as follows:

$$S(k)=\int_{1+k}^{W_0} P(W_e)\Phi(W_e,k)dW_e, \tag{5}$$

where $P(W_e)$ is the normalized beta-spectrum for which the experimental spectrum may be used and

$$\Phi(W_e,k)=\frac{\alpha p_e}{\pi p_e k}\left\{\frac{(W_e^2+W_e^2)}{W_e p_e}\ln(W_e+p_e)-2\right\}, \tag{6}$$

where W_e is the "created" electron energy; p_e is the "created" electron momentum, $(W_e^2-1)^{\frac{1}{2}}$; W_e is the observed electron energy, (W_e-k); p_e is the observed electron momentum, $[(W_e-k)^2-1]^{\frac{1}{2}}$; α is the fine structure constant, 1/137; and k is the photon energy. All energies are in units of mc^2, and all momenta in units of mc.

This factoring implies that the beta-decay and radiation can be considered to be independent processes.

Equation (5) was integrated numerically using normalized energy spectra obtained from P^{32} and RaE spectra given respectively by Siegbahn[12] and Neary.[13] The results multiplied by the photon energy k in order to remove the low energy divergence are shown as the solid lines in Figs. 7 and 8.

These theories neglect the effect of nuclear charge on the radiation, but it has been shown by Hellund (unpublished calculations) that these effects are unimportant.

Both the P^{32} and RaE spectra show a peaking in the region of 80 kev. One would expect an amount of K x-rays from RaE due to electronic excitation during beta-decay of the order of $0.6/Z^2$ or 10^{-4} K x-ray per beta-decay.[14] This is in rough agreement with the number of photons corresponding to the area in the peak in the RaE curve. In addition to this, some K x-rays arising from photoelectric absorption of outer or inner bremsstrahlung in the faces of the conical slit would contribute to both curves.

The higher intensity shown in P^{32}, Run 1, at low energies is probably due to the larger amount of outer bremsstrahlung present in this case. The effect would tend to concentrate at low energies because the multiple scattering process involved in beta-absorption would lower the average energy of the radiating electrons and thus lower the average energy of the bremsstrahlung.

In view of the above considerations and the difficulties involved in the accurate application of the many correction factors described in Sec. II C, these measurements are considered to be in good agreement with the predictions of the theory.

III. BETA-INNER BREMSSTRAHLUNG ANGULAR CORRELATION

A. Experimental

The apparatus is shown schematically in Fig. 9. A plastic vacuum chamber is used to reduce electron scattering and outer bremsstrahlung production. The chamber body is made of $\frac{1}{8}$-inch Bakelite-impregnated fiber tubing and the top and bottom of $\frac{1}{2}$-inch Bakelite using O rings for vacuum seals. The sources are mounted on thin films supported on an aluminum ring in turn supported by a Lucite mount centered in the chamber.

The electron detector is a stilbene crystal cemented into a Lucite light guide which is in turn cemented onto the face of a 5819 photomultiplier tube with Gelva V-1.5 cement. A unit of this type can be assembled in an oven at 75°C after careful warming of the crystal wrapped in several layers of cleansing tissue. The Gelva cement should previously have been melted in a vacuum and dissolved gases pumped out.

The face of the crystal is coated with a very thin layer of silicone stopcock grease and 0.2 mg/cm² aluminum foil adhered to the surface to serve as a light reflector and to reduce the rate of sublimation in the vacuum.

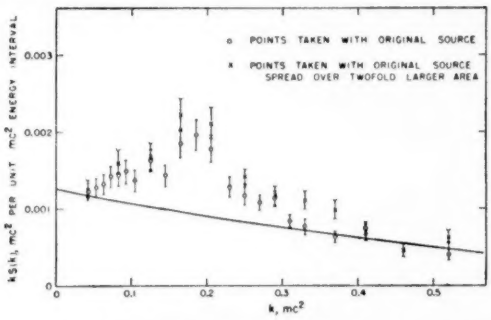
o POINTS TAKEN WITH ORIGINAL SOURCE
x POINTS TAKEN WITH ORIGINAL SOURCE SPREAD OVER TWOFOLD LARGER AREA
kS(k), mc² PER UNIT mc² ENERGY INTERVAL
k, mc²

FIG. 8. RaE inner bremsstrahlung energy intensity spectrum, $kS(k)$, mc^2 per unit mc^2 energy interval *vs* k in units of mc^2.

[12] K. Siegbahn, Phys. Rev. **70**, 133 (1946).
[13] G. J. Neary, Proc. Roy. Soc. (London) **A175**, 71 (1940).
[14] A. Migdal, J. Phys. (U.S.S.R.) **IV**, 449 (1941).

The vacuum seal is made by means of an *O* ring seal to the tube face.

The chamber and detector are fastened to a table which can be automatically rotated in 15° steps at predetermined time intervals. The timing clock also trips a single-frame movie camera which records the necessary counting data from the scaling circuit registers.

The gamma-detector is a NaI(Tl) scintillator as described in Sec. II. The pulses are double delay line shaped[15] to reduce the pulse width below 0.1 μsec. A diagram of the coincidence system is shown in Fig. 10. The pulses are fed through distributed line amplifiers with a gain of 100 on each side, delay line shaped, and fed through cascades to a 12AT7 coincidence mixer and to trigger pairs delivering 0.3-μsec pulses. The output of the mixer drives a trigger pair delivering a 0.5-μsec pulse. The trigger-pair pulses are fed into a simple crystal diode triple coincidence circuit to insure that only pulses which have been recorded as singles counts can record as a coincidence.

The coincidence circuit was designed and built by B. Norris of this laboratory and was designed to be used in conjunction with the 200-ohm distributed line amplifiers which are available commercially. The coincidence circuit has built into it pulse shaping delay lines which allow pulses to be shaped at 0.015, 0.03, 0.075, and 0.15 microsecond width. The minimum resolving time of the coincidence circuit is thus 0.03 microsecond. For this experiment the stilbene pulses were shaped at 0.015 μsec. In conjunction with the double delay line pulse shaping of the sodium iodide pulses at 0.075 μsec, the measured resolving time was about 0.11 microsecond. Owing to the fact that the pulse size of the photon pulses is reduced by a factor of about 7 by the pulse shaping networks, for low energy photons the pulse sizes begin to fall into the tube noise region. Consequently, in order to obtain a high detection efficiency, i.e., close to 100 percent for photons of energies down to 40 kev, it is necessary to operate at a photomultiplier voltage such that the noise background is of the order of a few thousand counts per minute. The beta-particles are detected down to energies of about 50 kev. Thus the coincidences detected are

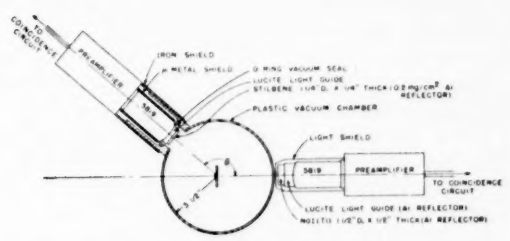

FIG. 9. Beta-gamma angular correlation apparatus.

[15] T. B. Novey and D. W. Engelkemeir, Rev. Sci. Instr. **22**, 841 (1951).

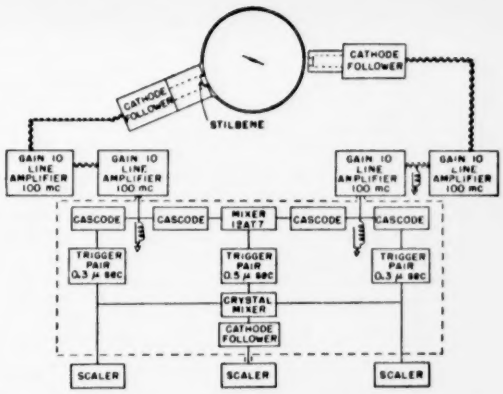

FIG. 10. Block diagram of electronic circuitry for beta-inner bremsstrahlung angular correlation measurements.

between β-particles of energies down to 50 kev and photons with energies down to about 40 kev.

The experimental angular correlation measurements were made at angles from 180° to 45° on both sides. In the case of P^{32} a point at 33° was obtained by crowding the detectors as close as possible. The correlation curves thus obtained were averaged and corrected for the finite angular resolution (20° full detector angle, about 1 percent geometrical efficiency).

The chance contributions to the coincidence rates were measured carefully as they were often equal to or greater than the true rates. The measurement was made using duplicate sources located and shielded so that while the singles rates and the pulse-height distributions were the same as with the single source, no true coincidences could occur.

As will be shown in the next section, no inner bremsstrahlung radiation is emitted in the directions colinear with the electron path, i.e., at 0° and 180°. Thus, the chance rate should equal the total coincidence rate at 180°. This agreement was never obtained probably owing to some contribution from scattering in the apparatus.

The rates at 180° varied from 10 to 15 percent above the measured chance rates, and the excesses amounted to 10 to 15 percent of the true rates at 35°. When the source and detectors were suspended in air with as much material as possible removed from around them to a distance of one or two feet, these percentages decreased to 5 percent.

It was not known whether this "scattering" correction was constant with angle between the detectors, but as it was small compared to the true coincidence rate at low angles, it was added to the chance rate and subtracted as a constant from the total coincidence rate. The correlation curves could not be compared to the theory on an absolute basis as the efficiency of the coincidence circuit is not well known but were normalized to agree at 45°.

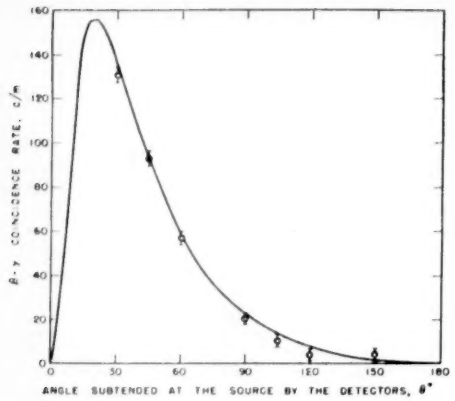

FIG. 11. Beta-inner bremsstrahlung angular correlation in P^{32}. Comparison of experiment (circles) with theory (solid line) normalized at 45°, Φ.

The data are given by the points in Figs. 11 and 12.

B. Comparison with Theory

The approximations valid for $k \ll W_{e\,\max}$ which were used in Sec. II **E** in obtaining the inner bremsstrahlung spectra also hold for the experimental conditions of the angular correlation measurements, and as shown by Wang Chang and Falkoff[5] and Madansky *et al.*,[6] the correlations for low energy photons are insensitive to the degree of forbiddenness or type of interaction involved in the beta-decay. To be sure, if the correlation of higher energy photons were measured, as pointed out by the latter authors, there would be a considerable effect. As the number of these photons is very low, the measurement is difficult, though not impossible with high efficiency liquid scintillators and very fast ($2\tau \sim 10^{-9}$ sec) coincidence circuits.

The probability $d\Phi$ that a beta-particle emitted with energy W_e will radiate a photon of energy k per unit photon energy interval at an angle θ between **k** and $\mathbf{p}_e$ is given by

$$d\Phi(W_e, k, \theta) = \frac{\alpha p_e}{4\pi^2 p_e k}\left[\frac{W_e^2+W_e^2}{W_e(W_e - p_e\cos\theta)} - \frac{1}{(W_e - p_e\cos\theta)^2} - 1\right] d\Omega_k. \quad (7)$$

As shown by Wang Chang and Falkoff[5] on the assumption that k is small and thus that $W_e = W_e$, $P_e = P_e$ and as $P/W = \beta$, $W^2 = 1/1-\beta^2$, Eq. (7) becomes

$$d\Phi = \frac{\alpha}{2\pi k}\frac{\beta^2 \sin^3\theta}{(1-\beta\cos\theta)^2} d\theta,$$

or

$$\frac{d\Phi}{d\Omega}(W, k, \theta) = \frac{\alpha}{4\pi^2 k}\frac{\beta^2 \sin^2\theta}{(1-\beta\cos\theta)^2}. \quad (8)$$

They also obtained this result by a purely classical relativistic calculation.

For the case at hand this must be integrated over the beta-spectrum detected and the range of gamma-energies detected; thus,

$$\frac{d\Phi(\theta)}{d\Omega} = \frac{\alpha}{4\pi^2}\int_{W_{\min}}^{W_{\max}}\int_{k_{\min}}^{W}\frac{P(W)\beta^2\sin^2\theta}{k(1-\beta\cos\theta)^2} dk dW, \quad (9)$$

where $k_{\min}$ is the detector energy cutoff at 40 kev. The minimum beta-energy detected is about 50 kev, and as electrons below this energy produce essentially no radiation above 40 kev, the beta lower limit can be

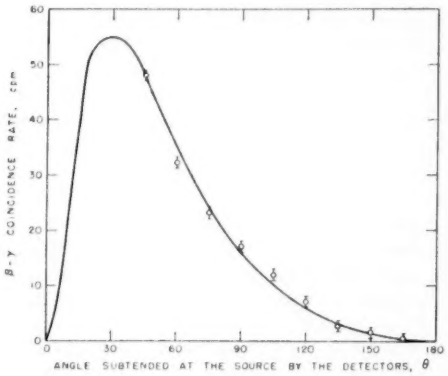

FIG. 12. Beta-inner bremsstrahlung angular correlation in RaE. Comparison of experiment (circles) with theory (solid lines) normalized at 45°.

taken as zero. Integrating over the photon energy Eq. (8) becomes

$$\frac{d\Phi(\theta)}{d\Omega} = \frac{\alpha}{4\pi^2}\int_0^{W_{\max}} \ln(W/k_{\min}) \times P(W)\frac{\beta^2\sin^2\theta}{(1-\beta\cos\theta)^2} dW. \quad (10)$$

This expression was evaluated numerically, and the normalized results are shown as the solid lines in Figs. 10 and 11.

The experimental angular correlation is an excellent agreement with that predicted by the theory.

I wish to express my appreciation to Dr. E. Hellund who gave much time to theoretical investigation of problems arising during this research, and to Dr. D. Engelkemeir for many helpful discussions during the course of the experiments and for permission to include some of his unpublished data in this paper.

The Continuous Gamma-Ray Spectrum Accompanying Beta-Decay*

P. Bolgiano, L. Madansky, and F. Rasetti
The Johns Hopkins University, Baltimore, Maryland

(Received September 19, 1952)

The spectral distribution and absolute intensity of the internal bremsstrahlung emitted in beta-decay was investigated in P^{32}, Y^{91}, and RaE. The gamma-radiation was detected by means of a NaI(Tl) crystal, phototube, linear amplifier and one-channel discriminator. Care was taken to avoid spurious effects, and corrections were made for several factors. Both the spectral distributions and the absolute intensities of the continua are in excellent agreement with theoretical predictions. The differences in the spectra due to allowed or forbidden types of the beta-transition and to different forms of interaction are too small to be detected in these experiments. Observations on the angular correlation of the internal bremsstrahlung of beta-emitters and on the internal bremsstrahlung emitted in K capture are also reported.

I. INTRODUCTION

THE spectral distribution of the continuous gamma-ray spectrum accompanying beta-decay has been reported previously.[1-4] The work reported here represents more complete results and extends the range of investigations to 20 kev. Some results on the angular correlation between the beta-ray and its associated bremsstrahlung are also given.

The theory of the spectral distribution of the internal bremsstrahlung was first given by Knipp and Uhlenbeck,[5] and Bloch.[6] Further calculations on the bremsstrahlung from first and second forbidden beta-transitions were made by Chang and Falkoff[7] for scalar interactions. A calculation of the first forbidden case for tensor interaction with the selection rule ($\Delta J=2$; yes) was made by Madansky *et al.*[8] The expressions for the spectral distribution of the gamma-rays for the allowed and forbidden cases are given below.

The following expressions utilize the notation of Chang and Falkoff,[7] where $x=W_0-k$.

Allowed beta-transition:

$$S(k)=\frac{\alpha G^2|M|^2}{4\pi^4}\frac{1}{k}\left\{\left[W_0^2\left(\frac{2}{3}x^3+x\right)-W_0\left(x^4+x^2-\frac{1}{8}\right)+\frac{7}{15}x^5-\frac{3}{8}x\right]\ln[x+(x^2-1)^{\frac{1}{2}}]-\left[W_0^2\left(\frac{11}{9}x^2+\frac{4}{9}\right)-W_0\left(\frac{7}{4}x^3+\frac{1}{8}x\right)+\frac{689}{900}x^4-\frac{1021}{1800}x^2-\frac{8}{75}\right](x^2-1)^{\frac{1}{2}}\right\}.$$

First forbidden beta-transition; scalar interaction:

$$S(k)=\frac{\alpha G^2|M|^2}{12\pi^4}\frac{1}{k}\left\{\left[W_0^4\left(\frac{2}{3}x^3+x\right)+W_0^3\left(-\frac{7}{3}x^4-3x^2+\frac{1}{8}\right)+W_0^2\left(\frac{18}{5}x^5+5x^3\right)+W_0\left(-\frac{13}{5}x^6-\frac{14}{3}x^4-\frac{15}{8}x^2-\frac{5}{24}\right)+\left(\frac{76}{105}x^7+\frac{5}{3}x^5+\frac{11}{6}x^3+\frac{3}{8}x\right)\right]\ln[x+(x^2-1)^{\frac{1}{2}}]-\left[W_0^4\left(\frac{11}{9}x^2+\frac{4}{9}\right)+W_0^3\left(-\frac{151}{36}x^3-\frac{73}{72}x\right)+W_0^2\left(\frac{163}{25}x^4+\frac{152}{75}x^2+\frac{4}{75}\right)+W_0\left(-\frac{4303}{900}x^5-\frac{5783}{1800}x^3-\frac{2441}{1800}x\right)+\left(\frac{14{,}741}{11{,}025}x^6+\frac{8133}{4900}x^4+\frac{135{,}853}{88{,}200}x^2+\frac{136}{2205}\right)\right](x^2-1)^{\frac{1}{2}}\right\}.$$

First forbidden beta-transition; tensor interaction; special case of selection rule ($\Delta J=2$; yes):

$$S(k)=\frac{\alpha G^2|M|^2}{12\pi^4}\frac{1}{k}\left\{\left[W_0^4\left(\frac{2}{3}x^3+x\right)+W_0^3\left(-2x^4-2x^2+\frac{1}{4}\right)+W_0^2\left(\frac{43}{15}x^5+\frac{8}{3}x^3-\frac{3}{8}x\right)+W_0\left(-\frac{31}{15}x^6-\frac{7}{3}x^4-\frac{3}{8}x^2-\frac{1}{12}\right)+\left(\frac{64}{105}x^7+\frac{8}{15}x^5+\frac{1}{12}x\right)\right]\ln(x+(x^2-1)^{\frac{1}{2}})\right.$$

(formula continued on next page)

* Work supported by the U. S. Atomic Energy Commission.

[1] L. Madansky and F. Rasetti, Phys. Rev. **83**, 187 (1951), also includes references to earlier work.
[2] T. B. Novey, Phys. Rev. **83**, 145 (1951).
[3] T. B. Novey, Phys. Rev. **86**, 619 (1952).
[4] D. Maeder and P. Preiswerk, Phys. Rev. **84**, 595 (1951).
[5] J. K. Knipp and G. E. Uhlenbeck, Physica **3**, 425 (1936).
[6] F. Bloch, Phys. Rev. **50**, 272 (1936).
[7] C. S. Wang Chang and D. L. Falkoff, Phys. Rev. **76**, 365 (1949).
[8] Madansky, Lipps, Bolgiano, and Berlin, Phys. Rev. **84**, 596 (1951).

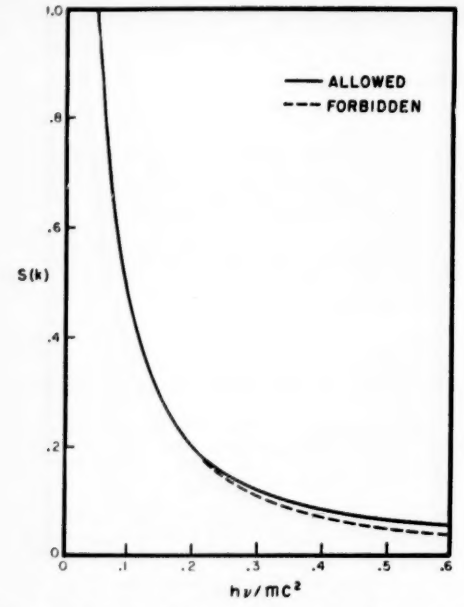

FIG. 1. Energy distribution of gamma-rays following allowed and first forbidden beta-transitions. $W_0=4$ in relativistic units. Ordinate $S(k)$ normalized to unity for $k=0.05$. Abscissa k measured in relativistic units. The dotted curve represents both the scalar theory and the tensor theory. The solid curve represents the allowed theory.

(*formula continued from preceding page*)

$$-\left[W_0^4\left(\frac{11}{9}x^2+\frac{4}{9}\right)+W_0^3\left(-\frac{7}{2}x^3-\frac{1}{4}x\right)+W_0^2\left(\frac{4481}{900}x^4+\frac{97}{600}x^2+\frac{4}{225}\right)+W_0\left(-\frac{363}{100}x^5-\frac{1337}{1800}x^3-\frac{437}{900}x\right)+\left(\frac{1306}{1225}x^6-\frac{769}{22{,}050}x^4+\frac{7733}{44{,}100}x^2+\frac{24}{1225}\right)\right](x^2-1)^{\frac{1}{2}}\Bigg\}.$$

A plot of the gamma-ray spectrum is shown in Fig. 1. In the energy range of 20–200 kev, one finds that the shapes of the allowed and forbidden cases are almost identical. The ratio of the total intensity of gamma-rays (in units of mc^2) to the total number of beta-rays for an allowed beta-transition can also be computed theoretically and is tabulated in Sec. 4.

Phosphorus 32, yttrium 91, and radium E are all pure beta-emitters and, hence, were chosen for the experiment. P^{32} exhibits an allowed shape for its beta-spectrum.[9] Yttrium 91 has the unique α-2 type spectrum[9] where the form of the beta-interaction is tensor or axial vector with the selection rule ($\Delta J=2$; yes). The radium E beta-spectrum also differs from the allowed shape. A mixture of interactions[10] gives a reasonable fit to the shape of its beta-spectrum. However, no calculation using this particular mixture of interactions (tensor and pseudoscalar) has been made for the internal bremsstrahlung. No calculations have been made employing the correct Z dependence for these three cases. Since the allowed and forbidden cases yield internal bremsstrahlung spectra which differ by only a small fraction of our experimental error in the energy range investigated, the experimental data have been compared with the allowed theory in each case. The results are described in Sec. 3.

The angular correlation of the beta-ray and its bremsstrahlung also has been derived for the case of an allowed beta-transition,[5,6] and for the unique α-2 first forbidden transition.[8] The correlation function depends on the range of beta-ray and gamma-ray energies used in the experiment. For a given range of energies the calculations show that for the special first forbidden beta-transition[8] discussed, the angular correlation functions differ from the allowed ones. Recent work by Horowitz,[11] however, indicates that if one considers an alternative mechanism for the bremsstrahlung, namely,

$$\begin{array}{ccc} & N_0^*+\gamma & \\ \nearrow & & \searrow \\ N_0 & & N_1+\nu+e+\gamma, \\ \searrow & & \nearrow \\ & N_1^*+e+\nu & \end{array}$$

in contrast to the usual one,

$$N_0\rightarrow N_1+\nu+e'\rightarrow N_1+\nu+e+\gamma,$$

then for a forbidden transition the angular correlation function becomes practically identical with the allowed one. This nuclear effect could certainly be present.

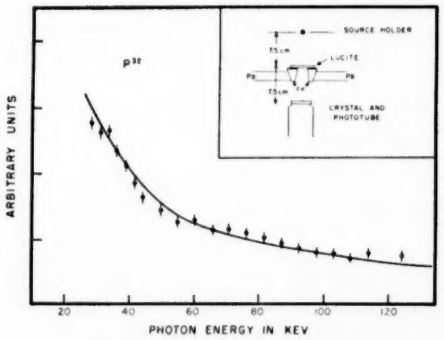

FIG. 2. Corrected theoretical spectrum for P^{32} and experimental data. Experimental arrangement is shown in inset.

[9] C. S. Wu, Revs. Modern Phys. **22**, 386 (1950).

[10] A. G. Petschek and R. E. Marshak, Phys. Rev. **85**, 698 (1952). C. S. Wu, Proc. Intern. Conf. Nuclear Phys. and Phys. Fundamental Particles, p. 160 (Sept. 1951).

[11] J. Horowitz, J. phys. et radium **13**, 429 (1952); and private communication.

However, this result is also based on calculations which do not include the Z dependence.

The experiments described below were designed to verify the theoretical predictions of the shapes of the internal bremsstrahlung continua. Some experiments were also conducted to obtain the qualitative behavior of the internal bremsstrahlung angular correlation.

II. EXPERIMENTAL PROCEDURE FOR MEASURING ENERGY SPECTRA

The experimental arrangement used with the beta-sources is shown in Fig. 2. The source was mounted about 15 cm above the NaI crystal. In order to stop the beta-particles and to prevent their being scattered into the crystal, a lead table top (1×20×20 inches) covered with ½-inch plywood was placed with its top surface half-way between the source and crystal. The center of the table contained a copper plug with a hole about ½ inch in diameter to pass the radiation to be examined and covered with a $\frac{3}{16}$-inch Lucite plate to stop the beta-particles in such a manner as to avoid admixture of the ordinary bremsstrahlung produced in stopping the beta-rays.[1]

Sources of the order of 0.1 millicurie were used. The gamma-radiation was measured by means of NaI(Tl) crystals (about 2×2×1 cm), a 5819 phototube, a linear amplifier and a one-channel discriminator. The P^{32} and Y^{91} sources were evaporated on small circular disks of 3-mg/cm² tissue paper about 10 mm in diameter. The RaE source was deposited electrochemically on one side of an 0.2-mil nickel foil strip of similar area.

By backing the source with mica and Lucite, it was determined that the external bremsstrahlung originating in the source holder was at most 1 percent of the total count observed. The relative contribution of external bremsstrahlung originating in the Lucite plate "beta-stopper" was ascertained to be of the order of 3 percent by varying the solid angle which it subtended at the scintillation crystal. Small amounts of lead in the vicinity of the crystal were sufficient to enhance the observed spectrum by ten percent or more by re-radiation of the lead K x-ray. Accordingly, the only Pb shielding used was the thick lead table provided with a copper-lined aperture. Source and crystal were enclosed together in the same light-tight covering, since as little as two strips of black scotch electrical tape between source and crystal absorbed sufficient radiation to alter the spectrum by about ten percent. The crystal was calibrated in the region from 20 to 60 kev with monochromatic x-rays from a Bragg-focusing x-ray spectrometer, and at higher energies with the line spectra of Cd^{109} (22.8-kev x-ray and 89-kev gamma-ray) and Os^{185} (62.8-kev x-ray). The pulse-height spectra obtained were Gaussian within 2 or 3 percent, and at the higher energies showed a smaller peak of about 30 kev less energy, owing to escape of the iodine K x-ray, in quantitative agreement with the data of West, Meyerhof, and Hofstadter,[12] and with a theoretical computation for the particular geometry used. The line-width dependence on energy is shown in Fig. 3.

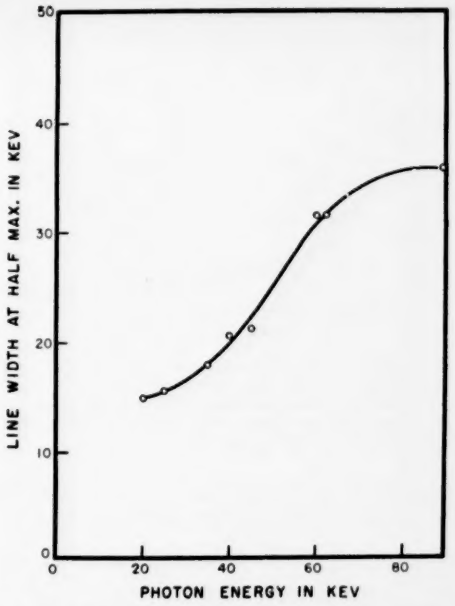

FIG. 3. Plot of the width at half-maximum of the pulse-height distribution for monochromatic gamma-rays.

III. CORRECTIONS

For comparison with experiment the theoretical spectra were corrected for absorption in the Lucite beta-stopper and aluminum foil, crystal efficiency, K x-ray escape, and instrumental resolving power. Measured x-ray absorption coefficients given by Compton and Allison[13] were used to correct for Lucite absorption and crystal efficiency. Absorption in the Lucite and the strong photoelectric absorption of iodine combined to make these particular corrections small over most of the energy ranges examined. It has been pointed out by West, Meyerhof, and Hofstadter[12] that near the K-absorption limit of iodine the K x-rays of iodine emitted subsequent to a photoelectric gamma-ray absorption will frequently escape from the crystal instead of being absorbed. The result is that a fraction of the gamma-rays will give rise to pulses of lower height. A quantitative prediction of this effect which considers the fluorescence yield of iodine as measured by Martin[14] was used to correct the spectrum for this effect. Figure 4 shows the theoretical spectrum of RaE both with and without the above corrections. The third curve shown has been corrected for instrumental resolving power by

[12] West, Meyerhof, and Hofstadter, Phys. Rev. **81**, 141 (1951).
[13] A. H. Compton and S. K. Allison, *X-Rays in Theory and Experiment* (D. Van Nostrand Company, Inc., New York, 1935).
[14] L. H. Martin, Proc. Roy. Soc. (London) **A115**, 420 (1927).

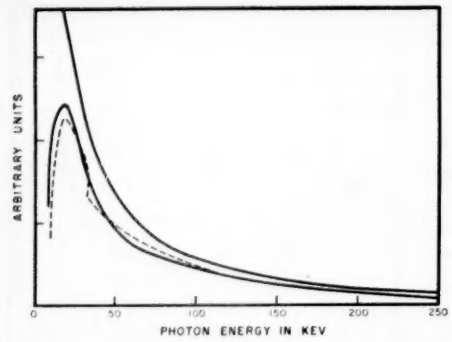

FIG. 4. Effect of corrections on the shape of the spectrum. The upper solid curve is the pure theoretical spectrum. The dotted curve includes all corrections except the folding due to the spread in pulse height for a monochromatic gamma-ray. The lower solid curve shows the final fully corrected spectrum.

folding it with a Gaussian curve whose empirical half-width varies with energy as shown in Fig. 3.

IV. RESULTS

The spectral shape is found to agree with the theory within the experimental error from 30 to 150 kev. Figures 2, 5, and 6 show corrected theoretical curves compared with the experimental data above 30 kev. No experimental points are shown below this limit, since the rapid rise of the theoretical curve combined with the fast increase of the absorption coefficient in Lucite, make it impossible to state with any assurance that the theory is verified within better than 20 percent in this region. Measurement of the total energy in the bremsstrahlung spectrum (above 90 kev) per electron emitted has been repeated in the manner previously reported.[1] The ratios I_γ/N_β of the gamma-ray energy (in units of mc^2) in the entire spectrum per beta-particle (assuming that the ratio of gamma-energy above 90 kev to that below 90 kev is the one theoretically predicted for an allowed transition) are given in Table I for the three sources investigated.

The theoretical ratio was computed using the formula for I_γ given by Chang and Falkoff (reference 7, p. 367), which was obtained by exact integration of their exact formula (5). Novey[3] finds a somewhat higher gamma-intensity from RaE, but it is believed this discrepancy might be explained by our uncertainties involved in evaluating the effects of scattering of the low energy beta-particles from RaE. Levinger[15] has computed theoretically that a Po x-ray of strength $0.64/Z^2$ per beta-particle should be present in addition to the RaE bremsstrahlung spectrum. The expected effect of such an x-ray is shown in Fig. 6 and is seen to be within our experimental error. Novey has reported the existence of such an x-ray.[4]

The bremsstrahlung accompanying K capture has also been observed for Fe^{55}. We find an end-point energy of 200 ± 10 kev, in good agreement with the end-point energy of 205 kev reported by Maeder and Preiswerk.[4] The correction procedure described above was applied to the theoretical spectrum to obtain this figure.

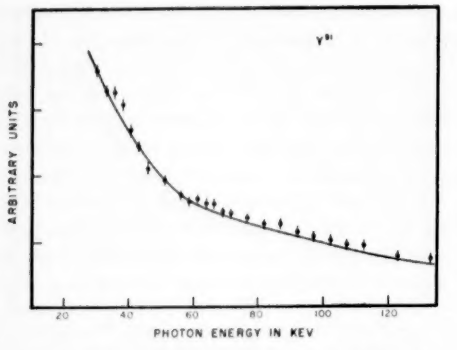

FIG. 5. Corrected theoretical spectrum for Y^{91} and experimental data.

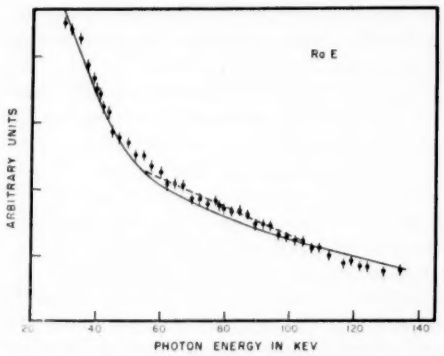

FIG. 6. Corrected theoretical spectrum for radium E and experimental data. The dotted portion shows the additional effect of Po x-rays from the photoeffect due to the beta-decay as calculated by Levinger.

V. ANGULAR CORRELATION EXPERIMENTS

An experimental determination of the angular correlation between the beta-particles and the bremsstrahlung from P^{32} and Y^{91} was also attempted. The source was mounted on the axis of a cylindrical evacuated Lucite chamber. The β-particles were counted with a 5819 phototube and a cylindrical stilbene crystal 1 inch in diameter and $1\frac{3}{16}$ inches long with a $\frac{1}{2}$-inch diameter hole running $\frac{3}{4}$ inch into the crystal to admit the particles and avoid their being scattered out of the crystal. This crystal was mounted within the vacuum system and separated from the phototube by a vacuum tight Lucite covering about $\frac{1}{16}$ in. thick. The photons were counted with a solid stilbene crystal $1\frac{5}{8}$ in. in diameter and $1\frac{1}{4}$ in. in length which together with a 5819 phototube could be rotated about the evacuated chamber. This crystal was placed with its front face

[15] J. S. Levinger, thesis, Cornell University, unpublished (1949) and private communication.

an inch and a half further from the source than the beta-counter and shielded with ½-inch lead to avoid scattering between the crystals.

Coincidences were detected electronically with a coincidence circuit of 2×10^{-8} second resolving time. The gamma-counter pulses were inverted and delayed electronically by approximately 100 mμ-seconds with respect to those from the beta-counter, and both displayed on a synchroscope with a 50 mμ-seconds per cm sweep triggered by the coincident circuit. The resulting traces were photographed and analyzed with respect to pulse heights and separations.

A rough calibration of the beta-crystal was made by finding the pulse heights corresponding to the upper end points of known beta-spectra. Known gamma-sources were used to calibrate the gamma-counter. An experiment was performed in which all beta-pulses corresponding to electrons of energies greater than 250 kev, and all gamma-pulses corresponding to photons of energies greater than 100 kev were recorded. The results of this experiment were compared with the distribution derived from quantum mechanical allowed theory, suitably integrated and corrected for this experimental situation, and are as shown in Fig. 7. Also shown is the distribution derived from the classical theory[7] as integrated for a similar situation by Novey.[3] The experiment appears to favor the correct quantum mechanical theory. The experimental point at 40° might be explained by scattering of photons greater than 300 kev from the beta-crystal into the gamma-crystal and from external bremsstrahlung originating in the beta-crystal from the impinging beta-particle. Since it was not possible to obtain a pulse-height resolution better than 30 percent for given beta-energies, no experimental curves are shown for the correlation associated with beta-rays of selected pulse heights. It was true, however, that Y^{91} and P^{32}, which have similar beta end-point energies, gave correlations which did not differ from each other within an experimental error of 10 percent at each position when the correlation was plotted for beta-counter pulses of only a 20 percent range of pulse amplitudes corresponding on the average to kinetic energies in the region of the order of 500 kev. Novey[3] has recently reported good agreement with the theoretical result for allowed transitions.

TABLE I. Gamma-ray energy per beta-particle, I_γ/N_β.

Source	Maximum beta-energy Mev	I_γ/N_β in units of mc^3 Theory (allowed transition)	Experimental
P^{32}	1.72	2.38×10^{-3}	2.32×10^{-3}
Y^{91}	1.5	1.97×10^{-3}	1.90×10^{-3}
RaE	1.17	1.11×10^{-3}	0.84×10^{-3}

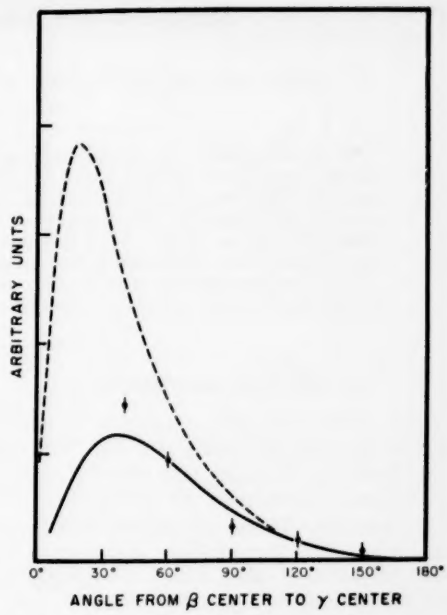

FIG. 7. Theoretical angular correlation curves for an allowed transition. The solid curve is calculated for the condition that one accepts all β-rays above 250 kev and all γ-rays above 100 kev. The dotted curve represents the classical correlation function derived for the same conditions. Both curves are corrected for solid angle of the counter.

VI. CONCLUSIONS

The experiments show excellent agreement with the predicted internal bremsstrahlung spectra. The calculations of Levinger on the relative amount of K-electron ejection appear to fall within our experimental error. The interesting question of the existence of the "Horowitz effect," however, cannot be answered by our experiments. It would, therefore, be of extreme interest to perform the correlation experiment with a beta-ray spectrograph providing good energy resolution.

We wish to thank Professor J. A. Bearden and Mr. C. Roos for their generous help with the x-ray spectrometer.

Three-Nucleon Interactions in Yukawa Theory

G. WENTZEL
Institute for Nuclear Studies and Department of Physics, University of Chicago, Chicago, Illinois
(Received October 24, 1952)

The method of Salpeter and Bethe is applied to the three-nucleon bound state problem. In a first approximation involving only multiple ladder-type diagrams, and neglecting retardation effects altogether, an equivalent Hamiltonian is derived which contains as potential energy merely the static Yukawa potentials of the three nucleon pairs. If the retardation corrections are treated as small perturbations, e.g., in a scalar theory, the resulting three-particle interactions prove to be small of the second order, and no larger than those deriving from other classes of Feynman diagrams.

Appendix I gives the static solution of the four-particle problem, and Appendix II the first-order retardation correction to the two-body potentials for scalar theories.

1. GENERAL ARGUMENTS

IF three or more particles (electrons or nucleons) interact by the intermediary of a field (Maxwell or Yukawa field), the resulting interaction Hamiltonian contains terms depending on the coordinates of more than two particles.[1] If the field-particle interaction is treated as a weak perturbation, involving a small coupling parameter g, these n-body interactions carry at least the factor $g^{2(n-1)}$.

According to Feynman's rules[2] for carrying out perturbation calculations, the three-body interactions of lowest order (g^4) can result from diagrams like Fig. 1 only. As the very structure of these diagrams indicates, they really describe iterated effects of (retarded) two-body interactions, rather than genuine three-body interactions. The same is true for all "multiple ladder-type" diagrams, an example of which is shown in Fig. 2. The lowest order true three-body interaction occurs in the order g^6; Fig. 3 gives an example of a diagram that is not "reducible" to successive two-body interaction diagrams.

The analysis is less simple if made from the viewpoint of a nonrelativistic approximation where the small effects of retardation are treated as corrections to the nonretarded forces.[1] Even the ladder diagrams may then, besides the iterated effects of *static* Coulomb or Yukawa potentials, give rise to interaction terms which may be classed as three-body interactions. However, the lowest order terms of this kind derive from the g^4 diagram Fig. 1, and it is easy to see that their effect, say, on the binding energy of the triton, can hardly be larger than that of the "genuine" three-body forces deriving from g^6 diagrams like Fig. 3, notwithstanding contradictory results previously reported on the basis of (old-style) fourth-order perturbation calculations.[3]

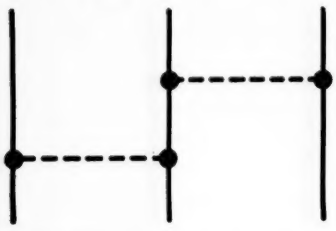

FIG. 1. Feynman diagram for three-body interactions of lowest order (g^4).

In atomic problems, as long as the nucleus can be regarded as a fixed center of force and the electron interactions as small corrections, a perturbation treatment is adequate. Not so in nuclear binding energy problems. For the two-nucleon problem, Salpeter and Bethe[4] have suggested the use, of a general integral equation following from Feynman's theory.[2] In a "first approximation," they retain in this equation all terms referring to ladder-type diagrams, but only these. Other classes of diagrams may be taken care of in higher approximations. It is obvious that similar methods, applied to the nonrelativistic three-nucleon problem, promise to be helpful in clarifying the problem of the three-body forces. In the "first approximation," involving multiple-ladder diagrams only, one may start out with a "static approximation," in which retardation effects are completely neglected. In this case no three-body interactions are expected to appear, and indeed, as will be shown, the problem reduces to a Schrödinger equation in which the potential energy consists merely of the ordinary static potentials of the three pairs. Then, re-introducing the retardation and also additional diagrams like Fig. 3, one should be able to correct this Schrödinger equation for three-body forces.

[1] H. Primakoff and T. Holstein, Phys. Rev. **55**, 1218 (1939).
[2] R. P. Feynman, Phys. Rev. **76**, 749, 769 (1949).

[3] This refers to the terms called "specifically quantum-mechanical" by Primakoff and Holstein, reference 1, and to all terms calculated by L. Jánossy, Proc. Cambridge Phil. Soc. **35**, 616 (1939). Actually these authors, neglecting nucleon recoils, disregard virtual intermediate states (called n' or II, respectively) with *no* mesons present. If one includes the corresponding matrix elements and expands into the small recoil energies, the first-order terms of this expansion cancel the "quantum-mechanical" terms resulting from intermediate states (n' or II) with two mesons present, calculated with neglect of recoil. The type of meson theory used (scalar-neutral or vector-charged, say) is irrelevant in this respect. (Dr. H. Primakoff has kindly informed me that he has been aware of the occurrence of such cancellations for some time: see the "Addendum" in reference 1.)

[4] E. E. Salpeter and H. A. Bethe, Phys. Rev. **84**, 1232 (1951). See also M. Gell-Mann and F. Low, Phys. Rev. **84**, 350 (1951), where a derivation from quantum field theory is given.

Only effects of retardation, linear in the nucleon velocities, are studied in the present paper.

2. THREE-PARTICLE PROBLEM IN FIRST APPROXIMATION

From the general integral equation for the three-body problem, which is obviously complicated, we immediately discard all terms referring to nonladder diagrams. The thus reduced equation [which corresponds to Eq. (11a) in Salpeter's and Bethe's paper,[4] with $\bar{G}$ already replaced by $G^{(1)}$, describing the retarded interaction of two particles resulting from a single quantum

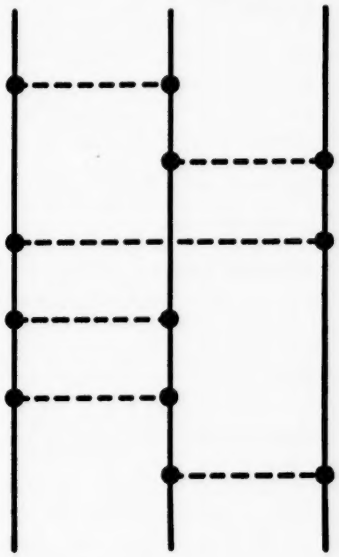

FIG. 2. A "multiple ladder-type" diagram.

link] has the following general structure:

$$
\begin{aligned}
&i\psi(1,2,3)\\
&=\int\int d\tau_2'd\tau_3'K(2,2')K(3,3')G(2',3')\psi(1,2',3')\\
&\quad+\int\int d\tau_3'd\tau_1'K(3,3')K(1,1')G(3',1')\psi(1',2,3')\\
&\quad+\int\int d\tau_1'd\tau_2'K(1,1')K(2,2')G(1',2')\psi(1',2',3). \quad (1)
\end{aligned}
$$

As a consequence, one derives a differential equation [analogous to Eq. (19a) of Salpeter and Bethe[5]]:

$$
\begin{aligned}
&(i\nabla_1-m_1)(i\nabla_2-m_2)(i\nabla_3-m_3)\psi(1,2,3)\\
&\quad=i[(i\nabla_1-m_1)G(2,3)+(i\nabla_2-m_2)G(3,1)\\
&\qquad+(i\nabla_3-m_3)G(1,2)]\psi(1,2,3). \quad (2)
\end{aligned}
$$

Analyzing into plane waves,

$$\exp[+i\textstyle\sum_s \mathbf{p}_s\cdot\mathbf{x}_s-i\sum_s E_s t_s],$$

[5] See also Y. Nambu, Prog. Theoret. Phys. **5**, 614 (1950), Eq. (82).

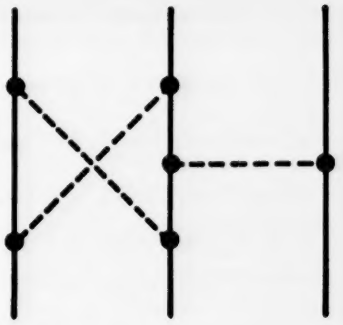

FIG. 3. A diagram that is not "reducible" to successive two-body interaction diagrams.

and using the center-of-mass frame,

$$\textstyle\sum_s \mathbf{p}_s=0,$$

one defines a bound stationary state of the system by requiring that, for all times t_s *equal*, ψ be purely periodical with time, with frequency less than $\sum m_s$:

$$\textstyle\sum_s E_s=\sum_s m_s-B, \quad B>0.$$

The single-time eigenfunction may then be written

$$U\times\exp[-i(\textstyle\sum_s m_s-B)t],$$

$$U=\int\int\int dE_1dE_2dE_3\delta(\textstyle\sum_s(E_s-m_s)+B)\psi(E_1,E_2,E_3).$$

It should be remembered that the masses m_s are supposed to contain small negative imaginary parts, and the same is true for the binding energy B, if the variables E_s are to be real.

In the following, we shall assume the three masses m_s to be equal (triton), and adopt the following notation:

$$E_s-m+B/3=\epsilon_s, \quad \textstyle\sum_s \epsilon_s=0, \qquad (3)$$

such that

$$U=\int d^3\epsilon\delta(\textstyle\sum_s \epsilon_s)\psi(\epsilon_1,\epsilon_2,\epsilon_3). \qquad (4)$$

The ϵ_s are strictly real variables.

To obtain a nonrelativistic approximation we may apply a Foldy-Wouthuysen transformation[6] with respect to each particle, leading to the substitution $i\nabla_s\rightarrow E_s-\mathbf{p}_s^2/2m$ in (2), provided, of course, that ψ and G are transformed accordingly and only "large" spinor components are retained. [Previous transformations are necessary in the pseudoscalar theory with pseudoscalar (γ_5) coupling which case will therefore be excluded.] With the notation (3) and

$$B/3+p_s^2/2m=T_s(p_s), \qquad (5)$$

the substitution to be made in (2) is

$$(i\nabla_s-m)\rightarrow(\epsilon_s-T_s(p_s)). \qquad (6)$$

Note that T_s carries the negative imaginary part of $B/3$ or m.

[6] L. L. Foldy and S. A. Wouthuysen, Phys. Rev. **78**, 29 (1950).

For a Yukawa theory involving only a single meson mass μ, the resulting equation reads

$$\prod_s[\epsilon_s - T_s(p_s)]\psi(\mathbf{p}_1, \epsilon_1; \mathbf{p}_2, \epsilon_2; \mathbf{p}_3, \epsilon_3)$$
$$= (g^2/2\pi i)\int d^3\kappa \int d\omega [2\pi^2(\mu^2+\kappa^2-\omega^2)]^{-1}$$
$$\times\{[\epsilon_1 - T_1(p_1)]\Gamma_{23}\psi(\mathbf{p}_1, \epsilon_1; \mathbf{p}_2+\boldsymbol{\kappa}, \epsilon_2+\omega; \mathbf{p}_3-\boldsymbol{\kappa}, \epsilon_3-\omega)$$
$$+[\epsilon_2 - T_2(p_2)]\Gamma_{31}\psi(\mathbf{p}_1-\boldsymbol{\kappa}, \epsilon_1-\omega; \mathbf{p}_2, \epsilon_2; \mathbf{p}_3+\boldsymbol{\kappa}, \epsilon_3+\omega)$$
$$+[\epsilon_3 - T_3(p_3)]\Gamma_{12}\psi(\mathbf{p}_1+\boldsymbol{\kappa}, \epsilon_1+\omega;$$
$$\mathbf{p}_2-\boldsymbol{\kappa}, \epsilon_2-\omega; \mathbf{p}_3, \epsilon_3)\}. \quad (7)$$

The symbols $\Gamma_{ss'}$ here indicate the spin and isotopic spin operators characterizing the coupling type of the particular Yukawa theory, in a nonrelativistic approximation.

3. STATIC APPROXIMATION

Following again Salpeter and Bethe, we now neglect the retardation in the Yukawa interaction operator:

$$(\mu^2+\kappa^2-\omega^2)^{-1} \to (\mu^2+\kappa^2)^{-1}.$$

[Should $\Gamma_{ss'}$ depend on ω, these ω's will be neglected too.] Then, defining static Yukawa interaction operators by

$$(Y_{23}f)(\mathbf{p}_1, \mathbf{p}_2, \mathbf{p}_3) = -g^2\int d^3\kappa [2\pi^2(\mu^2+\kappa^2)]^{-1}$$
$$\times\Gamma_{23}f(\mathbf{p}_1, \mathbf{p}_2+\boldsymbol{\kappa}, \mathbf{p}_3-\boldsymbol{\kappa}) \quad (8)$$

(similarly for the other nucleon pairs), and setting

$$\prod_s[\epsilon_s - T_s(p_s)]\psi(\epsilon_1, \epsilon_2, \epsilon_3) = \chi(\epsilon_1, \epsilon_2, \epsilon_3), \quad (9)$$

we obtain from (7) in the "static" approximation

$$\chi(\epsilon_1, \epsilon_2, \epsilon_3)$$
$$= Y_{23}\frac{1}{2\pi i}\int d\omega \frac{\chi(\epsilon_1, \epsilon_2+\omega, \epsilon_3-\omega)}{(\omega+\epsilon_2-T_2)(\omega-\epsilon_3+T_3)} + \cdots. \quad (10)$$

Note that the operator Y_{23} of Eq. (8) affects the arguments $\mathbf{p}_2$ and $\mathbf{p}_3$ (not written out) in χ as well as in T_2, T_3.

The first ω-integral in (10) is readily seen to be a function of ϵ_1 (and the $\mathbf{p}_s$) only [note that $\omega-\epsilon_3=(\omega+\epsilon_2)+\epsilon_1$]; consequently,

$$\chi = \sum_s f_s(\epsilon_s, \mathbf{p}_1, \mathbf{p}_2, \mathbf{p}_3).$$

Let

$$f_s(\epsilon_s, \mathbf{p}_1, \mathbf{p}_2, \mathbf{p}_3) - f_s(T_s(p_s), \mathbf{p}_1, \mathbf{p}_2, \mathbf{p}_3) = \chi_s(\epsilon_s, \mathbf{p}_1, \mathbf{p}_2, \mathbf{p}_3),$$
$$\sum_s f_s(T_s(p_s), \mathbf{p}_1, \mathbf{p}_2, \mathbf{p}_3) = \chi_0(\mathbf{p}_1, \mathbf{p}_2, \mathbf{p}_3).$$

Then

$$\chi = \chi_0(\mathbf{p}_1, \mathbf{p}_2, \mathbf{p}_3) + \sum_s \chi_s(\epsilon_s, \mathbf{p}_1, \mathbf{p}_2, \mathbf{p}_3), \quad (11)$$

$$\chi_s(T_s(p_s), \mathbf{p}_1, \mathbf{p}_2, \mathbf{p}_3) = 0. \quad (12)$$

Inserting (11) into the first integrand in (10), one can immediately carry out the ω-integrations[7] in the terms involving χ_0 and $\chi_1(\epsilon_1)$, whereas the "cross terms" involving $\chi_2(\epsilon_2+\omega)$ and $\chi_3(\epsilon_3-\omega)$ will be shown to vanish. Anticipating this result, one finds

$$\chi = -Y_{23}(\epsilon_1+T_2+T_3)^{-1}[\chi_0+\chi_1(\epsilon_1)] - \cdots. \quad (13)$$

A solution of this equation is most easily obtained by temporarily relinquishing the constraint $\sum\epsilon_s=0$.[8] Doing so, we may set $\epsilon_s = T_s(p_s)$ (for all s) in (13), whereby χ reduces to χ_0; the terms $Y_{23}(\sum T_s)^{-1}\chi_1$, etc., vanish because $\chi_1(\epsilon_1, \mathbf{p}_1, \mathbf{p}_2+\boldsymbol{\kappa}, \mathbf{p}_3-\boldsymbol{\kappa}) = 0$ for $\epsilon_1 = T_1(p_1)$ and for all values of $\boldsymbol{\kappa}$, according to (12). With the inotations

$$T = \sum_s T_s(p_s) = B + \sum_s p_s^2/2m, \quad (14)$$

$$T^{-1}\chi_0 = \varphi, \quad (15)$$

the resulting equation reads

$$(T+Y_{23}+Y_{31}+Y_{12})\varphi = 0. \quad (16)$$

Then, for arbitrary ϵ_1, (13) requires

$$[1+Y_{23}(\epsilon_1+T_2+T_3)^{-1}]\chi_1(\epsilon_1)$$
$$= (\epsilon_1 - T_1)Y_{23}(\epsilon_1+T_2+T_3)^{-1}\varphi, \quad (17)$$

or

$$\chi_1(\epsilon_1) = -(\epsilon_1 - T_1)\sum_{n\geq 1}[-Y_{23}(\epsilon_1+T_2+T_3)^{-1}]^n\varphi. \quad (17')$$

The situation is similar for χ_2 and χ_3. This completes the solution of Eq. (13), valid in particular for $\sum\epsilon_s=0$. Equation (16), combined with (14), is the Schrödinger equation in momentum space of the three-body problem, involving the static two-body potentials only.

We now prove the vanishing of the aforementioned "cross terms," like

$$Y_{23}\int d\omega \frac{\chi_2(\omega+\epsilon_2)}{(\omega+\epsilon_2-T_2)(\omega-\epsilon_3+T_3)}$$
$$= -Y_{23}\int \frac{d\omega}{(\omega-\epsilon_3+T_3)}\sum_{n\geq 1}\left[-Y_{31}\frac{1}{\omega+\epsilon_2+T_3+T_1}\right]^n\varphi.$$

Note that in such ω-integrals all poles of the integrand lie on the *same* side of the real ω axis (irrespective of how the p_s arguments of T_s are affected by the various Y operators, provided the p_s remain nonrelativistic); hence all such integrals are zero.

We finally want to calculate the single-time eigenfunction U given by (4), expressing ψ in terms of χ_0 and $\chi_s(\epsilon_s)$, by means of (9), (11), (15), and (17'). The

[7] Here the negative imaginary parts of T_s become important, e.g.,

$$(2\pi i)^{-1}\int d\omega(\omega+\epsilon_2-T_2)^{-1}(\omega-\epsilon_3+T_3)^{-1} = (\epsilon_2+\epsilon_3-T_2-T_3)^{-1}.$$

[8] This procedure can hardly impose undue restrictions on the solution. Indeed, a complete set of single-time eigenfunctions will be obtained.

contribution of χ_0 is

$$\chi_0 \int d^3\epsilon\delta(\epsilon_1+\epsilon_2+\epsilon_3)[\prod_s(\epsilon_s-T_s)]^{-1}$$

$$=T\varphi\int d\epsilon_1\int d\epsilon_2[(\epsilon_1-T_1)(\epsilon_2-T_2)(-\epsilon_1-\epsilon_2-T_3)]^{-1}$$

$$=(2\pi)^2\varphi. \tag{18}$$

On the other hand, the contribution of $\chi_1(\epsilon_1)$, as given by (17′), reduces to an ϵ_1 integral with all poles on the same side of the real axis. Therefore, (18) is the only nonvanishing term in U; in other words, except for a normalizing factor, the solutions of the Schrödinger equation (16) are the single-time eigenfunctions of the problem (7) in the static approximation. They obviously form a complete set, if negative values of B are admitted also.

The method used in this section for the construction of static solutions can be generalized to apply to four or more particles. For the four-body problem, the solution is stated without proof in Appendix I.

4. RETARDATION CORRECTIONS

Within the framework of our nonrelativistic approximation, characterized by the substitution (6), it is still meaningful to search for corrections to the static Yukawa potentials which are of the first order in the nucleon velocities $v=p/m$. In a closed system like the triton,

$$v\sim\mu/m, \quad T/\mu\sim mv^2/\mu\sim v.$$

We therefore assume $T\ll\mu$ and look for corrective terms of relative order T/μ in the Schrödinger equation (16), in particular for terms of the three-body interaction type.

We restore the full, ω-dependent, denominator $(\mu^2+\kappa^2-\omega^2)^{-1}$ in (7), but assume, for the sake of simplifying, that the operators $\Gamma_{ss'}$ are independent of ω (e.g., scalar theory). The first ω-integral in (10) (to be carried out before the κ space integration) is now replaced by

$$\int d\omega\frac{\chi(\epsilon_1,\ \epsilon_2+\omega,\ \epsilon_3-\omega)}{(\omega^2-\omega_\kappa^2)(\omega+\epsilon_2-T_2)(\omega-\epsilon_3+T_3)}. \tag{19}$$

Here $\omega_\kappa=(\mu^2+\kappa^2)^{\frac{1}{2}}$, containing like μ a negative imaginary part. The integrand is assumed to be known, from the static approximation, for ω-values such that $|\omega+\epsilon_2|$ and $|\omega-\epsilon_3|$ are of order T. If all $|\epsilon_s|\sim T$, integration between $-\tilde\omega$ and $+\tilde\omega$, where $T\ll\tilde\omega\ll\mu$, gives the same value as in the static case, except for terms of relative order $(T/\omega_\kappa)^2$ which are neglected. In the vicinity of the poles $\omega=\pm\omega_\kappa$, however, $\chi(\epsilon_1,\ \epsilon_2+\omega,\ \epsilon_3-\omega)$ cannot possibly be taken from the static approximation, but the integral equation itself indicates that[9]

$$\chi(\epsilon_1,\ \epsilon_2+\omega,\ \epsilon_3-\omega)=Y_{23}'\frac{1}{2\pi i}\int d\nu\frac{-\omega_\kappa^2}{\nu^2-\omega_\kappa^2}$$

$$\times\frac{\chi(\epsilon_1,\ \epsilon_2+\omega+\nu,\ \epsilon_3-\omega-\nu)}{(\nu+\omega+\epsilon_2-T_2)(\nu+\omega-\epsilon_3+T_3)}+\cdots. \tag{20}$$

can be calculated approximately for $|\omega|\gtrsim\mu$ by using the static approximation for the integrand near the poles $\nu=\pm\omega_\kappa$. This procedure should at least give the poles of the ω-function $\chi(\epsilon_1,\ \epsilon_2+\omega,\ \epsilon_3-\omega)$ in the regions $|\omega|\gtrsim\mu$ with the desired accuracy, and these poles are decisive when in (19) the contribution of the intervals $\omega>\tilde\omega$ and $\omega<-\tilde\omega$ (for $|\epsilon_s|\sim T$) are evaluated by contour integration.

Three-body interactions might be expected to arise from the terms χ_2 and χ_3 in (19) [see (11), (17′)] because they involve the operators Y_{31} and Y_{12}, and appear multiplied with a factor like Y_{23}. These terms, however, vanish in our approximation, because the respective groups of poles lie on the same side of the real axis, and contours can be chosen such as to make the integrals obviously small. For the remaining terms, in the region $|\epsilon_s|\sim T$, one obtains an equation of the form (13), with corrected Yukawa potentials $Y_{ss'}$, the corrections being of the order T/μ. These modified potentials are the same as derived from the two-body problem by a corresponding approximation (see Appendix II). Except for this change in the meaning of the symbols Y, the static solution (16), (17) remains valid.

Even if ω-dependent Γ-operators are admitted (e.g., vector mesons[10]) the result is the same, qualitatively. (Nuclear contact interactions and cut-off factors are implied if necessary.) The only exception, possibly, is the pseudoscalar theory with pseudoscalar (γ_5) coupling which we deliberately excluded in Sec. 2 because then the nonrelativistic interaction is not (or not entirely) of the Yukawa type.[11] This more complicated case must be studied separately. Otherwise, our result substantiates the expectation drawn from Feynman's perturbation theory that three-body interactions of relative order T/μ, caused by retardation, are nonexistent. The next order retardation correction will doubtless produce three-body terms, but in this approximation it is no longer permissible to disregard higher order irreducible Feynman diagrams like Fig. 3 which must give contributions of similar magnitude unless a major cancellation between various diagrams occurs. At the same time, since $T/\mu\sim v$, relativistic corrections to Eq. (7) will become significant.

[9] Y_{23}' is an integral operator like Y_{23} of Eq. (8) but including in its integrand the factor $-\omega_\kappa^2(\nu^2-\omega_\kappa^2)^{-1}$.

[10] This is the case treated by Primakoff and Holstein, and by Jánossy (see references 1 and 3).

[11] See L. L. Foldy, Phys. Rev. **84**, 168 (1951); G. Wentzel, Phys. Rev. **86**, 802 (1952). As for many-body interactions in such a theory, see G. Wentzel, Helv. Phys. Acta **25**, 569 (1952).

APPENDIX I

For the case of *four particles*, the generalization of Eqs. (1) to (10) is trivial. The static solution [corresponding to (11), (15), (16), (17)] is

$$\chi=T\varphi+\sum_s \chi_s(\epsilon_s)+\sum_{r<s}\chi_{rs}(\epsilon_r,\epsilon_s),\quad (T+\sum_{r<s}Y_{rs})\varphi=0,$$

$$[1+(Y_{34}+Y_{42}+Y_{23})(\epsilon_1+T_2+T_3+T_4)^{-1}]\chi_1 = (\epsilon_1-T_1)(Y_{34}+Y_{42}+Y_{23})(\epsilon_1+T_2+T_3+T_4)^{-1}\varphi,$$

$$\begin{aligned}[1+Y_{34}(\epsilon_1+\epsilon_2+T_3+T_4)^{-1}]\chi_{12} &= (\epsilon_1-T_1)(\epsilon_2-T_2)Y_{34}(\epsilon_1+\epsilon_2+T_3+T_4)^{-1}\\ &\times\{-[(\epsilon_1+T_2+T_3+T_4)^{-1}\\ &+(\epsilon_2+T_1+T_3+T_4)^{-1}]\varphi\\ &+(\epsilon_1+T_2+T_3+T_4)^{-1}(\epsilon_1-T_1)^{-1}\chi_1\\ &+(\epsilon_2+T_1+T_3+T_4)^{-1}(\epsilon_2-T_2)^{-1}\chi_2\}.\end{aligned}$$

φ is again the single-time eigenfunction.

APPENDIX II

For the *two-body* problem, the integral equation corresponding to (7) is

$$[\epsilon^2-(T(p)/2)^2]\psi(\mathbf{p},\epsilon)=-(g^2/2\pi i)\int d^3\kappa\int d\omega \times[2\pi^2(\omega_\kappa^2-\omega^2)]^{-1}\Gamma\psi(\mathbf{p}+\boldsymbol{\kappa},\epsilon+\omega),\quad (21)$$

where

$$\epsilon=\epsilon_1=-\epsilon_2,\quad \mathbf{p}=\mathbf{p}_1=-\mathbf{p}_2,\quad T(p)=B+p^2/m.$$

In the static approximation, the solution is

$$\psi=[\epsilon^2-(T/2)^2]^{-1}T\varphi,\quad (T+Y)\varphi=0^{13}\qquad (22)$$

[see Salpeter and Bethe,[4] Eqs. (26), (27)], valid for $\epsilon\sim T$ only. A more general expression, valid for $\epsilon\gtrsim\mu$ also, is found by the iteration procedure explained in Section 4 [see Eq. (20)]:

$$\psi=[\epsilon^2-(T/2)^2]^{-1}\chi,\qquad (23)$$

$$\chi(\mathbf{p},\epsilon)=g^2\int d^3\kappa[2\pi^2(\omega_\kappa^2-\epsilon^2)]^{-1}\Gamma\varphi(\mathbf{p}+\boldsymbol{\kappa}),\quad (24)$$

where φ is independent of ϵ. For $|\epsilon|\ll\mu$, χ becomes approximately $-Y\varphi$, and (23) leads back to (22). We now insert (23), (24) into (21), carry out the ω-integration rigorously, and satisfy the resulting equation for *small* values of $|\epsilon|(\sim T)$, leaving the extension to larger $|\epsilon|$-values to a later step in the iteration process. The result is a modified equation for φ, e.g., in a scalar theory:

$$(Y+YT^{-1}Y-Z)\varphi=0,\qquad (25)$$

$$(Z\varphi)(\mathbf{p})=\tfrac{1}{2}(g^2/2\pi^2)^2\int\int d^3\kappa d^3\kappa' \times[\omega_\kappa^2+\omega_\kappa\omega_{\kappa'}+\omega_{\kappa'}^2][(\omega_\kappa+\omega_{\kappa'})\omega_\kappa^3\omega_{\kappa'}^3]^{-1} \times\Gamma^2\varphi(\mathbf{p}+\boldsymbol{\kappa}+\boldsymbol{\kappa}').\quad (26)$$

It is readily seen that, in a bound state, Z in (25) is a correction of relative order T/μ. Therefore, after the substitution

$$T^{-1}Y\varphi=-\varphi',\qquad (27)$$

which makes $\varphi\approx\varphi'$ in the static approximation ($Y\varphi\approx-T\varphi$), $Z\varphi$ may be replaced by $Z\varphi'$, and (25) assumes the form of a Schrödinger equation with a corrected two-body potential $(Y+Z)$:

$$(T+Y+Z)\varphi'=0.\qquad (28)$$

Z is a repulsive potential in all scalar theories.

The single-time eigenfunction $\int d\epsilon\psi$ is easily expressed in terms of φ', namely,

$$\varphi'(\mathbf{p})-(g^2/4\pi^2)\int d^3\kappa\omega_\kappa^{-3}\Gamma\varphi'(\mathbf{p}+\boldsymbol{\kappa}).\qquad (29)$$

It obeys a more complicated equation obtainable immediately from (28).[14]

Obviously, the iteration method used here resembles the one proposed by Salpeter and Bethe (reference 4, Sec. V). The outstanding difference is that they replace the continuous set of poles of the function $\chi(\epsilon)$(24) (poles $\epsilon=\omega_\kappa$) by one single pole [$\epsilon=b(\mu^2+a^{-2}p^2)^{\frac{1}{2}}$, $b\gtrsim1$; see their Eqs. (30), (36)]. Our Ansatz (24) is probably the better initial approximation, although it may lead to difficulties in the practical evaluation of subsequent corrections.

Of course, Eq. (21) disregards contributions from nonladder type diagrams which will introduce into (28) further correction terms of the same order as Z. A study of the g^4 Feynman diagrams indicates that the inclusion of these additional terms in Z amounts to merely altering the numerical factor Γ^2 in (26). In the three scalar theories, namely,

neutral: $\Gamma=1$,
charged: $\Gamma=\tau_{1x}\tau_{2x}+\tau_{1y}\tau_{2y}$,
symmetric: $\Gamma=\boldsymbol{\tau}_1\cdot\boldsymbol{\tau}_2$,

the substitutions to be made in (26) are[15]

neutral: $\Gamma^2\to0$,
charged: $\Gamma^2\to-4\tau_{1z}\tau_{2z}$,
symmetric: $\Gamma^2\to-4\boldsymbol{\tau}_1\cdot\boldsymbol{\tau}_2$.

[13] $Y=Y_{12}$; see Eq. (8).

[14] In a recent paper by M. M. Lévy [Phys. Rev. **88**, 72 (1952), see Eqs. (47), (48), (52)] an equivalent equation is given, for the neutral scalar theory. Lévy's method of derivation seems to be practically identical with ours in the two-nucleon case. (This note was added after completion of this work.)

[15] These results confirm a general expression for the g^4 corrections to Y which H. Primakoff has derived by old-style perturbation methods (private communication). A statement in Lévy's paper (reference 14, p. 81) regarding the charge-symmetric scalar theory is incorrect.

Paramagnetic Relaxation in Metals*

ALBERT W. OVERHAUSER†
Department of Physics, University of California, Berkeley, California
(Received August 11, 1952)

The paramagnetic relaxation time of electron spins in a metal is calculated. Relaxation processes due to interaction with lattice vibrations, nuclear spins, other electrons, and impurity atoms are treated. It is found that the most important process of those considered is due to the interaction between electron magnetic moments and the fields caused by the translational motion of other electrons. A relaxation time of about one microsecond is calculated for this interaction at room temperature, and is approximately inversely proportional to the absolute temperature.

I. INTRODUCTION

IF a metal is placed in a magnetic field, the spin magnetic moments of the conduction electrons tend to line up parallel to the field. Such an alignment of spins does not take place immediately, but is limited by the speed of the dynamical mechanisms that produce alignment. This relaxation process, which gives rise to a net magnetization of the metal, depends upon the interactions between the electron spins and other parts of the system. In order to calculate the effects of such interactions we shall treat the degenerate electron gas by means of the single particle model, so that all interactions are assumed to be small perturbations. The results will depend, of course, on the validity of this approach. A further approximation will be the use of plane waves, $\exp(i\mathbf{k}\cdot\mathbf{r})$, for the wave functions of the single particle states, and the expression, $\hbar^2k^2/2m$, for the kinetic energy of such a state.

In this paper we shall consider only the spin interaction terms which cause transitions that change the net magnetic moment of the spin system. In other words, we shall determine the various contributions to what is commonly called the "spin-lattice" relaxation time. Interactions which tend to broaden the magnetic energy states without producing magnetic relaxation should not be important in metals, as they are in crystals, in view of the high velocity of the conduction electrons and the weakness of the spin-spin interaction studied in Sec. V.

Let us assume that a metal with N conduction electrons per cc is placed in a constant magnetic field $\mathfrak{IC}$ in the positive Z direction, which we shall call "up." The spin state of an electron can either be up or down, and, according to Fermi-Dirac statistics, the number of electrons n_+ or n_- per unit volume in k space with spin up or down is given by

$$n_\pm=\frac{1}{8\pi^3}\left[\exp\left(\frac{\hbar^2k^2/2m\pm\beta\mathfrak{IC}-\epsilon_\pm}{\kappa\theta}\right)+1\right]^{-1}. \quad (1)$$

Throughout the calculations the volume of the metal is taken to be 1 cc, β is the Bohr magneton, and θ is the absolute temperature. The parameters ϵ_+ and ϵ_- are the Fermi energies of the appropriate distributions. However, it follows from the fact that the total number of electrons is N that

$$\epsilon_++\epsilon_-=2\epsilon_0. \quad (2)$$

The constant ϵ_0 is the Fermi energy of the electron gas before $\mathfrak{IC}$ was applied. The one degree of freedom that remains permits the description of various amounts of bulk magnetization.

With approximations that are valid if $\beta\mathfrak{IC}\ll\kappa\theta$ and $\kappa\theta\ll\epsilon_0$, the total numbers of electrons N_+ and N_- with spin up and spin down are given by

$$N_\pm=N/2+mk_0(\epsilon_\pm-\epsilon_0\mp\beta\mathfrak{IC})/2\pi^2\hbar^2. \quad (3)$$

The constant k_0 is the wave number (times 2π) at the top of the Fermi distribution, so that $\epsilon_0=\hbar^2k_0^2/2m$. Equation (2) follows by setting $N_++N_-=N$. Furthermore, the net magnetization at any instant is βD, where

$$D=N_--N_+. \quad (4)$$

The condition that the system of electrons with spin up, $\{+\}$, and the system of electrons with spin down, $\{-\}$, be in equilibrium is that $\epsilon_+=\epsilon_-$. From (3) and (4) the equilibrium value of D is

$$D_0=m\beta k_0\mathfrak{IC}/\pi^2\hbar^2. \quad (5)$$

The progress of the combined system, $\{+\}+\{-\}$, towards equilibrium can then be described in terms of the process

$$D\rightarrow D_0.$$

One expects that the variation of D with time will be in accordance with the equation

$$dD/dt=(D_0-D)/T. \quad (6)$$

This equation serves as a definition of the relaxation time T, and we shall prove that this equation has the correct form. If there are several independent mechanisms which produce orientation, then

$$1/T=\sum 1/T_i,$$

where the T_i are the relaxation times to be associated

* Taken from a thesis submitted in partial satisfaction of the requirements for the degree of Doctor of Philosophy at the University of California.

† Now at the Physics Department, University of Illinois, Urbana, Illinois.

with the individual processes. Short relaxation times are most important, whereas long ones can be neglected.

Six interactions which can induce transitions between the spin states in a metal so as to cause such a relaxation process are: (a) Interaction of the electron spin with magnetic fields arising from transverse lattice vibrations. (b) Interaction with electric fields arising from longitudinal lattice vibrations. (c) Interaction with nuclear spins. (d) Interactions with spins of other electrons. (e) Interaction with electric currents due to the translational motion of other electrons. (f) Interaction with impurities. These couplings with electron spins are small compared to the electron lattice interactions that are important, for example, in the theory of conductivity. This fact allows us to assume that in times which are short with respect to the action of the above processes and long compared to the collision time (10^{-13} sec) of conductivity, $\{+\}$ and $\{-\}$ are independent but weakly interacting systems, each of which is in thermal equilibrium as regards its momentum distribution for the lattice temperature θ. Therefore, the distribution (1) holds throughout the relaxation process with the Fermi energies ϵ_+ and ϵ_- as time varying parameters.

Each of the relaxation times will be determined by the following scheme. We shall compute the number of spins, $W_{+,-}$, flipped per second from $\{+\}$ to $\{-\}$ and the number $W_{-,+}$ flipped from $\{-\}$ to $\{+\}$. The rate of change of D is then given by

$$dD/dt=2(W_{+,-}-W_{-,+}). \tag{7}$$

In each case we shall find that this quantity is proportional to $\epsilon_+-\epsilon_-$, which, by (3), (4), and (5) is related to D_0-D:

$$D_0-D=mk_0(\epsilon_+-\epsilon_-)/2\pi^2\hbar^2. \tag{8}$$

Therefore, (6) is proved to hold in each case and T can be identified from the coefficient of D_0-D. Also, since equilibrium obtains when $dD/dt=0$, one proves in a dynamical way that equilibrium is complete only if the Fermi energies are equal, which fact is, of course, a general result of statistical mechanics.

II. INTERACTION WITH TRANSVERSE PHONONS

In this section we shall compute the relaxation caused by the interaction between the electron magnetic moment, $-\beta\boldsymbol{\sigma}$, where $\boldsymbol{\sigma}$ is the Pauli spin vector, and the magnetic field $\mathfrak{IC}'(t)$ produced by the lattice vibrations of the metal. We will assume for the present that there is no correlation between the translational motions of the free electrons and the vibrational motions of the lattice. The field $\mathfrak{IC}'$ arises from the current $\mathbf{j}(t)$ produced by the mass motion of the charged lattice points. If $\mathbf{s}(t)$ is the displacement vector describing the lattice vibrations, the current density is given by

$$\mathbf{j}=Ne\dot{\mathbf{s}}/dt. \tag{9}$$

The assumption that there is one conduction electron per atom has been used here.

The magnetic field arising from such currents can be determined from the Maxwell curl equation.

$$\operatorname{curl}\mathfrak{IC}'=(d\mathfrak{D}/dt+4\pi\sigma_0\mathfrak{E}+4\pi\mathbf{j})/c. \tag{10}$$

However, the displacement current term is negligible and the conduction term is small for phonon frequencies greater than 10^7 per second. We may therefore use

$$\operatorname{curl}\mathfrak{IC}'=4\pi\mathbf{j}/c. \tag{11}$$

In writing Eq. (9) we have treated the positive ion lattice as a uniform distribution of positive charge. We shall also use the Debye model for the lattice vibrations and shall treat them by the method of field quantization. The displacement operator can then be written[1]

$$\mathbf{s}=(\hbar/2\rho\omega)^{\frac{1}{2}}\mathbf{e}_{\mathbf{K}\lambda}'(a_{\mathbf{K}\lambda}e^{i\mathbf{K}\cdot\mathbf{r}}+a_{\mathbf{K}\lambda}^*e^{-i\mathbf{K}\cdot\mathbf{r}}). \tag{12}$$

The summation sign over $\mathbf{K}$ and λ has been omitted. $\mathbf{e}_{\mathbf{K}1}'$ and $\mathbf{e}_{\mathbf{K}2}'$ are polarization vectors perpendicular to $\mathbf{K}$ and $\mathbf{e}_{\mathbf{K}3}'$ is parallel to $\mathbf{K}$. The velocity of sound in the metal is u and $\omega=uK$. The density of the metal is ρ, and $a_{\mathbf{K}\lambda}$ and $a_{\mathbf{K}\lambda}^*$ are destruction and creation operators, respectively, defined so that their nonzero commutators are 1. From (9), (11), and (12) the operator for the perturbing magnetic field is

$$\mathfrak{IC}'=4\pi Ne(\hbar u/2\rho c^2K)^{\frac{1}{2}}\mathbf{e}_{\mathbf{K}\lambda}(a_{\mathbf{K}\lambda}e^{i\mathbf{K}\cdot\mathbf{r}}+a_{\mathbf{K}\lambda}^*e^{-i\mathbf{K}\cdot\mathbf{r}}). \tag{13}$$

It can be shown that only transverse vibrations give rise to magnetic fields, so that λ is summed only over 1 and 2 in (13). Furthermore, $\mathbf{e}_{\mathbf{K}1}=-\mathbf{e}_{\mathbf{K}2}'$ and $\mathbf{e}_{\mathbf{K}2}=\mathbf{e}_{\mathbf{K}1}'$.

We will quantize the free electron field with the following conventions. The creation and destruction operators for particles with spin up will be indicated by b's, whereas the corresponding operators for electrons with spin down will be indicated by d's. The field operator for the system $\{+\}$ is then

$$\varphi=b_{\mathbf{k}}e^{i\mathbf{k}\cdot\mathbf{r}}.$$

Similarly, the field operator for the system $\{-\}$ can be taken:

$$\psi=d_{\mathbf{k}}e^{i\mathbf{k}\cdot\mathbf{r}}.$$

The phonon electron interaction is $\beta\mathfrak{IC}'\cdot\boldsymbol{\sigma}$, so that the perturbation operator of the electron phonon fields is

$$H=\int\begin{pmatrix}\varphi\\ \psi\end{pmatrix}^*\beta\mathfrak{IC}'\cdot\boldsymbol{\sigma}\begin{pmatrix}\varphi\\ \psi\end{pmatrix}d^3r. \tag{14}$$

Evaluation of this expression gives

$$\begin{aligned}H=4\pi Ne\beta(\hbar u/2\rho c^2K)^{\frac{1}{2}}\{&[(\mathbf{e}_{\mathbf{K}\lambda})_x-(\mathbf{e}_{\mathbf{K}\lambda})_y]\\&\times(\delta_{\mathbf{k}'-\mathbf{k}-\mathbf{K}}b_{\mathbf{k}'}^*d_{\mathbf{k}}a_{\mathbf{K}\lambda}+\delta_{\mathbf{k}'-\mathbf{k}+\mathbf{K}}b_{\mathbf{k}'}^*d_{\mathbf{k}}a_{\mathbf{K}\lambda}^*)\\&+[(\mathbf{e}_{\mathbf{K}\lambda})_x+(\mathbf{e}_{\mathbf{K}\lambda})_y](\delta_{\mathbf{k}'-\mathbf{k}-\mathbf{K}}d_{\mathbf{k}'}^*b_{\mathbf{k}}a_{\mathbf{K}\lambda}\\&+\delta_{\mathbf{k}'-\mathbf{k}+\mathbf{K}}d_{\mathbf{k}'}^*b_{\mathbf{k}}a_{\mathbf{K}\lambda}^*)\},\end{aligned}$$

[1] A. Sommerfeld and H. Bethe, *Handbuch der Physik* (Julius Springer, Berlin, 1933), second edition, Vol. XXIV, 2, pp. 500 ff.

plus four other terms which do not contribute to the relaxation process, and which we shall drop. The first term, for example, flips a spin up while absorbing a phonon. The conservation of wave number that obtains in emission or absorption of phonons is indicated by the symbols, $\delta_{\mathbf{k}'-\mathbf{k}-\mathbf{K}}$, which are 1 only if $\mathbf{k}'-\mathbf{k}-\mathbf{K}=0$. The above operator can be simplified by averaging the factors $(\mathbf{e}_{\mathbf{K}\lambda})_x^2+(\mathbf{e}_{\mathbf{K}\lambda})_y^2$ which enter the squares of the matrix elements and by summing over both directions of polarization. A factor 4/3 is obtained, so that we can set

$$H=8\pi Ne\beta(\hbar u/6\rho c^2K)^{\frac{1}{2}}(\delta_{\mathbf{k}'-\mathbf{k}-\mathbf{K}}b_{\mathbf{k}'}{}^{*}d_{\mathbf{k}}a_{\mathbf{K}}+\delta_{\mathbf{k}'-\mathbf{k}+\mathbf{K}}b_{\mathbf{k}'}{}^{*}d_{\mathbf{k}}a_{\mathbf{K}}{}^{*}+\delta_{\mathbf{k}'-\mathbf{k}-\mathbf{K}}d_{\mathbf{k}'}{}^{*}b_{\mathbf{k}}a_{\mathbf{K}}+\delta_{\mathbf{k}'-\mathbf{k}+\mathbf{K}}d_{\mathbf{k}'}{}^{*}b_{\mathbf{k}}a_{\mathbf{K}}{}^{*}). \quad (15)$$

We will now use first-order perturbation theory to calculate the number of electrons in $\{+\}$ which flip their spins down per second. Let us consider an electron in the state $\mathbf{k}$ in $\{+\}$ and calculate the transition probability per second that it flips its spin due to phonon emissions of wave number in the interval $(K, K+dK)$. We will assume for the present that the states $\mathbf{k}'$ in $\{-\}$ are unoccupied. The transition rate is given by

$$W_{\mathbf{k}\mathbf{k}'}{}^{em}dK=(2\pi/\hbar)|H_{\mathbf{k}\mathbf{k}'}|^2\rho_f. \quad (16)$$

The matrix element is that due to the first term in (15) and the square of its magnitude is

$$(8\pi Ne\beta)^2\hbar u(n_K+1)/6\rho c^2K.$$

Here, n_K is the average number of phonons in the state $\mathbf{K}$. The density of final states, ρ_f, is

$$\rho_f=(mK/4\pi^2\hbar^2k)dK.$$

Energy is conserved in the transitions so that we have

$$\hbar^2k'^2/2m+\beta\mathfrak{H}\mathcal{C}=\hbar^2k^2/2m+\hbar uK-\beta\mathfrak{H}\mathcal{C}. \quad (17)$$

There are similar transitions due to the absorption of phonons while the spin flips from up to down. The only difference is that n_K+1 must be replaced by n_K, and the phonon term in (17) is of opposite sign. The transition probabilities for the analogous cases when spins are flipped up instead of down are the same.

We may now proceed to calculate the total number of spins flipped down per second. To do this we multiply the number of electrons in the wave-number interval $(k, k+dk)$ by the transition probability, $W_{\mathbf{k}\mathbf{k}'}{}^{em}dK$ or $W_{\mathbf{k}\mathbf{k}'}{}^{ab}dK$, and then also by the appropriate Fermi function to describe the probability that the final electron states $\mathbf{k}'$ are unoccupied. We then integrate dk from 0 to ∞ and dK from $K_{\min}$ to $K_{\max}$. In order to account for the statistical factors we make the following definition:

$$g(k;x)=[\exp(\hbar^2k^2/2m\kappa\theta-x)+1]^{-1}. \quad (18)$$

The number of electrons in $\{+\}$ with k in the interval $(k, k+dk)$ is

$$(k^2dk/2\pi^2)g(k;\epsilon_+/\kappa\theta-\beta\mathfrak{H}\mathcal{C}/\kappa\theta).$$

The probability that the final electron state is unoccupied in processes of phonon emission is

$$1-g(k';\epsilon_-/\kappa\theta+\beta\mathfrak{H}\mathcal{C}/\kappa\theta).$$

On using (17) to eliminate k', this expression becomes

$$1-g(k;\epsilon_-/\kappa\theta-\beta\mathfrak{H}\mathcal{C}/\kappa\theta+\hbar uK/\kappa\theta).$$

Using the above results and the analogous ones for the case of phonon absorption, the number of spin flips from $\{+\}$ to $\{-\}$ per second is

$$W_{+,-}=\frac{8mu}{3\pi\rho}\left(\frac{Ne\beta}{\hbar c}\right)^2\int\left\{g\left(k;\frac{\epsilon_+-\beta\mathfrak{H}\mathcal{C}}{\kappa\theta}\right)\times\left[1-g\left(k;\frac{\epsilon_--\beta\mathfrak{H}\mathcal{C}+\hbar uK}{\kappa\theta}\right)\right](n_K+1)+g\left(k;\frac{\epsilon_+-\beta\mathfrak{H}\mathcal{C}}{\kappa\theta}\right)\times\left[1-g\left(k;\frac{\epsilon_--\beta\mathfrak{H}\mathcal{C}-\hbar uK}{\kappa\theta}\right)\right]n_K\right\}kdkdK.$$

The corresponding expression for $W_{-,+}$ is obtained by interchanging ϵ_+ and ϵ_- and by replacing $\beta\mathfrak{H}\mathcal{C}$ by $-\beta\mathfrak{H}\mathcal{C}$.

Before using (7) to obtain dD/dt, it is expedient to expand the functions $g(k;x)$ in a Taylor series about the point $x_0=\epsilon_0/\kappa\theta$. We will keep terms to the first order in the small quantities, $(\epsilon_+-\epsilon_0)/\kappa\theta$, $(\epsilon_--\epsilon_0)/\kappa\theta$, and $\beta\mathfrak{H}\mathcal{C}/\kappa\theta$. In order to make the writing simpler, we will use the following notation:

$$g=g(k;x_0),$$
$$g'=[\partial g(k;x)/\partial x]_{x=x_0},$$
$$g_{\pm K}=g(k;x_0\pm\hbar uK/\kappa\theta),$$
$$g_{\pm K}'=[\partial g(k;x)/\partial x]_{x=x_0\pm\hbar uK/\kappa\theta}.$$

The last two notations are necessary because $\hbar uK/\kappa\theta$ is not necessarily small. The integrand that occurs in the expression for dD/dt after expansion and subtraction is

$$[(\epsilon_+-\epsilon_-)/\kappa\theta]\{[g'(1-g_K)+gg_K'](n_K+1)+[g'(1-g_{-K})+gg_{-K}']n_K\}kdk+(2\beta\mathfrak{H}\mathcal{C}/\kappa\theta)\{[gg_K'-g'(1-g_K)](n_K+1)+[gg_{-K}'-g'(1-g_{-K})]n_K\}kdk.$$

It can be shown from the symmetry properties of $g(k;x)$ that

$$\int_0^\infty gg_{\pm K}'kdk=\int_0^\infty g'(1-g_{\pm K})kdk. \quad (19)$$

The second term above therefore gives zero upon

integration, and we obtain

$$\frac{dD}{dt}=\frac{32mu}{3\pi\rho}\left(\frac{Ne\beta}{\hbar c}\right)^2\frac{\epsilon_+-\epsilon_-}{\kappa\theta}\int[gg_K'(n_K+1)+gg_{-K}'n_K]kdkdK.$$

The remaining integrations can be performed as indicated, but it is simpler and sufficient for our purposes to make use of the high temperature approximation, where we can neglect the difference between n_K+1 and n_K, and can set

$$n_K=\kappa\theta/\hbar uK. \tag{20}$$

On integration and using (8) we obtain

$$\frac{dD}{dt}=\frac{16\pi N^2e^4\kappa\theta(D_0-D)}{3\rho\hbar k_0mc^4}\log\frac{K_{\max}}{K_{\min}}. \tag{21}$$

This equation is the desired result. We have only to discuss the determination of $K_{\min}$ and $K_{\max}$. At low phonon frequencies the induced electric fields resulting from the varying magnetic fields cause conduction currents which cancel out the magnetic fields. For such frequencies, then, there is a correlation between the electron motion and the lattice vibrations. It can be shown that this shielding effect decreases the magnitude of $|\mathcal{H}'|^2$ by the factor $K^2/(K^2+K_{\min}^2)$. The quantity $K_{\min}$ depends upon the electrical conductivity σ_0 and is given by $K_{\min}=4\pi\sigma_0u/c^2$. Its value for metallic lithium is 600 cm^{-1}.

If high frequency alternating fields are used to measure the relaxation time, the metal must be in the form of a fine powder of size small or comparable to the skin depth in order to prevent eddy current losses and excessive breadth of the absorption resonance due to the diffusion of the electrons in and out of the skin. The skin depth for Li is about 5×10^{-3} cm for a frequency of 10^7 cps, and 1/30 of this value for a frequency of 10^{10} cps. Particle sizes of about 10^{-3} cm and 10^{-4} cm, respectively, should be used. The minimum wavelength possible for phonons will be about twice the linear dimension of the particle. Assuming a spherical particle of diameter d, and letting $\frac{1}{2}\lambda_{\max}$ equal the cube root of the particle volume, we obtain

$$(4\pi/3)^{\frac{1}{3}}K_{\min}=2\pi/d.$$

$K_{\min}$ would be about $4\cdot10^3$ and $4\cdot10^4$, respectively. The restriction imposed by this last consideration would seem to be the more stringent in an ordinary practical case.

The expression for the maximum phonon wave number, as given by the Debye theory, is

$$(4\pi/3)^{\frac{1}{3}}K_{\max}=2\pi/a. \tag{22}$$

Here, a is the cube root of the atomic volume. The ratio $K_{\max}/K_{\min}$ is therefore d/a.

The relaxation time due to the interaction with transverse phonons is therefore

$$T=\frac{3\rho m\hbar k_0c^4}{16\pi N^2e^4\kappa\theta\log(d/a)}. \tag{23}$$

For the case of Li at room temperature, this expression has the value 6×10^{-2} sec.

III. INTERACTION WITH LONGITUDINAL PHONONS

In this section we shall compute the spin lattice relaxation caused by the interaction between electron spins and the electric fields of the lattice vibrations. The interaction energy of an electron spin with an electric field is given by[2]

$$H=(\beta/2mc)\boldsymbol{\sigma}\cdot(\mathbf{E}\times\mathbf{p}). \tag{24}$$

This term arises from the translational motion of the electron through the field, and is the origin of the spin orbit coupling in atoms, where E is taken to be the radial ion core field.

In metals and in the free electron approximation which we have been using, the fields that interest us are caused by the motion of the positive ions considered as a uniform distribution of positive charge. Electric fields will be associated with both longitudinal and transverse vibrations, but those due to the latter can be shown to be negligible. For longitudinal modes, however, the nonzero divergence of the lattice displacements will result in an accumulation of positive charge of amount

$$\delta\rho_+=-Ne\,\mathrm{div}\mathbf{s}.$$

This charge density will in turn be the source of electric fields that will induce spin transitions by means of (24). The above accumulation of charge is cancelled out in part by a corresponding aggregation of conduction electrons. We shall calculate this effect by means of the Fermi-Thomas statistical approximation.

Let $V(r)$ be the self-consistent potential arising from the accumulation of positive and negative charge. The maximum electron wave number, k_m, at each point in the lattice is given by

$$\hbar^2k_m^2/2m=\epsilon_0+eV.$$

The electron density as a function of position is then

$$n=[2m(\epsilon_0+eV)]^{\frac{1}{2}}/3\pi^2\hbar^3.$$

Since $|eV|\ll\epsilon_0$, this expression can be expanded in a power series and we can write

$$n=(2m\epsilon_0)^{\frac{1}{2}}(1+3eV/2\epsilon_0)/3\pi^2\hbar^3.$$

Hence the accumulation of electric charge due to the electrons is

$$\delta\rho_-=-me^2k_0V/\pi^2\hbar^2.$$

Consider, now, a Fourier component of the lattice displacement vector

$$\mathbf{s}_K=\mathbf{s}_K{}^0e^{i\mathbf{K}\cdot\mathbf{r}},$$

[2] Reference 1, pp. 509 ff.

and of the resulting self-consistent potential

$$V_{\mathbf{K}}=V_{\mathbf{K}}{}^{0}e^{i\mathbf{K}\cdot\mathbf{r}}.$$

The Maxwell equation which obtains is

$$\operatorname{div}\mathbf{E}=4\pi(\delta\rho_{+}+\delta\rho_{-}).$$

On inserting the expressions derived above, we obtain

$$V_{\mathbf{K}}=\frac{-4\pi Neis_{\mathbf{K}}}{K^{2}+4me^{2}k_{0}/\pi\hbar^{2}}. \tag{25}$$

The effect of electronic cancellation is given by the second term in the denominator. This interaction potential can be used, for example, to compute the electrical resistance of a metal and does in fact give results that agree with the more detailed theories. It seems reasonable to assume, therefore, that this simplified model will give a fair result for the relaxation problem at hand. It is easy to show that one does not make a significant error in neglecting spin orbit effects due to the ion core modulations of the crystalline field. It is sufficient to compare $(\Delta\epsilon|s_{\mathbf{K}}|/a)^{2}$ with (26) and to observe that they have the same magnitude. Here, $\Delta\epsilon$ can be taken to be the spin orbit splitting of the lowest p state in the atomic spectrum and a to be the lattice spacing.

If we expand (25) in a power series in K^{2} and keep only the first term, we obtain for a Fourier component of the electric field.

$$\mathbf{E}_{\mathbf{K}}=-K^{2}\pi^{2}\hbar^{2}N\mathbf{s}_{\mathbf{K}}/mek_{0}.$$

The mean square matrix element for spin flip transitions due to (24) will then be

$$|H|^{2}=\tfrac{2}{3}(\beta K^{2}\pi^{2}\hbar^{3}N/2m^{2}ce)^{2}|\mathbf{s}_{\mathbf{K}}|^{2}. \tag{26}$$

By $|s_{\mathbf{K}}|$ we mean:

Phonon absorption—$|s_{\mathbf{K}}|=(\hbar n_{K}/2\rho\omega)^{\frac{1}{2}}\delta_{\mathbf{k}'-\mathbf{k}-\mathbf{K}}$.

Phonon emission— $|s_{\mathbf{K}}|=(\hbar(n_{K}+1)/2\rho\omega)^{\frac{1}{2}}\delta_{\mathbf{k}'-\mathbf{k}+\mathbf{K}}$.

We have made use of the fact that $\mathbf{E}_{\mathbf{K}}$ and $\mathbf{p}$ are always about perpendicular due to conservation of energy and wave number. The factor $\frac{2}{3}$ comes from the average over-all directions and is half the factor obtained in Sec. II where two polarization directions were included. To perform the rest of the calculation it is sufficient to compare (26) with the square of the coefficients in (15) since all other details are identical. The ratio of the two expressions is found to be

$$\pi^{2}\hbar^{2}K^{4}/128m^{4}e^{4}u^{2}.$$

Furthermore, the final integration in K will be slightly different, so that the ratio of the relaxation rates is

$$\pi^{2}\hbar^{2}K_{\max}{}^{4}/512m^{4}e^{4}u^{2}\log(d/a).$$

Therefore, on dividing (23) by this factor we obtain the spin lattice relaxation time due to interaction with electric fields.

$$T=96\rho k_{0}m^{5}c^{4}u^{2}/\pi^{3}N^{2}\hbar^{5}K_{\max}{}^{4}\kappa\theta. \tag{27}$$

The sound velocity u can be estimated from the relation

$$\hbar uK_{\max}=\kappa\theta_{D}.$$

For the case of Li at room temperature, assuming $\theta_{D}=420°\mathrm{K}$, we obtain a value of 3×10^{-4} sec for the relaxation time.

IV. INTERACTION WITH NUCLEAR SPINS

In this section we will compute the paramagnetic relaxation due to the interaction of electron spins with the nuclear spins of the metal. We shall first consider the special case of a nucleus with spin $\frac{1}{2}$ and magnetic moment β_{n}, and shall generalize the calculation later for arbitrary nuclear spin. The most important interaction between the nuclear and electronic spins is that of the hyperfine coupling of an S state.[3] Because this interaction occurs entirely at the point of the nucleus it will not be permissible to use the plane wave approximation for the electrons without making an error of 10^{3} to 10^{4}. The perturbation can be written

$$H=(8\pi/3)\beta\beta_{n}\boldsymbol{\sigma}_{n}\cdot\boldsymbol{\sigma}\delta(\mathbf{r}). \tag{28}$$

Here $\boldsymbol{\sigma}_{n}$ is a Pauli spin operator for the nucleus and $\delta(\mathbf{r})$ is a delta-function with $\mathbf{r}$ the relative coordinate of the electron and the nucleus under consideration. If we expand $\boldsymbol{\sigma}_{n}\cdot\boldsymbol{\sigma}$ in terms of the raising and lowering operators, $\sigma_{\pm}=\frac{1}{2}(\sigma_{x}\pm i\sigma_{y})$, we obtain

$$\boldsymbol{\sigma}_{n}\cdot\boldsymbol{\sigma}=2\sigma_{n+}\sigma_{-}+2\sigma_{n-}\sigma_{+}+\sigma_{nz}\sigma_{z}.$$

The first term flips an electron spin from $\{+\}$ to $\{-\}$ and the nuclear spin from down to up. The transition probability per second for such a flip is

$$W_{\mathbf{k}\mathbf{k}'}=(2\pi/\hbar)(16\pi\beta\beta_{n}/3)^{2}|\psi(0)|^{4}\rho_{f}.$$

Because of the point nature of the interaction there is no interference condition and $|\psi(0)|$ is the magnitude of the wave function at the nucleus for an electron in the Fermi surface. The density of final states is

$$\rho_{f}=mk'/2\pi^{2}\hbar^{2}.$$

The number of transitions of a given type will depend upon the distribution in spin states of the nuclei. Let M_{+} and M_{-} be the number of nuclei with spin up and spin down, respectively. We have $M_{+}+M_{-}=N$, and we define

$$\Delta=M_{+}-M_{-},\quad \Delta_{0}=\beta_{n}N\mathfrak{H}/\kappa\theta.$$

It follows that $M_{\pm}=\frac{1}{2}(N\pm\Delta)$. The total number of electron flips per second from $\{+\}$ to $\{-\}$ is accordingly

$$W_{+,-}=\int W_{\mathbf{k}\mathbf{k}'}(k^{2}dk/2\pi^{2})M_{-}g(k;\epsilon_{+}/\kappa\theta-\beta\mathfrak{H}/\kappa\theta)\times[1-g(k';\epsilon_{-}/\kappa\theta+\beta\mathfrak{H}/\kappa\theta)]. \tag{29}$$

[3] J. Korringa, Physica **16**, 601 (1950).

The functions $g(k;x)$ are those defined in (18) and account for the Fermi statistics. The energy conservation equation for the above transitions is

$$\hbar^2k'^2/2m-\beta\mathfrak{H}-\beta_n\mathfrak{H}=\hbar^2k^2/2m+\beta\mathfrak{H}+\beta_n\mathfrak{H}.$$

Equation (29) can then be written

$$W_{+,-}=\frac{64m\beta^2\beta_n^2}{9\pi\hbar^3}|\psi(0)|^4(N-\Delta)\int g\left(k;\frac{\epsilon_{+,-}-\beta\mathfrak{H}}{\kappa\theta}\right)\times\left[1-g\left(k;\frac{\epsilon_{-,+}-\beta\mathfrak{H}-2\beta_n\mathfrak{H}}{\kappa\theta}\right)\right]k^3dk.$$

Transitions of the opposite type give a similar formula.

As in Sec. II we make a power series expansion of the functions in the integrands and compute dD/dt by keeping only first-order terms in the small quantities that occur (including Δ/N and Δ_0/N). After performing the various operations we have

$$dD/dt=256\pi mk_0N\beta^2\beta_n^2|\psi(0)|^4(D_0-D)/9\hbar^3+256m^2k_0^2\beta^2\beta_n^2\kappa\theta|\psi(0)|^4(\Delta_0-\Delta)/9\pi\hbar^5. \quad (30)$$

We have thus derived in a dynamical way the conditions of complete statistical equilibrium for two interacting spin systems in a magnetic field; that is, $dD/dt=0$ when $D=D_0$ and $\Delta=\Delta_0$. The calculation can be generalized to the case of arbitrary nuclear spin I by making the substitutions:

$$N/2\rightarrow N/(2I+1), \quad \beta_n\rightarrow\beta_n/2I.$$

We must also replace the square of the matrix element of σ_{n+} and σ_{n-}, which is 1 for $I=\frac{1}{2}$, by the quantity

$$G=\sum_{m=-I}^{I}(I+m+1)(I-m)=\tfrac{2}{3}I(I+1)(2I+1).$$

Furthermore, the quantities Δ and Δ_0 must be redefined to mean the difference of the number of nuclei in adjacent magnetic states, so that we now have

$$\Delta_0=\beta_nN\mathfrak{H}/I(2I+1)\kappa\theta.$$

Equation (30) becomes accordingly

$$dD/dt=(D_0-D)/T+G(\Delta_0-\Delta)/T_n. \quad (31)$$

It should be noted that (6) does not hold in general for the interaction with nuclear spins because the electronic relaxation depends upon the nuclear spin distribution as is shown by the second term in (31). T_n is the nuclear relaxation time and is

$$T_n=\frac{9\pi\hbar^5I^2}{64m^2k_0^2\beta^2\beta_n^2\kappa\theta|\psi(0)|^4}. \quad (32)$$

This is the same relaxation time as derived by Korringa[3] and is equivalent to Eq. (9) of his paper, though in a different form. The constant G appears in (31) because a given change in Δ requires G times as many transitions as an equal change in D. T is the electronic relaxation time and is

$$T=\frac{27\hbar^3I}{256\pi mk_0N\beta^2\beta_n^2(I+1)|\psi(0)|^4}. \quad (33)$$

It is interesting to note that this relaxation time is independent of temperature. It turns out that all other relaxation times increase with decreasing temperature, so that at very low temperatures this process will be the controlling one.

We will estimate this relaxation time for the isotope of lithium of mass seven, which has $I=\frac{3}{2}$. $|\psi(0)|^2$ can be determined as follows. We have defined it to be the square modulus of the metallic wave function, normalized in 1 cc, at the nucleus. Kohn and Bloembergen[4] have computed the electron density at the nucleus for the conduction electrons in the metal and have compared it to the corresponding density of the valence electron for a lithium atom. They find the ratio to be 1.0. From the measured hyperfine structure splitting[5] of Li and from the theoretical splitting of an S state,[6] we find $|\psi(0)|^2=34$, which means that the density of conduction electrons at the nucleus is greater by 34 than if the charge cloud were perfectly uniform. The relaxation time obtained from (33) is then $2\cdot10^{-4}$ sec.

From (32) and (33) one can derive the ratio of the nuclear and electronic relaxation times due to their mutual interaction.

$$T_n/T=8I(I+1)\epsilon_0/9\kappa\theta. \quad (34)$$

Since T_n can be measured directly in a nuclear resonance experiment, T could be determined from (34) without knowledge of the electronic wave functions

V. INTERACTION WITH ELECTRON SPINS

In this section we shall begin a study of the paramagnetic relaxation resulting from electron-electron interactions. From the classical point of view there are two terms in the interaction Hamiltonian which exert forces on the spins. The first is the spin-spin interaction which has the form[7]

$$H=(\beta^2/r_{12}^5)[(\boldsymbol{\sigma}_1\cdot\boldsymbol{\sigma}_2)r_{12}^2-3(\boldsymbol{\sigma}_1\cdot\mathbf{r}_{12})(\boldsymbol{\sigma}_2\cdot\mathbf{r}_{12})]. \quad (35)$$

The second is the spin-current interaction which is the coupling between the magnetic moment of one electron and the magnetic field produced by the translational motion of another. This term has the form[7]

$$H=(\beta e/mcr_{12}^3)[(\mathbf{r}_{12}\times\mathbf{p}_2)\cdot\boldsymbol{\sigma}_1+(\mathbf{r}_{21}\times\mathbf{p}_1)\cdot\boldsymbol{\sigma}_2]. \quad (36)$$

The exchange interaction does not have to be considered because it does not cause relaxation.

---

[4] W. Kohn and N. Bloembergen, Phys. Rev. **82**, 263 (1951).

[5] J. B. M. Kellogg and S. Millman, Revs. Modern Phys. **18**, 323 (1946).

[6] H. Bethe, *Handbuch der Physik* (Julius Springer, Berlin, 1933), second edition, Vol. XXIV, 1, p. 387.

[7] Reference 6, p. 377.

The spin-spin interaction can induce transitions in which there is a net flip of two spins up or down as well as those with a net flip of one spin up or down. On the other hand, the spin-current interaction can only cause single flip transitions. For the latter type processes both interactions must be treated simultaneously because interference effects are possible. The correct breakdown of the calculation is therefore into single flip relaxation and double flip relaxation. The relaxation time of the latter process is derived in this section, the former in the next.

We shall not use the above expressions for the electron-electron interaction because it is more convenient to use the relativistic wave equation of Dirac and to treat the interaction by the method of Moller. The calculations are thereby made more compact and the matrix elements are already provided. The Dirac equation for a free electron is

$$E\psi=(\boldsymbol{\alpha}\cdot\mathbf{p}+\mu\beta)\psi.$$

Here, $\mu=mc^2$ and $\mathbf{p}=c$ times the ordinary momentum vector. The plane wave solutions of positive energy are

$$\psi=u_{\mathbf{p}}{}^{+}\exp(i\mathbf{p}\cdot\mathbf{r}/\hbar c),\quad \psi=u_{\mathbf{p}}{}^{-}\exp(i\mathbf{p}\cdot\mathbf{r}/\hbar c).$$

The coefficients of the exponential factors are spinors and are given to the first order in p/μ by

$$\begin{aligned} u_{\mathbf{p}}{}^{+}&=(2\mu,\,0,\,p_z,\,p_+)/2\mu,\\ u_{\mathbf{p}}{}^{-}&=(0,\,2\mu,\,p_-,\,-p_z)/2u. \end{aligned}\tag{37}$$

We make use of the convention that for any vector $\mathbf{F}$

$$F_{\pm}=F_x\pm iF_y.\tag{38}$$

The Hamiltonian operator representing the interaction between electron pairs will be of the form

$$H=\tfrac{1}{2}\sum H_{\mathbf{p}'\mathbf{q}'\mathbf{p}\mathbf{q}}c_{\mathbf{p}'}{}^{*}c_{\mathbf{q}'}{}^{*}c_{\mathbf{q}}c_{\mathbf{p}}.\tag{39}$$

Here, the $c_{\mathbf{p}}$, $c_{\mathbf{p}}{}^{*}$, etc. are either the b's or d's as defined in II, or the corresponding operators for negative energy states. Because we are concerned with first-order transitions of low energy, we will not have to take the negative energy states into account. The coefficients of the above terms are the matrix elements of the Møller interaction[8]:

$$\begin{aligned} H_{\mathbf{p}'\mathbf{q}'\mathbf{q}\mathbf{p}}=4\pi\hbar^2c^2e^2[&(u_{\mathbf{p}'}{}^{*}u_{\mathbf{p}})(u_{\mathbf{q}'}{}^{*}u_{\mathbf{q}})\\ &-(u_{\mathbf{p}'}{}^{*}\boldsymbol{\alpha}u_{\mathbf{p}})\cdot(u_{\mathbf{q}'}{}^{*}\boldsymbol{\alpha}u_{\mathbf{q}})]/(R^2-\epsilon^2). \end{aligned}\tag{40}$$

Here $\mathbf{R}=\mathbf{p}-\mathbf{p}'$ and ϵ is the energy of the state $\mathbf{p}$ minus the energy of the state $\mathbf{p}'$. In this calculation ϵ^2 can always be neglected in comparison to R^2. The two term types in H which concern us here are: $d_{\mathbf{p}'}{}^{*}d_{\mathbf{q}'}{}^{*}b_{\mathbf{q}}b_{\mathbf{p}}$ which flip two spins down, and $b_{\mathbf{p}'}{}^{*}b_{\mathbf{q}'}{}^{*}d_{\mathbf{q}}d_{\mathbf{p}}$, which flip two spins up.

We will first treat the terms which flip two spins down. We must consider together all terms in (39) which connect the same initial and final states of the electron field, since they will interfere. Thus, for the transition $d_{\mathbf{p}'}{}^{*}d_{\mathbf{q}'}{}^{*}b_{\mathbf{q}}b_{\mathbf{p}}$ we must take, instead of $\frac{1}{2}H_{\mathbf{p}'\mathbf{q}'\mathbf{p}\mathbf{q}}$, the expression

$$\tfrac{1}{2}(H_{\mathbf{p}'\mathbf{q}'\mathbf{p}\mathbf{q}}+H_{\mathbf{q}'\mathbf{p}'\mathbf{q}\mathbf{p}}-H_{\mathbf{q}'\mathbf{p}'\mathbf{p}\mathbf{q}}-H_{\mathbf{p}'\mathbf{q}'\mathbf{q}\mathbf{p}}).$$

However, $H_{\mathbf{p}'\mathbf{q}'\mathbf{p}\mathbf{q}}=H_{\mathbf{q}'\mathbf{p}'\mathbf{q}\mathbf{p}}$, and $H_{\mathbf{q}'\mathbf{p}'\mathbf{p}\mathbf{q}}=H_{\mathbf{p}'\mathbf{q}'\mathbf{q}\mathbf{p}}$. When we use the above expression with four terms, we must sum over only one-quarter of the terms in (39), so that if we sum over all of them anyway, we need only multiply the coefficients by an extra factor of $\frac{1}{4}$. The matrix element can thus be taken:

$$H'=\tfrac{1}{2}(H_{\mathbf{p}'\mathbf{q}'\mathbf{p}\mathbf{q}}-H_{\mathbf{q}'\mathbf{p}'\mathbf{p}\mathbf{q}}).\tag{41}$$

Using (37), (38), and (40) and letting $\mathbf{S}=\mathbf{p}-\mathbf{q}'$, we obtain after some calculation the square modulus of (41):

$$|H'|^2=\left(\frac{\pi\hbar^2c^2e^2}{2\mu^2}\right)^2\left(\frac{R_+{}^2R_-{}^2}{R^4}+\frac{S_+{}^2S_-{}^2}{S^4}-\frac{R_+{}^2S_-{}^2+R_-{}^2S_+{}^2}{R^2S^2}\right).\tag{42}$$

We will now consider in a group all possible transitions which can be specified by the magnitudes p, q, and M, corresponding to the initial state, and the magnitude p'. We treat all such cases together because they will all have the same Fermi factors. The total momentum $\mathbf{M}=\mathbf{p}+\mathbf{q}$ is a constant during the collision. We can then average (42) over all possible orientations of the (χ,η,ζ) axes with respect to the original (X,Y,Z) axes; and then we must average this expression over the angle φ between the planes of the initial and final states (see Fig. 1). A lengthy computation gives for the average value of (42),

$$\langle|H'|^2\rangle_{\mathrm{Av}}=(2\pi\hbar^2c^2e^2)^2/10\mu^4.\tag{43}$$

The number of spin flips from $\{+\}$ to $\{-\}$ due to such double flip processes is given by

$$W_{+,-}=2\int(2\pi/\hbar)\langle|H'|^2\rangle_{\mathrm{Av}}\rho_fN_iG_iG_f.\tag{44}$$

Here, N_i is the number of initial states, ρ_f is the density

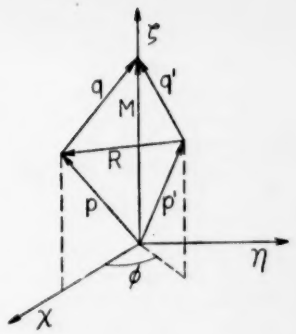

FIG. 1. Orientation of the electron momentum vectors with respect to the χ, η, ζ axes.

[8] W. Heitler, *The Quantum Theory of Radiation* (Oxford University Press, London, 1947), second edition, p. 101.

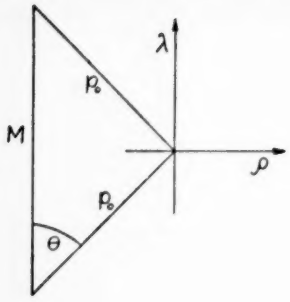

FIG. 2. Schematic section of electron momentum space, defining the quantities ρ, λ, and θ.

of final states for each initial state, G_i and G_f are the appropriate Fermi factors for the initial and final states. The extra factor of 2 is due to the fact that each transition flips two spins, and the integration is over all differentials that are necessary to specify ρ_f and N_i. Only electrons near the surface of the Fermi distribution, of momentum about p_0, will take part in such transitions. The phase space diagram will appear as in Fig. 2, which will serve as a definition of the quantities θ, ρ, λ for the initial state and the corresponding ones, ρ', λ', for the final. The energies of the various states have the form

$$E_p=\epsilon_0+(p_0/\mu)(\rho\sin\theta+\lambda\cos\theta)+\beta\mathfrak{IC}.$$

The energy conservation equation, $E_p+E_q=E_{p'}+E_{q'}$, gives

$$\rho'=\rho+2\mu\beta\mathfrak{IC}/p_0\sin\theta. \tag{45}$$

The number of initial states is

$$N_i=(4\pi M^2dM/c^3\hbar^3)(2\pi p_0\sin\theta d\lambda d\rho/c^3\hbar^3).$$

The number of final states for a given initial state is

$$Z_f=2\pi p_0\sin\theta d\lambda' d\rho'/c^3\hbar^3.$$

The spread in final energy is given by

$$\Delta E_f=(2p_0/\mu)\sin\theta d\rho'.$$

We therefore obtain the density of final states:

$$\rho_f=(\pi\mu/c^3\hbar^3)d\lambda'.$$

In order to specify the appropriate Fermi factors, we make the following definitions:

$$\begin{aligned} &g(\rho,\lambda;x)=\{\exp[(p_0/\mu\kappa\theta)(\rho\sin\theta+\lambda\cos\theta)-x]+1\}^{-1},\\ &g(\rho,\lambda)=g(\rho,\lambda;0),\\ &g'(\rho,\lambda)=[\partial g(\rho,\lambda;x)/\partial x]_{x=0}. \end{aligned} \tag{46}$$

We have then

$$\begin{aligned} G_i=g(\rho,\lambda;(\epsilon_+-\epsilon_0)/\kappa\theta-\beta\mathfrak{IC}/\kappa\theta)\\ \times g(\rho,-\lambda;(\epsilon_+-\epsilon_0)/\kappa\theta-\beta\mathfrak{IC}/\kappa\theta). \end{aligned}$$

Using (45) we obtain similarly

$$\begin{aligned} G_f=[1-g(\rho,\lambda';(\epsilon_--\epsilon_0)/\kappa\theta-\beta\mathfrak{IC}/\kappa\theta)]\\ \times[1-g(\rho,-\lambda';(\epsilon_--\epsilon_0)/\kappa\theta-\beta\mathfrak{IC}/\kappa\theta)]. \end{aligned}$$

Each factor in (44) has now been evaluated. In order to determine the relaxation we must also consider the reverse processes which flip two spins from $\{-\}$ to $\{+\}$. We will obtain an equation like (44) with G_i and G_f replaced by $\bar{G}_i$ and $\bar{G}_f$, which differ from the former only in that ϵ_+ and ϵ_- are interchanged and $\beta\mathfrak{IC}$ is replaced by $-\beta\mathfrak{IC}$. Using (7) we obtain

$$dD/dt=(8\pi/\hbar)\langle|H'|^2\rangle_{Av}\int\rho_fN_i(G_iG_f-\bar{G}_i\bar{G}_f). \tag{47}$$

We next expand G_iG_f and $\bar{G}_i\bar{G}_f$ in terms of the small quantities $(\epsilon_+-\epsilon_0)/\kappa\theta$, $(\epsilon_--\epsilon_0)/\kappa\theta$, and $\beta\mathfrak{IC}/\kappa\theta$. For example,

$$\begin{aligned} G_i=[g(\rho,\lambda)+g'(\rho,\lambda)(\epsilon_+-\epsilon_0-\beta\mathfrak{IC})/\kappa\theta]\\ \times[g(\rho,-\lambda)+g'(\rho,-\lambda)(\epsilon_+-\epsilon_0-\beta\mathfrak{IC})/\kappa\theta]. \end{aligned}$$

Only first-order terms are retained, and on using the relation

$$1-g(\rho,\lambda)=g(-\rho,-\lambda),$$

we obtain

$$\begin{aligned} &G_iG_f-\bar{G}_i\bar{G}_f\\ &=[(\epsilon_+-\epsilon_-)/\kappa\theta][g'(\rho,\lambda)g(\rho,-\lambda)g(-\rho,-\lambda')g(-\rho,\lambda')\\ &\quad+g(\rho,\lambda)g'(\rho,-\lambda)g(-\rho,-\lambda')g(-\rho,\lambda')\\ &\quad+g(\rho,\lambda)g(\rho,\lambda)g'(\rho,\lambda')g(-\rho,\lambda')\\ &\quad+g(\rho,\lambda)g(\rho,-\lambda)g(-\rho,-\lambda')g'(\rho,-\lambda')]\\ &\quad-(2\beta\mathfrak{IC}/\kappa\theta)[g'(\rho,\lambda)g(\rho,-\lambda)g(-\rho,-\lambda')g(-\rho,\lambda')\\ &\quad+g(\rho,\lambda)g'(\rho,-\lambda)g(-\rho,-\lambda')g(-\rho,\lambda')\\ &\quad-g(\rho,\lambda)g(\rho,-\lambda)g'(\rho,\lambda')g(-\rho,\lambda')\\ &\qquad-g(\rho,\lambda)g(\rho,-\lambda)g(-\rho,-\lambda')g'(\rho,-\lambda')]. \end{aligned}$$

Now, each of the above terms in square brackets is integrated over $d\rho$, $d\lambda$, and $d\lambda'$, and it can be seen that after integration the four terms in the coefficient of $(\epsilon_+-\epsilon_-)/\kappa\theta$ all give the same result. Thus the first term equals the second on the change of variable $\lambda\rightarrow-\lambda$ in the second term; the third equals the fourth on the substitution $\lambda'\rightarrow-\lambda'$ in the fourth; and, finally, the first term equals the third on the substitutions in the third, $\rho\rightarrow-\rho$, $\lambda'\rightarrow-\lambda$, and $\lambda\rightarrow-\lambda'$, while observing that $g'(\rho,\lambda)=g'(-\rho,-\lambda)$. The coefficient of $2\beta\mathfrak{IC}/\kappa\theta$ then integrates to zero and we can replace the coefficient of $(\epsilon_+-\epsilon_-)/\kappa\theta$ by $4g'(\rho,\lambda)g(-\rho,\lambda)g(\rho,\lambda')g(\rho,-\lambda')$. Combining the above results and remembering that $M=2p_0\cos\theta$, (47) becomes

$$\begin{aligned} \frac{dD}{dt}=\frac{128\mu\beta^4p_0^4(\epsilon_+-\epsilon_-)}{5\pi^3c^9\hbar^{10}\kappa\theta}\int g'(\rho,\lambda)g(-\rho,\lambda)g(\rho,\lambda')\\ \times g(\rho,-\lambda')\cos^2\theta\sin^2\theta d\theta d\rho d\lambda d\lambda'. \end{aligned}$$

The limits of integration are 0 to $\pi/2$ for θ and $-\infty$ to ∞ for the remaining variables. The integrals can be evaluated, and on using (8) we obtain the relaxation equation

$$dD/dt=8\pi e^4\kappa^2\theta^2(D_0-D)/15m\hbar^3c^4. \tag{48}$$

The relaxation time to be associated with the double flip action of spin-spin forces is therefore

$$T=15m\hbar^3c^4/8\pi e^4\kappa^2\theta^2. \quad (49)$$

It is interesting to note that (49) depends only upon the fundamental constants and the absolute temperature. The quadratic dependence of the relaxation rate with temperature results from the Fermi statistics. An electron in the Fermi surface can only collide with another electron in the Fermi surface, that is with a fraction of the electrons of about $\kappa\theta/\epsilon_0$. Similarly, of the possible final momentum states, only a fraction of about $\kappa\theta/\epsilon_0$ are permitted by the exclusion principle. Hence, two powers of $\kappa\theta/\epsilon_0$ would enter an order of magnitude calculation. For room temperature (49) has the value 6×10^{-3} sec.

VI. INTERACTION WITH ELECTRON CURRENTS

In this section we shall calculate the relaxation rate due to electron-electron collisions in which there is a net flip of one spin up or down. Such transitions can be due to spin-spin forces or spin-current forces, but it will be seen that the latter interaction is several orders of magnitude larger than the former in so far as these processes are concerned.

There are four term types in (39) which produce a net flip of one spin from $\{+\}$ to $\{-\}$. These four types must be grouped in pairs since they can connect the same initial and final states. The first pair gives the following terms:

$$\tfrac{1}{2}\sum(H^{\alpha}{}_{\mathbf{p}'\mathbf{q}'\mathbf{p}\mathbf{q}}b_{\mathbf{p}'}{}^*d_{\mathbf{q}'}{}^*b_{\mathbf{q}}b_{\mathbf{p}}+H^{\beta}{}_{\mathbf{p}'\mathbf{q}'\mathbf{p}\mathbf{q}}d_{\mathbf{p}'}{}^*b_{\mathbf{q}'}{}^*b_{\mathbf{q}}b_{\mathbf{p}}). \quad (50)$$

It is necessary to make the distinction between $H^{\alpha}{}_{\mathbf{p}'\mathbf{q}'\mathbf{p}\mathbf{q}}$ and $H^{\beta}{}_{\mathbf{p}'\mathbf{q}'\mathbf{p}\mathbf{q}}$ because the spin up spinor goes with the $\mathbf{p}'$ in the first and with the $\mathbf{q}'$ in the second. For a specific transition two terms of each type appear in (50), and, as before, one can show that the matrix element can be taken to be

$$H'=(H^{\alpha}{}_{\mathbf{p}'\mathbf{q}'\mathbf{p}\mathbf{q}}-H^{\alpha}{}_{\mathbf{p}'\mathbf{q}'\mathbf{q}\mathbf{p}})/\sqrt{2}.$$

Using (37), (38), and (40) one finds

$$H'=(\pi\hbar^2c^2e^2/\sqrt{2}\mu^2)\{[\tfrac{3}{2}i(\mathbf{R}\times\mathbf{M})_+-\tfrac{1}{2}i(\mathbf{R}\times\mathbf{S})_+ -R_zR_+]/R^2+[\tfrac{3}{2}i(\mathbf{S}\times\mathbf{M})_+-\tfrac{1}{2}i(\mathbf{R}\times\mathbf{S})_+-S_zS_+]/S^2]\}.$$

We must average the square modulus of this expression over all orientations of the (χ, η, ζ) axes in Fig. 1. We obtain

$$\begin{aligned}\langle|H'|^2\rangle_{Av}/8\pi^2\beta^4=&[3(\mathbf{R}\times\mathbf{M})^2/2+(\mathbf{R}\times\mathbf{S})^2/6\\ &+2R^4/15+(\mathbf{R}\times\mathbf{M})\cdot(\mathbf{R}\times\mathbf{S})]/R^4+[3(\mathbf{S}\times\mathbf{M})^2/2\\ &+(\mathbf{R}\times\mathbf{S})^2/6+2S^4/15+(\mathbf{S}\times\mathbf{M})\cdot(\mathbf{R}\times\mathbf{S})]/S^4\\ &+[(\mathbf{R}\times\mathbf{M})\cdot(\mathbf{R}\times\mathbf{S})+3(\mathbf{R}\times\mathbf{M})\cdot(\mathbf{S}\times\mathbf{M})\\ &+(\mathbf{S}\times\mathbf{M})\cdot(\mathbf{R}\times\mathbf{S})+7R^2S^2/15-(\mathbf{R}\cdot\mathbf{S})^2]/R^2S^2. \quad (51)\end{aligned}$$

Equation (51) must in turn be averaged over the angle φ. Near $\varphi=0$, R becomes very small; and near $\varphi=\pi$, S becomes very small. The presence of these near singularities is due to the action of spin current forces which have an interaction energy that varies in distance as $1/r^2$, so that the total scattering cross section would be infinite.[9] The presence of the magnetic field, however, removes the singularity because energy conservation for a collision in which one spin is flipped demands that R and S can never be smaller than

$$\delta=\mu\beta\mathfrak{H}/p_0\sin\theta.$$

This quantity is small, however, so that integration over φ makes several of the terms in (51) give a large contribution, of order of magnitude p_0/δ, which is from 10^4 to 10^6 larger than the remaining terms, as can be seen only by a close examination. Equation (51) can therefore be replaced by

$$\begin{aligned}\langle|H'|^2\rangle_{Av}=&8\pi^2\beta^4[3(\mathbf{R}\times\mathbf{M})^2/2R^4+3(\mathbf{S}\times\mathbf{M})^2/2S^4\\ &+(\mathbf{R}\times\mathbf{S})^2/6R^4+(\mathbf{R}\times\mathbf{S})^2/6S^4]. \quad (52)\end{aligned}$$

Actually, $(\mathbf{R}\times\mathbf{M})\cdot(\mathbf{R}\times\mathbf{S})/R^4$ and $(\mathbf{S}\times\mathbf{M})\cdot(\mathbf{R}\times\mathbf{S})/S^4$ give terms of the same order of magnitude, but it can be shown that they do not contribute to dD/dt, so that we will not carry them along. Further computation gives for the average of (52) over φ

$$\langle|H'|^2\rangle_{Av}=4\pi^2\beta^4p_0F(\lambda,\lambda',\theta)/3\sin^2\theta\cos^2\theta. \quad (53)$$

Here

$$\begin{aligned}F(\lambda,\lambda',\theta)=&(9\cos^4\theta\sin\theta+2\cos^2\theta\sin^3\theta)\\ &\times[((\lambda-\lambda')^2+\delta^2)^{-\frac{1}{2}}+((\lambda+\lambda')^2+\delta^2)^{-\frac{1}{2}}]\\ &+\delta^2(9\cos^4\theta\sin\theta-\cos^2\theta\sin^3\theta)\\ &\times[((\lambda-\lambda')^2+\delta^2)^{-\frac{1}{2}}+((\lambda+\lambda')^2+\delta^2)^{-\frac{1}{2}}].\end{aligned}$$

We can now compute the number of spin flips per second from $\{+\}$ to $\{-\}$ due to the spin-current interaction, and it is given by (44). The extra factor of 2 is now due to the extra two term types in the Hamiltonian operator, which in fact give the same transition rate as the two in (50). The factors ρ_f, N_i, and G_i are the same as before, whereas $\langle|H'|^2\rangle_{Av}$ is given by (53) and G_f is also new:

$$\begin{aligned}G_f=&[1-g(\rho',\lambda';(\epsilon_+-\epsilon_0-\beta\mathfrak{H}\mathcal{C})/\kappa\theta)]\\ &\times[1-g(\rho',-\lambda';(\epsilon_--\epsilon_0+\beta\mathfrak{H}\mathcal{C})/\kappa\theta)].\end{aligned}$$

The energy balance equation gives for this case

$$\rho'=\rho+\mu\beta\mathfrak{H}\mathcal{C}/p_0\sin\theta;$$

so that, finally,

$$\begin{aligned}G_f=&[1-g(\rho,\lambda';(\epsilon_+-\epsilon_0-2\beta\mathfrak{H}\mathcal{C})/\kappa\theta)]\\ &\times[1-g(\rho,-\lambda';(\epsilon_--\epsilon_0)/\kappa\theta)].\end{aligned}$$

Similar alterations must be made to $\bar{G}_f$ for the inverse processes. The relaxation rate from (7) is

$$dD/dt=(8\pi/\hbar)\int\langle|H'|^2\rangle_{Av}\rho_fN_i(G_iG_f-\bar{G}_i\bar{G}_f). \quad (54)$$

[9] N. F. Mott and H. S. W. Massey, *The Theory of Atomic Collisions* (Clarendon Press, Oxford, 1949), second edition, p. 40.

We have had to keep $\langle|H'|^2\rangle_{Av}$ inside the integral sign because it depends upon λ, λ', and θ. However, $\langle|H'|^2\rangle_{Av}$ is invariant under the substitutions $\lambda\rightarrow\lambda'$, $\lambda\rightarrow-\lambda$, etc., so that we can use the same methods as in V to simplify $G_iG_j-\bar{G}_i\bar{G}_j$. Computation shows that this factor in the integrand can be replaced by

$$2(\epsilon_+-\epsilon_-)g'(\rho,\lambda)g(-\rho,\lambda)g(\rho,\lambda')g(\rho,-\lambda')/\kappa\theta.$$

From (8), (54), and the expressions for the various factors we find

$$\frac{dD}{dt}=\frac{16\beta^4p_0^4(D_0-D)}{3c^6\hbar^7\kappa\theta}\int F(\lambda,\lambda',\theta)g'(\rho,\lambda)\times g(-\rho,\lambda)g(\rho,\lambda')g(\rho,-\lambda)d\theta d\rho d\lambda d\lambda'. \quad (55)$$

The integrals can be evaluated and yield (see appendix)

$$\frac{dD}{dt}=\frac{20\epsilon^4k_0^2\kappa\theta(D_0-D)\log(\kappa\theta\epsilon^{1.5}/\beta\mathfrak{H})}{9m^2c^4\hbar}. \quad (56)$$

Here $\epsilon=2.718$. The relaxation time due to the spin-current interaction is therefore

$$T=\frac{9m^2c^4\hbar}{20\epsilon^4k_0^2\kappa\theta\log(\kappa\theta\epsilon^{1.5}/\beta\mathfrak{H})}. \quad (57)$$

It is interesting to note that this relaxation time is dependent slightly upon the field strength $\mathfrak{H}$. For a magnetic field of 5 oersteds and a temperature of 293°K, (57) gives 8×10^{-7} second.

VII. INTERACTION WITH IMPURITIES

In this section we shall estimate the relaxation caused by the presence of impurity atoms in the metal. If the impurity is paramagnetic, the electron spins in the conduction band can interact by means of a spin-spin interaction, as in (35), where the second electron is in a bound state of the impurity atom. The interaction energy will be of the order of magnitude of β^2/a^3 within the region of the atom, where a is of the order of the atomic dimension. One can then show that, except for a numerical factor, the relaxation time due to such processes is given by

$$T\sim\hbar^3/mk_0N\beta^4f. \quad (58)$$

Here f is the fraction of paramagnetic impurity atoms in the metal. If f is 10^{-3}, (58) gives a value of 10^{-2} sec.

Relaxation can also be caused by the atomic electric fields of all impurity atoms by means of a spin orbit interaction, (24). The magnitude of this interaction energy will be $z\beta^2/a^3$, where z is the effective charge of the impurity atom as seen by a conduction electron. The relaxation time for such processes will therefore have the order of magnitude

$$T\sim\hbar^3/mk_0Nz^2\beta^4f. \quad (59)$$

For an impurity content of 10^{-3} and an effective charge z of say 3, an appropriate value which is sufficient to explain the contribution of impurities to the electrical resistance of metals, (60) gives a value of 10^{-3} sec. One can conclude that such impurity processes do not play an important role in electron paramagnetic relaxation.

VIII. CORRECTIONS TO THE RELAXATION TIMES

The preceding calculations were based upon the free electron model and the effects of binding to the crystalline lattice and the Coulomb interaction between the electrons were neglected. We will now take account of these effects in so far as they influence the spin susceptibility of the conduction electrons and the density of single particle states at the top of the Fermi distribution. We continue to assume that the single particle model is a valid approximation.

Let χ_0 and ρ_0 be the spin susceptibility and density of states for the free electron model without interactions, and let χ and ρ be the corresponding quantities when lattice, and exchange and correlation interactions are accounted for. One can then show that the relaxation times must be multiplied by the factor

$$(\chi/\chi_0)(\rho_0/\rho)^{2\text{ or }4}. \quad (60)$$

The 4 in the exponent applies to the calculations in V and VI, whereas the 2 applies to the others. The factor χ/χ_0 occurs because a larger susceptibility, and hence larger equilibrium value of D_0, means that the same number of electronic transitions will produce a fractional relaxation smaller by that same amount. A factor ρ_0/ρ occurs for each integration over the surface of the Fermi distribution, including the one in the derivation of the formula for transition probability.

Since a complete treatment of exchange and correlation effects has not been made to date, even in the single particle model, the numerical values of the factors in (60) are unknown. However, experimental data on susceptibilities and electronic specific heats seem to indicate that these factors are not very different from unity.

IX. CONCLUSION

The most important relaxation process of those considered is that due to the spin-current interaction in VI. The relaxation time of about 1 microsecond obtained for this process is at least two powers of ten shorter than the remaining ones, so that these latter processes may be neglected in comparison to the former. On the other hand, this figure is two or three powers of ten longer than the relaxation times characteristic of paramagnetic salts at room temperature.[10] One would therefore expect that a paramagnetic resonance in metals could be easily observed, and that a very narrow

[10] C. J. Gorter, *Paramagnetic Relaxation* (Elsevier Publishing Company, Inc., New York, 1947).

line of about 100 kc or 0.1 oersted in width would be seen. However, a number of investigators have looked for such a resonance, by both microwave and radio-frequency techniques,[11] and have failed to observe any resonance. It is at present difficult to explain these negative results. Yafet has shown that the energy of such a resonance would not be appreciably effected by interactions with the crystalline field.[12]

A possible explanation is that an interaction resulting in a relaxation time of 10^{-10} sec or less has been overlooked. One might suspect that second-order processes play a more important role than the first-order processes considered, as is actually the case in paramagnetic salts. However, this possibility can be ruled out by a simple argument. If one considers the various second-order calculations (double phonon emission and absorption, phonon Compton effects, simultaneous collision of two electrons and emission of a phonon, etc.), one observes that the relation of the second-order calculation to the first is similar in structure and magnitude to the corresponding relation in the theory of electrical resistance. Since second-order processes do not play an important role in electrical resistance, otherwise the linear dependence of resistance on temperature would not result, therefore second order processes do not play an important role in paramagnetic relaxation. The second-order processes which involve only the electron-electron interaction are not included in this argument, but it is unlikely that they are important.

Note added in proof: The metallic spin resonance has been observed[13] in Li, Na, and K at microwave frequencies. This recent success in finding the resonance resulted from the use of sufficiently small particle sizes, of the order of a micron or less, so that excessive width of such a resonance due to alternating current skin effects was reduced. Line widths of about 15, 80, and 120 oersteds were observed, respectively, in Li, Na, and K. These widths are probably caused by the modulation of the microwave field as seen by the electrons when they diffuse toward or away from the surface. More narrow lines would result, then, if even smaller particles or lower frequencies are used.

The author wishes to thank Professor Charles Kittel for proposing this problem and for helpful suggestions.

APPENDIX

We wish to compute the following integral occurring in (55):

$$\int F(\lambda, \lambda', \theta) g'(\rho, \lambda) g(-\rho, \lambda) g(\rho, \lambda') g(\rho, -\lambda') d\theta d\rho d\lambda d\lambda'.$$

Consider first the contribution of the first term of $F(\lambda, \lambda', \theta)$. We make the substitutions

$$y = (p_0 \cos\theta / 2\mu\kappa\theta)(\lambda + \lambda'), \quad x = \rho p_0 \sin\theta / \mu\kappa\theta,$$
$$y' = (p_0 \cos\theta / 2\mu\kappa\theta)(\lambda - \lambda'), \quad \alpha = \beta\mathfrak{H} \cot\theta / 2\kappa\theta.$$

Hence,

$$d\rho d\lambda d\lambda' = (2\mu\kappa\theta / p_0 \sin\theta)(\mu\kappa\theta / p_0 \cos\theta)^2 dx dy dy'.$$

The first term is, therefore,

$$\left(\frac{\mu\kappa\theta}{p_0}\right)^2 \int [(y^2+\alpha^2)^{-\frac{1}{2}} + (y'^2+\alpha^2)^{-\frac{1}{2}}] \frac{(9\cos^3\theta + 2\cos\theta\sin^2\theta) dx dy dy' d\theta}{(e^{x+y+y'}+1)(e^{-x-y-y'}+1)(e^{-x+y+y'}+1)(e^{x+y-y'}+1)(e^{x-y+y'}+1)}.$$

Because of the symmetry in y and y', we can consider only one of the terms in square brackets and then multiply by 2. We make the further substitutions

$$r = x + y', \quad s = x - y'$$

so that

$$dx dy' = \tfrac{1}{2} dr ds.$$

We obtain

$$\left(\frac{\mu\kappa\theta}{p_0}\right)^2 \int \frac{(9\cos^3\theta + 2\cos\theta\sin^2\theta) dr ds dy d\theta}{(y^2+\alpha^2)^{\frac{1}{2}}(e^{r+y}+1)(e^{-r-y}+1)(e^{r-y}+1)(e^{s+y}+1)(e^{-s+y}+1)}.$$

The integration in s gives

$$2y/(e^{2y}-1).$$

The integral in r gives

$$e^{2y}(e^{2y}-1-2y)/(e^{2y}-1)^2.$$

We obtain, therefore

$$\left(\frac{\mu\kappa\theta}{p_0}\right)^2 \int_0^{\pi/2} \int_{-\infty}^{\infty} \frac{(9\cos^3\theta + 2\cos\theta\sin^2\theta) x e^x (e^x - 1 - x) dx d\theta}{(x^2+4\alpha^2)^{\frac{1}{2}}(e^x-1)^3}.$$

[11] Unpublished research.
[12] Y. Yafet, Phys. Rev. **85**, 478 (1952).
[13] Griswold, Kip, and Kittel, Phys. Rev. **88**, 951 (1952), and private communication.

The integration in x can be manipulated to give

$$\int_0^\infty \frac{x^2e^x dx}{(x^2+4\alpha^2)^{\frac{1}{2}}(e^x-1)^2}.$$

If one takes advantage of the smallness of α, this integral can be shown to have the value $\log(\epsilon/\alpha)$, where $\epsilon=2.718\cdots$. We have then

$$(\mu\kappa\theta/p_0)^2\int_0^{\pi/2}(9\cos^3\theta + 2\cos\theta\sin^2\theta)\log(2\epsilon\kappa\theta\tan\theta/\beta\mathfrak{C})d\theta.$$

This integration can be carried out and gives finally

$$(20/3)(\mu\kappa\theta/p_0)^2\log(\kappa\theta\epsilon^{0.65}/\beta\mathfrak{C}).$$

We will now compute the contribution of the second term in $F(\lambda, \lambda', \theta)$. We make the same substitution and analysis as before and obtain similarly

$$\left(\frac{\mu\beta\mathfrak{C}}{p_0}\right)^2\int_0^{\pi/2}\int_0^\infty \frac{(9\cos^3\theta\cot^2\theta-\cos^3\theta)x^2e^x dx d\theta}{(x^2+4\alpha^2)^{\frac{1}{2}}(e^x-1)^2}.$$

If we integrate in x, observing as before the smallness of α for most all θ, this expression is

$$(\mu\kappa\theta/p_0)^2\int_0^{\pi/2}(9\cos^3\theta-\cos\theta\sin^2\theta)d\theta.$$

We obtain on further integration in θ

$$(17/3)(\mu\kappa\theta/p_0)^2=(20/3)(\mu\kappa\theta/p_0)^2\log\epsilon^{0.85}.$$

On inserting the sum of the two terms we have evaluated into (55), we obtain (56).

PHYSICAL REVIEW VOLUME 89, NUMBER 4 FEBRUARY 15, 1953

Induced Conductivity in Luminescent Powders. II. AC Impedance Measurements*

HARTMUT KALLMAN, BERNARD KRAMER, AND ARNOLD PERLMUTTER
Physics Department, New York University, Washington Square, New York, New York
(Received September 24, 1952)

Alternating current measurements of the impedance changes induced by ultraviolet, infrared, x-ray, and gamma-ray irradiation in (Zn:Cd)S luminescent powders are reported. These results are in agreement with previously reported dc measurements, and indicate that the observed impedance changes are primarily due to the change of the electron density in the conductivity band. Whereas the capacity changes show a monotonic increase, the Q values (X/R) show a pronounced minimum with increasing intensity. A model consisting of radiation sensitive and nonsensitive powder portions is proposed, and theoretical calculations based on such a model are shown to be in agreement with most of the experimental results. This ac measurement technique can be used to measure small exciting intensities (down to almost 1/1000 erg/sec cm²).

1. INTRODUCTION

IN a previous investigation[1] of the conductivity induced in luminescent type materials (in powder form) by ultraviolet radiation it was found that a non-ohmic relationship between the induced current and the applied field existed at all voltages except when the highest field strengths were used. Similar non-ohmic relationships were found in later experiments in which x-rays were used as the exciting radiation. With light excitation the powders are not uniformly excited and this nonuniform excitation is certainly responsible for at least part of the non-ohmic relationship observed. The x-rays used for these experiments penetrated these thin layers relatively uniformly; nevertheless, similar strong non-ohmic relationships were observed and this indicates that this non-ohmic characteristic is inherent to the powder structure. Since conductivity experiments with single crystals[2,3] irradiated with x-rays showed an ohmic relationship, this supports the idea that the non-ohmic characteristics are inherent to the grain structure.

With these results in mind it is assumed here, as a working hypothesis, that the powder has to be considered as an inhomogeneous system. Some parts of the powder sample (grain boundaries and air spaces) remain highly resistive even under strong excitation, while other parts, especially the interior of the grains, become highly conductive under excitation, much more than observed from dc measurements of the total resistance. To test this idea it was decided to duplicate many of the conductivity measurements with powders under ultraviolet, infrared, and high energy particle radiation using an alternating current field of low field strength instead of a dc field and measuring the effective resistive and reactive components of the impedance, hoping, in this way, to detect the true conductivity of the single grains.

Somewhat similar ac measurements have been reported by Garlick and Gibson,[4] who have thoroughly

* This work was supported by the Signal Corps Engineering Laboratories, Fort Monmouth, New Jersey.

[1] H. Kallmann and B. Kramer, Phys. Rev. **87**, 91 (1952).

[2] H. Kallmann and R. Warminsky, Ann. Physik **4**, 57 (1948) and **4**, 69 (1948); see also J. Fassbender, Ann. Physik **6**, 33 (1950) and R. Warminsky, Ph.D. thesis, Berlin Tech. Univ. (1948) (unpublished).

[3] H. Kallmann, Signal Corps Engineering Report E-1036 (Fort Monmouth, New Jersey) (unpublished).

[4] G. F. J. Garlick and A. F. Gibson, Proc. Roy. Soc. (London) **A188**, 485 (1947).

investigated the apparent change in dielectric constant and conductance of such luminescent powders in the frequency range of 0.1 to 10 megacycles. Their interpretation of such measurements is based upon a model in which the trapped electrons, assumed to be capable of remaining trapped while moving distances over 1000 times the inter-atomic spacing, are responsible for the impedance changes observed. de Groot[5] reports some ac measurements on luminescent powders and attributes the impedance changes to the electrons in the conductivity band; his measurements, however, are not extensive enough to confirm his interpretation.

The results of the ac measurements on luminescent powders reported in this paper are completely in agreement with the previously reported dc conductivity measurements[1] if, as assumed above, the inhomogeneity, that is, the relative insensitivity of parts of the powder to external radiation, is taken into account. This can be strikingly seen from the results obtained by the addition of infrared light during or after ultraviolet excitation. Corresponding to the observed initial dc current stimulation followed by current quenching, the ac measurements show an increase and then a decrease in the capacitance change values.

In our inhomogeneous system the impedance changes observed are ascribed to the fact that certain portions of the powder remain relatively nonconducting while other portions, especially the interior of the grains may become highly conductive (many electrons in the conduction band) under the influence of exciting radiation. Such a system could be treated theoretically by assuming the sample to be composed of some dielectric medium in which are embedded particles whose conductivity depends on the exciting radiation. The important feature of such a matrix is the increase of capacity to a saturation value with increasing excitation since the particles, when conductive, effectively decrease the spacing between the electrodes. The Q of such a system would be large (for a perfect dielectric) at low excitation, decreasing when the radiation sensitive particles become slightly conductive, and rising to a high value again when the particles become very conductive under strong excitation. Such an inhomogeneous system would exhibit an infinite dc resistivity; this is not in contradiction with the dc measurements since a resistivity $>10^{12}$ ohm-cm was obtained if the field strength was of the same value as that used in the ac measurements ($\sim$100 volt/cm).[6]

Since the computation of the impedance of such an inhomogeneous system would entail the use of various unknown parameters involving the shape and size of the particles as well as their spacing in the dielectric and would still be only an approximation, a very simplified model composed of layers of radiation sensitive portions alternating with high resistance radiation nonsensitive layers will be used. The high resistive layers essentially represent the high resistance grain boundaries and the air spaces between the grains while the radiation sensitive ones represent the interior of the grains. Such a layer model shows all the characteristic features of the above-described inhomogeneous system, and can be easily shown (see appendix) to be equivalent to two condensers in series, one of which is shunted by a radiation sensitive resistance. As this resistance decreases with increasing excitation, the effect of the capacitance in parallel with it becomes increasingly negligible, and finally only the capacitance of the nonconductive layer remains, which means the effective capacitance of the entire sample has increased. Increasing the intensity of excitation further can cause no further changes in the capacitance, and a saturation value is obtained. The effective resistive component of the impedance, however, shows no such monotonic change with intensity. As the radiation sensitive layer becomes slightly conducting, the shunt resistance decreases, and the effective series resistance of the sample increases. With much larger intensities this layer simply becomes a very low resistance in series with the nonconducting layer; the resistive component of the total impedance decreases. Thus, on the basis of this simple layer model, the resistive component may vary greatly and show a decided maximum. Since the capacitance changes measured are less than 100 percent, the ratio of the reactive to the resistive component of the impedance should show a definite minimum. The measurements described below show both the capacitance increase (also observed by Garlick and Gibson) and the predicted minimum of the "Q" value.

It should be noted that the inhomogeneous system described above is subject to at least two modifications which can also be illustrated by the layer model. First, the so-called nonconductive portion may also be somewhat responsive to the exciting radiation; this would lead to a nonsaturated change in capacitance as well as a Q value at higher radiation intensities that remained lower than the unexcited Q value. Secondly, the radiation may not be absorbed uniformly throughout the powder thickness. This is certainly true for ultraviolet radiation at around 3660A because of strong absorption in some of these samples as well as scattering in the powder. This effect tends to spread out the variation of capacitance and Q with intensity without changing the basic characteristics of such dependence curves.

On the basis of this simple layer model the following formulas (see appendix) for the capacitance change and Q values as functions of the exciting intensity are obtained for uniform excitation:

$$\Delta C = C - C_0 = \epsilon A d_2 / \{(d_1+d_2) \times [d_1+(d_1+d_2)\omega^2\epsilon^2/\gamma^2 I^2]\}; \quad \text{(A5)}$$

$$Q = (\omega\epsilon/\gamma I)(1+d_1/d_2)+\gamma I(d_1/d_2)/\epsilon\omega. \quad \text{(A7)}$$

[5] W. de Groot, Physica **12**, 402 (1946).

[6] The high dc photoconductivity occurs only at high field strengths where the nonconductive layers are bridged.

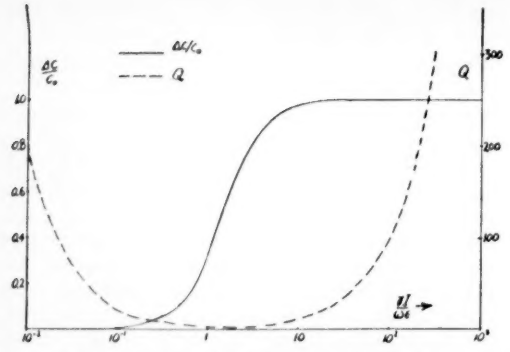

FIG. 1. Theoretical curves showing the capacitance change and Q value *versus* exciting intensity ($d_1=d_2$).

Curves showing relations (A5) and (A7) are given in Fig. 1 for $d_1=d_2$.

For nonuniform excitation the total impedance may be written as (see appendix)

$$Z=(d_2/d_0\Lambda\alpha\omega\epsilon)(\tan^{-1}\{(\omega\epsilon/\gamma I)(e^{\alpha d_0}-1)/[1+e^{\alpha d_0}(\omega\epsilon/\gamma I)^2]\}) - j(d_0/\Lambda\omega\epsilon)\{1-(d_2/2\alpha d_0^2)\times\ln[(\omega^2\epsilon^2+\gamma^2I^2)/(\omega^2\epsilon^2+\gamma^2I^2e^{-2\alpha d_0})]\}. \quad \text{(A11)}$$

The ΔC and Q curves obtained from (A11) are shown in Figs. 2 and 3, again for $d_1=d_2$. Since (A5), (A7), and (A11) give ΔC and Q as functions of I/ω, the curves should be shifted to lower intensities with decreasing frequencies.

This proposed representation does not delve into an atomistic explanation of the nonconductive behavior of the grain boundaries, but it is believed that both the grain boundaries and the air space may be considered as capacities with very high interior resistances only slightly influenced by radiation, while the grains themselves provide the capacities with an excitation sensitive interior resistance. The nonconductive portion may also be partly due to electron depleted barrier layers near the electrodes, but the capacitance saturation obtained at high exciting intensities indicates that such layers are not important in the powders investigated.

In Sec. 2 the experimental results of such impedance measurements are described. These investigations deal with the impedance changes induced in the powders by ultraviolet, x-ray, and gamma-radiation, as well as the influence of infrared radiation.

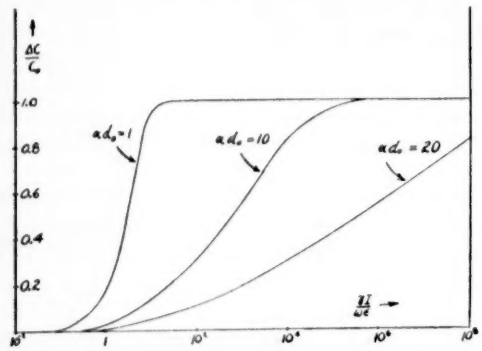

FIG. 2. Theoretical curves showing the capacitance change *versus* exciting intensity for various values of αd_0 ($d_1=d_2$).

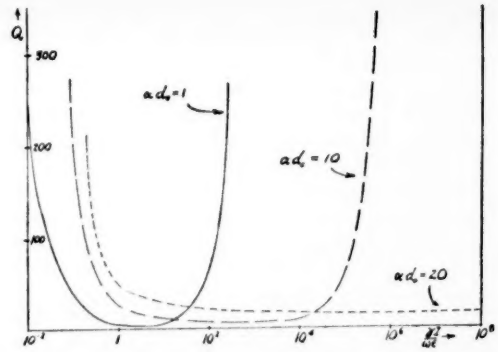

FIG. 3. Theoretical curves showing the Q values *versus* exciting intensity for various values of αd_0 ($d_1=d_2$).

2. EXPERIMENTAL RESULTS

Experiments were performed at 1 kc using a General Radio Bridge 650-A and at 4.6 kc, 80 kc, and 800 kc with a Boonton 160-A Q-meter.

The powders investigated were deposited on a piece of conductive glass, and a thin aluminum foil (about 4 cm² in area) was used as the other electrode. This method of preparing powders for conductivity measurements has previously been described.[1]

A. Results with Ultraviolet Irradiation

The ultraviolet source used was of the mercury discharge type (maximum energy around 3650A); about 10 microwatts per square centimeter was incident upon the powder. Calibrated neutral filters were used to decrease this intensity by a factor of up to 10^5.

In Fig. 4 the capacitance change and Q values for powder L (19 mg/cm²), a long-persistence [Zn:Cd]-

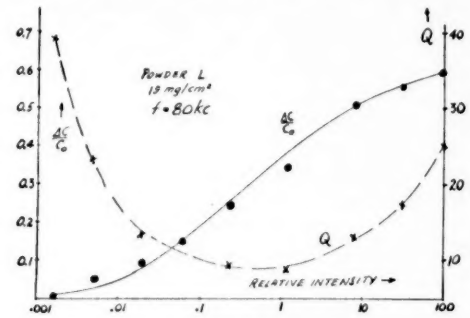

FIG. 4. Capacitance change and Q values for powder L *versus* ultraviolet exciting intensity.

S(Pb, Ag) material, are shown over a range of exciting intensities at a frequency of 80 kc. The characteristics of these curves are similar to those of the theoretical curves. The capacitance change curve shows the typical slow rise, relatively steep middle portion, and tendency toward saturation with increasing intensity, while the Q curve shows the pronounced minimum to be expected from the theoretical calculations.

Figures 5 and 6 show the capacitance change and Q values of powder L (19 mg/cm^2) at frequencies of 4600 cycles, 80 kc, and 800 kc for various values of exciting intensities. The capacitance change curve clearly shows how an increase in frequency shifts the curves to increased intensities; thus, a value of $\Delta C/C_0$ of 20 percent is reached at about $(5\times10^{-5})I_{\max}$ for $f=4600$ cps, at about $(10^{-3})I_{\max}$ for $f=80$ kc, and at $(10^{-1})I_{\max}$ for $f=800$ kc. For this powder at these intensities, the saturation part of the curve can be seen only at low frequencies, while the slow increase from zero capacitance change can be seen best at the highest frequency. At 80 kc, the intermediate frequency, the $\Delta C/C_0$ curve

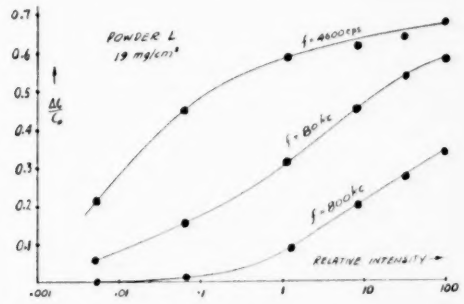

FIG. 5. Cpacitance change values for powder L *versus* ultraviolet exciting intensity at various applied frequencies.

is approximately linear with log$I$ over most of the measured range, similar to the curves obtained by Garlick and Gibson.

Although the theoretical calculations lead to the same value for $\Delta C/C_0$ at given values of I/ω, the experimental results indicate that the percentage change in I is considerably larger than the percentage change of ω to obtain the same capacitance change. The theoretical results were obtained by assuming ρ to vary inversely as I; if this dependence is changed to $\rho\propto 1/I^n$, where n is less than one, the theoretical curves would be in more accord with the measurements. In the results on dc measurements,[1] all powders showed a deviation from a linear relationship between the induced current and the exciting intensity; if the current density is expressed as $J=aI^n$, $n>1$ for the previously reported measurements. This is at variance with the relationship obtained from Fig. 5 where $n<1$ is a better fit for the experimental results. It may be that the shape of the dc current-intensity curves were considerably influenced by other factors, such as potential barriers and non-

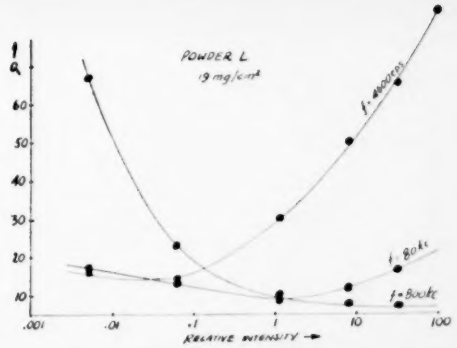

FIG. 6. Q values for powder L *versus* ultraviolet exciting intensity at various applied frequencies.

uniform field strength, which do not show up appreciably in the ac measurements. The theoretical calculations carried out previously[1] indicate that there are regions where $n>1$, $n=1$, and $n<1$.

Measurements of fluorescent emission (E) *versus* exciting intensity showed, in some of these powders, a dropping off from a linear relation at low intensities, indicating a relationship $E\propto I^n$, where $n>1$. Further investigations are being carried out to find explanations for these different behaviors.

Figure 6 shows the Q curves for powder L, and again the shift toward higher intensities with higher frequencies is easily noted. For the highest frequency used, 800 kc, the minimum of the Q curve is just reached, while at the lowest frequency (4600 cps), the minimum can just be seen at lowest intensities. The shifts are more difficult to determine because of the broadness of the curves; in addition, the Q values are probably not as accurate as the capacitance measurements.

Figure 7 shows the capacitance change and Q curves for powder N, a ZnS(Ag) long peristence luminescent powder of 26 mg/cm^2 thickness. The curve of $\Delta C/C_0$ *versus* the log of the exciting intensity is linear over a range of more than 5 orders of intensity magnitudes, and there is no sign of saturation. The departure from a straight line would probably be evident at both lower

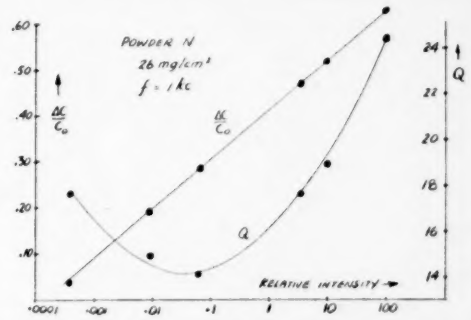

FIG. 7. Capacitance change and Q values for powder N *versus* ultraviolet exciting intensity.

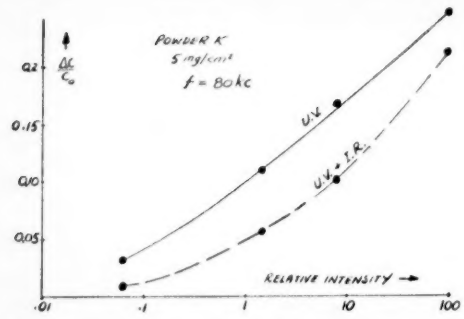

FIG. 8. Capacitance change values for powder K *versus* ultraviolet exciting intensity with and without infrared irradiation.

and higher frequencies. The Q curve shows the typical pronounced minimum.

Other $\Delta C/C_0$ and Q curves of other powders under ultraviolet excitation are shown and discussed together with ultraviolet plus infrared curves in the following section.

B. Results for Simultaneous Ultraviolet and Infrared Irradiation

The capacitance and Q values of these powders were measured when infrared irradiation was added to the ultraviolet excitation. The infrared source was a 250-watt heating lamp with a 7–56 Corning filter, and 1 milliwatt/cm² was incident upon the powder. The wavelength of the transmitted radiation was too long to excite the powder. In all powders measured, the equilibrium curves obtained with simultaneous infrared and ultraviolet radiation shifted as if the actual ultraviolet intensity were decreased; that is, a higher intensity was required to obtain a corresponding value of the ordinate. Thus, a definite "quenching" was observed, analogous to the current quenching observed with dc measurements. This shift is more pronounced at lower ultraviolet intensities; again in agreement with previous dc measurements where quenching always increases with decreasing excitation intensity. Figures 8 and 9 show the shift due to addition of infrared irradiation in the capacitance change and Q curves for a 5 mg/cm² sample of powder K; a [Zn:Cd]S(Pb, Cu, Ni) short-persistence luminescent powder. From Fig. 8 it can be seen that at high intensities the quenching is about 50 percent while at low intensities it is almost 90 percent, which checks with the dc measurements (where quenching is defined as $[(J_{UV}-J_{UV+IR})/J_{UV}]\cdot 100$ percent).

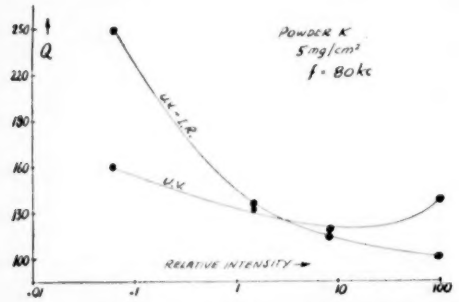

FIG. 9. Q values for powder K *versus* ultraviolet exciting intensity with and without infrared irradiation.

The Q curve (Fig. 9) also shows the same shift, but in addition there is now a definite change in the value of the minimum Q; this value changing from about 120 to 100, when infrared radiation is added to the existing ultraviolet excitation. Since an effective change of intensity should only shift the curve, this change in the minimum value indicates that the infrared radiation has some additional effect on the "nonconducting" portion of the powder; an effect not taken into account in the theoretical models proposed above.

Previous dc measurements have shown that a current stimulation occurs before quenching sets in when infrared irradiation is added to ultraviolet excitation, especially for powder K. Such a stimulation is difficult to note when using a Q meter or impedance bridge because the stimulation peak is rather fast and some time is required to obtain an impedance measurement. It was definitely noted, however, that at lower intensities (to the left of the cross-over point between the two Q curves of Fig. 9), the application of additional infrared irradiation caused a momentary decrease in the Q value before the equilibrium value was reached, while at intensities to the right of this point, first an increase and then a decrease in the Q value was noted. Thus, the infrared induced stimulation peak observed in dc measurements is also found in these impedance investigations. Since the infrared irradiation acts to empty the filled traps, the change in Q should be monotonic if only the filled traps influence the impedance measurements; if, however, the effects are primarily due to electrons in the conduction band, a nonmonotonic change may occur,

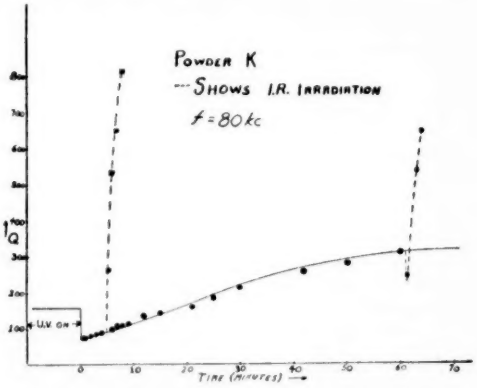

FIG. 10. Q values for powder K *versus* time after cessation of ultraviolet excitation showing effect of infrared irradiation at two points on decay curve.

since first there is an increase and then a decrease of the electron density in the conduction band due to the stimulation and overriding quenching effects of the infrared irradiation. This stimulation effect is more easily noted after ultraviolet excitation (during the decay period) and will be discussed below.

C. Measurements after Ultraviolet Excitation

Figure 10 shows the Q values obtained with powder K during and after ultraviolet excitation. As soon as the ultraviolet excitation is removed there is a sharp drop in the Q value followed by a slow build up to a Q value much higher than the Q with UV excitation. Thus the Q values again pass through a minimum, this time due to the decrease in conductivity with time rather than with intensity; effectively the Q values change from the extreme right-hand point of the UV curve (Fig. 9) through the minimum to the extreme left. The effects of infrared irradiation after ultraviolet excitation

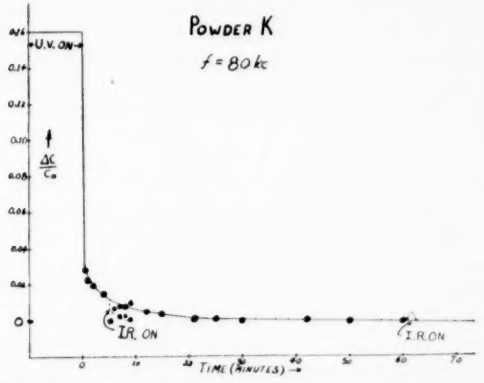

FIG. 11. Capacitance change values for powder K *versus* time after cessation of ultraviolet excitation showing effect of infrared irradiation at two points on decay curve.

are indicated by the dotted lines and are completely similar to the dc effects. Immediately after the ultraviolet radiation has been stopped, the effect of the infrared is to further decrease the conductivity. However, further along the decay curve (about 1 hour after ultraviolet excitation), a temporary decrease, then an increase of Q can be noted. This corresponds to a stimulation and subsequent quenching of the conductivity, respectively as in dc measurements. The stimulation is difficult to observe if the infrared is switched on at early portions of the decay curve; after longer time intervals the stimulation becomes more extended and can be noted on the Q meter.

The capacitance change (for this same sample) as a function of time after ultraviolet excitation is shown in Fig. 11. Corresponding to the fast decay of the conductivity a sharp decrease in the capacitance is seen. Infrared irradiation causes a further decrease in the capacitance if applied soon after ultraviolet excitation

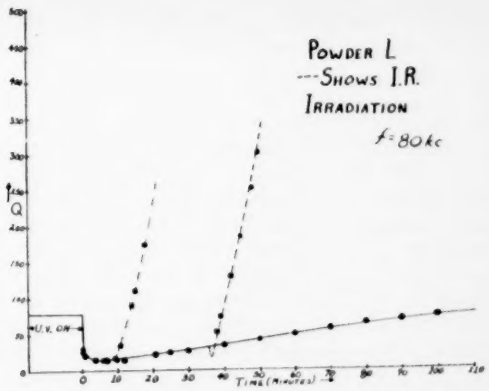

FIG. 12. Q values for powder L *versus* time after cessation of ultraviolet excitation showing effect of infrared irradiation at two points on decay curve.

has ceased, but if 1 hour elapses before infrared irradiation is applied, an increase in capacitance is noted. The latter is due to an increase of conductivity, corresponding to the decrease in Q seen in Fig. 10. Figures 12 and 13 show similar effects for powder L. Again, stimulation is observed only after a considerable time lapse after ultraviolet radiation has ceased. The decay of the capacitance change curve is considerably longer than that of powder K.

D. X-Ray and Gamma-Irradiation

Figures 14 and 15 show the effect of x-ray excitation on powder L at 80 kc.

X-ray experiments were undertaken to prove that the previously described results obtained with ultraviolet excitation are not primarily due to the nonuniform excitation of the powder. X-ray irradiation, although it excites these powders nearly uniformly (small α, Eq. (A9)), shows almost the same shape

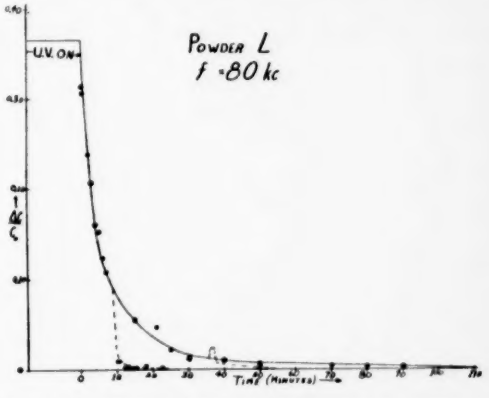

FIG. 13. Capacitance change values for powder L *versus* time after cessation of ultraviolet excitation showing effect of infrared irradiation at two points on decay curve.

of the $\Delta C/C_0$ and Q curves so that one can be sure that these effects are inherent to this type of material. X-rays of 50 kv were used, and intensities up to 300 r/min were obtained, which is roughly equivalent to the same amount of absorbed energy as in the light experiments. The $\Delta C/C_0$ curve shows a very sharp increase to its saturation value; this occurs over a range of about 2 magnitudes of intensity in comparison with about 3 orders of magnitude for the fastest rising curve for ultraviolet excitation. This is to be expected from the theoretical curves (Fig. 2), in which the smallest absorption (α) gives the steepest rise. Similarly, the Q curve is sharper than any of the other Q curves given above, again in agreement with the theoretical curves of Fig. 3.

Under gamma-irradiation, powder L evidenced a slow change in Q from over 1000 to 30 after a 150-minute exposure (irradiation of 10 r/hr). This gamma-irradiation corresponds to a very small ultraviolet excitation since the absorbed energy in the powder is of the order of 1/100 erg per second. The equilibrium Q value under gamma-irradiation would therefore correspond to the lowest intensity of Fig. 6. A similar slow build up in conductivity was noted in the dc measurements, where weak ultraviolet excitation was required for hours before an equilibrium current was reached, due to the fact that a large number of empty traps must be filled before an appreciable density of conduction band electrons becomes evident.

3. CONCLUSIONS

The above described experiments indicate that the changes of impedance induced by external radiation in (Zn:Cd)S powders can be essentially ascribed to a change in the density of electrons in the conduction band if the sample is considered to be an inhomogeneous material, a portion of which remains highly resistive even under strong irradiation. The observed impedance changes should, therefore, not be described as changes in the dielectric properties of the material, and the assumption of Garlick and Gibson of polarizable traps is not necessary, at least for these powders. It may be noted that the particular shape of the Q curve reported here has not yet been explained by the polarizable trap model. Such a shape could, to some extent, also be explained on the basis of nonuniform excitation without assuming an intrinsic inhomogeneity of the powder. From the x-ray experiments (Sec. 2, Part D) where the powders are uniformly excited and the Q curve has the same shape, it is concluded that it is the intrinsic inhomogeneity of the powder that is responsible for the shape of the Q curve.

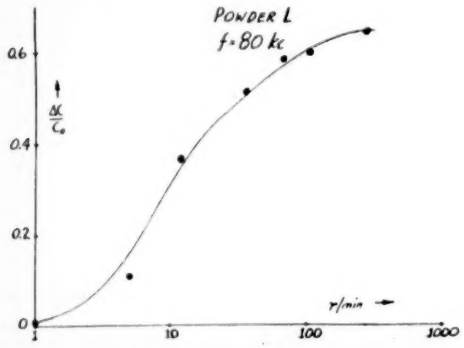

FIG. 14. Capacitance change for powder L values *versus* x-ray exciting intensity.

The close parallelism which was found between the radiation induced conductivity in dc measurements and the induced impedance changes in the ac measurements also strongly supports the above-mentioned conclusion. This parallelism is especially noticeable in the experiments where infrared light is directed at the powder after previous ultraviolet excitation. Corresponding to the observed dc current increase followed by a quenching there is first an increase, then a decrease in the capacitance (and a corresponding change in the Q value). If the impedance changes were due to electrons in traps, infrared irradiation would constantly decrease this amount, and there would be only a decrease in the capacitance and no such change in Q as found in Figs. 10 and 12.

Using the simplified layer model, an order of magnitude evaluation can also be made of the conductivity of the radiation sensitive portion. The result thus obtained is larger than that observed in the dc measurements (as is to be expected because of grain contact resistance), but is about the same as the experimental value found for single CdS crystals.[2,3]

APPENDIX

A. Uniform Excitation

If the powder can be considered to consist of a radiation sensitive portion and a permanently nonconducting portion, the impedance may be written as

$$Z=-j/\omega C_1+R_2/(1+R_2^2\omega^2C_2^2) \\ -jR_2^2\omega C_2/(1+R_2^2\omega^2C_2^2), \quad \text{(A1)}$$

since the arrangement described above is equivalent to two capacities in series.[7] C_1 is the capacitance of the nonconducting layer, C_2 is the capacitance of the radiation sensitive layer and R_2 is the shunt resistance of the radiation sensitive layer. If one considers the resistance of the conducting layer to vary inversely as the exciting untensity the impedance may be written as

$$Z=-jd_1/\omega\epsilon A+(d_1/\gamma IA)/(1+\omega^2\epsilon^2/\gamma^2I^2) \\ -(j\omega\epsilon d_2/\gamma^2I^2A^2)/(1+\omega^2\epsilon^2/\gamma^2I^2), \quad \text{(A2)}$$

where we have used $C_1=\epsilon A/d_1$; $C_2=\epsilon A/d_2$; $R_2=\rho d_2/A=d_2/\gamma IA$, and where A is the area, d_1 and d_2 are the thicknesses of the nonconducting and conducting layer

[7] See any textbook on electrical circuits.

respectively, and ϵ is assumed constant. Separating into real and imaginary components, the impedance may be written

$$Z=(d_2/A\gamma I)/(1+\omega^2\epsilon^2/\gamma^2I^2) -(j/\omega\epsilon A)\{[d_2/(1+\gamma^2I^2/\omega^2\epsilon^2)]+d_1\}. \quad \text{(A3)}$$

The apparent capacitance of the powder is obtained from the reactive part:

$$C=1/\omega X=\epsilon A/\{[d_2/(1+\gamma^2I^2/\omega^2\epsilon^2)]+d_1\}. \quad \text{(A4)}$$

The apparent change in capacitance of the powder is

$$\Delta C=C-C_0=(\epsilon Ad_2)/\{(d_1+d_2) \times[d_1+(d_1+d_2)\omega^2\epsilon^2/\gamma^2I^2]\}, \quad \text{(A5)}$$

where C_0 is the capacitance at zero intensity. The largest capacitance change obtainable (very large I) is

$$\Delta C_{\text{sat.}}=\epsilon Ad_2/d_1(d_1+d_2). \quad \text{(A6)}$$

The Q of the circuit (X/R) is

$$Q=(\omega\epsilon/\gamma I)(1+d_1/d_2)+\gamma I(d_1/d_2)/\epsilon\omega. \quad \text{(A7)}$$

Thus, Q becomes infinite for both $I=0$ and $I=\infty$, with a minimum given by

$$(\gamma I/\epsilon\omega)^2=(d_1+d_2)/d_1, \quad \text{(A8)}$$

at which point it has a value of $2[d_1(d_1+d_2)]^{\frac{1}{2}}/d_2$.

B. Nonuniform Excitation

If the incident radiation is strongly absorbed by the luminescent powder, there will be a nonuniform excitation throughout the powder. With x-rays, high energy beta-particles, and gamma-radiation such absorption is negligible and the powder can be considered uniformly excited. With ultraviolet or alpha-particle excitation, strong absorption sets in, and the layer of the powder facing the source is more strongly excited than the other side.

To consider the case of nonuniform excitation, the model again consists of N_1 nonconductive and N_2 conductive layers.

The impedance element of one layer of the radiation sensitive portion of the powder may be expressed as

$$dZ=dx/A(j\omega\epsilon+\gamma Ie^{-\alpha x}), \quad \text{(A9)}$$

where $A\epsilon/dx$ and $dx/\gamma Ie^{-\alpha x}A$ are the capacitance and resistance of the element considered; where the intensity of the radiation is assumed to fall off exponentially in the powder; and where x is the position of the layer. Each radiation insensitive layer has the same value as for uniform excitation and together have the impedance $1/j\omega C_1$. Therefore, the total impedance is

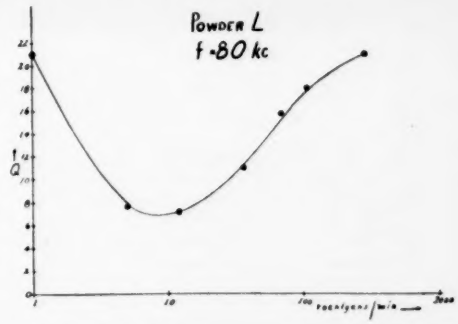

FIG. 15. Q values for powder L *versus* x-ray exciting intensity.

$$Z=(d_2/d_0A)\int_0^{d_0}dx/(j\omega\epsilon+\gamma Ie^{-\alpha x})+1/j\omega C_1, \quad \text{(A10)}$$

where $1/C_1=\sum 1/C_n$, for C_n the capacitance of each radiation insensitive layer. The integral is to be evaluated over the entire thickness of the powder (d_0); since the radiation sensitive portion is only the fraction d_2/d_0 of the entire sample, this factor must be placed in front of the integral. The integration is straightforward and yields

$$Z=(d_2/d_0A\alpha\omega\epsilon)(\tan^{-1}\{(\omega\epsilon/\gamma I)(e^{\alpha d_0}-1)/ [1+e^{\alpha d_0}(\omega\epsilon/\gamma I)^2]\}) -(jd_0/A\omega\epsilon)\{1-(d_2/2\alpha d_0^2) \times\ln[(\omega^2\epsilon^2+\gamma^2I^2)/(\omega^2\epsilon^2+\gamma^2I^2e^{-2\alpha d_0})]\}. \quad \text{(A11)}$$

For α approaching zero (negligible absorption) this equation reduces to (A3) above. However, the intensity dependence of Q and $\Delta C/C_0$ for intermediate values of intensity is considerably different from that obtained from (A3) for considerable absorption $(\alpha\gtrsim 1/d_0)$.

If, instead of using the simple model consisting of a conducting and nonconducting portion of the powder, these portions are differentiated by having different conductivities (γ_1 and γ_2) differing by at least several orders of magnitude, Eq. (A10) becomes

$$Z=(d_1/d_0A)\int_0^{d_0}dx/(j\omega\epsilon+\gamma_2Ie^{-\alpha x}) +(d_1/d_0A)\int_0^{d_0}dx/(j\omega\epsilon+\gamma_1Ie^{-\alpha x}). \quad \text{(A12)}$$

The change in the $\Delta C/C_0$ and Q curves using (A12) instead of (A10) would be that (1) the $\Delta C/C_0$ curve would not reach a saturation value but would continue to increase with intensity; (2) the Q curve, after going through a minimum, would tend to reach a maximum and then to decrease again at higher intensities.

Drift Velocity of Ions in Oxygen, Nitrogen, and Carbon Monoxide

ROBERT N. VARNEY*
Bell Telephone Laboratories, Murray Hill, New Jersey
(Received October 17, 1952)

The drift velocities of ions of the parent gas in oxygen, nitrogen, and carbon monoxide have been measured as a function of field strength to pressure ratio by techniques previously reported. Oxygen gave results similar to those in the rare gases reported previously. A log-log plot of drift velocity against E/p_0 in volts/(cm×mm Hg) starts with a slope near unity which gradually decreases to one-half at high values of E/p_0. The mobility, extrapolated to zero field and atmospheric pressure is 2.25 cm²/volt-sec. Nitrogen and carbon monoxide both show a novel characteristic; the drift velocity first rises with E/p_0 but reaches a maximum and actually decreases, then finally resumes a more normal rise with E/p_0 as described for oxygen. It is believed that at high E/p_0 the drift velocity is characteristic of N_2^+ ions and CO^+ ions, respectively. At low fields the ion in nitrogen is believed to be N_4^+. In CO the ion at low fields is believed to be CO^+, with $(CO)_2^+$ being formed at intermediate fields. The results are complicated by an additional ion which appears in the range of E/p_0 from 95 to 250 and which has a higher speed than the other ion. It is suspected of being C^+.

INTRODUCTION

THE apparatus for the present work has been described in detail in reference 1 and has been used previously to measure drift velocities of ions in the rare gases.[1,2] Briefly summarized, a field is applied between parallel-plate electrodes, and a pulse of electrons is released from the cathode by the radiation from an external spark of short duration. A typical Townsend avalanche results, and an exponential distribution of positive ions is left between the plates. The time needed (2 to 20 microseconds) to sweep out these ions is measured. The result, combined with the measured plate separation, yields the drift velocity.

The tube is thoroughly degassed until residual pressure readings are below 5×10^{-9} mm Hg, and highly purified gas from commercially available flasks (Airco) is then admitted. Liquid nitrogen cooling is continuously maintained on a connected trap. Pressures are read on a calibrated McLeod gauge.

The drift velocity is then plotted against E/p_0, the ratio of field strength to pressure, in a log-log form. The symbol p_0 is used to indicate that pressure readings are reduced to the corresponding value for 0°C. Also plotted is a graph of the mobility, defined as

$$\mu=(v\times p_0)/(760\times E),$$

as a function of E/p_0. At each value of E/p_0, readings of the velocity are taken with several values of p_0 spread over a range of a factor of 2, and with several values of X, the plate separation, spread over a range of a factor of 3. No significant changes in velocity are observed except as a function of E/p_0.

RESULTS

Figure 1 is the drift velocity plot for pure oxygen. It is seen to approach a slope of one-half at high E/p_0 and unity at low E/p_0 in accordance with the theory given by Wannier.[3] The slope of one-half is characteristic of a repulsive force field of fixed radius surrounding the gas molecules, hence frequently described as hard-sphere repulsion. The slope of unity at low E/p_0 leads

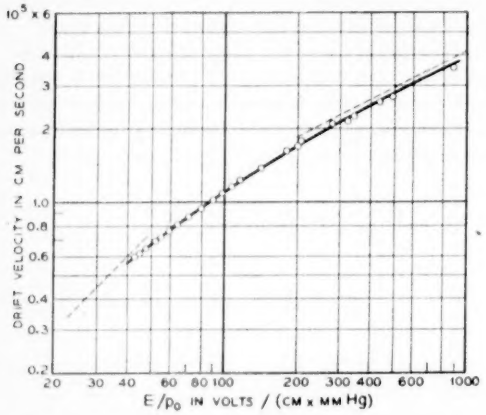

FIG. 1. Log-log plot of drift velocity of ions in oxygen *vs* E/p_0. The dashed lines are drawn at slopes of one-half and one, respectively.

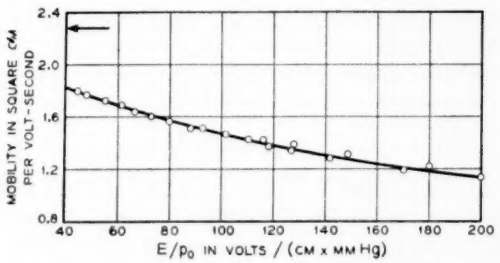

FIG. 2. Mobility of ions in oxygen plotted against E/p_0. The arrow at the left indicates an approximate extrapolated value for E/p_0 of zero. The arrow is at $\mu=2.30$ cm²/volt-sec, although any value between 2.15 and 2.35 is reasonably suitable.

* Now at Washington University, St. Louis, Missouri.
[1] J. A. Hornbeck, Phys. Rev. **83**, 374 (1951); **84**, 615 (1952).
[2] R. N. Varney, Phys. Rev. **88**, 362 (1952).
[3] G. H. Wannier, Phys. Rev. **83**, 281 (1951).

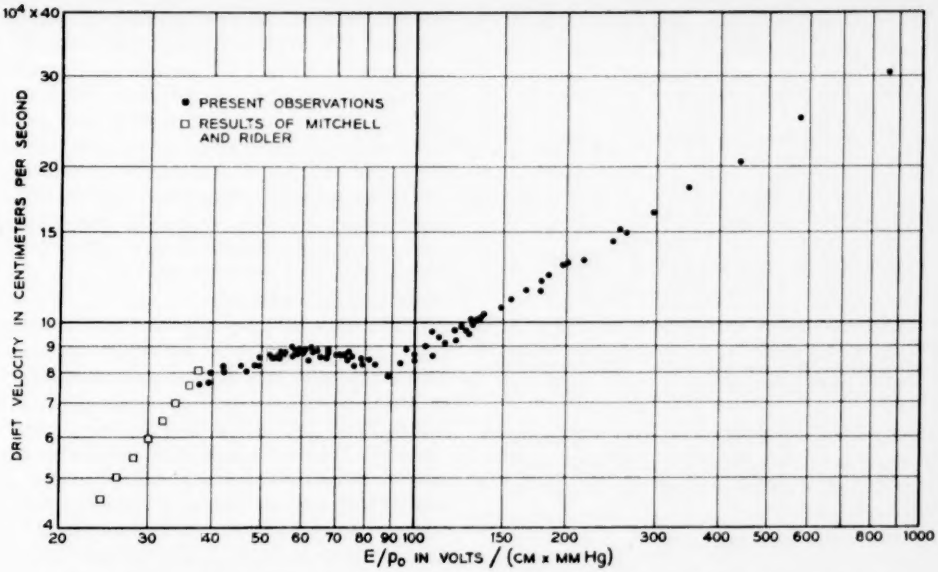

FIG. 3. Log-log plot of drift velocity of ions in nitrogen *vs* E/p_0. Actual points are shown to indicate the precision of observations. Mitchell and Ridler's results at low E/p_0, adjusted by the writer from 20°C to 0°C, are shown. It is proposed that at low E/p_0 the ions are largely N_4^+, at high E/p_0 they are N_2^+, and in the intermediate region each ion changes many times from N_2^+ to N_4^+ and back.

to the constant mobility characteristic of all ions in this range. Figure 2 shows the mobility *vs* E/p_0 for oxygen. The extrapolated mobility for E/p_0 of zero is estimated at 2.25 ± 0.1 cm²/volt-sec. Both Figs. 1 and 2 are similar to typical results in the rare gases.

The drift velocities of ions in nitrogen and in carbon monoxide are shown in Figs. 3 and 4, plotted logarithmically as before against E/p_0. Both graphs differ notably from the oxygen result in that after a preliminary rise in drift velocity with E/p_0, the velocity drops by several percent as E/p_0 grows. Finally, after an appreciable further increase in E/p_0, the drift velocity resumes a more uniform growth with E/p_0 at a rate approaching a slope of one-half on the log-log plot. The anomalous region of decreasing velocity with increasing E/p_0 ranges from E/p_0 of 60 to 88 in nitrogen and 100 to 150 in carbon monoxide. In nitrogen, however,the lower bound of abnormal behavior might be set as low as E/p_0 of 38 upon consideration of the mobility *vs* E/p_0 plot in Fig. 5. The limits in carbon monoxide may be regarded as extending from E/p_0 of 90 to 170 if the criterion for abnormal behavior is that the log velocity *vs* logE/p_0 curve has a slope of less than one-half.

In carbon monoxide, an additional ion appears in the range of E/p_0 from approximately 95 to 250. The pattern on the oscilloscope characteristic of this second and faster ion is considerably less sharp in form. Hence it is likely that this type of ion is not formed by the initial electron avalanche within the very short time interval of its duration, but rather is formed as a by-product of the other ions as they are swept out by the applied field. The drift velocity is correspondingly less clearly readable, and the scatter of points in Fig. 4 for the fast ion is a consequence. No similar ion is found in nitrogen.

The mobility *vs* E/p_0 curves for nitrogen and carbon monoxide are shown in Figs. 5 and 6. The curve for nitrogen is seen to join with that of Mitchell and Ridler.[4] (Mitchell and Ridler's results are presumed to refer to a temperature of 20°C and their pressures have been adjusted to 0°C both in E/p and μ.) The curve

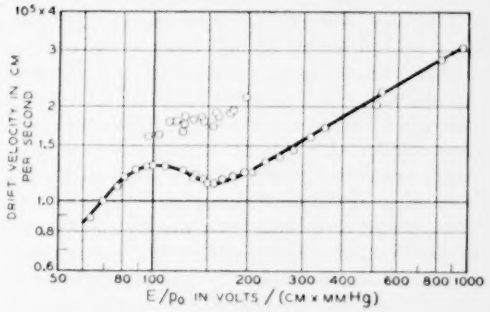

FIG. 4. Log-log plot of drift velocity of ions in carbon monoxide *vs* E/p_0. A second ion with higher velocity appears at values of E/p_0 between 95 and 250 volts/(cm×mm Hg). Since its oscilloscope pattern is less sharp, this drift velocity is less certain. Judgment errors in the case of the faster ion probably tend to give too low a velocity reading.

[4] J. H. Mitchell and K. E. W. Ridler, Proc. Roy. Soc. (London) **146**, 911 (1934).

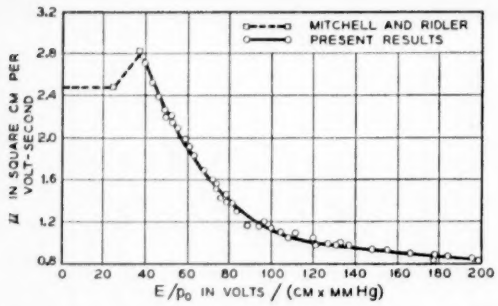

FIG. 5. Mobility of ions in nitrogen as a function of E/p_0. The present results join suitably with the older observations of Mitchell and Ridler at low E/p_0. Their results have been adjusted from 20°C to 0°C for this plot.

for carbon monoxide suggests a very much lower mobility at E/p_0 of zero for ions in this gas than for ions in nitrogen. The significance of this observation is discussed at a later point.

ANALYSIS OF RESULTS

By use of a previously established equation derived by Hornbeck and Wannier,[5] the molecular cross sections for the ions at high E/p_0 values are obtained shown in Table I. The low value for oxygen indicates that charge exchange occurs less readily in this gas than in N_2, CO, or A (from reference 1), a result that is not altogether surprising for oxygen because of its known electron affinity. The values for N_2 and CO are more nearly comparable with values for Ne and A.

The Langevin formula may be applied to predict zero field mobilities in these gases if several assumptions are made. The first assumption concerns the chemical formula of the ion; the second concerns the nature of the ion-molecule force interaction. In this paper, only two force laws will be considered. On the one hand, only attractive polarization forces may be used if the hard sphere repulsion is assumed to be negligible. On the other hand, the repulsive forces may be included by using the hard sphere radius obtained from Table I. The results are shown in Table II. (It was pointed out in references 2 and 5 that the repulsive forces treated in this way include the action of charge exchange.)

Examination of Table II and of the various drift velocity and mobility curves suggests certain possible explanations for the present results.

In oxygen, it is difficult to believe that any ion other than O_2^+ is present despite the poor agreement in mobility values shown in the table. The appearance potential[6] for O^+ in O_2 demands that electrons have 6 to 8 ev more energy to produce this ion than to give O_2^+. Such ions as O_3^+ and O_4^+ have been omitted from the table since they were not observed in the mass spectroscope by Luhr[7] with basic experimental conditions equivalent to the present ones.

[5] J. A. Hornbeck and G. H. Wannier, Phys. Rev. **82**, 458 (1951).
[6] H. D. Hagstrum, Revs. Modern Phys. **23**, 185 (1951).
[7] O. Luhr, Phys. Rev. **44**, 459 (1933).

Consider next the results obtained with nitrogen. The drift velocity curve (see Fig. 3) may be divided into three parts which will be referred to here as regions of high, intermediate, and low E/p_0. The two extremes are each reasonably similar, as far as they go, to curves obtained for single types of ions in the rare gases, but since the two sections are only connected by the decidedly unusual intermediate section which has a negative slope, it may be judged that a different ion exists at high fields than at low fields. In the intermediate region, a transition from one type of ion to the other must be occurring.

If the high field and the low field sections of the curve are each extended as might be guessed from comparison with rare gas curves, the high field section is seen to lie at lower velocity values than the low field section. This gives a first clue to the nature of the ions since it is reasonably well established that the slowest ion in a gas is the one which will exchange charge most readily with the gas molecules. Charge exchange always occurs with maximum cross section in any gas for the ion which becomes the normal gas molecule after exchange, in this case N_2^+;[8] in fact at the low energies involved, charge exchange occurs only for this case. Hence the ion at high E/p_0 is believed to be N_2^+.

The ion at low E/p_0 values is not likely to be N^+ since considerably more energy is needed to produce N^+ from N_2 than to give N_2^+. It is more probable that it is N_4^+, produced by attachment of N_2 gas molecules to the N_2^+ ions formed in the initial electron avalanche. Such attachment has been observed by Luhr[7] and the ions identified in the mass spectrograph.

It remains to explain the presence of only one observed velocity, especially through the transition region. The mechanism invoked is the reversible reaction system

$$N_2^+ + N_2 \rightarrow N_4^+, \quad N_4^+ + N_2 \rightarrow N_2^+ + 2N_2.$$

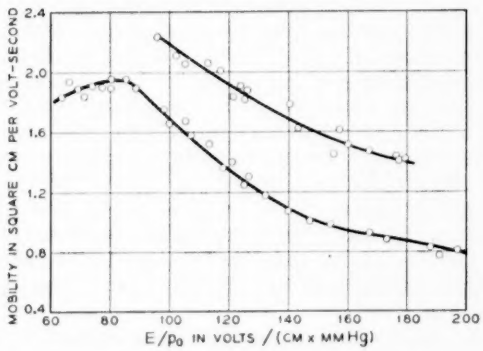

FIG. 6. Mobility of ions in carbon monoxide as a function of E/p_0. The mobility fails to show the very great increase with decreasing E/p_0 seen in Fig. 5 in nitrogen. The behavior of CO may thus be compared with that of N_2 only in the high field regime. The upper curve is for the faster ions suspected of being C^+ and observed only in a limited range of E/p_0 values.

[8] See, for example, H. Kallmann and B. Rosen, Z. Physik **61**, 332 (1930).

At low E/p_0, the reaction proceeds in the direction of the first equation by attachment, and detachment is much slower. At high E/p_0, N_4^+ might not even form, but any N_4^+ ions so formed break up rapidly by collision according to the second equation, which is now dominant. The necessary and sufficient condition that only one drift velocity be observed is that the mean free path for at least one of the above reactions be much less than the drift space. That is, at low E/p_0, the free path for the reaction $N_2^+ \rightarrow N_4^+$ is short, and at high E/p_0, the free path $N_4^+ \rightarrow N_2^+$ is short. In the intermediate region, each ion undergoes a long series of attachments and detachments giving, as a result, the average single observed velocity. If the interchanges were too infrequent, a measurable spread in drift velocity would be observed, because of the arrival of ions at the cathode with various histories. There are in fact some 10^4 collision free paths between the electrodes, so that if the attachment or detachment occurred only in one collision out of every 100 to 500, the spread in arrival times would be less than about 10 percent, and hence unobservable (a slight spread amounting to 10 percent is always present because of diffusion and pulse width).

TABLE I. Molecular cross sections of O_2, N_2, and CO at high E/p_0.

Molecule	Cross section
O_2	0.79×10^{-16} cm²
N_2	1.23
CO	1.45

In carbon monoxide, a similar analysis is applicable. At high fields, the ion is probably CO^+ since in CO gas this ion should have the largest charge exchange cross section and the smallest drift velocity. It may be noted that at high E/p_0 the CO and the N_2 drift velocity curves are nearly superposable. Since CO and N_2 bear many chemical and electronic resemblances to one another, it may be assumed that the nearly corresponding drift velocity curves indicate corresponding ions. Hence, the assumptions of N_2^+ ions and CO^+ ions at high E/p_0 mutually support one another.

At low E/p_0 the drift velocity curve in CO falls appreciably below the curve in nitrogen; in fact it may even be possible that the low E/p_0 region coincides with an extrapolation of the observed curve at high E/p_0. Finally, the low mobility in CO at low E/p_0 and the agreement of the zero field mobility seen in Table II combine to suggest that CO^+ is also the ion present in the low E/p_0 regime.

The transition region in CO, if it is to bear any relationship to the experimentally similar one in nitrogen, must then be governed by the attachment-detachment reactions

$$CO^+ + CO \rightarrow (CO)_2^+, \quad (CO)_2^+ + CO \rightarrow CO^+ + 2CO,$$

with the added provision that the first reaction occurs most favorably at an E/p_0 value above zero with the reverse reaction favored by a still higher E/p_0 value. Finally, since still another ion is observed but only in the intermediate E/p_0 band where this presence of $(CO)_2^+$ ions is likely, an irreversible disruption of this ion following the equation

$$(CO)_2^+ \rightarrow C^+ + CO_2$$

is suggested. There is evidence of deposition of carbon on the cathode and of accumulation of CO_2 in the liquid nitrogen trap. It must be emphasized that the scope of possibilities in carbon monoxide is considerably greater than in nitrogen rendering the present hypothesis notably more speculative.

TABLE II. Calculated and experimental zero-field mobilities of ions in O_2, N_2, and CO.

Gas	Assumed ion	Mobility without repulsive force	Mobility with repulsive force	Experimental mobility at zero field
O_2	O^+	5.37	...	2.25[a]
O_2	O_2^+	2.75	2.78	
N_2	N^+	3.42	...	2.49[b]
N_2	N_2^+	2.80	2.17	
N_2	N_3^+	2.55	...	
N_2	N_4^+	2.42	...	
CO	CO^+	2.19	1.58	1.6[a]
	$(CO)_2^+$	1.89	...	
	CO_2^+	1.93	...	
	C^+	2.82	...	

[a] Extrapolated from present data.
[b] From Mitchell and Ridler (reference 4).

CONCLUSION

The drift velocity curves in nitrogen and carbon monoxide have disclosed a definitely new and unexpected behavior of ions in these gases. The observations may have far reaching influence on the analysis of other observations, covering glow phenomena, afterglow, and catalysis. The hypotheses advanced to explain the observations must await further mass spectrographic studies for their confirmation but seem at the moment to offer the only reasonable ones.

The writer is particularly indebted to Dr. D. J. Rose for many discussions and suggestions without which the present results would have been unobtainable. He is also indebted to Dr. J. A. Hornbeck who designed and constructed the original apparatus. Dr. G. H. Wannier and Dr. K. G. McKay were most helpful in criticizing the manuscript. Mr. F. D. Dolezal contributed valuably to the experimental work as technical assistant.

A Cloud-Chamber Study of the Scattering of Fast Neutrons in Oxygen*

J. P. CONNER†
Rice Institute, Houston, Texas
(Received September 29, 1952)

Neutrons with an energy of 14.1 Mev have been scattered in oxygen gas, and the recoil oxygen nuclei observed in a cloud chamber operated at a pressure of ½ atmosphere. Recoils from elastically scattered neutrons were resolved from recoils due to inelastic scattering. The results indicate a strong asymmetry in the angular distribution of elastically scattered neutrons; the angular distribution has maxima at 0°, 80°, and 180° and minima at 60° and 130°. Within a factor of 2, the angular distribution for the inelastically scattered neutrons is symmetrical. The probability per unit energy interval that the oxygen nucleus will be left excited is about 5 times as large at 6-Mev excitation as at 12-Mev.

The cross section of oxygen for 14.1-Mev neutrons is 0.7×10^{-24} cm² for elastic scattering, 0.5×10^{-24} cm² for inelastic scattering, and 0.4×10^{-24} cm² for disintegration.

EXPERIMENTAL APPARATUS AND PROCEDURE

MONOENERGIC 14.1-Mev neutrons were produced in the Rice Institute Cockroft-Walton accelerator using the $H^3(d,n)He^4$ reaction. Targets were tritium absorbed in zirconium[1] with a thickness of about 300μ g/cm². The Cockroft-Walton was operated at about 160 kv, and the unresolved beam containing about 80 percent molecular ions was used. An aperture 5 mm in diameter was placed over the target to define the beam so that the size of the neutron source would be small. The cloud chamber was operated on a cycle of about 70 seconds with an electronic timer, which also pulsed the Cockroft-Walton ion source such that no neutrons were produced until the chamber became sensitive.

The cloud chamber was 24 cm in diameter and was placed with its center 32 cm from the neutron source at 90° to the beam. Stereoscopic photographs were taken with a single camera by photographing one direct view and one image reflected from a front surface mirror. The stereoscopic angle was 20°. The film was observed by removing the cloud chamber and projecting the images on the developed film through the same optical system including the camera. A white screen placed in the position of the chamber was then adjusted until both images of a track coincided; the coincident images gave the true length and orientation in space of the track.

The stopping power of the gas in the chamber was determined by placing a polonium alpha-particle source inside the chamber. The range[2] of the Po alpha-particles was taken to be 3.82 cm. The source was enclosed in a small cylinder the end of which was covered with a shield which could be moved with a small magnet from outside the chamber. At the beginning, in the middle, and at the end of each roll of film, 5 frames were taken of the alpha-particle tracks.

An upper limit for the fraction of neutrons which were scattered by surrounding equipment, the floor, etc., and then entered the chamber was obtained by observing the planes of the two forked-tracks from disintegrations produced by the neutrons. The initial direction of particles from a disintegration must be coplanar with the direction of the neutron initiating the disintegration; but, because of scattering of the charged particles, some tracks due to unscattered neutrons may appear noncoplanar. From the measurements, 80 percent of the neutrons came from within 10° of the direction to the source. The glass chamber wall (⅜ in. thickness) would scatter only 12 percent of the neutrons coming from the source, and most of the scattering would be at very small angles.

The chamber was refilled with 99.5 percent pure oxygen gas each day of the operation to be sure that the chamber filling had a known composition. Water only was used as the vapor in the chamber so that there would be no problem in identifying the tracks.

RESULTS

About 2300 recoil oxygen nuclei on about 450 pictures were measured. The true length of a recoil was taken to be the total length of the track less the width of the track. Recoils were measured down to a length of 0.1 cm, although a few between 0.1 and 0.2 cm may have been missed. It is felt that recoils with lengths greater than 0.2 cm were observed with 100 percent efficiency. The track lengths were estimated to 0.01 cm, and the angles were measured to 0.5°.

Figure 1 is a plot of the number of recoils observed as a function of the track length in certain angular intervals. The ordinate of a point is the number of tracks in a 2 mm track length interval. Points are plotted every mm of track length and so each track is counted twice, once in each plotted point adjacent to it in length. The limits of the angular intervals were chosen such that the recoils from elastically scattered neutrons were divided into 10 equal energy intervals. The short heavy vertical lines on the abscissa in Fig. 1 show the expected length of recoils corresponding to excitation of O^{16} to

* Supported by the U. S. Atomic Energy Commission.
† U. S. Atomic Energy Commission Predoctoral Fellow. Present address: Physics Division, Los Alamos Scientific Laboratory, Los Alamos, New Mexico.
[1] A. B. Lillie and J. P. Conner, Rev. Sci. Instr. **22**, 210 (1951).
[2] H. A. Bethe, Revs. Modern Phys. **22**, 213 (1950).

the amount indicated. Known excited states in O^{16} occur at 6.05, 6.13, 6.9, 7.1, 10.5, 10.8, and 11.2 Mev and perhaps at 8.6 and 9.5 Mev. In addition there are 5 states between 12.44 and 13.24 Mev.[3]

The range-energy relation for oxygen nuclei and the stopping power of the gas in the chamber must be known in order to calculate the expected track length of a recoil corresponding to a particular energy. The range-energy curve was obtained from results of Lillie.[4] The stopping power was determined from the length of Po alpha-particle tracks and was found to be 0.193 for the alpha-particles. A small correction to this figure was needed because the stopping power of hydrogen present in the water vapor was not the same for the fast alpha-particles and the relatively slow oxygen recoils. The corrected value of the stopping power for oxygen recoils was 0.197. Values of the stopping power of hydrogen were taken to be 0.35 for the oxygen nuclei and 0.20 for the alpha-particles.[5]

Elastic Scattering

One may see from Fig. 1 that recoils due to elastic scattering were resolved from those due to inelastic scattering; therefore, it was possible to obtain an angular distribution for elastically scattered neutrons. Angular intervals were chosen such that the total solid angle of the scattered neutrons was divided into 20 equal parts. The number of neutrons per unit solid angle was then plotted as a function of the angle of neutron scattering in the center-of-mass system. In order to include tracks due only to elastic scattering, recoils were counted which had a track length within 0.8 mm of the calculated track length. If the plane formed by the track and the incident neutron direction was at an angle greater than 45° to the horizontal, the tracks were not counted. The resulting angular distribution is given by the open circles in Fig. 2.

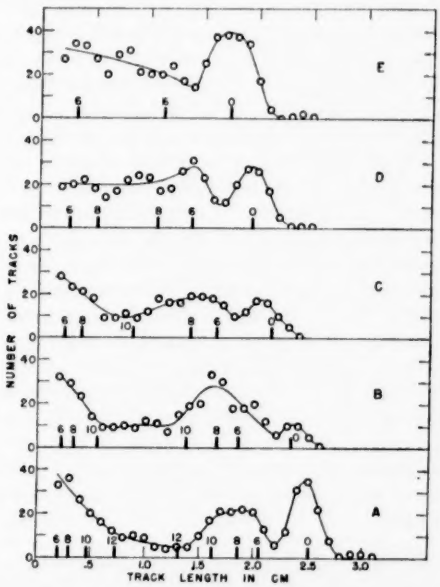

FIG. 1. Plot of number of tracks as a function of track length for tracks up to an angle of 45° in the laboratory system. Tracks due to inelastic scattering cannot take place at angles greater than 48°. The angular intervals of (*A*), (*B*), (*C*), (*D*), and (*E*) are 0° −18.4°, 18.4° −26.6°, 26.6° −33.2°, 33.2° −39.2°, and 39.2° −45.0°, respectively. The heavy short lines on the abscissa indicate the calculated lengths of tracks corresponding to excitation of the oxygen nuclei to an energy of 0, 6, 8, 10, and 12 Mev.

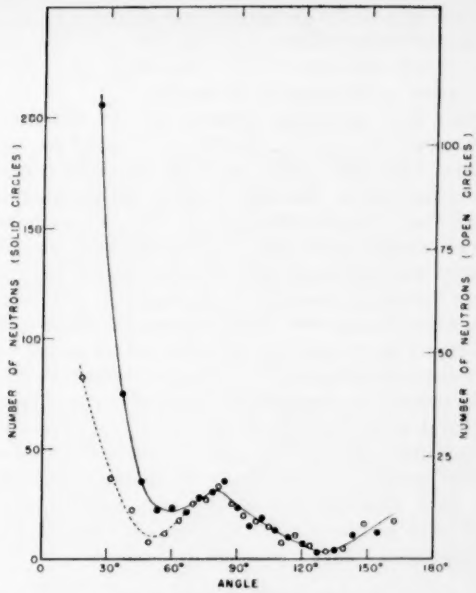

FIG. 2. Angular distribution of the elastically scattered neutrons. The ordinate is the number of neutrons per unit solid angle plotted as a function of the scattering angle in the center-of-mass system. The two methods of obtaining the angular distribution are indicated by the two kinds of points. In each case, the ordinate gives the number of recoil tracks counted.

At small angles this method is subject to large errors in measuring the angles of the recoils. Large angle scattering of the neutrons gives long oxygen recoils, and, therefore, accurate length and angle measurements, while small angle neutron scattering produces short recoils, whose direction cannot be determined as accurately. The data were considered in another way which took advantage of the fact that the length measurements were more accurate than the angle measurements for short tracks. The tracks due only to elastic scattering in all angular intervals were added together, and then the number of tracks with lengths between the calculated track lengths were plotted as the solid circles in Fig. 2. Again the plane formed by the track and the incident neutron was required to be within 45°

[3] Hornyak, Lauritsen, Morrison, and Fowler, Revs. Modern Phys. **22**, 291 (1950).
[4] A. B. Lillie, Phys. Rev. **87**, 716 (1952).
[5] C. M. Crenshaw, Phys. Rev. **62**, 54 (1942).

of the horizontal. This second type of plot is the same as that obtained with an ion chamber and differential pulse-height analyzer in the cases where no inelastic scattering or disintegration takes place.

Note that agreement between the two methods of obtaining the angular distribution is good at large angles. The solid circles are more accurate at small scattering angles. The curves show minima at about 55–60° and at 130° with maxima at 0°, 80°, and 180°. Other measurements with neutrons of about the same energy scattered from lead have indicated a large forward scattering, a minimum at about 25°, and a small maximum at about 40°.[6] Measurements at about 3-Mev neutron energy on several elements show a pronounced forward scattering with no indication of other maxima.[7]

In the present experiment the large forward scattering is about what is predicted for diffraction scattering.[8] The general shape of the curves is similar to that observed in stripping[9] and in the scattering of deuterons by light elements. It seems likely, because of the similarity in the angular distribution, that all these processes may have a common explanation.

Inelastic Scattering

As may be seen from Fig. 1, no angular distribution could be obtained for inelastically scattered neutrons involving a single excited state in oxygen. However, a rough average angular distribution from states with an excitation energy near 6 Mev was derived from the data by considering recoils with track lengths between those calculated for excitation energies of 5 and 7 Mev. The results indicate that the distribution is symmetrical within a factor of 2.

In order to obtain a probability distribution for excitation of oxygen nuclei, the angular distribution of inelastically scattered neutrons was assumed to be on the average symmetrical. Then by considering all tracks due to inelastic scattering, the probability per unit energy that the oxygen nuclei will be left excited was found to decrease by about a factor of 5 from 6-Mev excitation to 12-Mev excitation. This result is somewhat surprising since the density of excited states is expected to increase with increasing excitation. However, several units of angular momentum may be associated with the incident neutron, and the emitted neutron may be required to carry off several units also. The lower penetrability of lower energy neutrons from higher excited states could account for the experimental change in the excitation probability if most of the emitted neutrons had a large angular momentum.

CROSS SECTIONS

For determination of the cross sections the scattering in oxygen was compared to that in hydrogen by taking one roll of pictures with a gas mixture of 6.6 cm Hg hydrogen gas pressure and 12.7 cm Hg oxygen gas pressure in the chamber. The temperature during the run was 23.1°C at which the vapor pressure of water is about 2.2 cm Hg. Thus the ratio of number of atoms of hydrogen to that of oxygen was 0.61 during the time tracks were formed immediately after the expansion. To be counted a track was required to start at least 1 cm inside the light beam and 3 cm from the chamber walls. No measurements on length or angle of the recoils were made. The number of recoils counted was 166, the number of disintegrations was 53, and the number of recoil protons was 56. A value of 0.689 barn was taken for the cross section of hydrogen for 14.1-Mev neutrons.[10] The cross section of oxygen for neutron scattering was found to be 1.2 barns and for disintegration, 0.4 barn, giving a total of 1.6 barns, which is in good agreement with the value obtained from neutron transmission experiments.[11] The fact that some of the shortest tracks were not counted would make the value obtained for the total cross section slightly too small. Tracks of 0.1-cm length correspond to a neutron scattering angle of 9°. It is felt that most of the recoils over 0.1 cm long were counted. The ratio of elastic scatterings to inelastic scatterings as determined from measured tracks was 1.45. Only elastically scattered oxygen recoils are possible at laboratory angles greater than 48°, and at smaller angles the elastic scattering is well resolved from inelastic scattering. The cross section for elastic scattering is 0.7 barn, and that for inelastic scattering is 0.5 barn.

[6] Amaldi, Bocciarelli, Cacciapuoti, and Trabacchi, Nuovo cimento **3**, 15 and 203 (1946); International Conference on Fundamental Particles, Phys. Soc. (London), 97 (1947).

[7] Kikuchi, Aoki, and Wakatuki, Proc. Phys. Math. Soc. Japan **21**, 410 (1939); T. Wakatuki and S. Kikuchi, Proc. Phys. Math. Soc. Japan **21**, 656 (1939).

[8] G. Placzek and H. A. Bethe, Phys. Rev. **57**, 1075 (1940); Feld, Feshbach, Goldberger, Goldstein, and Weisskopf, Atomic Energy Commission Document NYO-636 (unpublished).

[9] S. T. Butler, Proc. Roy. Soc. (London) **A208**, 559 (1951).

[10] Poss, Salant, Snow, and Yuan, Phys. Rev. **87**, 11 (1952).

[11] L. S. Goodman, Argonne National Laboratory Report, ANL-4602 (1951) (unpublished); D. I. Meyer and W. Nyer, Los Alamos Report LA-1279 (1951) (unpublished).

The Measurement and Interpretation of the K Auger Intensities of Sn^{113}, Cs^{137}, and Au^{198}

C. D. Broyles,*† D. A. Thomas,*‡ and S. K. Haynes
Vanderbilt University, Nashville, Tennessee

(Received August 18, 1952)

Auger electron intensity measurements have been made on Cs^{137}, Au^{198}, and Sn^{113} with a magnetic lens spectrometer which is briefly described. K Auger yields for Ba and Hg of 0.130 ± 0.007 and 0.056 ± 0.008, respectively, were obtained. The K Auger electrons were resolved into three groups, K–LL, K–LX, and K–XY, according as two, one, or no L electrons were involved. The ratios of the intensities of the latter two to the K–LL were found to be for In 0.417 ± 0.016 and 0.076 ± 0.008; for Ba 0.40 ± 0.04 and 0.08 ± 0.02. The measured ratio of K–LX to K–LL for Hg was 0.71 ± 0.15. The relationship of these results to theory is discussed. A summary of measurements of K fluorescence yield and K Auger line intensity ratios is given. The Auger spectrum from Au^{198} indicates that K capture to Pt^{198} cannot occur in more than 0.5 percent of the disintegrations. A crude estimate of the L to K capture ratio for Sn^{113} indicates that it is not abnormally high.

I. INTRODUCTION

In the decay of radioactive nuclei, vacancies in the K electron shell are frequently created by internal conversion and by K capture. It is often desirable to determine the combined probability of these processes by counting the number of K vacancies produced per disintegration. As is well known,[1] a K vacancy is always filled by an electron from a shell of higher energy. The resulting energy can either be emitted as electromagnetic radiation (K x-rays), or be transferred to an electron in a shell of higher energy and eject it from the atom (K Auger electron).

If the K fluorescence yield w_K is known, a count of the empty shells can be made by a count of either the K x-rays or the K Auger electrons. The K fluorescence yield is defined as the number of K x-rays emitted per K vacancy. In the past, most of the measurements of vacancies in the K shells have been made by means of the K x-rays in spite of the difficulty in making absolute x-ray intensity measurements, because the K Auger electrons cannot penetrate the windows of most counters and ion chambers. A further difficulty is the lack of accurate knowledge of fluorescence yield, particularly for atomic number greater than fifty. This study attempts to increase the accuracy of our knowledge of the fluorescence yield for elements with atomic number greater than fifty, and to point out the possible usefulness of K Auger electron spectra obtained in a magnetic spectrometer with a very thin window.

II. EXISTING KNOWLEDGE OF THE FLUORESCENCE YIELD

A. Theoretical

Any complete and accurate theory of the Auger effect would be based on a proper theory of quantum electrodynamics, since the effect involves the interaction of several electrons.[2] Such a theory in a satisfactory state does not exist at present. Approximate theoretical treatments of the Auger effect, however, have been made by several workers. The first considerations were by Wentzel,[3] who found that the K Auger transition probability γ_A should be independent of the atomic number Z. Since the x-ray transition probability γ_X is approximately proportional[1] to Z^4, the K Auger yield should be approximately

$$a_K=\gamma_A/(\gamma_A+\gamma_X)=C_1/(C_1+C_2Z^4)=1/(1+bZ^4), \quad (1)$$

and the fluorescence yield

$$w_K=1-a_K=\gamma_X/(\gamma_A+\gamma_X)$$
$$=C_2Z^4/(C_1+C_2Z^4)=Z^4/(a+Z^4). \quad (2)$$

Wentzel did not make any numerical calculations, but Pincherle,[4] Burhop,[5] and Ramberg and Richtmyer[6] made use of the expressions derived by him to calculate values for some of the Auger transitions involving an

TABLE I. Transition probabilities per unit atomic time ($\times10^3$).[a]

Transition	Massey and Burhop Gold[r,s]		Burhop Silver[n,s]		Ramberg and Richtmyer Gold[n,f]		Pincherle[n,s]	
K–L_IL_I	1.74		2.54		2.02		2.50	
K–L_IL_{II}	9.52		2.88		2.36			
		18.73		8.65		6.82		8.81
K–L_IL_{III}	9.21		5.77		4.46			
K–$L_{II}L_{II}$			2.43					
				8.91		1.41		1.88
K–$L_{II}L_{III}$			6.48					
K–$L_{III}L_{III}$			8.20		17.88		22.44	
K–LX							25.7	
K–XY							2.70	

[a] Unit atomic time is the period of the electron of the first Bohr orbit of hydrogen. r—relativistic; n—nonrelativistic; s—screened hydrogen-like wave functions; u-unscreened hydrogen-like wave functions; f—Fermi-Thomas statistical model for potential field.

* U. S. Atomic Energy Commission Predoctoral Fellow.
† Present address: Sandia Corporation, Albuquerque, New Mexico.
‡ Present address: Rollins College, Winter Park, Florida.
[1] A. H. Compton and S. K. Allison, *X-Rays in Theory and Experiment* (D. Van Nostrand Company, Inc., New York, 1935), second edition, p. 482.
[2] N. F. Mott and I. N. Sneddon, *Wave Mechanics and Its Application* (Oxford University Press, London, 1948), pp. 338 and 342.
[3] G. Wentzel, Z. Physik **43**, 524 (1927).
[4] L. Pincherle, Nuovo cimento **12**, 81 (1935).
[5] E. H. S. Burhop, Proc. Roy. Soc. (London) **A148**, 272 (1935).
[6] E. G. Ramberg and F. K. Richtmyer, Phys. Rev. **51**, 913 (1937).

initial K shell vacancy. Table I lists these values as well as those of Massey and Burhop[7] discussed below. The first three calculations used nonrelativistic wave functions for the electrons. Pincherle used unscreened hydrogen-like wave functions in a Coulombian field; in this approximation the transition probability is completely independent of Z. He has made the most complete set of calculations of probabilities for the K Auger electrons, considering interactions of electrons in the K, L, M, and N shells. In the spectrometer used by the authors, the K Auger electrons are resolved into three groups or lines, which may be designated as the K–LL, K–LX, and K–XY Auger lines. Here X and Y are used to denote M, N, etc., shell electrons. Thus, the K–LX line is due to K–LM, K–LN, etc., Auger electrons, and the K–XY line is due to K–MM, K–MN, K–NN, etc., Auger electrons. It will be interesting to compare the observed ratios of intensities of these three lines to those obtained from the calculated probabilities of Pincherle. These calculated ratios are K–LL:K–LX:K–XY::1.00:0.716:0.103.

Burhop, using the more accurate screened hydrogen-like wave functions with effective nuclear charges for silver as determined by Slater,[8] has calculated the transition probabilities only for the K–LL interactions. Ramberg and Richtmyer used the still more accurate Fermi-Thomas statistical model for the potential field in calculating the K–LL probabilities for gold. The above three works are in reasonable agreement for the total probability of the K–LL interactions, the only ones common to the three calculations. The relative values of the probabilities of the various K–LL transitions are closely the same for Pincherle, and Ramberg and Richtmyer, though the absolute values of the latter are about twenty-five percent smaller. In a comparison of Burhop's and Pincherle's values, it is notable that the K–$L_{III}L_{III}$ probability of Burhop is only slightly more than one-third that of Pincherle, while his K–$L_{II}L_{II}$ and K–$L_{II}L_{III}$ values are several times greater than Pincherle's.

Relativistic calculations have been made by Massey and Burhop[7] for the K–L_IL_I, K–L_IL_{II}, and K–L_IL_{III} transition probabilities in gold and the K–L_IL_{II} probabilities in silver. The theoretical method, due to Møller,[9] on which Massey and Burhop base their work, considers only the two electrons directly involved in the transition. This is true of the nonrelativistic calculations also. In this method,[2] the charge and current densities associated with the electron transition to the K vacancy are written with the aid of the Dirac theory. The retarded potentials of the electromagnetic field due to the transition are then calculated from these densities. These potentials are then used as the perturbation in a first-order perturbation calculation of the transition probability for the ejection of another orbital electron. Using screened hydrogen-like wave functions, they find that the use of relativity increases the calculated Auger probability. For the transitions considered the increase is twenty percent for silver and almost one hundred percent for gold. In addition they find that the use of relativity decreases the calculated x-ray transition probability by a factor of 0.75 in gold so that the Auger yield for gold is slightly more than double the nonrelativistic value of 0.03. Using the K–LL Auger yields of Burhop, the relative values of the K–LL, K–LX, and K–XY yields of Pincherle, and corrections due to relativity based on their own calculations, Massey and Burhop constructed a theoretical curve of K Auger yield as a function of Z. Thus, the best theoretical curve available consists of a combination of several incomplete and approximate calculations. Values taken from this curve are $a_K=0.06$ for mercury, $a_K=0.15$ for barium, and $a_K=0.216$ for indium.

B. Experimental

Many workers have measured K fluorescence yields for low atomic number elements (Z less than fifty) by observation of incident and fluorescent x-ray intensities. The summaries of Arends[10] in 1935 and Backhurst[11] in 1936 cover the contemporary data very well. Backhurst points out that some persons have confused the K fluorescence yield with the number of K x-rays per orbital (K, L, M, etc.) vacancy. This confusion has occurred in summaries that include the results of Harms,[12] Balderston,[13] and Martin,[14] who report the latter quantity in their papers. The summaries of Compton and Allison,[1] Massey and Burhop,[7] Steffen *et al.*,[15] and Tellez-Plasencia[16] report the values of Harms, Balderston, and Martin as w_K. A summary by Stephenson[17] reports the work of Martin correctly, but omits the results of Harms, Locher,[18] and others, while Locher gives more weight to Harms' and Compton's[19] results than to Martin's. There is some reason for omitting the results of Berkey.[20] He finds a maximum value for w_K at $Z=42$. Such a maximum is not supported by any other experimental data or by theory. Backhurst suggests that this maximum is due to the fact that the incident x-rays used by Berkey may not have been monoenergetic. None of these summaries includes the several measurements of K yields made since 1940. These measurements include the only ones made for elements of high atomic number.[20a]

[7] H. W. S. Massey and E. H. S. Burhop, Proc. Roy. Soc. (London) **A153**, 661 (1936).
[8] J. C. Slater, Phys. Rev. **36**, 57 (1930).
[9] C. Møller, Z. Physik **70**, 780 (1931).
[10] E. Arends, Ann. Physik **22**, 281 (1935).
[11] I. Backhurst, Phil. Mag. **22**, 737 (1936).
[12] M. I. Harms, Ann. Physik **82**, 87 (1927).
[13] M. Balderston, Phys. Rev. **27**, 696 (1926).
[14] L. H. Martin, Proc. Roy. Soc. (London) **A115**, 420 (1927).
[15] R. Steffen *et al.*, Helv. Phys. Acta **22**, 167 (1949).
[16] H. Tellez-Plasencia, J. phys. et radium **10**, 14 (1949).
[17] R. Stephenson, Phys. Rev. **51**, 637 (1937).
[18] G. L. Locher, Phys. Rev. **40**, 484 (1932).
[19] A. H. Compton, Proc. Mag. **8**, 961 (1929).
[20] D. K. Berkey, Phys. Rev. **45**, 437 (1934).
[20a] *Note added during publication:* A recent book by Burhop, *The Auger Effect and Other Radiationless Transitions* (Cambridge

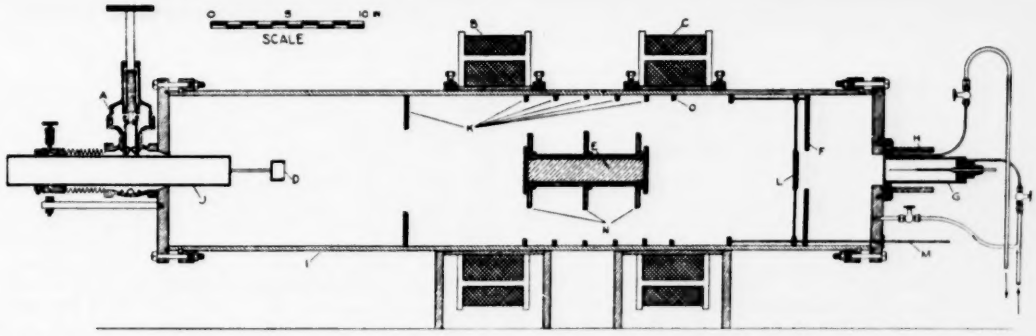

FIG. 1. Cross section of the lens spectrometer. (*A*) Vacuum lock, (*B*, *C*) lens coils, (*D*) source, (*E*) lead absorber, (*F*, *L*) ring baffles, (*G*) counter, (*H*) counter shield, (*I*) aluminum vacuum tank, (*J*) source holding tube, (*K*) anti-scattering baffles, (*M*) ring baffle position adjusting rod.

The experimental values support in a qualitative way the theoretical variation of a_K (or w_K) with atomic number, but none of the curves yet suggested, theoretical or semi-empirical, is in satisfactory agreement with all the available data. The relation

$$w_K = 0.957Z^4(0.984\times 10^6 + Z^4)^{-1}, \qquad (3)$$

given by Arends[10] and recommended by Tellez-Plascencia,[16] seems to give the best fit of those that have been proposed. A new and, it is hoped, complete and accurate summary is given in Sec. V.

In addition to the values of w_K, several measurements of the relative intensities of the various *K* Auger lines have been reported in the lireature. Ference,[21] using a magnetic spectrometer and Geiger-Mueller counter, studied the *K* Auger electrons from germanium. He reported the ratio K-LL:K-LX::1.00:0.31. He did not resolve the K-LL Auger electrons well enough to allow an accurate estimate of the ratio of the K-LL sublevels, but the shape of the line indicated three groups of electrons with the highest energy group being the most intense. He gave the ratios of intensities of these groups, to be taken as an order of magnitude only, as 1.00:0.26:0.26. In 1950 Bergstrom and Thulin,[22] using the same technique as the present authors, obtained the ratio K-LL:K-LX::1.00:0.48, for Cs^{133}. Steffen *et al.*,[15] using two isotopes of platinum, obtained average ratios of K-LL:K-LX:K-XY::1.00:0.86:0.025. Huber *et al.*[23] obtained the ratios K-LL:K-LX:K-XY::1.00:0.49:0.054 for silver and 1.00:0.44:0.056 for cadmium.[23a]

III. EXPERIMENTAL PROCEDURE

A. The Magnetic Lens Spectrometer

The lens spectrometer used in this work was designed for medium resolution and accurate relative intensities over a wide range of energies. A cross section of the vacuum chamber and coils is shown in Fig. 1, from which the many conventional details can be inferred. The chamber is unusual in that it is a machined aluminum cylinder (o.d. $10\frac{1}{4}$ in, i.d. $9\frac{1}{2}$ in.) with no welds whatever. The vacuum line is connected by an aluminum tube with a tapered pipe thread. Immediately before being screwed to a binding tightness both threads were painted with glyptal[24] lacquer. The end plates are each bolted to an aluminum collar, which fits snugly on the tube and is held fixed against a split ring which fits into a groove machined into the aluminum tube and projects $\frac{1}{8}$ in. above the surface of the tube.

The accuracy of intensity measurements is insured by the absence of any iron without four feet of the spectrometer, by coils which compensate for the earth's magnetic field to better than 0.1 percent,[25] by maintenance of a vacuum of 10^{-5} mm of mercury or better, and by the use of counter window thicknesses down to 10 μg cm^{-2}. Both Nylon and collodion windows supported by Lectromesh[26] have been used.

A gas flow ($\frac{2}{3}$ argon and $\frac{1}{3}$ ethylene) is continuously maintained through the counter at 4- to 6-cm pressure. It has been verified that at 6-cm pressure the counting rate is independent of electron energy up to 1.7 Mev. The counter voltage is adjusted to keep constant the pulse height as observed in an oscilloscope. It was found by observation of a constant strength source that this procedure maintained constant counter sensitivity even though, because of aging or change in gas pressure, the operating voltage varied as much as 10 percent.

University Press, Cambridge, England, 1952), pp. 44–51, has a more complete and more accurate summary. However, the values of Harms quoted are not for w_K as was pointed out by Backhurst, nor are those of Locher his preferred values. The summary in Section V attempts to rectify these and other minor errors and has a few additional references, some old and some published since 1950.

[21] M. Ference, Phys. Rev. **51**, 727 (1937).

[22] I. Bergstrom and S. Thulin, Phys. Rev. **79**, 539 (1950).

[23] O. Huber *et al.*, Helv. Phys. Acta **25**, 3 (1952).

[23a] *Note added during publication:* We had previously overlooked the work of Ellis and Flammersfeld (see references in Section V), who have measured the relative intensities of several of the lines for Bi ($Z=83$) using 180° magnetic spectrometers. From Ellis this K-LX to K-LL ratio is greater than 0.4 and from Flammersfeld it is at least 0.57.

[24] 1201 Glyptal lacquer, made by the General Electric Company.

[25] S. K. Haynes and J. W. Wedding, Rev. Sci. Instr. **22**, 97 (1951).

[26] Lektromesh, C. O. Jelliff Manufacturing Company, Southport, Connecticut.

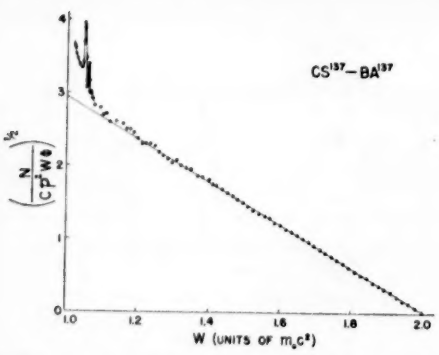

FIG. 2. Fermi-Kurie plot of the spectrum of the Cs^{137} source after subtraction of the 1.2-Mev beta-ray.

Each of the lens coils contains 1250 turns of 0.050 ×0.150 in. double Formex wire wound between sides composed of $\frac{3}{8}$ in. square copper tubing. A layer of tubing is also imbedded in the middle of each coil. Each coil is mounted on the main spectrometer tube by six adjustable screws. After the best possible visual alignment has been achieved, final adjustment is made with a low energy electron beam traversing the spectrometer without baffles. The compensating coil current is first adjusted so that the electron beam position is independent of beam energy.[25] Each lens coil is then adjusted individually until, as its current is varied, foci of all orders fall at the center of a fluorescent screen which replaces the counter.

The source of current for the lens coils is a 250-v, 6-kw dc generator controlled by an amplidyne. The input to the amplidyne is the amplified error signal between the desired current as set up on a type *K* potentiometer and the actual current as represented by the potential difference across a standard resistor. Negative feedback in the amplifier and a large *LC* filter keep current fluctuations of all frequencies to 0.1 percent or less.

The method of calculation of the electron trajectories from a point source in this spectrometer and the method of calculation of the ring baffle positions have already been described.[27] The theoretical resolution for a point source and a transmission (acceptance angle/4π) of 0.015 is $\Delta p/p=0.017$. In practice a resolution of 0.024 was obtained for the 3-mm diameter source of Au^{198} reported below. The run on In^{113} was made with different source diameter, coil geometry, and baffle arrangement, and the run on Cs^{137} with a different baffle arrangement which resulted in poorer resolution for these runs. Under optimum conditions the resolution for a source 6 to 8 mm in diameter is 0.030 for a transmission of 0.015.

[27] J. F. Perkins and A. W. Solbrig, Jr., Rev. Sci. Instr. **22**, 173 (1951).

B. Source Preparation

In order to measure intensities of electrons with energies between 20 and 80 kev one must have very thin uniform sources mounted on very thin backings. Vacuum distillation and electroplating are probably the only methods capable of giving sufficient uniformity. The former method was used for Cs^{137} and Au^{198} and could have been used for Sn^{113} if sufficient activity had been available. The Sn^{113} source was electroplated in order to conserve material.

The vacuum distillation chamber consists of a brass base covered with a "bell jar" about five inches high made from two-inch glass tubing. A $\frac{1}{16}$-inch rubber gasket with vacuum grease provides the seal between the base and the glass. Atmospheric pressure is sufficient to provide a good seal. The radioactive material is placed on a tantalum strip filament 0.001×0.050 in., which is supported by the filament leads through the base. The source film holder is mounted and centered 0.020 in. behind a radiation shield which is $\frac{1}{4}$ in. above the center of the filament. The source backing for the cesium and gold was of Formvar of thickness approximately 75 $\mu g\ cm^{-2}$ made conducting by a thin coat of evaporated aluminum.

For the cesium source a few drops of cesium chloride solution were dried on the filament. After evacuation the filament was heated to approximately 1000°C for one minute; the resulting source had an average thickness of 7 $\mu g\ cm^{-2}$ and a diameter of 3 mm. In the case of the gold source the strip of gold foil received from Oak Ridge was simply laid on the filament and after evacuation heated to about 1400°C for one minute. The resulting source had a thickness of about 20 $\mu g\ cm^{-2}$ and a diameter of 3 mm. The uniform density of autoradiographs and the lack of low energy tails on the lines in the spectrometer indicated, respectively, that the sources were uniform and thin.

The tin, enriched in Sn^{112} prior to irradiation,[28] was received in the form of 1 mg of SnO_2. It was reduced to metallic tin by being heated to approximately 1000°C in hydrogen gas. The metallic tin was dissolved in a hydrochloric acid plating solution by a procedure outlined by Sand.[29] A Formvar film of thickness less than 10 $\mu g\ cm^{-2}$ coated with about 75 $\mu g\ cm^{-2}$ of evaporated copper was mounted on an aluminum ring 1 in. in diameter. A piece of platinum gauze was placed so that a flat circular section about 0.5 cm in diameter was held $\frac{1}{8}$ in. above the film. After a positive potential of 1.12 volts with respect to the film had been applied, one to three drops of plating solution were dropped through the gauze so that they formed by surface tension a roughly cylindrical plating cell. The voltage was immediately raised to 1.9 volts. Plating continued for

[28] We are indebted to Dr. G. E. Boyd of Oak Ridge National Laboratory for the sample of Sn^{113} used.

[29] H. J. S. Sand, *Gravimetric Electrolytic Analysis* (Blackie and Son, Ltd, London and Glasgow, 1940), p. **72** (description of the method of A. C. Penney).

about 8 min at 1.5 ma. A uniform source of Sn^{113} having a thickness of much less than 0.1 mg cm^{-2} was plated out. The solution was neutralized with hydrazine hydroxide before the potential was disconnected. The source was washed by twenty additions and removals of two or three drops of distilled water. It should be emphasized that the potential must never be completely removed from the cell as long as the solution is acid. The acid solution demolishes the copper film rapidly and also tends to redissolve the tin already plated.

IV. EXPERIMENTAL RESULTS

A. Cs^{137}—Ba^{137}

The observations made were the time intervals required to accumulate a pre-set number of counts for different settings of the lens-coil current. The current was varied in steps of 0.2 percent in the region of the Auger and conversion electron lines, and in steps of 0.5 to 1.0 percent over the continuous spectrum. Eight runs were made across the desired current range alternately in the direction of increasing and decreasing current. A total of 3200 or more counts were obtained at each current setting. The current stability and counter sensitivity were checked at intervals by observation of the position and height of the *K* conversion line of the 661-kev gamma-ray.

The region below 320 kev was studied with a Nylon window of thickness approximately 18 μg cm^{-2}, mounted on Lektromesh. The low energy region was rerun with a 12 μg cm^{-2} Nylon window. This window gave the same counting rate as the 18 μg cm^{-2} window down to 15 kev. This indicates that the thicker window transmits completely above 15 kev. A 1.2-mg cm^{-2} Dacron window was used to study the region above 100 kev. Between 170 and 300 kev the ratio of the counting rates with the two windows was constant. This ratio gives the relative transmission of the two windows. The energy calibration was based on the *K* conversion line of the 661-kev[30] gamma-ray of the cesium. In analysis of the Cs—Ba data a Fermi plot of

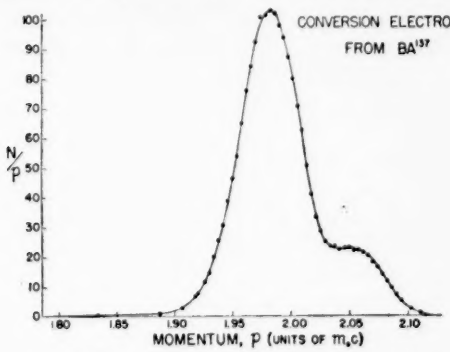

FIG. 3. *K* and *L* conversion lines of the 0.661-Mev gamma-ray of Cs^{137}.

[30] L. M. Langer and R. D. Moffat, Phys. Rev. **78**, 74 (1950).

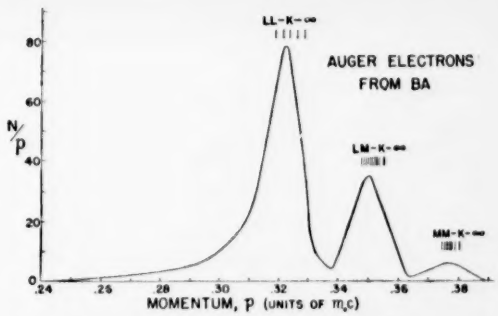

FIG. 4. Auger electrons of Ba from the Cs^{137} source.

the 1200-kev beta-group was made. This plot confirms the classification of this transition as second forbidden,[31] with spin change of 2, no parity change, and tensor interaction. By extrapolation of the straight line Fermi plot to low energy, this beta-group was subtracted from the 512-kev beta-group and the electron lines. Figure 2, a Fermi plot of the latter spectrum with the forbidden factor $C_{1T}=(W_0-W)^2+A(Z,W)(W^2-1)$,[32] gives a good straight line above 100 kev. The upward deviation below 100 kev is believed to be due to the inaccuracy for the forbidden factor[33] for small momenta and to the presence of the 90-kev beta-group of Cs^{134}. Since the Fermi plot was not a straight line in the region of the Auger electron lines, the continuous spectrum beneath these lines was obtained by a smooth joining of the continuous spectrum on each side of the lines.

Figures 3 and 4 show the conversion lines and Auger lines as counting-rate-per-unit-momentum interval *versus* momentum. The vertical lines above the Auger peaks mark the energy of the Auger electrons as calculated from x-ray spectra data given by Siegbahn.[34] For these calculations the energy levels of barium were used except for the level of the ejected electron. For this level, the value for the next higher atomic number element was used in order to approximate the doubly ionized state. The area beneath the curves is proportional to the intensity of the electrons producing the lines. The *K* to *L*–*M* conversion ratio of 4.64 measured by Graves *et al.*[35] was used to obtain the *K* conversion intensity from the measured total conversion intensity. The *K* Auger yield is the ratio of the *K* Auger electron intensity to the *K* conversion electron intensity. For barium this was found to be $a_K=0.130\pm0.007$. The ratios of the three *K* Auger lines were found to be $K\text{-}LL:K\text{-}LX:K\text{-}XY::1.00:0.40\pm0.04:0.08\pm0.02$. The probable errors given for the above values were obtained from a consideration of the statistical errors

[31] L. M. Langer and R. D. Moffat, Phys. Rev. **82**, 635 (1951).
[32] J. P. Davison, Phys. Rev. **82**, 48 (1951).
[33] M. E. Rose, of the Oak Ridge National Laboratory, is now calculating these factors accurately.
[34] M. Siegbahn, *Spektroskopie der Röentgenstrahlen* (Julius Springer, Berlin, 1931), p. 346.
[35] Graves, Langer, and Moffat, Phys. Rev. **88**, 169 (1952).

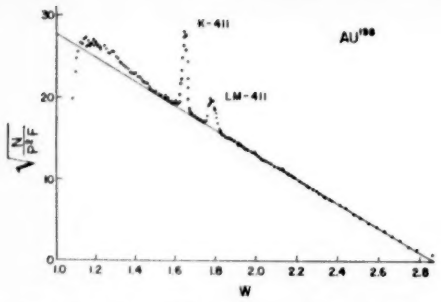

FIG. 5. Fermi-Kurie plot of the spectrum of the Au^{198} source.

of the individual points and what was believed to be the upper and lower limits for the position of the curves of the continuous spectrum beneath the lines.

B. Au^{198}—Hg^{198}

The data for the gold source were taken and analyzed in manner similar to that used for the cesium. The same 1.3 mg cm^{-2} Dacron window was used for the gold as for the cesium, but the thin window was made of collodion and was approximately 20 μg cm^{-2}. The K conversion line of the 411.2-kev gamma-ray[36] was used for calibration.

An allowed Fermi plot of the data taken with the thicker window is shown in Fig. 5. The deviation of the plot from linearity for energies below that of the K conversion line clearly shows the presence of low energy beta-groups. Figure 6 is a graph of the spectrum (taken with the thin window) in the region of the Auger lines after the 960-kev beta-group has been subtracted by extrapolation of the straight line Fermi plot. The lines marked A_1 and A_2 are the K Auger lines of mercury. The lines marked K_2, L_2, and M_2 are the K, L, and M conversion lines of the 159-kev gamma-ray, and K_3 is the K conversion line of the 209-kev gamma-ray of Au^{199}. The unmarked lines were unidentified. All attempts to identify these with known conversion lines of any impurity were unsuccessful. The presence of the Au^{199} conversion lines and their known intensities[37] were used to help fix the position of the continuous spectrum beneath the Auger electron lines. In the calculation of the K Auger yield, it was assumed that all of the K shell vacancies resulted from K conversion of the 159-, 209-, and 411-kev gamma-rays. The intensity of the K–XY Auger line relative to that of the K–LL line was assumed to be that calculated by Pincherle.[4] This resulted in a K Auger yield of $a_K=0.054\pm0.008$. The ratio of intensities of the two observed Auger lines was K–LL:K–LX::1.00: 0.71 ± 0.15. The percentage error is considerably greater for this measurement than for the barium Auger measurement. This is principally due to the fact that the continuous spectrum intensity is much larger in comparison with the Auger electron intensity than in the case of the barium measurements. If the unidentified lines were all K-conversion lines that contribute to the observed Auger electron peaks. the computed Auger yield would be reduced by three percent.

If K capture transitions occur in gold, they must give rise to platinum Auger electrons which would be approximately eight percent lower in energy than the mercury Auger electrons. It was estimated that if K capture transitions were 0.5 percent of the disintegrations, the presence of the platinum Auger electrons could have been detected.

C. Sn^{113}—In^{113}

In the work with the Sn^{113} source the region from 0.55 amp to 11.0 amp was covered by 400-count measurements in steps of 1 percent variation. Steps of 4 percent were used from 11.0 to 13.0 amp. On the peaks the number of counts per point was changed to 1000 and for the highest peaks to 3000, while the size of the current variations was reduced to about 0.3 percent. The region below the Auger peaks was covered four times; the Auger peaks nine times; the region between the Auger peaks and the conversion peaks twice; the conversion peaks eight times; the region above the conversion peaks twice. These data were taken with a four-layer (36-μg cm^{-2}) Nylon window. Figures 7 and 8 show the Auger peaks and conversion peaks, respectively. In order to guarantee that this window transmitted substantially all of the 20-kev Auger electrons, the Auger and conversion electron peaks were re-run with a window of only two layers (18 μg cm^{-2}) made at the same time as the four-layer window and with essentially identical layers. The 20-kev K–LL Auger peak was increased 3.8 percent by use of the thinner window. The cutoff of the thin window was below 3 kev, as is evidenced by the detection of a weak L Auger peak at 3.1 kev.

The 624-kev conversion line of Cs^{137} was used for energy calibration. Because of the poor resolution and a slight drift at the current necessary for the Cs^{137} line, the energies are not accurate to better than one percent. Within this error the K conversion line energy agrees with previous measurements, and the K Auger line

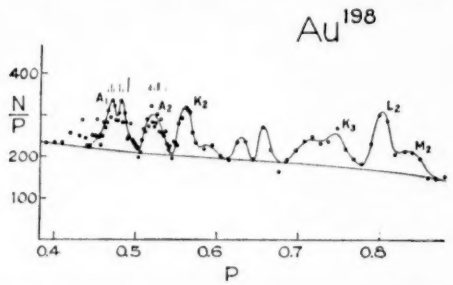

FIG. 6. The low energy portion of the spectrum of the Au^{198} source after subtraction of the 0.96-Mev spectrum of Au^{198}.

[36] DuMond, Lind, and Watson, Phys. Rev. **73**, 1392 (1948).
[37] P. M. Sherk and R. D. Hill, Phys. Rev. **83**, 1099 (1951).

energies agree with those calculated from x-ray measurements. A search was made for conversion lines of the 85-kev gamma-ray previously reported.[38] No conversion lines of intensity greater than one percent of the 360-kev line were found.

The experimental ratio of the *K* Auger intensity to the total conversion intensity (Figs. 7 and 8) is 0.54. In a previous report[39] a correction of 5 percent for window transmission was added. The work on $Cs^{137}-Ba^{137}$ reported above indicates that in all probability the 18 $\mu g\ cm^{-2}$ window transmits all electrons of 20 kev. A 4 percent correction for transmission of the conversion lines through the Lektromesh gives a final figure of 0.56 ± 0.03 for the ratio of *K* Auger intensity to conversion line intensity.[40]

The ratios of *K–LL* to *K–LX* to *K–XY* Auger electrons can be very accurately determined from Fig. 7 because the lines are fairly well resolved, and there is no beta-ray background as in the case of Ba^{137} and Hg^{198}. The ratios are *K–LL*:*K–LX*:*K–XY*::1.00:0.417 $\pm$0.016:0.076$\pm$0.008.

V. INTERPRETATION AND SUMMARY

A. *K* Fluorescence Yield and *K* Auger Yield

In studying the available theory and experimental results on *K* fluorescence and *K* Auger yield, one finds[1,7] that for elements of low atomic number $w_K \ll 1$ and $a_K \approx 1$ and for elements of high atomic number $w_K \approx 1$ and $a_K \ll 1$. Thus, it would seem that direct *K* Auger yield measurements would be more accurate than *K* Auger yields obtained from fluorescence yield measurements for elements of atomic number greater than 40 since $a_K > 0.5$ for these elements. Measurements of w_K based on x-ray intensities greatly outnumber the measurements of a_K based on electron intensities, but

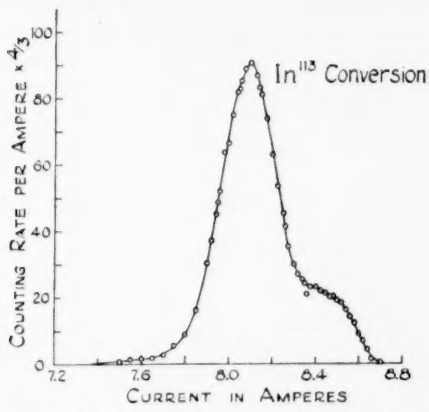

FIG. 7. *K* and *L* conversion lines of the 0.3917-Mev gamma-ray of In^{113}.

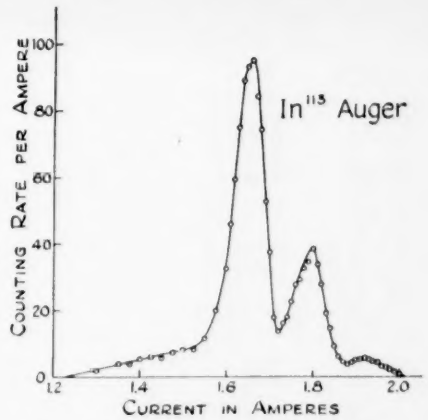

FIG. 8. Auger lines of In from the Sn^{113} source.

the former are confined principally to the elements with atomic number less than 50. The few cloud-chamber and photographic plate measurements of double electron tracks have been distributed over the whole atomic table and, in general, give values of w_K smaller than those obtained by other methods. Magnetic spectrometer measurements have been made only for elements with atomic number greater than 46.

In the present summary of the experimental results, the values are reported as $w_K = 1 - a_K$. Table II lists the numerical values followed by a lower case letter referring to the list of workers who obtained these values. This list gives the reference to the work and an indication of how the measurements were made. Figure 9 is a graph of these values. It appears that the $CZ^4/(a+Z^4)$ relation does not give a very good fit to these data, and that the proper analytical expression for the curve should probably involve an additional term or terms to include screening and relativistic effects. A least-squares fit to all these data would require a very thorough study of all the methods used, so that proper weights might be assigned the different values. The present authors have not attempted to carry out such a curve-fitting process, but have drawn an estimated curve that takes into consideration, in a rough way, what knowledge they have of the reliability of the various values. It is believed that the magnetic spectrometer measurements are the most accurate for the region in which they have been made.

In addition to the values of Auger yield, there are sufficient experimental measurements of the *K–LX* to *K–LL* Auger electron intensity ratios to indicate roughly the variation of this ratio with atomic number. Besides the ratios for indium, barium, and mercury reported in this paper, several measurements by other workers were mentioned in Sec. II. Figure 10 is a plot of these *K–LX* to *K–LL* ratios against atomic number. It is seen that this ratio increases with increasing atomic number, and for high atomic number is approximately that

[38] S. W. Barnes, Phys. Rev. **56**, 414 (1939).
[39] Thomas, Haynes, Broyles, and Thomas, Phys. Rev. **82**, 961 (1951).
[40] This figure replaces that previously reported in reference 39.

TABLE II. Summary of fluorescence yield measurements.

Element	Atomic number	K fluorescence yield							
C	6	0.0009[r]							
N	7	0.0015[r]							
O	8	0.0022[r]	0.082[j]						
Ne	10	0.0081[r]	0.083[j]						
Mg	12			0.013[ll]					
Si	14			0.038[ll]					
S	16			0.083[ll]				0.15[n]	
Cl	17	0.04[n]		0.108[ll]					
A	18	0.07[d]	0.149[j]	0.077[o]	0.06[y]	0.123[ee]			
Ca	20			0.15[ll]				0.207[n]	
Cr	24	0.26[a]	0.26[b]	0.263[ll]				0.265[n]	
Fe	26	0.37[a]		0.375[e]	0.314[f]	0.32[g]		0.343[n]	0.30[p]
Co	27						0.38[m]		
Ni	28	0.45[a]	0.385[t]	0.445[e]	0.374[j]	0.39[g]	0.39[m]	0.436[n]	0.364[p]
Cu	29	0.48[a]	0.41[t]	0.495[e]	0.419[f]	0.45[g]	0.43[m]	0.55[c]	0.401[p]
Zn	30	0.58[a]	0.48[t]	0.57[e]	0.444[f]	0.52[g]	0.45[m]	0.476[n]	0.450[p]
As	33						0.53[m]		
Se	34	0.68[h]	0.575[t]		0.578[f]	0.547[i]	0.55[m]	0.585[n]	0.550[p]
Br	35	0.68[h]	0.57[b]	0.56[k]		0.565[i]			
Kr	36	0.51[d]	0.53[a]	0.67[bb]					
Sr	38				0.644[f]		0.72[m]		
Zr	40		0.69[t]						
Mo	42	0.785[q]	0.735[t]	0.97[n]	0.826[f]	0.68[j]	0.79[m]		0.724[p]
Rh	45	0.801[q]	0.77[t]						
Pd	46	0.835[q]							
Ag	47	0.838[q]	0.81[t]	0.88[e]	0.83[ff]		0.72[m]	0.93[c]	0.795[p]
Cd	48	0.846[q]	0.79[t]		0.83[ff]		0.70[m]		
Sn	50	0.855[q]	0.81[t]				0.66[m]		0.825[p]
Sb	51	0.862[q]					0.64[m]		
Te	52	0.872[q]					0.59[m]		
I	53	0.88[h]							
Xe	54	0.70[l]	0.78[a]	0.81[bb]					
Cs	55	0.890[a]							
Ba	56	0.900[q]	0.870[gg]						
Pr	59	0.88[dd]							
Pt	78	0.942[s]							
Hg	80		0.946[gg]						
Pb	82	> 0.89[ee]							
Bi	83	0.934[v]	0.976[w]						
Po	84	0.894[aa]							

[a] W. Kossel, Z. Physik **19**, 333 (1923); x-ray intensity, ionization chamber, corrected for K jump by Broyles, Thomas, and Haynes.
[b] W. Bothe, Physik. Z. **26**, 40 (1925); x-ray intensity, ionization chamber, from the results of Barkla and Thomas, corrected for K jump by Broyles, Thomas, and Haynes.
[c] W. Bothe, Z. Physik **37**, 547 (1926); x-ray intensity.
[d] P. Auger, Ann. phys. **6**, 183 (1926); electrons, cloud chamber.
[e] M. Balderston, Phys. Rev. **27**, 676 (1926); x-ray intensity, ionization chamber, w_K as calculated by Backhurst.
[f] I. M. Harms, Ann. Physik **82**, 87 (1927); x-ray intensity, ionization chamber, w_K as calculated by Backhurst with minor corrections of Compton.
[g] L. H. Martin, Proc. Roy. Soc. (London) **A115**, 420 (1927); x-ray, ionization chamber, absorber.
[h] L. H. Martin, Proc. Roy. Soc. (London) **A115**, 420 (1927); deduced from Barkla and Philpot, Phil. Mag. **25**, 849 (1923) and Beatty, Proc. Roy. Soc. **A85**, 329 (1911), x-ray, ion chamber, change of ionization K edge.
[i] A. H. Compton, Phil. Mag. **8**, 961 (1929); x-ray intensity, ionization chamber.
[j] G. L. Locher, Phys. Rev. **40**, 484 (1932); electrons, cloud chamber, preferred values of Locher which seem also preferred in (1952).
[k] W. Stockmeyer, Ann. Physik **12**, 71 (1932); x-ray intensity, double ionization chamber, K edge.
[l] M. Haas, Ann. Physik **16**, 473 (1933); x-ray intensity, ionization chamber.
[m] D. K. Berkey, Phys. Rev. **45**, 437 (1934); x-ray intensity, ionization chamber.
[n] H. Lay, Z. Physik **91**, 533 (1934); x-ray intensity, photographic plate.
[o] Martin, Bower, and Laby, Proc. Roy. Soc. (London) **A148**, 40 (1935); electrons, cloud chamber.
[p] E. Arends, Ann. Physik **22**, 281 (1935); x-ray intensity, ionization chamber.
[q] I. Backhurst, Phil. Mag. **22**, 737 (1936); x-ray intensity, ionization chamber.
[r] W. Crone, Ann. Physik **27**, 405 (1936); x-ray intensity, ionization chamber, and counter.
[s] L. H. Martin and F. H. Eggleston, Proc. Roy. Soc. (London) **A158**, 46 (1936); electrons, cloud chamber.
[t] R. J. Stephenson, Phys. Rev. **51**, 637 (1937); x-ray intensity, ionization chamber.
[u] Weimer, Kurbatov, and Pool, Phys. Rev. **66**, 209 (1944); K-capture isotope, ionization chamber, window absorption.
[v] B. B. Kinsey, Can. J. Research **A26**, 421 (1948); data of Ellis, Proc. Roy. Soc. **A139**, 336 (1933); magnetic spectrum.
[w] B. B. Kinsey, Can. J. Research **A26**, 421 (1948); data of Flammersfeld, Z. Physik **114**, 227 (1939); magnetic spectrometer.
[x] Steffen, Huber, and Humbel, Helv. Phys. Acta **22**, 167 (1949); conversion electrons, magnetic spectrometer.
[y] Curran, Angus, and Cockroft (1949) value given by E. H. S. Burhop, *The Auger Effect and Other Radiationless Transitions* (Cambridge University Press, Cambridge, England, 1952), p. 28; proportional counter spectrometer.
[z] I. Bergstrom and S. Thulin, Phys. Rev. **79**, 539 (1950); conversion electrons, magnetic spectrometer.
[aa] L. S. Germain, Phys. Rev. **80**, 937 (1950); electrons, K-capture isotope, photographic plate.
[bb] D. West and D. Rothwell, Phil. Mag. **41**, 873 (1950); x-ray intensity, proportional counter spectrometer.
[cc] D. L. Dexter and W. W. Beeman, Phys. Rev. **81**, 456 (1951); width of x-ray absorption line.
[dd] E. Kondaiah, Phys. Rev. **83**, 471 (1951); conversion electrons, magnetic spectrometer.
[ee] H. M. Neuman, and I. Perlman, Phys. Rev. **81**, 958 (1951); deduced from Auger and conversion line intensities in magnetic spectrometer given by these authors without any allowance for K-capture transitions present. These transitions would probably increase the value to more than 0.95.
[ff] Huber, Humbel, Schneider, Shalit, Helv. Phys. Acta **25**, 3 (1952); coincidence measurements, magnetic spectrometer.
[gg] Broyles, Thomas, and Haynes, conversion electrons, magnetic spectrometer.
[ll] R. D. Evans, Phys. Rev. **45**, 29 (1934); x-ray intensity, ionization chamber.

obtained from Pincherle's[4] Auger transition probabilities.

B. Discussion of Sn^{113}—In^{113}

The summary of fluorescence yields given above indicates that the Auger yield of indium is appreciably less than the 0.20 lower limit assumed in a preliminary report of the work on Sn^{113}.[40] The conclusions reached there concerning the energy of the orbital capture transition to the 391.7-kev[35] state of In^{113}, concerning the parity of Sn^{113}, and concerning the impossibility of another transition preceding the 391.7-kev transition, are therefore unjustified. Cork[41] has since reported weak conversion lines which were assigned to gamma-rays of 255.2 kev and 400.9 kev. The data reported in Sec. IV indicate that conversion lines of the former must have an intensity of less than 1 percent of the conversion lines of the 391.7-kev gamma-ray. Conversion lines of the latter if present would not have been resolved from those of the 391.7-kev gamma-ray. That the 400.9-kev conversion lines are extremely weak compared to the 391.7-kev lines is indicated by the failure of Cork *et al.*[41] to observe the *L* line of the former whereas the *M* line of the latter was detected. Absorption curves, in addition to indicating the absence of 85-kev[38] gamma-radiation, indicate that the 255-kev radiation, if present, is probably an order of magnitude weaker than the 391.7-kev radiation.[38,39] That the intensity of the 400.9-kev gamma-radiation cannot be more than about 5 to 10 percent of that of the 391.7-kev gamma-ray is indicated by the close check between the

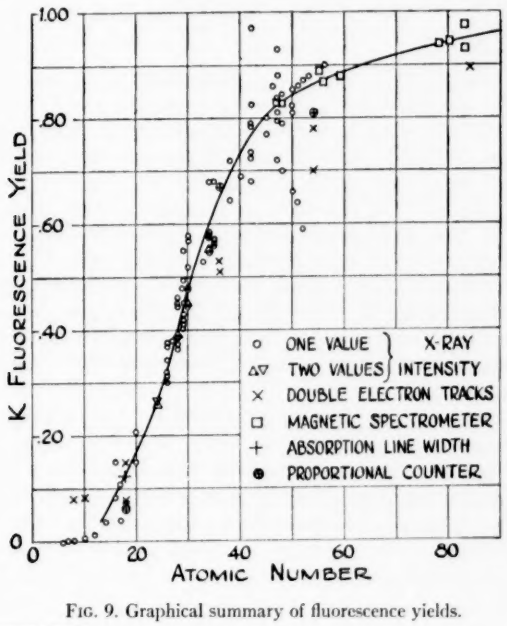

FIG. 9. Graphical summary of fluorescence yields.

[41] Cork, Stoddard, Branyan, Childs, Martin, and Leblanc, Phys. Rev. **84**, 596 (1951).

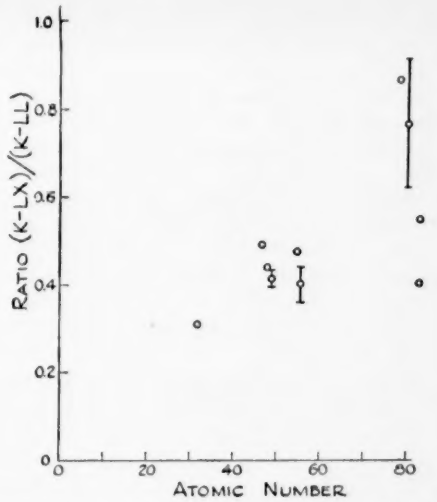

FIG. 10. Graphical summary of the ratio of *K*–*LX* to *K*–*LL* transitions as a function of atomic number as measured by various observers.

K conversion coefficient (0.445) of the latter gamma-ray obtained from the measurements of Cook and Haynes[42] and Graves, Langer, and Moffat[35] and the theoretical value for *M*4 radiation (0.47) computed by Rose *et al.*[43] Whether the weak transitions, if present, precede the 391.7-kev transition or are an alternative mode of disintegration is uncertain.

To illustrate the significance of the measured ratio of *K* Auger electrons to total conversion electrons, the decay scheme may be assumed to consist of a fraction p of the disintegrations through the 391.7-kev state and a fraction q of the disintegrations to the ground state through other levels but not through the 391.7-kev state. The ratio R of *K* Auger electrons to total conversion electrons is given by

$$R=R_p+a_K(q/p)(1+\alpha)/\alpha(1+\lambda_q), \tag{4a}$$

where

$$R_p=(a_K/\alpha)[(1+\alpha)/(1+\lambda_p)+\alpha_K], \tag{4b}$$

and λ_p and λ_q represent the ratio of *L* to *K* capture of the two branches, α and α_K represent, respectively, the conversion and *K* conversion coefficient of the 391.7-kev transition (other conversion lines have been neglected as negligible), and a_K represents the Auger yield of indium. R_p is the value if all transitions go through the 391.7-kev state.

The value of $\alpha_K=0.47\pm0.01$ is taken from Rose *et al.*[43] for *M*4 radiation. The value of $\alpha=0.58\pm0.01$ is computed from α_K with the help of the value of $\alpha_K/\alpha_{L+M}=4.21$ of Graves *et al.*[35] From the fluorescence yield curve $a_K=0.165\pm0.01$. With these values, the measured value of R, and by use of first-order error

[42] T.B. Cook, Jr., and S. K. Haynes, Phys. Rev. **86**, 190 (1952).
[43] Rose, Goertzel, Spinrad, Harr, and Strong, Phys. Rev. **83**, 79 (1951).

theory one obtains $\lambda_p=0.08\pm0.09$ for $R=R_p$, and $\lambda_p=0.18\pm0.09$ if 10 percent of the transitions go by an alternative route. The error is almost entirely due to the error in Auger yield. This fact indicates the great need for still more accurate knowledge of the value of a_K as a function of Z. It is clear, however, that if in 30 percent or more of the transitions of some radio-nuclide an L electron were captured ($\lambda_p>0.5$), the method outlined here would make possible a fairly accurate determination of the amount of L capture even with the present uncertainty in the value of a_K. An estimate of the disintegration energy could then be made by use of the results of Rose and Jackson[44] and Marshak[45] as previously indicated.[39]

[44] M. E. Rose and J. L. Jackson, Phys. Rev. **76**, 1540 (1949).
[45] R. E. Marshak, Phys. Rev. **61**, 446 (1942).

The authors wish to express their appreciation to Dr. I. Bloch and other members of the Physics Department Staff for their profitable discussions; Mr. R. Wymer of the Chemistry Department for his advice on the chemistry involved in the preparation of the radioactive sources; Mr. H. Carlton, Mr. E. B. Pflasterer, and Mr. T. N. Tyler for their skillful machine work and technical assistance; and Mr. J. E. Thomas, Mr. A. W. Smith, Mr. T. Baker, and Mr. C. W. Nestor for their assistance during long periods of continuous operation.

Financial assistance is gratefully acknowledged from The Research Corporation, The Carnegie Foundation for the Advancement of Teaching, The Natural Science Research Fund of Vanderbilt University, and a contract with the United States Atomic Energy Commission.

PHYSICAL REVIEW VOLUME 89, NUMBER 4 FEBRUARY 15, 1953

Neutron Energy Distribution from the Proton Bombardment of Li, Be, and C at 375 Mev*

WARREN F. GOODELL, JR., HOWARD H. LOAR, RICHARD P. DURBIN, AND WILLIAM W. HAVENS, JR.
Columbia University, New York, New York

(Received October 31, 1952)

High energy neutrons were produced by bombarding lithium, beryllium, and carbon targets with protons having a maximum energy of 375 Mev. The energy spectrum of the neutrons emitted in the forward direction was measured by determining the range spectrum of recoil protons scattered at 45° by a polyethylene scatterer. A telescope of stilbene crystals with copper range-determining absorbers was used as a detector. The neutron beam was monitored by a bismuth fission ionization chamber. For elements studied, the width of the neutron energy distribution broadens and the energy of the peak of the distribution decreases as the atomic number of the target material increases.

I. INTRODUCTION

AN investigation[1] was made of the energy spectra of neutrons emitted in the forward direction when several light elements were bombarded by 375-Mev protons. Targets of lithium, beryllium, and carbon were exposed to the internal proton beam of the Columbia University Nevis cyclotron. The energy of the protons was determined from the value of the magnetic field and the radial position of the target. The neutrons produced scattered protons in a polyethylene block. The range in copper of the scattered protons was determined, using a scintillation counter telescope. The energy distribution of the neutrons was then inferred from this proton-range spectrum.

II. DESCRIPTION OF THE EXPERIMENT

A diagram of the experimental arrangement is given in Fig. 1. The targets were placed inside the vacuum tank of the cyclotron in such a position that the neutrons emitted in the forward direction passed through collimating holes in the concrete shielding surrounding the cyclotron. The targets were rectangular slabs held by a clamp. All parts of the clamp were at least 2 in. from the leading edge of the target, so the clamp would not contribute to the neutron flux. The target thicknesses were 2 in. for lithium, $1\frac{3}{4}$ in. for beryllium, and $1\frac{1}{4}$ in. for carbon. The thicknesses of the beryllium and carbon targets were adjusted to give the same multiple scattering of protons, and hence to give roughly the same number of multiple traversals of the proton beam in the two targets. The targets were of sufficient height to intercept a major fraction of the internal beam of the cyclotron.

The neutron beam passed through a $\frac{3}{4}$ in. Plexiglas window and was collimated by a steel tube 4 in. in diameter and 6 in. long, which was imbedded in the lead and concrete shielding of the cyclotron. Two additional blocks of concrete were added to give better shielding to the counters. The neutrons were scattered alternately by carbon and polyethylene scatterers placed in the beam. The scatterers were 4 in. square, and had a thickness of 2.13 g/cm^2 for the carbon, and 2.38 g/cm^2 for the polyethylene. The thicknesses were

* This research was supported by the joint program of the Office of Naval Research and the Atomic Energy Commission.
[1] A preliminary report of this work was given by Goodell, Loar, and Durbin, Phys. Rev. **83**, 234 (1951).

adjusted to give the same number of carbon atoms in each scatterer. The recoil protons from the hydrogen in the polyethylene were detected by a triple coincidence scintillation counter telescope at an angle of 45° from the incident neutron beam, and the range spectrum of the protons was determined by copper absorbers. Stilbene crystals approximately 2 in. in diameter were viewed by two 1P21 photomultipliers in parallel per crystal. The details of the crystals are given in Table I.

A block diagram of the electronic equipment is shown in Fig. 2. The signals from the counters were fed to bridge-type coincidence circuits similar to those used by Neher[2] at Berkeley with a resolving time of approximately 10^{-7} second. The outputs of the bridges were connected to an Atomic Instrument 501 Coincidence Analyzer after amplification. An additional signal from the third crystal, passed through an amplifier with a rise time of about 0.04 microsecond, was then discriminated in amplitude to allow the recording of only those protons passing through the telescope and losing more than a given amount of energy in the last crystal.

The particles recorded corresponded to protons having a range between R_1 and R_2 before striking the copper absorber. Both R_1 and R_2 were changed by inserting different lengths of absorbers. The absorbers were $2\frac{3}{4}$-in. diameter cylinders of varying lengths and were placed as close as possible to the last crystal to minimize scattering losses in the absorber. By changing the absorbers, a range spectrum of the scattered protons was obtained, from which the energy distribution of the incident neutrons was calculated.

TABLE I. Crystal details.

Crystal	Position	Diameter (in.)	g/cm²
1	back	2.25	1.068
2	middle	2.25	0.932
3	front	1.94	0.957

The beam was monitored by a bismuth fission ionization chamber similar to those used by Wiegand.[3] For beryllium, typical counting rates were 300 monitor counts per minute, 100 coincidence counts per minute from polyethylene, 30 coincidence counts per minute from true recoil protons, and 1600 counts per minute in the third crystal alone.

III. TESTS OF EQUIPMENT

The plateaus of the counters were set with the help of a 240-Mev scattered proton beam from the cyclotron. After the initial adjustments, frequent check points were taken to insure that the operating characteristics of the system had not changed. Background runs with no scatterer indicated that the background was about 3 or 4 percent of the true coincidence rate. Crystals were moved out of line to determine the accidental coincidence rate, different thicknesses of scatterers were tried to check the linearity of the system, and the angular resolution of the system was varied by changing the positions of the crystals. No spurious effects were noted in any of these tests. Measurements with a collimated beta-source indicated that the response of the third crystal to a given energy particle was constant to within 15 percent over the face of the crystal. This proportionality was necessary for the differential range type of measurement used.

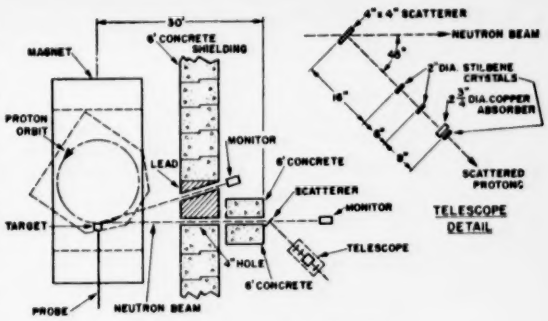

FIG. 1. Experimental arrangement.

IV. FACTORS DISTORTING ENERGY DISTRIBUTIONS

Certain factors contributed to the distortion of the neutron energy spectrum observed. The neutrons were absorbed to a slight extent in the target, in the Plexiglas window of the vacuum chamber, and in the polyethylene scatterer. Order of magnitude calculations showed that this absorption was negligible in comparison to other errors in the experiment, and in any case was approximately the same for all the spectra measured.

The major distortions were introduced by the interactions of the scattered protons in the scatterer and the absorbers. The energy loss in the scatterers was calculated using the curves of Aron.[4] Since the scatterers had been adjusted to contain the same number of carbon atoms, the stopping powers were somewhat dif-

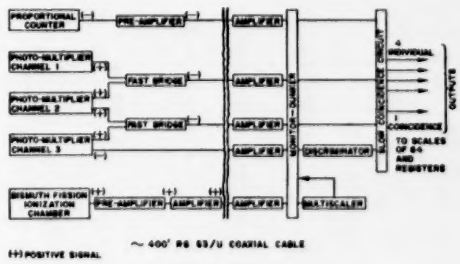

FIG. 2. Electronic equipment block diagram.

[2] L. F. Wouters, Nucleonics **10**, No. 8, 51 (1952).
[3] C. Wiegand, Rev. Sci. Instr. **19**, 790 (1948).
[4] Aron, Hoffman, and Williams, Atomic Energy Commission Report AECU 663 (UCRL 121) (unpublished).

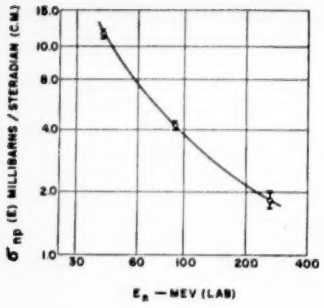

FIG. 3. Neutron-proton cross section at 45° in laboratory system.

ferent, and this introduced a small error in the determination of the number of protons in a given energy range.

The Coulomb scattering in the absorber was estimated by considering the absorber to be made up of a series of short pieces and calculating the mean scattering angle and scattering losses due to each section. Due to the particular geometry used, and the differential range method of measurement, the Coulomb-scattering losses were roughly constant with proton energy, and equal to about 8 percent.

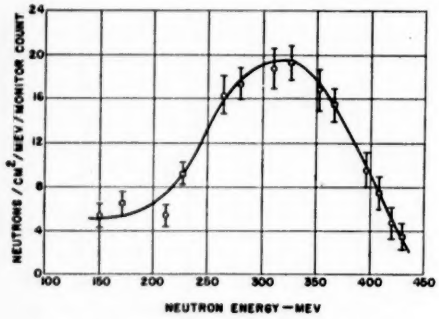

FIG. 4. Neutron energy distribution—lithium.

The nuclear cross section for protons in copper was assumed to be the same as that found by DeJuren[5] for neutrons of the same energy, as no other data were available. Half of this cross section was assumed to be due to elastic nuclear scattering, and half to absorption or inelastic scattering, as was found for protons.[6] Using the cross section and the distribution curves of Bratenahl *et al.*,[6] the percentage of protons missing the last crystal, because of diffraction scattering, was found to be about 3 percent. This varied with the energy of the detected protons, but since the absolute value was small the variation was neglected. The inelastic scattering was treated as an absorption of the protons with a cross section equal to half the total neutron cross section. The mean energy of the protons in each segment of the absorber was determined, and the absorption calculated for each segment. The fraction of protons which did not reach the last crystal because of absorption varied in approximately a linear manner with energy and had a maximum of about 30 percent.

These effects were combined to give the over-all distortion. Some of the calculations could be considerably improved, but the angular resolution of the detecting telescope introduced enough distortion by itself to make such improvements of little value.

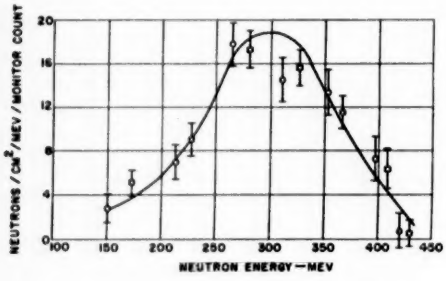

FIG. 5. Neutron energy distribution—beryllium.

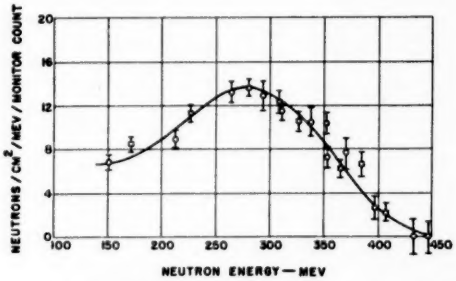

FIG. 6. Neutron energy distribution—carbon.

V. CALCULATIONS

To find the energy distribution of the neutron beam, different thicknesses of absorbers were placed between counters 2 and 3. For each thickness the normalized counting rate of coincidences between 1, 2, and all pulses in 3 greater than a certain size was obtained for the polyethylene and carbon scatterers. As the number of carbon atoms in the two scatterers was the same, a direct subtraction gave the number of counts due to recoil protons from hydrogen, the background counts automatically cancelling. The pulse-height discrimination in the third counter required that the proton counted be within a certain residual range or energy, as the specific ionization had to reach a preset value for the proton to register a coincidence. This in turn required that the energy of the proton before passing though the absorber lie within a certain energy range. Data were taken simultaneously for two different resolution widths to check the consistency and accuracy of the method. These widths correspond roughly to 40 and 60 Mev.

[5] J. DeJuren and B. J. Moyer, Phys. Rev. **81**, 919 (1951).

[6] Bratenahl, Fernbach, Hildebrand, Leith, and Moyer, Phys. Rev. **77**, 597 (1950).

The number of protons per unit proton energy was obtained by dividing the number measured per energy interval by the energy width of the interval, and correcting for the scattering losses. The mean energy of the interval was calculated from the thickness of the copper absorber, taking into account the energy loss in the scatterer and the crystals. To convert to the neutron energy distribution it was necessary to know the energy variation of the neutron-proton differential cross section at 45°. This was not known accurately above 90-Mev neutron energy. However, data from the Berkeley results[7,8] were plotted as shown in Fig. 3, and a smooth curve drawn through the points. This was combined with the angular resolution of the counter system and relativistic kinematic corrections to obtain the relative flux of neutrons.

The angle of 45° for the telescope was chosen as a compromise between distortions. The larger the angle, the smaller the energy of the scattered protons, and the less severe the scattering corrections in the absorbers—especially the nuclear absorption. As the cross section for this absorption is not too well known, the final result should depend as little as possible upon it. The neutron-proton cross section is also the flattest around 45°. However, the larger the angle, the greater the smearing of the angular resolution of the telescope.

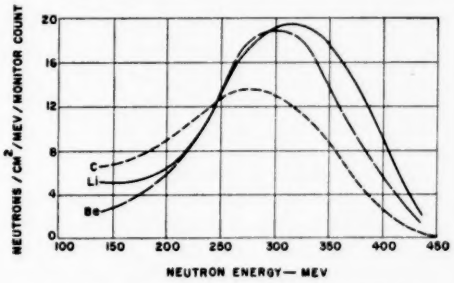

FIG. 7. Neutron energy distributions—comparison.

VI. RESULTS

The results of the experimental runs for lithium, beryllium, and carbon are shown in Figs. 4, 5, 6, and 7, and the comparative results for beryllium at several energies are shown in Fig. 8. These include the spectra taken at Harvard,[9] Harwell,[10] Rochester,[11] Berkeley,[12] and the present work.

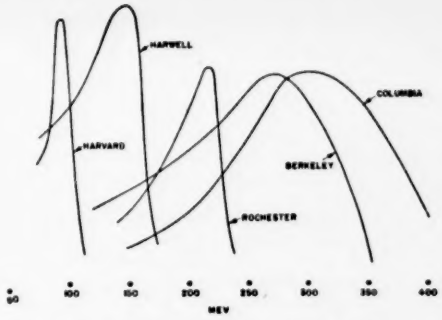

FIG. 8. Beryllium energy distributions for various proton energies.

These curves have been compared with symmetrical bell-shaped curves modified by the effects of the various resolution widths and distortions, and the parameters for best fit are given in Table II. The carbon curve is quite definitely a broader and lower energy curve than the others.

An order of magnitude comparison of the intensity of neutrons from the various targets was made, although no careful measurements were made of beam current. Multiple traversals of the proton beam were taken into account by calculating the mean scattering angle in the target, and assuming that the number of traversals was such that the same scattering angle was attained in each target.[13] With these assumptions, the number of neutrons emitted per nucleon of the target was roughly constant.

TABLE II. Parameters for best fit of observed energy spectra to $1/(p^2x^3)$ curve.

Parameter	Lithium	Beryllium	Carbon
Energy at peak	317 Mev	305 Mev	280 Mev
Full width at half-amplitude	160 Mev	150 Mev	200 Mev
Area under peak per nucleon	1.4	1.6	1.7

The general shapes of the spectra are seen to be in agreement with the data taken at lower energies.

We wish to thank Professor E. T. Booth, Professor J. Steinberger, and Professor A. Sachs for helpful discussions during the course of the work; the staff of the Nevis cyclotron, especially J. Spiro and the operating crew, for providing the neutrons; and Sue Goodell for many of the kinematic calculations.

[7] Hadley, Kelley, Leith, Segré, Wiegand, and York, Phys. Rev. **75**, 351 (1949).
[8] Kelly, Leith, Segré, and Wiegand, Phys. Rev. **79**, 96 (1950).
[9] D. Bodansky and N. F. Ramsey, Phys. Rev. **82**, 831 (1951).
[10] Cassels, Randle, Pickavance, and Taylor, Phil. Mag. **42**, 215 (1951).
[11] Nelson, Guernsey, and Mott, Phys. Rev. **88**, 1 (1952).
[12] Cladis, Hadley, and Hess, Phys. Rev. **86**, 110 (1952).
[13] W. J. Knox, Phys. Rev. **81**, 687 (1951).

The Dynamical Theory of Nuclear Induction*

R. K. WANGSNESS† AND F. BLOCH
Stanford University, Stanford, California
(Received November 10, 1952)

Starting from the microscopic viewpoint, the dynamics of nuclear induction is derived by means of statistical methods. The only essential lack of generality lies in the assumption that the nuclei in the sample are independent of each other, so that the treatment does not account for features arising from spin-spin interaction. By considering the simultaneous action of an arbitrary external field and of the molecular surroundings upon a representative nucleus a system of linear differential equations of the first order is derived for the "distribution matrix." It is analogous to the classical Boltzmann equation for the distribution function and allows, upon integration, to determine the macroscopic average value of any spin function in its dependence upon time. This general result is particularly applied to the time dependence of the macroscopic nuclear polarization, and the conditions are investigated under which it satisfies the phenomenological differential equation originally proposed by one of the authors (F.B.). Besides the fact that this equation does not describe line structures caused by the interaction of neighboring spins its validity is found to be seriously restricted only for nuclei having a spin larger than unity and in cases where, in addition, quadrupole relaxation is essential. It demands in these cases that the molecular surroundings are isotropic, e.g., as in gaseous and liquid samples, and further, that their characteristic frequencies of interaction with the nuclei are large compared to the Larmor frequency so that there exists equality between the longitudinal and the transverse relaxation time.

1. INTRODUCTION

IN his original paper on nuclear induction[1] one of the authors has proposed the differential equation,

$$d\mathbf{M}/dt=\gamma\mathbf{M}\times\mathbf{H}-\mathbf{i}M_x/T_2-\mathbf{j}M_y/T_2-\mathbf{k}(M_z-M_0)/T_1, \tag{1.1}$$

for the time dependence of the macroscopic nuclear polarization $\mathbf{M}(t)$ under the influence of an external field $\mathbf{H}(t)$. The vectors $\mathbf{i}$, $\mathbf{j}$, and $\mathbf{k}$ are here unit vectors in the x, y, and z directions, respectively, and

$$\gamma=\mu/Ih \tag{1.2}$$

is the gyromagnetic ratio of the nuclei under consideration with magnetic moment μ and spin I. It is further assumed that the external field has the form

$$\mathbf{H}(t)=\mathbf{k}H_0+\mathbf{H}_1(t), \tag{1.3}$$

where H_0 is strong and constant while H_1 is relatively weak and an arbitrary function of the time t. M_0 is the equilibrium polarization in the field H_0 and the establishment of thermal equilibrium is in Eq. (1.1) summarily described by two constants T_1 and T_2 in the following manner: Starting with an arbitrary magnitude and direction, the z component of $\mathbf{M}$ will, in the absence of the field $\mathbf{H}_1$, reach the value M_0 with a time constant T_1, the "longitudinal" relaxation time, and the x and y components will vanish with a time constant T_2, the "transverse" relaxation time.

While the phenomenological Eq. (1.1) is certainly not rigorously valid under all circumstances, it has nevertheless been found experimentally to represent, in many cases, the proper qualitative or even quantitative description of the observed phenomena; nuclear and molecular data of considerable interest can in these cases be inferred from the shape and magnitude of the observed signals under varying conditions of the external field. It seemed to us worth while, therefore, to develop a theory which starts from the microscopic viewpoint and derives the dynamics of nuclear induction by means of statistical methods. As an application of the considerably more general results, we shall determine the special conditions under which the phenomenological equations can be expected to be valid and where relaxation can be accordingly characterized by the two constants T_1 and T_2, without reference to particular mechanisms responsible for the greatly varying magnitude of these relaxation times. An excellent investigation of such mechanisms in a variety of important cases has been previously carried out by Bloembergen.[2] His approach is, however, rather different from ours in so far as the molecular surroundings are described by random varying external fields rather than as a quantum-mechanical system interacting with the nucleus, and his treatment of the problem does not include the general dynamical case.

The behavior of the polarization, due to a large number of identical nuclei in a macroscopic sample, is determined by the effect of the external field, of the molecular surroundings, and of neighboring nuclear moments upon the orientation of the magnetic moment of each nucleus. We shall here not attempt a perfectly general theory where all these features are treated

* This paper is based in part upon a thesis submitted by R. K. Wangsness to Stanford University in partial fulfillment of the requirements for the degree of Doctor of Philosophy (November, 1949). A brief report of this work was presented at the meeting of the American Physical Society in December, 1949 [Phys. Rev. **78**, 82 (1950)].

† AEC Predoctoral Fellow, July, 1948, to December, 1949. Present address: U. S. Naval Ordnance Laboratory, White Oak, Maryland.

[1] F. Bloch, Phys. Rev. **70**, 460 (1946).

[2] N. Bloembergen, Leiden thesis, 1948 (Schotanus and Gens, Utrecht).

rigorously but shall restrict ourselves to conditions, often experimentally realized, which lead to a relatively simple dynamical description.

Our problem is greatly simplified by assuming that each nucleus under consideration reacts independently of the other nuclei in the sample to the external field and the molecular surroundings and that the latter can be considered as a heat reservoir in thermal equilibrium. In making this assumption, the magnetic moments of neighboring nuclei are taken into account only in so far as they form part of the heat reservoir. We thus restrict the scope of the present paper by excluding those cases in which the magnetic field acting upon a nucleus depends essentially upon the orientation of its neighbors so that they may not be considered as independent. There are many cases where this feature is of importance; it can, for example, lead to a complex line structure in crystals and polyatomic liquids which our simplified approach is inadequate to describe. This approach is, however, perfectly applicable in other cases which are likewise of practical importance; in particular, in gases and dilute liquid solutions the distance between the nuclei under consideration is frequently so large that their interaction can be safely neglected. Furthermore, the action of the molecular surroundings is here often deliberately and greatly increased by adding to the substance paramagnetic atoms or molecules to serve as catalysts for a rapid establishment of thermal equilibrium. To the extent to which the coupling of a nucleus to its surroundings is primarily determined by such catalysts its interaction with the magnetic moments of other nuclei is negligible and our assumption becomes justified.

Treating the molecular surroundings of the nuclei as a general heat reservoir we shall derive, in analogy to the Boltzmann equation for the classical distribution function, a set of first-order linear differential equations for the "distribution matrix"; this matrix determines the average value of the nuclear polarization or of any other quantity which depends upon the orientation of the nuclear spins.

The equations for the distribution matrix will be used to express the time derivative of the average value of an arbitrary spin function in terms of the average value of other spin functions. The resulting set of relations is particularly convenient, in its general form, for finding the conditions under which it reduces to the phenomenological Eq. (1.1) for the components of the nuclear polarization itself. It will be shown that this reduction is automatic for nuclei with spin $\frac{1}{2}$; depending upon the coupling to the molecular surroundings through the nuclear electric and magnetic moments, the reduction for higher values of the spin will be found to take place under certain special conditions which, however, have still a considerable range of practical applicability.

2. FORMULATION OF THE PROBLEM

In a completely general theory it would be necessary to consider all the nuclei in interaction with each other and with the molecular system as the total system. Because of the simplifying assumptions, introduced in Sec. 1, it is, however, sufficient to treat only the combined system of one representative nucleus and its molecular surroundings. The macroscopic results for many identical and independent nuclei can then be obtained by statistical averages.

The Hamiltonian of this system will be assumed to have the form

$$\mathcal{H}=hE+hF+hG. \tag{2.1}$$

The first term represents the energy $-(\mathbf{H}\cdot\boldsymbol{\mu})$ of the nucleus in the external field $\mathbf{H}$. From Eq. (1.2), the magnetic moment $\boldsymbol{\mu}$ is related to the spin vector $\mathbf{I}$ through the relation $\boldsymbol{\mu}=h\gamma\mathbf{I}$, and we have therefore

$$E=-\gamma(\mathbf{H}\cdot\mathbf{I}). \tag{2.2}$$

The second and third terms in (2.1) represent the energies of the molecular surroundings and of their interaction with the nucleus, respectively.

We choose a representation in which I_z, the z component of the nuclear spin, is diagonal with its eigenvalues given by the magnetic quantum number $m=-I, -I+1, \cdots, +I$. The energy hF of the molecular surroundings will likewise be assumed to be diagonal and the eigenvalues of F will be denoted by a frequency f; acting as a heat reservoir, the molecular surroundings must be considered to have very many degrees of freedom so that its energy levels are not only practically continuous but in general also highly degenerate. We shall therefore use another symbol s, which will specify one of the possibly many states with the same energy hf.

The dynamical behavior of our system is then described by a set of probability amplitudes $a_{m,f,s}(t)$ or by the density matrix ρ, defined in Dirac's notation by

$$(mfs|\rho(t)|m'f's')=a_{m,f,s}(t)a_{m',f',s'}^{*}(t), \tag{2.3}$$

and satisfying the matrix equation

$$d\rho/dt=-(i/h)[\mathcal{H},\rho].$$

With (2.1), this equation can also be written as

$$d\rho/dt=-i[E+F+G,\rho], \tag{2.4}$$

where the square bracket stands as usual for the commutator. The condition of normalization for the probability amplitudes implies, according to (2.3), that the matrix ρ must be normalized so as to satisfy

$$\mathrm{Tr}\{\rho(t)\}=\sum_{mfs}(mfs|\rho(t)|mfs)=1.$$

From a normalized solution $\rho(t)$ of (2.4) the expectation value of any physical quantity Q, represented by the matrix $(mfs|Q|m'f's')$ is obtained in its time dependence

by the relation

$$\langle Q\rangle(t)=\mathrm{Tr}\{Q\rho(t)\}. \tag{2.5}$$

The right side of this equation represents the diagonal sum or "trace" of the matrix product $Q\rho$.

With the form (1.3) for the external field we can also write (2.2) in the form

$$E=E_0+E_1, \tag{2.6}$$

with

$$E_0=-\omega I_z, \tag{2.7}$$

$$E_1=-\gamma(\mathbf{H}_1\cdot\mathbf{I}), \tag{2.8}$$

and where we have used the abbreviation

$$\omega=\gamma H_0 \tag{2.9}$$

for the circular frequency of precession of the nucleus in the strong field H_0. We shall now consider the nucleus in the field H_0 and the molecular surroundings, uncoupled to each other, as the unperturbed system. With E of the form (2.6) the terms E_0 and F in (2.4) will thus be treated as large, while the terms E_1 and G will represent a small perturbation. In analogy to Dirac's perturbation theory we write therefore

$$\rho=AB\rho^*B^{-1}A^{-1}, \tag{2.10}$$

where $A=e^{-iE_0t}$ or, with (2.7),

$$A=e^{i\omega I_z t}, \tag{2.11}$$

and

$$B=e^{-iFt}. \tag{2.12}$$

One obtains then from (2.4),

$$d\rho^*/dt=-i[E_1^*+G^*,\ \rho^*], \tag{2.13}$$

with

$$E_1^*=A^{-1}EA, \tag{2.14}$$

and

$$G^*=B^{-1}A^{-1}GAB. \tag{2.15}$$

The validity of (2.13) is directly verified by substituting (2.10) in (2.4), using (2.6) and the equality

$$B^{-1}A^{-1}E_1AB=A^{-1}E_1A.$$

This equality holds since B, like F, is an operator which acts only upon the variables f, s of the molecular surroundings and therefore commutes with E_1, A, and A^{-1}, which act upon m alone.

Denoting ρ and ρ^* at the time $t=0$ by $\rho(0)$ and $\rho^*(0)$, respectively, we have from (2.10), (2.11), (2.12) that

$$\rho^*(0)=\rho(0). \tag{2.16}$$

From this initial value one obtains by forward integration in two successive approximations the value of $\rho^*(t)$ at a later time t in the form

$$\rho^*(t)=\rho(0)+\Delta^{(1)}\rho^*+\Delta^{(2)}\rho^*. \tag{2.17}$$

The first-order increment is

$$\Delta^{(1)}\rho^*=-i\int_0^t[E_1^*(t'),\ \rho(0)]dt'-i\int_0^t[G^*(t'),\ \rho(0)]dt'. \tag{2.18}$$

In the second-order increment we have to keep the terms which are quadratic in G^*, but we are allowed to neglect the cross terms of E_1^* and G^* as will be further discussed in the next section; it is then found to be

$$\Delta^{(2)}\rho^*=-\int_0^t\left(\int_0^{t'}[G^*(t'),[G^*(t''),\ \rho(0)]]dt''\right)dt'. \tag{2.19}$$

For the purposes of this investigation we are interested only in the expectation value of quantities concerning the nuclear spin alone, such as the components of $\mathbf{I}$, the angular momentum of the nucleus in units $\hbar$. Quantities of this nature will be generally designated as "spin functions"; in our chosen representation they are diagonal in the variables f and s, referring to the molecular surroundings and hence of the form

$$(mfs|Q|m'f's')=(m|Q|m')\delta_{ff'}\delta_{ss'}. \tag{2.20}$$

In order to evaluate their expectation values according to (2.5) it is sufficient to know the "distribution matrix" σ defined by

$$(m|\sigma|m')=\textstyle\sum_{fs}(mfs|\rho|m'fs), \tag{2.21}$$

instead of the general density matrix ρ. In fact, it follows directly from this definition and from (2.5) that

$$\langle Q\rangle=\mathrm{Tr}\{Q\sigma\}=\textstyle\sum_{mm'}(m'|Q|m)(m|\sigma|m') \tag{2.22}$$

is the expectation value of a spin function Q given by the matrix (2.20). In analogy to the transformation (2.10) we can introduce the matrix,

$$(m|\sigma^*|m')=\textstyle\sum_{fs}(mfs|\rho^*|m'fs), \tag{2.23}$$

which is related to σ by

$$\sigma=A\sigma^*A^{-1}. \tag{2.24}$$

To prove this last relation from (2.10) and from the definitions [(2.21), (2.23)], one merely has to note that F and, through (2.12), also B, is diagonal in m while A is, according to (2.11) a pure spin function and therefore diagonal in f and s. Inserting (2.17) in (2.23), we find that

$$(m|\sigma^*(t)|m')=(m|\sigma^*(0)|m')+(m|\Delta^{(1)}\sigma^*|m')+(m|\Delta^{(2)}\sigma^*|m'), \tag{2.25}$$

with

$$(m|\sigma^*(0)|m')=\textstyle\sum_{fs}(mfs|\rho(0)|m'fs), \tag{2.26}$$

$$(m|\Delta^{(1)}\sigma^*|m')=\textstyle\sum_{fs}(mfs|\Delta^{(1)}\rho^*|m'fs), \tag{2.27}$$

$$(m|\Delta^{(2)}\sigma^*|m')=\textstyle\sum_{fs}(mfs|\Delta^{(2)}\rho^*|m'fs). \tag{2.28}$$

In order to evaluate the matrix (2.26) and, by means of the expressions (2.18), (2.19) and the matrices (2.27), (2.28), a knowledge of the density matrix ρ at the time $t=0$ is required. Actually it is not this matrix $\rho(0)$ which is known but rather its statistical average, to be denoted by $\bar{\rho}(0)$. It indicates the fact that the surroundings are for $t=0$ in statistical equilibrium at the absolute

temperature T. This implies that there exists no phase relation between the probability amplitudes for different states, characterized by f and s, and that the probability of finding the surroundings in any one of these states is given by the Boltzmann factor $P(f)$, which depends only on the energy hf. Going back to the definition (2.3) of the density matrix and taking the statistical average of this equation for $t=0$, we have, therefore,

$$(mfs|\bar{\rho}(0)|m'f's')=(m|\sigma(0)|m')P(f)\delta_{ff'}\delta_{ss'}. \quad (2.29)$$

The appearance of the arbitrary matrix $(m|\sigma(0)|m')$ signifies that we maintain complete generality in regard to the initial state of the nucleus. The fact that this matrix represents indeed the distribution matrix at the time $t=0$ can be verified if one replaces $\rho(0)$ by $\bar{\rho}(0)$ in (2.26), noting further that

$$\sum_{f,s}P(f)=1, \quad (2.30)$$

and that by virtue of (2.11) and (2.24),

$$(m|\sigma^*(0)|m')=(m|\sigma(0)|m'). \quad (2.31)$$

We shall from now on be concerned with statistical averages which are obtained through the replacement of the matrix $\rho(0)$ by its average $\bar{\rho}(0)$ of Eq. (2.29). In a strictly consistent notation this replacement should be indicated by placing a bar over the corresponding quantities, such as $(m|\bar{\sigma}(t)|m')$, $\langle\bar{Q}\rangle$, etc. To avoid an overburdened notation we shall, however, omit this bar and keep the previous notations with the understanding that in the remaining part of this paper $\rho(0)$ will be replaced throughout by the matrix (2.29) and that all further relations for the distribution matrices σ, σ^* and for the expectation values of spin functions refer to their statistical averages.

The expressions (2.27), (2.28) for the statistical average of the increments $\Delta^{(1)}\sigma^*$ and $\Delta^{(2)}\sigma^*$ are thus directly obtained by writing Eqs. (2.18), (2.19) in matrix form, replacing $(mfs|\rho(0)|m'f's')$ by (2.29) and using the equality

$$(mfs|G^*|m'f's')=e^{i(f-m\omega-f'+m'\omega)t}(mfs|G|m'f's'), \quad (2.32)$$

which is valid by virtue of the relations (2.15) and (2.11), (2.12). For the summations over f, implied by (2.27), (2.28) as well as by the formation of matrix products in (2.18), (2.19) we shall from now on assume that the energy values hf of the molecular surroundings form practically a continuum. The number of states with a given quantum number s and with f between f and $f+df$ will be given by

$$dn_s=\eta_s(f)df, \quad (2.33)$$

so that the symbol $\sum_{fs}$ is to be replaced throughout by $\sum_s\int\eta_s(f)df$. The relation (2.30) has in this notation the form

$$\sum_s\int\eta_s(f)P(f)df=1, \quad (2.34)$$

and the Boltzmann factor $P(f)$ in (2.29) is to be written explicitly as

$$P(f)=e^{-hf/kT}\Big/\sum_s\int\eta_s(f')e^{-hf'/kT}df'. \quad (2.35)$$

Following the procedure indicated above and by virtue of (2.31) replacing in (2.29) $(m|\sigma(0)|m')$ by $(m|\sigma^*(0)|m')$, one obtains

$$\begin{aligned}(m|\Delta^{(1)}\sigma^*|m')=&\\ -i\sum_{m''}\int_0^t dt'\{&(m|E_1^*(t')|m'')(m''|\sigma^*(0)|m')\\ &-(m|\sigma^*(0)|m'')(m''|E_1^*(t')|m')\}\\ -i\sum_s\sum_{m''}\int\eta_s(f)P(f)df\int_0^t dt'&\\ \times\{&e^{-i\omega(m-m'')t'}(mfs|G|m''fs)(m''|\sigma^*(0)|m')\\ &-e^{-i\omega(m''-m')t'}(m|\sigma^*(0)|m'')(m''fs|G|m'fs)\},\end{aligned} \quad (2.36)$$

and

$$\begin{aligned}(m|\Delta^{(2)}\sigma^*|m')=&\\ -\sum_{s,s'}\sum_{m'',m'''}\int\eta_s(f)P(f)df\int\eta_{s'}(f')df'\int_0^t dt'\int_0^{t'}dt''&\\ \times\{e^{i(f-m\omega-f'+m''\omega)t'+i(f'-m''\omega-f+m'''\omega)t''}&\\ \times(mfs|G|m''f's')(m''f's'|G|m'''fs)(m'''|\sigma^*(0)|m')&\\ -e^{i(f'-m\omega-f+m'''\omega)t'+i(f-m'''\omega-f'+m'\omega)t''}&\\ \times(mf's'|G|m''fs)(m''|\sigma^*(0)|m''')(m'''fs|G|m'f's')&\\ -e^{i(f-m'''\omega-f'+m'\omega)t'+i(f'-m\omega-f+m''\omega)t''}&\\ \times(mf's'|G|m''fs)(m''|\sigma^*(0)|m''')(m'''fs|G|m'f's')&\\ +e^{i(f'-m'''\omega-f+m'\omega)t'+i(f-m''\omega-f'+m'''\omega)t''}&\\ \times(m|\sigma^*(0)|m'')(m''fs|G|m'''f's')(m'''f's'|G|m'fs)\}.&\end{aligned} \quad (2.37)$$

To obtain the first term in (2.36) from that in (2.18) it has to be noted that E_1, defined by (2.8), is a spin function and thus, according to (2.20), to be represented by the matrix

$$(mfs|E_1(t)|m'f's')=(m|E_1(t)|m')\delta_{ff'}\delta_{ss'}. \quad (2.38)$$

$E_1^*(t)$ is therefore by virtue of (2.14) and (2.11) likewise a spin function represented by the matrix

$$(mfs|E_1^*(t)|m'f's')=(m|E_1^*(t)|m')\delta_{ff'}\delta_{ss'} \quad (2.39)$$

with

$$(m|E_1^*(t)|m')=e^{-i\omega(m-m')t}(m|E_1(t)|m'). \quad (2.40)$$

3. THE BOLTZMANN EQUATION FOR THE DISTRIBUTION MATRIX

Equations (2.36), (2.37) for the increments yield, through (2.25), the transformed distribution matrix σ^* at a time t in terms of its initial value $\sigma^*(0)$. The time interval t must be chosen sufficiently small so that (2.25) represents a good approximation, i.e., that the omitted terms of higher order than the first in E_1 and the second in G are indeed negligible. To estimate orders of magnitude this condition may be considered equivalent to stating that the lower order terms themselves which have been kept in $\Delta^{(1)}\sigma^*$ and $\Delta^{(2)}\sigma^*$ cause these increments to be small compared to the initial value $\sigma(0)$. For the linear terms in E_1^* in Eq. (2.36) it requires

$$\gamma|H_1|t\ll 1, \tag{3.1}$$

where we may define $|H_1|$ as the "effective" magnitude of the weak variable field $\mathbf{H}_1$ of Eq. (1.3). Due to the fact that E_1^* occurs in (2.36) as the integrand in a time integral and because of the relation (2.40) and the definition of E_1 by (2.8), it is seen that the effective magnitude $|H_1|$ depends greatly upon the frequencies contained in the actual field $\mathbf{H}_1$. In the case of greatest practical importance, where $\mathbf{H}_1$ is transverse and varies with a frequency in the neighborhood of the resonance frequency ω, the effective magnitude is of the same order as the actual magnitude of $\mathbf{H}_1$; it is, however, smaller if $\mathbf{H}_1$ varies with a frequency which differs appreciably from ω. Concerning the increments due to the perturbation G it will be seen later that the linear terms in (2.36) do not have to be considered in this connection and that the quadratic terms in (2.37) become relatively important only after a time t of the order of the relaxation times T_1 or T_2, defined in Sec. 1. It is therefore necessary, besides the condition (3.1), to demand both

$$t\ll T_1 \quad \text{and} \quad t\ll T_2. \tag{3.2}$$

We shall now proceed to discuss separately the various terms in (2.36) and (2.37). If we introduce the commutator of the two matrices $(m|E_1^*|m')$ and $(m|\sigma^*(0)|m')$, the first term of (2.36) can be conveniently written in the form

$$-i\int_0^t (m|[E_1^*(t'),\sigma^*(0)]|m')dt'.$$

Upon carrying out the integration over t' and introducing the matrix

$$(m|K(t)|m')=\hbar\frac{1-e^{-i\omega(m-m')t}}{i\omega(m-m')}\sum_s\int\eta_s(f)\times P(f)(mfs|G|m'sf)df, \tag{3.3}$$

we find that the second term of (2.36) can be similarly written in the form

$$-(i/\hbar)(m|[K(t),\sigma^*(0)]|m').$$

Besides satisfying the conditions (3.1), (3.2), the time interval t will from now on be chosen so large that it contains many periods of precession in the constant field H_0; i.e., we demand also that

$$\gamma H_0 t=\omega t\gg 1. \tag{3.4}$$

The off-diagonal elements of the matrix (3.3) are small compared to the diagonal elements in the order $1/\omega t$ and hence negligible in view of (3.4); we can therefore effectively write

$$(m|K(t)|m')=t\Delta E_m\delta_{mm'}, \tag{3.5}$$

where

$$\Delta E_m=\hbar\sum_s\int\eta_s(f)P(f)(mfs|G|mfs)df \tag{3.6}$$

represents the average value of the interaction energy $\hbar G$. Equation (3.5) expresses the fact that the first-order effect of the surroundings causes merely a shift of the nuclear Zeeman levels by ΔE_m. While such shifts may actually occur, they are not essential for the following discussion and will for simplicity's sake be disregarded by assuming that $\Delta E_m=0$; this assumption is besides frequently justified by the fact that the perturbations upon the nucleus are of such fluctuating character as to render zero the diagonal matrix elements of G appearing in (3.6).

We are therefore justified in rewriting (2.36) in the simplified form

$$(m|\Delta^{(1)}\sigma^*|m')=-i\int_0^t(m|[E_1^*(t'),\sigma^*(0)]|m')dt', \tag{3.7}$$

being left solely with the second-order increment (2.37) for the effect of the coupling between the nucleus and its molecular surroundings.

To render the discussion of (2.37) more convenient we shall write this equation in the form

$$(m|\Delta^{(2)}\sigma^*|m')=-\sum_{s,s'}\int\eta_s(f)P(f)df\times\int\eta_{s'}(f')df'(mfs|L|m'f's'), \tag{3.8}$$

where it is seen from carrying out the integrations over t' and t'' in (2.37) that

$$\begin{aligned}(mfs|L|m'f's')=&\sum_{m'',m'''}\{(mfs|G|m''f's')(m''f's'|G|m'''fs)\\&\times(m'''|\sigma^*(0)|m')\varphi[f-f'-\omega(m-m''),m'''-m]\\&-(mf's'|G|m''fs)(m''|\sigma^*(0)|m''')(m'''fs|G|m'f's')\\&\times\varphi[f'-f-\omega(m-m''),m''-m+m'-m''']\\&-(mf's'|G|m''fs)(m''|\sigma^*(0)|m''')(m'''fs|G|m'f's')\\&\times\varphi[f-f'-\omega(m'''-m'),m''-m+m'-m''']\\&+(m|\sigma^*(0)|m'')(m''fs|G|m'''f's')(m'''f's'|G|m'fs)\\&\times\varphi[f'-f-\omega(m'''-m'),m'-m'']\},\end{aligned} \tag{3.9}$$

with

$$\varphi[x, n]=\frac{x(e^{in\omega t}-1)-n\omega(e^{ixt}-1)}{n\omega x(x-n\omega)}. \quad (3.10)$$

The integration over f' in (3.8) requires integrals of the form

$$\int \chi(x)\varphi[x, n]dx$$

$$=t\int \chi(\xi/t)\frac{\xi(e^{i\nu}-1)-\nu(e^{i\xi}-1)}{\nu\xi(\xi-\nu)}d\xi, \quad (3.11)$$

where

$$\xi=xt; \quad \nu=n\omega t. \quad (3.12)$$

For a sufficiently long interval t, the integration over ξ may be extended from $-\infty$ to $+\infty$ and the function χ may be replaced by its value for the argument zero, provided that it is a sufficiently slowly varying function. The expression (3.11) becomes thus effectively

$$t\chi(0)\int_{-\infty}^{+\infty}\frac{\xi(e^{i\nu}-1)-\nu(e^{i\xi}-1)}{\nu\xi(\xi-\nu)}d\xi=\pi t\chi(0)(e^{i\nu}-1)/i\nu. \quad (3.13)$$

It is seen from (3.9) and (3.10) that the quantity n appearing in the definition (3.12) of ν is an algebraic sum of two or four values of the magnetic quantum number and hence an integer. All those terms encountered in the summation over m' and m'' in (3.9) for which $n\neq 0$ yield a periodic dependence upon t and are of relative order of magnitude $1/\omega t$, compared to the terms with $n=0$, which yield a linear dependence upon t. The former are therefore negligible compared to the latter if t is again chosen long enough to satisfy the condition (3.4), so that we can write

$$\int \chi(x)\varphi[x, n]dx=\begin{cases}\pi t\chi(0) & \text{for } n=0,\\ 0 & \text{for } n\neq 0.\end{cases}$$

With Dirac's δ-function and the usual δ-symbol this result can be expressed in the form

$$\varphi[x, n]=\pi t\delta(x)\delta_{n,0}. \quad (3.14)$$

Using this property of φ in the summation over m'', m''' in (3.9) and in the integration over f' in (3.8) one obtains

$$(m|\Delta^{(2)}\sigma^*|m')$$
$$=t\sum_\tau\{2\Gamma_{m'+\tau,m+\tau}{}^{-\tau}(m+\tau|\sigma^*(0)|m'+\tau)$$
$$-(\Gamma_{mm}{}^{\tau}+\Gamma_{m'm'}{}^{\tau})(m|\sigma^*(0)|m')\}, \quad (3.15)$$

with

$$\Gamma_{mm'}{}^{\tau}=\pi\sum_{s,s'}\int \eta_s(f)P(f)$$
$$\times\eta_{s'}(f+\tau\omega)(mfs|G|m+\tau, f+\tau\omega, s')$$
$$\times(m'+\tau, f+\tau\omega, s'|G|m'fs)df. \quad (3.16)$$

Noting from (2.35) that

$$P(f+\tau\omega)=e^{-\kappa\tau}P(f),$$

with

$$\kappa=\hbar\omega/kT, \quad (3.17)$$

one obtains from (3.16) the relation

$$\Gamma_{m'+\tau,m+\tau}{}^{-\tau}=e^{-\kappa\tau}\Gamma_{mm'}{}^{\tau}. \quad (3.18)$$

The result (3.15) can thus be written in the more convenient form,

$$(m|\Delta^{(2)}\sigma^*|m')$$
$$=t\sum_\tau\{2e^{-\kappa\tau}\Gamma_{mm'}{}^{\tau}(m+\tau|\sigma^*(0)|m'+\tau)$$
$$-(\Gamma_{mm}{}^{\tau}+\Gamma_{m'm'}{}^{\tau})(m|\sigma^*(0)|m')\}. \quad (3.19)$$

In order that the derivation of the result (3.19) be valid another condition for the length of the time interval t has to be satisfied. Going back to Eqs. (3.8), (3.9) it is seen that the replacement of the function $\chi(x)$ by its value for the argument $x=0$ in (3.13), and hence the appearance of the Dirac δ-function in (3.14), requires that products formed by the function $\eta_{s'}(f')$ and matrix elements of the form $(mfs|G|m''f's')$ are sufficiently slowly varying functions of the variable f'. To formulate this condition in a quantitative manner we introduce a "characteristic frequency" ω^* of the molecular surroundings, which will indicate the effective scale in which the spread of the frequencies f' has to be measured. The condition justifying the step from Eq. (3.11) to (3.13) can then be written in the form

$$\omega^* t\gg 1. \quad (3.20)$$

The physical significance of the frequency ω^* depends entirely upon the nature of the surroundings, and its order of magnitude may be very different in different cases. In crystals, e.g., it must be expected to be of the order $k\theta/h$, where θ is the characteristic temperature, used in Debye's theory of the specific heat. In the case of gases, ω^* may have the significance of the inverse time during a collision or between collisions, depending upon whether the interaction with the nucleus is directly due to the colliding partner (e.g., if the latter consists of a paramagnetic molecule) or whether it consists of the coupling to the rotation of the molecule, containing the nucleus, whereby transitions between rotational states are of primary importance. A third example is encountered in liquids where $1/\omega^*$ may be primarily determined by the correlation time and thus dependent upon the viscosity.[2]

The validity of the results (3.7) and (3.19) for the increments of σ^* demands that one can choose a time interval t which is neither too short nor too long so that all four conditions [(3.1), (3.2), (3.4), (3.20)] are simultaneously satisfied. This evidently requires six conditions which all can be formulated by the relation

$$(\gamma|H_1|, 1/T_1, 1/T_2)\ll(\gamma H_0, \omega^*), \quad (3.21)$$

in the sense that each of the three quantities on the left side must be small compared to each of the two quantities on the right side. It is seen that the relative strength of the constant field H_0 in comparison to the effective magnitude $|H_1|$ of the variable field, mentioned in Sec. 1, is only a necessary but not a sufficient condition. Neither this condition nor the others implied by (3.21) is of course automatically fulfilled, and they may actually be violated in extreme cases (e.g., in the presence of a very weak constant field). In most practical cases they are, however, well fulfilled so that the conditions (3.21) represent no serious restriction for the applications of our results.

Assuming these conditions to be satisfied, we shall now, as mentioned in the beginning of this section, choose the time interval t short enough so that the expressions (3.7) and (3.19) represent the corresponding small increments of σ^*. Equation (2.25) can then be written in the differential form

$$d(m|\sigma^*|m')/dt=-i(m|[E_1^*(t),\sigma^*]|m') +\sum_\tau\{2e^{-\kappa\tau}\Gamma_{mm'\tau}(m+\tau|\sigma^*|m'+\tau) -(\Gamma_{mm}{}^\tau+\Gamma_{m'm'}{}^\tau)(m|\sigma^*|m')\}. \quad (3.22)$$

We shall claim this differential equation to be valid at any time t despite the fact that Eq. (2.25) refers to a specific initial time $t=0$. One might consider this claim to be obviously justified since any one instant can be chosen to be "initial" as well as any other. It must be kept in mind, however, that we have actually distinguished the time $t=0$ by choosing at this instant the specific form (2.29) for the statistical average of the density matrix. This choice would evidently be strictly satisfied under the hypothetical condition that the interaction between the nucleus and its surroundings is ineffective up to the time $t=0$ and that the latter had come to thermal equilibrium previous to this instant. However, because of the interaction, this equilibrium would be upset at a later time; and since in reality the interaction remains, of course, always effective, it might seem that our choice is based upon an inconsistency. Nevertheless, it is actually seen to be justified if one considers that the molecular surroundings normally have so very many degrees of freedom that it takes a long time before the interaction with the nucleus affects a sufficient number of them to cause an appreciable deviation from equilibrium conditions. We may safely assume either that this time is too long to matter for our considerations or that the molecular system is in sufficient contact with a "heat reservoir" which re-establishes equilibrium conditions more rapidly than they would be upset by the sole action of the nuclei. Physically this means that the "local heating" in the neighborhood of each nucleus is negligible, i.e., that the heat conduction of the molecular system is sufficiently high so that the heat transferred from the nucleus is carried away before it can effectively react backward upon the latter.

Under these circumstances it is legitimate to obtain the transformed distribution matrix σ^* as a solution of the differential equation (3.22). It remains to derive an equivalent equation for the distribution matrix σ related to σ^* by (2.24). This relation has, in view of (2.11), the matrix form

$$(m|\sigma|m')=e^{i\omega(m-m')t}(m|\sigma^*|m'), \quad (3.23)$$

so that with the further use of (2.7),

$$d(m|\sigma|m')/dt=-i(m|[E_0,\sigma]|m') +e^{i\omega(m-m')t}d(m|\sigma^*|m')/dt. \quad (3.24)$$

Inserting in the last term of (3.24) the expression (3.22), replacing σ^* by σ through (3.23), and using (2.6), one obtains thus

$$d(m|\sigma|m')/dt=-i(m|[E,\sigma]|m') +\sum_\tau\{2e^{-\kappa\tau}\Gamma_{mm'\tau}(m+\tau|\sigma|m'+\tau) -(\Gamma_{mm}{}^\tau+\Gamma_{m'm'}{}^\tau)(m|\sigma|m')\}. \quad (3.25)$$

In analogy to the classical Boltzmann equation for distribution functions, we shall refer to this system of differential equations as the Boltzmann equation for the distribution matrix σ. It allows the determination of the matrix elements of σ in an external field as a function of time in terms of their values at a given instant and represents the most general result of this investigation. Once this time dependence has been determined, that of the expectation value of any spin function Q is obtained from (2.22).

Before discussing this problem we shall note some of the properties of (3.25). From the condition of normalization,

$$\sum_{mfs}(mfs|\rho(t)|mfs)=1,$$

for the density matrix (2.3) given in Sec. 2, one obtains from (2.21) for the distribution matrix σ the normalization,

$$\sum_m(m|\sigma(t)|m)=1. \quad (3.26)$$

The fact that this condition is compatible with the Boltzmann equation (3.25) can be directly verified by showing that the time derivative of the left side vanishes by virtue of this equation and the relation (3.18).

It can also be verified that the spin states have a stationary Boltzmann distribution in the absence of the alternating field H_1, where one has from (2.6) and (2.8) $E=E_0$. It is expressed by the fact that (3.25) has in this case the time-independent normalized solution,

$$(m|\sigma|m')=e^{\kappa m}\delta_{mm'}\sinh(\kappa/2)/\sinh[\kappa(I+\tfrac{1}{2})], \quad (3.27)$$

and is essentially based upon the circumstance that E_0 is, according to (2.7), represented by a diagonal matrix so that it commutes with (3.27).

Another case of considerable practical interest is that in which kT is large compared to the separation $\hbar\omega$ of the nuclear Zeeman levels in the external field H_0, so

that according to (3.17) $\kappa \ll 1$. Keeping only the linear terms in κ, one has here

$$(m|\sigma|m') = (m|\sigma_0|m') + \kappa(m|\sigma_1|m'), \quad (3.28)$$

with

$$(m|\sigma_0|m') = \delta_{mm'}/(2I+1), \quad (3.29)$$

and where the matrix σ_1 is a solution of

$$\begin{aligned} &d(m|\sigma_1|m')/dt = \\ &\quad -i(m|[E, \sigma_1]|m') - \sum_\tau \{2\Gamma_{mm}{}^\tau (m+\tau|\sigma_1|m'+\tau) \\ &\quad -(\Gamma_{mm}{}^\tau + \Gamma_{m'm'}{}^\tau)(m|\sigma_1|m')\} \\ &\qquad -(2\delta_{mm'}/2I+1)\sum_\tau \tau \Gamma_{mm}{}^\tau. \end{aligned} \quad (3.30)$$

4. EXPECTATION VALUES OF SPIN FUNCTIONS

We shall here consider the manner in which expectation values of spin functions vary with the time t; in particular, we shall restrict ourselves to the case where the spin function Q and thereby, according to (2.20), the matrix $(m|Q|m')$, does not explicitly depend upon t. Nevertheless, its expectation value (2.22) will in general be a function of t through the time dependence of the distribution matrix σ, obtained by integrating the Boltzmann equation (3.25). While this procedure can in principle always be carried out, it may lead to rather involved calculations; an explicit knowledge of the distribution matrix is, however, in many cases not required. Particularly in those cases which lead to the phenomenological equations (1.1) and in which we are especially interested, it is possible to establish directly differential equations for expectation values which are far easier to treat than the general Boltzmann equation (3.25).

We shall therefore form directly

$$d\langle Q\rangle/dt = \sum_{mm'}(m'|Q|m)d(m|\sigma|m')/dt, \quad (4.1)$$

and insert on the right side of the equation the expression for the time derivative of σ, obtained from (3.25). While this insertion leads to no difficulty it does not, in itself, present a simple basis of discussion. A simple form is, however, obtained if we assume that the interaction operator G of Eq. (2.1) can be expanded in the form

$$G = \sum_{l,\tau} I_l{}^\tau F_l{}^{-\tau}, \quad (4.2)$$

where the operators $I_l{}^\tau$ will be a pure spin function while the operators $F_l{}^\tau$ will act upon the variables of the molecular surroundings alone, and are to be represented by matrices of the form

$$(mfs|F_l{}^\tau|m'f's') = (fs|F_l{}^\tau|f's')\delta_{mm'}. \quad (4.3)$$

It will further be assumed that $I_l{}^\tau$ is represented by a matrix of the form

$$(m|I_l{}^\tau|m') = I_{lm}{}^\tau \delta_{m,\,m'+\tau}. \quad (4.4)$$

The form (4.2) corresponds to the usual expansion of the energy of interaction between the nucleus and an external electromagnetic field in magnetic dipole, electric quadrupole, and higher terms. With the indices $l=1$, 2 for magnetic dipole- and electric quadrupole-interaction, respectively, one has for $l=1$,

$$\begin{aligned} &I_1{}^0 = I_z, \quad F_1{}^0 = -\gamma H_z', \\ &I_1{}^{\pm 1} = I^\pm, \quad F_1{}^{\pm 1} = -\tfrac{1}{2}\gamma(H_x' \pm iH_y'), \\ &I_1{}^\tau = 0, \quad \text{for } |\tau|>1; \end{aligned} \quad (4.5)$$

and for $l=2$,

$$\begin{aligned} &I_2{}^0 = 2I_z{}^2 - I_x{}^2 - I_y{}^2, \\ &F_2{}^0 = -\{q/4hI(2I-1)\}\partial E_z'/\partial z, \\ &I_2{}^{\pm 1} = I_z I^\pm + I^\pm I_z, \\ &F_2{}^{\pm 1} = -\{q/4hI(2I-1)\}(\partial E_z'/\partial z \pm i\partial E_y'/\partial z), \\ &I_2{}^{\pm 2} = (I^\pm)^2, \\ &F_2{}^{\pm 2} = -\{q/8hI(2I-1)\}(\partial E_x'/\partial x \\ &\qquad -\partial E_y'/\partial y \pm 2i\partial E_x'/\partial y), \\ &I_2{}^\tau = 0, \quad \text{for } |\tau|>2, \end{aligned} \quad (4.6)$$

where we have used the abbreviation

$$I^\pm = I_x \pm iI_y. \quad (4.7)$$

γ stands further for the gyromagnetic ratio (1.2) of the nucleus, and q for its electric quadrupole moment. The magnetic field components H_x', H_y', H_z', as well as the derivatives of the electric field components E_x', E_y', E_z', are to be taken at the position of the nucleus and refer to the fields produced by the molecular surroundings; they are therefore to be represented by matrices acting only upon the variables f and s. The terms for higher values of l in (4.2) correspond to higher multipole interactions and their explicit form will not be needed in our further discussion.

Using the form (4.2) of G and the Eqs. (4.3) and (4.4), one obtains now from (3.16)

$$\Gamma_{mm'}{}^\tau = \sum_{l,l'} I_{lm}{}^{-\tau} I_{l',\,m'+\tau}{}^\tau \Phi_{ll'}{}^\tau, \quad (4.8)$$

with

$$\begin{aligned} \Phi_{ll'}{}^\tau = \pi \sum_{s,s'} \int &\eta_s(f)P(f)\eta_{s'}(f+\tau\omega)(fs|F_l{}^\tau|f+\tau\omega, s') \\ &\times (f+\tau\omega, s'|F_{l'}{}^{-\tau}|fs)df. \end{aligned} \quad (4.9)$$

By expressing the time derivative of the distribution matrix through the Boltzmann equation (3.25) with the expression (4.8) inserted and using the relation (4.4), one obtains now from (4.1)

$$\begin{aligned} d\langle Q\rangle/dt = -i\langle[Q, E]\rangle + \sum_{\tau,l,l'} &\Phi_{ll'}{}^\tau \{2e^{-\kappa\tau}\langle I_{l'}{}^\tau Q I_l{}^{-\tau}\rangle \\ &-\langle QI_l{}^{-\tau}I_{l'}{}^\tau\rangle - \langle I_l{}^{-\tau}I_{l'}{}^\tau Q\rangle\}. \end{aligned} \quad (4.10)$$

Noting the relation

$$\Phi_{l'l}{}^{-\tau} = e^{-\kappa\tau}\Phi_{ll'}{}^\tau, \quad (4.11)$$

which follows from (4.9) in analogy to (3.18), and the

identity

$$2I_l^{-\tau}QI_{l'}^{\tau}-QI_l^{-\tau}I_{l'}^{\tau}-I_l^{-\tau}I_{l'}^{\tau}Q = I_l^{-\tau}[Q, I_{l'}^{\tau}]+[I_l^{-\tau}, Q]I_{l'}^{\tau},$$

the equation (4.10) can be written in the still simpler form,

$$d\langle Q\rangle/dt=-i\langle[Q, E]\rangle + \sum_{\tau ll'}\Phi_{ll'}{}^{\tau}\langle I_l^{-\tau}[Q, I_{l'}^{\tau}]+[I_l^{-\tau}, Q]I_{l'}^{\tau}\rangle, \quad (4.12)$$

which is particularly suitable for our further discussions.

We are for our purposes particularly interested in the case where Q stands for any one of the components of the spin vector $\mathbf{I}$. In fact, the expectation value of the magnetic moment $\boldsymbol{\mu}$ of the nucleus is directly given by that of $\mathbf{I}$ through

$$\langle\boldsymbol{\mu}\rangle=\gamma h\langle\mathbf{I}\rangle, \quad (4.13)$$

where γ is the gyromagnetic ratio (1.2). If there are n nuclei of the considered kind per unit volume whose molecular surroundings have the same properties, one has for the macroscopic polarization vector

$$\mathbf{M}=n\langle\boldsymbol{\mu}\rangle=n\gamma h\langle\mathbf{I}\rangle, \quad (4.14)$$

where the expectation values refer to the representative single nucleus, treated in the previous sections. The fact that the macroscopic quantity $\mathbf{M}$ has to be obtained from a statistical average over expectation values of the microscopic quantities $\boldsymbol{\mu}$ and $\mathbf{I}$ needs no further consideration here; it has been taken into account in the previous replacement of the actual density matrix by its statistical average through Eq. (2.29). The time dependence of $\mathbf{M}$ is thus directly given by that of $\langle\mathbf{I}\rangle$, and the validity of the phenomenological equation (1.1) demands that the equations obtained from (4.12) with $Q=I_{x,y,z}$ result in a system of linear differential equations which differs from (1.1) merely by the factor $n\gamma h$.

The fact that the first term on the left side of (4.12) has indeed the proper structure, demanded by the corresponding term in (1.1), is immediately seen from the commutation rules

$$[I_x, I_y]=iI_z; \quad [I_y, I_z]=iI_x; \quad [I_z, I_x]=iI_y, \quad (4.15)$$

which yield, with the expression (2.2) for E,

$$-i\langle[\mathbf{I}, E]\rangle=\gamma\langle\mathbf{I}\times\mathbf{H}\rangle. \quad (4.16)$$

For the discussion of the second term we neglect the contributions for the values $l, l'>2$. This means that we shall consider only magnetic dipole and electric quadrupole interactions of the nucleus and its surroundings; the higher moments will be neglected both for simplicity's sake and because of their subordinate practical importance. With this understanding, it is also permissible to omit the mixed terms with $l=1$, $l'=2$, or vice versa, for with the magnetic field of Eqs. (4.5) an axial vector and the electric field of Eqs. (4.6) a polar vector, there is no relation between their signs so that the corresponding quantities $\Phi_{12}{}^{\tau}$ and $\Phi_{21}{}^{\tau}$, defined by (4.9), must be indeed expected to vanish.

Using the abbreviation

$$S_l(Q)=\sum_{\tau}\Phi_{ll'}{}^{\tau}\langle I_l^{-\tau}[Q, I_{l'}^{\tau}]+[I_l^{-\tau}, Q]I_{l'}^{\tau}\rangle, \quad (4.17)$$

we can thus write the result of substituting for Q the components of $\mathbf{I}$ in (4.12) in the form

$$d\langle\mathbf{I}\rangle/dt=\gamma\langle\mathbf{I}\times\mathbf{H}\rangle+S_1(\mathbf{I})+S_2(\mathbf{I}). \quad (4.18)$$

The evaluation of the expressions $S_1(\mathbf{I})$ and $S_2(\mathbf{I})$ is straightforward; one has merely to use the expressions of $I_1{}^{\tau}$ and $I_2{}^{\tau}$, given in (4.5) and (4.6), to apply the commutation relations (4.15), and to use the fact that $I_x^2+I_y^2+I_z^2=I(I+1)$. The procedure is, however, somewhat lengthy, and we shall therefore omit intermediate steps and give the results directly. Combining terms with equal and opposite values of τ by means of the relation (4.11) one finds that

$$S_1(I_z)=-2\Phi_{11}{}^{1}(1+e^{-s})\langle I_z\rangle + 2\Phi_{11}{}^{1}(1-e^{-s})\langle I(I+1)-(I_z)^2\rangle, \quad (4.19)$$

$$S_1(I_{x,y})=-\Phi_{11}{}^{0}\langle I_{x,y}\rangle-\Phi_{11}{}^{1}(1+e^{-s})\langle I_{x,y}\rangle - \Phi_{11}{}^{1}(1-e^{-s})\langle I_{x,y}I_z+I_zI_{x,y}\rangle, \quad (4.20)$$

$$\begin{aligned}S_2(I_z)=&-2\Phi_{22}{}^{1}(1+e^{-s})\langle 8(I_z)^3-4I(I+1)I_z+I_z\rangle\\ &+2\Phi_{22}{}^{1}(1-e^{-s})\langle 4I(I+1)(I_z)^2-4(I_z)^4\\ &-5(I_z)^2+I(I+1)\rangle+4\Phi_{22}{}^{2}(1+e^{-2s})\\ &\times\langle 4(I_z)^3-4I(I+1)I_z+2I_z\rangle\\ &+4\Phi_{22}{}^{2}(1-e^{-2s})\langle I^2(I+1)^2-2I(I+1)(I_z)^2\\ &+(I_z)^4+5(I_z)^2-2I(I+1)\rangle, \quad (4.21)\end{aligned}$$

$$\begin{aligned}S_2(I_{x,y})=&-9\Phi_{22}{}^{0}\langle 2(I_{x,y}(I_z)^2+(I_z)^2I_{x,y})-I_{x,y}\rangle\\ &+\Phi_{22}{}^{1}(1+e^{-s})\langle(3-4I(I+1))I_{x,y}\rangle\\ &-\Phi_{22}{}^{1}(1-e^{-s})\langle 4(I_{x,y}(I_z)^3+(I_z)^3I_{x,y})\\ &+7(I_{x,y}I_z+I_zI_{x,y})\rangle+\Phi_{22}{}^{2}(1+e^{-2s})\\ &\times\langle 6(I_{x,y}(I_z)^2+(I_z)^2I_{x,y})-4I(I+1)I_{x,y}\rangle\\ &+\Phi_{22}{}^{2}(1-e^{-2s})\langle 2(I_{x,y}(I_z)^3+(I_z)^3I_{x,y})\\ &+(4-2I(I+1))(I_{x,y}I_z+I_zI_{x,y})\rangle. \quad (4.22)\end{aligned}$$

The relation of these expressions to the validity of the phenomenological equations will be discussed in the following section.

5. CASES OF VALIDITY OF THE PHENOMENOLOGICAL EQUATION

Equation (4.18) with the general expressions for S_1 and S_2, given by (4.19) to (4.22), has the same range of validity as the Boltzmann equation simplified by the omission of higher multipole interactions. It has the advantage that it relates the time derivative of the expectation value of $\mathbf{I}$ directly to the expectation values of other functions of its components. The time dependence of the latter would, however, have to be known in order to integrate (4.18), and it would thus seem that one is led back to the distribution matrix, i.e., to the integration of the general Boltzmann equa-

tion (3.25). Yet there exists a number of important special cases where the expectation values appearing in $S_1(\mathbf{I})$ and $S_2(\mathbf{I})$ can be reduced to contain only those of the components of $\mathbf{I}$ itself. Equation (4.18) represents in this case a set of three simultaneous linear differential equations of the first order between these components, which is not only easier to integrate than (3.25) but actually results, as we shall see, in Eq. (1.1) for the macroscopic polarization. We will now discuss these cases separately.

Case a, $I=\frac{1}{2}$: This case is particularly simple since a nucleus with spin $\frac{1}{2}$ has no electric quadrupole moment so that the term S_2 in (4.18) is absent. Noting further that one has here

$$I(I+1)-(I_z)^2=\tfrac{1}{2}; \quad (I_zI_{x,y}+I_{x,y}I_z)=0,$$

one obtains from (4.19)

$$S_1(I_z)=-\langle I_z\rangle/T_1+I_0/T_1, \tag{5.1}$$

$$S_1(I_{x,y})=-\langle I_{x,y}\rangle/T_2, \tag{5.2}$$

with

$$1/T_1=2\Phi_{11}{}^1(1+e^{-\kappa}), \tag{5.3}$$

$$1/T_2=(1/2T_1)+\Phi_{11}{}^0, \tag{5.4}$$

$$I_0=(1/2)\tanh(\kappa/2). \tag{5.5}$$

Inserting this result in (4.18) and multiplying this equation according to (4.14) with $n\gamma h$, it is seen that one obtains here indeed Eq. (1.1) for the macroscopic polarization with

$$M_0=n\gamma hI_0=n\mu\tanh(H_0\mu/kT) \tag{5.6}$$

as the correct equilibrium polarization of nuclei with spin $\frac{1}{2}$ and magnetic moment μ in an external field H_0. The second equality in (5.6) has been obtained from (5.5), using further (1.2) for $I=\frac{1}{2}$, (2.9), and (3.17). We see thus that the general Boltzmann equation (3.25) leads for nuclei with spin $\frac{1}{2}$ rigorously to the phenomenological equation (1.1).

Case b, $\kappa\ll 1$: The range of validity of the phenomenological equations is considerably extended by assuming $\kappa\ll 1$; this means, according to Eq. (3.17), that the Zeeman splitting of the nuclear energy levels due to the external field H_0 is small compared to kT. Actually this is hardly a restriction of the practical applications since κ is of the order of 10^{-6} for fields of about 10^4G and at normal temperatures; it becomes comparable to unity only at exceedingly low temperatures or in exceedingly strong fields.

The expressions for S_1 and S_2, given in Eqs. (4.19) to (4.22), are greatly simplified by this assumption which will be made from now on. It has been seen in Sec. 3 that the distribution matrix has in this case the form (3.28) with the dominant part σ_0 given by (3.29). Keeping only terms linear in κ it is, in fact, permissible to replace in S_1 and S_2 the terms $(1+e^{-\kappa})$ and $(1+e^{-2\kappa})$ by 2 since these two expressions appear only in products containing the expectation values of I_z, $I_{x,y}$, $I_z{}^3$, and $(I_{x,y}I_z{}^2+I_z{}^2I_{x,y})$ which are themselves of order κ. To the same order one can replace $(1-e^{-\kappa})$ by κ and $(1-e^{-2\kappa})$ by 2κ and evaluate the expectation values of the spin functions with which these expressions are multiplied by substituting for the distribution matrix its dominant part (3.29). Denoting the approximate expectation values, thus obtained, by the subscript 0, one has

$$\langle I_z{}^2\rangle_0=(1/3)I(I+1);$$

$$\langle I_z{}^4\rangle_0=(1/15)I(I+1)[3I(I+1)-1],$$

and further

$$\langle I_{x,y}I_z+I_zI_{x,y}\rangle_0=0; \quad \langle I_{x,y}(I_z)^3+(I_z)^3I_{x,y}\rangle_0=0.$$

If we omit all terms of higher order in κ than the first, the expressions (4.19) to (4.22) to thus simplify

$$S_1(I_z)=-4\Phi_{11}{}^1\langle I_z\rangle+(4\kappa/3)\Phi_{11}{}^1I(I+1), \tag{5.7}$$

$$S_1(I_{x,y})=-(2\Phi_{11}{}^1+\Phi_{11}{}^0)\langle I_{x,y}\rangle, \tag{5.8}$$

$$\begin{aligned}S_2(I_z)=32(\Phi_{22}{}^2-\Phi_{22}{}^1)\langle I_z{}^3\rangle+4\{&\Phi_{22}{}^1[4I(I+1)-1]\\&-\Phi_{22}{}^2[2I(I+1)-1]\}\langle I_z\rangle+(4\kappa/15)\\&\times(\Phi_{22}{}^1+4\Phi_{22}{}^2)[4I(I+1)-3]I(I+1),\end{aligned} \tag{5.9}$$

$$\begin{aligned}S_2(I_{x,y})=6(2\Phi_{22}{}^2-3\Phi_{22}{}^0)&\langle I_{x,y}(I_z)^2+(I_z)^2I_{x,y}\rangle\\&+\{9\Phi_{22}{}^0+\Phi_{22}{}^1[6-8I(I+1)]\\&-8\Phi_{22}{}^2I(I+1)\}\langle I_{x,y}\rangle.\end{aligned} \tag{5.10}$$

It is seen that the magnetic dipole terms (5.7) and (5.8) have the same form as those given by (5.1) and (5.2), respectively, in the previous case of spin $\frac{1}{2}$ and thus would, by themselves, lead in the same way to the phenomenological Eq. (1.1) with

$$1/T_1=4\Phi_{11}{}^1, \tag{5.11}$$

$$1/T_2=(1/2T_1)+\Phi_{11}{}^0, \tag{5.12}$$

$$I_0=(\kappa/3)I(I+1), \tag{5.13}$$

and where

$$M_0=n\gamma hI_0=(n\mu^2H_0/3kT)(I+1)/I \tag{5.14}$$

represents the correct value of the equilibrium polarization up to terms of order κ and therefore linear in H_0.

The electric quadrupole terms (5.9) and (5.10) are in general not of the form leading to (1.1) and may invalidate this equation since nuclei with $I>\frac{1}{2}$ can have a finite quadrupole moment. Their relative importance is, however, frequently found to be small; in the presence of paramagnetic catalysts particularly the magnetic dipole relaxation can easily become dominant unless one is dealing with nuclei of rather large quadrupole moments. Besides, it will be shown below that these terms likewise reduce in certain cases to a form leading to the phenomenological equation so that it remains here valid, even if quadrupole interaction contributes appreciably to the relaxation.

Case c, $I=1$: Since nuclei with spin 1 can have no higher moments than those due to a magnetic dipole

and an electric quadrupole, one is here rigorously justified in the earlier omission of all higher interaction terms. One has here further

$$(m|I_z^3|m')=m^3\delta_{mm'}=m\delta_{mm'}=(m|I_z|m'), \quad (5.15)$$

since $m^3=m$ for the three possible values $m=0, \pm 1$; and

$$(m|I_{x,y}(I_z)^2+(I_z)^2I_{x,y}|m') = (m^2+m'^2)(m|I_{x,y}|m')=(m|I_{x,y}|m'), \quad (5.16)$$

since $(m|I_{x,y}|m')$ differs from zero only for $m=0$, $m'=\pm 1$ or $m'=0$, $m=\pm 1$, in all of which cases $m^2+m'^2=1$. Using the ensuing relations,

$$\langle I_z^3\rangle=\langle I_z\rangle, \quad (5.17)$$

and

$$\langle I_{x,y}(I_z)^2+(I_z)^2I_{x,y}\rangle=\langle I_{x,y}\rangle, \quad (5.18)$$

one obtains thus from (5.9) with $I=1$

$$S_2(I_z)=-4(\Phi_{22}{}^1+4\Phi_{22}{}^2)(\langle I_z\rangle-(2\kappa/3)), \quad (5.19)$$

and from (5.10)

$$S_2(I_{x,y})=-(9\Phi_{22}{}^0+10\Phi_{22}{}^1+4\Phi_{22}{}^2)\langle I_{x,y}\rangle. \quad (5.20)$$

Combining these results with (5.7) and (5.8) for $I=1$, we see therefore that

$$S_1(I_z)+S_2(I_z)=-(\langle I_z\rangle-I_0)/T_1, \quad (5.21)$$

$$S_1(I_{x,y})+S_2(I_{x,y})=-\langle I_{x,y}\rangle/T_2, \quad (5.22)$$

with

$$1/T_1=4(\Phi_{11}{}^1+\Phi_{22}{}^1+4\Phi_{22}{}^2), \quad (5.23)$$

$$1/T_2=\Phi_{11}{}^0+2\Phi_{11}{}^1+9\Phi_{22}{}^0+10\Phi_{22}{}^1+4\Phi_{22}{}^2, \quad (5.24)$$

and

$$I_0=2\kappa/3. \quad (5.25)$$

Inserting (5.21) and (5.22) in (4.18) and multiplying with $n\gamma\hbar$, one is thus led again to Eq. (1.1) with the proper value for the equilibrium polarization $M_0=n\gamma\hbar I_0$. In order to obtain for spin 1 from the general Boltzmann equation the phenomenological equation (1.1) one needs thus merely the condition $\kappa\ll 1$, which is practically always satisfied.

Case d, isotropic molecular surroundings: For spin values larger than unity it is not possible, in general, to reduce the expressions (5.9) and (5.10) to a form which leads to the phenomenological equation. The only cases where this equation can here still be expected to be valid are those in which the coefficients of the expectation values $\langle I_z^3\rangle$ and $\langle I_{x,y}I_z^2+I_z^2I_{x,y}\rangle$ vanish, i.e., where one has the relations

$$\Phi_{22}{}^2=\Phi_{22}{}^1=3\Phi_{22}{}^0/2. \quad (5.26)$$

Even in cases where there exist certain relations among the operators $F_2{}^\tau$ ($\tau=0, \pm 1, \pm 2$), defined in (4.6), there is still in general no relation among the corresponding values $\Phi_{22}{}^\tau$ because of the different arguments $f+\tau\omega$ which appear in the integration over f in (4.9).

The situation is different, however, if the functions containing these arguments are sufficiently slowly varying so that they do not change appreciably if f is increased by ω or 2ω. If we use again the "characteristic frequency" ω^* of the molecular surroundings, introduced in Sec. 3, this condition can be formulated by

$$\omega^*\gg\omega=\gamma H_0, \quad (5.27)$$

which is evidently compatible with, but more stringent than, the conditions (3.21) for ω^*. One has in this case from (4.9)

$$\Phi_{ll'}{}^\tau\cong\pi\sum_{s,s'}\int\eta_s(f)P(f)\eta_{s'}(f)(fs|F_l{}^\tau|fs') \times(fs'|F_{l'}{}^{-\tau}|fs)df. \quad (5.28)$$

If the molecular surroundings have no preferred directions, there exist relations between the quantities $F_1{}^\tau$ ($\tau=0, \pm 1$) and likewise between the quantities $F_2{}^\tau$ ($\tau=0, \pm 1, \pm 2$), since it is seen from (4.5) and (4.6) that they are proportional to the components of the vector $\mathbf{H}'$ and to those of the second-rank tensor, formed by the derivatives of $\mathbf{E}'$, respectively. As a consequence, there exist here also relations between the corresponding quantities $\Phi_{ll'}{}^\tau$, given by (5.28).

The manner in which these relations can be obtained will first be illustrated for the quantities $\Phi_{11}{}^0$ and $\Phi_{11}{}^1$: Under a rotation of the coordinate system, characterized by three Euler angles, the three quantities $F_1{}^0$, $F_1{}^1$, and $F_1{}^{-1}$ given by (4.5) will transform according to the vector transformation of H_z', H_y', H_z'. The same transformation as that of the quantities $F_1{}^\tau$ is undergone by their matrix elements, appearing in (5.28), and the quantities $\Phi_{11}{}^\tau$ will therefore undergo the same transformation as the corresponding products of two vector components. In a notation emphasizing this transformation property, we can write

$$\Phi_{11}{}^0\sim\{H_z'{}^2\}, \quad (5.29)$$

$$\Phi_{11}{}^1\sim\tfrac{1}{4}\{(H_x'+iH_y')(H_z'-iH_y')\}. \quad (5.30)$$

The result for an isotropic medium can now be obtained from that obtained for a given rotation of the coordinate system by averaging with uniform weight over all three Euler angles. Indicating this process by a bar, we have therefore, in this case,

$$\Phi_{11}{}^0\sim\{\overline{H_z'{}^2}\}, \quad (5.31)$$

$$\Phi_{11}{}^1\sim\tfrac{1}{4}\{\overline{H_x'{}^2}+\overline{H_y'{}^2}\}, \quad (5.32)$$

and since

$$\overline{H_x'{}^2}=\overline{H_y'{}^2}=\overline{H_z'{}^2},$$

we have

$$\Phi_{11}{}^0=2\Phi_{11}{}^1. \quad (5.33)$$

Using this result for the formulas (5.11) and (5.12), obtained for the relaxation times due to pure magnetic dipole interaction, it is seen that one here obtains

$$1/T_1=1/T_2=2\Phi_{11}{}^0, \quad (5.34)$$

i.e., the well-known fact that the longitudinal and

transverse relaxation times are equal in an isotropic medium whose characteristic frequency ω^* is large compared to the Larmor frequency ω of the nuclei.

An analogous procedure leads to the desired relations between the quantities $\Phi_{22}{}^r$. In analogy to (5.29) and (5.30) and using the expressions (4.6) for $F_2{}^r$, we write

$$\Phi_{22}{}^0 \sim \{(\partial E_z'/\partial z)^2\}, \tag{5.35}$$

$$\Phi_{22}{}^1 \sim \{[(\partial E_x'/\partial z)+i(\partial E_y'/\partial z)] \times[(\partial E_x'/\partial z)-i(\partial E_y'/\partial z)]\}, \tag{5.36}$$

$$\Phi_{22}{}^2 \sim \frac{1}{4}\left\{\left(\frac{\partial E_x'}{\partial x}-\frac{\partial E_y'}{\partial y}+2i\frac{\partial E_x'}{\partial y}\right) \times\left(\frac{\partial E_x'}{\partial x}-\frac{\partial E_y'}{\partial y}-2i\frac{\partial E_x'}{\partial y}\right)\right\}. \tag{5.37}$$

By averaging over the Euler angles of rotation, one has

$$\overline{(\partial E_x'/\partial x)^2}=\overline{(\partial E_y'/\partial y)^2}=\overline{(\partial E_z'/\partial z)^2}.$$

Further, because of the condition $\operatorname{div}\mathbf{E}'=0$

$$\overline{\left(\frac{\partial E_x'}{\partial x}\frac{\partial E_y'}{\partial y}\right)}=\overline{\left(\frac{\partial E_y'}{\partial y}\frac{\partial E_z'}{\partial z}\right)} =\overline{\left(\frac{\partial E_z'}{\partial z}\frac{\partial E_x'}{\partial x}\right)}=-\frac{1}{2}\overline{\left(\frac{\partial E_z'}{\partial z}\right)^2}$$

and

$$\overline{(\partial E_x'/\partial z)^2}=\overline{(\partial E_y'/\partial z)^2}=\overline{(\partial E_x'/\partial y)^2}=\tfrac{3}{4}\overline{(\partial E_z'/\partial z)^2}.$$

The use of these relations in the averages of the right side of the equations (5.35) to (5.37) yields directly the equalities (5.26). With these relations between the quantities $\Phi_{22}{}^r$ and the relation (5.33) between the quantities $\Phi_{11}{}^r$, one obtains now from Eqs. (5.7) to (5.10):

$$S_1(I_z)+S_2(I_z)=-(\langle I_z\rangle-I_0)/T_1, \tag{5.38}$$

$$S_1(I_{x,y})+S_2(I_{x,y})=-\langle I_{x,y}\rangle/T_2, \tag{5.39}$$

with

$$1/T_1=1/T_2=2\Phi_{11}{}^0+6\Phi_{22}{}^0[4I(I+1)-3], \tag{5.40}$$

and

$$I_0=\tfrac{1}{3}\kappa I(I+1). \tag{5.41}$$

Equations (5.38) to (5.41) lead again to the phenomenological equation (1.1). It is interesting to note, however, that the condition of an isotropic molecular medium with high characteristic frequency, which we have here needed for the validity of the phenomenological equation, leads at the same time to the equality (5.40) of the longitudinal and the transverse relaxation time. While the condition of isotropy is well satisfied in gases and liquids, there exists the possibility, as shown by Bloembergen,[2] that the viscosity of liquids prevents the existence of a sufficiently high characteristic frequency ω^* to satisfy the condition (5.27), with the ensuing result that T_2 is appreciably shorter than T_1. One has therefore to conclude that, with the exception of nuclei of spin 1, the phenomenological equation is in such cases invalid if electrical quadrupole interaction contributes appreciably to relaxation.

6. CONCLUSIONS

The dynamics of nuclear induction has been treated here with considerable generality, the only serious restriction lying in the omission of those features for which the spin-spin interaction between neighboring nuclei is essential. Particularly the differential equation (3.25) has, except for this restriction, a practically perfect and general validity. It is true that its derivation required the further conditions (3.21); one must note, on the other hand, that the largest of the three quantities on the left side of this inequality measures the order of magnitude of the line width in the frequency scale so that their required smallness is equivalent to the requirement of relatively narrow resonance lines.

While this condition and thereby the validity of the Boltzmann equation (3.25) is practically always ensured, there are more serious further restrictions to the validity of the very much simpler phenomenological equation (1.1). We shall here briefly summarize them:

1. For $I=\frac{1}{2}$: No further restrictions.
2. For $I=1$: $H_0\mu \ll kT$.
3. For $I>1$ and negligible quadrupole-relaxation: $H_0\mu \ll kT$.
4. For $I>1$ and appreciable quadrupole-relaxation: $H_0\mu \ll kT$; the molecular surroundings are further required to be isotropic and to have a characteristic frequency large compared to the Larmor frequency of the nuclei. As a consequence of these requirements one has $T_1=T_2$. It is only the last-mentioned restriction which represents a serious limitation to the validity of the phenomenological equation; it demands in practice that the sample consist of a gas or a liquid with low viscosity.

This investigation shows, nevertheless, that there exists a considerable range of validity for the phenomenological equation which accounts for its empirical usefulness. It may finally be hoped that a treatment of similar generality can be developed to include also features of spin-spin interaction and line structure.

Interpretation of High Energy $p-p$ Scattering*

DON R. SWANSON†
Radiation Laboratory, Department of Physics, University of California, Berkeley, California
(Received September 19, 1952)

A study is made of the scattering of high energy protons by protons. Several types of "cutoffs" are introduced into the singular tensor interaction proposed by Christian and Noyes; the triplet P state radial equations are then solved by essentially exact numerical integration methods. The resulting cross sections show a more pronounced disagreement with experiment than do the Born approximation cross sections of Christian and Noyes. Calculations were carried out in the vicinity of 350 Mev and 120 Mev.

INTRODUCTION

SEVERAL experiments have been carried out on the scattering of protons by protons at energies greater than 100 Mev.[1–4] The resulting differential cross sections are characterized by spherically symmetric angular distributions (in the center-of-mass system) and by a lack of dependence on energy. Between scattering angles of 20° and 160° and between energies of 120 Mev and 350 Mev the cross section is about four or five millibarns per steradian. The results have been interpreted by Christian and Noyes[5] (hereafter referred to as "CN"), by Jastrow,[6] and by Case and Pais.[7] In the CN analysis (350 Mev) a square well singlet interaction was used which gave almost no scattering at angles greater than 40°. The problem then was to find a triplet interaction yielding an essentially isotropic differential cross section. It was observed that any triplet central potential is undesirable since the cross section due to it would vanish at 90° (the wave function is antisymmetric), accordingly a tensor force model was chosen. (The wave function must of course still be antisymmetric; however, with a noncentral potential the antisymmetrization is not expressed in terms of the polar scattering angle θ alone, but by the azimuthal angle ϕ as well. The antisymmetric spin scattering matrix $S(\theta,\phi)-S(\pi-\theta,\phi+\pi)$ does not necessarily vanish at $\theta=\pi/2$ as it would if there were no ϕ dependence.)

In order to obtain the desired "flat" cross section, Christian and Noyes found it necessary to use a potential with a "highly singular" radial dependence $e^{-r/R}/r^2$. All triplet state calculations were carried out in Born approximation. Jastrow, on the other hand, attempted to obtain agreement with experiment by introducing a hard core into the singlet interaction, thus permitting greater momentum transfers and accordingly a substantial amount of large angle (90°) scattering. The triplet interaction was not then required to yield an isotropic cross section. Neither the CN nor the Jastrow interpretation was entirely successful in fitting the experimental data, the principal difficulty being too large a theoretical peak in the forward direction due mostly to scattering of the singlet D state. However, it was not in the spirit of the analyses to indulge in a detailed program of "curve fitting" but rather to illustrate the important features of the various interactions chosen. This philosophy applies as well to the present paper.

It is proposed here to examine more critically the triplet state calculations of Christian and Noyes, and, in particular, to investigate the validity of their use of the Born approximation. Singlet scattering will be ignored. There is reason to suspect that results of the Born approximation applied to a highly singular potential may not be even qualitatively correct. Consider, for example, the radial equation for the $^3P_0$ state [Appendix, Eq. (A18)]. In the vicinity of the origin this takes the form

$$d^2u/dy^2+\lambda_0 u/y^2=0, \quad y=kr. \tag{1}$$

(Choosing $\lambda_0>0$ implies that the nuclear potential is effectively attractive in this state, and sufficiently deep to dominate the centrifugal term as $r\to 0$.) The solution, for $\lambda_0>\frac{1}{4}$, is composed of spherical Bessel functions of imaginary order having an oscillatory singularity at the origin:[8]

$$u\underset{y\to 0}{\longrightarrow} y^{\frac{1}{2}}\cos[(\lambda_0-\tfrac{1}{4})^{\frac{1}{2}}\log y+B].$$

An interaction of this nature can be treated in a physically meaningful way only if the singularity at the origin is in some arbitrary way "cut off." It is evident, however, that the region of the cutoff cannot be arbitrarily small since several oscillations of the wave function within the region would lead to bound states of the diproton. Consider the integral equation satisfied by the solution to Eq. (A18):

$$u=A_1 g_1(y)+4\lambda g_{-1}(y)\int_0^y \frac{e^{-ay}}{y^2}ug_1 dy +4\lambda g_1(y)\int_y^\infty \frac{e^{-ay}}{y^2}ug_{-1}dy. \tag{2}$$

* This work was performed under the auspices of the U. S. Atomic Energy Commission.
† Now at Hughes Aircraft Company Research and Development Laboratories, Culver City, California.
[1] Chamberlain, Segrè, and Wiegand, Phys. Rev. **83**, 923 (1951).
[2] C. L. Oxley and R. D. Schamberger, Phys. Rev. **85**, 416 (1952).
[3] Birge, Kruse, and Ramsey, Phys. Rev. **83**, 274 (1951).
[4] Cassels, Staford, and Pickavance, Nature **168**, 468 (1951).
[5] R. S. Christian and H. P. Noyes, Phys. Rev. **79**, 85 (1950) (referred to as "CN" in the text).
[6] R. Jastrow, Phys. Rev. **81**, 165 (1950).
[7] K. M. Case and A. Pais, Phys. Rev. **80**, 203 (1950).
[8] K. M. Case, Phys. Rev. **80**, 797 (1950).

The left-hand side of the equation becomes the wave function in Born approximation if the plane wave solution $u=g_1(y)$ is inserted as a trial function in the integrand. The Born approximation is valid if the exact solution does not deviate greatly from the free particle trial function. Near the origin the latter, $g_1(y)$, becomes just $\frac{1}{3}y^2$; the next zero occurs beyond the region in which the nuclear interaction is appreciable, even for energies as high as 350 Mev. It is therefore evident that for sufficiently short cutoffs the Born approximation is invalid since the exact (possibly oscillatory) solution does not resemble the trial function. Examination of the integral equation (2) shows, moreover, that the presence of a short range cutoff has a negligible influence on the Born calculation itself, simply because the singularity in the potential is masked by the $\frac{1}{3}y^2$ factor from the trial function. (For convenience a square well cutoff may be visualized here; that is, the potential e^{-ay}/y^2 for $y\geq y_0$ is placed equal to the constant e^{-ay_0}/y_0^2 for $y\leq y_0$.) It is evident that the larger the cut-off radius the more nearly valid becomes the first-order iteration procedure. On the other hand, a long range cutoff cannot be ignored in a Born calculation. It seems, then, that the CN procedure (Born approximation without explicit introduction of cutoff) can be taken seriously only if there exists some kind of cutoff of sufficiently long range to permit first-order perturbation methods to have real meaning, yet short enough so that the perturbation calculation itself is not appreciably influenced by its presence. It will be shown here that, strictly speaking, a cutoff fulfilling these two conditions does not exist.

PROCEDURE

The procedure adopted here is to introduce specific cutoffs into the CN interaction and obtain an essentially exact solution to the scattering problem by a numerical integration procedure. The cutoffs considered will be of two types: tensor force "square wells," in which the potential is given by

$$V(r)=\mp 15.2 S_{12}\frac{e^{-r/R}}{(r/R)^2}\ \text{Mev}\quad \text{for}\quad r\geq r_0, \tag{3}$$

$$V(r)=\mp 15.2 S_{12}\frac{e^{-r_0/R}}{(r_0/R)^2}\ \text{Mev}=\text{constant}\quad \text{for}\quad r\leq r_0,$$

$$r^2S_{12}\equiv 3\boldsymbol{\sigma}_1\cdot\mathbf{r}\boldsymbol{\sigma}_2\cdot\mathbf{r}-r^2\boldsymbol{\sigma}_1\cdot\boldsymbol{\sigma}_2,\quad R=1.6\times10^{-13}\ \text{cm},$$

and "hard cores," where

$$V(r)=\infty\ \text{for}\ r\leq r_0,\qquad V(r)=\text{Eq. (3) for}\ r\geq r_0. \tag{4}$$

The $\mp$ sign refers to what will be called "attractive" and "repulsive" interactions, respectively. The Born cross section of course is the same for the two signs of the interaction.

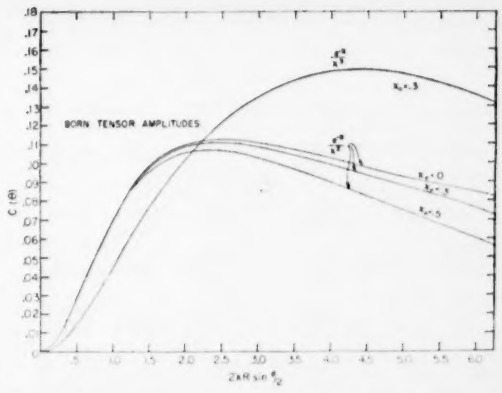

FIG. 1. Born tensor amplitudes, $C(\theta)$ [Eq. (A14)], for singular potentials with various ranges $[x_0=(r_0/R)]$ of square well cutoffs. The radial dependence of the potentials is indicated on the plot. $x=r/R$.

In attempting to choose a more or less physically meaningful cut-off radius, r_0, the "nucleon Compton wavelength" $\hbar/Mc$ is a convenient guide. Part of the motivation for choosing a radial dependence of the form $e^{-r/R}/r^2$ is its similarity to terms in the phenomenological interactions predicted by meson theories. Such motivation hardly exists at distances as short as $\hbar/Mc$ where, for example, the nucleon structure, as well as relativistic effects, may be expected to play an important role. On the other hand, to introduce a cutoff as large as $3\hbar/Mc$ (about $\frac{1}{2}$ the meson Compton wavelength) more or less abandons the similarity to meson potentials. Essentially the same limits on r_0 are obtained by a few rough calculations which indicate that a cutoff somewhat smaller than $\hbar/Mc$ would lead to a bound di-proton, and a radius greater than $3\hbar/Mc$ tends to destroy the desired isotropy of the cross section even in Born approximation. (The latter point is illustrated by a plot of the Born tensor amplitude in Fig. 1.) The calculations were therefore carried out using a "short range cutoff," $r_0\approx\hbar/Mc$, and a "long range cutoff," $r_0\approx 2\hbar/Mc$, for both the square well and the hard core. The four cases considered will be denoted by the following abbreviations:

SRSW: short range square well cutoff; Eq. (3) with $r_0=0.24\times10^{-13}$ cm.
LRSW: long range square well cutoff; Eq. (3) with $r_0=0.48\times10^{-13}$ cm.
SRHC: short range hard core cutoff; Eq. (4) with $r_0=0.24\times10^{-13}$ cm.
LRHC: long range hard core cutoff; Eq. (4) with $r_0=0.48\times10^{-13}$ cm.

The ${}^3P_0$, ${}^3P_1$ and ${}^3P_2$, ${}^3F_2$ states for the SRSW case were solved by numerical integration and checked by iterating the resulting radial functions (using the integral equations) to produce the same phase shifts and amplitudes to within a few percent. All other states

TABLE I. Triplet $p-p$ phase shifts at 350 Mev for singular tensor potential with various cutoffs. (Cross sections plotted in Fig. 2.)

		Short range square well cutoff			Long range square well cutoff		Short range hard core		Long range hard core	
		Attractive	Repulsive	Born (Repulsive)	Attractive	Repulsive	Attractive	Repulsive	Attractive	Repulsive
$^3P_2, {}^3F_2$	B_1^2	-0.002 $+i.242$	-0.048 $+i.184$	${}^B\delta_1^{20}=-0.033$	Same as SRSW		0.005 $+i.170$	-0.029 $+i.116$	-0.035 $-i.185$	-0.008 $-i.239$
	A_1^2	-0.022 $-i.100$	-0.152 $+i.567$	${}^B\delta_1^{21}=0.169$	Same as SRSW		-0.028 $-i.171$	-0.119 $+i.503$	-0.129 $-i.514$	-0.027 $+i.158$
	B_3^2	-0.017 $-i.016$	0.018 $-i.060$	${}^B\delta_3^{20}=-0.014$	Same as SRSW		-0.013 $-i.016$	0.013 $-i.062$	0.012 $-i.020$	-0.016 $-i.066$
	A_3^2	-0.037 $-i.357$	-0.086 $+i.323$	${}^B\delta_3^{21}=0.188$	Same as SRSW		-0.045 $-i.356$	-0.078 $+i.325$	-0.082 $-i.349$	-0.035 $+i.331$
$^3P_0$	δ_1^0	-0.626	2.00	0.880	-0.616	1.24	-0.64	0.91	-0.66	0.32
$^3P_1$	δ_1^1	0.580	-0.360	-0.440	0.540	-0.351	0.38	-0.37	0.04	-0.47

($^3F_3$ $^3F_4$, $^3H_4$, etc.) were included in Born approximation, with cutoffs ignored. Some details of the procedure are given in the Appendix.

The phase shifts for the LRSW cutoff were then obtained by a perturbation method using as trial functions in the integral Eqs. (A21) the radial functions for the SRSW case, except in the $^3P_0$ state of the "repulsive" interaction, which was integrated numerically. (The $^3P_0$ state is effectively attractive in the "repulsive" interaction and repulsive in the "attractive" because of a minus sign appearing in the corresponding matrix element of the tensor operator S_{12}.) Inspection of the differential Eqs. (A18) and (A19) shows that the effective well depth in the $^3P_0$ state is twice as great and of the opposite sign as that of the $^3P_1$ state. From the remarks following Eqs. (A23) in the Appendix, it is apparent that the most important quantity in the coupled system is the P-dominant P phase shift. Furthermore, in the P-dominant mode the term

$$(e^{-ay}/y^2)3(6)^{\frac{1}{2}}w$$

is asymptotically smaller than the term $(e^{-ay}/y^2)u$; from the power series expansion it is clear that it also starts out much smaller near the origin. Ignoring for the moment this coupling term, then, and comparing the size of the $^3P_2$ potential to the $^3P_1$ and $^3P_0$, it is seen that the latter are, in absolute value, five and ten times as large as the former. Accordingly it is reasonable to think that the $^3P_0$ phase shift in the "repulsive" case and the $^3P_1$ in the "attractive" will exhibit a great deal more sensitivity to the nature of the cutoff than will the coupled $^3P_2$, $^3F_2$ states. The perturbation calculations for the long range square well cutoffs indeed show just this sort of behavior. The coupled phase shifts in fact differ negligibly from those of the SRSW cutoff.

The foregoing arguments indicate that a fair approximation to the hard core cut-off cross sections should result from taking the core into consideration only in the $^3P_0$ and $^3P_1$ states and using the square well cut-off phase shifts in the coupled states. However, the following somewhat more refined procedure was used which still avoids the labor of repeating the coupled numerical integrations. Starting with the unperturbed SRSW solutions, the P-dominant P phase shift, δ_{11}^2, is added to the "hard sphere" P phase shift,

$$\tan\delta_p^{hs}=+J_{\frac{3}{2}}(y_0)/J_{-\frac{3}{2}}(y_0).$$

The nature of the approximation can be readily seen by considering a similar procedure for an uncoupled

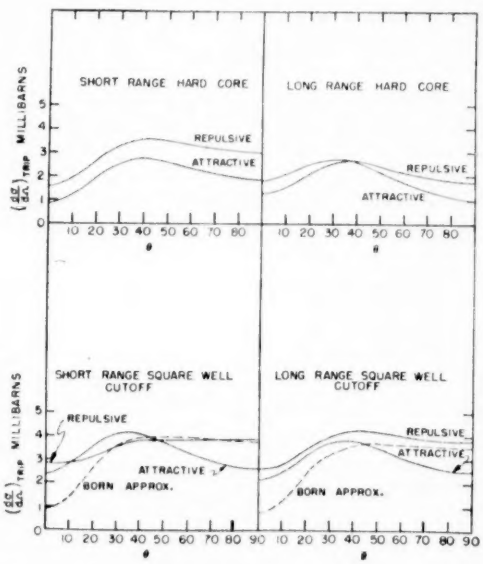

FIG. 2. Differential cross sections (center-of-mass system) for triplet $p-p$ scattering (neglecting Coulomb) at 350 Mev using a singular tensor potential $\mp 15.2S_{12}e^{-r/R}/(r/R)^2$ Mev with various cutoffs. Dotted curves shown Born cross sections, solid curves are "exact." Phase shifts are in Table I. "Short range" means $r_0=0.24\times10^{-13}$ cm; "long range" $=0.48\times10^{-13}$ cm.

integral equation (see Appendix for notation):

$$\sin\delta_{hc} \approx \int_0^{y_0} U_a u_a g_1 dy + \int_{y_0}^{\infty} U_b u_b g_1 dy$$

$$\approx \sin\delta_p{}^{hs} + \sin\delta_{sw}, \quad \delta_{hc} \approx \delta_p{}^{hs} + \delta_{sw}, \quad (5)$$

where U_a = strong repulsion (approximates hard core); $U_b = e^{-ay}/y^2$ for $y \geq y_0$, $= e^{-ay_0}/y_0^2$ = constant for $y \leq y_0$; trial function u_a = exact solution when $U_b = 0$; trial function u_b = exact solution when $U_a = 0$; δ_{sw} = phase shift for square well cutoff; δ_{hc} = phase shift for hard core cutoff; and $\delta_p{}^{hs} = P$ phase shift for hard core alone.

$$\int_0^{y_0} U_b u_b g_1 dy$$

is neglected. Analogous treatment of $a_{13}{}^2$, $a_{31}{}^2$, $a_{33}{}^2$ shows that the influence of the hard core on these quantities is negligible. The phase shifts $\delta_{13}{}^2$, $\delta_{31}{}^2$ (unperturbed SRSW value is $\pi/2$) feel the core somewhat more strongly; however, they may deviate as much as 20 percent from $\pi/2$ without changing the $\delta_l{}^{Jm_s}$ by more than a few percent [Eqs. (A8)].

All hard core coupled PF phase shifts were obtained in the manner just indicated; all uncoupled P-state equations were integrated numerically.

RESULTS AND CONCLUSIONS

Phase shifts and differential cross sections at 350 Mev are given in Table I and Fig. 2. The "attractive" interaction evidently leads to a greater anisotropy of the triplet cross section than does the "repulsive," regardless of the nature of the cutoff. The near agreement of the exact cross sections at 350 Mev with those calculated in Born approximation is surprising in view of the large discrepancies in the corresponding phase shifts. Similar discrepancies at 129 Mev lead to an exact cross section much larger than that obtained in Born approximation (Fig. 3); apparently, then, the close agreement at 350 Mev is accidental. Figure 2 also indicates that the greater the "volume" of potential removed by the cutoff the greater is the angular variation of the cross section; Fig. 1 illustrates the same point in Born approximation.

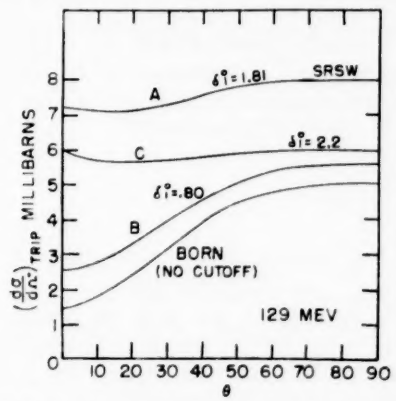

FIG. 3. Differential cross sections for triplet p-p scattering (neglecting Coulomb) at 129 Mev using cutoff singular tensor potential. Curve A: SRSW cutoff. Curves B, C have cutoffs adjusted to give the $^3P_0$ phase shifts indicated on the plot.

TABLE II. Phase shifts for triplet p-p scattering at 129 Mev, using repulsive singular tensor interaction with short range square well (SRSW) cutoff.

	Exact	Born
$^3P_0$	$\delta_1{}^0 = 1.81$	${}^B\delta_1{}^0 = 0.590$
$^3P_1$	$\delta_1{}^1 = -0.240$	${}^B\delta_1{}^1 = -0.295$
$^3P_2, {}^3F_2$	$B_1{}^2 = -0.008 + i.012$	${}^B\delta_1{}^{20} = -0.021$
	$A_1{}^2 = -0.037 + i.228$	${}^B\delta_1{}^{21} = 0.112$
	$B_3{}^2 = 0.002 - i.082$	${}^B\delta_3{}^{20} = -0.024$
	$A_3{}^2 = -0.027 + i.195$	${}^B\delta_3{}^{21} = 0.109$

The SRSW cutoff for the "repulsive" case was calculated in detail at 129 Mev. The results, Fig. 3 (curve A) and Table II, show that the predicted scattering is much too great. The trouble comes almost entirely from the large $^3P_0$ phase shift. To investigate the effect (at 129 Mev) of modifying the cutoff, attention will be restricted to the $^3P_0$ state. (The arguments of the preceding section indicate that the coupled phase shifts are only slightly influenced by the nature of the potential at short range; the $^3P_1$ state is repulsive and so obviously insensitive to the cutoff.) A $^3P_0$ phase shift of 0.80 (instead of the 1.8 of Table II) yields roughly the desired cross section (Fig. 3, curve B). The required phase shift can be produced, for example, by the combination of a square well cutoff at 0.48×10^{-13} cm and a hard core of radius 0.24×10^{-13} cm, (or, of course, by a hard core alone of radius somewhat larger than 0.24×10^{-13} cm). The cross section at 350 Mev will then in any case lie between that of the SRHC and the LRHC cutoffs shown in Fig. 2.

It is concluded, therefore, that, within the framework of the singlet and triplet models adopted by Christian and Noyes, something similar to the following triplet potential seems to yield the closest approach to the experimental cross sections (Fig. 4) at 120 Mev and 350 Mev:

$$V(r) = 15.2 S_{12} \frac{e^{-r/R}}{(r/R)^2} \text{ Mev}, \quad r \geq r_1 = 0.48\times10^{-13} \text{ cm},$$

$$V(r) = 15.2 S_{12} \frac{e^{-r_1/R}}{(r_1/R)^2} \text{ Mev} = \text{constant}, \quad r_0 \leq r \leq r_1, \quad (6)$$

$$V(r) = \infty, \quad r \leq r_0 = 0.24\times10^{-13} \text{ cm}.$$

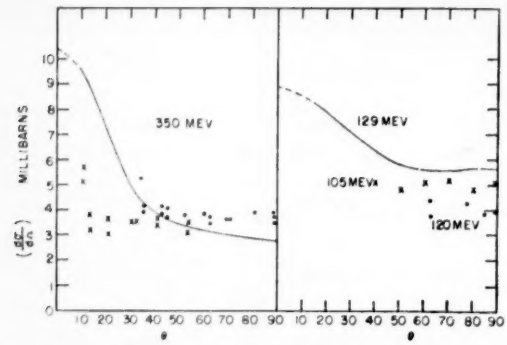

FIG. 4. $P-p$ scattering at 350 Mev, 129 Mev using the cut-off singular tensor potential given by Eq. (6) and a square well singlet interaction (Christian and Noyes). Coulomb scattering neglected. The experimental points at 350 Mev and those at 120 Mev denoted by ● are taken from Chamberlain, Segrè, and Wiegand. (See reference 1.) The points, x, at 105 Mev are from Birge, Kruse, and Ramsey (see reference 3).

It is to be emphasized that significance should be attached only to the necessary degree of "severeness" (i.e., volume of potential affected) of the cutoff and not to its precise nature.

It should be mentioned that a cutoff sufficiently short to increase the $^3P_0$ phase shift at 129 Mev to 2.2 is not obviously less desirable than (6) (see Fig. 3, curve C); the 350-Mev scattering would be changed, but not drastically. The effect of so short a cutoff would be more pronounced at some energy less than 120 Mev where the $^3P_0$ phase shift will have decreased to $\pi/2$.

By using the potential given by (6), the discrepancy with the experimental forward scattering is considerably greater than originally was indicated by the CN calculations. The disagreement seems sufficiently conclusive to justify ruling out a large class of static potentials for the $p-p$ interaction. The class of inacceptable potentials is by no means exhaustive, however. Whenever a strong short range component (e.g., hard core) is included in the singlet interaction (thus permitting large angle scattering), the triplet potential acquires several more degrees of freedom since the requirement of isotropy may be dropped. In particular, triplet central potentials then merit consideration.

APPENDIX

The nucleon-nucleon scattering problem for a noncentral static potential will be formulated and discussed. The notation and method of treatment adapts conveniently to a description of polarization effects carried out in a concurrent paper.[9]

The asymptotic form of the triplet state wave function can be written[10]

$$\psi \sim e^{ikz}\chi_{\text{inc}}+(e^{ikr}/r)S\chi_{\text{inc}}. \tag{A1}$$

χ_{inc} is the triplet spin function of the initial state, where $S(\theta,\phi)$ is the triplet spin scattering operator, the matrix for which is given explicitly in terms of the complex phase shifts, $\delta_l{}^{Jm_s}$, by

$$S=\frac{1}{2ik}\sum_{J,m_s,l}(2l+1)[\exp(2i\delta_l{}^{Jm_s})-1]\prod_l{}^{Jm_s}P_l(\cos\theta)$$

$$=\frac{1}{4ik}\begin{vmatrix} A & \sqrt{2}Be^{-i\phi} & Ce^{-2i\phi} \\ -\sqrt{2}De^{i\phi} & 2E & \sqrt{2}De^{-i\phi} \\ Ce^{2i\phi} & -\sqrt{2}Be^{i\phi} & A \end{vmatrix}\begin{matrix} 1 \\ 0. \\ -1 \end{matrix}\quad\begin{matrix} 1 & 0 & -1 \quad m_s' \\ & & m_s \end{matrix} \tag{A2}$$

$$A=\sum_l[(l+2)A_l{}^{l+1}+(2l+1)A_l{}^l+(l-1)A_l{}^{l-1}]P_l,$$

$$B=\sum_l[B_l{}^{l+1}-B_l{}^{l-1}]P_l{}^1,$$

$$C=\sum_l\left[\frac{1}{l+1}A_l{}^{l+1}-\frac{2l+1}{l(l+1)}A_l{}^l+\frac{1}{l}A_l{}^{l-1}\right]P_l{}^2,$$

$$D=\sum_l\left[\frac{l+2}{l+1}A_l{}^{l+1}-\frac{2l+1}{l(l+1)}A_l{}^l-\frac{l-1}{l}A_l{}^{l-1}\right]P_l{}^1,$$

$$E=\sum_l[(l+1)B_l{}^{l+1}+lB_l{}^{l-1}]P_l,$$

$$A_l{}^J=\exp(2i\delta_l{}^{J,\pm1})-1$$

$$B_l{}^J=\exp(2i\delta_l{}^{J,0})-1. \tag{A3}$$

$\prod_l{}^{Jm_s}P_l$ is an operator in triplet spin space defined by Eq. (A6). Coulomb scattering is neglected. The boundary conditions of the scattering problem yield also the relationship between the complex phase shifts and the asymptotic form of the radial wave functions. To obtain this relationship, first expand the wave function of the system in eigenfunctions, ψ^{Jm}, of total angular momentum J^2 and J_z. Separate the radial from the spin-angular dependence by means of the expansion

$$\psi^{Jm}=\sum_l(u_l{}^J(r)/r)\psi_l{}^{Jm},$$

where the $\psi_l{}^{Jm}$ are eigenfunctions of J^2, J_z and the orbital angular momentum L^2. The Schrödinger equation for the radial functions becomes

$$\frac{d^2u_l{}^J}{dr^2}-\frac{l(l+1)}{r^2}u_l{}^J+k^2u_l{}^J-\frac{M}{\hbar^2}\sum_{l'=J-1}^{J+1}V_{ll'}{}^J(r)u_{l'}{}^J=0, \tag{A4}$$

where $V_{ll'}{}^J(r)=(\psi_l{}^{Jm}, V(\mathbf{r},\boldsymbol{\sigma}_1,\boldsymbol{\sigma}_2)\psi_{l'}{}^{Jm})$ is independent of m. The scalar product denotes an integration over the surface of a sphere and summation over spin variables.

For a tensor interaction, the orbital angular momentum is not a constant of the motion and $V(\mathbf{r},\boldsymbol{\sigma}_1,\boldsymbol{\sigma}_2)$ contains off-diagonal elements between states of the

[9] Don R. Swanson, Phys. Rev. **89**, 749 (1953).
[10] J. Ashkin and T. Wu, Phys. Rev. **73**, 973 (1948).

same parity.[11]

$$S_{12}=\frac{1}{2J+1}\begin{vmatrix} -2(J-1) & 0 & 6[J(J+1)]^{\frac{1}{2}} \\ 0 & 2(2J+1) & 0 \\ 6[J(J+1)]^{\frac{1}{2}} & 0 & -2(J+2) \end{vmatrix}\begin{matrix} J-1 \\ J \\ J+1 \end{matrix}\quad \begin{matrix} l'/l \end{matrix} \tag{A5}$$

The orthonormal set of spin-angular functions, $\psi_l{}^{Jm}$, can be expressed in terms of spherical harmonics and spin functions by means of the Clebsch-Gordon expansion:

$$\psi_l{}^{Jm}=\sum_{m_l,m_s}(lsJm|lsm_lm_s)Y_{m_l}{}^l(\theta,\phi)\chi^{sm_s}$$

and

$$Y_{m_l}{}^l\chi^{sm_s}=\sum_J(lsJm|lsm_lm_s)\psi_l{}^{J,m_l+m_s},$$

where $m=m_l+m_s$. Defining the projection operator, $\prod_l{}^{Jm}$, by

$$\Pi_l{}^{Jm}Y_{m-m_s}{}^l\chi^{sm_s}=(lsJm|ls,\ m-m_s,\ m_s)\psi_l{}^{Jm},$$

so that

$$(l1Jm_s|l10m_s)\psi_l{}^{Jm_s}=\prod_l{}^{Jm_s}Y_0{}^l\chi^{1m_s}, \tag{A6}$$

the general expansion for the wave function of the system takes the form

$$\bar{\psi}=\sum_{Jm}\sum_{l=J-1}^{J+1}\sum_{i=1}^{2}\frac{C_i{}^{Jm}}{(l1Jm|l1,\ m-m_s,\ m_s)}\frac{u_{li}{}^J(r)}{r}\times\prod_l{}^{Jm}Y^{l}{}_{m-m_s}\chi^{1m_s}, \tag{A7}$$

$u_{li}{}^J\sim a_{li}{}^J\sin(kr-l\pi/2+\delta_{li}{}^J)$. The subscript i is summed over the two regular solutions to the coupled equation in (A4) [see discussion following Eqs. (A20)]. For uncoupled states, put $C_2{}^{Jm}=0$. The asymptotic form of (A7) is the same as (A1) with S defined by (A2) provided that[5]

$$\begin{aligned} D_J\exp(2i\delta_{J-1}{}^{J,\pm1})&=E_J+2i[J/(J+1)]^{\frac{1}{2}}W \\ &=[D_J\exp(2i\delta_{J+1}{}^{J,0})]^*, \\ D_J\exp(2i\delta_{J-1}{}^{J,0})&=E_J-2i[(J+1)/J]^{\frac{1}{2}}W \\ &=[D_J\exp(2i\delta_{J+1}{}^{J,\pm1})]^*, \end{aligned} \tag{A8}$$

where

$$\begin{aligned} D_J\equiv&\exp[-i(\delta^J{}_{J-1,J-1}+\delta^J{}_{J+1,J+1})] \\ &-a^J{}_{J-1,J+1}a^J{}_{J+1,J-1} \\ &\times\exp[-i(\delta^J{}_{J-1,J+1}+\delta^J{}_{J+1,J-1})], \\ E_J\equiv&\exp[i(\delta^J{}_{J-1,J-1}-\delta^J{}_{J+1,J+1})] \\ &-a^J{}_{J-1,J+1}a^J{}_{J+1,J-1} \\ &\times\exp[i(\delta^J{}_{J-1,J+1}-\delta^J{}_{J+1,J-1})]. \end{aligned}$$

$$\begin{aligned} W&=a^J{}_{J-1,J+1}\sin(\delta^J{}_{J-1,J-1}-\delta^J{}_{J-1,J+1}) \\ &=a^J{}_{J+1,J-1}\sin(\delta^J{}_{J+1,J+1}-\delta^J{}_{J+1,J-1}), \end{aligned} \tag{A9}$$

$a^J{}_{J-1,J-1}=a^J{}_{J+1,J+1}=1$.

$\delta_l{}^{Jm_s}=\delta_l{}^J$ for all uncoupled states.

[11] W. Rarita and J. Schwinger, Phys. Rev. **59**, 556 (1941).

The subscript i in Eqs. (A7) here takes on the values $J-1$, $J+1$ instead of 1, 2. The Wronskian conditions (A9) follow immediately from the differential equations (A4) or (A20):

$$u_1u_2'-u_2u_1'+w_1w_2'-w_2w_1'=\text{constant}. \tag{A10}$$

Boundary conditions at the origin require the constant to be zero; the asymptotic form of (A10) is (A9).

In Born approximation, Eqs. (A2) and (A8) become

$${}^BS=\frac{1}{k}\sum_{J,l,m_s}(2l+1)\,{}^B\delta_l{}^{Jm_s}\prod_l{}^{Jm_s}P_l, \tag{A11}$$

$${}^B\delta_l{}^{Jm_s}={}^B\delta_{ll}{}^J-\epsilon_l{}^{Jm_s}\,{}^Ba_{lL}{}^J,\quad l=J-1,\ J+1;\ L=2J-l.$$

$$\begin{aligned} \epsilon_{J-1}{}^{J\pm}&=-\epsilon_{J+1}{}^{J,0}=1/\epsilon_{J+1}{}^{J\pm} \\ &=-1/\epsilon_{J-1}{}^{J,0}=[J/(J+1)]^{\frac{1}{2}}. \end{aligned} \tag{A12}$$

For any linear combination of central and tensor potentials, with arbitrary exchange dependence, $V(\mathbf{r},\boldsymbol{\sigma}_1,\boldsymbol{\sigma}_2)=[-J(r)S_{12}-J_c(r)][a+bP_x]$, Eq. (A11) can be written in the closed form[10]

$${}^BS=F1+\begin{vmatrix} C_1 & C_2e^{-i\phi} & C_3e^{-2i\phi} \\ C_2e^{i\phi} & -2C_1 & -C_2e^{-i\phi} \\ C_3e^{2i\phi} & -C_2e^{i\phi} & C_1 \end{vmatrix}, \tag{A13}$$

where

$$\begin{aligned} &F=aF(\theta)+bF(\pi-\theta)\equiv aF_K+bF_L; \\ &F(\theta)=\frac{M}{\hbar^2}\int r^2J_C(r)\frac{\sin Kr}{Kr}dr, \\ &C_1=-\tfrac{1}{2}C_++\tfrac{3}{2}\cos\theta C_-, \\ &C_2=(3/\sqrt{2})\sin\theta C_-, \\ &C_3=-\tfrac{3}{2}[C_++\cos\theta C_-], \\ &C_\pm=aC_K\pm bC_L\equiv aC(\theta)\pm bC(\pi-\theta), \\ &C(\theta)=\frac{M}{\hbar^2}\int r^2J(r)\frac{g_2(Kr)}{Kr}dr. \end{aligned} \tag{A14}$$

The procedure for calculating S will be to remove from the Born scattering matrix (A13) the first few terms of its partial wave expansion (A11), and to replace them by the corresponding terms in the exact scattering matrix. The result will then correspond to a scattering matrix containing explicitly the phase shifts of the few lowest angular momentum states and implicitly the Born approximation on all higher states.

$$\begin{aligned} &S={}^BS+S' \\ &A_l'{}^J=\exp(2i\delta_l{}^{J,\pm1})-1-2i\,{}^B\delta_l{}^{J,\pm1}; \\ &B_l'{}^J=\exp(2i\delta_l{}^{J,0})-1-2i\,{}^B\delta_l{}^{J,0}, \end{aligned} \tag{A15}$$

where S' is defined analogously to Eqs. (A2), (A3), but with $A_l'{}^J$, $B_l'{}^J$ replacing $A_l{}^J$, $B_l{}^J$.

For p-p scattering, replace $S(\theta,\phi)$ with $S(\theta,\phi)-S(\pi-\theta,\phi+\pi)$.

The triplet contribution to the differential scattering cross section, reduced to terms containing just Legendre

polynomials, is

$$(d\sigma/d\Omega)_{\text{triplet}}=(d\sigma/d\Omega)_{\text{trip}}{}^{\text{Born}}+(d\sigma/d\Omega)_{\text{TI}}$$
$$+(d\sigma/d\Omega)_{\text{CI}}+(d\sigma/d\Omega)'=\tfrac{1}{4}\,\text{Tr}(S^{\dagger}S),$$
$$(d\sigma/d\Omega)_{\text{trip}}{}^{\text{Born}}=\tfrac{1}{4}\,\text{Tr}({}^{B}S^{\dagger}\,{}^{B}S)=\tfrac{3}{4}|F|^2$$
$$+6[a^2C_K{}^2+b^2C_L{}^2-abC_KC_L],$$
$$(d\sigma/d\Omega)_{\text{TI}}=-(1/4k)\{[aC_K+bC_L]$$
$$\times[\epsilon_0(\Delta_0+\Delta_2P_2)+\epsilon_2(\Delta_1P_1+\Delta_3P_3)]$$
$$+[aC_K-bC_L][\epsilon_2(\nu_0+\nu_2P_2)+\tfrac{1}{3}\epsilon_0\nu_1P_1]\},$$
$$(d\sigma/d\Omega)_{\text{CI}}=(1/4k)[aF_K+bF_L]$$
$$\times[\epsilon_0(\Delta_0{}^C+\Delta_2{}^CP_2)+\epsilon_2(\Delta_1{}^CP_1+\Delta_3{}^CP_3)],$$
$$(d\sigma/d\Omega)'=(\epsilon_4/4k^2)[\Lambda_0+\Lambda_1P_1+\Lambda_2P_2$$
$$+\Lambda_3P_3+\Lambda_4P_4]=\tfrac{1}{4}\,\text{Tr}(S'^{\dagger}S'). \quad \text{(A16)}$$

(For $n-p$ scattering, $\epsilon_0\equiv\epsilon_2\equiv\epsilon_4\equiv 1$.) (For $p-p$ scattering, $\epsilon_0\equiv 0$, $\epsilon_2\equiv 2$, $\epsilon_4\equiv 4$ and $a\equiv 1$, $b\equiv -1$.)

$$\Delta_0=-\Delta_0{}^{10}+\Delta_0{}^{11}+\tfrac{3}{2}\Delta_2{}^{11}-(5/2)\Delta_2{}^{21}+\Delta_2{}^{31},$$
$$\Delta_2=-2\Delta_2{}^{10}-\Delta_2{}^{11}+5\Delta_2{}^{21}+\Delta_2{}^{31}-3\Delta_2{}^{30},$$
$$\Delta_1=-\Delta_1{}^{00}+\tfrac{3}{2}\Delta_1{}^{11}+\tfrac{3}{2}\Delta_1{}^{21}-2\Delta_1{}^{20}+3\Delta_3{}^{21},$$
$$\Delta_3=-2\Delta_3{}^{21}-3\Delta_3{}^{20},$$
$$\Delta_0{}^C=\Delta_0{}^{10}+2\Delta_0{}^{11},$$
$$\Delta_2{}^C=2\Delta_2{}^{10}+\Delta_2{}^{11}+5\Delta_2{}^{21}+3\Delta_2{}^{30}+4\Delta_2{}^{31},$$
$$\nu_0=3\Delta_1{}^{00}+\tfrac{3}{2}\Delta_1{}^{21}+\Delta_3{}^{21}-(9/2)\Delta_1{}^{11},$$
$$\nu_2=6\Delta_1{}^{20}-6\Delta_1{}^{21}+9\Delta_3{}^{20}-4\Delta_3{}^{21},$$
$$\nu_1=3\Delta_0{}^{10}-3\Delta_0{}^{11}+6\Delta_2{}^{10}-\tfrac{3}{2}\Delta_2{}^{11}$$
$$-(15/2)\Delta_2{}^{21}+3\Delta_2{}^{31},$$
$$\Delta_1{}^C=\Delta_1{}^{00}+3\Delta_1{}^{11}+2\Delta_1{}^{20}+3\Delta_1{}^{21},$$
$$\Delta_3{}^C=3\Delta_3{}^{20}+2\Delta_3{}^{21}.$$
$$\Lambda_0=\Delta_{11}{}^{000}+3\Delta_{11}{}^{111}+2\Delta_{11}{}^{220}+3\Delta_{11}{}^{221}+3\Delta_{33}{}^{220}$$
$$+2\Delta_{33}{}^{221}+\Delta_{00}{}^{110}+2\Delta_{00}{}^{111}+2\Delta_{22}{}^{110}$$
$$+\Delta_{22}{}^{111}+5\Delta_{22}{}^{221}+3\Delta_{22}{}^{330}+4\Delta_{22}{}^{331}.$$
$$\Lambda_2=4\Delta_{11}{}^{020}+\tfrac{3}{2}\Delta_{11}{}^{111}+9\Delta_{11}{}^{121}+2\Delta_{11}{}^{220}+\tfrac{3}{2}\Delta_{11}{}^{221}$$
$$+6\Delta_{13}{}^{020}+6\Delta_{13}{}^{121}+(12/7)\Delta_{13}{}^{220}-(6/7)\Delta_{13}{}^{221}$$
$$+(24/7)\Delta_{33}{}^{220}+(8/7)\Delta_{33}{}^{221}+4\Delta_{02}{}^{110}+2\Delta_{02}{}^{111}$$
$$+10\Delta_{02}{}^{121}+6\Delta_{02}{}^{130}+8\Delta_{02}{}^{131}+2\Delta_{22}{}^{110}-\tfrac{1}{2}\Delta_{22}{}^{111}$$
$$+(25/14)\Delta_{22}{}^{221}+(24/7)\Delta_{22}{}^{331}+(24/7)\Delta_{22}{}^{330}$$
$$+5\Delta_{22}{}^{121}+(40/7)\Delta_{22}{}^{231}-(8/7)\Delta_{22}{}^{131}$$
$$+(12/7)\Delta_{22}{}^{130}.$$
$$\Lambda_4=(72/7)\Delta_{13}{}^{220}+(48/7)\Delta_{13}{}^{221}+(18/7)\Delta_{33}{}^{220}$$
$$-(8/7)\Delta_{33}{}^{221}+(40/7)\Delta_{22}{}^{221}+(100/7)\Delta_{22}{}^{331}$$
$$+(4/7)\Delta_{22}{}^{331}+(36/7)\Delta_{22}{}^{131}+(72/7)\Delta_{22}{}^{130}$$
$$+(18/7)\Delta_{22}{}^{330}.$$
$$\Lambda_1=2\Delta_{10}{}^{010}+6\Delta_{01}{}^{111}+6\Delta_{01}{}^{121}+4\Delta_{01}{}^{120}+4\Delta_{12}{}^{010}$$
$$+3\Delta_{12}{}^{111}+9\Delta_{12}{}^{121}-\tfrac{3}{5}\Delta_{21}{}^{121}+\tfrac{4}{5}\Delta_{21}{}^{120}+3\Delta_{12}{}^{221}$$
$$+(48/5)\Delta_{12}{}^{231}+(36/5)\Delta_{12}{}^{230}.$$
$$\Lambda_3=6\Delta_{12}{}^{121}+(18/5)\Delta_{21}{}^{121}+(36/5)\Delta_{21}{}^{120}+12\Delta_{12}{}^{221}$$
$$+6\Delta_{12}{}^{030}+12\Delta_{12}{}^{131}+(12/5)\Delta_{12}{}^{231}$$
$$+(24/5)\Delta_{12}{}^{230}+4\Delta_{03}{}^{121}+6\Delta_{03}{}^{120}, \quad \text{(A17)}$$

where

$$\Delta_l{}^{J1}=\Delta_l{}^{J,-1}=\text{Im}A_l{}'^J,$$
$$\Delta_{ll'}{}^{JJ',-1}=\Delta_{ll'}{}^{JJ'1}=\tfrac{1}{4}\Re[A_l{}'^J(A_{l'}{}'^{J'})^*],$$
$$\Delta_l{}^{J0}=\text{Im}B_l{}'^J, \qquad \Delta_{ll'}{}^{JJ'0}=\tfrac{1}{4}\Re[B_l{}'^J(B_{l'}{}'^{J'})^*]. \quad \text{(A17b)}$$

The identity $A_{J-1}{}^J-A_{J+1}{}^J=B_{J-1}{}^J-B_{J+1}{}^J$ follows from (A8), (A9). The summation has been carried out explicitly over the ${}^3S_1$, ${}^3P_0$, ${}^3P_1$, ${}^3P_2$, ${}^3D_1$, ${}^3D_2$, ${}^3D_3$, and ${}^3F_2$ states. In $(d\sigma/d\Omega)'$, DF interference has been omitted. For $p-p$ scattering, terms which contain an even subscript do not appear and (A17) simplifies considerably.

The radial differential equations for which "exact" solutions were obtained in the present paper will be considered now in more detail.

Let

$$U=e^{-ay}/y^2 \text{ for } y\geq y_0,$$
$$=e^{-ay_0}/y_0{}^2 \text{ for } y\leq y_0=\text{constant}.$$

$${}^3P_0: \quad \frac{d^2u^0}{dy^2}-\frac{2}{y^2}u^0+u^0=4\lambda Uu^0; \quad \text{(A18)}$$

$${}^3P_1: \quad \frac{d^2u^1}{dy^2}-\frac{2}{y^2}u^1+u^1=-2\lambda Uu^1; \quad \text{(A19)}$$

$$\left.\begin{aligned} {}^3P_2: &\quad \frac{d^2u}{dy^2}-\frac{2}{y^2}u+u=\tfrac{2}{5}\lambda U(u-3(6)^{\frac{1}{2}}w);\\ {}^3F_2: &\quad \frac{d^2w}{dy^2}-\frac{12}{y^2}w+w=\tfrac{2}{5}\lambda U(4w-3(6)^{\frac{1}{2}}u);\end{aligned}\right\} \quad \text{(A20)}$$

$a=1/kR$; $\lambda=MV_0R^2/\hbar^2$; $k^2=ME/\hbar^2$; $y=kr$.

The potential $V(r)$ is given in Eq. (3). There are four independent sets of solutions,

$$\begin{Bmatrix} u_1 \\ w_1 \end{Bmatrix}, \quad \begin{Bmatrix} u_2 \\ w_2 \end{Bmatrix}, \quad \begin{Bmatrix} u_3 \\ w_3 \end{Bmatrix}, \quad \begin{Bmatrix} u_4 \\ w_4 \end{Bmatrix}$$

to Eq. (A20). Examination of the power series representation in the neighborhood of the origin shows that two of the solutions always vanish at the origin, and the other two are irregular and must be discarded because of the usual arguments on quadratic integrability and conservation of current. The two regular solutions,

$$\begin{Bmatrix} u_1 \\ w_1 \end{Bmatrix}, \quad \begin{Bmatrix} u_2 \\ w_2 \end{Bmatrix},$$

will be called a "fundamental set." Any set of solutions arising from a linear transformation of the fundamental set will also satisfy all of the boundary conditions of the scattering problem and hence may be used to calculate the complex phase shifts $\delta_l{}^{Jm_s}$. It is not difficult to give a plausible argument showing that

there ought to be one pair of solutions,

$$\left\{\begin{matrix} u_1 \to u_{11}^2 \\ w_1 \to u_{31}^2 \end{matrix}\right\},$$

in which the P-state is dominant, at least asymptotically, and another pair,

$$\left\{\begin{matrix} u_2 \to u_{13}^2 \\ w_2 \to u_{33}^2 \end{matrix}\right\},$$

in which the F-state is dominant. Consider the integral equations corresponding to the coupled differential equations (A20) and their boundary conditions:

$$u_{1\alpha}^2(y) = A_{1\alpha}^2 g_1(y) + \tfrac{2}{5}\lambda g_{-1}(y)\int_0^y U(u_{1\alpha}^2 - 3\sqrt{6}u_{3\alpha}^2)g_1 dy$$

$$+ \tfrac{2}{5}\lambda g_1(y)\int_y^\infty U(u_{1\alpha}^2 - 3\sqrt{6}u_{3\alpha}^2)g_{-1}dy;$$

$$u_{3\alpha}^2(y) = A_{3\alpha}^2 g_3(y) + \tfrac{2}{5}\lambda g_{-3}(y)\int_0^y U(4u_{3\alpha}^2 - 3\sqrt{6}u_{1\alpha}^2)g_3 dy$$

$$+ \tfrac{2}{5}\lambda g_3(y)\int_y^\infty U(4u_{3\alpha}^2 - 3\sqrt{6}u_{1\alpha}^2)g_{-3}dy;$$

$$g_{\pm l}(y) = (\tfrac{1}{2}\pi y)^{\frac{1}{2}} J_{\pm(l+\frac{1}{2})}(y); \quad g_1 \underset{y\to 0}{\longrightarrow} \frac{y^2}{3}; \quad g_3 \underset{y\to 0}{\longrightarrow} \frac{y^4}{105}. \tag{A21}$$

The constants $A_{1\alpha}^2$, $A_{3\alpha}^2$ are arbitrary; the subscripts α denote the duplicity of regular solutions and take on the values 1, 3. The asymptotic form of (A21) yields integral expressions for the amplitudes and phase shifts:

$$A_{1\alpha}^2 = a_{1\alpha}^2 \cos\delta_{1\alpha}^2,$$

$$a_{1\alpha}^2 \sin\delta_{1\alpha}^2 = -\tfrac{2}{5}\lambda\int_0^\infty U(u_{1\alpha}^2 - 3\sqrt{6}u_{3\alpha}^2)g_1 dy;$$

$$A_{3\alpha}^2 = a_{3\alpha}^2 \cos\delta_{3\alpha}^2,$$

$$a_{3\alpha}^2 \sin\delta_{3\alpha}^2 = -\tfrac{2}{5}\lambda\int_0^\infty U(4u_{3\alpha}^2 - 3\sqrt{6}u_{1\alpha}^2)g_3 dy, \tag{A22}$$

where

$$u_{1\alpha}^2 \sim a_{1\alpha}^2 \sin(y - \pi/2 + \delta_{1\alpha}^2),$$

$$u_{3\alpha}^2 \sim a_{3\alpha}^2 \sin(y - 3\pi/2 + \delta_{3\alpha}^2).$$

The weighting influence of the $g_3(y)$ term (which is small throughout the region in which the nuclear potential is large) in the various integrands suggests that the "subdominant" amplitudes a_{13}^2, a_{31}^2 might best be kept small by placing $A_{13}^2 = A_{31}^2 = 0$, which amounts to choosing $\delta_{13}^2 = \delta_{31}^2 = \pi/2$. In Born approximation, for which the free particle trial functions $u_{11}^2 = a_{11}^2 g_1(y)$, $u_{13}^2 = u_{31}^2 \equiv 0$, $u_{33}^2 = a_{33} g_3(y)$ are used, Eqs. (A22) become

$${}^B\delta_{11}^2 = -\frac{2}{5}\lambda\int_0^\infty U(g_1)^2 dy, \quad {}^B a_{13}^2 = {}^B a_{31}^2 = -\frac{6}{5}\sqrt{6}\lambda\int_0^\infty U g_1 g_3 dy,$$

$${}^B\delta_{33}^2 = -\frac{8}{5}\lambda\int_0^\infty U(g_3)^2 dy, \quad \delta_{13}^2 = \delta_{31}^2 = \pi/2. \tag{A23}$$

It is evident from the behavior of the functions $g_1(y)$ and $g_3(y)$ that, of the four quantities now describing the coupled state scattering (δ_{11}^2, a_{13}^2, a_{31}^2, δ_{33}^2), δ_{11}^2 might be large but the other three are small. (a_{11}^2 and a_{33}^2 may be normalized to unity since only the ratios

$$a_{13}^2/a_{33}^2 \text{ and } a_{31}^2/a_{11}^2 \text{ are relevant.})$$

In general, wherever a comparison of the exact solution with the Born approximation could be made, the latter was found to be quite accurate for the three small quantities (a_{13}^2, a_{31}^2, δ_{33}^2), with only δ_{11}^2 showing marked deviations. Table III gives the comparison at 350 Mev for the SRSW case.

TABLE III. Triplet $p-p$ phase shifts and amplitudes at 350 Mev for singular tensor potential with short range square well cutoff (SRSW case).

	δ_{11}^2	a_{13}^2	a_{31}^2	δ_{33}^2	δ_{31}^2	δ_{13}^2
Repulsive exact	0.218	−0.101	−0.098	0.050	$\pi/2$	$\pi/2$
Attractive exact	0.918	0.084	0.085	−0.077	$\pi/2$	$\pi/2$
Repulsive Born	0.088	−0.099	−0.099	0.067	$\pi/2$	$\pi/2$
Attractive Born	−0.068	0.099	0.099	−0.067	$\pi/2$	$\pi/2$

To integrate Eqs. (A20) numerically, it is convenient to start with a power series solution near the origin (where the potential is constant). The roots of the indicial equations are

$$\begin{aligned} \alpha_1 &= 6, & \beta_1 &= 4, \\ \alpha_2 &= 2, & \beta_2 &= 4, \\ \alpha_3 &= -1, & \beta_3 &= 1, \\ \alpha_4 &= -1, & \beta_4 &= -3, \end{aligned}$$

where

$$u_i = \sum_{n=0}^\infty a_n{}^i y^{n+\alpha_i}, \qquad w_i = \sum_{n=0}^\infty b_n{}^i y^{n+\beta_i}. \tag{A24}$$

The fundamental set of regular solutions can therefore be taken[12] to be

$$u_1 = \sum_0^\infty a_n y^{n+6}, \quad u_2 = u_1 \log y + \sum_0^\infty C_n y^{n+2},$$

$$w_1 = \sum_0^\infty b_n y^{n+4}, \quad w_2 = w_1 \log y + \sum_0^\infty d_n y^{n+4}. \tag{A25}$$

[12] E. T. Whittaker and G. N. Watson, *A Course of Modern Analysis* (The Macmillan Company, New York, 1946), Chap. X.

The recurrence relations are

$$a_n[(n+6)(n+5)-2]+K_1a_{n-2}+Kb_n=0,$$
$$b_n[(n+4)(n+3)-12]+K_2b_{n-2}+Ka_{n-4}=0,$$
$$a_{n-4}(2n+3)+C_n[(n+2)(n+1)-2]+K_1C_{n-2}+Kd_{n-4}=0,$$
$$b_n(2n+7)+d_n[(n+4)(n+3)-12]+K_2d_{n-2}+KC_n=0, \quad \text{(A26)}$$

where

$$K_0=\tfrac{2}{3}\lambda e^{-\alpha y_0}/y_0^2; \quad K=\pm 3(6)^{\frac{1}{2}}K_0;$$
$$K_1=1\mp K_0; \quad K_2=1\mp 4K_0.$$

(Upper sign: "attractive," lower sign: "repulsive.")

The quantities a_0 and d_0 are undetermined; the former merely defines the normalization and the latter represents the arbitrary amount of solution $\alpha=1$ that may be mixed in solution $\alpha=2$.

In some cases the coupled equations were integrated on a differential analyzer; in others, a desk calculator was used. To check the phase shifts, the resulting radial functions were used as trial functions in the integral equations. For the uncoupled equations, a method recently described by Kynch[13] was used. Its advantage lies in the fact that the nuclear phase shift is integrated directly, whereas in an integration of the wave function most of the effort is "wasted" in obtaining the centrifugal phase shift. If the quantity $\tan^{-1}(-1^l S(y'))$ represents the phase shift which would obtain if the potential for $y\geq y'$ were placed equal to zero, then

$$(-1)^{l+1}\, dS_l/dy = V(g_l+Sg_{-l})^2 \quad \text{(A27)}$$

where $d^2u/dy^2-l(l+1)u/y^2+u=Vu$. $S(y)$ is either monotonically increasing or decreasing depending on whether the potential is repulsive or attractive. For a square well cutoff, the power series expansion for $S(y)$ (P-state) is given by

$$S(y)=S_0y^5+S_2y^7+S_4y^9+S_6y^{11}.$$

Let $V=\epsilon=$ constant.

$$S_0=\frac{\epsilon}{45}, \qquad S_4=\frac{\epsilon}{9}\left(S_0^2-\frac{4}{15}S_0-\tfrac{2}{3}S_2+\frac{1}{525}\right),$$
$$S_2=-\frac{2\epsilon}{21}\left(S_0+\frac{1}{30}\right), \quad S_6=\frac{\epsilon}{11}\left(S_0^2+2S_0S_2+\frac{4}{35}S_0-\frac{4}{15}S_2-\tfrac{2}{3}S_4-\frac{4}{42\,525}\right). \quad \text{(A28)}$$

Within a hard core $S(y)=-g_1(y)/g_{-1}(y)$ (P-state).

The author wishes to express his sincere thanks to Professor Robert Serber, Dr. R. S. Christian, Professor Owen Chamberlain, and Dr. Robert Jastrow for many stimulating discussions and helpful suggestions. The assistance of Mr. John Killeen and the operating crew of the differential analyzer was invaluable. The excellent computational work of Mr. Victor Brady was also much appreciated.

[13] G. J. Kynch, Proc. Phys. Soc. (London) **65**, 2, 83 (1952).

Polarization Effects in Nucleon-Nucleon Scattering*

DON R. SWANSON†
Radiation Laboratory, Department of Physics, University of California, Berkeley, California
(Received September 19, 1952)

If a beam of unpolarized nucleons is scattered from a target of unpolarized nucleons, the scattered particles are polarized (in a direction normal to the scattering plane) provided that the interaction contains tensor or spin-orbit forces. The polarization can be detected by means of a second similar scattering since the cross section then contains an azimuthal dependence:

$$I(\theta, \phi) = I_0(\theta)(1+\epsilon \cos\phi),$$

where $\epsilon(\theta)$ is essentially the square of the polarization. Calculations are carried out by the author for a double $p-p$ scattering using the tensor interaction described in the preceding paper, and for a double $n-p$ scattering using the central and tensor potential of Christian and Hart (containing the "half-exchange" dependence proposed by Serber). The polarization produced by the first scattering at the optimum angle of $\theta \approx 50°$ was found to vary from 6 percent at 40 Mev to 33 percent at 285 Mev for $n-p$ scattering and from 10 percent 129 Mev to 15 percent at 350 Mev for $p-p$ scattering. The $n-p$ results (previously published) are consistent with the azimuthal asymmetry detected in a double scattering experiment reported by L. Wouters.

SCATTERING OF A POLARIZED BEAM

FOR a single nucleon-nucleon collision in a definite initial spin state χ_i, the intensity of the scattered state is given by $(\bar{S}\chi_i, \bar{S}\chi_i)$, the expectation value of $\bar{S}^\dagger\bar{S}$. S is the 3×3 triplet spin scattering matrix defined in the Appendix of the preceding paper[1]; $\bar{S}$ (4×4 dimensions) is the same with singlet states included. The result of a measurement to which many scattering events contribute is necessarily the average expectation value of the measured quantity taken over an ensemble of all possible initial states of the system. The totality of information concerning a system can be expressed in terms of the q-dimensional density matrix, $\rho_{ji}{}^{(q)} = \sum_\alpha g_\alpha (a_i{}^\alpha)^* a_j{}^\alpha$, where $\sum_i a_i{}^\alpha u_i$ is the wave function of the system in the state α, g_α is probability of occurrence, and u_i a complete set of expansion functions. Following the method of Wolfenstein and Ashkin,[2,3] let $\rho^{(4)}$ refer to the initial spin states of the two-nucleon system; then the differential scattering cross section is given by $\mathrm{Tr}(\rho^{(4)}\bar{S}^\dagger\bar{S})$. Consider for the moment an ensemble of one particle (spin $\frac{1}{2}$) systems; a measurement of spin will yield the result $\langle\boldsymbol{\sigma}_1\rangle = \mathrm{Tr}(\rho^{(2)}\boldsymbol{\sigma}_1)$, from which it follows that the (two-dimensional) density matrix can be written $\rho^{(2)} = \frac{1}{2}[1+\langle\boldsymbol{\sigma}_1\rangle\cdot\boldsymbol{\sigma}_1]$. The four-dimensional density matrix describing a spin state ensemble of two-particle systems is given by the "direct product"[4] of the density matrices for the one-particle ensembles, provided that the states of one particle are not correlated with those of the other:

$$\rho^{(4)}(1, 2) = \rho^{(2)}(1) \times \rho^{(2)}(2),$$

or

$$(\rho^{(4)})_{ij;i'j'} = [\rho^{(2)}(1)]_{ii'}[\rho^{(2)}(2)]_{jj'}.$$

Hence,

$$\rho^{(4)} = \tfrac{1}{4}(1+\langle\boldsymbol{\sigma}_1\rangle\cdot\boldsymbol{\sigma}_1)\times(1+\langle\boldsymbol{\sigma}_2\rangle\cdot\boldsymbol{\sigma}_2). \quad (1)$$

The differential cross section for a beam of particles of polarization $\mathbf{P}_1 = \langle\boldsymbol{\sigma}_1\rangle/I_1$ scattered from an unpolarized target $\langle\boldsymbol{\sigma}_2\rangle = 0$ is therefore given by

$$\begin{aligned}\mathrm{Tr}(\rho^{(4)}\bar{S}^\dagger\bar{S}) &= \tfrac{1}{4}I_0\,\mathrm{Tr}(\bar{S}^\dagger\bar{S}) + \tfrac{1}{4}\langle\boldsymbol{\sigma}_1\rangle\cdot\mathrm{Tr}(\boldsymbol{\sigma}_1\times 1\bar{S}^\dagger\bar{S}) \\ &= \tfrac{1}{4}I_0\,\mathrm{Tr}(\bar{S}^\dagger\bar{S}) + \tfrac{1}{8}\langle\boldsymbol{\sigma}_1\rangle\cdot\mathrm{Tr}(\boldsymbol{\sigma}S^\dagger S),\end{aligned} \quad (2)$$

where $\boldsymbol{\sigma}$ is the triplet spin operator and I_0 the intensity of the incident beam. The second equality follows from the absence of matrix elements in S between triplet and singlet states; hence the latter do not contribute to the "polarization term" $\frac{1}{8}\langle\boldsymbol{\sigma}_1\rangle\cdot\mathrm{Tr}(\boldsymbol{\sigma}S^\dagger S)$.

For an interaction of the form

$$[A(r)+\boldsymbol{\sigma}_1\cdot\boldsymbol{\sigma}_2 B(r)][a+bP_x],$$

S is proportional to the (triplet) unit matrix and so the polarization term vanishes. In the case of a tensor or spin-orbit force, it follows from Eq. (A2)[1] (or can be proved by symmetry arguments[5]) that the polarization term in Eq. (2) is nonvanishing and proportional to the component of polarization of the incident beam normal to the scattering plane. Detection of an azimuthal dependence of this type in the nucleon-nucleon scattering cross section would therefore constitute direct evidence for the presence of noncentral forces. The problem now to be considered is that of producing the incident polarized beam of high energy (S states alone do not contribute to polarization) nucleons.

If an unpolarized beam strikes an unpolarized target, the polarization of the scattered beam is given by

$$(\bar{S}\chi_i, \boldsymbol{\sigma}_i\bar{S}\chi_i)/(\bar{S}\chi_i, \bar{S}\chi_i) = \mathrm{Tr}(\boldsymbol{\sigma}SS^\dagger)/\mathrm{Tr}(\bar{S}\bar{S}^\dagger),$$

where $\rho^{(4)} = \frac{1}{4}1$ is the density matrix describing the initial system. A proof, based on the transformation

---

* This work was performed under the auspices of the U. S. Atomic Energy Commission.
† Now at Hughes Aircraft Company Research and Development Laboratories, Culver City, California.
[1] Don R. Swanson, Phys. Rev. **89**, 740 (1953). The notation of this reference will be used throughout.
[2] L. Wolfenstein, Phys. Rev. **76**, 541 (1949).
[3] L. Wolfenstein and J. Ashkin, Phys. Rev. **85**, 947 (1952).
[4] H. Weyl, *Theory of Groups and Quantum Mechanics* (Methuen and Company, Ltd., London, 1931), Chap. II.
[5] L. Wolfenstein, Phys. Rev. **75**, 1664 (1949).

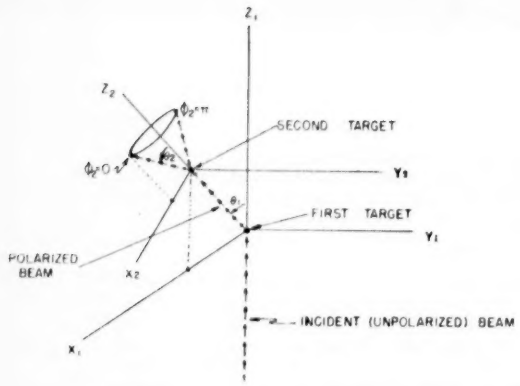

FIG. 1. Coordinate axes for double scattering problem.

properties of S, that

$$\mathrm{Tr}(\boldsymbol{\sigma}SS^{\dagger})=\mathrm{Tr}(\boldsymbol{\sigma}S^{\dagger}S)$$

has been given by Wolfenstein and Ashkin.[3] An algebraic *tour de force*, however, using the form (A2) (reference 1) for S, yields the equality

$$\mathrm{Tr}(\sigma_{y}S^{\dagger}S)-\mathrm{Tr}(\sigma_{y}SS^{\dagger})=\frac{\tan\theta\cos\phi}{4k^{2}}$$
$$\times Im\sum_{J}[P_{J+1}{}^{2}+J(J+1)P_{J+1}][(A_{J+1}{}^{J}-A_{J-1}{}^{J})$$
$$-(B_{J+1}{}^{J}-B_{J-1}{}^{J})][A-E-C]=0, \quad (3)$$

which vanishes immediately for purely central or $\mathbf{S}\cdot\mathbf{L}$ forces (uncoupled, therefore $\delta_l{}^{Jm_s}=\delta_l{}^{J}$) and does so for tensor forces as a consequence of the Wronskian conditions (A9), (A17b), reference 1.

If the z_1 direction is taken as that of the incident beam, then $\mathrm{Tr}(\sigma_{z_1}S^{\dagger}S)\equiv 0$ may be readily confirmed. Placing the x_1 axis in the scattering plane, $(\phi_1=0)$, the polarization is given by

$$P_{1y_1}(\theta_1,\phi_1=0)=\frac{1}{8I_1}\mathrm{Tr}(\sigma_{y_1}S_1{}^{\dagger}S_1)=\frac{Q_1(\theta_1)}{I_1(\theta_1)};$$
$$P_{x_1}=P_{z_1}=0; \quad I_1=\tfrac{1}{4}\,\mathrm{Tr}(S_1{}^{\dagger}S_1), \quad (4)$$

where the subscripts 1 will be used throughout to denote the first scattering.

In the first scattering, introduce the subscript (b) to represent the particles originally in the incident beam, and (t) to denote those from the target. The polarization of the two scattered beams is the same:

$$\langle\boldsymbol{\sigma}_b\rangle=\mathrm{Tr}(\boldsymbol{\sigma}_b\times 1\bar{S}^{\dagger}\bar{S})=\mathrm{Tr}(1\times\sigma_t\bar{S}^{\dagger}\bar{S})=\langle\boldsymbol{\sigma}_t\rangle$$
$$=\tfrac{1}{2}\,\mathrm{Tr}(\boldsymbol{\sigma}S^{\dagger}S). \quad (5)$$

The nucleons emerging at some laboratory angle (Θ,Φ) will be used to form the incident beam for a second scattering. If particles (b) are to be used, the center-of-mass angles are $\theta=2\Theta$ and $\phi=\Phi$; for particles (t), however, $\theta=\pi-2\Theta$ and $\phi=\Phi+\pi$. Consider, for example, the experiment of Wouters[6] in which incident protons produce a neutron beam by means of a (p,n) reaction. The (p,n) collision is described by $S(\theta,\phi)$, and the polarization of neutrons observed at Θ, Φ is $\langle\sigma_t\rangle(\theta,\phi)/I(\theta)$ where $\theta=\pi-2\Theta$ and $\phi=\Phi+\pi$. The scattering matrix itself carries all information on the exchange nature of the interaction. In the case of two protons the S matrix is antisymmetric, so it is of course immaterial whether $\theta=2\Theta,\phi=\Phi$ or $\theta=\pi-2\Theta,\phi=\Phi+\pi$ is used.

The subscript 1 will be used hereafter in place of (b) or (t) to indicate that the operator in question refers to once-scattered particles which form an incident beam for the second scattering.

THE DOUBLE SCATTERING PROBLEM

The coordinate system for the second scattering $(x_2y_2z_2)$ is obtained by rotating $(x_1y_1z_1)$ about the y_1 axis until the z axis lies along the new incident beam (Fig. 1). Hence $P_{y1}=P_{y2}$ is unchanged and represents (in the form of $\langle\boldsymbol{\sigma}_1\rangle$) just the quantity that must appear in the density matrix for the new initial state

$$\boldsymbol{\rho}^{(4)}=\boldsymbol{\rho}_1{}^{(2)}\times\boldsymbol{\rho}_2{}^{(2)}=\tfrac{1}{4}(1+\langle\boldsymbol{\sigma}_1\rangle\cdot\boldsymbol{\sigma}_1)\times(1+\langle\boldsymbol{\sigma}_2\rangle\cdot\boldsymbol{\sigma}_2). \quad (6)$$

The subscript 2 refers to particles of the second target. The latter is supposed to be unpolarized, so that $\langle\boldsymbol{\sigma}_2\rangle=0$. The differential cross section for the second scattering

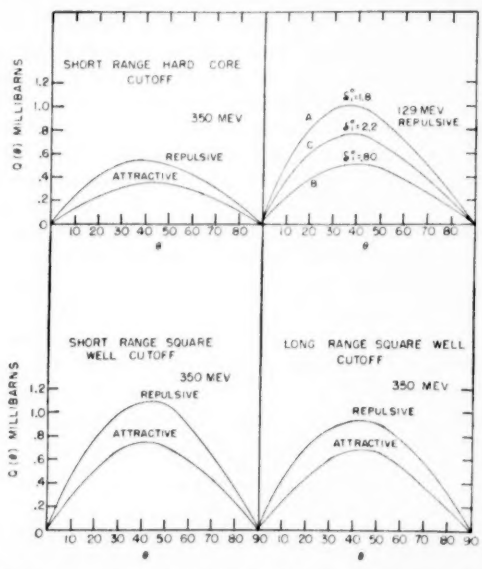

FIG. 2. Values of $Q(\theta)=\frac{1}{8}\,\mathrm{Tr}(\sigma_{y}S^{\dagger}S)$ for $p-p$ scattering at (lab. system) energies of 350 Mev, 129 Mev. θ=scattering angle in center-of-mass system. The interactions indicated (cut-off singular tensor) are those for which cross sections were computed in reference 1 (Figs. 2, 3).

[6] L. Wouters, Phys. Rev. **84**, 1069 (1951).

is obtained from (6), (2), (3), and (4):

$$(d\sigma/d\Omega)_2 = J(\theta_1, \theta_2, \phi_2) = I_1(\theta_1)I_2(\theta_2) + Q_1(\theta_1)Q_2(\theta_2)\cos\phi_2. \quad (7)$$

$I_1(\theta_1)$ and $I_2(\theta_2)$ are the differential cross sections with polarization terms omitted.

In the case of $p-p$ scattering, or $n-p$ scattering with exchange dependence $1\pm P_x$, so that interaction occurs only in orbital angular momentum states of the same parity, then the condition

$$(S^\dagger S)(\theta, \phi) = (S^\dagger S)(\pi-\theta, \phi+\pi)$$

implies $Q(\theta) = -Q(\pi-\theta)$ so that $Q(\pi/2)=0$. The contribution to the polarization at $\theta=\pi/2$ must therefore come exclusively from odd-even interference terms; the possibility of such a measurement suggests a test of the $1+P_x$ dependence proposed by Serber.

Ignoring for the moment the fact that the second scattering occurs at a somewhat lower energy than the first, and assuming the two involve the same types of particles (i.e., both $n-p$ or both $p-p$), then the measured ratio at the optimum angles $\theta_1=\theta_2=\theta_{max}$ is

$$R \equiv \frac{J(\phi_2=0)}{J(\phi_2=\pi)} = \frac{1+(Q/I)^2}{1-(Q/I)^2} \geq 1. \quad (8)$$

Barring a somewhat remarkable dependence of $Q(\theta)$ on energy, a ratio greater than 1 should in general be expected as the experimental result whenever $\theta_1 \approx \theta_2$. A relationship which led to Eq. (3),

$$\sqrt{2}(B-D)\cot\theta - (A-C-E) = \sum_J [P_{J+1}{}^2 + J(J+1)P_{J+1}][(A_{J+1}{}^J - A_{J-1}{}^J) - (B_{J+1}{}^J - B_{J-1}{}^J)] = 0, \quad (9)$$

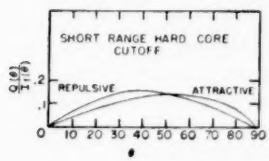

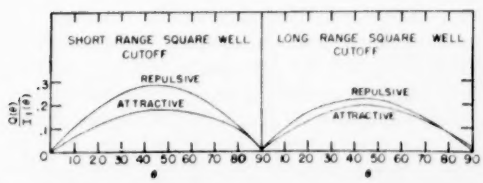

FIG. 3. Values of $Q(\theta)/I_t(\theta)$ for $p-p$ scattering at 350 Mev. $I_t(\theta)$ = triplet cross section. Polarization is given by

$$Q(\theta)/[I_t(\theta)+I_s(\theta)];$$

$I_s(\theta)$ = singlet cross section. The function plotted hence represents the polarization at those angles ($\theta>50°$ for Christian and Noyes model) for which singlet scattering is negligible. The interactions indicated (cut-off singular tensor) are those for which cross sections were computed in reference 1.

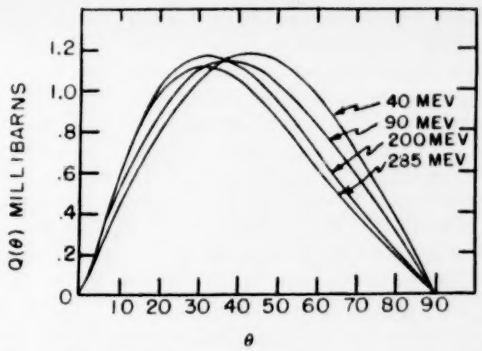

FIG. 4. Values of $Q(\theta)=\frac{1}{4}\,\mathrm{Tr}(\sigma_y S^\dagger S)$ for $n-p$ scattering at the energies indicated. The interaction used is that of Christian and Hart. A similar plot of polarization (Q/I) is given in reference 7.

can be used to simplify appreciably the form of $Q(\theta)$ by eliminating $A-C$.

$$Q(\theta) = \frac{\epsilon_4}{8k^2} Im[E'(B'+D')^* + D^{*\prime}B'\cot\theta] + \frac{\epsilon_2}{4k}(C_+ + F)\Re(B+D) \equiv Q' + Q_I. \quad (10)$$

ϵ_2, ϵ_4 are defined in Eq. (A17) of reference 1.

RESULTS AND CONCLUSIONS

For $p-p$ scattering, $Q(\theta)$ is plotted in Fig. 2 for all cases considered in reference 1 except the long-range hard core model which has been omitted because the coupled phase shifts were found only roughly. The dominant term of Eq. (10), which alone yields a value of $Q(\theta)$ correct to within 50 percent or so is quite simple; for singular potentials (C_K-C_L) is very small, so that $Q' \gg Q_I$; only P states have been kept:

$$Q(\theta) \approx Im\{B_1{}'^2{}^*[B_1{}'^0 + \tfrac{3}{2}(A_1{}'^1 - A_1{}'^2)]\}P_2{}^1(\cos\theta). \quad (11)$$

The importance of obtaining accurate values for the coupled ${}^3P_2$ phase shifts is clear; even rigorously there is no contribution to the polarization from the ${}^3P_0$ and ${}^3P_1$ states alone. The polarization,

$$P(\theta, \phi=0) = Q(\theta)/I(\theta),$$

is plotted in Fig. 3; the value of $I(\theta)$ was taken in all cases to be the predicted triplet cross section for the potential model used; that is, the singlet scattering is assumed negligible for $\theta \geq 50°$. If, instead, it is assumed that singlet scattering can be introduced in such a way as to bring the cross section in each case up to the experimental value of 4 millibarns, then Fig. 2, rather than Fig. 3, shows more clearly the dependence of polarization on choice of cutoff. With the potential given by Eq. (6) of reference 1, the polarization (at $\theta \approx 50°$) is 10 percent ($R \approx 1.02$) at 129 Mev and 15 percent ($R \approx 1.05$) at 350 Mev.

For $n-p$ scattering, the tensor and central inter-

action of Christian and Hart (containing the "half-exchange" dependence proposed by Serber) is used. In Fig. 4, $Q(\theta)$ is plotted for energies of 40, 90, 200, 285 Mev. A similar plot of the polarization $Q(\theta)/I(\theta)$ was given in an earlier report.[7] A comparison of $Q(\theta)$ with Q/I illustrates the point that $I(\theta)$ alone carries almost the entire energy dependence of the polarization.

If odd-state forces were introduced into the triplet $n-p$ interaction (by changing the $1+P_x$ dependence), the polarization could be considerably larger because of the contribution from $S-P$ interference:

$$Q_{SP}=(1/8k^2)Im\{B_0{}^1[B_1{}^2-B_1{}^0+\tfrac{3}{2}(A_1{}^2-A_1{}^1)]^*\}\sin\theta. \quad (12)$$

[7] Don R. Swanson, Phys. Rev. **84**, 1068 (1951).

To obtain some idea of the magnitude of this term, suppose the same amount of triplet odd-state interaction were introduced into the $n-p$ Hamiltonian as was used for the $p-p$ interaction in the preceding paper.[1] Interpolating the $p-p$ phase shifts to obtain rough values at 200 Mev, the result is $Q_{SP}\approx 0.5\sin\theta$ millibarns leading to $R(\pi/2)\approx 1.03$. Hence, although the asymmetry is appreciably influenced by the presence of odd states, the quoted uncertainty in the experimental results of Wouters[6] is too great to permit any sharp conclusions to be drawn on the question of the exchange dependence of the $n-p$ interaction. The desirability of further experiments on $n-p$ double scattering is, however, indicated.

PHYSICAL REVIEW VOLUME 89, NUMBER 4 FEBRUARY 15, 1953

Isomeric Transitions in Tc^{93} and Tc^{96}†

HARRY T. EASTERDAY AND HEINRICH A. MEDICUS*
Radiation Laboratory, Department of Physics, University of California, Berkeley, California
(Received October 31, 1952)

The 390-kev γ-line reported to be associated with Tc^{92} is found to be Tc^{93} and is shown to be a $M4$ isomeric transition. Mass assignment to Tc^{96} is made for the isomeric transition previously known to have 34.4-kev energy and 51.5-minute half-life, and a weak positron branching was found.

MASS assignment of the many technetium activities which are usually produced by irradiation of molybdenum is quite difficult because the latter element has seven stable isotopes of roughly equal natural abundance. From the standpoint of nuclear shell structure, knowledge of these activities is of particular interest since according to this model, technetium with 43 protons lies in a region of isomerism. Until now characteristics of isomeric transitions were known for the odd-even isotopes 95, 97, and 99. This report concerns isomeric states in the nuclei 93 and 96.

The three strongest activities produced when enriched Mo^{92} is bombarded with protons of energies between 5 and 10 Mev decay with half-lives of 4.5 minutes, 43.5 minutes, and 2.7 hours.[1-3] At the proton energies used (p, n) and (p, γ) reactions are the most probable, so the activities are expected to be associated with Tc^{92} or Tc^{93}. In order to attempt to fix the mass of the 390-kev γ-transition of 43.5-minute half-life as being Tc^{93}, the activity was produced by two additional separate reactions. Thresholds calculated from the empirical mass formula[4] for (d, n) and $(d, 2n)$ reactions on Mo^{92} are -2 Mev and $+10$ Mev. The 390-kev line was observed in 1-mil molybdenum foils throughout the full range of 20-Mev deuterons; however, it could not be produced with neutron bombardment on the same type of foil. Thresholds for $(\alpha, 4n)$ and $(\alpha, 5n)$ on Nb^{93} are calculated to be 34 and 45 Mev, respectively. The activity was found to be produced in slight amount with α's between 39 and 40 Mev. Although this evidence cannot be considered conclusive, it appears to indicate that the 390-kev line is Tc^{93} instead of Tc^{92} as previously reported.

The multipole order of the 390-kev line was determined by measurement of the K/L ratio and the conversion coefficient. The activity for the multipole order measurements was produced by bombardment of enriched Mo^{92} with 9.5-Mev protons from the 60-inch cyclotron and the activity observed in a β-spectrometer. Chemical separation of the Tc activities was made by heating the bombarded molybdenum oxide in a glass tube open at one end. By controlling the temperature, the technetium oxide can be made to condense in the cooler part of the tube whereas the less volatile molybdenum oxide is not affected. The activity is removed with a drop of dilute ammonium hydroxide and mounted on a thin Tygon foil. Figure 1 shows the K- and L-

† This work was supported by the U. S. Atomic Energy Commission.
* Fellow of the Swiss Arbeitsgemeinschaft für Stipendien in Mathematik and Physik, now at Massachusetts Institute of Technology, Cambridge, Massachusetts.
[1] E. E. Motta and G. E. Boyd, Phys. Rev. **73**, 1470 (1948).
[2] D. N. Kundu and M. L. Pool, Phys. Rev. **74**, 1775 (1948).
[3] Medicus, Preiswerk, and Scherrer, Helv. Phys. Acta. **23**, 299 (1950).
[4] E. Fermi, *Nuclear Physics* (University of Chicago Press, Chicago, 1950), p. 7.

conversion lines measured with a double focusing spectrometer of 1 percent resolution. It was not possible to separate the L and M lines. The result of the $K/(L+M)$ ratio is 5.8 ± 0.3. Determination of the conversion coefficient was made with a lens spectrometer by measuring the intensities of the conversion electron line and of the photoelectrons from a uranium converter. The converter efficiency was determined using the 390-kev K-line of Sr^{87} which Mann and Axel[5] have shown to be an $M4$ transition. Taking the theoretical K-conversion coefficient of 0.194 from the new tables of Rose *et al.*[6] for the Sr^{87} isomer, the K-conversion coefficient for Tc^{93} is 0.31 ± 0.07. This is in good agreement with the theoretical value of 0.295 given by Rose for magnetic 2^4-pole emission at this energy and Z value. The measured K/L ratio is within experimental error on the curves given by Goldhaber and Sunyar.[7] The half-life of 43.5 minutes is too small by a factor of at least three to agree with the empirical formula of Goldhaber and Sunyar even if one assumes that the initial state has spin $\frac{1}{2}$. Since the decay scheme of Tc^{93} is not known at present, it is possible that the apparent half-life is shortened by competing processes, K-capture and positron emission.

An isomer of 51.5 ± 1.0 minutes half-life and 34.4-kev transition energy is produced among the other activities formed by the irradiation of isotopes of natural molybdenum.[3] Until now it has not been possible to assign this isomer to a given Tc isotope. The obvious solution of assigning this activity to the positron emitter Tc^{94}, which has a half-life (52.5 ± 1.0 minutes) within the experimental error of that of the isomer, has been proved incorrect.[3]

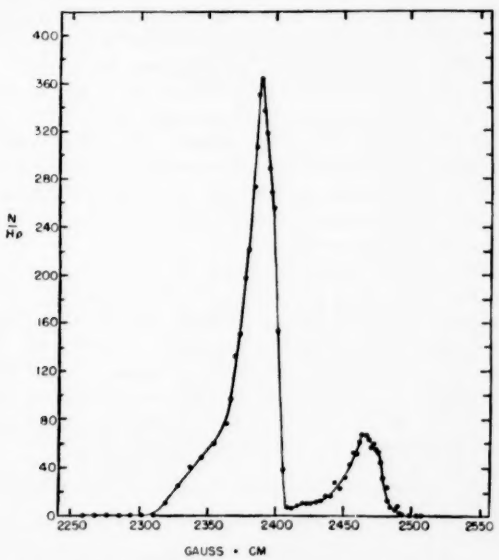

FIG. 1. K- and L-conversion electrons from the 390-kev transition in Tc^{93}.

TABLE I. Relative counting rates for different Tc isotopes produced by proton bombardment of enriched Mo isotopes.

Enriched isotope	Isomer 51.5-min 34.4-kev L-line	Tc^{93} 43.5-min 390-kev K-line	Tc^{94} 52.5-min β^+-spectrum at 835 kev	Tc^{95} 20-hour 762-kev line	Tc^{96} 104-hour 842-kev line	Tc^{97} 90-day 96-kev K-line
Mo^{92}	1000	1080	170	0.32	0.19	0.32
Mo^{94}	1000	3.6	5400	0.69	0.31	
Mo^{95}	1000	58	23	4.4	0.22	0.08
Mo^{96}	1000		0.80	0.050	0.18	0.017
Mo^{97}	1000		67		0.28	20.0
Mo^{98}	1000	6.3	79	0.80	0.28	
Mo^{100}	1000	3.4	43	0.19	0.16	0.30
Natural Mo	1000	9.9	91	0.35	0.22	1.1

By bombarding enriched molybdenum oxides[8] with 9.5-Mev protons, it has been possible to fix the mass number of the isomer. Only activities produced by (p, n) processes are important at this energy. The $F^{18}\beta^+$-activity of 0.64-Mev maximum energy produced by O^{18} did not interfere with the measurements since a helical baffle could be used in the spectrometer to block all positrons. The intensity of the L-line of the isomer was compared in each sample with intensities of known lines of Tc isotopes 93, 95, 96, and 97 and the positron spectrum of Tc^{94} at 835 kev. No comparison of Tc^{98} and Tc^{100} could be made, since the energy and half-life of these activities are not known at present. Table I gives the relative counting rates with that of the isomer normalized to 1000. All values are corrected in time to the end of bombardment (as a rule, $1\frac{1}{4}$ hour in duration). It will be noticed that among the ratios for the various isotopes, only those for Tc^{96} give a reasonably constant value.

Tc^{96} alone was produced by irradiating Nb^{93} foils with α-particles of 13.5 and 15 Mev. These energies were chosen in order to suppress the $(\alpha, 2n)$ reaction which at 17.5 Mev was found to have a small cross section compared to (α, n). In both cases the L-line of the isomer was observed. As a further proof that the activity is not associated with the positron emitter Tc^{94}, the isomer was produced with 3.5–4.0 Mev protons from the Radiation Laboratory electrostatic accelerator on natural molybdenum. According to the decay scheme,[3] the (p, n) threshold energy required to produce the Tc^{94} activity is at least 5.1 Mev.

It appears that the ground state of Tc^{96} and the isomer are formed by bombardment in amounts of comparable magnitude. This results from knowing the number of L-conversion electrons for the isomeric transition along with the number of $K+L$ electrons for the three 0.8-Mev transitions in cascade. By considering the K/L ratio of the isomeric transition, the ab-

[5] L. G. Mann and P. Axel, Phys. Rev. **80**, 759 (1950).
[6] Rose, Goertzel, and Perry, Oak Ridge National Laboratory Report 1023 (unpublished).
[7] M. Goldhaber and A. W. Sunyar, Phys. Rev. **83**, 906 (1951).
[8] The degree of isotopic enrichment estimated by comparing line intensities with those of natural molybdenum varied between 80 percent and 90 percent.

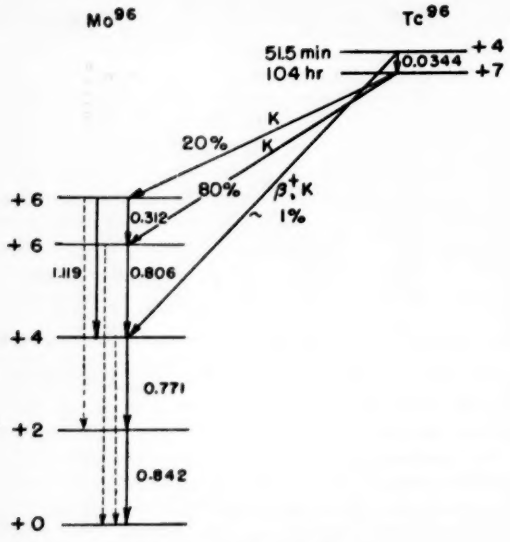

FIG. 2. Decay scheme for Tc^{96}.

sorption in the counter window (0.4-mg/cm² Nylon), and the decay, and by assuming that all three 0.8-Mev γ-rays have conversion coefficients corresponding to $E2$ transitions,[9] one should be able to find the ratio of the number formed in the ground state to the number formed in the isomeric state. However, this result is subject to a large error due to the difficulty in making counter window and backscattering corrections at the low energy of the isomer.

If one assumes that the isomeric state decays exclusively to the ground state of Tc^{96} with no branching in the form of positron emission or K-capture, an increase in the 104-hour activity should be observed immediately after bombardment. Attempts to observe this increase with one-hour bombardments of Nb foils with 18-Mev α-particles were not successful because the intensity of the sources was too small. It is not possible to observe the increase by bombarding enriched Mo^{96} with protons because the 20-hour Tc^{95} produced from Mo^{95} contamination is strong enough to mask any increase in the 104-hour activity. Branching from the isomeric state was found to occur by observing with a trochoidal analyzer a 51.5-minute positron activity in the separated Tc activity produced by 17-Mev α's on Nb. At this energy the $(\alpha, 3n)$ reaction leading to the 52.5-minute positron emitter, Tc^{94}, is excluded. By comparing the intensity of these positrons with the 104-hour activity, it can be concluded that there is roughly one positron for each 10^4 transitions to the ground state. Although it was not possible to measure the maximum energy of the positrons directly, some estimations can be made. The branching ratio of the K-capture from the Tc^{96} ground state to the two upper states of Mo^{96} is known (Fig. 2). If one assumes that the ft values of these two transitions are equal, one can establish the energy difference between the Tc^{96} and Mo^{96} levels and thus determine the maximum positron energy from the isomeric state as being about 400 kev. The only allowed positron transition from the isomeric state is to the second excited state of Mo^{96}. Another estimate can be made by using the (p, n) threshold for Mo^{96} of 3.8±0.3 Mev found by Blaser *et al.*[10] This also leads to a value of 0.4±0.3 Mev for the maximum positron energy. At this energy the K-capture to positron ratio given by Moskowski[11] is 50 to 1, so that the branching ratio for the isomeric transitions to K-capture plus positron emission is in the order of 200 to 1. Since the ratio of half-lives of the ground state to isomeric state is 120 to 1, the expected increase in the 104-hour activity is more or less compensated by direct decay.

The modified decay scheme for Tc^{96} is shown in Fig. 2. The dotted lines indicate weak cross-over transitions of 1.65, 1.89, and 2.39-Mev energy reported by Boyd and Ketelle.[12] A spin of at least 7 must be assigned to the ground state in order to be in agreement with the data for the 104-hour activity (i.e., no strong cross-over transitions in the triple γ-cascade, no positron emission, no direct transitions to the ground state). The half-life of 51.5 min and K/L ratio of 1.2±0.3 allow the assignment of a magnetic 2^3-pole γ-ray to the isomeric transition and a spin of +4 to the excited state. Since Tc^{96} contains an odd number of both neutrons and protons, a high spin value is not unreasonable. A proton in the $g_{9/2}$ state and a neutron in the $g_{7/2}$ state as given by the shell model[13] for the 43rd proton and 53rd neutron might add to a spin of 7. One interpretation of the spin of 4 for the excited state would be that the proton remains in the $g_{9/2}$ state while the neutron goes over into a $s_{1/2}$ state.

We wish to thank Professor A. C. Helmholz for helpful discussions and Professor M. Goldhaber, who suggested the work with the 390-kev line. We wish also to thank G. O'Kelley for his cooperation in the use of the β-spectrometer and Bernd Crasemann for the trochoidal analysis. Thanks are due G. B. Rossi, R. D. Watt, and the crews of the 60-inch cyclotron and proton linear accelerator for the many bombardments.

[9] P. Preiswerk and P. Stähelin, Helv. Phys. Acta **24**, 300 (1951).

[10] Blaser, Boehm, Marmier, and Scherrer, Helv. Phys. Acta **24**, 440 (1951).

[11] S. A. Moskowski, Research Program with the Chicago Cyclotron, Report NP-1493 (unpublished).

[12] G. E. Boyd and B. H. Ketelle, Phys. Rev. **83**, 216 (1951).

[13] M. G. Mayer, Phys. Rev. **78**, 16 (1950).

Certain Explicit Relationships between Phase Shift and Scattering Potential

NORMAN LEVINSON*
Massachusetts Institute of Technology, Cambridge, Massachusetts
(Received October 21, 1952)

An intuitive account is given of recent important results of Gelfand and Levitan for the determination of the potential in the one-dimensional Schrödinger equation from the S-phase shift, the bound states, and certain normalizing parameters.

The method is then used to obtain the first variation in the potential corresponding to a small change in the phase shift, bound states, and normalizing parameters.

I.

THE determination of the potential from a given S-phase shift has been considered in a number of recent papers. For particulars see the introduction and references of Jost and Kohn.[1] The method of Jost and Kohn for constructing a potential from a phase shift has much to commend it. However, as the authors point out, it has a limited range of convergence, and of necessity is ambiguous in case bound states occur.

Here methods developed recently by Gelfand and Levitan[2] for the determination of the potential from the spectral function will be presented in intuitive form. These methods introduce a number of quite new ideas which are of great interest in themselves.

The problem may be described as follows. The Schrödinger equation,

$$\phi''+k^2\phi=V(r)\phi, \tag{1}$$

is considered over the interval $0<r<\infty$. It is assumed that

$$\int_0^\infty r^j|V(r)|dr<\infty, \quad j=1, 2.$$

Let $\phi(k, r)$ be the resolution of (1) satisfying $\phi(k, 0)=0$, $\phi'(k, 0)=1$. It is well known that as $r\to\infty$ and for real $k>0$

$$\phi(k, r)\sim\frac{|f(k)|}{k}\sin[kr+\eta(k)], \tag{2}$$

where $\eta(k)$ is the phase function and $f(k)$ is $f(k, 0)=g(k)$ as given in Jost and Kohn.[1] Let $ik_1, \cdots, ik_m$ denote the values of k for which there are bound states of energy $-k_1^2, \cdots, -k_m^2$. That m is finite has been shown by Levinson.[3] The eigenfunctions associated with the bound states are $\phi(ik_j, r)$, $j=1, \cdots, m$, and will be denoted by $\phi_j(r)$.

The expansion theorem associated with the eigenvalue problem states that, for any suitably restricted function $F(r)$,

$$F(r)=\sum_{j=1}^{n}c_j\phi_j(r)\left[\int_0^\infty F(r)\phi_j(r)dr\right]+\frac{2}{\pi}\int_0^\infty\frac{k^2}{|f(k)|^2}\phi(k, r)\left[\int_0^\infty F(r)\phi(k, r)dr\right]dk, \tag{3}$$

where $f(k)$ is as given in Eq. (2) and the $c_j^{\frac{1}{2}}$ are the normalizing factors for $\phi_j(r)$.

Let $k^2=\lambda$ and let $\phi(k, r)=\phi(\sqrt{\lambda}, r)$ be denoted by $y(\lambda, r)$. Let $\rho(\lambda)$ be a monotone nondecreasing function which for $\lambda<0$ is constant except for jumps at $\lambda=-k_j^2$, the magnitude of each jump being c_j. Let $\rho(0)=0$ and let

$$\rho(\lambda)=\frac{1}{\pi}\int_0^\lambda\frac{\lambda^{\frac{1}{2}}}{|f(\lambda^{\frac{1}{2}})|^2}d\lambda$$

for $\lambda>0$. Then Eq. (3) becomes

$$F(r)=\int_{-\infty}^\infty y(\lambda, r)\left(\int_0^\infty F(r)y(\lambda, r)dr\right)d\rho(\lambda). \tag{4}$$

The problem of determining $V(r)$ when $\eta(k)$ is given has been shown by Bargmann[4] not to have a unique solution. It has been shown by Levinson[3] that if no bound states exist $\eta(k)$ does determine $V(r)$ uniquely. Jost and Kohn[1] showed that this uniqueness proof could be extended to the case where bound states exist, providing the normalizing factors $c_1, \cdots c_m$ are also given.

Suppose now that $\eta(k)$, ik_j, and c_j, $j=1, \cdots, m$ are given. Then proceeding as in Jost and Kohn,[1] §2, $f(k)$ may be found. Once $f(k)$ is known, $\rho(\lambda)$ as defined below Eq. (3) is completely determined. The function $\rho(\lambda)$ is known as the spectral function. It will be shown how $\rho(\lambda)$ determines $V(r)$ explicitly and uniquely.

II.

This section will develop the motivation for the method of Gelfand and Levitan.[2]

* The preparation of this paper is sponsored in part by the U. S. Office of Naval Research.

[1] Res Jost and Walter Kohn, Phys. Rev. **87**, 977 (1952).

[2] I. M. Gelfand and B. M. Levitan, Izvest. Akad. Nauk S.S.S.R., Math. Series **15**, 309 (1951).

[3] N. Levinson, Kgl. Danske Videnskab Selskab, Mat.-fys. Medd. **25**, No. 9 (1949).

[4] V. Bargmann, Phys. Rev. **75**, 301 (1949); Revs. Modern Phys. **21**, 488 (1949).

The function $\phi(k, r)=y(\lambda, r)$ is written in the form

$$\phi(k, r)=\frac{\sin kr}{k}+\int_0^r K(r, \xi)\frac{\sin k\xi}{k}d\xi. \tag{5}$$

It must now be shown that $K(r, \xi)$ exists. Integrating Eq. (5) by parts twice yields

$$k^2\phi=k\sin kr-K(r, r)\cos kr+K(r, 0)+\frac{\partial K(r, r)}{\partial \xi}\frac{\sin kr}{r}-\int_0^r \frac{\partial^2 K}{\partial \xi^2}\frac{\sin k\xi}{k}d\xi.$$

Computing ϕ'' directly from Eq. (5) and using the above result, it is found that

$$\phi''+k^2\phi=2\frac{\sin kr}{k}\frac{dK(r, r)}{dr}+K(r, 0)+\int_0^r\left(\frac{\partial^2 K(r, \xi)}{\partial r^2}-\frac{\partial^2 K(r, \xi)}{\partial \xi^2}\right)\frac{\sin k\xi}{k}d\xi.$$

By Eqs. (1) and (5) the right side above must be equal to

$$V(r)\frac{\sin kr}{r}+V(r)\int_0^r K(r, \xi)\frac{\sin k\xi}{k}d\xi.$$

This will be true if, for $0\leq\xi\leq r$,

$$\partial^2 K/\partial r^2-\partial^2 K/\partial \xi^2=V(r)K(r, \xi), \tag{6}$$

and the boundary conditions

$$K(r, 0)=0, \quad K(r, r)=\tfrac{1}{2}\int_0^r V(r)dr, \tag{7}$$

hold. If the range $0\leq\xi\leq r$ is replaced by $-r\leq\xi\leq r$, $r\geq 0$ and the boundary conditions by

$$K(r, r)=-K(r, -r)=\tfrac{1}{2}\int_0^r V(r)dr,$$

then the problem is the standard one of solving a linear hyperbolic partial differential equation with boundary conditions prescribed on two intersecting characteristic curves. Thus $K(r, \xi)$ is determined.

In case $V(r)\equiv 0$ then it is readily seen that the $\rho(\lambda)$ in (4) becomes $2\lambda^{\frac{1}{2}}/(3\pi)$ for $\lambda\geq 0$ and zero for $\lambda<0$. The $\rho(\lambda)$ for (1) is written as

$$\begin{aligned}&\rho(\lambda)=2\lambda^{\frac{1}{2}}/3\pi+\sigma(\lambda), \quad \lambda\geq 0\\ &\rho(\lambda)=\sigma(\lambda), \quad \lambda<0.\end{aligned} \tag{8}$$

In much the same way as Eq. (5) is justified it can be shown that there exists a $K_0(r_1, \xi)$ such that

$$\frac{\sin kr_1}{k}=\phi(k, r_1)+\int_0^{r_1} K_0(r_1, \xi)\phi(k, \xi)d\xi. \tag{9}$$

Recalling that $k^2=\lambda$, and that

$$\int_{-\infty}^{\infty}\phi(k, r_1)\phi(k, r)d\rho(\lambda)=\delta(r-r_1),$$

where δ is the Dirac function, it is seen that

$$\int_{-\infty}^{\infty}\phi(k, r)\phi(k, r_1)d\rho(\lambda)=0, \quad r\neq r_1.$$

If this is used in Eq. (9) there results for $r>r_1\geq 0$

$$\int_{-\infty}^{\infty}\frac{\sin kr_1}{k}\phi(k, r)d\rho(\lambda)=0.$$

Then if one refers to Eq. (5), this implies that for $r>r_1\geq 0$

$$\int_{-\infty}^{\infty}\frac{\sin kr\sin kr_1}{k^2}d\rho(\lambda)+\int_0^r K(r, \xi)d\xi\int_{-\infty}^{\infty}\frac{\sin k\xi\sin kr_1}{k^2}d\rho(\lambda)=0.$$

If Eq. (8) is used in the above equation in conjunction with the fact that

$$\int_0^{\infty}\frac{\sin kr\sin kr_1}{k^2}d\left(\frac{2\lambda^{\frac{1}{2}}}{3\pi}\right)=\delta(r-r_1),$$

there results for $r>r_1\geq 0$,

$$\int_{-\infty}^{\infty}\frac{\sin kr\sin kr_1}{k^2}d\sigma(\lambda)+\int_0^r K(r, \xi)d\xi\int_{-\infty}^{\infty}\frac{\sin k\xi\sin kr_1}{k^2}d\sigma(\lambda)+K(r, r_1)=0. \tag{10}$$

Let

$$\frac{1}{2}\int_{-\infty}^{\infty}\frac{1-\cos ku}{k^2}d\sigma(\lambda)=\Phi(u). \tag{11}$$

Then

$$\Phi(r+r_1)-\Phi(r-r_1)=P(r, r_1)=\int_{-\infty}^{\infty}\frac{\sin kr\sin kr_1}{k^2}d\sigma(\lambda). \tag{12}$$

Thus (10) becomes

$$P(r, r_1)+\int_0^r K(r, \xi)P(\xi, r_1)d\xi+K(r, r_1)=0. \tag{13}$$

From continuity considerations this holds for $0\leq r_1\leq r$. It is (13) which forms the point of departure for the determination of $V(r)$ from $\rho(\lambda)$. It is clear from (12) that $P(r, r_1)=P(r_1, r)$.

III.

Suppose now that $\rho(\lambda)$ is given. Then $\sigma(\lambda)$ is determined by (8), and thus $P(r, r_1)$ from (11) and (12). It is clearly the case that for each fixed $r>0$, Eq. (13) is a Fredholm equation with $K(r, r_1)$ as an unknown function of r_1.

It will now be shown that the homogeneous equation,

$$\int_0^r P(r_1, \xi)h(\xi)d\xi+h(r_1)=0,$$

has only the null solution, $h\equiv 0$.

Let

$$I=\int_0^r\int_0^r P(r_1, \xi)h(\xi)h(r_1)d\xi dr_1+\int_0^r h^2(r_1)dr_1.$$

Clearly $I=0$. By using (12), it is found that

$$P(r_1, \xi)=\int_{-\infty}^{\infty}\frac{\sin kr_1 \sin k\xi}{k^2}d\sigma(\lambda)$$

$$=\int_{-\infty}^{\infty}\frac{\sin kr_1 \sin k\xi}{k^2}d\rho(\lambda)-\delta(r_1-\xi).$$

Thus

$$I=\int_0^r\int_0^r h(\xi)h(r_1)d\xi dr_1\int_{-\infty}^{\infty}\frac{\sin kr_1 \sin k\xi}{k^2}d\rho(\lambda)$$

$$-\int_0^r\int_0^r h(\xi)h(r_1)\delta(r_1-\xi)d\xi dr_1+\int_0^r h^2(r_1)dr_1.$$

Or, since the last two integrals are equal,

$$I=\int_{-\infty}^{\infty}\left(\int_0^r\frac{h(\xi)\sin k\xi}{k}d\xi\right)^2 d\rho(\lambda).$$

Since

$$\frac{1}{k}\int_0^r h(\xi)\sin k\xi d\xi \qquad (14)$$

is an entire function of λ and since $\rho(\lambda)$ has a continuous spectrum for $\lambda>0$, it follows that $I>0$ unless (14) is identically zero. This last implies $h(\xi)\equiv 0$ so that indeed the homogeneous equation has only the null solution, and thus by the Fredholm theorem the nonhomogeneous integral equation (13) has a unique solution, $K(r, r_1)$. If it is assumed that $\Phi''(u)$ exists, then it can be shown that the first and second partial derivatives of $K(r, r_1)$ exist. As suggested by (7) let $V(r)=2dK(r, r)/dr$. Then $\phi(k, r)$ given by (5) satisfies (1), and $\rho(\lambda)$ is the spectral function of (1) with boundary condition $\phi(k, 0)=0$.

In summarizing, it is found that a knowledge of the phase function $\eta(k)$, the bound states $k_1, \cdots k_m$, and the normalizing factors $c_1, \cdots c_m$ determines the spectral function $\rho(\lambda)$. By Eq. (8) this determines $\sigma(\lambda)$. From $\sigma(\lambda)$, $\Phi(u)$ is determined in Eq. (11), and $P(r, r_1)$ by Eq. (12). The function $K(r, r_1)$ is then determined from the Fredholm equation (13) for $0\leq r_1\leq r$. The variable r appears in the Fredholm equation as a parameter, and thus the determination of $K(r, r_1)$ computationally may be a long process. Once $K(r, r_1)$ is found, $V(r)$ is given by $2dK(r, r)/dr$.

IV.

Suppose the potential $V(r)$ corresponding to a given spectral function $\rho(\lambda)$ is sought. Let $\rho_0(\lambda)$ be another spectral function, and suppose its potential function $V_0(r)$ is known or has been determined. Then what is the relationship between $V(r)-V_0(r)$ and $\rho(\lambda)-\rho_0(\lambda)$? The case treated above corresponds to $V_0(r)\equiv 0$.

Let $\phi_0(k, r)$ denote the solutions of Eq. (1) where V is replaced by V_0. Let $\rho(\lambda)-\rho_0(\lambda)=\sigma(\lambda)$. Then the same argument as used above, for the case $V_0(r)\equiv 0$, shows that

$$V(r)-V_0(r)=2dK(r, r)/dr, \qquad (15)$$

where K is the solution of

$$K(r, r_1)+P_0(r, r_1)+\int_0^r K(r, \xi)P_0(\xi, r_1)d\xi=0, \qquad (16)$$

and

$$P_0(r, r_1)=\int_{-\infty}^{\infty}\phi_0(k, r)\phi_0(k, r_1)d\sigma(\lambda).$$

If $\rho(\lambda)-\rho_0(\lambda)$ is small, then P_0 is small and as a *first approximation*, Eq. (16) yields

$$K(r, r_1)\sim -P_0(r, r_1).$$

In Eq. (15) this gives

$$V(r)-V_0(r)\sim -4\int_{-\infty}^{\infty}\phi_0(k, r)\phi_0'(k, r)d\sigma(\lambda),$$

or, if $V-V_0=\delta V$ and $\rho-\rho_0=\delta\rho$, then

$$\delta V(r)\sim -4\int_{-\infty}^{\infty}\phi(k, r)\phi'(k, r)d(\delta\rho(\lambda)).$$

These formulas are, of course, only approximations which neglect terms of higher order than the first in $\delta\rho(\lambda)$.

A Test of the Charge Symmetry Hypothesis: Positive to Negative Pion Production Ratio Obtained in Bombarding Carbon with Alpha-Particles and Protons

H. W. WILSON* AND WALTER H. BARKAS
Radiation Laboratory, Department of Physics, University of California, Berkeley, California
(Received October 24, 1952)

A measurement of the plus/minus ratio for the production of pions by alpha-particles incident on carbon nuclei has been carried out to test the charge symmetry hypothesis. Employing an experimental procedure which eliminates residual errors in geometry, etc., the ratio was found to be 0.72 ± 0.17. The alpha-particle energy was 375 Mev and the meson energy was 15 Mev observed at 90° to the beam. Coulomb effects are expected to bring about a depression of the production ratio from unity of about this magnitude. The experimental result, therefore, provides support for the charge symmetry hypothesis.

As supplementary information the same apparatus was used to measure the pion plus/minus ratio for 330-Mev protons incident on carbon. The ratio found was 5.4 ± 0.8.

INTRODUCTION

IN nuclei neutrons and protons seem to play symmetrical roles, but it has not been established nearly so well in meson production that the charge symmetry hypothesis is valid. Some measurements have been made of pion production ratios when neutrons and protons separately bombard carbon. Bradner, O'Connell, and Rankin[1] observed a positive to negative ratio of $1/12.6\pm12$ percent for mesons of 50–65 Mev emerging from a carbon target at $\approx90°$ to a neutron beam. The neutrons had an energy spectrum peaked near 270 Mev. Richman, Weissbluth, and Wilcox[2] measured the ratio for 340-Mev protons bombarding carbon. For mesons of 12–20 Mev emerging at $90°\pm12°$, they found a ratio of 3.4 ± 0.8, and for the integral ratio, 5.1 ± 1. Block, Passman, and Havens[3] also reported measurements for carbon bombarded by protons of 381 Mev. For 18-Mev mesons observed at 90° to the beam, their experimental points imply a ratio of 17 ± 8, and for the integral ratio they give 11 ± 3. These results indicate that protons yield a large excess of positive mesons, and neutrons a large excess of negative mesons, but only weak evidence is offered of an actual symmetry in production, particularly because no absolute production cross sections have been measured for neutrons.

EXPERIMENTAL METHOD

In order to obtain identical conditions for neutron and proton bombardment, we have carried out an experiment in which carbon was bombarded by the internal 375-Mev alpha-particle beam of the 184-inch cyclotron. Pions emerging from a target at 90° to the beam were observed using nuclear track plates as detectors.

Various experimental arrangements were tried, and the one finally adopted is shown in Fig. 1. The apparatus was placed in the magnetic field of the cyclotron and mesons of opposite signs passed into stacks of plates A and B. To eliminate any lack of perfect symmetry for detection of positive and negative mesons, two bombardments were made. Without altering the positions of the plates between bombardments, the beam was reversed (by reversing the cyclotron magnetic field) so that the signs of mesons entering plates A and B were reversed. It is easy to show that one can thus eliminate the effects of unsymmetrical geometry and other experimental inequalities. The true plus/minus ratio, R, is given by

$$R=\left[\left(\frac{N_+}{N_-}\right)_A\left(\frac{N_+}{N_-}\right)_B\right]^{\frac{1}{2}},$$

where $(N_+/N_-)_A$ and $(N_+/N_-)_B$ are the plus/minus ratios found in plates A and B, respectively. Pions in the range 11–21 Mev were detected so that the ratio obtained is for this range of energies. The yield of mesons compared to background was very low and examination of 12 plates all exposed at the same time, six in position A and six in position B, yielded only 82 mesons, excluding ρ mesons. The ratio of positive to negative mesons obtained was 0.72, with a standard deviation of 0.17. To determine the ratio, $\pi-\mu$ decays and star forming mesons were counted, and it was assumed that 73 percent of the π^- mesons produced stars in the Ilford $C2$ emulsion employed. Practically complete discrimination was obtained between one-prong stars and $\pi-\mu$ decays, in the few cases where ambiguity existed, by grain counting. All doubtful events were studied by two or more observers. To reduce the Coulomb barrier effect, another experiment at higher meson energy (≈30 Mev) was carried out. The meson yield was so low in this case, however, that the experiment was impractical.

DISCUSSION

The experimental ratio is significantly near unity, but at the same time the probability is low that true value may actually be as high as unity.

For every process leading to the production of a

* Present address: Department of Natural Philosophy, The University, Glasgow, Scotland.
[1] Bradner, O'Connell, and Rankin, Phys. Rev. **79**, 720 (1950).
[2] Richman, Weissbluth, and Wilcox, Phys. Rev. **85**, 161 (1952).
[3] Block, Passman, and Havens, Phys. Rev. **83**, 167 (1951).

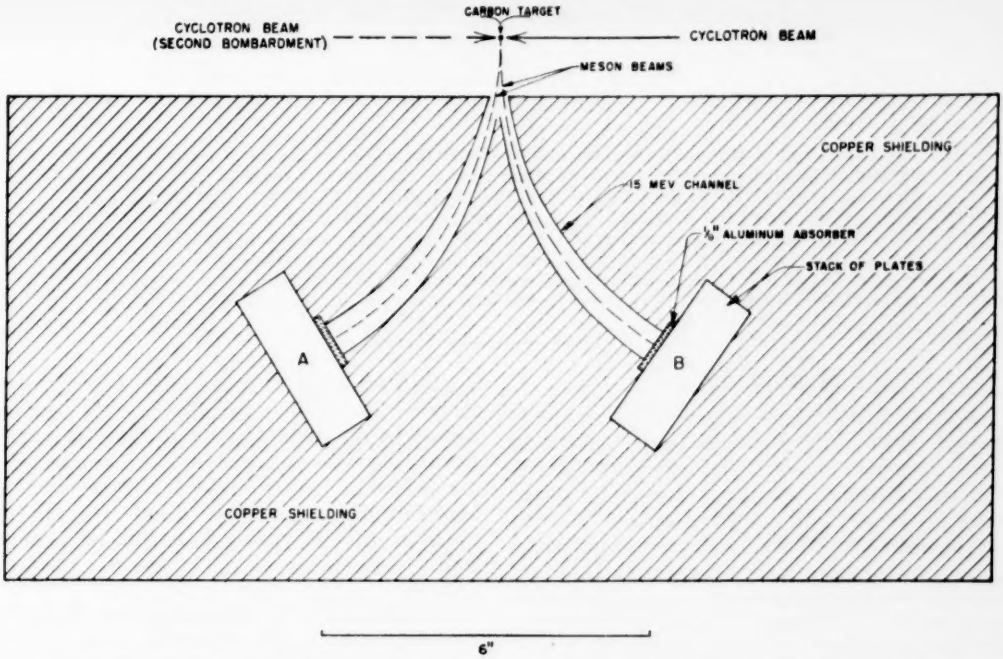

FIG. 1. Median plane section of plus/minus apparatus. The magnetic field, which is nearly constant along the meson paths, is perpendicular to the paper. The apparatus was made as symmetrical as possible. The target was in the form of a carbon rod $\frac{1}{16}$ in.$\times\frac{1}{4}$ in. in cross section. The beam traversed the $\frac{1}{4}$-inch dimension. The channels were 1 inch deep.

positive meson, this experimental arrangement provides a mirror process leading to the production of a negative meson. Aside from slight mass differences of the mirror disintegration products, Coulomb effects are the only ones which would cause the experimental ratio to deviate from unity if the hypothesis is valid. In this case they tend to depress the ratio. The effect of the barrier was first observed by one of the writers[4] who investigated the alpha-particle plus/minus ratio at 0° as a function of target atomic number for mesons having very low kinetic energies in the effective center-of-mass system. For targets of high atomic number the Coulomb effect was shown to be profound. In the present experiment, however, the meson energy is several times greater than the barrier height. In addition the effective barrier height must be somewhat reduced by the fact that the system of nucleons, while the meson is escaping, is rapidly disintegrating. To estimate correctly the effect of the barrier on the ratio under these conditions offers difficulties. Fried and Gasiorowicz[5] have calculated the expected ratio for a point nucleus and obtained a value of about 0.5. This calculation certainly overestimates the Coulomb effect on the ratio. A calculation is being carried out on the assumption that mesons are created in the Coulomb field of the residual finite size nucleus before the latter disintegrates. It is reasonably certain that the experimental ratio agrees within its standard deviation with the value anticipated on the basis of the charge symmetry hypothesis.

[4] Walter H. Barkas, Phys. Rev. **75**, 1467 (1949) and University of California Radiation Laboratory Report UCRL 486.
[5] B. Fried and S. Gasiorowicz (private communication).

PROTON PLUS/MINUS RATIO

The ratio of positive to negative mesons obtained in bombarding carbon by 330-Mev protons was also found using the apparatus of Fig. 1. It was thought worth while to carry out such a separate experiment to determine this ratio afresh in view of the divergence of the published ratios. The higher yield of mesons relative to background under proton bombardment made the accumulation of data less tedious in this case. There were 449 mesons, excluding ρ-mesons, counted, and the plus/minus ratio obtained was 5.4 ± 0.8.

In conclusion, one of us (H.W.W.) wishes to thank Professor E. O. Lawrence for his kindness in permitting him to work in the Radiation Laboratory and for his encouragement in the work carried out therein.

Levels of Al^{25} from the $Mg^{24}(d,n)Al^{25}$ Reaction*

E. GOLDBERG†
University of Wisconsin, Madison, Wisconsin
(Received October 27, 1952)

A 67-kev target of Mg^{24} was bombarded with 4.007-Mev deuterons, and the neutron groups from the $Mg^{24}(d,n)Al^{25}$ reaction were studied at seven different angles with Ilford C2 emulsions. The observed Q values are $+0.07\pm0.06$, -0.38 ± 0.06, -0.88 ± 0.05, -1.74 ± 0.04, (-1.87 ± 0.04), -2.44 ± 0.04, -2.67 ± 0.04, (-2.85 ± 0.04), and -3.04 ± 0.03 Mev. The neutron groups with the Q values -2.44, -2.67, and -3.04 Mev correspond to virtual states of Al^{25} which have previously been seen as $Mg^{24}+p$ resonances. From the Butler theory for the angular distribution of the stripped neutrons, the ground state of Al^{25} is described by $J=3/2$ or $5/2$, even parity; the first excited state is $J=1/2$, even parity, and the second excited state is likely to be $J=3/2$ or $5/2$, even parity. The level structure of Al^{25} is compared to that of Mg^{25}.

I. INTRODUCTION

A KNOWLEDGE of the energy level structure of light nuclei which includes parity and total angular momentum values of the individual levels as well as their excitation energies is valuable for testing theories concerned with nuclear structure and the nature of nuclear forces. The low-lying levels of mirror nuclei, for example, may be compared to judge the validity of the charge symmetry hypothesis. Theories which predict the quantum numbers of the levels may be tested directly.

The recent work of Butler[1] which has stimulated experimental and theoretical interest in (d,p) and (d,n) reactions provides a method for determining the parity and, to a degree, the angular momentum of the levels of the residual nuclei from these reactions. A reduction of ambiguity in level assignments may be achieved in the study of these reactions by choosing a target nucleus of zero spin.

The study of Al^{25} by way of the $Mg^{24}(d,n)Al^{25}$ reaction is of particular interest, since the mirror nucleus Mg^{25} has been subjected to some rather thorough spectral analyses. The nucleus Al^{25} has recently been investigated[2] by the elastic scattering of protons from Mg^{24}, and a phase shift analysis of the data has made possible the assignments of several of the higher levels.[3] The $Mg^{24}(d,n)Al^{25}$ reaction would yield information on the bound levels of Al^{25}, and any levels in the overlapping region could serve as checks on the classification arguments.

An incidental bit of information from the $Mg^{24}(d,n)$-Al^{25} reaction is the ground-state Q value which would provide an independent value for the mass of Al^{25}. This value of 24.998306 ± 0.000099 amu may be compared to the value of 24.99817 amu derived from the $Al^{25}(\beta^+)Mg^{25}$ end-point energy of 3.1 Mev.[4,5]

II. EXPERIMENTAL PROCEDURE

Deuterons having an energy of 4.007 Mev were allowed to fall on a thin Mg^{24} target. The outgoing neutrons were detected at various angles with 200-micron Ilford C2 emulsions positioned in air 10 cm from

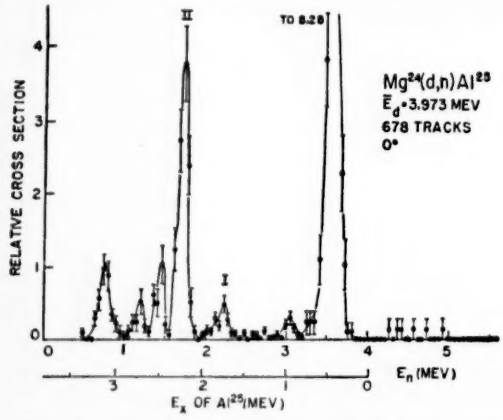

FIG. 1. Neutron energy spectrum at 0° to the incident deuteron beam. The $O^{16}(d,n)F^{17}$ groups are identified by I and II.

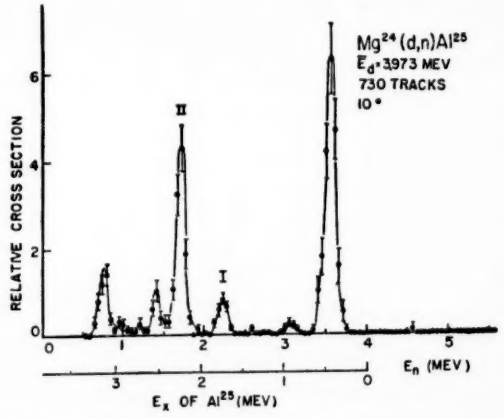

FIG. 2. Neutron energy spectrum at 10° to the incident beam.

* Work supported by the Wisconsin Alumni Research Foundation and the U. S. Atomic Energy Commission.
† Atomic Energy Commission Predoctoral Fellow.
[1] S. T. Butler, Proc. Roy. Soc. (London) **208**, 559 (1951).
[2] Mooring, Koester, Goldberg, Saxon, and Kaufmann, Phys. Rev. **84**, 703 (1951).
[3] L. J. Koester, Jr., Phys. Rev. **85**, 643 (1952).
[4] Atomic masses of Mg^{24} and Mg^{25} taken from the table of C. W. Li, Phys. Rev. **88**, 1038 (1952).
[5] D. Van Patter (private communication).

the target. The plates were exposed for 1.28 microampere-hours. The laboratory angles of observation were 0°, 10°, 30°, 40°, 60°, and 150°. A total of 5736 acceptable tracks were measured according to standards adopted earlier.[6]

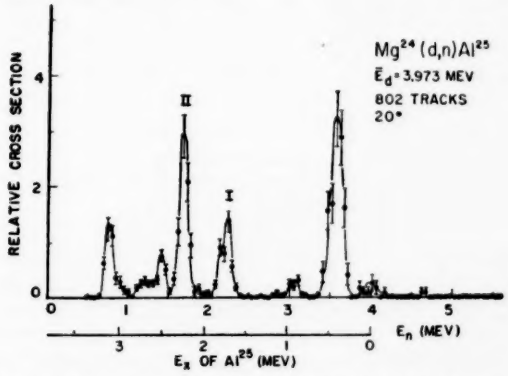

FIG. 3. Neutron energy spectrum at 20° to the incident beam.

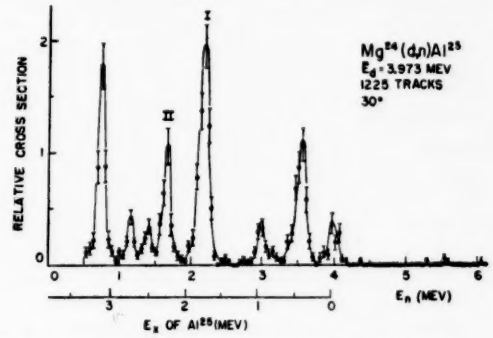

FIG. 4. Neutron energy spectrum at 30° to the incident beam.

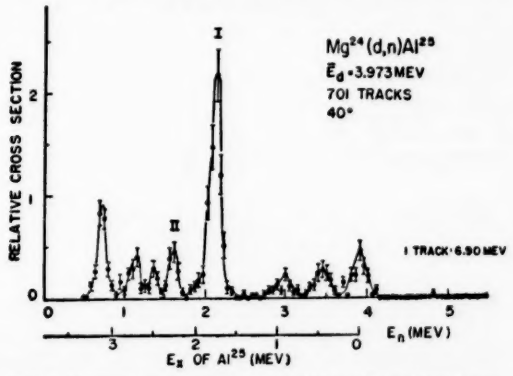

FIG. 5. Neutron energy spectrum at 40° to the incident beam.

The target was prepared by heating $Mg^{24}O$ on a tantalum strip in vacuum, slowly raising the temperature of the strip until a metallic deposit was seen

[6] Johnson, Laubenstein, and Richards, Phys. Rev. **77**, 413 (1950).

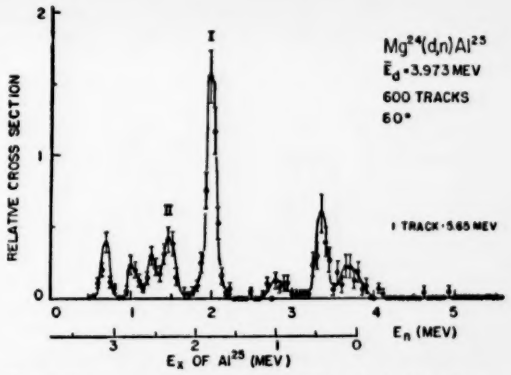

FIG. 6. Neutron energy spectrum at 60° to the incident beam.

on a glass plate placed beyond the target backing.[7,8] Ten successive evaporations were necessary to deposit a satisfactory layer (i.e., 45 kev for 4.0-Mev deuterons) on a ten mil tantalum backing positioned two inches from the oxide. The thickness was determined by measuring the increase in mass of the target backing. The target was set at an angle to increase its thickness to 67 kev. Oxygen in the target, identified by neutrons from the $O^{16}(d,n)F^{17}$ reaction, may have arisen from the brief exposures to air when the target was being prepared, or may indicate some direct evaporation of the MgO. The oxygen content was, however, less than one-third that of MgO, indicating that the tantalum does partially reduce the oxide.[9]

III. EXPERIMENTAL RESULTS

A. Neutron Spectra

The neutron spectra from the $Mg^{24}(d,n)Al^{25}$ reaction are shown in Figs. 1 to 7. The two neutron groups

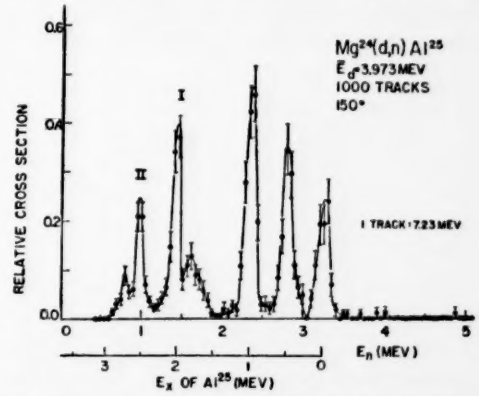

FIG. 7. Neutron energy spectrum at 150° to the incident beam.

[7] Mg^{24} isotope supplied by the Y-12 Plant, Carbide and Carbon Chemicals Division, Union Carbide and Carbon Corporation, Oak Ridge, Tennessee.

[8] The author would like to thank Dr. J. N. Cooper for informing him of this technique. Revs. Sci. Instr. **23**, 764 (1952).

[9] The comparison with MgO targets is based on some unpublished neutron spectra measurements made by the author.

TABLE I. Q values from the $Mg^{24}(d,n)Al^{25}$ reaction and excitation energies of Al^{25} (Mev.)

Laboratory angle of observation							Weighted average Q value	Other Q values	Best excitation energy	Total No. of tracks
0°	10°	20°	30°	40°	60°	150°				
...	...	+0.09	+0.10	+0.07	+0.02	+0.08	+0.07±0.06		0	267
−0.38	−0.37	−0.34	−0.34	−0.38	−0.38	−0.40	−0.38±0.06		0.45±0.03	1100
−0.88	−0.86	−0.85	−0.86	−0.88	−0.82	−0.89	−0.88±0.05		0.95±0.03	430
−1.78	...	−1.76	...	...	...	−1.73	−1.74±0.04		1.81±0.04	103
(−1.87)	(−1.86)	(−1.90)	...	...	...	...	−1.87±0.04		1.94(?)	14
−2.43	−2.46	−2.44	−2.43	−2.45	−2.48	−2.43	−2.44±0.04	−2.439[a]	2.51±0.05	372
−2.66	−2.65	−2.64	−2.67	−2.67	−2.71	...	−2.67±0.04	−2.626[a]	2.70±0.05	302
...	(−2.87)	...	(−2.82)	(−2.84)	...	...	−2.85±0.04		2.92(?)	35
−3.06	−3.05	−3.05	−3.05	−3.03	−3.03	...	−3.04±0.03	−3.018[b]	3.09±0.06	750

[a] This value was computed from values of capture gamma-ray resonance energies (see reference 16) and the binding energy of the deuteron [R. Mobley and R. Laubenstein, Phys. Rev. **80**, 309 (1950)].
[b] See reference 2 and Mobley and Laubenstein, reference a.

labeled I and II occur at the correct energies and with the correct angular distributions[10] to be attributed to $O^{16}(d,n)F^{17}$ reaction. Group I corresponds to the formation of F^{17} in the ground state, and group II corresponds to the first excited state. The observed ranges of group I were paired with the computed energies of this group[11] to check the calibration of these plates. The points were seen to agree with Rotblat's table for Ilford C2 emulsions,[12] although the latter was meant to apply to emulsions exposed in vacuum. The table was used with no correction made for exposure in air. The correction was expected to be of the order of two percent.[13]

The data have been corrected for variation of the n-p cross section with energy[14] and for variation of the probability that the tracks leave the emulsion.[15] To improve the statistics of weak groups, additional plate area was scanned and measurements made for certain energy intervals. It was necessary to normalize according to the area of the particular plate scanned. This normalization was also applied to all the plates to facilitate comparison of the group intensities at different angles.

Figure 1 illustrates the data at 0°. All groups other

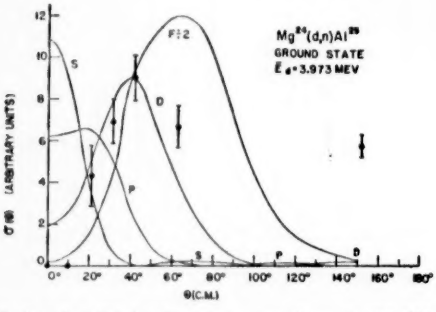

FIG. 8. Angular distribution of neutrons from the $Mg^{24}(d,n)Al^{25}$ reaction, with the Al^{25} in the ground state.

than those arising from the $O^{16}(d,n)F^{17}$ reaction are attributed to the $Mg^{24}(d,n)Al^{25}$ reaction by noting the energy variation of the groups with angle of observation. There was no evidence of carbon contamination of the target at this angle or at the other angles. The group of lowest neutron energy corresponds to a level of Al^{25} seen[2] through the elastic scattering of protons from Mg^{24}. This level will be discussed later when the interpretation of the angular distributions is considered. The groups at 1.2 and 1.4-Mev neutron energies are identified as those corresponding to levels of Al^{25} which were inferred from the study of the $Mg^{24}(p,\gamma)Al^{24}$ reaction.[16]

Background plates exposed at this angle do not account for the six tracks which have neutron energies in excess of 4.2 Mev. The data at other angles give no evidence for a level of Al^{25} which would account for all of these tracks. A few near 4.0 Mev might be associated with the ground-state group that begins to appear at 20°, while the tracks of higher energies might possibly be attributed to the $Mg^{25}(d,n)Al^{26}$ or $Mg^{26}(d,n)Al^{27}$ reactions which are highly exoergic. The Mg^{25} impurity is assayed to be 0.301 percent, Mg^{26} is 0.114 percent, and Mg^{24} is 99.59 percent.[7]

Figures 2 to 7 illustrate the remaining data. At 150° (Fig. 7), the first three levels of Al^{25} are clearly defined, and one neutron group which was not resolved at the other angles is now visible at the right of group I. This

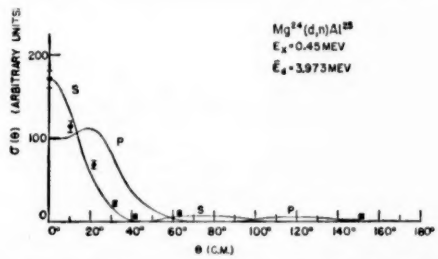

FIG. 9. Angular distribution of neutrons from the $Mg^{24}(d,n)Al^{25}$ reaction, with the excitation energy of 0.45 Mev for Al^{25}.

[10] F. Ajzenberg, Phys. Rev. **83**, 693 (1951).
[11] T. W. Bonner and J. W. Butler, Phys. Rev. **83**, 1091 (1951).
[12] J. Rotblat, Nature **167**, 550 (1951); **165**, 387 (1950).
[13] A. J. Dyer, Australian J. Sci. Research **A5**, 104 (1952).
[14] R. K. Adair, Revs. Modern Phys. **22**, 249 (1950).
[15] H. T. Richards, Phys. Rev. **59**, 796 (1941).
[16] Grotdal, Lönsjö, Tangen, and Bergström, Phys. Rev. **77**, 296 (1950).

group is associated with the marked asymmetry of group I at 0° and 20°. The more rapid variation of the neutron energy with angle for the $O^{16}(d,n)F^{17}$ neutrons permits resolution of these two groups at large angles. A level of Al^{25} at an excitation energy of 1.81 Mev may be inferred from this group. At a few angles, there is a suggestion of neutron groups which would be associated with levels at 1.94 and 2.92 Mev (see Table I). The intensities of these groups are such that it is possible, but unlikely, that they arise from the Mg^{25} or Mg^{26} impurities.

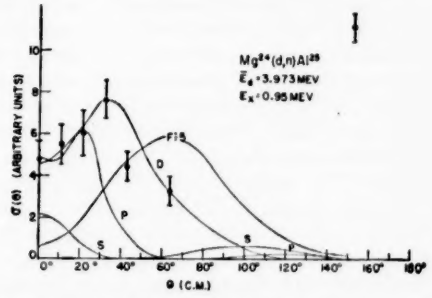

FIG. 10. Angular distribution of neutrons which correspond to the 0.95-Mev level of Al^{25}.

Table I lists the Q values of the $Mg^{24}(d,n)Al^{25}$ reaction for the various neutron groups. The average Q value for each group is computed after weighting each value according to the number of tracks in the group at that angle. The cited uncertainties of the Q values represent not only the variation of the calculated Q values among the plates which is ± 20 kev in most cases but also the

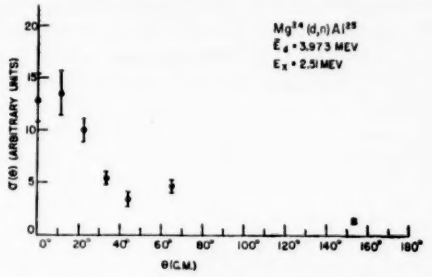

FIG. 11. Angular distribution of neutrons which correspond to the 2.51-Mev level of Al^{25}.

uncertainty in the range energy relation and geometric uncertainties. The latter includes orientation of the target, finite target size, and width of region of emulsion scanned; these should contribute not more than ± 10 kev. The beam energy uncertainty is less than ± 5 kev. For 4.0-Mev neutrons, the range-energy relation contributes ± 40 kev, this being reduced for lower energy neutrons. However, the excitation energies of Al^{25} close to the ground state are known with greater certainty because the uncertainty of the range-energy relation tends to cancel out.

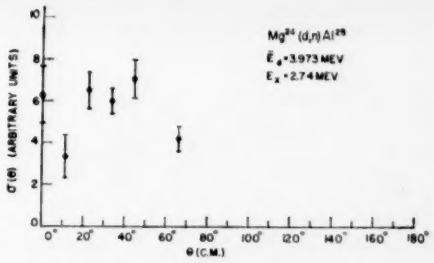

FIG. 12. Angular distributions of neutrons which correspond to the 2.74-Mev level of Al^{25}.

It is possible to calculate the absolute differential cross sections if the density of hydrogen atoms in the emulsion and the number of target nuclei per square centimeter are known along with the total charge collected by the target. The cross section for the neutron group at 10° corresponding to the first excited state of Al^{25} (i.e., $E_x = 0.45$ Mev) was computed to be $(4\pm 2)\times 10^{-26}$ cm² per steradian. This yields a factor of 0.7×10^{-26} cm² per steradian per ordinate unit on the first seven figures.

B. Angular Distributions

The availability of the data at the seven angles permits an examination of the angular distributions of several neutron groups. They are given in Figs. 8 to 13, and are identified by the corresponding excitation energies of Al^{25} as derived from this experiment. The points were computed on the basis of the number of tracks in the particular group, rather than the height of that group as it appeared in foregoing figures. The angles of observation and intensities have been converted to the center-of-mass system.[17]

IV. INTERPRETATION OF THE ANGULAR DISTRIBUTIONS

According to Butler's theory,[1] the angular distribution of the neutrons from a particular reaction will depend very markedly on the orbital angular momentum l_p attributed to the proton before capture. If zero spin and even parity are assumed for the ground

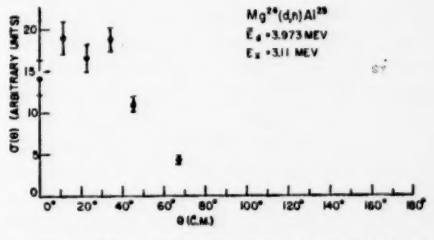

FIG. 13. Angular distribution of the neutrons from the $Mg^{24}(d,n)Al^{25}$ reaction with Al^{25} excitation energy of 3.11 Mev.

[17] M. Moskow, Master's Essay, The Johns Hopkins University (1948) (unpublished).

TABLE II. Behavior of the nuclear factor N.

E_x(Mev)	l_p	$C_1\sigma(\theta)_{calc}$ / N	$C_2\sigma(\theta)_{exp}$	$NC_2\sigma(\theta)_{exp}$ / $C_1\sigma(\theta)_{calc}$
0.00	2	1.00	1.00	1.00
0.45	0	0.68	19.1±0.4	28.1
0.95	2	1.86	0.86±0.21	0.46

state of Mg^{24}, the total angular momentum of the residual nucleus Al^{25} will be $J=l_p\pm\frac{1}{2}$. The parity of this state will be even if l_p is even and odd if l_p is odd. The ambiguity for J is removed in the case $l_p=0$, where $J=\frac{1}{2}$. Butler's expression [i.e., Eq. (34)][1] when applied to this reaction is explicit in so far as the angular distribution is concerned except for the choice of the nuclear radius. The equation $r_0=1.49\ (A^{\frac{1}{3}}+1)\times10^{-13}$ cm yields a value 5.80×10^{-13} cm. The solid lines which appear in Figs. 8 to 10 have been computed from Butler's expression employing this nuclear radius. No correction was made for the Coulomb effect.

The comparison of experimental points to the theoretical curves in Fig. 8 would prompt an assignment of $J=3/2$ or $5/2$, even parity, to the ground state of Al^{25}. As in Figs. 9 and 10, the curve which best fits the data has been drawn to the appropriate scale while the companion curves have magnitudes in relation to the chosen curve designated according to the Butler expression, neglecting the nuclear factor N and the statistical factor $(2J+1)$. This assignment is consistent with the known spin assignment[18] of $J=5/2$ for the ground state of Mg^{25}, the mirror nucleus of Al^{25}. It is also in agreement with the prediction of the Mayer spin-orbit model[19] which requires $J=5/2$, even parity. Deviations of the points from the curves at larger angles may be attributed to compound nucleus formation which is expected to be noticeable because of the small differential cross sections for this state. The angular distribution associated with the first excited state of Al^{25} is shown in Fig. 9. The data clearly show the level to be $J=\frac{1}{2}$, even parity, because the forward maximum implies the capture of a proton by Mg^{24} with $l_p=0$. The cross section is quite small at $\theta_{lab}=150°$ compared to values in the forward direction. The data for the second excited state (i.e., $E_x=0.95$ Mev) would suggest $J=3/2$ or $5/2$, even parity, but there is a slight possibility that the designation is $J=\frac{1}{2}$ or $\frac{3}{2}$, odd parity, for this level. The experimental cross-section value at $\theta_{lab}=150°$ is very large compared to values in the forward direction and deviates markedly from the P and D (i.e., $l_p=1$ and $l_p=2$, respectively) curves. The values of the absolute differential cross sections are rather small for this reaction.

It should be emphasized that since Butler's analysis treated only bound levels of the residual nucleus, there is no justification in applying it to states unstable against emission of the captured particle. Also the singularity of Butler's expression for $k_p=0$ (k_p being the wave number of the captured particle) is not experimentally realized. This observation further suggests a failing of the theory in this region. Consequently, the three remaining angular distributions were not compared to the theoretical curves. A more recent extension of this theory by Friedman and Tobacman[20] considers the virtual states as well as the bound states. The expression for the angular distributions for bound states is found to be similar to that of Butler and lacks the singularity. The expression for virtual states has additional incoherent terms, and a quantity df/dE which depends on the behavior of the wave function at the nuclear surface. The partial widths for particle and gamma-emission also enter. These quantities are not explicitly known. The Born approximation has been employed by Bhatia, Huang, Huby, and Newns[21] to calculate the angular distributions of (d,p) and (d,n) reactions. The results agree with Butler's where the latter theory is applicable and do not exhibit singularities at $k_p=0$.[22] The expression, however, does possess more parameters than Butler's expression.

A possible check on these theories may be afforded by consideration of the data of Fig. 13 since the level to which the data applies has already been assigned $J=\frac{3}{2}$, odd parity from the partial wave analysis of the elastic scattering data.[3] The neutron distribution is noted to have a slight minimum in the forward direction and drops rapidly beyond θ(c.m.)$=34°$. If reasonable assumptions are made regarding df/dE in Friedman and Tobacman's expression, and gamma-emission is assumed to be negligible, the theoretical curve for $l_p=1$ has a forward maximum, decreasing monotonically to one-half the peak value at 60°. The prediction of Bhatia and Huang is that of a forward maximum which drops steadily to one-fifth the maximum value at 60°. Neither of these curves fits the data well enough to suggest the

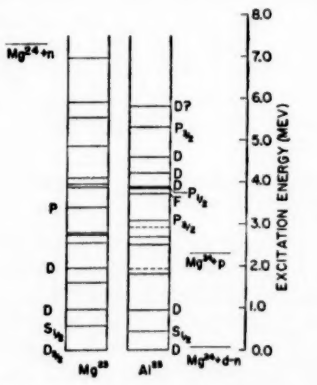

FIG. 14. Energy levels diagrams of Al^{25} and Mg^{25}.

[18] J. E. Mack, Revs. Modern Phys. **22**, 64 (1950).
[19] M. G. Mayer, Phys. Rev. **78**, 16 (1950).
[20] F. L. Friedman and W. Tobacman (to be published).
[21] Bhatia, Huang, Huby, and Newns, Phil. Mag. **43**, 485 (1952).
[22] The equivalence of the essential features of the Butler theory to the Born approximation calculation has been demonstrated by P. B. Daitch and J. B. French [Phys. Rev. **87**, 900 (1952)]; and R. G. Thomas, private communication.

assignment of $l_p=1$. One is prompted to consider an extrapolation of the Butler curves from the range of validity and notes in contrast to the above treatments a preference for an $l_p=1$ assignments. If this procedure is tolerated, it is tempting to go a step further and hazard guesses for the levels at 2.51- and 2.74-Mev excitation energies. That at 2.51 Mev would appear to have an assignment of $l_p=0$ making it $J=\frac{1}{2}$, even parity, while the level at 2.74 Mev would be described with $l_p=1$ or 2. It may be noted in passing that while the level at 2.51-Mev excitation energy corresponds to the k_p close to zero, the absolute cross section of the $Mg^{24}(d,n)Al^{25}$ reaction for this level is not noticeably greater than the cross sections for the other levels.

Butler's expression for $\sigma(\theta)$ contains an angle independent coefficient N which is a function of the initial and final nuclei. It may be of interest to note the variation of this nuclear factor among the levels of Al^{25} which have been classified in the experiment. The levels are assumed to be $J=5/2$, even parity, for the ground state, $J=\frac{1}{2}$, even parity, for the first excited state, and $J=\frac{3}{2}$, even parity, for the second excited state. The experimental and theoretical values are compared at the peaks of the angular distributions which are 40°, 0°, and 35°, respectively. The theoretical values are not sensitive to the choice of J (i.e., either 3/2 or 5/2) which enters in by way of the statistical factor $(2J+1)$. The comparison is shown in Table II. The third and fourth columns are normalized to unity for the ground-state entry. The last column is the ratio of these values.

It is clear from this comparison that the nuclear factor for the two levels with $l_p=2$ varies by only a factor of two, but the nuclear factor is more than an order of magnitude larger for the level involved in the S wave proton capture. A similar analysis of the $Be^9(d,n)B^{10}$ reaction[23] for which the first five states of B^{10} are described by the designation $l_p=1$ yields a result that this nuclear factor has a variation of only a factor of three among these levels. All these observations suggest a strong dependence of the nuclear factor on l_p.

V. ENERGY LEVELS OF THE MIRROR NUCLEI Al^{25} AND Mg^{25}

A description of the level structure of Al^{25} from its ground state to 6.1 Mev can now be given, for the region from 2.7 to 6.1 Mev has been investigated by the elastic scattering of protons.[2,3] The data of the present experiment overlap the above mentioned region with the 3.11-Mev level in common, and confirm the two levels reported from the study of the $Mg^{24}(p,\gamma)Al^{25}$ reaction.[16] The structure of Mg^{25} is also presented in Fig. 14 for the purpose of comparison. This latter diagram is a compilation of levels seen from the $Al^{27}(d,n)Mg^{25}$ and $Mg^{24}(d,p)Mg^{25}$ reactions.[24,25] The assignments are those

TABLE III. Cross sections of the $Mg^{24}(d,n)Al^{25}$ and $Mg^{24}(d,p)Mg^{25}$ reactions.

$Mg^{24}(d,n)Al^{25}$		$Mg^{24}(d,p)Mg^{25}$	
E_x(Mev)	$\sigma(\theta)$(cm²/sterad.)	E_x(Mev)	$\sigma(\theta)$(cm²/sterad.)
0.00	$3.0\cdot10^{-27}$	0.000	$1.7\cdot10^{-26}$
0.45	$5.7\cdot10^{-26}$	0.583	$2.3\cdot10^{-25}$
0.95	$2.5\cdot10^{-27}$	0.976	$9.3\cdot10^{-27}$

of Holt, deduced from a study of the angular distributions of the proton groups from the $Mg^{24}(d,p)Mg^{25}$ reaction.[26] The designations of the upper levels of Al^{25} were made from a partial wave analysis of the $Mg^{24}(p,p)$-Mg^{24} data,[3] while those for the lowest three levels are derived from the data of this experiment. The symbols are not meant to imply any particular nuclear model. The value for the total angular momentum of the state, as has been stated, it $J=l_p\pm\frac{1}{2}$ except when $l_p=0$ in which case $J=\frac{1}{2}$. The parity is even if l_p is even and odd if l_p is odd, for the ground state of Mg^{24} is assumed to have zero spin and even parity. The two dashed lines on the diagram for Al^{25} indicate the doubtful levels previously mentioned. Because nuclear emulsions cannot resolve levels with a spacing smaller than 100 kev, it is possible that doublets are present and undetected in the region of Al^{25} below 3.0-Mev excitation energy. This remark also applies to the region of Mg^{25} above 4.0-Mev excitation energy.

The absolute cross section of the $Mg^{24}(d,n)Al^{25}$ and $Mg^{24}(d,p)Mg^{25}$ reactions for the three lowest states are compared in Table III. The values given are the differential cross sections at the peaks of the angular distributions. It is seen from the level diagrams that the l_p assignments agree. The values from the (d,p) reaction are from four to six times larger than the corresponding values from the (d,n) reaction. This is reasonable, for the (d,p) reaction is expected to have a larger cross section than the (d,n) reaction because of the Coulomb effect.[27] Since the $Mg^{24}(d,p)Mg^{25}$ reaction was studied with 8.0-Mev deuterons while 4.0-Mev deuterons were employed for the $Mg^{24}(d,n)Al^{25}$ reaction, the expectation is even greater for a larger (d,p) than (d,n) cross section in this case. The levels of Al^{25} and Mg^{25} are seen, therefore, to correspond very nicely below 1.0-Mev excitation energy. An unambiguous correspondence of levels above 1.0 Mev cannot be made at this time. However, one can see that the level densities of the regions to 6.0 Mev are approximately equal.

The author would like to express his gratitude to Professor H. T. Richards for many helpful and stimulating discussions, and to Dr. F. Ajzenberg for advice on the techniques of nuclear emulsions. The assistance of Mr. R. E. Benenson, Dr. J. R. Cameron, and Dr. Ajzenberg in the operation of the electrostatic generator is gratefully acknowledged.

[23] F. Ajzenberg, Phys. Rev. **88**, 298 (1952).
[24] Endt, Enge, Haffner, and Buechner, Phys. Rev. **87**, 27 (1952).
[25] Toops, Sampson, and Steigert, Phys. Rev. **85**, 280 (1952).
[26] The author is indebted to Dr. J. R. Holt for communicating his results prior to publication.
[27] D. C. Peaslee, Phys. Rev. **74**, 1001 (1948).

Photoproduction of π^0 Mesons in Hydrogen and Deuterium*

NORMAN C. FRANCIS†
University of Rochester, Rochester, New York
(Received September 8, 1952)

Photoproduction of π^0 mesons in hydrogen and deuterium is calculated in the weak coupling theory under several different assumptions regarding the interaction Hamiltonian. All calculations are performed non-relativistically taking into account the anomalous magnetic moments of the nucleons. The contribution of the negative energy states for the nucleons and of the nucleon current are isolated. Calculations are also performed with a phenomenological Hamiltonian which yields a $(2+3\sin\theta')$ angular distribution in the center-of-mass system for the photoproduction of π^0 mesons in hydrogen. In the case of deuterium, the relative importance of elastic and inelastic photoproduction is examined as a function of photon energy, meson angle, and the theoretical results are compared with recent experimental data. Best agreement with experiment is obtained if nucleon current effects are neglected.

INTRODUCTION

THE standard weak coupling theory which was used to calculate the photoproduction of π^+ mesons in hydrogen predicts much too small a cross section for π^0 meson production.[1] However, when the anomalous magnetic moment of the proton is assumed to interact directly with the electromagnetic field and the π^0 meson is treated as a pseudoscalar particle, the cross section for π^0 production becomes comparable to the π^+ cross section.[2] If the anomalous magnetic moment of the proton is responsible for π^0 production in hydrogen, then the neutron should contribute an almost equal amount to the π^0 photoproduction in a nucleus like deuterium. Indeed, the elastic production process

$$\gamma+D\rightarrow\pi^0+D$$

at all meson angles, and the total cross section (elastic plus inelastic) for π^0 meson produced in the forward direction, are especially interesting because of their dependence, due to interference effects, on the relative sign of the neutron and proton π^0 coupling constants. In practice, it is easier to measure the total deuteron cross section at large angles with respect to the photon beam where the proton and neutron make their separate contributions.

At least two objections can be raised against the relativistic weak coupling calculation carried out by Kaplon[2] to explain the photoproduction of π^0 mesons in hydrogen. The first objection is that while the proton cross section calculated in this way agrees well with experiment[3] both as regards absolute magnitude and variation with energy, it predicts an approximately isotropic angular distribution in the laboratory system, which seems to contradict experiment. The origin of the isotropic distribution can be traced to interference between the probability amplitudes for transitions to positive and negative energy intermediate states. Since the odd part of the (PS, PV) meson-nucleon interaction Hamiltonian is needed to give a large amplitude for negative energy state transitions, if for an as yet unknown reason the odd part of the (PS, PV) meson-nucleon operator is suppressed[4] and only the $(\boldsymbol{\sigma}\cdot\mathbf{q})$ part ($\boldsymbol{\sigma}$ is the proton spin and $\mathbf{q}$ is the meson momentum) is retained, the interference between negative and positive energy transitions is eliminated and the proton cross section favors the emission of π^0 mesons in the forward direction. For this reason the deuteron elastic π^0 production is calculated with an interaction which contains only the even part of the (PS, PV) interaction. The elastic production is also calculated with the entire (PS, PV) interaction Hamiltonian since the experimental angular distribution from hydrogen is not final.

A second possible objection to a weak coupling calculation which includes the anomalous magnetic moment of the proton is that the anomalous moment, which presumably is due to virtual charged meson currents, may be more important for the photoproduction of π^0 mesons than the Dirac moment associated with the bare proton. With this in mind, a third model is considered in which the charge of the proton is completely ignored and the proton is assumed to interact with the radiation field through its anomalous moment alone. If the proton and neutron anomalous moments are assumed equal, the photoproduction of π^0 mesons is independent of the charge state of the nucleon target. Since the explicit version of the (PS, PV) theory which is used may be incorrect, it is interesting to inquire into the most general phenomenological interaction possible within the context of weak coupling theory. It turns out that, for a pseudoscalar π-meson, one can

* This work was assisted by the U. S. Atomic Energy Commission.
† Now at Indiana University, Bloomington, Indiana.
[1] K. A. Brueckner, Phys. Rev. **79**, 641 (1950).
[2] M. F. Kaplon, Phys. Rev. **83**, 712 (1951), and Aidzu, Fujimoto, and Fukuda, Prog. Theoret. Phys. **6**, 193 (1951).
[3] A. Silverman and M. Stearns, Phys. Rev. **83**, 206 (1951).

[4] Similar *ad hoc* assumptions are needed to explain both the forward maximum in the differential cross section for the reaction $p+p\rightarrow D+n$ [see Chew, Goldberger, Steinberger, and Yang, Phys. Rev. **84**, 581 (1951)] and the π^+ to π^- meson ratio of about one in the reactions

$$\gamma+D\rightarrow\pi^++n+n$$

and

$$\gamma+D\rightarrow\pi^-+p+p$$

[see R. E. Marshak, *Meson Physics* (McGraw-Hill Book Company, Inc., New York, 1952)].

use a linear combination of the following five terms: $(\boldsymbol{\sigma}\cdot\boldsymbol{\lambda}')$, $(\boldsymbol{\sigma}\cdot\boldsymbol{\lambda}')(\mathbf{k}'\cdot\mathbf{q}')$, $(\boldsymbol{\sigma}\cdot\mathbf{k}')(\mathbf{q}'\cdot\boldsymbol{\lambda}')$, $(\boldsymbol{\sigma}\cdot\mathbf{q}')(\mathbf{q}'\cdot\boldsymbol{\lambda}')$, $[\mathbf{q}'\cdot(\mathbf{k}'\times\boldsymbol{\lambda}')]$, where $\boldsymbol{\sigma}$ is the spin of the nucleon, $\mathbf{q}'$ is the meson momentum, $\mathbf{k}'$ and $\boldsymbol{\lambda}'$ are the photon momentum and polarization, respectively—all quantities measured in the center-of-mass system. Coefficients are, in general, arbitrary functions of q' and k'.

If, in particular, the phenomenological interaction is chosen as

$$2\mathbf{q}'\cdot(\mathbf{k}'\times\boldsymbol{\lambda}')+i[(\boldsymbol{\sigma}\cdot\mathbf{k}')(\mathbf{q}'\cdot\boldsymbol{\lambda}')-(\boldsymbol{\sigma}\cdot\boldsymbol{\lambda}')(\mathbf{q}'\cdot\mathbf{k}')],$$

the proton cross section is proportional to $(2+3\sin^2\theta')$. This angular dependence is especially interesting because it agrees with the results of a quantum mechanical, strong coupling calculation[5] as well as corresponding to the angular dependence which is associated with the $l=1$, $j=\frac{3}{2}$ state (l being the orbital and j the total angular momentum) of the meson-nucleon system.[6]

THE METHOD

The production of π^0 mesons in photon-nucleon collisions is calculated with four nonrelativistic interaction Hamiltonians. The first of these may be obtained directly from the relativistic (PS, PV) Hamiltonian. To lowest order in $1/M$ (M is the nucleon mass), the Hamiltonian for a proton may be written

$$H_1(p)=H_{MN}(p)+H_{RN}(p)+H_{MRN}(p), \tag{1}$$

where

$$H_{MN}(p)=g_P(\boldsymbol{\sigma}\cdot\boldsymbol{\nabla})U/\mu,$$

$$H_{RN}(p)=-e\mu_P[\boldsymbol{\sigma}\cdot(\boldsymbol{\nabla}\times\mathbf{A})]/2M-e(\mathbf{p}\cdot\mathbf{A})/M,$$

$$H_{MRN}(p)=-eg_P(\boldsymbol{\sigma}\cdot\mathbf{A})\frac{\partial U}{\partial t}\Big/M\mu.$$

Here $\boldsymbol{\sigma}$ and μ_P are the spin and magnetic moment of the proton, respectively; $\mathbf{A}$ is the vector potential evaluated at the position of the proton; μ is the meson mass; U is the π^0 meson wave function; e is the charge of the proton, and g_P is the coupling constant of the proton to the π^0 meson field.

$H_{MN}(p)$ and $H_{RN}(p)$ are the usual nonrelativistic approximations to the pure meson-nucleon and radiation-nucleon interactions, respectively. The catastrophic term, $H_{MRN}(p)$, can be shown to result from negative energy state transitions. If the catastrophic term is neglected, the interaction becomes

$$H_2(p)=H_{MN}(p)+H_{RN}(p). \tag{2}$$

Similarly, if the anomalous moment of the proton is assumed to be entirely responsible for the π^0 production, the interaction Hamiltonian takes the form

$$H_3(p)=\frac{g_P'}{\mu}(\boldsymbol{\sigma}\cdot\boldsymbol{\nabla})U-\frac{e\mu_P'}{2M}[\boldsymbol{\sigma}\cdot(\boldsymbol{\nabla}\times\mathbf{A})], \tag{3}$$

where μ_P' is the anomalous moment of the proton and g_P' is a constant.

Of all the interaction terms, H_{MRN} is the only one which has a diagonal matrix element; all the others require second-order calculations. It is therefore convenient to define an effective interaction $(H)_e$ which enables the process to be calculated in first order. Clearly, to determine $(H)_e$, we need only sum the second order matrix element over all of the intermediate states. After performing this calculation we obtain the following effective Hamiltonians:

$$[H_1(p)]_e=\frac{ie}{M\mu}\frac{2\pi}{(k\epsilon)^{\frac{1}{2}}}e^{i\mathbf{K}\cdot\mathbf{r}}\left\{\boldsymbol{\sigma}\cdot\left[-\epsilon\boldsymbol{\lambda}+\frac{(\mathbf{q}\cdot\boldsymbol{\lambda})\mathbf{q}}{\epsilon}-\frac{\mu_P\mathbf{q}\times(\mathbf{k}\times\boldsymbol{\lambda})}{k}\right]\right\}g_P, \tag{4}$$

$$[H_2(p)]_e=\frac{ie}{M\mu}\frac{2\pi}{(k\epsilon)^{\frac{1}{2}}}e^{i\mathbf{K}\cdot\mathbf{r}}\left\{\boldsymbol{\sigma}\cdot\left[\frac{(\mathbf{q}\cdot\boldsymbol{\lambda})\mathbf{q}}{\epsilon}-\frac{\mu_P\mathbf{q}\times(\mathbf{k}\times\boldsymbol{\lambda})}{k}\right]\right\}g_P, \tag{5}$$

$$[H_3(p)]_e=-\frac{ie}{M\mu}\frac{2\pi}{(k\epsilon)^{\frac{1}{2}}}e^{i\mathbf{K}\cdot\mathbf{r}}\{\boldsymbol{\sigma}\cdot[\mathbf{q}\times(\mathbf{k}\times\boldsymbol{\lambda})]\}\mu_P'g_P', \tag{6}$$

where $\mathbf{q}$ and ϵ are the momentum and energy of the meson, respectively; $\boldsymbol{\lambda}$ is the photon polarization whose momentum is $\mathbf{k}$; $\mathbf{r}$ is the position vector of the proton and $\mathbf{K}=\mathbf{k}-\mathbf{q}$.

As a fourth effective Hamiltonian we take the following:

$$[H_4(p)]_e=\frac{eG_P}{M\mu^2}\frac{2\pi}{\{k'\epsilon'\}^{\frac{1}{2}}}e^{i\mathbf{K}'\cdot\mathbf{r}'}[2\mathbf{q}'\cdot(\mathbf{k}'\times\boldsymbol{\lambda}')+i\boldsymbol{\sigma}\cdot\mathbf{q}'\times(\mathbf{k}'\times\boldsymbol{\lambda}')], \tag{7}$$

where the primes indicate that the variables are measured in the center-of-mass system and G_P is a constant. In the center-of-mass system, this phenomenological interaction gives rise to a $(2+3\sin^2\theta')$ angular distribution, and this is at present the sole reason for choosing it.

After squaring the matrix element of the effective Hamiltonians, performing the usual summations and averages, and introducing the statistical factor, we obtain the following proton cross sections in the laboratory system:

$$\left(\frac{d\sigma}{d\Omega}\right)_1^P=\frac{\Lambda_1^2g_P^2}{2}\left\{\frac{2\epsilon^2}{q^2}+\frac{q^2\sin^2\theta}{\epsilon^2}+\mu_P^2(1+\cos^2\theta)-2\sin^2\theta-4\frac{\epsilon}{q}\mu_P\cos\theta\right\}, \tag{8}$$

[5] Y. Fujimoto and H. Miyazawa, Prog. Theoret. Phys. **5**, 1052 (1950).

[6] K. A. Brueckner and K. Watson, Phys. Rev. **86**, 923 (1952).

where

$$\Lambda_1^2=\left(\frac{e^2q^3}{\mu^2M^2k}\right)\Big/\left[1+\frac{\epsilon}{M}\frac{(q-k\cos\theta)}{q}\right],$$

$$\Lambda_2^2=\left(\frac{e^2q^3}{\mu^2M^2k}\right)\Big/\left[1+\frac{\epsilon}{2M}\frac{(q-k\cos\theta)}{q}\right];$$

$$\left(\frac{d\sigma}{d\Omega}\right)_2^P=\frac{\Lambda_1^2F_P}{2}, \tag{9}$$

$$F_P=g_P^2[\mu_P^2(1+\cos^2\theta)+(\sin^2\theta)q^2/\epsilon^2];$$

$$\left(\frac{d\sigma}{d\Omega}\right)_3^P=\frac{\Lambda_1^2\mu_P'^2g_P'^2(1+\cos^2\theta)}{2}, \tag{10}$$

$$\left(\frac{d\sigma}{d\Omega}\right)_4^P=\frac{q^2q'^2k'^2[2+3(\sin^2\theta)q^2/q'^2]e^2G_P^2}{2\mu^4kM(k+M)[q-k\epsilon\cos\theta/(k+M)]}, \tag{11}$$

with θ the angle between $\mathbf{k}$ and $\mathbf{q}$.

The cross section $(d\sigma/d\Omega)_4{}^P$ is accurate to the first power in $1/M$, while Eqs. (8), (9), and (10) are accurate to lowest order in $1/M$ since they are obtained from effective Hamiltonians which are also accurate to lowest order in $1/M$. However, the statistical factor in these and in several of the following equations contain higher order corrections to insure a meaningful comparison between these results and the plane wave approximation to the total cross section.

The effective Hamiltonian for a neutron target may be written

$$[H_1(n)]_e=[H_2(n)]_e=[H_3(n)]_e=\frac{\mu_Ng_N'}{\mu_P'g_P'}[H_3(p)]_e, \tag{12}$$

where μ_N and g_N' are the neutron's magnetic moment and coupling constant, respectively.

We may assume that

$$[H_4(n)]_e=[H_4(p)]_e. \tag{13}$$

The proton and the neutron effective Hamiltonians are indeed equal if the π^0 meson is produced in $\frac{3}{2}$ isotopic spin state.[7]

The cross sections for the process

$$\gamma+n\rightarrow\pi^0+n$$

are, therefore,

$$\left(\frac{d\sigma}{d\Omega}\right)_1^N=\left(\frac{d\sigma}{d\Omega}\right)_2^N=\left(\frac{d\sigma}{d\Omega}\right)_3^N=\frac{(g_N'\mu_N)^2}{g_P'^2\mu_P'^2}\left(\frac{d\sigma}{d\Omega}\right)_3^P, \tag{14}$$

and

$$\left(\frac{d\sigma}{d\Omega}\right)_4^P=\left(\frac{d\sigma}{d\Omega}\right)_4^N. \tag{15}$$

The first three neutron cross sections are equal because the catastrophic term vanishes for a neutron target and the neutron moment is entirely anomalous.

[7] K. Watson, Phys. Rev. **85**, 852 (1952).

ELASTIC PRODUCTION

The cross section for the process[8] $\gamma+D\rightarrow\pi^0+D$ is calculated with the effective Hamiltonians defined by Eqs. (4) through (7) and Eqs. (12) and (13). However, since these interactions were derived for a free nucleon at rest, their application in the deuteron calculation must be justified.

In deriving Eqs. (4) to (6), it was necessary to sum over free nucleon intermediate states. For the deuteron problem, on the other hand, the intermediate states are no longer free but are the states of a two-nucleon system with a potential. However, the energy denominator to lowest order in $1/M$ is independent of the energy of the nucleons in the intermediate state and therefore the application of closure over all intermediate states results in the free nucleon effective Hamiltonians.

A further objection to the employment of Eqs. (4) to (7) and Eqs. (12) and (13) is that the momentum operator p appearing in the corresponding Hamiltonians is evaluated for a target at rest. The validity of this approximation has been checked, and the error in this instance is also negligible.

Furthermore, with the use of the effective Hamiltonian, one neglects processes in which one particle in the deuteron absorbs the photon and the other emits the meson. This two-body effect clearly depends strongly on the behavior of the nucleon potential at small distances. If the Hulthen potential is assumed and if the energy of the incident photon is 300 Mev, the two-body terms may be calculated and these terms may also be neglected.

Finally, in this work the D state admixture to the deuteron wave function is neglected. If the Hulthen potential

$$-(\beta^2-\alpha^2)/(e^{(\beta-\alpha)r}-1)$$

is assumed, the deuteron wave function becomes

$$\psi_0(\mathbf{r})=N(e^{-\alpha r}-e^{-\beta r})/r,$$

where $-\alpha^2/M$ is the binding energy of the deuteron and where β and N are related to the triplet effective range r_0.

The effective Hamiltonians which were used to calculate the proton and neutron cross sections may be used to obtain the deuteron elastic result if we label particles 1 and 2 the proton and neutron, respectively. Then the $\mathbf{r}$ and $\boldsymbol{\sigma}$ appearing in $[H(p)]_e$ and $[H(n)]_e$ will have subscripts 1 and 2, respectively. The deuteron matrix element may now be written

$$\mathfrak{M}_D{}^t={}^3\chi_{m'}{}^*\int\psi_0(\mathbf{r})e^{-i\mathbf{P}\cdot\mathbf{R}}\{[H_1(p)]_e+[H_1(n)]_e\}\times\psi_0(\mathbf{r})d\mathbf{r}_1d\mathbf{r}_2\,{}^3\chi_m, \tag{16}$$

where ${}^3\chi_m$ is the triplet spin function, $\mathbf{r}=\mathbf{r}_1-\mathbf{r}_2$, and

[8] N. Francis and R. E. Marshak, Phys. Rev. **85**, 496 (1952); Heckrotte, Henrich, and Lepore, Phys. Rev. **85**, 490 (1952).

$\mathbf{R}=(\mathbf{r}_1+\mathbf{r}_2)/2$. The superscript i indicates which of the four effective Hamiltonians is being considered. When $i=1$, 2 or 3, the evaluation of the matrix element is straightforward and requires no further discussion. To find $\mathfrak{M}_D{}^4$, however, $[H_4(p)]_e$ and $[H_4(n)]_e$ must be expressed in the laboratory system. In the laboratory system

$$[H_4(p)]_e=\frac{eG_P e^{i\mathbf{K}\cdot\mathbf{r}}}{M\mu^2(k\epsilon)^{\frac{1}{2}}}[2\mathbf{q}'\cdot(\mathbf{k}'\times\boldsymbol{\lambda}')+i\boldsymbol{\sigma}\cdot\mathbf{q}'\times(\mathbf{k}'\times\boldsymbol{\lambda}')], \quad (17)$$

where $\mathbf{q}'=\mathbf{q}-\beta\epsilon$, $\mathbf{k}'=\mathbf{k}-\beta k$, $\beta=(\mathbf{p}+\mathbf{k})/(M+k)$. The momentum of the target nucleon is p. If the gauge is chosen so that the fourth component of the vector potential vanishes either in the laboratory or in the center-of-mass system, $\boldsymbol{\lambda}=\boldsymbol{\lambda}'$. It should also be remarked that in calculating the deuteron matrix element, the $\mathbf{p}$ appearing in β must be treated as the momentum operator which acts on the proton coordinate if the $\mathbf{p}$ appears in $[H_4(p)]_e$ and on the neutron coordinate if the $\mathbf{p}$ appears in $[H_4(n)]_e$.

After the conventional manipulations the elastic cross section for the four different effective Hamiltonians may be written

$$\left(\frac{d\sigma}{d\Omega}\right)_1^D=\tfrac{1}{3}\Lambda_2{}^2I^2(\tfrac{1}{2}\mathbf{K})\left\{\frac{g_P{}^2q^2\sin^2\theta}{\epsilon^2}+2g_P{}^2\frac{\epsilon^2}{q^2}+(\mu_P g_P+\mu_N g_N)^2(1+\cos^2\theta)-2g_P{}^2\sin^2\theta-4(\mu_P g_P+\mu_N g_N)g_P\frac{\epsilon}{q}\cos\theta\right\}; \quad (18)$$

$$\left(\frac{d\sigma}{d\Omega}\right)_2^D=\tfrac{1}{3}\Lambda_2{}^2I^2(\tfrac{1}{2}\mathbf{K})[F_P+F_N+2F_{PN}]; \quad (19)$$

$$\left(\frac{d\sigma}{d\Omega}\right)_3^D=\tfrac{1}{3}\Lambda_2{}^2I^2(\tfrac{1}{2}\mathbf{K})\mu_N{}^2(g_P{}'-g_N{}')^2(1+\cos^2\theta); \quad (20)$$

$$\left(\frac{d\sigma}{d\Omega}\right)_4^D=\frac{4}{3}\Lambda_2{}^2I^2(\tfrac{1}{2}\mathbf{K})G_P{}^2\frac{k^2}{\mu^2}\left\{(5\sin^2\theta+2)\left[1-\frac{3k+\epsilon}{2(M+k)}\right]-\frac{q^2+3k\epsilon}{q(M+k)}\cos\theta\right\}; \quad (21)$$

where

$$I(\mathbf{K})=\int e^{\pm i\mathbf{K}\cdot\mathbf{r}}\psi_0{}^2(\mathbf{r})d\mathbf{r},$$

F_P is defined above, $F_N=g_N{}^2\mu_N{}^2(1+\cos^2\theta)$, and $F_{PN}=\mu_P g_P\mu_N g_N(1+\cos^2\theta)$. In the elastic cross sections, we have neglected $1/M^2$ terms in $(d\sigma/d\Omega)_4{}^D$ and have neglected $1/M$ terms in the other three cross sections.

TOTAL CROSS SECTION

An upper and lower limit to the total cross section, elastic plus inelastic, for the photoproduction of π^0 mesons in deuterium will be obtained assuming a central nuclear potential that vanishes for odd parity states ("Serber mixture"). The effect of the distorted S state will be considered but all other partial waves will be assumed undistorted. Since the plane wave cross section may be considered to be a sum of terms, each with a different orbital angular momentum, and since the distortion is considered in only the final S states, the total cross section will be the plane wave cross section less its S part plus the cross section calculated with the distorted final S state. That is,

$$\left(\frac{d\sigma}{d\Omega}\right)_T=\int_\mu^{\epsilon_{\max}}\left[\left(\frac{d^2\sigma}{d\Omega d\epsilon}\right)_{P.W.}-\left(\frac{d^2\sigma}{d\Omega d\epsilon}\right)_S\right]d\epsilon+\left(\frac{d\sigma}{d\Omega}\right)_S', \quad (22)$$

where $(d\sigma/d\Omega)_T$ is the total cross section, $(d^2\sigma/d\Omega d\epsilon)_{P.W.}$ is the spectrum derived assuming plane waves for the final nuclear state, $(d^2\sigma/d\Omega d\epsilon)_S$ is the S part of the plane wave result and $(d\sigma/d\Omega)_S'$ is the cross section calculated with the distorted S state. The plane wave spectrum and its S part can be derived with relative ease but the calculation of the cross section for the distorted S state is tedious. We will therefore determine $(d^2\sigma/d\Omega d\epsilon)_{P.W.}$ and $(d\sigma/d\Omega d\epsilon)_S$ exactly and find an upper limit to $(d\sigma/d\Omega)_S'$.

Although the following procedure may be applied to a calculation involving any of the four effective Hamiltonians defined above, for definiteness we shall calculate the upper and lower limits to the total cross section using $H_e=[H_2(p)]_e+[H_2(n)]_e$. The effective Hamiltonian may be written

$$H_e=(\boldsymbol{\sigma}_1\cdot\mathbf{L}_1)e^{i\mathbf{K}\cdot\mathbf{r}_1}+(\boldsymbol{\sigma}_2\cdot\mathbf{L}_2)e^{i\mathbf{K}\cdot\mathbf{r}_2}, \quad (23)$$

where

$$\mathbf{L}_1=\frac{ie}{M\mu}\frac{2\pi}{(k\epsilon)^{\frac{1}{2}}}g_P\left[\frac{(\mathbf{q}\cdot\boldsymbol{\lambda})}{\epsilon}\mathbf{q}-\mu_P\mathbf{q}\times(\mathbf{k}\times\boldsymbol{\lambda})\right],$$

and

$$\mathbf{L}_2=-\frac{ie}{M\mu}\frac{2\pi}{(k\epsilon)^{\frac{1}{2}}}g_N\mu_N\mathbf{q}\times(\mathbf{k}\times\boldsymbol{\lambda}).$$

Using the effective Hamiltonian defined by Eq. (23), the cross section for transitions to plane wave final states is easily found to be

$$\left(\frac{d^2\sigma}{d\Omega d\epsilon}\right)_{P.W.}=\frac{\Lambda^2MN^2}{K}\{A(F_P+F_N)+\tfrac{2}{3}BF_{PN}\}, \quad (24)$$

where

$$\Lambda^2=\frac{e^2q^3}{M^2\mu^2k}; \quad A=\frac{1}{a-pK}-\frac{1}{a+pK}+\frac{1}{b-pK}-\frac{1}{b+pK}-\frac{2}{b-a}\log Q;$$

$$B=\frac{b-a}{b+a}\left[\frac{1}{a}\log\left(\frac{a+pK}{a-pK}\right)-\frac{1}{b}\log\left(\frac{pK+b}{-pK+b}\right)\right];$$

$$a=\alpha^2+p^2+K^2/4;\quad b=\beta^2-\alpha^2+a;\quad \mathbf{p}=(\mathbf{p}_1-\mathbf{p}_2)/2,$$

and

$$Q=\frac{a+pK}{a-pK}\frac{b-pK}{b+pK}.$$

The part of the plane wave spectrum corresponding to final S states is

$$\left(\frac{d^2\sigma}{d\Omega d\epsilon}\right)_S=\Lambda^2N^2M[F_P+F_N+\tfrac{2}{3}F_{PN}]\times(\log^2Q)/2K^2p. \quad (25)$$

The matrix element for transitions to distorted S states may be written

$$\mathfrak{M}_{S'}=\chi_f^*\int\psi_f^*(\mathbf{r})e^{-i\mathbf{P}\cdot\mathbf{R}}[(\boldsymbol{\sigma}_1\cdot\mathbf{L}_1)e^{i\mathbf{K}\cdot\mathbf{r}_1}+(\boldsymbol{\sigma}_2\cdot\mathbf{L}_2)e^{i\mathbf{K}\cdot\mathbf{r}_2}]\times\psi_0(\mathbf{r})d\mathbf{r}_1d\mathbf{r}_2{}^3\chi_m, \quad (26)$$

where ψ_f is the distorted S state wave function. The cross section for distorted final S states is as follows:

$$\left(\frac{d\sigma}{d\Omega}\right)_S'=\tfrac{1}{3}\sum_f{}'\left\{\frac{\epsilon q\sum_m\langle|\mathfrak{M}_{S'}|^2\rangle}{(2\pi)^2[1+(\epsilon/2M)(q-k\cos\theta)/q]}\right\}, \quad (27)$$

where $\sum'$ implies a summation over all final spin states and only those nuclear final states that conserve energy. An upper limit to $(d\sigma/d\Omega)_S'$ is obtained by replacing q by its maximum value and summing over the complete set of final nuclear states. We finally obtain

$$\left(\frac{d\sigma}{d\Omega}\right)_S'\leq\left[\left\{\frac{8\pi\Lambda_2{}^2N^2J}{K^2}\right\}\left\{F_P+F_N+\tfrac{2}{3}F_{PN}\right\}\right]_{q=q_{\max}}\equiv\left(\frac{d\sigma}{d\Omega}\right)_S', \quad (28)$$

where

$$J=\left\{\frac{K}{2}\left[\tan^{-1}\frac{K}{2\alpha}+\tan^{-1}\frac{K}{2\beta}-2\tan^{-1}\frac{K}{\alpha+\beta}\right]-\frac{\alpha}{2}\log\frac{4\alpha^2+K^2}{4\alpha^2}+\frac{\beta}{2}\log\frac{4\beta^2+K^2}{4\beta^2}+\frac{(\alpha+\beta)}{2}\log\frac{(\alpha+\beta)^2+K^2}{(\alpha+\beta)^2}\right\}.$$

Therefore,

$$\left(\frac{d\sigma}{d\Omega}\right)_T\leq\left(\frac{d\sigma}{d\Omega}\right)_S''+\int_\mu^{\epsilon_{\max}}\left[\left(\frac{d^2\sigma}{d\Omega d\epsilon}\right)_{P.W.}-\left(\frac{d^2\sigma}{d\Omega d\epsilon}\right)_S\right]d\epsilon. \quad (29)$$

If the π^0 meson spectra calculated with and without distortion are compared, it is apparent that the effect of the distortion is to increase the spectrum for low nucleon energies and decrease it for high nucleon energies. Due to the closure principle, the integral over all relative nuclear energies of the undistorted and distorted spectra are equal. Therefore, if the integration over the relative momentum extends from zero to a finite upper limit, the distorted integral exceeds the undistorted and the plane wave result is a lower limit to the total cross section.[9]

Since both an upper and a lower limit to the total cross section have been derived, it is instructive to determine when one limit may be more accurate than the other. For mesons produced in the forward direction, the distorted S state spectrum is sharply peaked at a very high meson energy. Consequently, above photon energies of about 1.5μ, when the half-width of the spectrum is small compared to the entire energy range, the error introduced by replacing q by $q_{\max}$ and summing over a complete set of final states is quite small and the upper limit to the total cross section is very accurate. However, as the meson angle increases, the distorted S state spectrum becomes diffuse and remains appreciable from $\epsilon_{\max}$ to ϵ_0 where $\epsilon_{\max}=(q_{\max}{}^2+\mu^2)^{\frac{1}{2}}$ and ϵ_0 is the energy of a π^0 meson photoproduced by a nucleon at rest. ($\epsilon_{\max}-\epsilon_0=K_0{}^2/4M$ where K_0 is the momentum transfer to a free nucleon.) Therefore for large meson angles, when K_0 is also large, $(d\sigma/d\Omega)_S''$ is a good deal larger than $(d\sigma/d\Omega)_S'$. This difference, though significant compared to $(d\sigma/d\Omega)_S'$, will be small compared to $(d\sigma/d\Omega)_T$ if many partial waves contribute to the photoproduction as they generally do.

If a single curve representing the total cross section as a function of angle is desired, a reasonably accurate result could be obtained if it is assumed that

$$\left(\frac{d\sigma}{d\Omega}\right)_T=\frac{1}{2\pi}\left[\theta\left(\frac{d\sigma}{d\Omega}\right)_{P.W.}+(2\pi-\theta)\left\{\left(\frac{d\sigma}{d\Omega}\right)_S''+\int_\mu^{\epsilon_{\max}}\left[\left(\frac{d^2\sigma}{d\Omega d\epsilon}\right)_{P.W.}-\left(\frac{d^2\sigma}{d\Omega d\epsilon}\right)_S\right]d\epsilon\right\}\right]. \quad (30)$$

A simple and fast method,[10] which yields an upper limit to the total cross section approximately equal to the upper limit obtained with the procedure mentioned above, will now be applied to the problem when

$$H_e=[H_4(p)]_e+[H_4(n)]_e.$$

This method, which is applicable when the energy of the incident photon is high, involves the replacement of the rigorous conservation of energy equation which appears in the cross section as the argument of a δ-function with the conservation of energy condition for a free nucleon at rest. Then, if the summation over

[9] This argument is due to G. Chew (private communication).
[10] M. Lax and H. Feshbach, Phys. Rev. **81**, 189 (1951).

final states is extended to include the complete set of final states, the result is an upper limit to the total cross section and may be written

$$\left(\frac{d\sigma}{d\Omega}\right)_T \leq \frac{\Lambda_1^2 k^2}{\mu^2}\left\{\eta^2\left[(2+3\cos^2\theta)-\frac{4k\epsilon\cos\theta}{q(k+M)}\right]+\frac{I(\mathbf{K})}{3}\left[\left(1-\frac{(k+\epsilon)}{k+M}\right)(11\sin^2\theta+2)-\frac{2(q^2+k\epsilon)\cos\theta}{q(k+M)}\right]\right\}_{t=t_0},$$

where $\eta=M/(M+k)$. This result is quite near the correct total cross section for small θ but is about 20 percent high in the backward hemisphere.

RESULTS AND CONCLUSIONS

The most recent measurement[11] of the angular dependence of the photoproduction of π^0 mesons in hydrogen indicates that for mesons produced between 45° and 135° in the laboratory system, the yield is large at 45° and decreases sharply as the meson angle increases to 135°. This experimental result should be compared with the theoretical predictions which were calculated for a photon energy of 300 Mev since the experiment was performed with a photon beam whose average energy was 290 Mev. The cross sections calculated for $k=300$ Mev/c using both $[H_1(p)]_e$ and $[H_2(p)]_e$ are shown in Fig. 1 as curves A_1 and A_2, respectively. The curve A_1 is far too isotropic in the angular region in question to agree with the experimental results. The curve A_2 increases steeply from $\theta=90°$ to 45° in qualitative agreement with experiment, but its behavior from $\theta=90°$ to 135° is too slowly varying. The closest agreement is obtained if the cross section is assumed to have the form $(2+3\sin^2\theta')$ in the center-of-mass system. If this theoretical cross section is transformed to the laboratory system, the resulting differential cross section in the laboratory decreases monotonically as θ increases from 45° to 135° and is shown in Fig. 9 as curve P.

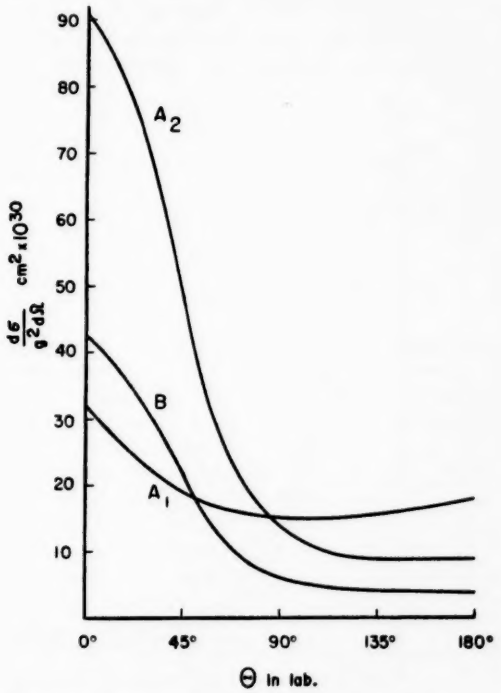

FIG. 1. Curves A_1 and A_2 give the differential cross section at $k=300$ Mev/c for the process $\gamma+p\rightarrow\pi^0+p$, considering and neglecting negative energy state transitions, respectively. The curve B gives the differential cross section at $k=300$ Mev/c for the process $\gamma+n\rightarrow\pi^0+n$.

[11] G. Cocconi and A. Silverman, private communication.

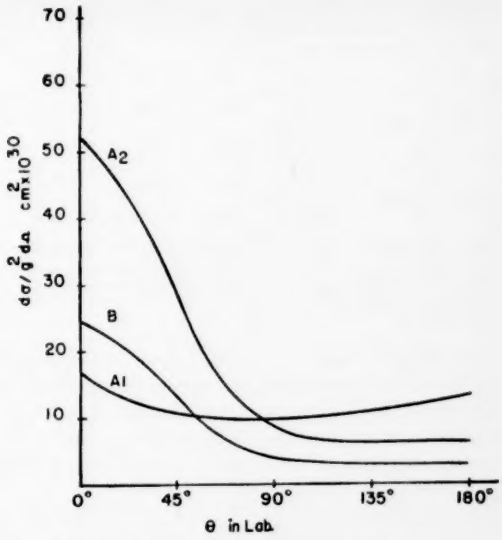

FIG. 2. Same as Fig. 1 at $k=250$ Mev/c.

The curve A_1 of Fig. 1 is a plot of the proton cross section calculated nonrelativistically with the catastrophic term included and, therefore, may be compared with the results of the relativistic calculation.[2] At $\theta=0$, where $k=\epsilon$, the relativistic and nonrelativistic results are equal. However, as θ increases, the relativistic curve remains constant while curve A_1 of Fig. 1 decreases. The difference in the shapes of the two curves is a result of neglecting terms of order $1/M$ in the nonrelativistic calculation. The error is especially large because of the destructive interference present when the catastrophic term is included.

If $\mu_P'=-\mu_N$, and if the effect of the proton charge is neglected, the proton and neutron cross sections are equal and their angular dependence is the same as curve B of Figs. 1 and 2. These curves, like A_2 of Fig. 1, are too flat from $\theta=90°$ to 135°.

TABLE I. Ratio R of deuteron elastic cross section when $g_P=-g_N$ to that when $g_P=g_N$.[a]

			R_1	R_2	R_3
k	300	0°	28.5	221	∞
		90°	16.7	11.2	∞
k	250	0°	28.5	123	∞
		90°	19.4	10.3	∞

[a] The subscript on R defines which effective Hamiltonian is used. The R_1 and R_2 are calculated neglecting and considering negative energy state transitions, respectively, while R_3 is calculated assuming that the anomalous moment alone contributes.

The deuteron elastic cross section depends strongly on the relative sign of the neutron and proton coupling constants. If we define $(d\sigma/d\Omega)_D^-$ and $(d\sigma/d\Omega)_D^+$ to be the elastic cross sections when $g_P=-g_N$ and when $g_P=g_N$, respectively, and if we define their ratio to be R, we obtain the values given in Table I.

The significant feature of Table I is the large values of R for all three theories. Therefore, if $g_P=-g_N$, the elastic deuteron cross section is appreciable, but if $g_P=g_N$, the calculated elastic result is so small that it is probably not measurable with the present techniques.

Figures 3 and 4, and Fig. 9, curve D, show the angular dependence of the cross section for the reaction

$$\gamma+D\rightarrow\pi^0+D.$$

For meson angles near zero, the relatively well-known low momentum components of the deuteron wave function contribute while at large meson angles, where the momentum transfer K is not small, the high momentum components of the deuteron wave function are needed. Therefore, at the small meson angles the elastic cross section is quite accurate as well as large. At the large meson angles, where the cross section is small, the result is uncertain because the high momentum components of the deuteron S state wave function are not well known and because the D state admixture of the deuteron wave function, which we

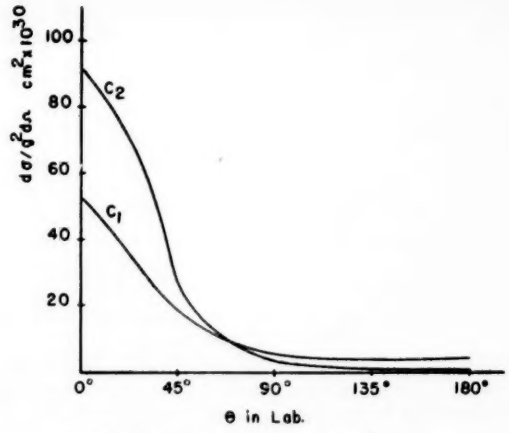

FIG. 4. Same as Fig. 3 at $k=250$ Mev/c.

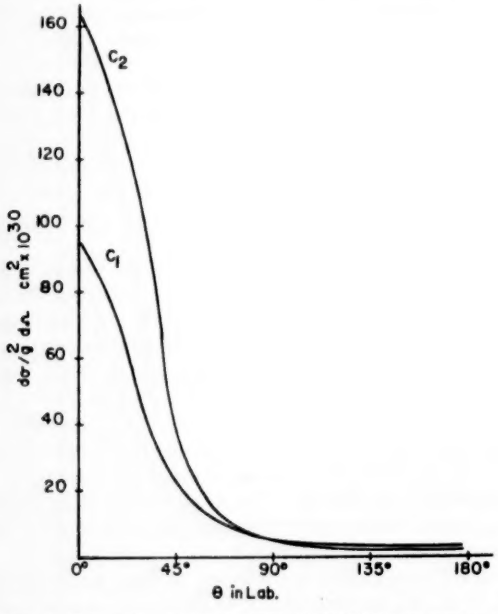

FIG. 3. Curves C_1 and C_2 give the differential cross section at $k=300$ Mev/c for the process $\gamma+D\rightarrow\pi^0+D$, assuming $g_P=-g_N$ and considering and neglecting negative energy state transitions, respectively.

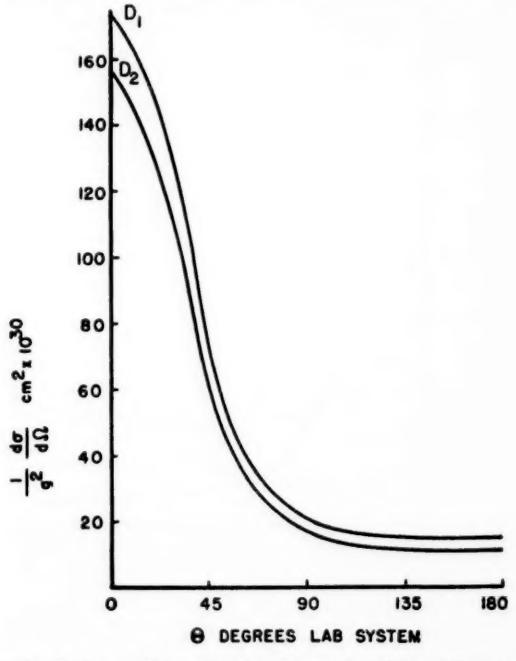

FIG. 5. Curves D_1 and D_2 give the upper and lower limits to the total cross section for the photoproduction of π^0 mesons in deuterium at 300 Mev/c with $g_P=-g_N$ and neglecting negative energy state transitions.

have neglected, might introduce an appreciable correction to the cross section.[12]

The point at $\theta=0°$ of Fig. 9, curve D, is uncertain due to the cancellation of the first and second order terms in $1/M$.

Figures 5–8 show the variation with angle of the upper and lower limits of the total cross section for the photoproduction of π^0 mesons in deuterium calculated with $[H_2(p)]_e+[H_2(n)]_e$, that is, neglecting negative energy state transitions. At the meson angles near zero, where transitions to S states are important, the upper limit is quite accurate. For mesons emitted in the backward direction, many partial waves contribute to the cross section and therefore the lower limit, which is actually the plane wave result, is likely to be as close to the total cross section as the upper limit.

We have observed that the measurement of the elastic production at any angle determines the sign of g_P/g_N. That is, the coherent production determines the relative phase of the proton and the neutron amplitudes. For $\theta>90°$, the total cross section is chiefly incoherent and is, therefore, essentially independent of the relative sign of g_P and g_N. However, the cross section at these angles is quite sensitive to the neutron contribution and, thus, the comparison of the theoretical results with experiment at large meson angles offers a good method for determining the neutron contribution to the π^0 production.

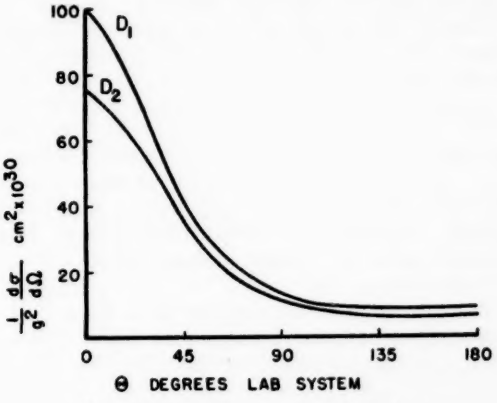

FIG. 6. Same as Fig. 5 at $k=250$ Mev/c.

Cocconi and Silverman[11] have measured the ratio of the deuterium total cross section to the hydrogen cross section when the maximum photon energy is 310 Mev and for $\theta=45°$, 90°, and 135° in the laboratory system. We will first consider the 90° ratio. The measured result is

$$\left[\left(\frac{d\sigma}{d\Omega}\right)_T \Big/ \left(\frac{d\sigma}{d\Omega}\right)_P\right]_{\theta=90°}=1.91\pm0.09.$$

[12] Chew, Goldberger, Steinberger, and Yang, Phys. Rev. **84**, 581 (1951).

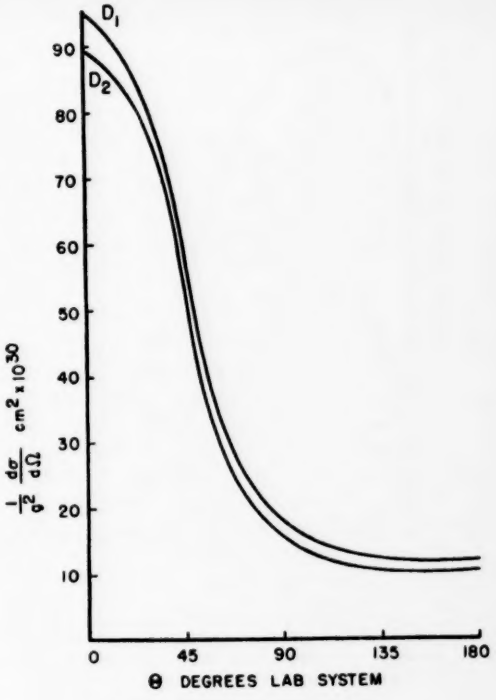

FIG. 7. Same as Fig. 5 with $g_P=g_N$.

The upper limits to the calculated ratios assuming no negative energy state transitions are 1.51 and 1.29 when $g_P=-g_N$ and when $g_P=g_N$, respectively. The larger calculated ratio is smaller than the experimental result by about 20 percent which is outside the range of the experimental error. The reason why the calculated cross section is small is because the neutron con-

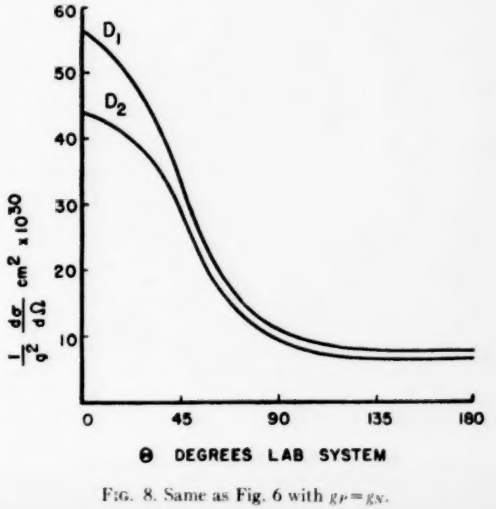

FIG. 8. Same as Fig. 6 with $g_P=g_N$.

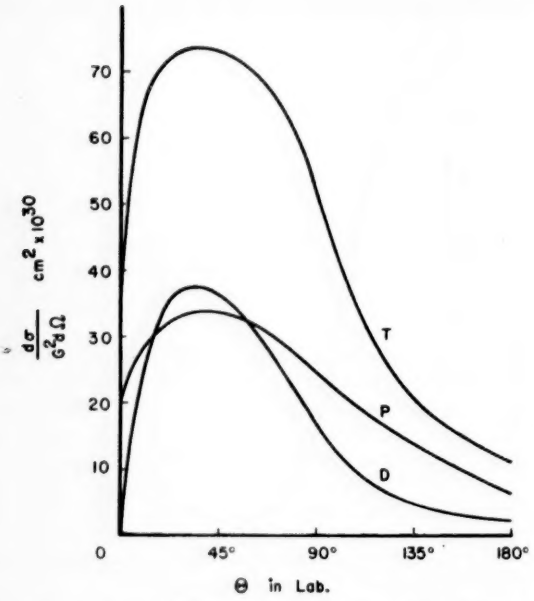

FIG. 9. Curves P, D, and T are the proton, elastic deuterium, and upper limit to the total deuterium cross section, respectively, for $k=300$ Mev/c, assuming an interaction which gives a $(2+3\sin^2\theta')$ proton cross section in the center-of-mass system.

tribution is only about one-half that of the proton when the measured magnetic moment of the latter is used.

If we assume that $\mu_P'=-\mu_N$ and that the proton current does not contribute, however, and furthermore that $g_P'=-g_N$, the upper limit to the ratio of the total deuteron to the proton cross sections at $\theta=90°$ may be estimated to be about 2 in rough agreement with the experimental value (see Fig. 9). When $\theta=135°$ the lower limit to the ratio of the total deuteron cross section to the proton cross section is about 1.5, which may be compared with an experimentally measured result of 1.53. Therefore, the measured ratio of the total cross sections is not inconsistent with the hypothesis that the anomalous moment alone contributes to the photo π^0 meson production. The ratio of the upper limit to total cross section in deuterium to the hydrogen result is 2.1 at 90° and 2.0 at 135° when the proton's cross section is $(2+3\sin^2\theta')$ in the center-of-mass system. The ratio at 135° is approximately 33 percent above the experimental value, which is not inconsistent considering that the experiment at 135° is uncertain to about 20 percent and the upper limit is probably large by about 10 to 20 percent.

Finally, we may predict that if the anomalous moments of the proton and neutron alone contribute to the photoproduction of π^0 mesons, then for $k=300$ Mev and for $\theta=90°$

$$\left(\frac{d\sigma}{d\Omega}\right)_D \Big/ \left(\frac{d\sigma}{d\Omega}\right)_P = 0.5.$$

A ratio of 0.65 is obtained if the calculation is performed with the interaction which yields a $(2+3\sin^2\theta')$ distribution for the proton.

In conclusion, the only interactions which yield a ratio of about 2 in agreement with experiment for $(d\sigma/d\Omega)_T/(d\sigma/d\Omega)_P$ at $\theta=90°$ are the interactions which give approximately equal proton and neutron cross sections. The production of π^0 mesons in photon-nucleon collisions thus appears to be charge independent, although further experiments are clearly necessary.

The author wishes to thank Dr. R. E. Marshak for suggesting this problem and for his continued stimulating guidance. He is also indebted to Dr. C. Longmire and Dr. R. Scaletar for their aid in the early stages of this research.

Average Neutron Total Cross Sections in the 3- to 12-Mev Region*

NORRIS NERESON AND SPERRY DARDEN
University of California, Los Alamos Scientific Laboratory, Los Alamos, New Mexico
(Received October 31, 1952)

An experiment is described for measuring average neutron total cross sections over the 3- to 12-Mev energy region. The neutron source is a collimated beam of fast neutrons emerging from the Los Alamos Fast Reactor, and the detector is a proton recoil ionization chamber which serves as a neutron spectrometer. The average energy spread of the measurements is around 10 percent, and the over-all accuracy of the cross-section determinations is ±10 percent or better. Total cross-section results are presented for H, Be, C, O, Al, Si, S, Fe, Cu, Zr, Pb, Bi, and U. Neighboring elements above Fe are observed to exhibit regularities in their total cross-section patterns.

I. INTRODUCTION

A SURVEY of average neutron total cross sections in the 3- to 12-Mev energy range has been carried out using a method outlined previously.[1] This report presents total cross-section results obtained for thirteen elements scattered throughout the periodic table. Most of the elements were selected on the basis that previous cross-section data were available as a check over part of the energy range. This procedure has provided comparisons with other total cross-section data and has given information on the accuracy, resolution, and general reliability of the present method. This type of average cross-section information will be useful for checking theories treating the variation of total cross section with energy.

II. NEUTRON SOURCE

The neutron source in these experiments is the Los Alamos Fast Reactor.[2] This reactor possesses ports from which collimated beams of fast neutrons can be obtained. These beams have a maximum diameter of about 1 inch, are collimated to within 1°, and possess cadmium ratios of 1.00±0.01 as observed with a U^{235} foil. Above 2 Mev the energy spectrum of the neutrons emerging from these ports is similar to that of a fission neutron spectrum, i.e., the neutron flux decreases exponentially with energy such that approximately every 3 Mev the intensity diminishes by a factor of 10. For example, at a reactor power of 20 kw, the collimated neutron flux at an energy of 3 Mev is 5×10^6 neutrons cm^{-2} sec^{-1} Mev^{-1}, while at 10 Mev the corresponding flux is 3×10^4.

By using a neutron spectrometer type of detector the continuum of neutron energies present in the reactor beam can be converted into pulses whose heights are proportional to the neutron energies. The resulting pulse-height distribution can then be recorded on a multichannel pulse-height analyzer where each channel represents a small neutron energy interval. If an absorber is inserted in the beam, the transmission and total cross section of the material can be determined as a function of neutron energy.

The rapid decrease of the neutron flux with energy sets an upper energy limit to the method at about 13 Mev; above this energy the reactor neutron flux is so small that excessive running times are required to obtain adequate statistical accuracy. At energies below 12 Mev, it is possible to attain 5 percent statistics on cross-section determinations within several hours. A lower energy limit of 3 Mev was selected in this cross-section survey since a considerable amount of cross-section data have already been obtained with better resolution below an energy of 3 Mev.

III. DETECTION SYSTEM

A. Ionization Chamber

The neutron spectrometer detector is a parallel plate ionization chamber. The chamber operates directly in the collimated neutron beam from the reactor port. A radiator containing hydrogen or deuterium[3] (polyethylene) is used to convert the neutrons into proton or deuteron recoils. A platinum collimator immediately following the radiator allows the collimated particles emerging up to 10° of the forward direction to enter

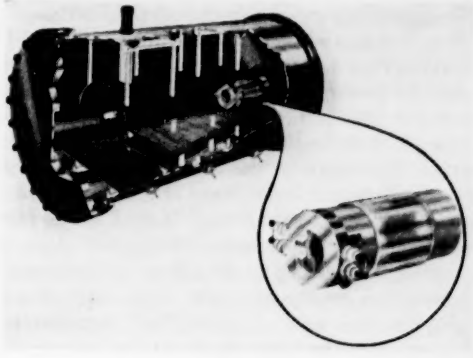

FIG. 1. Perspective view of ionization chamber.

* This work was performed under the auspices of the U. S. Atomic Energy Commission.
[1] N. Nereson, Phys. Rev. **87**, 221 (1952).
[2] Rev. Sci. Instr. **18**, 688 (1947).
[3] The polyethylene with its hydrogen replaced by deuterium was prepared by Dr. Anthony Ronzio of this Laboratory.

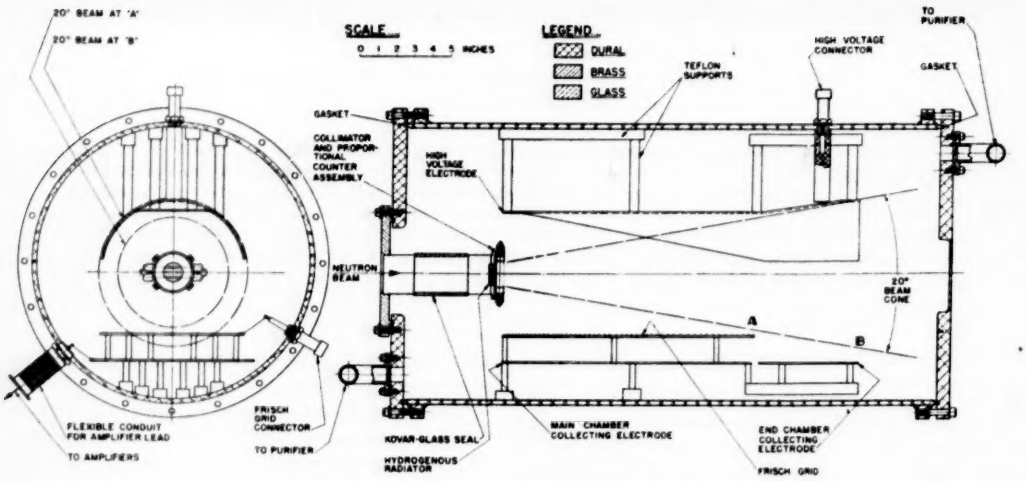

FIG. 2. Front and side views of ionization chamber.

the chamber volume. The energies of these collimated proton or deuteron recoils are determined by measuring their pulse height in a parallel plate ionization chamber equipped with a Frisch grid. In order to reduce background effects, the charged particles first pass through a small proportional counter before entering the main chamber volume. The proportional counter signal is operated in coincidence with the main chamber signal. However, only the pulse height from the main chamber is measured; the energy deposited by the recoil particles in the collimator and proportional counter is only a few percent of their total energy and can be calculated with sufficient accuracy. In order to avoid measuring recoils which leave the main chamber volume, another separate electrode is used which immediately follows the main collecting electrode. The signal from this end electrode operates in anticoincidence with the coincidence signal obtained from the main chamber and proportional counter.

A perspective view of the chamber is illustrated in Fig. 1, and front and side views are given in Fig. 2. The high voltage or top electrode is curved in order to increase the probability of the electrons being directed toward the grid rather than the outer walls of the chamber. Both collecting electrodes operate at ground potential. The shape of the collecting, grid, and high voltage electrodes is in the form of a trapezoid whose width is about 1 in. greater than that of the emerging proton beam. The main reason for this particular shape is to reduce the capacity of the collecting electrodes. In the present design, the capacities of the main chamber and end chamber are 35 $\mu\mu$f and 20 $\mu\mu$f, respectively.

The length of the collecting electrode is designed so that useful signal output is secured over a factor of two in neutron energy using one type of recoil particle with one gas filling. By a combination of proton and deuteron radiators, a factor of three in neutron energy can be covered with one gas filling. For example, at an absolute pressure of 40 psi the neutron energy range from 4.5 to 13.5 Mev can be investigated. The gas filling has usually consisted of a mixture of welding argon plus 2 percent carbon dioxide. With the above gas filling, the average time for the pulse from the main chamber to reach maximum height is about 1 μsec.

A weak Pu^{239} alpha-source, permanently mounted on the high voltage electrode, serves as a check on the operation of the chamber and amplifier in addition to calibrating the pulse height in terms of energy. A deposition of 5 Mev of energy in the main chamber gives a pulse height which is about 25 times the rms noise level of the amplifier system. A pulse-height distribution curve from this alpha-source gives a total width of about 3 percent at half-maximum height. This width is almost entirely due to amplifier noise and,

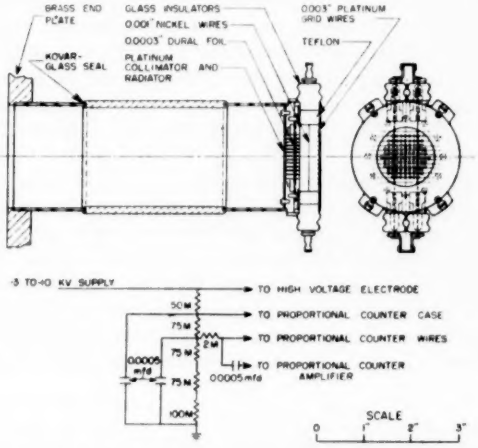

FIG. 3. Detail of collimator and proportional counter.

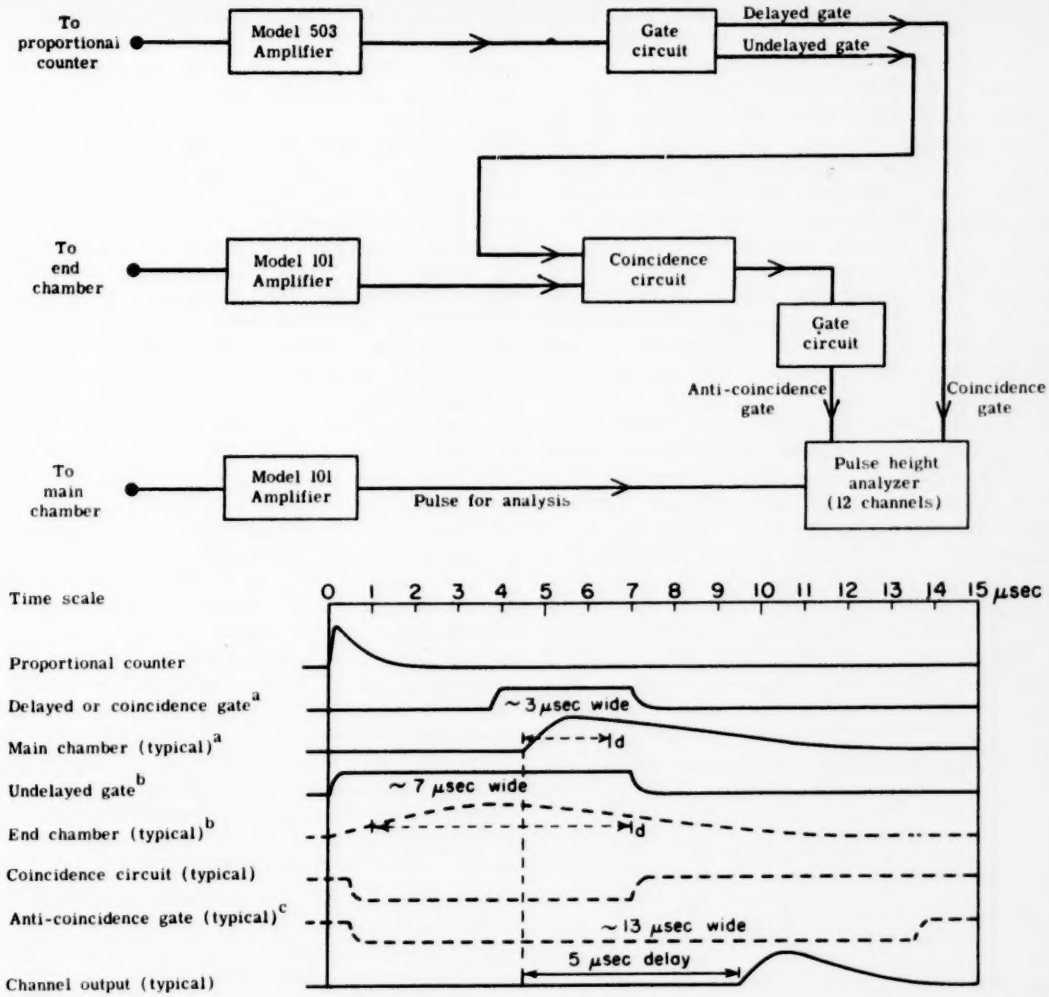

FIG. 4. Instrumentation and pulse shapes associated with ionization chamber. a. Coincidence between these two signals necessary for analyzer to count; b. coincidence necessary for anti-coincidence gate output; c. occurrence of this gate prevents analyzer from counting; d. dotted lines show approximate range of pulse-height peaks.

consequently, would be expected to increase with decreasing energy. In its present design, the chamber has been mainly used for neutron energies above 3 Mev. The practical lower energy limit of the present chamber design is about 2 Mev.

The alpha-source on the top electrode was used to determine the saturation characteristics and proper operating potentials for the chamber. Curves of pulse height *vs* top electrode potential (V_p) at a fixed grid potential (V_g) show a rising characteristic followed by a broad maximum. This maximum region is undoubtedly due to the variation of electron drift velocity in the argon-carbon dioxide gas mixture.[4] The same maximum value of alpha pulse height was observed at all pressures below 40 psi. However, at 49 psi the curves show the saturation pulse height is 3 percent less than at the lower pressures; a 4 percent decrease in maximum pulse height was observed at a pressure of 57 psi. Apparently electron attachment begins to have a noticeable effect at the higher pressures. The curves of pulse height *vs* V_g at a fixed V_p also show a rise followed by an extended maximum. The center of this maximum region occurs at about $V_g = V_p/4$, and the chamber was usually operated at this grid potential value. The potential which would normally exist at the position of the grid due to V_p alone amounts to $V_p/5.5$. A conventional calcium purifier maintained continuously at a temperature of 275°C keeps the pulse height constant. A

[4] See, for example, E. Klema and J. Allen, Phys. Rev. **77**, 661 (1950).

representative example for a fixed gas filling shows that the alpha pulse height did not deviate more than ±0.5 percent during two months of operation.

A detail of the collimator and proportional counter assembly is illustrated in Fig. 3. The collimator consists of about 250 holes, each 0.047 inch in diameter, drilled with a 1 inch diameter circle in a 0.27 inch thick piece of platinum. The collimator is divided into two parts with a 0.0003-inch dural foil sandwiched between the two pieces. The dural foil serves as a pressure seal and thin window for admitting the proton or deuteron recoils to the chamber. This construction has the advantages of permitting radiators to be exchanged or removed on the exterior of the chamber and of not disturbing the gas filling during this procedure. In order to reduce background counts, i.e., counts obtained with the radiator removed, it is essential to remove all traces of grease and organic material from the collimator.

The small proportional counter following the collimator consists of two wires 1 mil in diameter mounted between two plane surfaces spaced 1 cm apart. One of these surfaces is the inside face of the collimator, and the other surface consists of a wire grid mounted on a platinum ring. The grid wires define the field of the counter and permit the recoil particles to pass through the interspaces into the main chamber.[5] Two collecting wires were used in order to insure adequate field strength over the entire collimator area. The counter multiplication depends upon the particular pressure and voltage in use and varies over a range from 5 to 20.

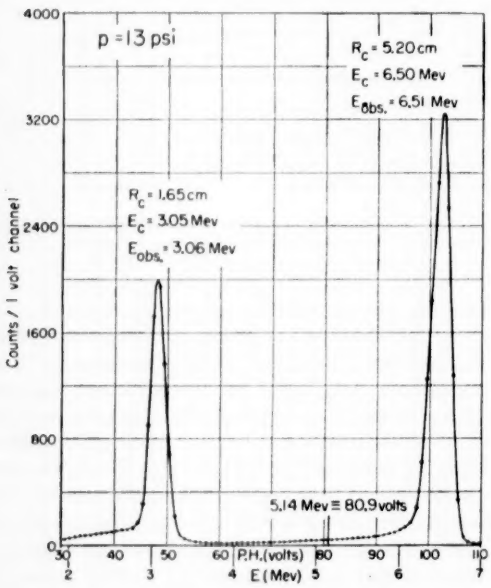

FIG. 5. Pulse-height distribution obtained from chamber with an alpha-source placed in front of collimator.

[5] The twelve platinum grid wires occupy 3 percent of the area which the protons recoils pass through.

The total rise time of the proportional counter signal is about 0.1 μsec for an argon—2 percent carbon dioxide gas mixture. As shown in Fig. 3, the potentials for this counter are derived from the main chamber high voltage supply.

The various electronic units and pertinent signal shapes associated with the ionization chamber are diagrammed in Fig. 4. A 12-channel pulse-height analyzer[6] is used to sort out the pulses from the main amplifier. The analyzer can register a count only during the occurrence of a coincidence gate signal which is initiated by the proportional counter. The delay and width of this gate is adjusted to coincide with the signals from the main chamber. The actual delay and time spread of the main chamber signals vary with the particular pressure and voltage in use on the chamber, but these factors can easily be ascertained by oscilloscope observation. Usually, the width of the gate is adjusted to approximately 3 μsec since the time spread of the main chamber signals averages about 2 μsec.

The analyzer cannot register a count during the period of an anticoincidence gate which is initiated by the end chamber. The end-chamber anticoincidence signal must logically occur shortly after a proportional counter signal; this is assured by having the end-chamber signal in coincidence with an undelayed gate produced by the proportional counter. The analyzer circuit delays each analyzed signal by 5 μsec before the signal goes to the scaler units. This is advantageous in the present case since late anticoincidence gates produced by protons near the high voltage electrode have ample time to nullify the channel output signal.

B. Check with Alpha-Particles

Preliminary testing of the chamber was carried out by placing an alpha-source at the position normally occupied by the radiator. The alpha-source consisted of the active deposit of thorium; this source has a half-life of 10.6 hours and emits two main alpha-groups having energies of 8.776 and 6.054 Mev. The source was deposited within a 1-in. diameter circle on a platinum disk. With the source placed 0.15 in. away from the front face of the collimator, the pulse-height distribution shown in Fig. 5 was obtained. The designations R_c and E_c refer, respectively, to the range and energy of the alpha-particles in the main chamber and were calculated from standard range-energy curves.[7] The energy E_{obs} is the main chamber energy calculated from the above pulse-height distributions using the 5.14-Mev alpha-source for a pulse height *vs* energy calibration. The values of E_c and E_{obs} are in good agreement which proves: (1) the main chamber collects all of the ionization produced beyond the grid wires of the proportional counter, and (2) it is satisfactory to use an alpha-source

[6] Wilkin Johnstone of this Laboratory is responsible for the design of the multichannel analyzer and gating circuits.

[7] Aron, Hoffman, and Williams, Atomic Energy Commission Report AECU-663 (1949), unpublished.

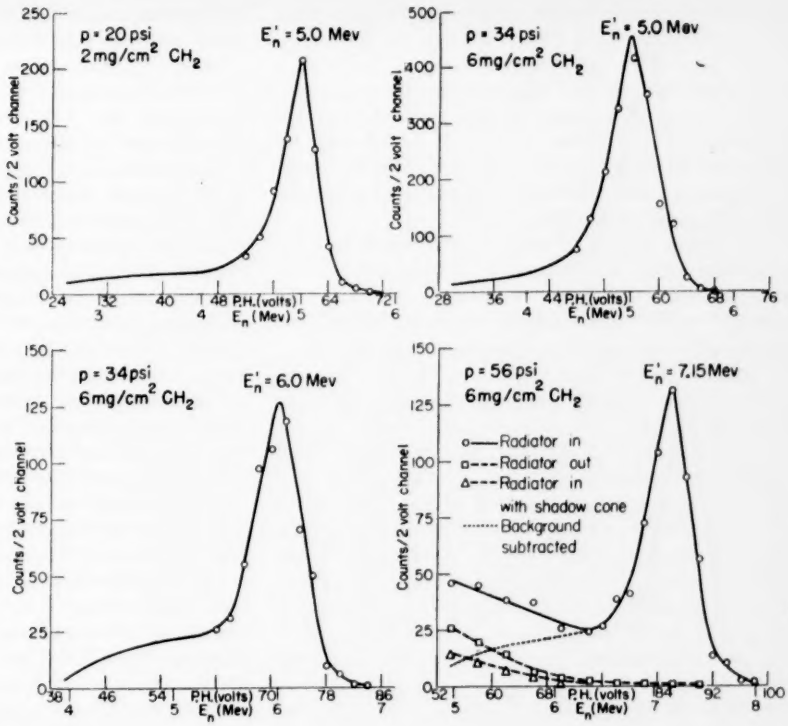

FIG. 6. Chamber pulse-height distributions obtained from monoergic neutrons.

mounted on the high voltage electrode as an energy standard for determining the energy deposited in the main chamber by particles arriving from the collimator.

The alpha-particle distributions show a total width at half-maximum of 7.5 percent and 4 percent, respectively, for the low and high energy distributions. Since the width of the 5.14-Mev alpha-source on the high voltage electrode is about 3 percent, the larger widths for the collimated alphas mainly arise from energy straggling in the collimator, dural foil, and proportional counter. The energy spread is less when the collimated particles deposit a greater fraction of their total energy within the main chamber volume, e.g., when the chamber is operated at a lower pressure. Another factor which broadens the energy spread at lower energies is the noise level of the amplifier; at low energies the noise level is a larger fraction of the pulse height than at the high energies.

The collimated alpha-particle distributions exhibit low energy areas which amount to 12 and 18 percent respectively of the total areas under the high and low energy distribution curves. The alpha-source on the high voltage electrode does not show the above effect. Since similar low energy regions are observed in the distributions for collimated protons and deuterons, it seems reasonable to conclude that these extraneous low energy particles are produced in the collimator. Their source probably arises from the original particles penetrating the edges of the collimating tubes or being scattered by the walls of the collimating holes.

C. Check with Neutrons

It seemed essential to test the chamber with monoergic neutrons in order to duplicate the actual conditions in which the chamber would be used. A Los Alamos electrostatic accelerator, utilizing the d,d reaction, provided a monochromatic source of neutrons within the 5-Mev to 7-Mev energy range. In all of these tests the radiator was located 8.5 in. from the end of the deuterium gas target of the accelerator. The target pressure was usually about 6 psi absolute; this pressure gave a total neutron energy spread ranging from 0.3 to 0.2 Mev for the 5- to 7-Mev range. The chamber was filled with the customary filling of welding argon plus 2 percent carbon dioxide. Irradiations were made with chamber pressures varying from 20 to 57 psi absolute and with polyethylene foil radiators in the 2 to 10 mg/cm² region. The bias on the proportional counter gate circuit was adjusted for normal operation, i.e., set slightly lower than that required to detect those protons traveling the full range of the main collecting electrode.

Typical results of the neutron bombardments are illustrated in Fig. 6 where the number of main chamber pulses in 2-volt channels are shown as a function of pulse-height and neutron energy. The energy E_n is the neutron energy calculated from the 5.14-Mev alpha-

source standard and other chamber constants, while E_n' is the neutron energy derived from the d,d source. Out of a total of ten irradiations the peak of the chamber pulse-height (or energy) distributions always agreed within 1 percent with the energy derived from the accelerator source. When obtaining the neutron or proton recoil energy from the alpha-source pulse height, it is important that the chamber is operated at saturation voltage for the alpha-particles.

The curves in Fig. 6 have a total width at half-maximum which ranges from 9 to 11 percent of the mean neutron energy; this is consistent with the expected width. For example, with a polyethylene radiator of 6 mg/cm^2 at a neutron energy of 6 Mev, the following quantities contribute to the resolution width: (1) the radiator gives a total energy spread of 8 percent, (2) the gas target on the accelerator produced an energy spread of 4 percent, (3) amplifier noise and chamber collection characteristics show a combined width of 3 percent as determined by the alpha-source pulse distribution, (4) the angular divergence of the protons from the collimating holes produces an energy width of about 2 percent, (5) the analyzer channel width of 2 volts contributes a width of 3 percent, and (6) proton energy straggling in the collimator, dural foil, and proportional counter probably contributes about 1 percent to the width. The resultant width of the above six contributions is slightly over 10 percent which agrees with the experimental result in Fig. 6. Since the radiator is responsible for the largest contribution to the energy width, the resolution can be improved slightly by using a thinner radiator. For example, with a 3 mg/cm^2 radiator at 6 Mev, the energy spread from the radiator is 4 percent and the expected resultant width would be about 8 percent; experiments verify this value.

All of the curves except one are shown with background effects subtracted. Two types of chamber background were experimentally measured: (1) that obtained with the hydrogenous radiator removed, and (2) that resulting with the radiator in place when a polyethylene shadow cone was placed between the target and radiator. The exact source of these background contributions is not known but it seems probable that the first type of background arises mainly from organic matter present on the inside face of the collimator and also from n,α reactions in the argon gas. The second background effect is most likely caused by neutrons being scattered into the radiator by the large frontal surfaces of the chamber. Typical magnitudes of the above two background effects obtained with the accelerator source are shown in the lower right corner of Fig. 6. These background curves represent upper limits since subsequent experiments showed that the first type of background can be reduced by a better cleaning of the collimator, and both types of background were improved by using delay line clipping instead of RC clipping on the main chamber pulses. Little effort was directed towards securing the lowest possible chamber background since in the practical application of the chamber these background effects were small and usually did not enter directly into the measurements.

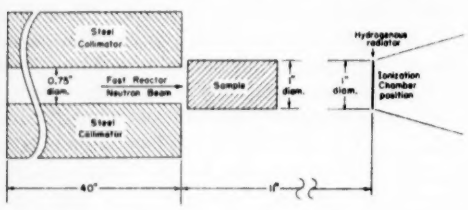

FIG. 7. Experimental arrangement for measuring neutron total cross sections.

The curves in Fig. 6 show an extraneous low energy region which comprises about 25 percent of the total proton recoils. As in the case with alpha-particles, these low energy recoils are believed to arise from protons being scattered by the collimator walls or protons penetrating the edges of the collimating holes. Scattering effects would be expected to decrease with energy whereas penetration effects would increase with the energy and range of the particle. Deuteron radiators instead of proton radiators have been used at neutron energies above 7 Mev in an attempt to diminish penetration effects. Unfortunately, no monoergic neutron checks using deuteron radiators in the chamber have been made since these radiators were not available at the time of the accelerator tests.[8]

The presence of the low energy component in the energy distributions of Fig. 6 is the main reason why the present chamber design is not suitable as a general fast neutron spectrometer. The above effect probably could be minimized by designing a collimator with a smaller ratio of wall surface to hole area.[9] Also, the use of deuteron recoils will improve the distribution.

The present ionization chamber detector is well suited for use with a fission type neutron spectrum. In this type of spectrum the extraneous low energy component produced in the platinum collimator is a smaller percentage of the total neutron intensity than in the case of a monoergic source. For example, using the

[8] Supporting experiments have been carried out using the electrostatic accelerator as a 6.3-Mev neutron source, a proton or deuteron radiator followed by an identical collimator to that used in the chamber, and a nuclear plate as a detector. The resulting recoil distributions showed (1) no low energy area with the collimator removed, (2) a 25 percent low energy region with the collimator and proton radiator, and (3) a 20 percent low energy region with the collimator and deuteron radiator. These experiments proved that an improved distribution curve is obtained with deuteron recoils and that the collimator itself (rather than some part of the main chamber) is entirely responsible for the energy degradation effect.

[9] The simplest way to accomplish this is to employ larger collimating holes so recoil particles could emerge at angles greater than 10°. This change would also aid in increasing the intensity of the recoils but would demand further separation of the chamber electrodes as well as increasing their width. Another suggestion is to make the collimating holes taper toward the center, i.e., have an hour-glass shape.

6-Mev energy distribution curve of Fig. 6 and a neutron spectrum which decreases exponentially by a factor of 10 every 3 Mev, a calculation shows that this low energy contribution is about 15 percent of the total proton recoil intensity at 6 Mev.

Other background effects associated with the above spectrum can be measured experimentally with the fast reactor neutron beam. First, the background obtained with the proton radiator removed is a maximum of 8 percent at energies around 3 Mev and decreases to a minimum of 2 percent at energies around 13 Mev.[10] With a deuteron radiator, the above background figures are reduced by a factor of two. This background is observed with the coincidence gate rate adjusted to the same value as with the radiator in place. The latter procedure is followed in order to include accidental coincidences in this same background figure. The ungated main chamber counts increase only by 20 percent when a radiator is inserted and, as a result, the accidental counts do not decrease appreciably with the radiator removed provided that the coincidence gate rate is adjusted to its normal value. The accidental counts comprise about one-third of the above background percentages and are determined by setting the delay of the coincidence gate at a large time value like 20 μsec or longer. Second, the background arising from neutrons scattered by the chamber walls into the radiator is negligible. This was checked by inserting a 10-in. length of polyethylene in the beam and noting that the observed small intensity corresponded to the transmission expected from this absorber length.

A check on the operation of the chamber in the fast reactor neutron beam consisted of verifying the exponential absorption law for neutrons. The chamber counting rate was observed as various thicknesses of carbon were placed in the beam. The results show that the intensity varies exponentially with carbon thickness down to transmissions of about 0.25. Below transmissions of 0.25, the observed values lie about 1 to 2 percent above the line determined by the previous points; evidently, multiple-scattering effects begin to appear in the results obtained with long absorbers. In order to minimize multiple-scattering effects, total cross-section measurements are made with absorbers having transmissions greater than 0.3 (usually 0.5).

IV. TOTAL CROSS SECTIONS

A. Experimental

The experimental arrangement for measuring neutron total cross sections is illustrated in Fig. 7. Since the majority of neutrons originate just beyond the far end of the steel collimator, the neutron source is about 40 in. distant from the sample. The experimental geometry on the source side of the sample is therefore very good, but the geometry on the detector side is only fair. When the above geometry is used, the correction for in-scattering in the light elements can be neglected, since it does not exceed 0.6 percent for energies below 12 Mev. For the heavy elements, this correction amounts to a maximum of 1.3 percent at 12 Mev.[11] All of the absorbers employed were checked for uniform density and were at least 98 percent pure.

TABLE I. Energy spread of entire detector system for different radiators.

Radiator	Neutron energy Mev	Energy resolution percent
2 mg/cm² CH_2	3.0	10.5
	6.0	5.5
6 mg/cm² CH_2	5.5	11.0
	8.5	7.0
7 mg/cm² CD_2	7.0	13.0
	10.5	8.0
16 mg/cm² CD_2	10.0	16.0
	13.0	11.0
25 mg/cm² CD_2	12.0	20.0
	14.0	15.0

In a typical cross-section measurement the open beam intensity I_0 and the intensity I resulting with an absorber inserted in the beam are observed on the 12-channel analyzer over an energy interval of 3 to 4 Mev. The radiator is then removed,[12] and the corresponding background intensities I_{0b} and I_b are recorded. The transmission $T=(I-I_b)/(I_0-I_{0b})$ can then be obtained and the total cross section calculated for a maximum of 12 energy values. With certain radiators the percent background is the same for the open beam run as for the sample run (i.e., $I_b/I=I_{0b}/I_0$), and in this case it is not necessary to take background runs. A maximum numerical difference of 2 percent has been observed between background percentages taken with the open beam and with a sample.

Statistical reasons account for restricting a given set of data to a 3- or 4-Mev energy interval. The neutron source intensity decreases by a factor of 20 every 4 Mev and the cross section of hydrogen diminishes by approximately a factor of 1.5 over this energy interval. Therefore, if a cross section is measured to ± 1 percent statistical accuracy at the beginning of the interval, the corresponding accuracy at the end of a 4 Mev interval is approximately ± 8 percent. The data for next higher energy intervals are made to overlap the previous one, and the data for this interval are taken with a thicker radiator and a greater analyzer channel width in order to improve the accuracy at the end of the previous energy interval. The radiator thickness is usually chosen so that the energy spread of the entire

[10] This background, when expressed in percent, will vary with radiator thickness. The thicknesses used here were such that the energy spread from the radiator alone never exceeded 10 percent of the mean neutron energy.

[11] Calculated from neutron diffraction scattering curves, B. Feld *et al.*, Atomic Energy Commission Report NYO-636 (1951), unpublished.

[12] More precisely, a blank piece of platinum is substituted for the radiator and its associated platinum backing. A $\frac{1}{32}$-in. thick piece of platinum precedes the radiator in order to prevent charged particles, created externally to the radiator, from entering the chamber volume.

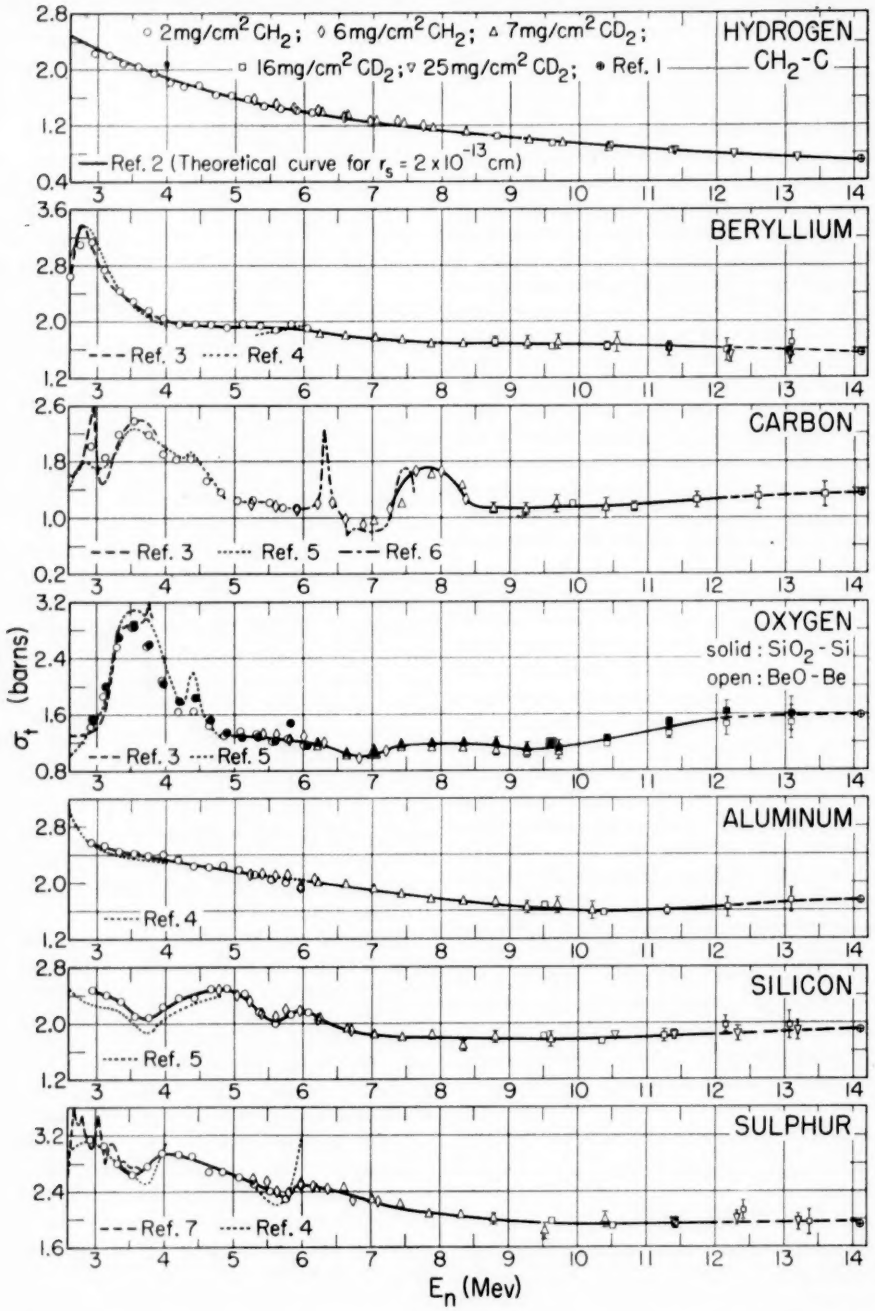

FIG. 8. Average neutron total cross sections of H, Be, C, O, Al, Si, and S. The references in the figure are (1) Coon, Graves, and Barschall, Phys. Rev. **88**, 562 (1952); (2) J. M. Blatt and J. D. Jackson, Phys. Rev. **76**, 18 (1949); (3) R. Ricamo and W. Zünti, Helv. Phys. Acta **8**, 419 (1951); (4) G. H. Stafford, Proc. Phys. Soc. (London) **A64**, 388 (1951); (5) Frier, Fulk, Lampi, and Williams, Phys. Rev. **78**, 508 (1950); (6) Los Alamos Electrostatic Accelerator Group, unpublished data, 1952; (7) R. Ricamo, Nuovo cimento **8**, 383 (1951); (8) Miller, Adair, Bockelman, and Darden, Phys. Rev. **88**, 83 (1952).

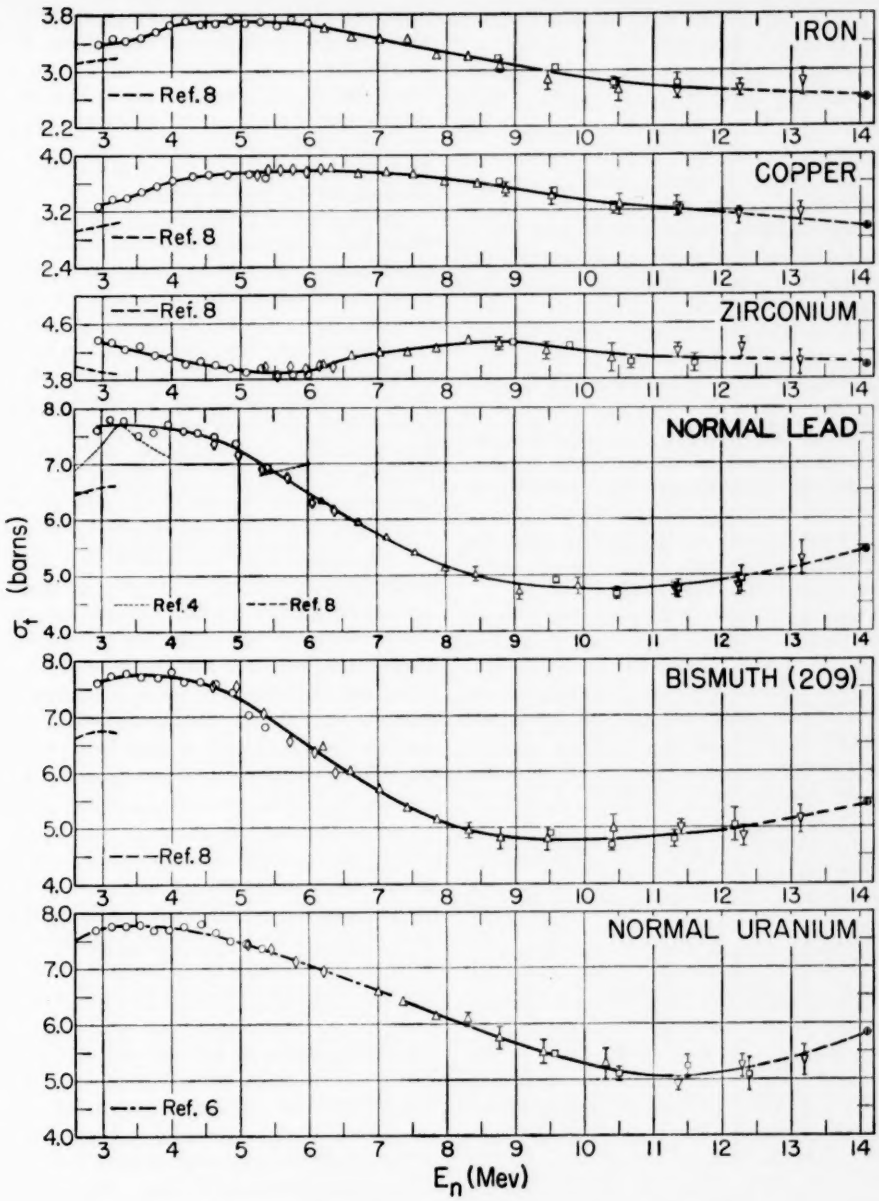

FIG. 9. Average neutron total cross sections of Fe, Cu, Zr, Pb, Bi, and U.

detector system is slightly greater than 10 percent at the beginning of the energy interval (see Table I). However, for neutron energies above 10 Mev the average energy spread has been increased to about 14 percent so as to obtain better accuracy in the 10–13-Mev energy region.

All of the radiator thicknesses listed in Table I are not always used in every cross-section determination. For example, the 6 mg/cm² CH_2 radiator is frequently omitted if the cross section does not vary rapidly in the 5.5 to 7.5-Mev energy region. Also, the 25 mg/cm² CD_2 radiator has been only used to obtain better statistical accuracy in the 12- to 14-Mev energy region. Although the present experiment is capable of providing only ±5 percent statistical accuracy over the 3- to 12-Mev energy region, it is nevertheless useful to obtain a point around 13 Mev in order that the data can be extended closer to the 14.1-Mev value which is accurately known.

B. Results

The results of the measurements are shown in Figs. 8 and 9 where the average neutron total cross section σ_t is plotted against neutron energy E_n. The data obtained with the various radiator thicknesses are identified by separate symbols. A solid line representing the average cross section has been drawn through the present experimental points only in energy regions where better resolved data do not already exist. Where more accurate cross-section information is available, the points from the present experiment are plotted merely for comparison purposes. Since the present method gives poor statistical accuracy above 12 Mev, a dashed line over the 12- to 14-Mev region indicates that the cross-section behavior in this energy interval is uncertain. In conformity with the objective of measuring average cross sections, a smooth curve has been generally drawn through the data points rather than a detailed curve following small fluctuations. This procedure has been especially followed in regions where cross-section variations are smaller than the resolution of the measurements and where the errors are large, as over the 12- to 14-Mev range.

Hydrogen provides a good check measurement on an average cross section since this cross section contains no resonances and is well known. The hydrogen data were obtained by employing polyethylene and carbon absorbers. The results agree well with the theoretical curve of hydrogen for the case of the singlet effective range $r_s = 2\times10^{-13}$ cm. It is interesting to note that a better fit can be observed for $r_s = 2\times10^{-13}$ cm than for $r_s = 1$ or 3×10^{-13} cm.

The resonances in the cross sections of beryllium and carbon provide information on the resolution of the present measurements. The wide resonances, such as the 3.6-Mev carbon resonance, are satisfactorily reproduced by the present method. The 2.75-Mev beryllium resonance (15 percent energy width) is not accurately followed near the peak of the resonance and therefore probably represents the limiting resolution of the method at this energy; this is consistent with the fact that the 2 mg/cm^2 CH_2 radiator contributes an energy spread of 14 percent at the above energy. The beryllium resonance check indicates that it is satisfactory to determine the energy resolution from the detector constants. Narrow resonances (2–3 percent energy width), such as the 6.3-Mev carbon resonance and the 4.4-Mev oxygen resonance, show as slight rises in the present measurements.

The carbon measurements are a representative example of how the present data average out the narrow peaks and dips in cross-section determinations using better resolution; however, in the energy regions where the carbon cross section does not fluctuate rapidly, the data agree well with the other measurements. The electrostatic accelerator check measurements indicate multiple structure is present in the large carbon resonance centering at 7.8 Mev. The low energy side of the above resonance demonstrates how the resolution is improved with the 6 mg/cm^2 CH_2 radiator over that of the 7 mg/cm^2 CD_2 radiator. In energy regions where cross-section results vary with energy, the better resolved values from the thinner radiator have usually been given preference to the more statistically accurate results from the thicker radiator.

The two sets of oxygen measurements were made by using the combinations beryllium oxide-beryllium and quartz-silicon. In regions where statistical errors are small, the differences between these two sets of measurements are probably indicative of the systematic errors present in this experiment, *viz.*, sample purity, sample measurement and weighing, amplifier drift, and analyzer instability. Except for three points, the two sets of data are in agreement within ±10 percent. It is difficult to understand why the data do not agree better with the high energy side of the oxygen resonance centering at 3.5 Mev; the discrepancy is in the wrong direction to be accounted for by poor resolution.

Except possibly for silicon and sulfur, no outstanding similarities in cross-section behavior are observed in the light element results of Fig. 8. It is interesting to note that both silicon and sulfur show cross-section minima in the energy regions of 3.5–3.7 and 5.6–5.8 Mev.[13] However, this common feature may be accidental rather than a regularity since the adjacent element, aluminum, does not show a similar pattern. More information on neighboring elements is needed to establish conclusive cross-section trends for elements in this region.

Common tendencies in average cross-section patterns of neighboring elements are much more evident for the heavier elements illustrated in Fig. 9. Both iron and copper possess broad maxima centering about 5 to 6 Mev and show a decrease in cross section at higher energies. Zirconium, removed from the above elements, shows an entirely different behavior, *viz.*, a minimum in the 5- to 6-Mev region and a considerably smaller percentage change in cross section at higher energies. The heavy elements, bismuth, lead and uranium, show the cross-section regularities of a broad maximum around 3.5 Mev, a rather rapid decrease from 5 to 9 Mev, a minimum in the 9.5- to 11.0-Mev region, and a slow increase towards 14 Mev. The above minimum appears to shift towards higher energies with increasing atomic number. (The lead cross-section measurements consistently showed a small dip at 3.5 Mev.)

The above results are similar to the cross-section regularities observed by Barschall[14] and by Miller and others[15] in the 0.1- to 3-Mev energy region. Further

[13] The second minimum is probably not resolved by the present measurements.

[14] H. Barschall, Phys. Rev. **86**, 431 (1952).

[15] Miller, Adair, Bockelman, and Darden, Phys. Rev. **88**, 83 (1952).

measurements are being carried out on additional elements as more information is desirable to confirm the cross-section trends observed for the present elements.

The authors wish to thank the electrostatic accelerator group for using their machine to check the ionization chamber detector and also for measuring the total cross section of carbon as a check on the present measurements. Edward Jurney of this laboratory assisted materially in the early development of the detector.

PHYSICAL REVIEW VOLUME 89, NUMBER 4 FEBRUARY 15, 1953

Cross Section for the Reaction $D(d,p)H^3$†

C. F. Cook and J. R. Smith*
Rice Institute, Houston, Texas
(Received October 31, 1952)

Cross sections for the reaction $D(d,p)H^3$ have been measured between 50 and 100 kev, using thin targets of deuterium absorbed in zirconium. With the angular distribution data of Wenzel and Whaling, the total cross sections have been calculated. The total cross section at 100 kev is measured to be 14.8 millibarns. A gas target was used to determine the cross section at 420 kev. The value obtained was 49.3 millibarns.

INTRODUCTION

MEASUREMENT of the cross section for the reaction $D(d,p)H^3$ has been the object of several experiments,[1–4] using both thick and thin targets. The present investigation utilizes thin targets of deuterium absorbed in zirconium films evaporated on to ½-in. aluminum disks. Targets of this type have been successfully used to measure the d-T cross section, and the paper by Conner, Bonner, and Smith[5] discusses their preparation.

EXPERIMENTAL METHOD

The experimental apparatus used was essentially the same as that employed in measuring the d-T cross section at low energies, and the reader is referred to the earlier paper for details of the construction. The deuteron beam from the Cockroft-Walton accelerator was separated into its mass components and deflected 10° by a magnetic field. The beam was collimated by two $\frac{3}{16}$-in. diameter apertures, one of which was 10 cm above, the other 30 cm below the center of the 2½-in. diameter pole faces of the magnet. Deuterons then struck the target at an angle of 20° to the normal. Disintegration protons were counted at an angle of 90° to the incident deuteron beam by a counter filled to a pressure of ½ atmosphere with a mixture of argon plus 5 percent CO_2. The counter accepted protons in a solid angle defined by a 1.00-cm circular aperture located 7.64 cm from the center of the target. The solid angle was thus 0.01346 steradian. With a voltage of 1300 v on the counter, the bias curve showed a plateau 40 volts wide.

The number of incident deuterons was determined by measuring the charge deposited on the target with a current integrator of the type described by Watt.[6] Secondary electrons produced at the lower slit and at the target were electrostatically repelled to their respective origins. Correction for neutralized deuterons in the beam was made by taking a background count with the charged beam bent away from the target by a strong permanent magnet placed between the target and the lower slit. At the highest energies the neutral correction amounted to 2 percent; at 50 kev it was 4 percent.

The number of deuterium atoms per square centimeter of the Zr targets was determined by comparing the proton yield of each target with that of a deuterium gas target. The gas target is illustrated in Fig. 1. The deuteron beam from the Van de Graaff generator was defined by S' to be 5 mm in diameter and then entered the target through an aluminum foil having a thickness of 1.26 mg/cm². The energy of the deuterons incident on the foil was 800 kev. The energy loss in the foil was calculated from the data of Warshaw[7] to be 380 kev, so that the energy of the deuterons incident on the deuterium gas was 420 kev. Protons from the d-D reaction were counted at an angle of 90° to the beam by a counter consisting of thin anthracene flakes mounted on a 5819 photomultiplier tube. The solid angle was defined by aperture B, a ⅜-in. hole covered with an aluminum foil 0.020 mm thick and located 4.4 cm from the center of the beam. When the yield of the gas target was to be determined, slit A, 0.626 cm

† This work was supported by the U. S. Atomic Energy Commission.
* National Science Foundation Predoctoral Fellow.
[1] Bretscher, French, and Seidl, Phys. Rev. **73**, 815 (1948).
[2] Moffat, Roaf, and Sanders, Proc. Roy. Soc. **A212**, 220 (1952).
[3] Arnold, Phillips, Sawyer, Stovall, and Tuck, Phys. Rev. **88**, 159 (1952).
[4] W. A. Wenzel and W. Whaling, Phys. Rev. **88**, 1149 (1952).
[5] Conner, Bonner, and Smith, Phys. Rev. **88**, 468 (1952).
[6] B. E. Watt, Rev. Sci. Instr. **17**, 334 (1946).
[7] S. D. Warshaw, Phys. Rev. **76**, 1759 (1949).

wide, defined a length of beam as the source of protons. The effective length of beam seen by the counter was calculated to be 0.690 cm. When the yields from the Zr–D targets were to be determined, slit A was removed and a target holder inserted. The Zr–D targets were held so that the deuteron beam struck them at an angle of 20° to the normal, which is the same angle at which data were taken on the Cockroft-Walton accelerator.

RESULTS

Three calibrated targets were used to determine the D–D cross section at 100 kev. Two of these had Zr deposits of 50 $\mu g/cm^2$, and the third had 25 $\mu g/cm^2$. The respective energy losses for deuterons at 100 kev, including the loss in the deuterium, were 8 and 4 kev.[7,8]

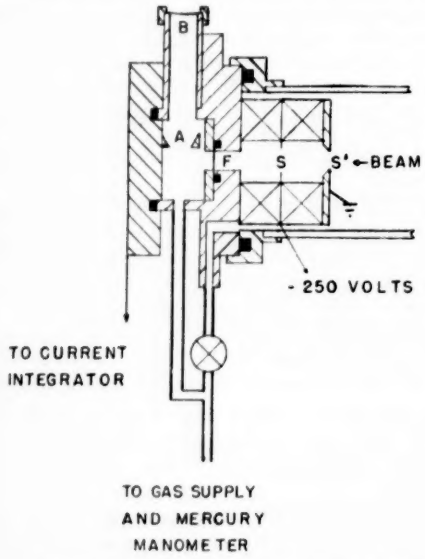

FIG. 1. Gas target arrangement for calibration of zirconium-deuterium filled targets with the Van de Graaff. The analyzed beam passed through collimator S', through the secondary electron guard electrode S, through the foil F into the gas target. Connections to S' and S were made by colloidal graphite lines painted on the inside of the glass tube. The slits A and B defined the counting length of the beam as seen by the photomultiplier.

The average value for the differential cross section at 90° was found to be 1.01 mb/steradian at 100 kev. The total cross section was computed from the differential cross section, using the angular distribution data of Wenzel and Whaling.[4] The value obtained was 14.8 mb. The probable error, computed from the deviations from the mean with the three targets, was 4 percent. Total error is estimated at 6 percent.

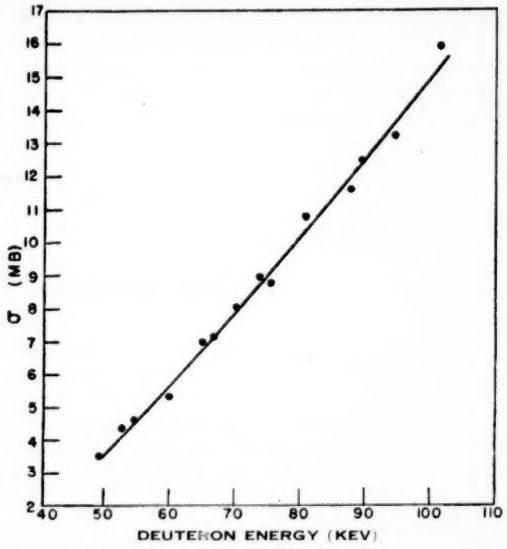

FIG. 2. D(d,p)H^3 total cross section. Deuteron energies plotted are those at the center of the target.

Cross sections below 100 kev were obtained with a Zr–D target for which the energy loss for 100-kev deuterons was 8.5 kev. This target was not calibrated, but absolute magnitudes were obtained by normalizing the yield curve to the mean value given by the three calibrated targets at 100 kev. The d–D excitation curve for the region 50–100 kev appears in Fig. 2. Since the curve is approximately linear in this region, deuteron energies plotted are those at the center of the target.

The gas target yield obtained during the Zr–D target calibration was used to calculate a value for the cross section at 420 kev. The resulting value was 2.88 mb/steradian at 90° in the laboratory system. Using the angular distribution data of Wenzel and Whaling, we obtain 49.3 mb as the total cross section at 420 kev.

Our measurements using Zr–D targets are from 4 percent (at 100 kev) to 17 percent (at 60 kev) lower than the recent measurements of Arnold *et al.*,[3] and from 7 percent to 25 percent below the results of Wenzel and Whaling.[4] The value for the cross section at 420 kev is 8 percent below that reported by Wenzel and Whaling.

[8] C. M. Crenshaw, Phys. Rev. **62**, 54 (1942).

Nuclear Alignment and the Entropy of Liquid He^3

BERNARD WEINSTOCK, BERNARD M. ABRAHAM, AND DARRELL W. OSBORNE
Argonne National Laboratory, Lemont, Illinois

(Received November 10, 1952)

By consideration of the melting pressure data it is shown that calculations implying that the nuclear spins in liquid He^3 are appreciably aligned at temperatures above 0.5°K are inconsistent with the assumption that the nuclear spins are randomly oriented in the solid. The expression

$$S_{liq}=R\ln 2+0.344RT+0.013RT^3$$

for the entropy of liquid He^3 (including the nuclear spin entropy) is consistent with the vapor pressure data from 1.0°K to 2.5°K and with the melting pressure data from 0.5°K to 1.5°K.

SINCE He^3 has a nuclear spin of $\frac{1}{2}$, there is a contribution of $R\ln 2=1.38$ cal deg^{-1} mole^{-1} to the entropy at temperatures where the spins are randomly oriented. At sufficiently low temperatures the spins in solid and liquid He^3 will be aligned in an ordered fashion, and the nuclear spin entropy will become zero. It is well known that solids (excluding those with *ortho* and *para* modifications) do not begin to lose their nuclear spin entropy until temperatures below 0.01°K have been reached; therefore, it is expected that the entropy of solid He^3 will be $R\ln 2$ or more down to at least 0.01°K. In liquid He^3, however, according to the calculations of Pomeranchuk,[1] Lifshitz,[2] and Singwi,[3] there is an appreciable ordering of the spins and an accompanying decrease of the entropy below $R\ln 2$ at temperatures near 1°K. It is the purpose of this article to point out that these calculations disagree with the melting pressure data.[4,5] Further, an expression for the entropy of liquid He^3 will be presented which is consistent with both the vapor pressure[6] and the melting pressure measurements.

In a paper published before the solidification of He^3 was reported Pomeranchuk[1] predicted that in liquid He^3 the effects connected with the exchange of two He^3 atoms would lead to the antiparallel orientation of neighboring nuclear spins for $T\lesssim 1$°K, and that the nuclear spin entropy would then fall linearly with temperature. Since that part of the entropy not due to nuclear spins also falls, he estimated that the total entropy of the liquid would become less than $R\ln 2$ below *ca* 1°K. On the other hand, the exchange effects are not important in the solid, because the amplitude of the zero oscillations is considerably less than the distance between the atoms, and hence the nuclear spins are freely oriented down to temperatures so low (*ca* 10^{-7}°K) that kT is comparable with their magnetic interactions. Consequently, down to *ca* 10^{-7}°K the entropy of solid He^3 is equal to $R\ln 2$ plus a negligible contribution from the vibrational modes of motion. If the Debye θ is approximately 30, as in solid He^4, the latter contribution is only 0.02 cal deg^{-1} mole^{-1} at 1.5°K. In short, he predicted that the entropy of the liquid is less than that of the solid for temperatures less than about 1°K and greater than that of the solid for higher temperatures. He further pointed out it would follow from the Clapeyron equation,

$$dp/dT=(S_{liq}-S_{sol})/(V_{liq}-V_{sol}), \qquad (1)$$

and from the fact that the molal volume of the liquid is greater than that of the solid, that the melting pressure curve would have a minimum at *ca* 1°K and a negative slope from this temperature down to 10^{-7}°K.

The measurements[4,5] of the melting pressure of He^3 (the circles in Fig. 1) show, however, that Pomeranchuk's prediction regarding the liquid is incorrect. From 1.5°K down to 0.5°K the slope of the melting pressure curve is positive, and hence in this range the entropy of the liquid is greater than that of the solid. The measurements below 0.5°K, which approach a constant melting pressure of 29.3 atmos, are possibly in error due to poor thermal contact in the apparatus and are excluded from this discussion. It is entirely possible that at an experimentally realizable temperature below 0.5°K the exchange effects will result in alignment of the spins in the liquid and a consequent decrease of the entropy below $R\ln 2$. Since this would cause the melting pressure to rise with decreasing temperature, measurements of the melting pressure with improved thermal contact below 0.5°K are in progress to investigate this possibility. However, at present it can be concluded that there is no appreciable alignment of the nuclear spins in liquid He^3 down to 0.5°K.

Although it is now clear from the melting pressure that the entropy of the liquid is greater than $R\ln 2$ at 0.5°K, Lifshitz[2] had shown that the vapor pressure data are consistent with Pomeranchuk's prediction that the entropy of the liquid has already fallen to $R\ln 2$ at 1°K. This was done by computing the chemical potential of the liquid from the vapor pressure measurements in the range 1°K to 3°K. The chemical

[1] I. Pomeranchuk, J. Exptl. Theoret. Phys. (U.S.S.R.) **20**, 919 (1950).
[2] E. M. Lifshitz, J. Exptl. Theoret. Phys. (U.S.S.R.) **21**, 659 (1951).
[3] K. S. Singwi, Phys. Rev. **87**, 540 (1952).
[4] Osborne, Abraham, and Weinstock, Phys. Rev. **82**, 263 (1951).
[5] Weinstock, Abraham, and Osborne, Phys. Rev. **85**, 158 (1952).
[6] Abraham, Osborne, and Weinstock, Phys. Rev. **80**, 366 (1950).

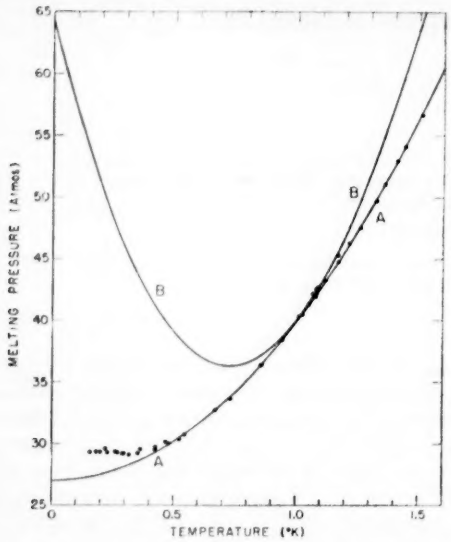

FIG. 1. Comparison of the experimental melting pressure of He^3 (circles) with curves calculated from the vapor pressure data. Curve *A*, calculated from Eq. (13), corresponds to no nuclear alignment in the solid and the liquid. Curve *B*, calculated from Eq. (7), corresponds to nuclear alignment in the liquid but not in the solid.

potential of the liquid at its vapor pressure, μ_{liq}, including the contribution $RT\ln 2$ due to nuclear spin, is given by the familiar relation

$$\mu_{liq}=\mu_{gas}=RT\ln p-2.5RT\ln T-RT\ln 2 -RT\ln(2\pi m)^{3/2}k^{5/2}h^{-3}+Bp-\tfrac{1}{2}B^2p^2/RT. \quad (2)$$

In his calculation Lifshitz omitted the terms in the second virial coefficient, B, which are due to the gas imperfection. He then fitted an expansion in powers of T^2 to μ_{liq}, a form suggested by the expression for the chemical potential of a degenerate Fermi-Dirac gas at low temperatures, and thus obtained

$$\mu_{liq}/R=2.82-0.38T^2+0.017T^4. \quad (3)$$

The entropy of the liquid at its saturated vapor pressure can be calculated from the thermodynamic relation

$$S_{liq}=-(d\mu/dT)_{sat}+V_{liq}(dp/dT)_{sat}, \quad (4)$$

or, if the volume of the liquid is neglected,

$$S_{liq}/R=0.76T-0.068T^3. \quad (5)$$

According to this expression the entropy of the liquid becomes $R\ln 2$ at 1°K, as predicted by Pomeranchuk.

Since the gas imperfection corrections are significant even at 1°K, the authors have repeated Lifshitz' analysis of the vapor pressure data retaining the terms due to the gas imperfection, $Bp-\frac{1}{2}B^2p^2/RT$, in Eq. (2). This was done in order to determine whether or not the calculated liquid entropy would become $R\ln 2$ at less than 0.5°K due to the influence of these terms. The values of the second virial coefficient, B, were interpolated graphically from the theoretical calculations of de Boer, van Kranendonk, and Compaan.[7] The range of the vapor pressure measurements was 1.02°K to 3.35°K, but the computations were limited to the temperature range 1°K to 2.5°K, because the virial expansion becomes inadequate for the saturated vapor above 2.5°K. The following expressions, in which account was also taken of the volume of the liquid,[8] were obtained for the chemical potential and entropy of the liquid:

$$\mu_{liq}/R=-2.715-0.489T^2+0.0133T^4 +R^{-1}\int_0^T V_{liq}(dp/dT)_{sat}dT, \quad (6)$$

and

$$S_{liq}/R=0.978T-0.053T^3. \quad (7)$$

According to Eq. (7), the entropy of the liquid falls to $R\ln 2$ at 0.73°K, instead of 1°K, but this result too is inconsistent with the melting pressure data.

It is also interesting to note that Singwi[3] has calculated the entropy of a degenerate Fermi-Dirac gas with a molecular weight of 3 and a density equal to that of liquid He^3 and has shown that these values agree fairly well with the entropy[6] of liquid He^3 derived from the vapor pressure measurements in the range 1°K to 2.5°K. The entropy of a degenerate Fermi-Dirac gas at low temperatures is given by the expansion

$$\frac{S}{R}=\frac{\pi^2}{2}\left(\frac{T}{T_0}\right)-\frac{\pi^4}{20}\left(\frac{T}{T_0}\right)^3+\cdots, \quad (8)$$

where

$$T_0=h^2(3/\pi)^{2/3}\rho^{2/3}/8m^{5/3}k. \quad (9)$$

When the mass of the He^3 atom and the density of liquid He^3 at low temperatures (0.0792 g/cm³)[8] are inserted in these expressions, it is found that T_0 is 4.85°K and

$$S/R=1.02T-0.043T^3. \quad (10)$$

According to Eq. (10), the temperature at which the entropy of the liquid falls to $R\ln 2$ is 0.69°K. The agreement between the theoretical coefficients in Eq. (10) and the empirical coefficients in Eq. (7) is indeed striking, but the agreement must be considered to be fortuitous. As was shown above, any treatment which predicts an entropy of less than $R\ln 2$ for the liquid at or above 0.5°K disagrees with the melting pressure data and the concept that there is no nuclear alignment in the solid above 0.01°K.

During the course of this analysis the previously published values of the entropy[6] of liquid He^3 were re-evaluated. These values were derived from the vapor

[7] de Boer, van Kranendonk, and Compaan, Physica **16**, 545 (1950).
[8] Grilly, Hammel, and Sydoriak, Phys. Rev. **75**, 1103 (1949).

pressure equation,

$$\log_{10}p_{mm} = -0.97796/T + 2.5\log_{10}T + 0.000302T^3 + 1.91594, \quad (11)$$

which represents the experimental data very accurately over the entire range of the measurements, 1.02°K to 3.35°K. However, a numerical error was found in the values of $(S_{\text{real}} - S_{\text{ideal}})$ that were used to correct the entropy of the ideal gas for gas imperfection. The corrected values (including the nuclear spin entropy) are given in Table I.

Equation (11) is unsatisfactory below 1°K because it gives an extrapolated entropy of 1.80 cal deg^{-1} mole^{-1} (including the nuclear spin entropy) at 0°K, rather than the value $R\ln 2 = 1.38$ cal deg^{-1} mole^{-1} that is expected in the absence of nuclear alignment. A relation that fits the vapor pressure data from 1° to 2.5°K as well as Eq. (11) and that in addition gives $S_{\text{liq}} = R\ln 2$ at 0°K was obtained as follows. The chemical potential of the liquid, calculated from the vapor pressure data and Eq. (2), was fitted by an expression of the form

$$\mu_{\text{liq}}/R = -A - T\ln 2 - CT^2 - DT^4 + R^{-1}\int_0^T V_{\text{liq}}(dp/dT)_{\text{sat}}dT. \quad (12)$$

The empirical values found for the coefficients are $A = 2.323$, $C = 0.172$, and $D = 0.0032$. The entropy and the heat capacity derived from (12) are

$$S_{\text{liq}}/R = \ln 2 + 0.344T + 0.013T^3, \quad (13)$$

and

$$C_{\text{liq}}/R = 0.344T + 0.039T^3. \quad (14)$$

The entropies from Eq. (13) are in satisfactory agreement with those given in Table I, and in view of the melting pressure results Eqs. (12), (13), and (14) can be extrapolated with some degree of confidence down to at least 0.5°K. These equations will fail only when the temperature is so low (below 0.5°K) that nuclear alignment occurs in the liquid. The vapor pressure equation corresponding to Eq. (12) is not convenient for calculation, but fortunately it need not be used, because there is no significant difference between the pressures calculated from it and from Eq. (11) down to 0.5°K.

The agreement between the melting pressure data and Eq. (13) can easily be shown by integrating the Clapeyron equation [Eq. (1)] after substituting Eq. (13) for S_{liq} and $R\ln 2$ for S_{sol}. It is only necessary to make the reasonable assumption that $(V_{\text{liq}} - V_{\text{sol}})$ is a constant over the range of the measurements. The value of $(V_{\text{liq}} - V_{\text{sol}}) = 1.12$ cm^3/mole is then determined from the observed slope, and the constant of integration is determined from the observed melting pressure at one temperature. The resultant equation,

$$p = 27.0 + 12.6T^2 + 0.2T^4 \text{ atmos}, \quad (15)$$

is shown as curve A in Fig. 1, and it can be seen to agree very well with the experimental points from 1.5°K to 0.5°K. The experimental data are also represented adequately by the simpler equation which was previously reported:

$$p = 26.8 + 13.1T^2 \text{ atmos}. \quad (16)$$

In contrast, the melting pressure calculated from Eq. (7) and the Clapeyron equation, with $S_{\text{sol}} = R\ln 2$, is shown as curve B in Fig. 1. $(V_{\text{liq}} - V_{\text{sol}})$ was again assumed to be constant and was evaluated as 0.73 cm^3/mole from the slope at 1°K; the constant of integration was chosen to fit the observed pressure at the same temperature. The curves calculated from any of the equations that imply alignment of the nuclear spins in the liquid above 0.5°K [Eqs. (5), (7), or (10)] are similar to curve B, and all are in striking disagreement with the melting pressure measurements. It must be pointed out, however, that if there were nuclear alignment in solid He^3 in the temperature range 1.5°K to 0.5°K the melting pressure calculated from any of these equations would agree with the experimental melting pressure data.

For these computations the small difference between the entropies of the liquid at its saturated vapor pressure and at the melting pressure was neglected. Since $(\partial V_{\text{liq}}/\partial T)_p$ is probably positive for liquid He^3, the entropy of the liquid is smaller under compression. However, the effect is merely to decrease the calculated value of $(V_{\text{liq}} - V_{\text{sol}})$ and to raise the temperature at which any minimum might occur in the calculated melting pressure curve; the conclusion that there is no appreciable nuclear alignment in liquid He^3 down to 0.5°K is unaffected.

The discussion in this article is based on the accepted view that down to at least 0.01°K there is no appreciable alignment of the nuclear spins in solid He^3. It then follows from a consideration of the observed melting pressure curve, as shown above, that the nuclear spins in liquid He^3 are randomly oriented down to 0.5°K.

TABLE I. Entropy of liquid He^3. (eu = cal deg^{-1} mole^{-1}.)

T (°K)	$\Delta H_{\text{vap}}/T$ (eu)	$S_{\text{ideal gas}}$ (eu)	$S_{\text{real}} - S_{\text{ideal}}$ (eu)	S_{liq} (eu)
1.0	9.12	11.25	−0.04	2.09±0.14
1.5	7.10	9.75	−0.15	2.50±0.17
2.0	5.67	9.00	−0.33	3.00±0.22
2.5	4.32	8.54	−0.56	3.66±0.29

Electron-Positron Annihilation in Flight

S. A. COLGATE AND F. C. GILBERT
Radiation Laboratory, Department of Physics, University of California, Berkeley, California
(Received November 4, 1952)

The positron-electron annihilation cross section has been measured for 50-, 100-, and 200-Mev incident positron energies. Three small proportional counters in a magnetic field determined the incident electron or positron momentum, and a large scintillation counter immediately behind the absorber indicated the disappearance of a particle. The positron annihilation cross section was determined by subtracting the electron loss rate (due mainly to bremsstrahlung energy losses) from the positron loss rate. The cross sections obtained at 50, 100, and 200 Mev were, respectively, 11.0 ± 2.5, 6.3 ± 1.2, and 3.7 ± 0.6 millibarns per electron in a beryllium absorber, in good agreement with Dirac's two-quantum annihilation cross section. The presence of annihilation radiation was detected in coincidence with the disappearance of a positron within a small cone in the forward direction.

DURING the course of searching nuclear plates for electron-electron scattering events with 200-Mev incident electrons, Barkas, Deutsch, Gilbert, and Violet[1] observed two events that corresponded to the disappearance in flight of a high energy electron. These two events appeared quite real with no plausible explanation.

The following experiment was done to gain more information about electron and positron disappearances in general and if possible to explain the two disappearance events observed above.[2,3]

At the outset it was well recognized that positrons should disappear in flight by annihilating with an electron at rest, giving rise to two gamma-rays. This is a second-order process in electrodynamics, and the theoretical cross section was known with some confidence.[4] It was therefore proposed at the beginning to try to observe the annihilation in flight of positrons by a balance type of experiment comparing the "disappearance" cross section of positrons to that of electrons.

A thin radiator (placed in the magnetic field of the pair spectrometer) in the path of the bremsstrahlung beam of the synchrotron is an excellent symmetric source of high energy positrons and electrons. Reversing the direction of the magnetic field changes only the sign of the particles observed in a given direction. The number and direction of the particles relative to the background should stay the same. With this symmetric type source a comparison could be made of the "poor geometry" absorption of positrons *versus* electrons.

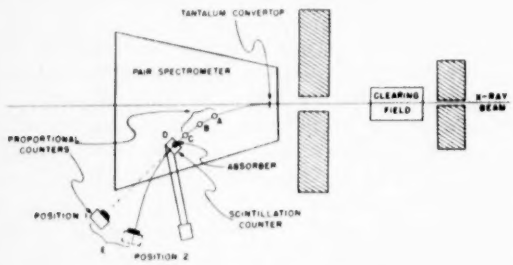

FIG. 1. Experimental arrangement.

At this point it is necessary to consider the absorption processes involved when a 200-Mev electron or positron passes through matter. The known processes are as follows: (1) ionization loss; (2) bremsstrahlung or radiation loss; (3) multiple scattering; (4) Single large angle scattering; and (5) annihilation in flight (positrons only).

Inverse beta-decay is theoretically too small to be considered a competing process. The first four processes should be essentially the same for positrons and electrons.[5] Therefore if we are looking for a difference in the absorption between positrons and electrons, the loss due to these processes should be made small, i.e., the absorber should be thin compared to the range and of low Z. Processes 2, 3, and 4 are proportional to the square of the nuclear charge Z of the absorber, while the anihilation cross section is proportional to Z. For the experimental conditions of a low Z absorber ($Z<10$), a solid angle of the absorber to the detector of 2π, and 50- to 200-Mev incident particles, processes 1, 3, and 4 are small compared to 2 and 5. Bremsstrahlung gives rise to an apparent absorption in the following manner. The incident electron or positron radiates a large fraction of its energy in one event leaving the primary particle with a small energy, say less than 5 Mev. If this residual energy is less than what is required for the particle to get out of the absorber into the detector, then the event appears as an absorption. The absorber thickness then had to be chosen so that the probability of bremsstrahlung loss by this process was smaller than the annihilation cross section. It turned out that 2

[1] Barkas, Deutsch, Gilbert, and Violet, Phys. Rev. **86**, 59 (1952).
[2] Barkas, Deutsch, Gilbert, and Violet, Phys. Rev. **88**, 1435 (1952).
[3] After the initiation of this work, a further search of plates exposed at the same time but at lower energy was made which showed more disappearances of one sign of particles and none of the other. The conclusion drawn in the erratum (reference 2) is that the magnetic field was somehow reversed and that the disappearances observed were annihilations of positrons in flight.
[4] P. A. M. Dirac, Proc. Cambridge Phil. Soc. **26**, 361 (1930).
[5] Electron-electron and positron-electron scattering are different, but at high energy both processes cause only a very small angular deviation of the incident particle and so are not observed as an absorption.

cm of Be gave a bremsstrahlung loss about $\frac{1}{4}$ that of annihilation. Annihilation in flight would occur once in every 300 traversals of the absorber so that an extremely small loss had to be detected.

The apparatus used is schematically shown in Fig. 1. A, B, and C are three thin-walled proportional counters[6] in triple coincidence that defined the presence of a particle of a given momentum. Counter D is a stilbene scintillation crystal 4 cm in diameter by 4 cm thick with a cylindrical well in it 2 cm deep to hold the absorber. When there is no absorber in place, every time a triple coincidence occurs showing that a particle has passed through A, B, C, a fourth pulse should be observed from counter D. The loss of particles between counters C and D is the triple coincidence rate minus the quadruple coincidence rate.

The sensitive volume of counters A, B, and C was roughly a sphere $\frac{1}{4}$ inch in diameter. The alignment was performed both by maximizing the triples to singles ratio, and by accurately locating the counters on a circle, i.e., the orbit of a particle in the uniform magnetic field. Both methods agreed. The ratio of triples to counter C singles rate was roughly 40 percent, showing that the electrons or positrons had small deviation from their calculated orbits. Counter D was required to be extremely efficient if it was to introduce no additional loss factor. The efficiency of a scintillation counter is determined by both the bias setting of the pulse detector and by the number of photoelectrons ejected in the photo tube per incident particle. The counter used had to have a long light pipe to remove the photo tube from the effects of the magnetic field, but in spite of this gave approximately 150 photoelectrons per incident particle. With the electronic bias set at a pulse height corresponding 10 to 15 photoelectrons, the statistical efficiency was better by many orders of magnitude than what was needed. The effective pulse size from a small gamma-source was unchanged for +, 0, and − magnetic field showing that the phototube was sufficiently shielded. The coincidence circuits and gate generators for each counter were standard in design with the exception that the gate generator for counter D had to have zero dead time. In order to record the triples minus the quadrupole coincidence, it was felt at the beginning that a more reliable result could be obtained by recording both the triple and quadruple coincidences separately and then subtracting rather than using an anticoincidence circuit. In order to record reliably the large numbers associated with the triples and quadruples rates, three or more scalers were used in parallel for each.

The reduction of the background loss rate was the major problem in the success of the experiment. This turned out to be principally a counting rate problem, not just a chance coincidence one, but also dependent upon such effects as overloading amplifier *D* with a resulting change of bias and after pulsing of the small proportional counters. During normal running conditions a run of 3000 triples took 15 minutes with a background loss rate of 1 to 3 counts. Both the triples rate and loss rate were essentially entirely due to particles from the radiator. When the radiator was removed the triples rate was reduced by a factor of 800 and the loss rate relative to the primary synchrotron beam was reduced by approximately a factor of 4, so that background from surrounding objects did not have to be considered.

[6] These were Victoreen Geiger tubes cut down in length and refilled.

TABLE I. Experimental results.

Particle	Energy	Absorber	Observed loss per 1000 traversals	Net loss minus background
Positrons	200	Be	5.1	
				3.75±0.5
Positrons	200	none	1.4	
Electrons	200	Be	0.77	
				0.1 ±0.3
Electrons	200	none	0.65	
Positrons	100 Mev	Be	10.5	
				9.5 ±1.0
Positrons	100 Mev	none	1.0	
Electrons	100 Mev	Be	3.7	
				3.2 ±0.6
Electrons	100 Mev	none	0.5	
Positrons	50 Mev	Be	21.0	
				20.4 ±2.0
Positrons	50 Mev	none	0.6	
Electrons	50 Mev	Be	10.0	
				9.4 ±1.0
Electrons	50 Mev	none	0.6	
Positrons	200 Mev	2-cm LiH	2.8	
				2.0 ±0.4
Positrons	200 Mev	none	0.8	
Electrons	200 Mev	2-cm LiH	1.0	
				0.7 ±0.3
Electrons	200 Mev	none	0.3	
Electrons	200 Mev	2-cm Al	4.5	
				3.8 ±0.6
Electrons	200 Mev	none	0.7	
Electrons	200 Mev	3.7 g/cm² Ag	4.2	
				3.0 ±0.6
Electrons	200 Mev	none	0.7	

Positron loss minus electron loss per 1000 traversals	Energy	Absorber	Experimental cross section *per electron* of absorber in millibarns	Theoretical positron annihilation cross section per electron of absorber in millibarns
3.65±0.6	200 Mev	Be	3.7±0.6	3.53
6.3 ±1.2	100 Mev	Be	6.3±1.2	6.35
11.0 ±2.5	50 Mev	Be	11.0±2.5	10.8
1.3 ±0.5	200 Mev	LiH	2.6±1.0	3.53

RESULTS

Table I displays the results on disappearances. Many short runs of background and absorber were used to balance out the effects of changing background. Also the experiment was set up at three different times with at least a month's interval in between, and with different counters. The results were always consistent. The direction of the magnetic field was determined by the force on a current carrying wire, and for no run with a low *Z* absorber was the electron loss rate as large as the positron loss rate.

The Be absorber was used the most to get statistically meaningful cross sections for the positron annihilation in flight process. LiH was used to check the Z dependence of disappearances at 100 and 200 Mev, but counting times were much longer due to its low density. Aluminum and silver absorbers showed too much bremsstrahlung loss at 200 Mev to get meaningful answers for the positron annihilation cross section, but the total loss for electrons was less by a factor of 5 than the cross section that could be ascribed to the two disappearances in nuclear plates. Similarly the electron loss cross section in beryllium and LiH at 200 Mev was less by a factor of 40 than the two disappearances in nuclear plates.

It was felt then that it had been reasonably established that electrons do not disappear in flight in low Z materials by a substantially large factor less than the two events observed in nuclear emulsion. Also, if the electron loss rate is subtracted from the positron loss rate, the remainder loss rate equals the theoretical annihilation cross section at 200, 100, and 50 Mev within statistical accuracy. There remained, however, the need for additional proof that the disappearances of positrons was associated with the annihilation in flight process.

CONFIRMATION OF ANNIHILATION IN FLIGHT

When a high energy positron annihilates with an electron at rest, two high energy gamma-rays are given off which are strongly correlated in the forward and backward direction in the center-of-mass system. In the laboratory system then, there is one gamma-ray with nearly all the energy directed forward and another low energy gamma at large angle. It was attempted then to observe the high energy gamma-ray going forward in coincidence with the disappearance of a positron in the beryllium absorber.

The disappearance or annihilation of the positrons in beryllium was observed essentially the same as before; namely, three counters A, B, and C in coincidence proved the presence of a high energy positron, while a fourth counter D monitored its passage through the absorber. However, instead of determining disappearances by the difference between two large coincidence rates (triples minus quadruples), an anticoincidence circuit was used which finally worked as reliably as the subtraction method. The anticoincidence pulse was then used in coincidence with a fifth counter E. Counter E could be placed in two general positions: (1) the extrapolated positron trajectory in the magnetic field, and (2) the extrapolated gamma-ray trajectory (namely, the tangent to the positron trajectory at the point of the absorber). With counter E in position (1), an efficiency was determined for counting 200-Mev positrons to be (triples+counter E)/triples=70 percent. This efficiently dropped to less than one percent when counter E was moved to position (2), saying that position (2) was essentially outside the positron orbit. With counter E in position (2) in coincidence with the anticoincidence disappearance pulse, i.e., with counter E looking at the gamma-ray trajectory in coincidence with annihilations, the ratio (anticoincidence and counter E)/anticoincidence was less than 5 percent. Counter E was a thin wall proportional counter, and should not detect high energy gamma-rays alone. However, when $2\frac{1}{2}$ radiation lengths of lead (the maximum of the shower curve for 200-Mev gamma-rays) was put in front of counter E in position (2), the the ratio (anticoincidence and counter E)/anticoincidence increased to 50 ± 8 percent. This says that with counter E made sensitive to gamma-rays we see a gamma-pulse in coincidence with the positron annihilation. The half-width of the positron curve for this ratio was approximately the width of the counter, showing that the gamma-rays were directly forward. When electrons were used, these ratios were essentially the same, except that the disappearance rate for electrons was $\frac{1}{4}$ that of positrons. The disappearance of electrons is due to high energy bremsstrahlung loss, which should give one high energy gamma going forward. These facts support the concept of positron annihilation in flight giving rise to at least one high energy gamma-ray.

ACKNOWLEDGMENTS

We particularly appreciate the excellent suggestions of Dr. Barkas and Dr. Alvarez towards the successful completion of the experiment. The extra help and time from the operating crew of the synchrotron under the direction of Mr. George McFarland and Professor A. C. Helmholz was similarly invaluable.

Irreversible Processes with Application to Helium II and the Knudsen Effect in Gases*

O. K. RICE
Department of Chemistry, University of North Carolina, Chapel Hill, North Carolina
(Received October 27, 1952)

It is generally conceded that the pressure difference dp which develops in a steady state, when two portions of helium II are kept at different temperatures and separated by a capillary, is given by $dp/dT = Q/TV$, where Q is the heat absorbed as volume V leaves the capillary at absolute temperature T. London gives $Q=TS$ where S is the entropy, for the case where no heat is absorbed along the capillary ($c=0$), while Gorter gives $Q=Tx_1(\partial S/\partial x_1)$ where x_1 is the mole fraction of normal helium in the helium II. Gorter's equation coincides with London's, which is reasonably well confirmed experimentally, only if $\bar{S}_2$ the partial molal entropy of superfluid is zero. In this paper an analysis of the situation, including a careful discussion of the meaning of Q, is attempted, and it is shown that for $c=0$ London's equation follows from the equation for dp/dT and the conservation of energy. The equations which are developed are quite general, and can be applied directly to other cases, for example, the Knudsen effect in gases. They still do not permit an answer to the question concerning $\bar{S}_2$ for helium, however, and for this purpose an analysis of the processes occurring *within* the capillary is required. It is found that if the thermodynamic properties of the fluid in the capillary are not changed from those of bulk liquid, then Gorter's equation is correct. There seems, however, to be no reason to suppose that they may not be changed, so it is concluded that no direct information regarding $\bar{S}_2$ can be obtained from experiments on the thermomechanical effect. This last statement is considered in connection with some speculations concerning the state of liquid helium in a capillary and in a Rollin film.

1. GENERAL FORMULATION OF THE PROBLEM

IF two portions of liquid helium kept in vessels in thermal contact with reservoirs at slightly different temperatures are connected by a very narrow tube or slit, a pressure difference develops between them, which gives rise to the well-known fountain effect. Fundamentally the phenomenon is of much the same nature as thermal electromotive force. It is related to the fact that when helium enters the capillary a certain amount of heat is given to the reservoir, or, when helium leaves the capillary a corresponding amount of heat is absorbed. The quantitative relationships involved were first investigated by London,[1] following Kelvin's treatment of the thermocouple, which has since been called the method of "pseudo-thermodynamics." More recently they have been discussed by de Groot, Jansen, and Mazur,[2] using the "thermodynamics of irreversible processes" which is based on Onsager's reciprocal relations. It is agreed that

$$dp/dT=Q/TV, \tag{1}$$

where Q is the heat given to the reservoir when a volume V of liquid at absolute temperature T enters the capillary. dp is the pressure difference resulting in a steady state when the temperature difference between the two reservoirs has the value dT, both dp and dT being very small.

The validity of Eq. (1) is not confined to the case of liquid helium. It should hold for any system of one component (in the phase-rule sense) when two portions of the system are separated by a capillary or membrane of any sort, if heat is evolved or absorbed when the liquid enters the capillary or membrane. We shall, in fact, later illustrate this point by considering the application to the Knudsen effect in a gas.

Though there is general agreement as to the validity of Eq. (1) there are also certain difficulties and points of disagreement. One of these has to do with the very general matter of the exact meaning of the quantity Q and its relation to the so-called heat of transfer. Another has to do specifically with the evaluation of Q in the case of liquid helium. It is closely connected with the first question, but can be formulated rather precisely in terms of the two-fluid theory of helium II. In this theory it is supposed that helium II is a mixture of normal fluid and superfluid and that only the superfluid is capable of passing through a very fine capillary. London claims to show, on the basis of the assumption that no heat is absorbed by the superfluid as it passes along the capillary, that

$$Q=TS, \tag{2}$$

where S is the entropy of the fluid passing into or out of the capillary. On the other hand, Gorter[3] claims to have proved that

$$Q=Tx_1(\partial S/\partial x_1)_T, \tag{3}$$

where x_1 is the mole fraction of normal fluid in the mixture. This equation is concurred in by de Groot.

The difference between Eqs. (3) and (2) is perhaps best brought out by noting that $(\partial S/\partial x_1)_T=\bar{S}_1-\bar{S}_2$, where $\bar{S}_1$ and $\bar{S}_2$ are the partial molal entropies, the

* Work assisted by the Smith Research Fund of the University of North Carolina and the Office of Naval Research.
[1] H. London, Proc. Roy. Soc. (London) **A171**, 484 (1939).
[2] de Groot, Jansen, and Mazur, Physica **16**, 691 (1950); S. R. de Groot, *Thermodynamics of Irreversible Processes* (North Holland Publishing Company, Amsterdam, 1951), Chap. VI.
[3] C. J. Gorter, Physica **15**, 523 (1949).

subscript 1 being used always for normal fluid and subscript 2 for superfluid (where there is no subscript, reference will be to the mixture); here we consider Q, V, and S to be associated with one mole. Thus we have, from Eq. (3),

$$Q=Tx_1(\bar{S}_1-\bar{S}_2). \tag{3a}$$

On the other hand, $S=x_1\bar{S}_1+x_2\bar{S}_2$, so Eq. (2) is equivalent to

$$Q=T(x_1\bar{S}_1+x_2\bar{S}_2). \tag{2a}$$

If $\bar{S}_2$ is zero it is seen that Eqs. (3a) and (2a) become identical.

Now it is commonly assumed that the intrinsic entropy of superfluid is zero, or at least negligible. If $\bar{S}_2=0$, however, this means not only that the intrinsic entropy is zero, but also the entropy of mixing with the normal fluid. This is, indeed, the assumption that has been made by Tisza[4] and Gorter. On the other hand, in recent work[5] I assumed that the entropy of mixing is not zero, and hence $\bar{S}_2\neq 0$. The question now arises as to whether experimental confirmation of Eq. (2), or of Eq. (1) with Eq. (2) inserted (and this has been demonstrated at least approximately[6]), is sufficient evidence for deciding that $\bar{S}_2$ must equal zero. This can be determined only by a careful examination of the basis of these equations. In order to effect such an examination we shall turn first to a detailed consideration of the meaning of the quantity Q in Eq. (1). Then we shall discuss the evaluation of Q by a method similar to that of London,[7] but using Eq. (1) instead of the second law of thermodynamics, and finally turning to a detailed consideration of the processes taking place in the capillary.

2. DEFINITION OF Q AND THE HEAT OF TRANSFER

Q has been defined as the heat given to the reservoir when a volume V of liquid, at a particular temperature T and pressure p, enters the capillary or membrane,

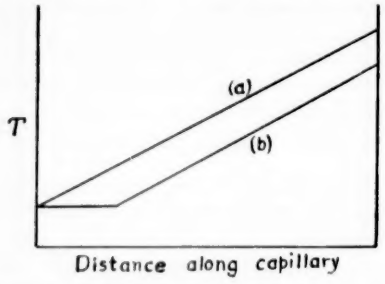

FIG. 1. Temperature distribution in an insulated capillary before and after motion of fluid through the capillary.

[4] L. Tisza, Phys. Rev. **72**, 838 (1947).
[5] O. K. Rice, Phys. Rev. **76**, 1701 (1949); **78**, 182 (1950).
[6] P. L. Kapitza, J. Phys. U.S.S.R. **5**, 59 (1941); L. Meyer and J. H. Mellink, Physica **13**, 197 (1947); Kramers, Wasscher, and Gorter, Physica **18**, 329 (see especially p. 337) (1952).
[7] See W. H. Keesom, *Helium* (Elsevier Publishing Company, Amsterdam, 1942), p. 358 ff.

Q being, of course, a function of T and p and proportional to V. It may be readily shown that this is the negative of the quantity Q^*, which is called the heat of transfer by Denbigh[8] and by de Groot in their consideration of irreversible processes. According to de Groot,[9] Q^* is the amount of heat which is transferred from a vessel in reservoir I, let us say, to one in reservoir II by a unit quantity of matter (which may just as well be taken as the amount having the volume V at temperature T and pressure p) when there is a steady state of the second order between the two reservoirs. A steady state of the second order is one in which the difference of temperature between the reservoirs, which we have called dT, is zero. Under these circumstances dp is also necessarily zero for a one-component system.[10] This being the case, the only things that happen when a volume V of material moves from the vessel in reservoir I to that in reservoir II are that (1) a certain amount of work pV is done on the system in reservoir I and the same amount is done by the other system; and (2) an amount of heat Q is given to reservoir I from the vessel within it, and is taken from reservoir II. Therefore, the transfer of the volume V from I to II results in the transfer of Q units of heat from reservoir II to reservoir I; hence $Q^*=-Q$.

In de Groot's treatment Q^* was originally introduced through its relation to a quantity U^* which is called the energy of transfer. U^* can be defined in terms of the phenomenological coefficients of the Onsager theory, but has been shown by de Groot to be equal to the energy accompanying unit mass (having volume V) from system and reservoir I to system and reservoir II, when they are in a steady state of the second order.[11] The energy which enters system and reservoir II is the intrinsic energy E of the material which enters it, plus the work done on the piston, namely pV, plus the heat Q^* supplied to the thermostat. The same amount of energy leaves system and reservoir I. Thus,

$$U^*=E+pV+Q^*,$$

or

$$Q^*=U^*-H,$$

where H is the enthalpy of an amount of fluid having volume V.

[8] K. G. Denbigh, *Thermodynamics of the Steady State* (Methuen and Company, Ltd., London, 1951), Chap. II.
[9] S. R. de Groot, reference 2, page 88.
[10] Helium II is treated by de Groot as a two-component system in which the two components are in instantaneous equilibrium with each other; this is a one-component system in the phase rule sense. On page 83 of his book (see reference 2) he shows that in such a two-component system in a steady state of the second order the composition in both vessels is constant in time and that the net rate of total chemical production is zero. Thus, if material flows from one vessel to the other the compositions must be the same; otherwise there would be net chemical production. Since the temperatures are the same, the pressures on the two vessels must be the same.
[11] This is true even if they are not in a steady state, so long as they are at the same temperature, but in deriving the connection between U^* and Q^* a steady state of the second order must be considered, since Q^* is defined for such a state.

The quantity Q^* is handled in a somewhat different way by Denbigh, though it is again introduced through its relation to U^* (called Q by Denbigh). He considers a dividing surface between system and reservoir I, and system and reservoir II. Practically all of system I and all of reservoir I are at temperature T and pressure p, while practically all of system II and all of reservoir II are at $T+dT$ and $p+dp$. Since the transfer that occurs is essentially from constant pressure p to constant pressure $p+dp$, we see that the net absorption of heat from the two reservoirs is essentially equal to dH, where dH is the change of enthalpy of material having volume V on going across the boundary line from I to II. Thus, if Q_{I} is the heat given to reservoir I and Q_{II} that absorbed from reservoir II,

$$Q_{\mathrm{II}}-Q_{\mathrm{I}}=dH.$$

If dH is sufficiently small, however, $Q_{\mathrm{II}}=Q_{\mathrm{I}}=-Q^*$, so that Denbigh's interpretation of Q^* is quite equivalent to de Groot's. The utility of Denbigh's formulation is that he can separate the heats absorbed or evolved into three parts, a part Q_{I} absorbed from one reservoir, an equal part given to the other, and a part dH absorbed from one reservoir or another, the exact source of the heat dH making no difference since the amount is so small. This procedure leads to a neat deduction of the fundamental Eq. (1).

It should not, however, be allowed to obscure the fact that Q or Q^* is a quantity which depends on the temperature. It is the quantity which is characteristic of the flow of material from bulk into a capillary or membrane at a given temperature (and pressure). If we have systems I and II at different temperatures, connected by a capillary with a uniform temperature gradient, such as shown in Fig. 1(a), and allow a flow of material to take place in such a way that no heat is transferred to or from the capillary, then after a small amount of flow has taken place, the temperature gradient in the capillary will be disturbed and will look something like that shown in Fig. 1(b). It will now be necessary for heat to flow into the capillary to restore the original gradient. This heat must come from one or both of the reservoirs, and will be added to or subtracted from Q_{I} or Q_{II} or both. This is of no importance to Q_{I} or Q_{II} as long as the temperature difference between I and II is small, but if it is larger it adds an entirely extraneous quantity of heat to Q_{I} and Q_{II}, i.e., one which is not characteristic of the passage of fluid at constant temperature from bulk to capillary or vice versa. It is, therefore, more apropos, if one wishes to consider the variation of Q with temperature, to consider a set-up in which heat can be added or removed along the capillary, assuming the capillary to be in contact at each point with a thermostat which has a fixed temperature, intermediate to the temperatures of the reservoirs I and II. This, it is to be emphasized, can have no effect on the validity of Eq. (1). It is merely a device for finding how Q varies with the temperature.

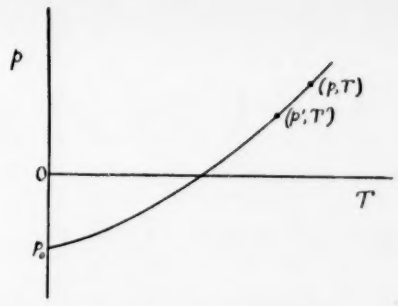

FIG. 2. A quasi-equilibrium line.

3. THE INTERPRETATION OF EQ. (1) AND THE EVALUATION OF Q

It is to be noted that Eq. (1) relates a quantity Q, which—as should now be clear and has been stressed by de Groot—has to do with a process which occurs at constant temperature, to a differential quotient dp/dT, in which the total differentiation indicates a change between two states of the fluid which can exist in a steady state with each other when connected by a capillary or membrane. We will describe two such states as being in quasi equilibrium. Presumably if state A and state B can exist in quasi equilibrium, and the same is true for states B and C, then A and C can also exist in quasi equilibrium. Q and V being functions of p and T, Eq. (1) is the equation for a family of curves in the p *vs* T diagram, which may be called quasi equilibrium lines. We shall discuss some particular quasi equilibrium line, as indicated in Fig. 2, and we shall use the notation indicated. In particular, we shall find it convenient to consider the quasi equilibrium between two states (p, T) and (p', T') as indicated on the figure.

Suppose one mole of fluid were pushed through a capillary from a system at temperature T' and pressure p' to another at T and p. Let Q' be the heat given out when volume V' of the liquid enters the capillary at T', p' and Q the heat absorbed when it emerges at T, p, and let cdT be the heat absorbed from reservoirs along the capillary (as suggested at the end of Sec. 2) when the portion of liquid changes in temperature by an amount dT on passing along the capillary (c is the "Thomson coefficient"). Then the total change of energy of the fluid will be[7]

$$Q-Q'+\int_{T'}^{T} cdT+p'V'-pV, \qquad (4)$$

the pV terms being the respective work terms on or by pistons connected with the vessels at the ends of the capillary. Suppose now the liquid at T' were merely heated up to T and compressed to p, along the quasi-

equilibrium line. Let C_0 be the specific heat under such circumstances. Then the change of energy would be[7]

$$\int_{T'}^{T}\frac{dE}{dT}dT=\int_{T'}^{T}C_0dT-\int_{T'}^{T}p\frac{dV}{dT}dT. \tag{5}$$

By equating (4) and (5), we obtain

$$Q-Q'+\int_{T'}^{T}(c-C_0)dT-\int_{T'}^{T}V\frac{dp}{dT}dT=0. \tag{6}$$

Differentiating Eq. (6) with respect to the upper limit T gives

$$dQ/dT+(c-C_0)-Vdp/dT=0. \tag{7}$$

Now, inserting Eq. (1) in Eq. (7),

$$dQ/dT+(c-C_0)-Q/T=0. \tag{8}$$

Integrating this equation divided by T, we see that

$$\frac{Q}{T}-\left(\frac{Q}{T}\right)_{T=0}=\int_0^T\frac{C_0-c}{T}dT. \tag{9}$$

If we assume that $Q/T=0$ at $T=0°$K, which seems to be experimentally confirmed for helium II, and if $c=0$, it then appears that

$$\frac{Q}{T}=\int_0^T\frac{C_0}{T}dT=S. \tag{10}$$

We thus see clearly the assumptions on which Eq. (2) is based. The most important of these is that $c=0$, and if c is greater than zero, dp/dV will be less than given by Eqs. (1) and (2), which, as remarked, seem to be reasonably well confirmed by experiment. It is still not certain whether these assumptions also require $\bar{S}_2=0$ until we consider the processes in the capillary in somewhat more detail. Before doing this, however, we shall apply the equations of this section, which are actually quite general, to a discussion of the Knudsen effect in a gas.

4. DISCUSSION OF THE KNUDSEN EFFECT

The Knudsen effect occurs when two portions of gas are separated by a very fine capillary or a porous plate with openings so small that collisions between the gas molecules in the capillary or the pores are infrequent compared with the collisions of the gas molecules with the walls.[12] If under these circumstances the two portions are kept at different temperatures, a steady state is set up such that the pressures on the two sides are different. This steady state can be treated by Eq. (1). We shall consider the case of perfect gases which do not interact specifically with the walls of the capillary or pores sufficiently to affect their average energy, but which can, of course, exchange energy with these walls.

The average energy of the molecules of a gas which hit a wall, or an opening in a wall, exceeds the average energy of all the molecules by $\frac{1}{2}RT$ per mole. This amount of heat is absorbed from the thermostat.[13] However, simultaneously the piston operating on the gas does an amount of work equal to $pV=RT$, and this work appears as heat. The net heat flowing into the reservoir is thus $\frac{1}{2}RT$, which is equal to Q. It is shown by de Groot and by Denbigh that using this value of Q in Eq. (1) leads to the correct relationship, $p/p'=(T/T')^{\frac{1}{2}}$.

Since all the equations of Sec. 3, except Eq. (10) are quite general it should be possible, if one can evaluate c, to use them as an alternative method of finding Q. From footnote 13 it is clear that we must have

$$c=C_v+\tfrac{1}{2}R,$$

where C_v is the specific heat at constant volume. It is not necessary to add any term to take care of expansion of the gas in the capillary, since any change of pressure is effected by motion of individual molecules which exchange energy only with the walls. On the other hand, C_0 in this case will be given by

$$\begin{aligned}C_0&=C_v+pdV/dT\\&=C_v+d(pV)/dT-Vdp/dT\\&=C_v+R-Vdp/dT.\end{aligned}$$

Inserting these values of c and C_0 into Eq. (7), we see that $dQ/dT=\frac{1}{2}R$, so if $Q=0$ when $T=0$, we find $Q=\frac{1}{2}RT$, as before. This shows that Sec. 3 is quite consistent with the usual treatment of the Knudsen effect. It is, however, not expeditious to attempt to apply Eq. (9) in this case. For, by Eq. (1), it is readily seen that $Vdp/dT=\frac{1}{2}R$, which makes C_0 equal to c. Only at very low temperatures, where quantum effects are important, will this equality break down, and so only at these low temperatures will there be any contribution to the integral of Eq. (9).

5. THE THERMOMECHANICAL EFFECT IN HELIUM II

We now attempt to give a more detailed discussion of the thermomechanical effect in helium II. This discussion has to be based upon some hypotheses of a speculative nature, for only by a detailed consideration of the properties of helium II and its behavior in a capillary can further light be thrown on the thermomechanical effect. While the conclusions which we can draw are thus tentative, they may throw some light on

[12] See K. F. Herzfeld and H. M. Smallwood in H. S. Taylor and S. Glasstone, *Treatise on Physical Chemistry* (D. Van Nostrand Company, Inc., New York, 1951), third edition, Vol. 2, pp. 134–135.

[13] One may ask why this heat is not immediately given back to the thermostat, as the gas exchanges energy with the walls of the capillary in immediate contact with the thermostat, and presumably regains its normal distribution of velocities. However, the gas which *passes* any point in the capillary must possess an excess of energy of $\frac{1}{2}RT$, just as that which passes into the capillary; so any *net flow* through the capillary carries with it the extra energy which is only given out again when it leaves the capillary.

the possibilities involved. We will make no *a priori* assumptions as to whether the energy or the entropy of mixing is zero,[14] but leave ourselves free to discuss the various possibilities mentioned in Sec. 1.

We start with the two-fluid theory and the usual assumption that only superfluid can move in a capillary. We add to this the more questionable assumption that the superfluid in the capillary behaves as an approximately continuous medium any part of which exerts a pressure on the contiguous parts, and that molecular flow of the type responsible for the Knudsen effect does not occur. We designate the effective pressure of the superfluid as p_{2c} and assume that its effective molal volume can be set equal to $\bar{V}_{2c}$ (the additional subscript c is used to designate quantities in the capillary).

Let us now consider the transport of superfluid along the capillary. There is good evidence that superfluid is mixed with normal fluid, and the equilibrium conditions in the capillary are not very different from those in the bulk liquid.[15] The capillary is, however, able to maintain pressure differences and prevents any motion of the normal fluid. If a portion of superfluid of volume $\bar{V}_{2c}$ goes along the capillary from pressure p_{2c} to pressure $p_{2c}+dp_{2c}$, an amount of work equal to $d(p_{2c}\bar{V}_{2c})$ is done by it upon the surrounding portions of the fluid.[16] This work is furnished by (1) a decrease in the velocify of the fluid, (2) from a change in the intrinsic energy to the system, (3) by forces exerted by its surroundings (e.g., forces of interaction with the normal fluid) upon the portion of superfluid, or (4) as heat absorbed. The role of the capillary is to allow a steady state to be set up in which all fluid velocities are zero, and inasmuch as we wish to consider only situations which are slightly removed from a steady state, the contribution (1) to the work may be ignored. Contributions (2) and (3) —or, rather, the negative of these contributions— may be combined as $d\bar{E}_{2c}$, the change in the partial molal energy, for this is equal to the energy change when the portion of superfluid is transferred from the one portion of the capillary to the other. The heat cdT absorbed when the portion of fluid moves along the capillary through a temperature difference dT will be given by

$$cdT=d(\bar{E}_{2c}+p_{2c}\bar{V}_{2c})=d\bar{H}_{2c}, \tag{11}$$

which is equivalent to de Groot's equation for the heat of transfer in a continuous system with bulk flow. We have set $\bar{E}_{2c}+p_{2c}\bar{V}_{2c}=\bar{H}_{2c}$, the enthalpy of superfluid in the capillary. It is usual to define the partial molal enthalpy of component n of a solution as $\bar{E}_n+p\bar{V}_n$, where p is the total pressure. In this case of the capillary, however, the total pressure is not susceptible of exact definition, and if the chemical potential is defined as $\mu_{2c}=\bar{H}_{2c}-T\bar{S}_{2c}=\bar{E}_{2c}+p_{2c}\bar{V}_{2c}-T\bar{S}_{2c}$, the work done on introducing a certain quantity of superfluid into the capillary has the proper relation to the chemical potential.

Combining Eq. (11) with Eq. (6), we find

$$Q-Q'=\int_{T'}^{T}C_0dT+\int_{T'}^{T}V\frac{dp}{dT}dT-\int_{T'}^{T}\frac{d\bar{H}_{2c}}{dT}dT. \tag{12}$$

If Q is zero when $T=0°$K,

$$Q=\int_{0}^{T}C_0dT+\int_{0}^{T}V\frac{dp}{dT}dT-\int_{0}^{T}\frac{d\bar{H}_{2c}}{dT}dT. \tag{13}$$

Since for the bulk liquid $dH/dT=dE/dT+pdV/dT+Vdp/dT=C_0+Vdp/dT$, we see that Eq. (13) becomes

$$Q=H-H_0-\bar{H}_{2c}+\bar{H}_{2c,0}, \tag{14}$$

where the subscript zero denotes values at $T=0°$K and $p=p_0$. If it is permissible to assume that $\bar{H}_{2c}$ is the same as the corresponding quantity in bulk liquid (i.e., the same function of temperature and of pressure), and if, further, the pressure in the capillary connecting the reservoirs at $T=0°$K and $T=T$ changes uniformly from p_0 to p, the corresponding pressures on the quasi-equilibrium line,[17] then $\bar{H}_{2c,0}=H_0$ and Eq. (14) becomes

$$Q=H-\bar{H}_2=x_1(\bar{H}_1-\bar{H}_2). \tag{15}$$

If the bulk liquid is in internal equilibrium, the chemical potentials of the two fluids must be equal or

$$\bar{H}_1+T\bar{S}_1=\bar{H}_2+T\bar{S}_2, \tag{16}$$

which combined with Eq. (15) gives just Eq. (3a), a form of de Groot's equation. This is of interest because it shows exactly the assumptions upon which de Groot's equation is based. If these assumptions are correct, then it is true that an experimental proof of London's equation would demand that $\bar{S}_2=0$, which is equivalent to saying that c could not be equal to zero unless $\bar{S}_2$ were equal to zero.

However, it is by no means certain that the assumptions which give Eq. (15) are correct.[18] In particular it is not at all certain that the thermodynamic properties are the same in the capillary as in the bulk liquid. It is, indeed, possible to make a quite general statement;

[14] They cannot both be zero. See O. K. Rice, Phys. Rev. **79**, 1024 (1950).

[15] See, e.g., H. P. R. Frederikse, Physica **15**, 860 (1949).

[16] Suppose a portion of fluid of volume V_2 is moved a distance Δx along a capillary of cross section a with a pressure gradient of dp/dx. The difference in pressure at the two ends of the capillary is $(V_2/a)dp/dx$, and the work done by the portion of fluid on the surrounding portions is $a(V_2/a)(dp/dx)\Delta x=V_2\Delta p$ if V_2 remains constant. If V_2 changes there is an added term $p\Delta V_2$, so the total work done in first approximation is $\Delta(pV_2)$.

[17] The conclusion concerning the pressure follows if the thermodynamic properties of liquid in the capillary are the same as in bulk liquid, since we expect thermodynamic equilibrium at the ends of the capillary between superfluid in the bulk liquid and the superfluid in the capillary.

[18] These assumptions, as well as various aspects of both de Groot's and London's treatments, have also been questioned by J. E. Verschaffelt, Bull. Acad. Roy. Belg. **37**, 1120 (1951), who also deals with what happens in the capillary, but apparently has not considered all the possibilities that we discuss below.

namely, we can write

$$T d\bar{S}_{2c} = c dT, \tag{17}$$

which merely states that the change of entropy as the superfluid moves along the tube is equal to the heat absorbed by it. There is, of course, no net increase of entropy indicated by this equation, for the increase of entropy of the helium II is balanced by the decrease in entropy of the reservoirs. This is in accord with the general principle discussed by Prigogine and de Groot that the rate of production of entropy is a minimum when there is a steady state. Thus, a small change in the system such as could produce a very slow flow of material down the capillary, would produce no appreciable change (i.e., a change of higher order) in the rate of production of entropy, which occurs through the steady flow of heat along the capillary due to conduction, and which is not, as we see, augmented by the entropy considered in Eq. (17).

Though Eq. (17) indicates that for c to be zero is a sufficient condition[19] for $\bar{S}_{2c}$ to be zero, we cannot, even admitting this, conclude that $\bar{S}_2$ for bulk liquid would have to be zero. Indeed, it seems not unreasonable to suppose that the capillary produces a greater state of order in the helium II, removing the entropy of mixing. London's original hypothesis was that only pure superfluid (with no entropy) could exist in the capillary. It now seems unlikely that this is the case; however, if the effect of the capillary is to remove any entropy of mixing as well as to allow only superfluid to move in the capillary, much the same effect is produced.

We may expect in any case that the superfluid in the bulk liquid will be in thermodynamic equilibrium with the superfluid in the capillary at its end. We note that if $\bar{S}_{2c}=0$, the chemical potential μ_{2c} of superfluid is the same along the capillary. For $d\mu_{2c}=d\bar{H}_{2c}-Td\bar{S}_{2c}-\bar{S}_{2c}dT$, and the first two terms of the expression cancel according to Eqs. (11) and (17), respectively. In order to have thermodynamic equilibrium at the ends of the capillary μ_{2c} must be equal to the Gibbs free energy G of the bulk liquid. We thus conclude that if $\bar{S}_{2c}=0$, the condition that two portions of the bulk liquid should be in quasi equilibrium is that G should be the same for them, and the equation for a quasi-equilibrium line becomes under these conditions, as has been noted by Tisza,[4]

$$\begin{aligned} dG &= (\partial G/\partial p)_T dp + (\partial G/\partial T)_p dT \\ &= V dp - S dT = 0. \end{aligned} \tag{18}$$

This, of course yields London's equation [Eq. (1) with Eq. (2) inserted].

As noted by Tisza, if $dG=0$ along a quasi-equilibrium line, there is an analogy between the thermomechanical effect and an osmotic pressure. It is important to remember that this analogy is dependent on the assumption that $\bar{S}_{2c}=0$.

[19] It is not a necessary condition, and this will be discussed later.

It is of interest to note that it is necessary for $\bar{S}_{2c}$ to be equal to zero in order for London's equation to hold. It is not sufficient for $\bar{S}_{2c}$ to be constant, although this is enough to cause c to be equal to zero. The more stringent condition $\bar{S}_{2c}=0$ is equivalent to the extra condition $Q/T=0$ at 0°K used in Sec. 3. If $\bar{S}_{2c}=0$, then when we approach 0°K where $\bar{S}_2$ must approach zero, we must have Q/T approach 0; otherwise, the transfer to material from bulk liquid to capillary would be accompanied by a change of entropy of the thermostat which was not matched by a change in entropy of the helium, as it must be if the liquid at the end of the capillary is in equilibrium with bulk liquid.

The deduction of London's equation just given throws further light on the conditions under which London's equation can hold, and we can also learn something about the conditions under which Gorter's equation and London's equation can be true simultaneously. Thus, if $\bar{S}_2$ and $\bar{S}_{2c}$ are both zero, the results obtained are quite in accord with Eq. (14). If $\bar{S}_{2c}$ is zero, then by Eq. (11) the integrand of the last integral in Eq. (13) is zero, and Eq. (14) becomes $Q=H-H_0$. Since G remains constant along a quasi equilibrium line, we must in the case of $\bar{S}_2=0$ also have $\bar{H}_2$ constant along such a line, the change in the enthalpy of mixing being balanced by the change of enthalpy due to pressure. Thus $H_0=\bar{H}_2$ and the above equation reduces to Eq. (15). Furthermore, if $\bar{S}_2$ and $\bar{S}_{2c}$ are both zero, then to have thermodynamic equilibrium between superfluid in the bulk liquid and at the end of the capillary we must have $\bar{H}_{2c}=\bar{H}_2$ as assumed following Eq. (14).

On the other hand, it is perfectly clear that while an experimental proof of London's equation does show that $\bar{S}_{2c}$ is zero, it is not necessary to conclude from such a proof that $\bar{S}_2$ is zero also. If $\bar{S}_2$ is not zero then the establishment of thermodynamic equilibrium between the superfluid in the bulk liquid and the liquid near the end of the capillary requires that there be a change in enthalpy of the superfluid at the end of the capillary. This, in itself, is not surprising; several questions may, however, be raised in this connection. The behavior of the liquid in a capillary is probably quite similar to the behavior of a Rollin film. It is, then, necessary to consider the way in which superfluid may be transferred along a Rollin film, and this clearly requires more knowledge than we now possess about the nature of the Rollin film. Some speculations may, however, be in order. From the experiments of Frederickse on the specific heat of thin absorbed films of helium we know something about the behavior of these films. In the first place we may say that for very thin films, a few molecules thick, the λ-transition is spread out over a greater than normal range of temperatures, so some superfluid must still be present even above the normal λ-point. This superfluid is not in a condition—perhaps not in a sufficiently connected state—so that it can actually show the properties of superfluidity.

Now the Rollin film is of the order of 100 molecular layers thick, and it forms over available surfaces quite suddenly as the temperature is lowered past the λ-point. In the outer edges of the Rollin film the liquid must be in nearly the same state as bulk liquid. This does not say, however, that the superfluid cannot be in a somewhat different condition near the wall, and for a greater distance than the natural thickness of the film *above* the λ-point; in fact, the peculiar ability of the superfluid to stabilize so thick a film would imply that this must be the case. If it is true that $\bar{S}_2 \neq 0$, and still London's equation holds, then it must follow on the basis of the above picture, that the partial molal entropy of the superfluid near the wall must be zero (and its enthalpy must have the proper value for it to exist in equilibrium) and the superflow must take place in these layers. One might question the hypothesis, and feel that it is easier to believe from the experimental check of London's equation simply that $\bar{S}_2$ is equal to zero for bulk liquid as well as for layers near the wall of the tube. However, the thermomechanical effect alone cannot prove this, and the discussion of the effect of He^3 on the λ-point does offer some, at least circumstantial evidence, that $\bar{S}_2$ may not be zero.[20]

In conclusion we should call attention once more to the tentative character of the very mechanistic approach used in this section. Gorter's equation appears to rest necessarily on some such mechanistic approach with, in addition, some such special assumptions as we have indicated. London's equation, on the other hand, can be based upon a much more general type of deduction and related directly to a quantity like c which can be, at least in principle, experimentally determined.

Without committing them to any of the views expressed in this paper, I wish to thank Professor S. R. de Groot and Dr. K. G. Denbigh for stimulating discussions.

[20] J. C. Morrow, Phys. Rev. **84**, 502 (1951).

PHYSICAL REVIEW VOLUME 89, NUMBER 4 FEBRUARY 15, 1953

Field Emission: Large Current Densities, Space Charge, and the Vacuum Arc*†

W. P. DYKE AND J. K. TROLAN
Physics Department, Linfield College, McMinnville, Oregon

(Received October 16, 1952)

Field emission was obtained from a single crystal tungsten emitter under conditions of very high vacuum and clean surfaces. The geometry of the emitter was determined by electron microscopy permitting accurate calculation of both the surface electric field and an average current density. The use of pulse electronic techniques extended the observations to the upper limit of the current densities for which the normal field emission was stable. Above this limit an explosive vacuum arc occurred between electrodes.

From these experiments the following conclusions were drawn. (1) The wave mechanical, image force corrected theory quantitatively predicted the observed average current density up to that density for which space charge dominated the emission. (2) Space charge was effective at a current density of the order of 10^7 amperes/cm^2, where a marked deviation occurred from the usual current-voltage relationship. Space charge effects permitted the simultaneous operation of multiple emitting areas of differing geometries. (3) At a still higher critical current density in the range 10^7 to 10^8 amperes/cm^2, a field emission initiated vacuum arc occurred between electrodes resulting in a change of emitter geometry. Current density was the dominant criterion for the initiation of the vacuum arc.

THE field emission of electrons from a cold metallic cathode occurs in the presence of a large surface electric field. Observations on the effect were published by Lilienfeld[1] in 1922 following the initial report of Wood;[2] later, Millikan and Lauritsen[3] introduced the following empirical relationship describing the phenomena:

$$I = C \exp(-B/V), \tag{1}$$

where I and V are current and voltage, respectively, and C and B are constants.

Classical theory[4] fails completely to provide a field emission mechanism. According to wave mechanics, which has been applied with increasing success, the copious conduction electrons penetrate the potential barrier at the metallic surface when the barrier is thinned by the applied field. Comparisons between experiment and the original theory of Fowler and Nordheim,[5] which assumed a simple triangular poten-

* This work was supported by the Research Corporation, the U. S. Office of Naval Research and Linfield College; additional support during the later part of the work was received from the Microwave Laboratory of the University of California.

† Preliminary reports on this work were given at several meetings of the Division of Electron Physics of the American Physical Society: Phys. Rev. **82**, 575 (1951); **85**, 391 (1952); **85**, 752 (1952). As partial fulfillment for the Ph.D. degree, preliminary data to part of this work was submitted to the Physics Department, Oregon State College by the second author.

[1] J. E. Lilienfeld, Physik. Z. **23**, 506 (1922).

[2] R. W. Wood, Phys. Rev. **5**, 1 (1897).

[3] R. A. Millikan and C. C. Lauritsen, Proc. Natl. Acad. Sci. U. S. **14**, 1 (1928).

[4] W. Schottky, Z. Physik **14**, 80 (1923).

[5] R. H. Fowler and L. W. Nordheim, Proc. Roy. Soc. (London) **A119**, 173 (1928).

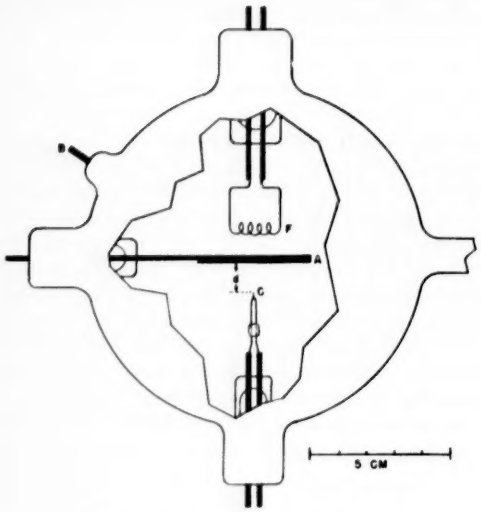

FIG. 1. Experimental field emission tube.

tial barrier, have been well summarized by Jenkins.[6]

When the theory[5] is modified to include the effect of the electron image force,[7] there results the relationship[8]

$$J=1.55\times10^{-6}\frac{F^2}{\phi}\exp\left[\frac{-6.85\times10^7\phi^{\frac{1}{2}}f(y)}{F}\right], \quad (2)$$

where J is the current density in amperes/cm^2, F is the electric field in volts/cm, ϕ is the work function in electron volts, and $f(y)$ is an elliptic function of the variable

$$y=3.78\times10^{-4}F^{\frac{1}{2}}/\phi.$$

Values of $f(y)$ are available in tabular[7] or graphic[9] form.

Early comparisons between experiment and theory were limited by the inability to resolve field emitter geometries by use of optical microscopy. Haefer[10] improved the resolution of the emitter geometry by use of electron microscopy and verified Eq. (2) within a rather large experimental error, which was due to the use of an approximate electric field calculation[11] and the inability to view the emission pattern[12] and hence to judge the surface cleanliness while the current-voltage relationship was observed. Current densities up to 10^6 amperes/cm^2 were recorded for the steady state emission to which observations were limited.

Since the theory (2) predicts current densities in excess of 10^{10} amperes/cm^2, which is considerably greater than those reported previously[10] by direct current methods, it is of interest to extend the comparison between experiment and theory by the use of suitable pulse electronic techniques with which improved cathode stability would be expected, since positive ion bombardment, resistive heating, surface contamination, migration, etc., are thus minimized.

The predicted field current densities are sufficiently large to stimulate interest in the practical application of field emission and to support its proposed contribution to voltage breakdown in vacuum. It was therefore desirable that the experimental observations include the upper limit of current densities for which the normal field emission was stable at microsecond pulse lengths and those densities above which voltage breakdown occurred between electrodes.

EXPERIMENTAL METHOD

The experimental tube envelope (Fig. 1), which was Pyrex, enclosed a needle shaped tungsten field emission cathode (C) which faced the anode (A) a sheet of 5-mil molybdenum, with an anode-cathode spacing $d=0.5$ cm. Electrons from the filament F were used to heat the anode by bombardment during the outgassing procedure.

A thin aluminum coating was evaporated onto the interior of the glass envelope of the experimental tube and connected electrically to the inseal B. It was held at anode potential in order to prevent the glass envelope from charging electrically. It has been found impossible to obtain reliable, reproducible data when uncoated envelopes of the same type were used.

The present anode structure was chosen to inhibit cathode contamination and voltage breakdown due to anode effects when large field currents were emitted. The anode was outgassed, cleaned, and smoothed at high temperature to minimize the bombardment of the cathode by anode material, ions, or clusters. The cathode surface was known to be clean and smooth (prior to breakdown) judged from electron micrographs, electrical behavior, and from the operation of numerous similar cathodes in preliminary experiments in which the emission pattern was viewed on metal backed phosphor anode screens. Suitable techniques for emitter fabrication, conditioning, and high vacuum were thus chosen;[11] however, metal backed phosphor anodes, which were not readily outgassed, contributed excessive cathode contamination when the emitted direct current was large, and were thus not suited to the present experiments.

The field emission cathode was electrolytically etched from a blank of commercial 5-mil tungsten wire (Callite 200H) mounted at the apex of a hairpin filament which was used to outgas and smooth the emitter.[11]

The experimental tube was evacuated with a type GHG-10-02 D.P.I. mercury diffusion pump and liquid air traps. The high vacuum side of the system was baked at 500°C, after which all metal parts (except the

[6] R. O. Jenkins, *Reports on Progress in Physics* (The Physical Society, London, 1943), Vol. IX, p. 177.
[7] L. W. Nordheim, Proc. Roy. Soc. (London) **A121**, 626 (1928).
[8] A. Sommerfeld and H. Bethe, *Handbuch der Physik* (J. Springer, Berlin, 1933), Vol. XXIV, No. 2, p. 441.
[9] F. R. Abbott and J. E. Henderson, Phys. Rev. **56**, 113 (1939).
[10] R. H. Haefer, Z. Physik **116**, 604 (1940).
[11] Dyke, Trolan, and Dolan (to be published).
[12] E. W. Mueller, Z. Physik **106**, 541 (1937).

coating *B*) were outgassed simultaneously at a temperature above which evaporation was appreciable. After a minimum of four such cycles, the experimental tube, a Bayard-Alpert ionization gauge,[13] and a separate Pyrex envelope housing a tantalum getter filament were sealed off as a unit at a pressure of 10^{-9} mm of Hg or better as indicated by the gauge. Subsequently, a layer of tantalum was evaporated onto the wall of the getter tube, after which all metal parts of the experimental tube were again heated. Residual gas was thus transferred to the active tantalum layer, and after several such cycles the pressure of chemically active gases was reduced to 10^{-12} mm of Hg or better, judged by the contamination rate of the field emission cathode.[14] The final vacuum was thus sufficiently good to insure that the electrode surfaces remained free from contamination by residual gases for a time that was long compared with that needed for the experiment, i.e., several hours.

Under these conditions it was possible to draw stable direct currents up to 8 milliamperes at 20 kv, corresponding to a cathode current density of the order to 10^6 amperes/cm^2 as will be shown later. Although the cathode would probably emit larger stable direct currents, the 8-milliampere current limitation was imposed to avoid excessive anode temperature which accelerates the contamination process. At this level the contamination of the cathode surface was evidenced by a decrease in direct current over a period of seconds, the cathode returning to its initial condition following a flash at 2200°C for a few seconds in the absence of field. The contaminant was probably oxygen[12] liberated at the anode, whose temperature exceeded 1000°C at the current and voltage levels indicated above. Pulsed currents considerably larger than those achieved with direct current techniques were drawn without evidence of cathode contamination.

Figure 2 describes the experimental system. Potentials in the range 0–20 kv were furnished by a rectified 800-cycle power supply whose input was regulated mechanically by the inertia of a motor-generator set. During direct current operation, potentials were read by a Weston Model 622 milliammeter in series with a 20-megohm Weston Type 2 resistor. Currents were indicated by a current sensitive Leeds & Northrup Type R galvanometer.

During pulsed operation, a positive potential which approximated a square wave of either $\frac{1}{2}$ or 2 microsecond duration and whose amplitude was variable from 2 to 35 kv was furnished by a pulse generator which included a conventional 4 section, 6.7 ohm line (for 2 μsec operation) or a 50-ohm coaxial cable (for $\frac{1}{2}$ μsec operation) either of whose outputs (8 kv or less) was switched by a triggered spark gap directly to the experimental tube or to the primary of a pulse transformer (T807, AN/APS-3). Its output potential, which was applied directly to the anode of the experimental tube, was divided by a conventional calibrated capacity divider[15] whose output was connected to the deflection plates of a Tektronix Type 511 oscilloscope (CRT_1). A Fairchild Type A, 35 mm f/2.3 automatic camera (C_1) recorded the current which was drawn by the experimental tube. For this purpose, a noninductive carbon resistance was inserted between the cathode and ground and was connected at the cathode end directly to the deflection plates of CRT_2. A Tektronix 517 oscilloscope was used to record the current in the latter part of the work.

Pulsed data were taken on a single-shot basis. A key activated the trigger generator, Fig. 2, whose voltage impulse caused the system to cycle once and then return to the quiescent state. It simultaneously triggered the pulse generator and the sweeps of both oscilloscopes and opened the shutters of the cameras (C_1) and (C_2) and advanced their films. Filament temperatures were measured with a Leeds & Northrup optical pyrometer.

A Sorenson voltage regulator stabilized the primary supply for both oscilloscopes.

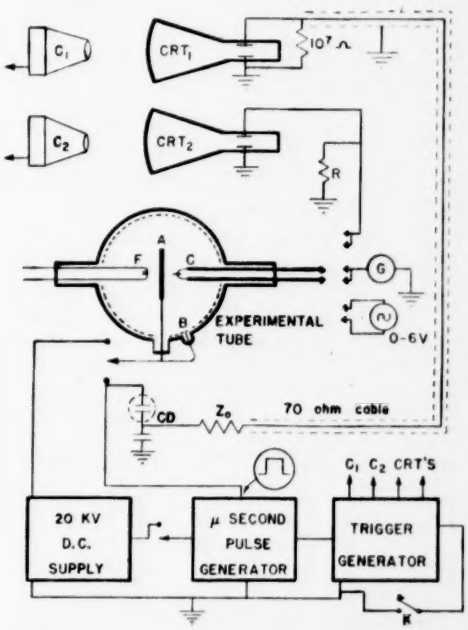

FIG. 2. Experimental electronic circuit used for both pulse and direct current measurements. C—camera; CRT—oscilloscope; G—galvanometer; CD—capacity divider.

[13] R. T. Bayard and D. Alpert, Rev. Sci. Instr. **21**, 6, 571 (1950).

[14] J. A. Becker, Report Eleventh Annual Conference on Physical Electronics, Massachusetts Institute of Technology, 1951 (unpublished).

[15] G. N. Glasoe and J. V. Le Bacqz, *Pulse Generators* (McGraw-Hill Book Company, Inc., New York, 1948), Radiation Laboratory Series.

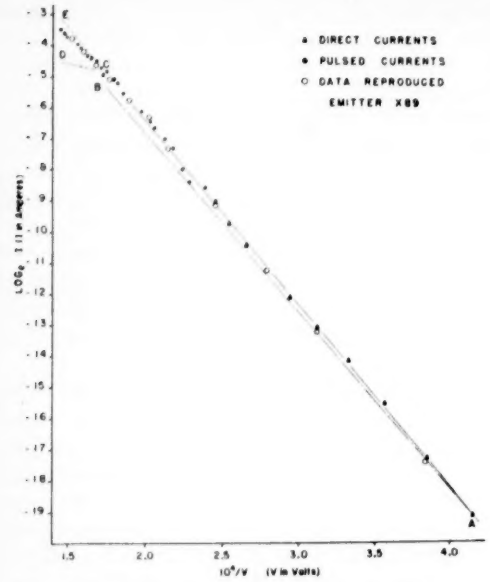

FIG. 3. Field current-voltage characteristic for combined pulse and direct current operation of emitter X-89. Curve AB represents the characteristic for the hypothetical case of a constant emitting area equal to that at A. Curve CE was predicted by the theory (2) and curve CD from $J \propto V^4$, both assuming a uniform distribution of current density and a constant emitting area.

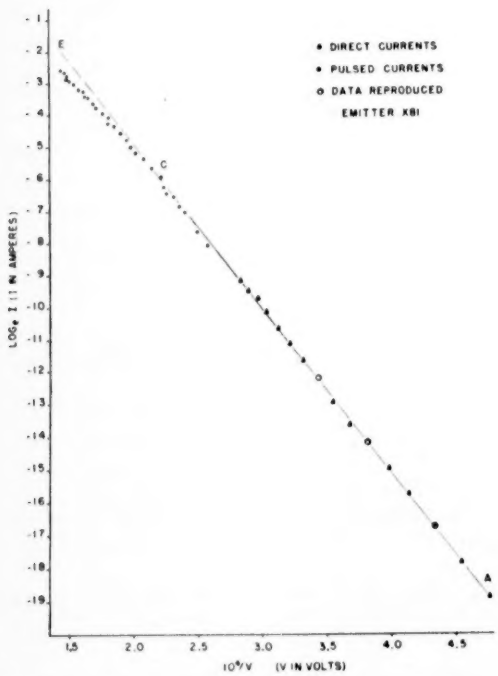

FIG. 4. Field current-voltage characteristic for combined pulse and direct current operation of emitter X-81.

EXPERIMENTAL RESULTS

The current-voltage relationships for emitters X-89, X-81, N-10, and Q-7 for combined direct current and pulsed operations are shown in Figs. 3, 4, 5, and 6, respectively.

Figure 3 illustrates the typical experimental procedure. Direct current readings were taken, then repeated (not shown). Pulsed currents of 1 μsec duration were then drawn, immediately following which the data were reproduced in the sense of decreasing currents, the reproducibility precluding the possibility of significant

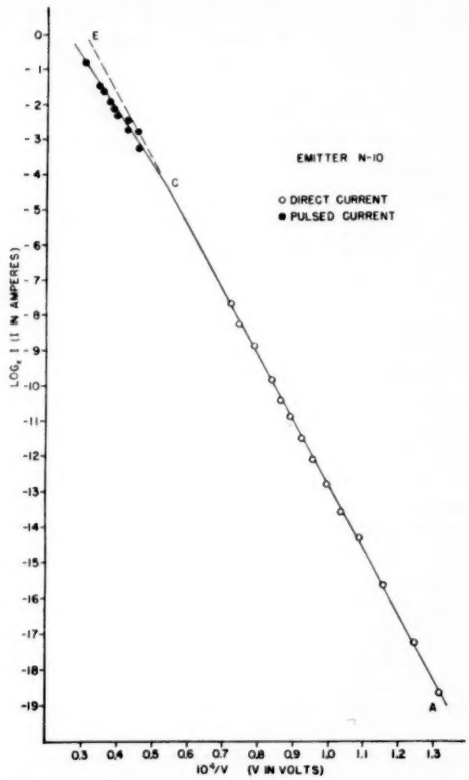

FIG. 5. Field current-voltage characteristic for combined pulse and direct current operation of emitter N-10.

cathode contamination or geometric alteration during the experiments.

The current-voltage relationships in Figs. 3, 4, 5, and 6 have several characteristics in common.

1. Each graph is linear for a considerable range of currents (A to C) below a critical current I_C, in which range the empirical equation (1) was confirmed.

2. At currents greater than I_c the current-voltage relationships depart from linearity in the direction of lower current for a given voltage, the departure presumably being due to space charge, since cathode contamination or geometric alteration are precluded by the reproducibility of the data.

3. At voltages slightly higher than the maximum value shown on each graph the normal field emission was abruptly terminated

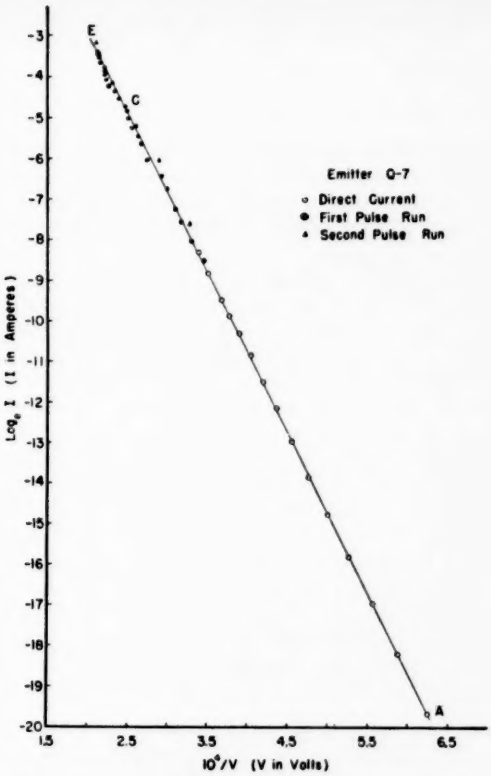

FIG. 6. Field current-voltage characteristic for combined pulse and direct current operation of emitter Q-7.

by a low impedance vacuum arc (except for emitter X-89). While the pulsed field emission was stable at current densities a factor of two or more lower than the arc level, the emitter tip was usually damaged (melted) during the arc.

The emission from X-89 was discontinued at a current level slightly below that for which an arc was expected, and the emitter was removed from the experimental tube in order to obtain the electron micrographs of two profiles of the emitter shown in Fig. 7.

Electron micrographs of two profiles of emitter N-10 are shown in Fig. 8A, prior to insertion into the experimental tube (the radius of this emitter was later increased slightly by surface migration at high temperature during the final outgassing procedure, judged from its subsequent electrical behavior). After arc damage this emitter appeared as in Fig. 8B, which is a composite of several electron micrographs. Figure 9 shows a typical profile of emitter Q-7 after arc damage.

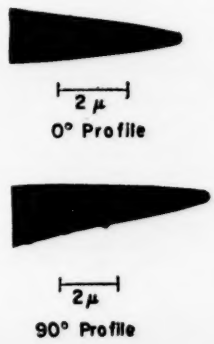

FIG. 7. Electron micrographs of two profiles of emitter X-89 following its experimental use as a field emitter.

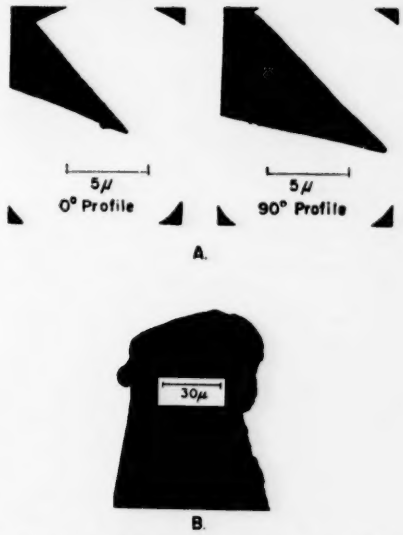

FIG. 8. A. Electron micrographs of two profiles of emitter X-89 prior to its insertion into the experimental tube; B. a composite of several electron micrographs showing one profile of emitter N-10 after a vacuum arc.

RESULTS

The analysis of the present experimental data (I) over most of its range further supports the validity of the wave mechanical, field emission theory involving the electron image force and extends its comparison with experiment to higher current densities than those previously reported, (II) presents evidence for the presence of space charge limited field emission, and (III) suggests mechanisms which may have initiated the voltage breakdown leading to the vacuum arc. This analysis follows.

I. Comparison between Experiment and Theory

A current density J, an average for the emitting area A, was derived from the present data and com-

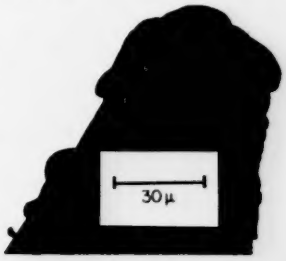

FIG. 9. A composite of several electron micrographs showing one profile of emitter Q-7 after vacuum arc.

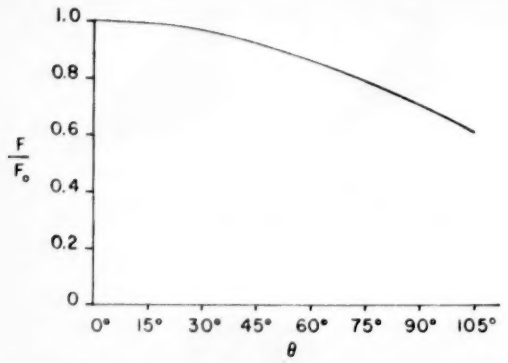

FIG. 10. The dependence of electric field F upon polar angle θ for emitter X-89 calculated with use of an equipotential surface which was closely fitted to the emitter profile judged from its electron micrographs ($\theta=0°$, $F=F_0$ at the apex).

pared with the current density J predicted by the theory (2) when the electric field F_0 at the emitter apex and the value $\bar{\phi}=4.5$ ev were used. When A was known, values of $\bar{J}$ were readily calculated from

$$\bar{J}=I/A, \tag{3}$$

where I was the experimental current.

For emitter X-89, the emitting area was estimated from the measured emitter radius and the calculated dependence of current density on polar angle θ, measured from the emitter apex. For this emitter, whose geometry was determined from electron micrographs (Fig. 7) the ratio F/F_0 as a function of θ calculated by a previous method[11] is shown in Fig. 10. This, with the theory (2) and $\phi=4.5$ ev, predicted the ratio J/J_0 as a function of θ shown in Fig. 11. Curve C resulted from $F_0=7\times10^7$ volts/cm, curve A from $F_0=3\times10^7$ volts/cm, these two values of F_0 corresponding to the points C and A on the graph of Fig. 3, i.e., to the extremities of its linear portion, as will be shown.

Eighty-five percent of the total current was emitted by the area bounded by $\theta=53°$ for the curve C and $\theta=40°$ for curve A (Fig. 11). An extension of these boundaries to larger values of θ would result in an unreasonable increase in area without significant current increase. With the emission boundary thus arbitrarily defined, and with the emitter radius $r=2.3\times10^{-5}$ cm, averaged from the two micrographs of Fig. 7, the areas corresponding to C and A are $A_C=1.2\times10^{-9}$ cm², $A_A=7.6\times10^{-10}$ cm². These, with Eq. (3) and currents at C and A from Fig. 3, yielded current densities $\bar{J}_C=6\times10^6$ amperes/cm², and $\bar{J}_A=6$ amperes/cm². This part of the data was readily compared with the theory (2), as follows.

The electric field F_0 at the emitter apex was calculated from

$$F_0=\beta_0 V, \tag{4}$$

where V was the measured value of the applied potential.

The geometric factor β_0, calculated for emitter X-89 using Eq. (3) of reference 11 with $a=0.33\times10^{-5}$ cm, $r_0=1.8\times10^{-5}$ cm, and $n=0.07$, was

$$\beta_0=(9.9\pm1.5)\times10^3 \text{ cm}^{-1}. \tag{5}$$

The significant experimental errors in β_0 occurred in the calibration of the electron microscope (10 percent) and the determination of emitter geometry averaged from the electron micrographs of its several profiles (5 percent).

Equation (5) includes a 7 percent correction to account for the effect of the supporting filament structure.[16] No significant correction was required for the effect on β_0 introduced by the difference between the experimental anode (Fig. 1) and the theoretical anode used for the calculation of β_0 [reference 11, Eq. (2)] since the effect was necessarily small compared to the 10 percent change in β_0 noticed when the aluminum coating on the inner surface of the envelope of the experimental tube (Fig. 1) was changed from anode potential to emitter potential. This value of β_0 agrees within the experimental error with the value β_m which the theory (2) required in order to predict the observed experimental current-voltage curve. Use of Eqs. (2) and (3) with the assumptions of a uniform work function $\bar{\phi}$ and a constant emitting area A over which the electric field had the constant value F_m gave

$$\beta_m=\left[\frac{d(\ln J)}{d(10^8/F)}\Big/\frac{d(\ln I)}{d(10^4/V)}\right]\times10^4. \tag{6}$$

To evaluate β_m in the present case the theory (2) was

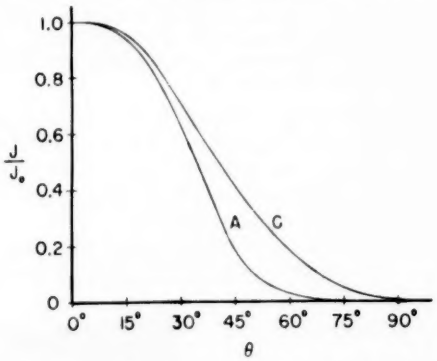

FIG. 11. The dependence of current density J upon polar angle θ (measured from the emitter apex) calculated for emitter X-89 from the field emission theory (2) and the data in Figure 10, assuming a constant work function $\phi=4.5$ ev. Curve A for $F_0=3\times10^7$ volts/cm; curve C for $F_0=7\times10^7$ volts/cm corresponding to the points A and C of Fig. 3.

[16] Emission was obtained from a long, needle-shaped field emitter in another experimental tube, with and without the effect of a typical filament structure which was slid along the needle in the final vacuum with the aid of an external magnet. The filament was moved from its normal position (2 mm from the emitter tip), to another position far removed from the tip. The corresponding change in β_0 was calculated from the change in applied potential required to establish a common current.

TABLE I. Data for several emitters.

A	B	C	D	E	F	G	H	K
Emitter number	β_0 cm^{-1}	β_m cm^{-1}	$\bar{J}_C$ amp/cm^2	$\bar{J}_A$ amp/cm^2	Emitter radius cm	Emitter cone angle in degrees	$\bar{J}_X$ amp/cm^2	V_{max} kv
X-89	9.9×10^3	12.8×10^3	6×10^6	6	2.2×10^{-5}	13	2×10^7	6.9
X-81		14.6×10^3	7×10^6	11	2.7×10^{-5}	10	3×10^7	6.9
N-10		4.0×10^3	9×10^6	6	2.5×10^{-5}	32	2×10^8	32.1
Q-7		19.5×10^3	1×10^7	3×10^2	1.5×10^{-5}	6.5	6×10^7	4.75

graphed in Fig. 12 with $\bar{\phi}=4.5$ ev; the current-voltage relationship AB (Fig. 3) for emitter X-89 was calculated for the required hypothetical case of a constant emitting area with the aid of the data from Fig. 11. According to (6), the ratio of the slopes of these two graphs yield

$$\beta_m=(12.8\pm1.9\times10^3\ \text{cm}^{-1}). \tag{7}$$

The error in β_m due to the ignored variation of F with θ (Fig. 10) was less than 5 percent; that introduced by the neglect of the known distribution of work function with crystallographic direction[17] was less than 7 percent. With other minor errors such as those inherent in the current and voltage measurement, β_m was known within ±15 percent. While β_0 and β_m for emitter X-89 agree within the combined experimental error, additional data from four other emitters indicated that $\beta_m>\beta_0$ by approximately the same percentage in each case.

Careful inspection of the electron micrographs of emitter X-89 revealed that the radius of curvature of the surface near the tip varied slightly with crystallographic direction; apparently the simple crystallographic faces (probably 110) were planes of small but significant area. The surface at other crystallographic directions had smaller than average radii of curvature and hence larger values of β than apparent from (5) and Fig. 10; these surfaces were probably those for which $\phi<\bar{\phi}$ according to Nichols;[17] hence most of the current originated at these surfaces. These effects account at least in part for the observed difference between β_m and β_0, the former being probably more correct than the latter.

This conclusion was strengthened when the experimental current densities $\bar{J}_C$ and $\bar{J}_A$, previously calculated for emitter X-89, were graphed in Fig. 12 at electric field values calculated from the corresponding voltages V_C and V_A from Fig. 3, using β_m from (6). Thus, the theory (2) and experiment agree in the range of current densities $6<\bar{J}<6\times10^6$ amps/cm^2 within the present experimental error.

Haefer[10] used the hyperboloidal approximation to evaluate β_0 in experiments whose agreement with theory appears to be subject to a larger experimental error than that claimed. No mention was made of the uncertainty in β_0 resulting from the use of the hyperboloidal geometry with emitters whose shapes approximated a cone with a hemispherical cap. A hyperboloid tangent to the emitter at the apex can intersect the emitter at only one other polar angle; either the apex of the hyperboloid has a smaller radius than the emitter, or it diverges from the emitter along the shank. β_0 is increased by the former and decreased by the latter, being sensitive to both.[11] With Haefer's formula for β_0, the two surfaces are coincident at $\theta=0°$ and $\theta=10°$, and fortunately the two opposing errors in β_0 are comrable for this fit.

Haefer's formula yields $\beta_0=8.0\times10^3$ cm^{-1} for emitter X-89, a value lower than the present value (5) by 19 percent. This error, if assigned to Haefer's values of β_0, may be compensated for by the previously ignored effect of the filament structure on β_0, which effect is not less than 25 percent judged from the reported filament structure in his work and the present experiments. Further error in Haefer's work may have resulted from surface contamination, since the published emission pattern [his Fig. 12(a)] is not that now generally accepted for clean tungsten[18,19] as was claimed.

Current densities $\bar{J}_C$ and $\bar{J}_A$ for emitters X-81, N-10, and Q-7 are shown in Table I, columns D and E. When

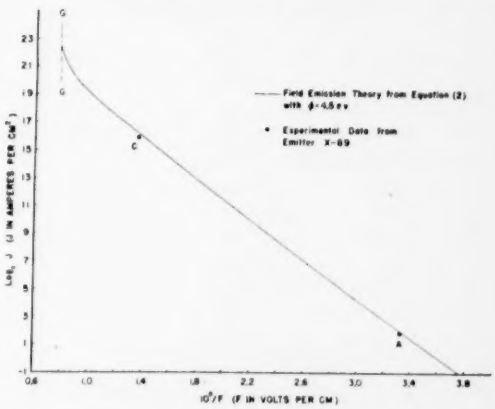

FIG. 12. A graph showing the dependence of current density upon electric field. The solid line resulted from the field emission theory (2) with $\phi=4.5$ ev; the experimental data at A and C represent the average current densities $\bar{J}_A$ and $\bar{J}_C$ with corresponding values of F from $F=\beta_m V$, for emitter X-89. The theory is terminated at the dashed line GG when the surface potential barrier is reduced to the top Fermi electron energy level.

[17] M. H. Nichols, Phys. Rev. **57**, 297 (1940).

[18] E. W. Mueller, Z. Physik **120**, 270 (1943).

[19] J. A. Becker, Bell System Tech. J. **30**, 907 (1951).

the radii of these emitters were obtained from a comparison between the data in Figs. 4, 5, and 6 with the theory (2), current densities were calculated by the method used with emitter X-89. The data from Fig. 11 were assumed applicable to all emitters. This method was used since the required emitter radii were not available from micrographs after use due to arc damage (Figs. 8 and 9); micrographs taken before the emitter was inserted into the experimental tube accurately identified emitter cone angles (Table I, column G) and provided an estimate of emitter radii within a factor of 2 (surface migration caused subsequent changes in radii during the outgassing procedure). Current densities $\bar{J}$ for these three emitters are known within a factor of 3.

The following conclusions were drawn from the foregoing discussion and an inspection of Table I and Figs. 3, 4, 5, 6, and 12: 1. The empirical equation (1) is valid in the range $\bar{J}_A<\bar{J}<\bar{J}_C$ for each emitter. 2. Experimental values of $\bar{J}$ for emitter X-89 agree with those predicted by the theory (2) in the range $6<\bar{J}<6\times10^6$ amps/cm^2, within the experimental error. 3. β_0 and β_m agree within the experimental error; β_0 is sensitive to both emitter radius and cone angle. 4. It is significant that the lowest average current density $\bar{J}_C$ for which space charge effects were observed was of nearly the same value for each emitter; these values of $\bar{J}_C$ were in the range $6\times10^6<\bar{J}_C<1\times10^7$ amperes/cm^2.

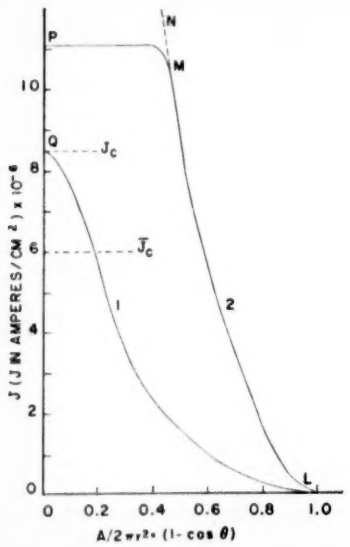

FIG. 13. The surface distribution of current density J for emitter X-89. The abscissas were chosen so that the area under each curve is proportional to the corresponding total current. Curve 1, which is a replot of curve C, Fig. 11, corresponds to the point C, Fig. 3 just prior to the onset of space charge effects ($J=J_C$ at the emitter apex, the average current density being $\bar{J}_C$). Curve 2 corresponds to the largest current shown in Fig. 3, the portion PM resulting from use of Eq. (8) for the space charge limited region, and the portion LM resulting from the use of Eq. (2) for areas in which space charge was absent.

II. Space Charge

It will be shown that space charge necessarily influenced the emission when the current density exceeded a critical value J_C, the effect being confined mainly to the area from which the charge originated provided that J was not considerably greater than J_C. Because the largest value of J was found at the emitter apex where the electric field was greatest (Fig. 11) space charge first influenced the emission from a small area at the apex, the effect spreading to neighboring areas (at larger θ) as the applied voltage was increased sufficiently to increase J to J_C in those regions.

At an area where the emission was space charge limited, i.e., $J\geq J_C$, further increases in current density followed approximately[20]

$$J\propto V^{\frac{1}{2}}, \tag{8}$$

while at areas for which $J<J_C$, the emission increased according to (2). The total observed current increase above I_C (Fig. 3), therefore, fell between the values predicted by (8) (curve CD) and by (2) (curve CE). For both of these limiting curves, a constant emitting area and a uniform current density distribution were assumed; hence, neither of them represents the true experimental situation.

In order to show first that space charge influenced the emission when $J>J_C$, the space charge q_s within a distance $s\ll r$ from a unit emitting area of radius of curvature r was approximated as follows:

The average space charge density $\bar{\rho}_s$ within the distance s was

$$\bar{\rho}_s=J/\bar{v}\ \text{esu/cm}^3, \tag{9}$$

where

$$\bar{v}=\tfrac{1}{2}[v_0+(2e/m)^{\frac{1}{2}}(F_0s)^{\frac{1}{2}}]\ \text{cm/sec}.$$

The initial velocity v_0 (if any) was negligible. Now,

$$q_s=s\cdot\bar{\rho}_s=2Js^{\frac{1}{2}}(m/2e)^{\frac{1}{2}}F_0^{-\frac{1}{2}} \tag{10}$$

for a unit emitting area. A 1 percent change in β [see Eq. (4)] which was detectable experimentally, would be expected from space charge effects when

$$q_s=0.01\sigma, \tag{11}$$

where σ was the induced surface charge per unit area. Combining (9), (10), and (11) with $\sigma=F_0/4\pi$, $F_0=2.3\times10^5$ esu/cm and $J=3\times10^{16}$ esu/cm^2, the latter two being typical of the experimental data when $V=V_C$, one obtains

$$s=2\times10^{-6}\ \text{cm}. \tag{12}$$

The charge q_s within this distance s from the emitter surface was sufficient to cause a measurable change in the electric field in the proper direction and of sufficient magnitude to account for the departure from linearity observed at the points C of the current-voltage relationships of Figs. 3, 4, 5, and 6. Since s was approxi-

[20] Stern, Gossling, and Fowler, Proc. Roy. Soc. (London) **A124**, 699 (1929).

mately one-tenth of an emitter radius, the charge q_s evidently affected mainly the emission from its area of origin.

Thus, space charge affected only the emission from a small area at the apex of emitter X-89 where $J=J_C$, when $V=V_C$, and the corresponding current-density distribution was that shown in Fig. 11, curve *C*. These data from curve *C* were replotted in Fig. 13, curve 1, using values of the variable $A/2\pi r^2=(1-\cos\theta)$ as abscissae (the emitting area being hemispherical), in order that the area under the curve be proportional to the total emission current. During the subsequent voltage increase V_C to V_E (Fig. 3), current densities were assumed to increase in accordance with (8) at areas for which $J>J_C$, and in accordance with (2) at areas for which $J<J_C$. The former required the portion *PM* of curve 2, (Fig. 13) and the latter gave the portion *LM*. This interpretation attributes most of the current increase above I_C to an increase in the effective emitting area rather than to a large increase in current density at the emitter apex.

Areas under curves 1 and 2, Fig. 13, are proportional to the respective total currents, their ratio being 2.4. The corresponding ratio of the maximum experimental current I_{max} to I_C (from Fig. 3) was 3.3. Thus, the present assumptions lead to approximately the observed increase of the total current above I_c for emitter X-89; improved agreement should result when the distribution of ϕ with crystallographic direction[17] is recognized. Such experiments are in progress.

As a result of the effects of space charge, the total emission current from a cathode was increased by the effective operation of emitting areas in parallel at approximately a common current density, although the individual areas had widely different values of current density at lower voltage in the absence of space charge, due to differences in both β_0 and ϕ. This technique was experimentally demonstrated to be valid for multiple emitters.

III. The Field Emission Initiated Vacuum Arc

The foregoing data described the normal behavior of field emitters whose emission was stable and reproducible over a large range of currents extending into the space charge region. It is of particular interest to investigate the phenomena which occurred when attempts were made to extend the emission to still higher currents. When this was done an explosive breakdown occurred between electrodes even under the best initial conditions of vacuum and surface cleanliness, the breakdown phenomena being commonly described as the "vacuum arc." In much of the earlier work with voltage breakdown, the values of the significant variables such as current density, electric field, work function (surface contamination) were uncertain. In the present work these variables were known accurately prior to breakdown.

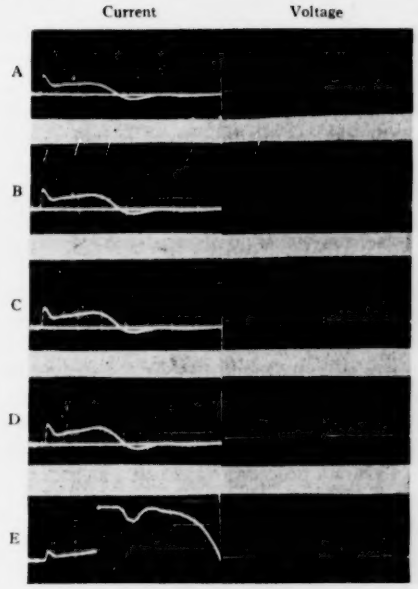

FIG. 14. Current and voltage oscillographs from emitter Q-7 during its transition from the normal field emission (at *A*) to the vacuum arc (at *E*) corresponding to a total voltage change of 5 percent. Both current and voltage plateaus are of approximately one microsecond duration. The current oscilloscope sensitivity at *E* was less by a factor of 2.5 than that at *A*, *B*, *C*, and *D*.

Breakdown occurred between electrodes when the current density, averaged over the cross-sectional area of the emitter cone at its junction with the emitter hemisphere, exceeded a critical value J_z; to a good approximation

$$J_z=(I_{max}/\pi r^2)\ \text{amperes/cm}^2, \tag{7}$$

where I_{max} was the largest value of the normal, stable field current prior to breakdown shown in the curves of Figs. 4, 5, and 6, and r was the average radius of the emitter hemisphere (Table I, column F). The values of J_z from the several emitters (column H) are in sufficient agreement to suggest that current density was the most important variable in the present voltage breakdown; no correlation with voltage was apparent from an inspection of column K.

The current and voltage oscilloscope traces from emitter Q-7 taken during the transition between the normal, stable field emission, Fig. 14A, and the terminating vacuum arc, Fig. 14E, are instructive. The current trace *A*, for which $I=2.2\times10^{-2}$ ampere, was typical of all smaller currents. It exhibits a constant current plateau of approximately 1 microsecond duration (the anomalies at the leading and trailing edges of the current pulse were characteristic of the cathode circuit and are not related to the emission current). A 4 percent increase in voltage which would normally result in a 25 percent current increase caused the change *A* to *D*, marked by a "tilted" current trace

indicating an increase of current with time during a single pulse (with constant voltage), the degree of tilt increasing with current level. The series A–D was reversible and reproducible, the emitter apparently suffering little change in the process as indicated by the similarity between the first and second pulse runs (Fig. 6) made, respectively, before and after several cycles A–D–A (Fig. 14). A one percent increase in voltage yielded the nonreversible change D–E, voltage breakdown occurring near the expected peak of the current pulse. The time of formation of the ensuing vacuum arc was less than 5×10^{-8} sec, judged from an inspection of the current trace E (total current during the arc was greater than that indicated by the current trace E, due to saturation of the oscilloscope amplifier, Tektronix Type 517). Emitter Q-7 appeared as in Fig. 9, after arc, its radius increased by a factor of approximately 150 by a process in which it was melted.

The foregoing data suggest that voltage breakdown resulted from increased emitter temperature due to a current density dependent mechanism accompanying the emission process. Possible mechanisms which might have produced the required heating are resistive heating and the Nottingham mechanism.[21] The former is favored by the sensitive dependence of the breakdown process to current increase indicated in Fig. 14. A solution for the adiabatic case applied to the present emitters showed that resistive heating would yield an excessive emitter temperature rise in a microsecond when $J\geq10^7$ amperes/cm^2. The increase in emitter temperature predicted by the two mechanisms when heat conduction is considered will be presented in a forthcoming paper together with additional experimental evidence.

The foregoing interpretation is reasonable if the thermal component of the emitted current was comparable in magnitude to the normal field current (accounting for the tilted current pulse, Fig. 14D), a result that is expected according to Le Page and Du Bridge,[22] when the surface potential barrier is not large compared with kT (the barrier in the present case was about 1 ev above the top Fermi level[7] when $F_0=8\times10^7$ v/cm. The work of Guth and Mullin[23] concerning electron emission at intermediate electric fields and temperatures adds further support. The required temperature dependent current increase probably originated in part at least at areas whose normal field emission was not space-charge saturated.

During the formation of the vacuum arc (Fig. 14E) the current increased by approximately two orders of magnitude in 5×10^{-8} second, the normal field emission prior to the arc being space-charge limited in part. The observed current increase required either that $\bar{J}$ was considerably greater than $\bar{J}_C$ in which case space charge was necessarily neutralized, or that the effective emitting area was correspondingly increased, or both. The positive ions required by the former may have been supplied by the heated emitter whose surface material was evaporated as ions or as neutral atoms which were ionized near the emitter surface in the high density electron beam. In view of the required rate of ion delivery, the excellence of the present vacuum, and transit time considerations it is unlikely that the present breakdown was initiated by ions[24] or clusters[25] liberated at the anode.

The observed current increase of two orders of magnitude which accompanied the formation of the vacuum arc was certainly sufficient to account for the additional heating required for the geometric deformation shown in Figs. 8B and 9.

The authors express their appreciation to Professor J. E. Henderson of the University of Washington, who suggested the original line of investigation and who has maintained a continued interest throughout this work. Considerable technical assistance was rendered by L. M. Perry and others of the Physics department at Linfield College.

[21] W. B. Nottingham, Phys. Rev. **59**, 907 (1941).
[22] W. R. Le Page and L. A. Du Bridge, Phys. Rev. **58**, 61 (1940).
[23] E. Guth and C. J. Mullin, Phys. Rev. **61**, 339 (1942).
[24] Webster, Van de Graaff, and Trump, J. Appl. Phys. **23**, 264 (1952).
[25] Lawrence Cranberg, J. Appl. Phys. **23**, 518 (1952).

Nuclear Gamma-Rays from Low Energy Proton Bombardment of Sodium, Magnesium, and Aluminum

HARVEY CASSON*
Department of Physics and Institute for Nuclear Studies, University of Chicago, Chicago, Illinois
(Received September 22, 1952)

Gamma-rays produced by the resonance capture of 200–415-kev protons in sodium, magnesium, and aluminum have been investigated with a single crystal NaI(Tl) scintillation spectrometer. Excited states in Mg^{24}, Al^{25}, Al^{27}, and Si^{28} with energies above the ground state of 12 Mev, 2.5 Mev, 8.6 Mev, and 12 Mev, respectively, were found to decay by cascade gamma-emission. Direct transitions to the ground state of Mg^{24}, Al^{27}, and Si^{28} were not observed. Observed pulse-height distributions, location of observed peaks, identifiable gamma-rays and their relative intensities are given. Decay schemes are proposed to account for the observed gamma-rays of Al^{27}, Si^{28}, and Al^{25}. They are found to involve energy levels which are in general agreement with levels found in (d,n) and (p,p) scattering experiments; in the case of Al^{25}, with levels found in the mirror nucleus Mg^{25}. An estimate is made of the absolute proton capture probability in the targets used.

I. INTRODUCTION

TANGEN,[1] using G-M counter detection, has investigated a number of (p,γ) resonances among the lighter elements for proton energies up to 500 kev but, using absorption techniques, was only able to report the mean gamma-ray energies. Since the mean energies have frequently been considerably lower than the calculated excitation energies, this suggests the likelihood of cascade emission. In the present work the energies and relative intensities of the gamma-rays arising from several such (p,γ) resonances were measured, using a sodium iodide (single crystal) scintillation spectrometer. In simple cases, at least, such an energy study might be expected to indicate the most probable modes of decay to the ground state of the nucleus resulting from the proton capture.

The materials selected for proton bombardment were sodium, magnesium, and aluminum, each of which exhibits several sharp but weak (p,γ) resonances within the range of our proton accelerator.

II. SOURCE OF THE BOMBARDING PROTONS

Protons in the energy range from 200–400 kev were obtained from the new Cockcroft-Walton accelerator, or "kevatron" of the Institute for Nuclear Studies at the University of Chicago.

The protons were extracted from a capillary type ion source,[2] accelerated down a quartz tube containing 15 accelerating sections, and were then magnetically deflected through 15° into the target chamber. Fine adjustment of the position of the beam on the target was accomplished by a pair of electrostatic deflection plates (horizontal and vertical) located just before the magnet.

The high voltage through which the ions were accelerated was determined by measuring the current passing to ground through a 10^{10}-ohm resistor stack made up of 1000 10-megohm resistors in series.

In frequent practice, the voltage scale was checked by excitation of the gamma-rays from the well-known fluorine reaction: $F^{19}(p;\alpha,\gamma)O^{16}$, which is sharply resonant at a proton energy of 340.4 kev.[2]

III. TARGET CHAMBER

Owing to the very low yield of γ-rays from the resonances under investigation, the target chamber with which most of the measurements were made was designed to have as small as possible a distance between the target and the detector (see Fig. 1). The target could be preheated to drive off any oil vapors which would be carbonized when struck by the beam. The end of the chamber had attached to it a cooling coil which kept it near room temperature. This allowed the gamma-detector to be moved up to within 3.5 mm of the target surface. The target material was either evapoporated (in vacuum) or fused onto pure copper disks, 1 inch in diameter and $\frac{3}{32}$ inch thick. These target disks were dropped into position in the center of the heater assembly and were held in place by means of a split ring of spring wire which slipped into a groove and could easily be removed with forceps.

The target chamber as a whole was insulated from ground and used as a Faraday cup to measure the beam current hitting the target, and electrically biased diaphragms were used (see Fig. 1) to prevent error in the beam current readings from secondary electrons.

IV. BEAM CURRENT INTEGRATOR

The beam current integrator has been in the laboratory in satisfactory operation for several years. It involves a feedback circuit which prevents the input lead from rising very much above ground potential, thus minimizing spurious leakage currents. It was started simultaneously with the gamma-ray count and after a preset number of microcoulombs of protons hitting the target, the count was automatically stopped. The integrator could be set for 250, 500, 1250, or 2500

* Now at Argonne National Laboratory, P. O. Box 299, Lemont, Illinois.

[1] R. Tangen, "Experimental Investigations of Proton Capture Processes in Light Elements," Kgl. Norske Videnskab. Selskabs, Skrifter, No. 1 (1946).

[2] A. H. Morrish, Phys. Rev. **76**, 1651 (1949).

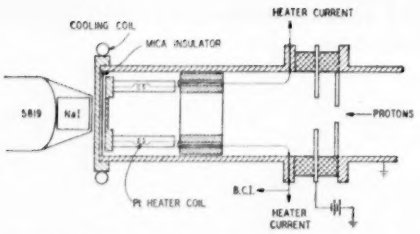

FIG. 1. Target chamber, designed for heating of target, and close proximity of target and sodium iodide crystal.

microcoulombs. Proton beam currents between 6 and 12 microamperes were ordinarily used.

V. THE SCINTILLATION SPECTROMETER

The scintillating crystals used in this work were 1-in. cubes of NaI(Tl).[3] The surfaces of the crystal were cut parallel to the cleavage planes. Because of the hygroscopic property of sodium iodide, the crystals were stored in dried mineral oil when not in use, and a thin layer of either mineral oil or vacuum grease was kept over their surfaces under all other circumstances.

The crystals, with their surfaces cleaned,[4] were placed in optical contact with the entrance window of the photomultiplier tube (RCA 5819) and covered with a reflector of shiny aluminum foil.

Two photomultiplier tubes were used at various times during the research. They were selected from about six tubes of the same type. The pulse output of the photomultiplier went to a pre-amplifier of the type described by Allen;[5] the pre-amplifier output went to a Los Alamos Model 500 linear amplifier, as described by Elmore and Sands.[6]

A single-channel differential discriminator (Fig. 2) was constructed for the analysis of pulse heights. It consisted of two Schmidt[7] discriminator circuits, two univibrator circuits,[7] and one anticoincidence gate circuit, operated by a regulated power supply. The common cathodes of the two Schmidt circuits were kept at a fixed difference in bias. (This determined the channel width.) The input grids were tied together to the variable arm of a ten-turn 0.1 percent linearity helipot whose dial setting determined the voltage of the base of the channel. The univibrator which followed the lower discriminator was used as a time-delay pulse shaper; the univibrator following the upper one provided a rectangular gating pulse. Only when the lower, but not the upper, of the two discriminator circuits was triggered would a pulse arrive at the output.

The time delay was about 5 microseconds; the gating pulse had a width of about 10 microseconds. The rise time of the pulses from the amplifier was about 1 microsecond. The circuit was fast enough to handle adequately the counting rates ordinarily observed in our work.

The output of the single-channel discriminator went to a Los Alamos Model 200 scale of 64,[8] whose input was either shorted or open as determined by the relay circuit associated with the beam current integrator.

VI. INTERPRETATION OF PULSE-HEIGHT DISTRIBUTIONS

It has been shown experimentally[9] that when a clear NaI(Tl) crystal (that is, a sodium iodide crystal grown with a few percent of thallium iodide added as an impurity) is bombarded with γ-radiation, the light output is strictly proportional to the energy absorbed, over a large range of energies.

Whereas alphas or betas slow down directly, a photon of energy E_0 must first produce electrons in motion by (1) photoelectric effect, (2) Compton effect, (3) pair production in the crystal. Although (1) leaves an atom with a vacancy in the K or L shell, the resultant x-radiation is usually reabsorbed in the crystal so that the light pulse corresponds to energy E_0. (2) produces a continuous distribution of electron energies up to a maximum which is less than E_0 and may be expressed, by direct calculation from the Compton equation,[10] in the following form:

$$(E_e)_{\max}=\frac{1}{1+mc^2/2E_0}\times E_0=E_0-\frac{mc^2/2}{1+mc^2/2E_0}. \quad (1)$$

This point is referred to as the Compton edge.

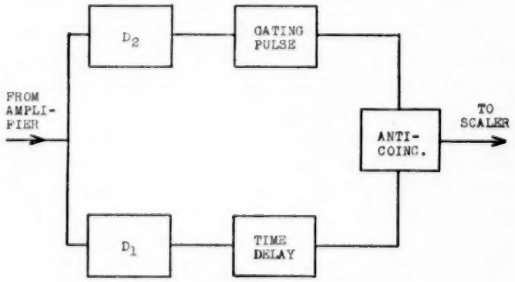

FIG. 2. Block diagram of the single-channel differential discriminator.

[3] Harshaw Chemical Company, Cleveland, Ohio.

[4] Fresh, transparent surfaces on the crystals were obtained by placing them successively in baths of (a) *n*-butyl alcohol, (b) *n*-butyl alcohol mixed with xylene, and (c) xylene, following a technique privately communicated by W. Bernstein of the Brookhaven National Laboratory.

[5] J. S. Allen, Rev. Sci. Instr. **18**, 743 (1947).

[6] W. C. Elmore and Matthew L. Sands, *Electronics: Experimental Techniques* (McGraw-Hill Book Company, Inc., New York, 1949), p. 167 and Sec. 7.2.

[7] Reference 6, pp. 99 ff, Chap. IV, 87 ff, pp. 120–123.

[8] Reference 6, p. 218.

[9] See, for example, R. Hofstadter and J. A. McIntyre, Nucleonics **7**, 32 (1950).

[10] See, for example, W. Heitler, *Quantum Theory of Radiation* (Oxford University Press, London, 1947), second edition, p. 146. The maximum electron energy is obtained for backscattering of the radiation. Putting $\cos\theta=-1$ and evaluating the change in quantum energy gives the result stated.

For $E_0 \gg mc^2$, Eq. (1) shows that the Compton edge occurs at approximately $E_0 - \frac{1}{2}mc^2$. Evaluation of the Klein-Nishina formula to obtain the energy distribution of the Compton electrons gives an almost flat distribution which rises to a sharp maximum at the Compton edge and is zero above the edge. Experimentally, we find this maximum to lie between $E_0 - mc^2$ and $E_0 - \frac{1}{2}mc^2$.

In case (3), an electron and positron are created in the crystal with kinetic energies initially adding up to $E_0 - 2mc^2$. They are slowed down to zero energy and the positron is annihilated, yielding 2 quanta of energy mc^2. If both quanta are absorbed in the crystal, the total light pulse corresponds to E_0; if one escapes, $E_0 - mc^2$; and if both escape, $E_0 - 2mc^2$. For the case of pairs produced close enough to a surface of the crystal to allow one or both of the electrons to leave the crystal before being completely stopped, a continuous distribution of pulses less than E_0 is obtained.

The resultant pulse-height distribution due to an incident gamma-quantum of energy $E_0 \gg mc^2$ may be described as follows. Three peaks may be observed: P_3 at pulse height E_0, owing to a superposition of all processes in which the full gamma-ray energy is absorbed in the crystal (i.e., all secondary radiations are absorbed); P_2 at pulse height approximately $E_0 - mc^2$, arising from pair production with one of the annihilation quanta captured, superimposed on the peak of the Compton distribution; and P_1 at pulse height $E_0 - 2mc^2$ from pair production with both annihilation quanta escaping. The observed *continuous* distribution of lower energy pulses is mainly due to a superposition of the Compton distribution and the distribution due to pair, photo, and Compton electrons which are not completely stopped in the crystal.

Since the above processes have different energy dependence, the appearance of a distribution may be expected to change considerably with the energy of the incident gamma.

For a 1-inch cubic NaI crystal, and gamma-energy E_0 less than 0.5 Mev, the peak E_0 tends to predominate due to large photoeffect and large probability that any secondary radiations will be absorbed in the crystal. Between 0.5 Mev and about 2 Mev one observes mainly the Compton peak and the photopeak. Between 2 and 4 Mev, one observes $E_0 - 2mc^2$, $E_0 - mc^2$, with a much smaller peak at E_0. Above 4 Mev the peak at E_0 was not observed. Instead, $E_0 - mc^2$ decreases relative to $E_0 - 2mc^2$ (because of the decrease in the Compton cross section relative to the cross section for pair production), and the latter peak predominates. At some energy above 4 Mev, depending on the resolution of the spectrometer, the smaller peak $E_0 - mc^2$ ceases to be resolved from the larger peak $E_0 - 2mc^2$, and as a result only one peak is seen.

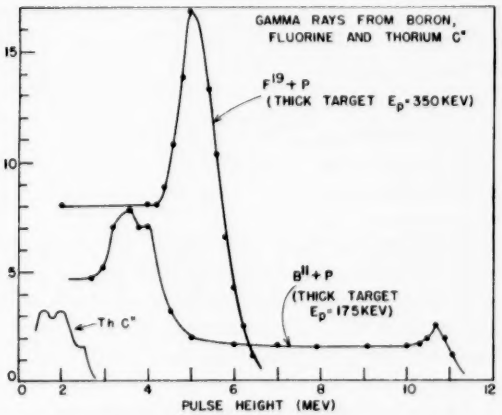

FIG. 3. Spectra of gamma-rays of various energies used in calibrating the spectrometer.

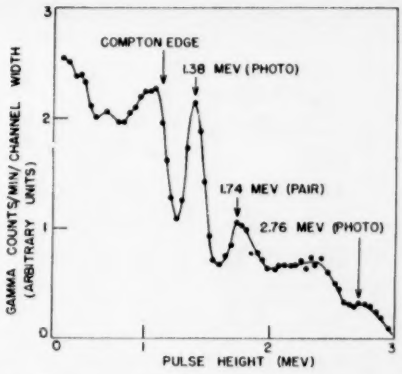

FIG. 4. Gamma-ray spectrum from a Na^{24} source. The distributions due to the 1.38-Mev and 2.76-Mev cascade gamma-rays are superimposed.

For gamma-rays above 6 Mev (and at least up to 11.5 Mev), the observed distribution was especially simple in form. It consisted of a long flat portion with the peak at $E_0 - 2mc^2$ superimposed.

Figures 3 and 4 show the pulse-height distributions due to gamma-rays of various energies.

Where more than one gamma-ray is present, the interpretation of the peaks may be difficult. This is especially true in the region 2 to 4 Mev since all three of the peaks may be observable.

VII. CALIBRATION AND PERFORMANCE OF THE SCINTILLATION SPECTROMETER

The response of the scintillation spectrometer was calibrated using the following known gamma-ray sources:

Na^{22} and Na^{24}	Hg^{203}
$B^{11}(p,\gamma)C^{12}$	Hf^{181}
$F^{19}(p;\alpha,\gamma)O^{16}$	Se^{75}

Since the amplifier saturated above 90 volts, and the discriminator did not operate satisfactorily below 10 volts, the range of pulse heights which could be reliably analyzed at a given gain setting of the analyzer was somewhat restricted. In order to cover the gamma-ray

TABLE I. Gamma-ray absorption coefficients.

	Sodium iodide				Copper
E_γ(Mev)	Compton absorption coeff. (cm^{-1})	Pair absorption coeff. (cm^{-1})	Photo absorption coeff. (cm^{-1})	Total absorption coeff. (cm^{-1})	Total absorption coeff. (cm^{-1})
0.5	0.268	···	0.059	0.327	0.72
1.0	0.196	···	0.011	0.207	0.52
2.0	0.136	0.008	0.004	0.148	0.36
3.0	0.106	0.022	0.002	0.130	0.32
4.0	0.086	0.035	0.002	0.123	0.30
5.0	0.074	0.048	0.001	0.123	0.28
6.0	0.066	0.059	0.001	0.126	0.27
7.0	0.060	0.068	0.001	0.129	0.27
8.0	0.056	0.077	···	0.133	0.27
9.0	0.051	0.085	···	0.136	0.27
10.0	0.047	0.092	···	0.139	0.27
11.0	0.044	0.100	···	0.144	0.27
12.0	0.041	0.107	···	0.148	0.27

energy range from 0.5 to 12 Mev, the range was divided up into several parts each of which was separately calibrated. In the low energy range, the 0.51-Mev and 1.28-Mev gammas of Na^{22} were used; in the high energy range, the Na^{22} 1.28 Mev and fluorine 6.13-Mev gammas were used for the calibration. The ranges were selected by changing the amplifier gain. The channel width most frequently used was about 2 volts, although a 5 volt channel was used when intensities were very low. The results of the calibration confirmed the conclusions of previous investigators concerning the linearity of the pulse height *versus* energy release relation.

The resolution of the spectrometer is defined as the full width at half-maximum of the photopeak of a low energy gamma ($E_\gamma<3$ Mev, where the photopeak is visible) and is expressed as a percentage of the pulse height at the peak. The best resolution obtained was about 12 percent at 1.28 Mev and 17 percent at 0.5 Mev. At 6 Mev, the peaks at $E-2mc^2$ and $E-mc^2$ are unresolved giving a single peak. If the resolution for this case is defined as the width of the peak considering the *plateau* to be the zero line, then a value of about 6 percent was obtained. Using the full height of the peak, the width at half-maximum was about 17 percent.

It is believed that by finding a better photomultiplier tube, the resolution could have been improved by about a factor of 2, which would bring it close to the best values attained by other investigators.

VIII. CALCULATION OF INTENSITIES AND YIELDS

The total area under the distribution curve due to a monochromatic beam of γ-rays should be equal to the number of primary gammas which have been absorbed by the crystal. (Secondary absorption and resolution factors would ordinarily affect the location of pulses in the distribution, and hence its shape, but should not change their total number.) The assumption made here is that each time a gamma is absorbed and a light pulse is produced, there are enough photons in the light pulse to assure a probability of unity that the detector will register the pulse. Only for very low energy pulses (say, pulses corresponding to less than 50 kev of gamma-ray energy) might this assumption be invalid. Since we are concerned at present with gammas of energy greater than 500 kev and extrapolate to zero the observed higher energy part of the pulse-height distribution, such a low energy "cutoff" would not affect the results.

This extrapolated area under the distribution curve owing to a given gamma-ray, we call the "extrapolated yield." The observed pulse-height distributions generally involved a number of gamma-rays. The plateau level due to the highest energy gamma was determined first, either by direct observation when possible, or else by estimation of the expected level in terms of the height of the pair peak. The extrapolated yield was then determined by extending this plateau to zero and calculating the area under this distribution. The plateau of this gamma was assumed to be the zero line of the next lower gamma-ray, and in like manner, the extrapolated yields of this, and successive lower gamma-rays were determined. For γ-rays below 3 Mev, the extrapolation was performed by comparison with known distributions (Na^{24}, Na^{22}, ThC″, etc.).

In certain cases where a number of peaks were so close to each other that identification of the gamma-rays involved was not certain or else the height of a peak could not be established because of poor statistics, the extrapolated yield for the *sum* of the gamma-rays involved was determined.

In order to be able to compare the various gamma-rays from the point of view of their relative frequency of production in the (p,γ) reactions, it was necessary to know the variation with energy of the total absorption coefficients (photoelectric+Compton+pair) of the gammas in sodium iodide. On the basis of data given in Heitler[11] this was calculated; the results are given in Table I.

Since there was about $\frac{1}{8}$ inch of copper between the target surface and the detector, Heitler's values of the total absorption coefficients in copper are also included in Table I. The attenuation of the beam due to the presence of this material (about 15 percent for most of the gamma-rays observed) did not seriously distort the components of the pulse-height distribution, and it should be remembered that calibration of the spectrometer was carried out with the same target and crystal geometry which was later used in investigating the new gamma-rays.

The "*relative intensity*" of an observed gamma-ray was obtained from the *extrapolated yield* by converting the latter to the extrapolated yield which would have been obtained from a hypothetical gamma of energy 6 Mev and having the same absolute intensity. Both the relative efficiency for absorption in sodium iodide and the relative transmission through the copper were con-

[11] Reference 10, Chaps. III, IV, and V.

sidered. Taking these two factors into account mathematically, we may write for the relative intensity

$$I_\gamma=\frac{1-\exp[-\tau_{\mathrm{NaI}}(6)\bar{x}]}{1-\exp[-\tau_{\mathrm{NaI}}(\gamma)\bar{x}]}\times\frac{\exp[-\tau_{\mathrm{Cu}}(\gamma)\bar{y}]}{\exp[-\tau_{\mathrm{Cu}}(6)\bar{y}]}\times Y_{\mathrm{ext}}, \quad (2)$$

where τ_{NaI} and τ_{Cu} are the linear absorption coefficients taken from Table I, $\bar{x}$ is the effective thickness of the crystal, $\bar{y}$ the effective thickness of copper, and Y_{ext} is the extrapolated yield.

It should be emphasized that the above definition of "relative intensity" refers to the *number* of gamma-quanta absorbed by the crystal, rather than the number of gamma-quanta multiplied by their energy.

Between 2 and 10 Mev, the relative intensity turns out to be numerically almost the same as the extrapolated yield (within 20 percent). In this region of energies, the exponentials in Eq. (2) may be expanded in series. The first-order approximation, which gave sufficient accuracy, involves merely the ratio of the absorption coefficients $\tau(\gamma)$ and $\tau(6)$ in sodium iodide.

In view of the difficulties involved in obtaining extrapolated yields from a complex distribution to an accuracy of much better than 50 percent (uncertainty in extrapolation, decrease in effective target thickness during the course of a run, statistics, etc.), the labor of substitution into Eq. (2) was not warranted for most of the observed gamma-rays.

The analysis of 0.5-Mev radiation must be considered as a special case. The absorption of high energy gammas due to the pair production cross section in the copper resulted in the emanation of annihilation quanta of energy 0.51 Mev from the copper. The excitation of positron-emitting states of short half-life would also produce annihilation radiation (a long half-life would enable this radiation to be detected in the background runs).

Before one can make any claims about the existence of nuclear 0.5-Mev gamma-rays it is necessary to compare the observed intensity of radiation with the total estimated annihilation intensity. A significant difference between the two would then be attributable to nuclear radiation.

For the purpose of estimating absolute gamma-ray yields, a calculation was made of the effective geometry of a cylindrical crystal relative to a point source located along its axis. The assumption was made that the attenuation of the gamma-ray beam on passing through the crystal was negligible.

Straightforward integration gave the following expression for the number Y of gammas absorbed per unit time for a point source of strength S:

$$Y=\frac{S\tau a}{4}\left\{\frac{x+L}{a}\ln\left[1+\frac{a^2}{(x+L)^2}\right]-\frac{x}{a}\ln\left(1+\frac{a^2}{x^2}\right)+2\left[\tan^{-1}\frac{x+L}{a}-\tan^{-1}\frac{x}{a}\right]\right\}, \quad (3)$$

where τ is the gamma-absorption coefficient; a the radius of the crystal; and x the distance from the point source to the front surface of the crystal. As x is increased, the expression is rapidly asymptotic to an inverse square law where the distance is measured to the center of the crystal.

IX. EXPERIMENTAL OBSERVATIONS

The order in which the materials were studied was (a) aluminum, (b) sodium, and (c) magnesium. Since small amounts of the target materials tended to evaporate from certain targets due to the heating induced by the proton beam, and thus contaminated the target chamber and associated piping, it became necessary to exert care with regard to the types of materials introduced into the target chamber, previous to, or during a given investigation. The only contaminant possible during (a) was fluorine which had been used for calibration purposes. The fluorine gammas were observed. Hence, the presence of 6-Mev gammas in an Al+p spectrum could at least in part be ascribed to this impurity. In (b), the possible contaminants were aluminum and fluorine. Since the previously observed Al+p peaks were not observed to any significant extent in (b), there was no danger of falsely assigning any aluminum impurity peaks to the sodium reaction. In (c) the possibility of target chamber contamination was increased to include sodium. This contamination was observed, and it became necessary to disassemble the target chamber and clean it.

Excitation curves were run for each resonance in order to determine the yield of the reaction, detect impurities and check the voltage scale. The area under pulse-height distributions generally agreed within 10 percent with the excitation curves run with the integral discriminator. The observed yields and calculated extrapolated yields are given in Table II. The integral discriminator was generally set to count pulses greater than 1 Mev in height.

(a) Aluminum Bombarded with Protons. $Al^{27}+p\rightarrow Si^{28}$

Since the excitation curves obtained using ordinary aluminum indicated the presence of impurity radiations, specially purified aluminum was procured from our Institute for the Study of Metals. With this aluminum whose purity was specified as greater than 99.99 percent, only the aluminum resonances were observed. The targets were machined into disk form using a clean, sharp tool.

The two resonances which gave enough intensity for gamma-energy analysis were located at 325 kev and 404 kev. Thick target spectra were obtained at 415 kev and in the region 335 to 350 kev. The former included both resonances; the latter only the 325-kev resonance. A 6-Mev gamma-ray appeared on both sets of curves and was attributed to fluorine contamination. The two

TABLE II. Total gamma-ray yields.

Reaction	Target	Observed thick target yield of pulses >1 Mev (counts of 64/500 μcoul)	Total extrapolated yield[a] (counts of 64/500 μcoul)
$Na^{23}+p\rightarrow Mg^{24}$ (305-kev resonance)	Na_2SO_4	80	94
$Mg^{24}+p\rightarrow Al^{25}$ (222-kev resonance)	Magnesium (evaporated)	4.5	8
$Mg^{26}+p\rightarrow Al^{27}$ (314-kev resonance)	Magnesium (evaporated)	4	6
$Mg^{26}+p\rightarrow Al^{27}$ (336-kev resonance)	Magnesium (evaporated)	60	80
$Al^{27}+p\rightarrow Si^{28}$ (325-kev resonance)	Solid pure aluminum	7	9
$Al^{27}+p\rightarrow Si^{28}$ (404-kev resonance)	Solid pure aluminum	28	37

[a] Gamma components of 0.5 Mev or less are not included.

spectra appeared to be of the same shape with all other components occurring in the same proportions. The observed peaks, their interpretation in terms of gamma-energies, and estimated intensities are given in Table III. It should be noted that the intensity values given at $E_p=415$ kev include both resonances. If the lower voltage yields are subtracted from the upper ones, a ratio of about 5:1 is obtained for the relative intensity of the two resonances. Over a dozen runs in total were made, and average spectra are shown in Figs. 5(a) and 5(b). The pulse-height distribution for the 7-Mev gamma-rays at $E_p=415$ kev was compared with the corresponding part of the distribution at 330 kev by alternately running over the peaks observed at these proton energies. The results were very nearly the same. The difference in the average values listed in Table III is not believed to be significant.

Although the pulse-height analyses were not carried out beyond pulse heights of about 7.5 Mev (gamma-energies greater than 8.5 Mev), the absence of any appreciable plateau above the peaks due to the observed 7–7.5 Mev gamma-rays indicates that no higher energy gammas of comparable intensities were being emitted.

The characteristics of the spectrum may be described by dividing it into three parts: gammas of energy 1.8–2.8, 4.5–5, and 7–7.5 Mev. (The possible presence of gammas below 1 Mev was not investigated.) The interpretation of the peaks in the 1.8–2.8-Mev region was made difficult by their spacing of approximately 0.5 Mev. Although only the 1.8- and 2.8-Mev values are quoted, a 2.3-Mev gamma might be present with low intensity. In the 4.5–5-Mev region, at least two gamma-rays were present, making the identification of peaks even more difficult.

In the case of 7–7.5-Mev gamma-rays, the appearance of a distinct peak in the distribution is clearly evident. Although the presence of two components is indicated in Fig. 5 and Table III, the combination of insufficient resolving power and poor statistics do not permit this to be done with absolute certainty.

(b) Sodium Bombarded with Protons. $Na^{23}+p\rightarrow Mg^{24}$

As investigated by Tangen,[12] the 305-kev resonance in sodium is the only relatively strong resonance in the neighborhood of, or below, 300 kev. Other possible

TABLE III. Gamma-rays from reaction $Al^{27}+p\rightarrow Si^{28}+h\nu$.

P_1: pair peak with escape of both annihilation quanta, at $E_\gamma-2mc^2$.
P_2: pair peak with escape of one of the annihilation quanta, and Compton peak superimposed, at approximately $E_\gamma-mc^2$.

Resonances involved (kev)	(a) Gamma-energies: Observed peak location (Mev)	Identification on Figs. 5(a), 5(b) and interpretation		Energy of associated γ-ray (Mev)	(b) Gamma-intensities: E_γ (Mev)	Extrapolated yield (counts of 64/500 μcoul)	Relative intensity (counts of 64/500 μcoul)
	1.81±0.05	*B*	Photo	1.81±0.05	1.81±0.05	14	12
			P_1	2.83±0.07			
	2.31±0.07	*C*	P_2	2.82±0.07	2.82±0.07	12	12
404+325	2.82±0.07	*D*	Photo	2.82±0.07			
(E_p=415	3.63±0.10	*E*	P_1	4.65±0.10	4.65±0.10	Sum ~5	Sum ~5
kev)	4.02±0.10	*F*	P_2	4.65±0.10			
			P_1	5.04±0.10	5.04±0.10		
	4.47±0.13	*G*	P_2	5.04±0.15			
	5.11±0.15	···	P_1	6.13±0.15	6.13±0.15	2	2
	6.10±0.15	*H*	P_1	7.12±0.15	7.12±0.15	Sum ~12–16	Sum ~ 12–16
	6.44±0.15	*I*	P_1	7.46±0.15	7.46±0.15		
	1.75±0.10	Interpretations same as above			1.75±0.10	2	2
	2.73±0.13				2.73±0.13	2	2
	3.66±0.14						
325	4.07±0.16				4.67±0.14	Sum ~1	Sum ~1
	5.20±0.15				5.09±0.16		
	6.14±0.18				6.22±0.15	1.7	1.7
	6.60±0.23				7.16±0.18	Sum 2	Sum 2
					7.60±0.23		

[12] Reference 1, p. 56 ff.

resonances in this region of operating voltage are about a factor of 100, or more, lower in intensity.

The excitation curves obtained in the present work were consistent with the above, and hence any gamma-rays observed could be assigned to this resonance.

The data were obtained from about eight runs using both thick and thin targets of sodium sulfate. A spectrum obtained with sodium nitrite showed the same features as the others.

A gamma-ray in the region 10–10.5 Mev, at least one in the neighborhood of 7.5 Mev, and one at about 1.38 Mev are clearly visible. In the pulse-height region 2 to 3.5 Mev which would correspond to gamma-rays of energy 2 to 4.5 Mev, the intensity is relatively high but the peaks are poorly resolved. Since the peaks could not be interpreted with certainty in the latter region, the yield and intensity (given in Table IV) were estimated for the sum of all components present there. A typical spectrum is shown in Fig. 6.

(c) Magnesium Bombarded with Protons

The work of Tangen and others[13] has resulted in the identification of the 290, 314, 336, and 388 kev resonances in magnesium with the reaction $Mg^{26}(p,\gamma)Al^{27}$, and the 222-kev resonance[14] with the reaction $Mg^{24}(p,\gamma)Al^{25}$. In the present work, the 222, 314, and 336 kev resonances were studied. The 290-kev resonance, being just detectable on the excitation curves, was too weak to be analyzed.

The magnesium targets, both thick and thin, were prepared by evaporation in vacuum onto the copper target disks.

A total of nine thick target and eight thin target runs were made. Since more peaks were detectable on the higher energy thick target curves than the sum total of peaks on the thin target curves, it was concluded that small amounts of impurities were present. For this reason, the results of thin target bombardment were used to identify the gamma-ray peaks associated with the 336 and 314 kev resonances.

(*1*) $Mg^{24}(p,\gamma)Al^{25}$ (*222 kev Resonance*)

The measurements on this resonance were carried out using thick targets only. The existence of the resonance was verified by running an excitation curve with the discriminator set to count all pulses greater than 0.5 Mev in height. A sharp step appeared at 222 kev (an increase by a factor of about 4 above background). The curve then remained flat up to and above 280 kev. From this, it was concluded that resonances due to impurities were not present in this region, and since larger beam currents were obtainable at the higher proton energies, the data for this resonance were taken at 270 kev.

[13] Reference 1, p. 58 ff.
[14] Grodtal, Lönsjö, and Tangen, Phys. Rev. **77**, 296 (1950).

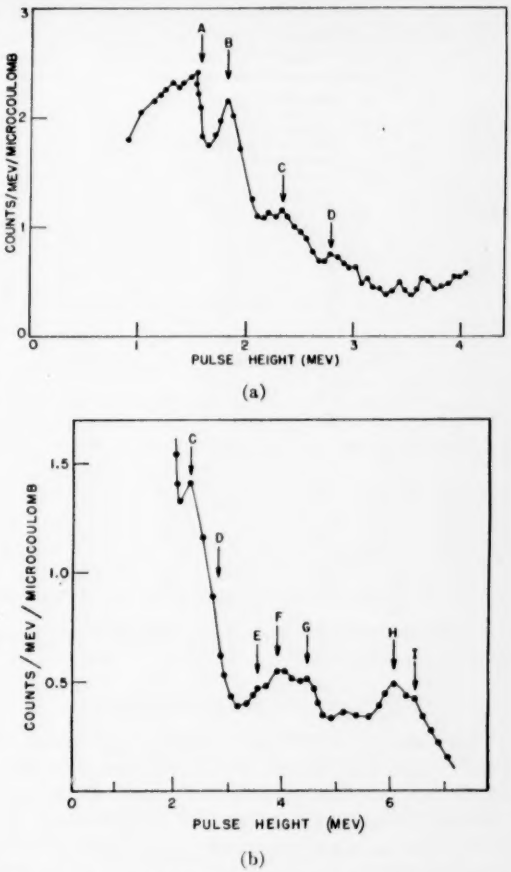

FIG. 5. (a) $Al^{27}(p,\gamma)Si^{28}$ low energy gamma-spectrum. (E_p=415 kev.) In this region, two gamma-rays are observed: a 1.8-Mev gamma-ray, with Compton edge and photopeak at *A* and *B*, respectively; and a 2.8-Mev gamma-ray, with peaks at *B*, *C*, and *D*. (b) $Al^{27}(p,\gamma)Si^{28}$ high energy gamma-spectrum (thick target), showing gamma-peaks above 2 Mev. Peak *C* is the same as peak *C* in Fig. 5(a); peak *D* of that figure is not resolved here. The presence of two gamma-rays of energy 4.65 and 5.04 Mev is determined from peaks *E*, *F*, and *G*. (Since two peaks are generally observed per gamma-ray in this energy region, *F* is considered to be an unresolved double peak.) Peaks *H* and *I* are the pair peaks (P_1) due to the 7.12 and 7.46-Mev gamma-rays (only one peak per gamma is resolved in this energy region).

Two spectra covering the pulse-height region 0.5–2.5 Mev were obtained (see Fig. 7). The absence of γ-rays above 2.5 Mev in energy was obvious in that with the integral discriminator set to count pulses above 2.5 Mev, the number of counts obtained was negligible.

The Compton distribution and photopeak of a 1.9-Mev gamma-ray appeared. There is a peak at 0.9 Mev which could be the pair peak. A smaller peak at 2.3 Mev may be interpreted as the photopeak of a 2.3-Mev gamma-ray.

A photopeak is also observed at 0.5 Mev which may be due to the annihilation of the decay positrons of Al^{25}, a nuclear γ-ray of this energy, or a combination of

TABLE IV. Gamma-rays from reaction: $Na^{22}+p\rightarrow Mg^{24}$ proton resonance at 305 kev.

P_1: pair peak with escape of both annihilation quanta, at $E_\gamma-2mc^2$.
P_2: pair peak with escape of one of the annihilation quanta, and Compton peak superimposed, at approximately $E_\gamma-mc^2$.

(a) Gamma-ray energies				(b) Gamma-ray intensities		
Observed peak location	Identification in Fig. 6, and probable interpretation		Energy of associated γ-ray	E_γ	Extrapolated yield (counts of 64/500 μcoul)	Relative intensity (counts of 64/500 μcoul)
1.00±0.03	—	Compton	1.38			
1.38±0.04	*A*	Photo	1.38	1.38±0.04	36	28
		P_1	2.40	(?)1.90±0.11		
		Photo	1.90			
1.90±0.11	*B*	P_2	2.4		Sum ≦5	Sum ≦4
		P_1	2.92			
		Photo	2.41	2.41		
2.41±0.12	*C*	P_2	2.9			
		P_1	3.43			
		Photo	2.88	2.88		
2.88±0.14	*D*	P_2	3.4			
		P_1	3.90	3.9	Sum ≈24	Sum ≈24
3.22±0.13	*E*	P_2	3.7	3.7		
		P_1	4.24			
3.65±0.14	—	P_2	4.2	4.2		
		P_1	4.67			
4.74±0.14	—	P_1	5.76	5.76−0.14	≦5	≦5
5.13±0.15	—	P_1	6.15	6.15−0.15	≦2	≦2
5.82±0.24	*F*	P_1	6.84	6.84−0.24	Sum ≈20	Sum ≈20
6.48±0.20	*G*	P_1	7.50	7.50−0.20		
9.3 ±0.3	*H*	P_1	10.3	10.3−0.3	12	11

both. The spectrum interpretation and yield estimates are given in Table V.

(2) $Mg^{26}(p,\gamma)Al^{27}$ (*336-kev Resonance*)

The presence of only two gamma-rays was discernible from the thin target curves: a 5.8-Mev and a 2.8-Mev gamma-ray (see Fig. 8). The intensities of the two gamma-rays were comparable. The observed yield for the 2.8-Mev gamma-ray, as given in Table VI was lower than for the 5.8-Mev gamma-ray. However, since the thin magnesium targets were difficult to work with, having a tendency to evaporate under bombardment, these relative yield figures are probably not very reliable.

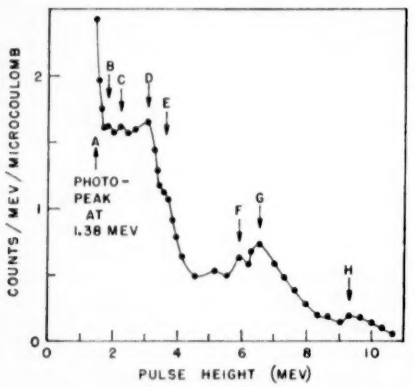

FIG. 6. $Na^{23}(p,\gamma)Mg^{24}$ gamma-ray spectrum (305-kev resonance). Peaks *B*, *C*, *D*, and *E* are not sufficiently well resolved to permit certain identification of the gamma-rays involved. Peaks *F*, *G*, and *H* are the pair peaks (P_1) due to the 6.8-, 7.5-, and 10.3-Mev gamma-rays, respectively.

(3) $Mg^{26}(p,\gamma)Al^{27}$ (*314-kev resonance*)

This resonance is about 1/12 as strong as the 336-kev resonance. The observed thin target yield above 1 Mev was about twice background. Because of very poor statistics in this case (this being the weakest of all the resonances analyzed), the interpretation of the observed spectrum is somewhat in doubt. The information about the spectrum was obtained from one thick target and two thin target curves.

To make sure that the observed pulse-height distributions were actually due to this resonance, the areas under the thin target curves were calculated. The results were compared with the yield at 314 kev obtained from the excitation curves and were essentially the same.

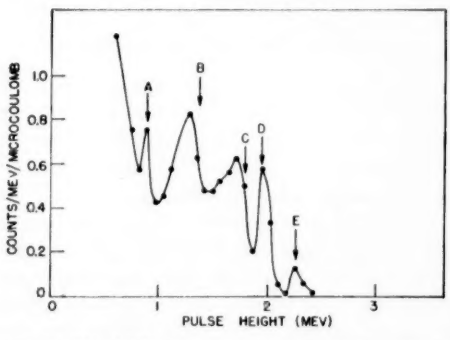

FIG. 7. $Mg^{24}(p,\gamma)Al^{25}$ gamma-spectrum due to the resonance at a proton energy of 222 kev. Thick target: $E_p=270$ kev; 500 microcoulombs per point. Peak *D* is interpreted as the photopeak of a 1.95-Mev gamma-ray, with pair peak (P_1) at *A* and Compton edge at *C*; peak *E*, the photopeak of a 2.3-Mev gamma, with pair peak (P_1) at *B*.

TABLE V. Gamma-rays from reaction: $Mg^{24}+p \rightarrow Al^{25}+h\nu$.

P_1: pair peak with escape of both annihilation quanta, at $E_\gamma - 2mc^2$.
P_2: pair peak with escape of one of the annihilation quanta, and Compton peak superimposed, at approximately $E_\gamma - mc^2$.

Resonance energy (kev)	Observed peak location (Mev)	Identification in Fig. 7 and interpretation		Energy of associated γ ray (Mev)	Extrapolated yield (counts of 64/500 μcoul)	Relative intensity (counts of 64/500 μcoul)
	0.48±0.05	...	Annihilation photo *or* nuclear photo	0.48±0.05	30	~6 (nuclear component)
222	0.94±0.05	*A*	P_1			
	1.60±0.06	*C*	Compton	1.95±0.06	6	6
	1.94±0.06	*D*	photo			
	1.30±0.05	*B*	P_1	2.35±0.1	2	2
	2.35±0.1	*E*	photo			

As a further check, the 314-kev and 336-kev resonance yields were calculated, giving a ratio of about 1/14. From the data obtained by Tangen, who used G-M counter detection, a ratio of about 1/12 was estimated for the two resonance yields, which would seem to be a satisfactory agreement. The location of the resonance also agreed with his value (314) within 1 kilovolt.

In spite of the low yield, it is concluded that the 5.8-Mev gamma-ray which predominated at the 336 kev resonance did *not* appear at 314 kev. Instead, the observed increased counting rates were observed in the region of 3 to 3.5 Mev pulses, corresponding to one or more gamma-rays in the neighborhood of 4 Mev in energy.

X. DISCUSSION AND CONCLUSIONS

The "relative intensity" numbers listed in Tables III–VI (definition given in Sec. VIII) are proportional to the number of quanta of each energy which would have been *absorbed in the crystal* if the efficiency of the crystal had been a constant, independent of gamma-energy. Assuming that differences in the angular distributions of the emitted gamma-rays are not important (in view of the large solid angle accepted by the crystal, and the rather broad target), the "relative intensity" numbers are then proportional to the number of quanta of each gamma-energy *emitted from the target* per incident proton.

(1) $Al(p,\gamma)Si^{28}$

At the 325- and 404-kev resonances in aluminum, excited states of Si^{28} are produced having excitation energies of approximately 12.00 and 12.08 Mev, respectively,[15] in the center-of-mass system.

In the absence of any competing reactions, the full energy, which is about the same in the laboratory system, must be release by the emission of gamma-rays, either directly to the ground state, or in cascade, via intermediate levels.

The observed gamma-rays, 1.81±0.04, 2.82±0.07, 4.65±0.10, 5.04±0.10, 7.12±0.15, and 7.46±0.15 Mev, can be accounted for in a decay scheme (the same for both resonances) involving levels in Si^{28} at 1.81±0.05, 4.63±0.10, and 7.12±0.15 Mev. If the 7.12-Mev gamma is emitted first, and the present work cannot rule out this possibility, then an additional level, at 5.04±0.10, is involved. The "relative intensities" given in Table III for a proton energy of 415 kev (including both the 325 and 404 kev resonances), are the same for the 1.81 and 2.82-Mev gammas, each having the value 12, indicating that they may be in cascade; the sum of the intensities of the 4.65- and 5.04-Mev gammas is about 5; and the sum of the intensities of the 7.12- and 7.46-Mev gammas is between 12 and 16. These observed "relative intensities" are seen to be consistent

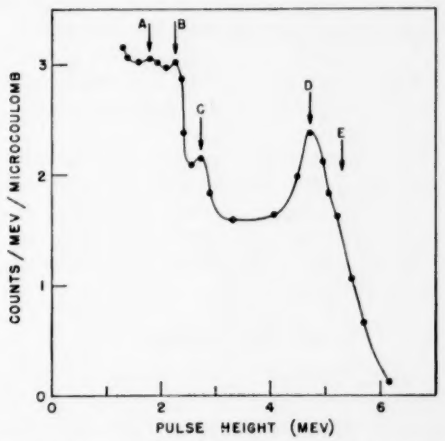

FIG. 8. Thin target gamma-spectrum from $Mg^{26}(p,\gamma)Al^{27}$ at the 336-kev resonance. $E_p = 336$ kev. Peaks *A*, *B*, and *C* are associated with a single gamma-ray of energy 2.8 Mev. Peak *D* is the pair peak (P_1) due to a 5.8-Mev gamma-ray whose second peak (P_2) at *E* is not resolved.

[15] D. E. Alburger and E. M. Hafner, Revs. Modern Phys. **22**, 376 (1950).

TABLE VI. Gamma-rays from reaction: $Mg^{26}+p \rightarrow Al^{27}+h\nu$.

P_1: pair peak with escape of both annihilation quanta, at $E_\gamma - 2mc^2$.
P_2: pair peak with escape of one of the annihilation quanta, and Compton peak superimposed, at approximately $E_\gamma - mc^2$.

Resonance energy (kev)	Observed peak location (Mev)	Identification in Fig. 8 and interpretation		Energy of associated γ-ray (Mev)	Extrapolated yield (counts of 64/500 μcoul)	Relative intensity (counts of 64/500 μcoul)
	1.85±0.10	*A*	P_1			
	2.25±0.12	*B*	P_2	2.83±0.14	35	35
336	2.83±0.14	*C*	Photo			
	4.78±0.25	*D*	P_1	5.80±0.25	45	45
	5.30±0.25	*E*	P_2			
314	(?)3.20±0.2	—	P_1	(?)4.2±0.2	3	3
	(?)3.70±0.2	—	P_2			

with the requirements of the proposed decay scheme, which is drawn in Fig. 9.

Levels in Si^{28} at 1.78±0.13, 4.47±0.10, 4.91±0.21, and 7.10±0.12 Mev have been determined by Peck[16] from the neutrons emitted in the reaction $Al^{27}(d,n)Si^{28}$. These levels are seen to be consistent with the ones proposed for the decay scheme.

Rutherglen *et al.*,[17] bombarding thick targets of aluminum with 750-kev protons, observed the gamma-rays with a pair spectrometer. Their bombardment included at least eight resonances between 404 kev and 750 kev in addition to the 404-kev and 325-kev resonances involved in this work. They were able to resolve three gamma-rays of energies 7.62±0.1, 10.46±0.07, and 12.12±0.1 Mev, but suggested the possibility of other gamma-rays in the neighborhood of 7.6 Mev. The 7.62±0.1 Mev gamma-ray is possibly the same as the 7.46±0.15 Mev gamma-ray observed in the present work.

Since no gamma-energies greater than 7.5 Mev were observed for the 415-kev proton bombardments, whereas at 750 kev, 10 to 12-Mev gammas are present, it is evident that other modes of decay of the excited states of Si^{28} must be more probable in the higher resonances. According to Tangen, the mean gamma-ray energy at the 503-kev resonance (which is about six times more intense than the 404-kev resonance) is 9.2 Mev compared with 5.4 Mev at both the 404- and 325-kev resonances.

It should be mentioned that decay through a level in the neighborhood of 6.1 Mev has not been entirely excluded. Since there was known to be a small amount of fluorine contamination present, however, the observed gamma-ray of this energy was assigned to the reaction $F^{19}(p;\alpha,\gamma)O^{16}$.

(2) $Na^{23}(p,\gamma)Mg^{24}$

The excited state of Mg^{24} produced here has 12.0_3 Mev of energy, about the same as the previously discussed Si^{28}. The observed gamma-rays: 1.38±0.04 Mev ("relative intensity" 28); 6.84±0.24 and 7.50±0.20 Mev (sum of intensities 20); 10.3±0.3 Mev (intensity 11); a probable gamma-ray at 3.6±0.2 Mev; and others in the region 2–4.5 Mev *do not* appear to be sufficient to determine a complete decay scheme, which is consistent with the observed relative intensities. The intensity of the 1.38-Mev gamma-ray seems to be too large to be accounted for entirely by the simple cascade:

$$(10.3\pm0.3)+(1.38\pm0.04)=11.7\pm0.3.$$

Possible emission of the 7.50±0.20 Mev gamma-ray to the well-known 4.14-Mev level in Mg^{24} (the 4.14 level decays by emission of a 2.76-Mev gamma to a level at 1.38 Mev) seems to be somewhat outside the limits of experimental error as far as the energy is concerned.

Since the intensity of the 1.38-Mev gamma is of the order of the sum of the intensities of the 6.84±0.24, 7.50±0.20, and 10.3±0.3 gammas, it seems likely that each of these high energy gammas is part of a cascade passing through the 1.38-Mev level. Energy considerations suggest the presence of at least one gamma-ray of energy less than or equal to 0.5 Mev.

One possible decay scheme which is consistent with the experimental data would require levels at 5.1, 4.6, 1.8, and 1.38 Mev. The gamma-rays in this scheme would be 10.3, 7.4, 6.9, 3.7, 3.2, and 0.4 Mev.

(3) $Mg^{26}(p,\gamma)Al^{27}$

The excited state of Al^{27} produced at the 336-kev resonance appears to decay by means of two gamma-rays: 5.8 and 2.8 Mev. The excitation energy, as given in the paper of Alburger and Hafner, is 8.61 Mev. Energy levels at both 5.8 and 2.8 Mev are both known from other researches.[18] Hence, the decay with either order of emission is shown in the decay scheme proposed in Fig. 9.

The 314-kev resonance, producing Al^{27} with approximately the same excitation energy of 8.6 Mev, showed no evidence of a 5.8-Mev gamma-ray. Low intensity prevented an extended search of the pulse-height distribution, but gamma-rays in the region of 4 Mev were indicated. It is suggested that the decay takes place

[16] R. A. Peck, Phys. Rev. **76**, 1279 (1949).
[17] Rutherglen, Rae, and Smith, Proc. Phys. Soc. (London) **64**, 913 (1951).
[18] For data on Al^{27} levels, see H. F. Stoddard and H. E. Gove, Phys. Rev. **87**, 238, 262 (1952); Reilley, Allen, Arthur, Bender, Ely, and Hausman, Phys. Rev. **86**, 857 (1952).

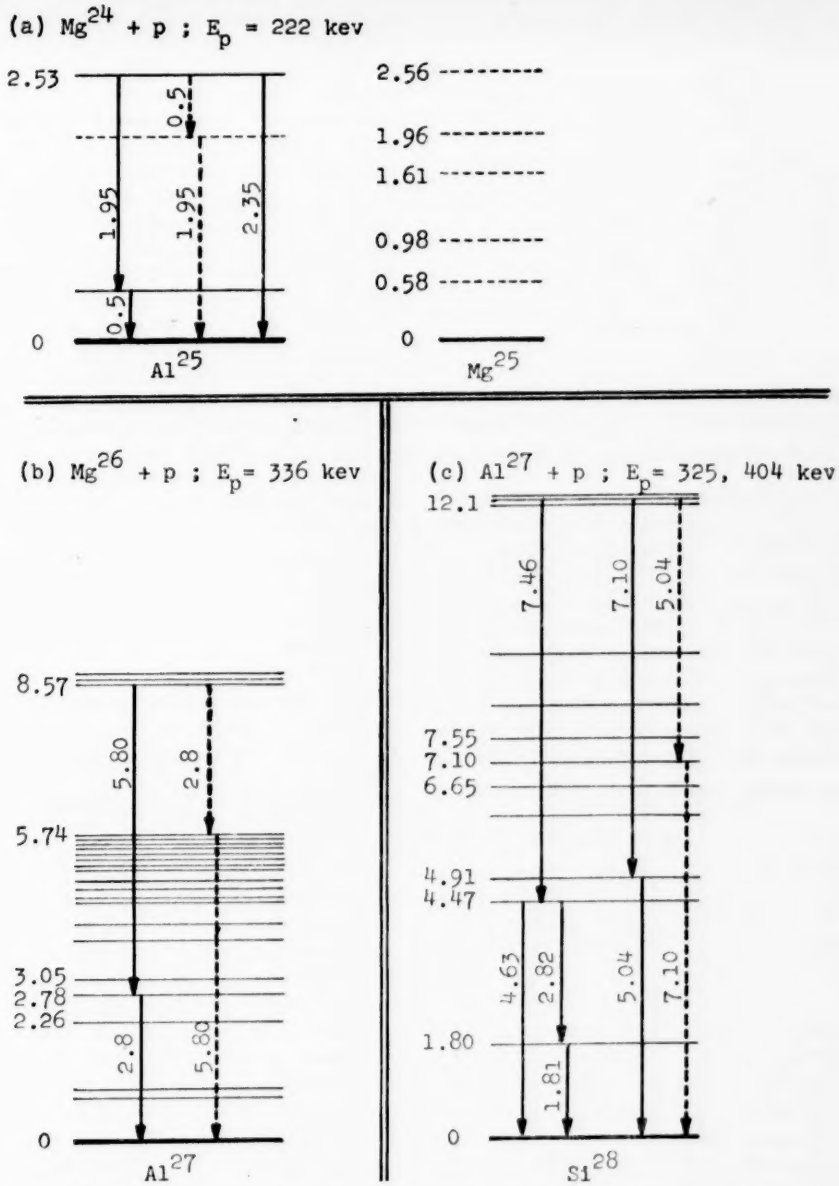

FIG. 9. Energy level diagrams drawn for Al^{25}, Al^{27}, and Si^{28} with level positions obtained from the literature. The gamma-transitions indicated are the probable modes of decay from the excited states, as determined from the observed gamma-rays. A permutation of the order of emission of 2 gammas, which is also consistent with the experimental results and a known intermediate level, is indicated by dashed lines. The known levels of Mg^{25} are drawn in dashed lines for comparison with the present results for the mirror nucleus Al^{25}.

either through a 4.3-Mev (known) level with emission of two 4.3-Mev gammas, or through some other level in the neighborhood of 4 Mev of excitation energy.

(4) $Mg^{24}(p,\gamma)Al^{25}$

The observed gamma-rays 1.95±0.06 Mev (intensity 6), 0.48±0.05 Mev (intensity 6), and 2.35±0.1 Mev (intensity 2) can be combined into the decay scheme shown in Fig. 9. This scheme is in reasonable agreement with an estimated excitation energy of 2.3+0.21=2.5 Mev, where 2.3 Mev is the estimated[19] binding energy of a proton added to Mg^{24}, and 0.21 Mev is the kinetic

[19] See, for example, Louis T. Koester, Phys. Rev. **85**, 643 (1952).

TABLE VII. Estimated yields.

Reaction	Proton energy at resonance (kev)	Target	Estimated number of reactions per proton $\times 10^{12}$
$Na^{23}(p,\gamma)Mg^{24}$	305	Thick Na_2SO_4	19
$Mg^{24}(p,\gamma)Al^{25}$	222	Thick magnesium	5.0
$Mg^{26}(p,\gamma)Al^{27}$	314	Thick magnesium	1.9
	336	Thick magnesium	25
$Al^{27}(p,\gamma)Si^{28}$	325	Thick aluminum	1.3
	404	Thick aluminum	7.5

energy of a proton in the center-of-mass system for the 222-kev resonance. It should be noted that the presence of 0.9- and 1.6-Mev gamma-rays, whose energies would also add up to the estimated excitation energy, cannot be excluded, as may be seen from Table IV. Support for the above results may be obtained by comparison with the energy levels of the mirror nucleus Mg^{25} as given by Endt *et al.*[20] They give 0.583, 0.976, 1.611, 1.957, and 2.562 Mev for the first five excited states.

On the basis of the proposed decay schemes, the relative intensities, and the geometry of the detecting system, it becomes possible to estimate the reaction probabilities, i.e., the number of (p,γ) reactions taking place per proton hitting each of the thick targets. In the case of the sodium reaction, even without a complete decay scheme, it seems reasonable to assume that the 10.3, 7.5, and 6.8 Mev gammas are the members of three distinct cascades which are the principle ones that occur. Adding the relative intensities of the primary γ-rays of the various modes of decay gives the total relative probability that the (p,γ) reaction takes place.

Using Eqs. (2) and (3) and a distance of about 0.8 in. between target and the center of the crystal, with 0.135 in. of copper in between, an over-all detection efficiency at 6 Mev of about 3.2 percent is obtained.

The resultant calculated reaction probabilities are given in Table VII. They are believed to be correct within about a factor of 2. It may be noted that the most probable of these reactions is less probable by a factor of about 10^3 than the fluorine reaction at 340 kev in CaF_2. The latter is given in the literature as 1.7×10^{-8}.

I wish to express my gratitude to Professor Samuel K. Allison, in whose laboratory this work was done, for suggesting that the problem be undertaken, and for giving invaluable assistance and guidance whenever it was most needed. Thanks are due Gordon duFloth, Peter K. Weyl, and Elias Snitzer for their help with operational problems of the kevatron, and special thanks to Mrs. Sophie Casson who spent many evenings assisting in the taking of data, checking calculations, and helping in the preparation of this paper.

[20] Endt, Enge, Haffner, and Buechner, Phys. Rev. **87**, 27 (1952).

An Anomalous Critical Current Effect in Superconducting NbN†

FLOYD C. HALEY* AND DONALD H. ANDREWS
Department of Chemistry, The Johns Hopkins University, Baltimore, Maryland
(Received November 6, 1952)

Observations have been made of thirty transitions from the normal to the superconducting state occurring in four samples of NbN over a range of current from 0.01 ma to 10 ma. The samples were made from 5 and 10 mil diameter wire and from ¼ to 1-mil thick sheets. For $H_I > 100$ oersted evidence was found for the usual parabolic relation between T and H_I, the field produced at the surface of the wire by currents just sufficient to make $R = 0.5\ R_n$; but for $H_I < 100$ oersted the curve tailed off to higher values of temperature, approaching the axis for $H_I = 0$ tangentially several tenths of a degree above the value of T_0 where it is normally assumed to intersect the axis as a straight line. This is further evidence in support of Mendelssohn's suggestion of a sponge-like structure for superconducting alloys.

ALMOST immediately after his initial discovery of superconductivity forty years ago, Kammerlingh Onnes[1] observed that at temperatures several degrees below the transition point, normal resistance could be restored either by a sufficiently strong electric current (I_c) passing through the metal or by a critical magnetic field (H_c) external to it. Silsbee[2] then showed, in the case of elementary superconductors in the form of wires with circular cross section, that $H_c = H_I$ where H_I is the magnetic field at the surface of the wire produced by the current I_c flowing through it. Further experiments disclosed that, over the range readily observable, the graphs of either H_c or H_I plotted against T were parabolic and followed the relation

$$H_c = H_I = a(T_0^2 - T^2), \tag{1}$$

where T_0 is the temperature of the mid-point of the transition at which, extrapolated to $H_c = 0$ or $H_I = 0$, the resistance R is equal to one-half of the normal resistance R_n, and H_c and H_I are the values which likewise make $R = 0.5\ R_n$ at the temperature T.

As experiments were extended from pure elements to alloys, it was found that in the latter class H_c was usually considerably larger than H_I, but the shape of the graph of either plotted against T was consistent with Eq. (1), as shown in the experiments of Rjabinin and Schubnikow.[3] Moreover, in all the experiments on elements and alloys the evidence indicated that Eq. (1) was obeyed down to the smallest fields or currents which would yield observable changes in resistance. This relation was assumed by London[4] in his treatment of the intermediate state in a wire as the current is increased to I_c. It has been confirmed again in the recent work of Mendelssohn, Squire, and Teasdale[5] dealing with the effect of current on the transition of tin.

Contrary to this assumption, recent studies of the effect of current on the transition of the interstitial alloy NbN have shown[6] that Eq. (1) is not obeyed for small currents (*ca* 1 ma) and that dR/dI becomes a hundred to a thousand times larger than the values obtained with currents above 1 ma, such as are customarily used in making observations of H_I as a function of T. The purpose of this communication is to present more extensive evidence on this point for samples of NbN of different sizes and shapes at values of the current considerably lower than those hitherto employed.

MATERIALS

The niobium was obtained from the Fansteel Metallurgical Corporation of North Chicago, Illinois and was guaranteed to be 99.7 percent pure, the principal impurity being oxygen. Four samples of NbN were prepared by heating the Nb in an atmosphere of NH_3 as described in a previous publication.[7] The details for each sample are as follows:

W5 (five-mil wire). Length 5.5 mm, diam. 0.127 mm. $R_{300°} = 0.2$ ohm. Heated in NH_3 at 1225°C for 30 min.

W10 (ten-mil wire). Length 6.5 mm, diam. 0.254 mm. $R_{300°} = 0.05$ ohm. Nitriding same as W5.

R1 (ribbon cut from 1-mil foil). $3.3 \times 0.45 \times 0.025$ mm³. $R_{300°} = 0.19$ ohm. Heated in NH_3 at 1550°C for 90 min.

R1/4 (ribbon cut from ¼-mil foil). $5.0 \times 0.7 \times 0.0062$ mm³. Heated in NH_3 at 1350°C for 30 min.

Each sample was mounted on the flat surface of a small copper post, using bakelite lacquer to provide thermal contact and electrical insulation between the

† The work reported here is taken from a dissertation submitted by one of the authors (F.C.H.) in partial fulfillment of the requirement for the degree of Doctor of Philosophy at The Johns Hopkins University. Support was obtained from the Office of Naval Research and from the U. S. Department of the Army, Philadelphia Ordnance District, Ballistic Research Laboratories, Aberdeen, Maryland.

* Now at the Engineering Research Laboratory, Experimental Station, E. I. du Pont de Nemours and Company, Wilmington, Delaware.

[1] H. Kammerlingh Onnes, Leiden Physical Lab. Comm. **133**, 3 (1913); **139**, 65 (1914).

[2] F. B. Silsbee, J. Washington Acad. Sci. **6**, 597 (1916).

[3] J. N. Rjabinin and L. W. Schubnikow, Physik. Z. Sowjetunion **7**, 122 (1935).

[4] F. London, *Superfluids I* (John Wiley and Sons, Inc., New York, 1950), p. 123.

[5] Mendelssohn, Squire, and Teasdale, Phys. Rev. **87**, 589 (1952).

[6] D. H. Andrews and C. W. Clark, Nature **158**, 945 (1946); also, Lebacqz, Clark, Williams, and Andrews, Proc. Inst. Radio Engrs. **37**, 1147 (1949).

[7] Andrews, Milton, and DeSorbo, J. Opt. Soc. Am., **36**, 518 (1946).

TABLE I. Values of temperature (°K) at different percent R_n with various values of current (I) used for measurement.

I (ma)	Percent R_n 87.5 percent	75.0 percent	62.5 percent	50.0 percent	37.5 percent	25.0 percent
			R-1 (Ribbon from 1-mil sheet)			
0.010	16.081°K	16.045	16.026	16.015	16.006	15.995°K
0.025	16.069	16.029	16.012	15.998	15.985	15.965
0.050	16.053	16.022	16.005	15.992	15.980	15.943
0.100	16.067	16.034	16.017	16.002	15.981	15.930
0.501	16.049	16.016	15.996	15.978	15.958	15.863
1.005	16.040	16.004	15.983	15.966	15.948	15.883
5.088	16.027	15.987	15.962	15.941	15.921	15.824
10.376	16.016	15.977	15.950	15.929	15.906	15.815
			R-½ (Ribbon from ½-mil sheet)			
0.010	15.798°K	15.777	15.763	15.751	15.741	15.728°K
0.052	15.757	15.738	15.720	15.707	15.688	15.675
0.105	15.759	15.737	15.722	15.706	15.691	15.673
0.210	15.746	15.727	15.710	15.696	15.682	15.667
1.074	15.734	15.710	15.691	15.677	15.662	15.646
2.083	15.706	15.682	15.648	15.648	15.632	15.613
			W-5 (5-mil wire)			
0.025	16.171°K	15.980	15.854	15.697	15.520	15.350°K
0.050	16.130	15.983	15.846	15.695	15.501	15.293
0.075	16.110	15.950	15.790	15.631	15.431	15.227
0.100	16.099	15.940	15.761	15.616	15.436	15.233
0.250	16.057	15.895	15.733	15.575	15.384	15.185
0.500	16.039	15.866	15.708	15.543	13.354	15.141
0.749	16.056	15.857	15.683	15.502	15.306	15.102
1.001	16.021	15.841	15.670	15.492	15.296	15.087
2.496	15.976	15.778	15.590	15.419	15.238	15.033
5.005	15.964	15.743	15.559	15.378	15.189	14.983
7.478	15.909	15.698	15.514	15.331	15.140	14.935
9.936	15.878	15.657	15.474	15.284	15.093	14.888
			W-10 (10-mil wire)			
0.100	16.061°K	15.891	15.794	15.708	15.645	15.552
0.401	15.840	15.724	15.619	15.520	15.376	15.112
1.000	15.845	15.700	15.597	15.497	15.379	15.142
4.021	15.740	15.587	15.460	15.340	15.206	14.991

sample and the post. The ends of the samples were copper plated and tinned and had power and potential leads soldered on.

APPARATUS

Tests were carried out with the samples mounted in the vacuum chamber of a small liquid hydrogen cryostat previously described.[6] As the sample passed through the transition the electrical potential across it was measured by a Leeds and Northrup (Type K) potentiometer-galvanometer assembly. The master potentiometer was made to follow the potential by a servo-mechanism controlled by photocells receiving signals from the galvanometer. Another Type K potentiometer (slave) was geared to the first and in turn fed its potential to a Brown recording potentiometer. Thus a potential of 1μv measured on the master potentiometer would produce a potential of 100 μv on the slave potentiometer. This, in turn, was recorded by the Brown potentiometer which had a full scale reading of 2.5 mv. In this manner a continuous record was obtained of the change of resistance through the transition, even for currents one hundred times smaller than those for which the potential could be measured directly on the Brown recorder. The time rate of change of temperature was normally about 0.01 deg min^{-1}. A typical run would cover the range from the normal to the superconducting state continuously or vice versa, with temperatures read every half-minute from the vapor pressure of the liquid hydrogen.

Cooling was effected by reducing the pressure in the space above the liquid hydrogen to a value slightly less than the vapor pressure of the liquid hydrogen itself; warming was produced by the effect of the normal heat leak, when pumping on the hydrogen vapor was cut off. The agreement between points determined by cooling and by warming indicate a relative accuracy of 0.002°. The thermal contact, between the sample and the copper base in contact with the liquid hydrogen, was determined by experiments with pulsed infrared signals falling on the sample. The results showed that any temperature errors due to the heating of the sample by the measuring current through it, could be neglected for currents <10 ma.

RESULTS

The usual S-type transition curves were obtained with all four samples. Temperature was plotted as a function of time directly on the Brown recorder sheets, based on the observed vapor pressures of hydrogen read at half-minute intervals, and the sets of temperature readings corresponding to a standard set of percentages of R_n were then tabulated as shown in Table I. In plotting the results the field at the surface of the wires was used as ordinate. For the ribbons the field was calculated for a wire of the same cross section as the ribbon. This does not alter the shape of the curve and provides a rough basis of comparison with the results for the wires.

The values of H_1 for sample W-5 are shown in Fig. 1, plotted with the notation used by Burton, Wilhelm, and Smith[8] in a discussion of the current and magnetic

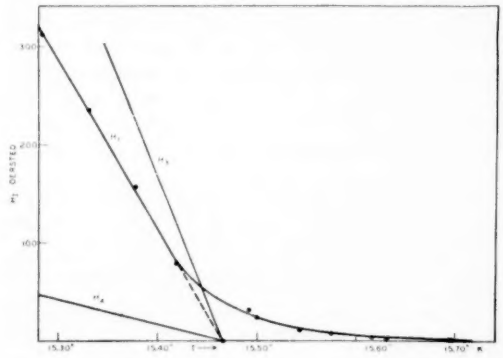

FIG. 1. Critical fields for 5-mil wire sample; H_1 surface field calculated from observed critical current; H_3 externally imposed critical field; H_4 critical field calculated from $C_s - C_n$.

[8] Burton, Smith, and Wilhelm, *Phenomena at the Temperature of Liquid Helium* (Reinhold Publishing Corporation, New York, 1940), p. 309.

field relations in alloys. H_1 shows the field corresponding to the value of the critical current which raises the resistance to 0.5 R_n. H_3 is the external magnetic field required to restore the resistance to 0.5 R_n. This is based on a few rough measurements made in our laboratory on sample R-1/4. No results were available for estimating H_2, the field for the commencement of penetration. H_4 is the field calculated from the results of Armstrong[9] for the difference in heat capacity between NbN powder in the normal and in the superconducting states, using the formula proposed by Rutgers[10] and rigorously established by Gorter and Casimir.[11]

According to previous measurements on superconductors one would expect curve H_1 to follow Eq. (1). For the range of our observations, plotted on the scale of Fig. 1, this would be a straight line intersecting the temperature axis at $H_I=0$. Within the limit of experimental error the four points for $H_I=312$, 235, 157, and 78.4 oersted do lie on a straight line. The points for smaller values of H_I, however, deviate markedly from this straight line and follow a curve with a logarithmic decrement, becoming tangent to the temperature axis several tenths of a degree above the temperature one would have taken normally as the T_0 for Eq. (1). The values for H_3 and H_4 lie on either side of H_1 as might be expected. A curve for H_3 with a slope corresponding to the results of Cook, Zemansky, and Boorse[12] would lie still farther to the right, rising more steeply. It is interesting to note that the results of the above authors showed a suggestion of a decreasing value of dH_c/dT as the effects of fields of less than 500 oersted were observed.

The four points obtained for sample W-10 show the same behavior as may be seen by inspection of Table I.

The points for samples R-1 and R-1/4 are plotted in Fig. 2 and show also the logarithmic decrement instead of following Eq. (1).

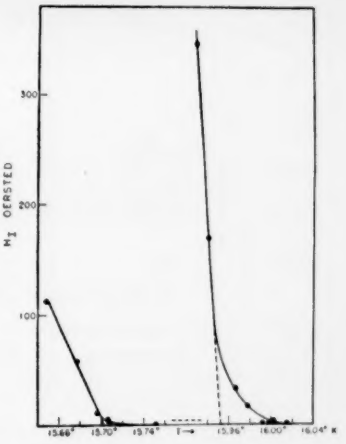

FIG. 2. Values of the surface field calculated from observed values of the critical current for 1-mil ribbon (left) and ¼-mil ribbon (right).

CONCLUSIONS

In the interpretation of results of experiments on superconducting alloys or even on elementary "hard" superconductors one must always be cautious because of the enhanced effect of impurities or inhomogeneities. The departure from linearity of the relation between H_I and T for small values of H_I can, of course, be due to such causes; but considerable evidence against such a conclusion lies in the fact that (a) the samples were prepared from different samples of niobium, (b) two were rolled in the form of sheets and two drawn as wires, (c) the methods of nitriding were quite different, yet the nonlinear anomaly is strikingly the same in all four samples.

Again one might conclude that this anomaly is due to the nature of the change of the intermediate state with current, a relationship which is scarcely understood for elementary superconductors and far less for alloys. Yet it must be born in mind that this anomaly occurs, not in a curve representing the growth of the intermediate state from a condition of little superconductivity to large, but in a relationship between temperature and the current necessary to produce $R=0.5\,R_n$, i.e., the resistance is being held constant and therefore the nature of the intermediate state may be assumed to maintain a constant character while I_c is determined as a function of T.

Mendelssohn[13] has proposed that an alloy just below the superconducting transition consists of a sponge-like network of superconducting filaments imbedded in a matrix of normal metal. If this is true, and if these filaments are of graduated sizes, one can understand how a small current can find a path of low resistance through the metal with values of local H_I at the surface of the filaments not exceeding the critical H_I for the greater part of the path, whereas a larger current destroys superconductivity over a large part of the path and thereby produces a much higher resistance. If this be the case, these results indicate a striking uniformity of filament size distribution, considering the regularity shown in the curves.

Finally, it should be pointed out that there is a region of irregularity in the curves in the neighborhood of about 0.1 ma which is marked enough to suggest something beyond experimental error. Further observation along these lines might be fruitful in obtaining more information on the nature of the intermediate state in alloys of this type.

The authors wish to express their sincere appreciation of the help of Miss Mary Camilla Williams in carrying out the experimental observations.

[9] G. T. Armstrong, J. Am. Chem. Soc. **71**, 3583 (1949).
[10] A. J. Rutgers, Leiden Comm. Suppl. **75b** (1933).
[11] C. J. Gorter and H. Casimir, Physica **1**, 305 (1934); Z. tech. Phys. **15**, 539 (1934).
[12] Cook, Zemansky, and Boorse, Phys. Rev. **79**, 1021 (1950).
[13] K. Mendelssohn, Proc. Roy. Soc. (London) **A152**, 34 (1935).

Electrostatic Analysis of Nuclear Reaction Energies. III*

D. J. Donahue,† K. W. Jones, M. T. McEllistrem, and H. T. Richards
University of Wisconsin, Madison, Wisconsin

(Received October 27, 1952)

Electrostatic analysis of incident and product particles has been used to measure the following reaction energies: $Na^{23}(p,\alpha)Ne^{20}$ (2.379±0.003 Mev); $Na^{23}(p,\alpha)Ne^{20*}$ (0.745±0.002); $Na^{23}(p,p')Na^{23*}$ (−0.439 ±0.001 Mev); $Mg^{24}(p,p')Mg^{24*}$ (−1.371±0.002 Mev); $Al^{27}(p,p')Al^{27*}$ (−0.843±0.002 Mev); $Al^{27}(p,\alpha)Mg^{24}$ (1.594±0.002 Mev); $Al^{27}(p,\alpha)Mg^{24*}$ (0.228±0.003 Mev).

I. INTRODUCTION

ACCURATE measurements of nuclear reaction energies by electrostatic deflection of incident and product particles in high resolution cylindrical[1] and spherical analyzers[2] have been reported in previous communications[3,4] which shall henceforth be referred to as I and II. The present paper reports further measurements using the same equipment and procedures (except for minor modifications which will be explicitly stated). In the present work thin targets of Na^{23}, Mg^{24}, and Al^{27} have been bombarded with protons and various ground-state and excited-state reactions observed and measured. These are individually discussed below and the results summarized in Table I. Figures 1 and 2 are typical figures showing some of the observed reaction edges.

II. PROCEDURE

The only significant change in procedure over that described in I and II is that the spherical analyzer calibration was used as a secondary voltage standard rather than the cylindrical analyzer. In the earlier work (I, II) extreme fluctuations of 0.1 percent in over-all calibration (cylindrical plus spherical analyzer) had been observed over an extended period of time. Insufficient data were then available to determine which of the analyzers was at fault. In the present work observations of narrow resonances in the $Al^{27}(p,\alpha)Mg^{24}$ and $Mg^{24}(p,p')Mg^{24*}$ reactions definitely established that it was the cylindrical analyzer which was drifting. The cause of the drifting was not easily established. Therefore, instead of constant recalibrations of the cylindrical analyzer with the $Li^7(p,n)Be^7$ threshold, the spherical analyzer was calibrated with protons scattered by platinum immediately before and after the cylindrical analyzer was checked with the $Li^7(p,n)Be^7$ threshold. Then, subsequently, the cylindrical analyzer was checked before and after each reaction edge in terms of the spherical analyzer measurement of the elastically scattered protons from a platinum foil. With this arrangement the over-all calibration fluctuation was in general less than 0.03 percent, although occasionally larger fluctuations did occur. To cover these we have assigned an uncertainty in T_1 of 0.05 percent.

We have continued to include an error of 0.1 percent in the final Q value as representing the uncertainty in the absolute voltage scale, though there are probably

TABLE I. Summary of present measurements. T_1 is the energy of the incident particle; T_2 is the energy at 134° 33′ of the light outgoing particle.

Reaction	T_1 (Mev)	T_2 (Mev)	Q (Mev) Q	dQ
$Na^{23}(p,\alpha)Ne^{20}$	1.458	2.893	2.378±0.003	
	1.457	2.894	2.380±0.003	
$Na^{23}(p,\alpha)Ne^{20*}$	2.925	2.610	0.745±0.002	
$Na^{23}(p,p')Na^{23*}$	1.457	0.849	−0.439±0.001	
$Mg^{24}(p,p')Mg^{24*}$	2.412	0.822	−1.371±0.002	
$Al^{27}(p,p')Al^{27*}$	2.309	1.244	−0.843±0.002	
$Al^{27}(p,\alpha)Mg^{24}$	1.187	2.179	1.594±0.002	
	1.187	2.179	1.594±0.002	
$Al^{27}(p,\alpha)Mg^{24*}$	2.742	2.200	+0.230±0.003	
	3.405	2.684	0.225±0.003	
	3.402	2.684	0.229±0.003	

* Work supported by the U. S. Atomic Energy Commission and the Wisconsin Alumni Research Foundation.

† Now at General Electric, Hanford, Washington.

[1] Warren, Powell, and Herb, Rev. Sci. Instr. **18**, 559 (1947).

[2] Browne, Craig, and Williamson, Rev. Sci. Instr. **22**, 952 (1951).

[3] Williamson, Browne, Craig, and Donahue, Phys. Rev. **84**, 731 (1951), referred to as I.

[4] Craig, Donahue, and Jones, Phys. Rev. **88**, 808 (1952), referred to as II.

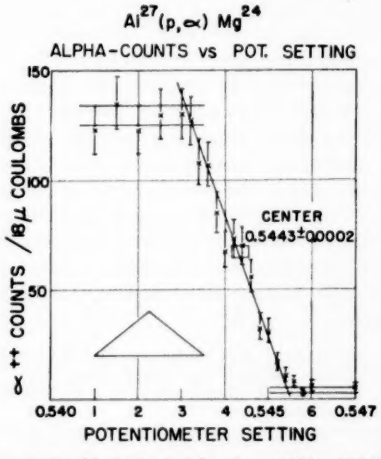

FIG. 1. Doubly ionized alphas from $Al^{27}(p,\alpha)Mg^{24}$.

enough independent checks[5] of this scale that one could with fair assurance reduce this uncertainty by perhaps a factor of two.

The angle between the incident beam and the reaction particles was 134° 33±3′ as in II.[4] The error quoted in all of our present results is simply the square root of the sum of the squares of all the estimated individual uncertainties. This is the error which has been referred to as the "probable" error in I and II. For most of the reactions the largest individual uncertainty is the 0.1 percent of Q which arises from the 0.1 percent systematic uncertainty in the absolute voltage scale.

III. RESULTS AND DISCUSSION

Targets of sodium, magnesium, and aluminum were prepared by evaporation of the metal upon 1000A

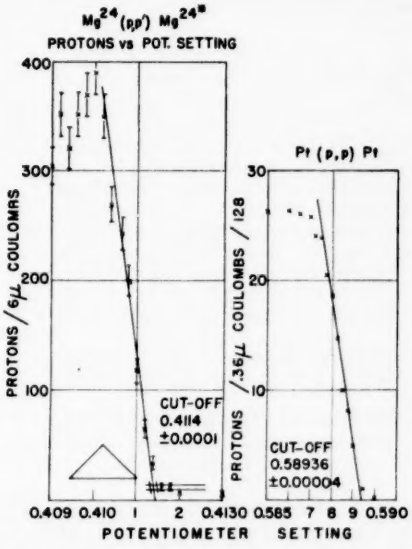

FIG. 2. Protons scattered inelastically from the ~1.37-Mev level of Mg^{24} and the elastically scattered protons from platinum used for analyzer calibration.

nickel foils.[6] For some of the sodium and aluminum data, targets were also prepared by evaporation of the metal upon thick diamond backings. These targets were used when the reaction products happened to come at energies close to that of the elastically scattered protons from the thin nickel backing.

In general targets were "thin" with respect to the energy of the incident particle but were "thick" compared to the spherical analyzer resolution. (The magnesium target was an exception in this respect. The reason for choice of a target "thick" compared to spherical analyzer resulution is discussed in I. The thinness of the magnesium target required an analysis of the reaction data in terms of the extrapolated cut-off energy rather than the half-yield point used for the "thick" target.) To avoid contamination build-up, freshly evaporated targets were used for each reaction edge. In addition, whenever feasible the targets were checked for contamination build-up by examination of the elastically scattered protons from carbon. Targets were kept heated to ~200°C, and only in one case was any measurable carbon build-up observed. In that instance the correction to the Q value necessitated by the contamination was only 0.4 kev.

First-order relativistic corrections were applied throughout the analysis as in I and II.

Table II displays the component errors making up the over-all uncertainty in the Q value for the $Al^{27}(p,\alpha)Mg^{24}$ reaction and is typical of the other data.

Table III compares our present reaction measurements with the best of the other available data. In general, there is very satisfactory agreement of most

TABLE II. Tabulation of component errors for the $Al^{27}(p,\alpha)Mg^{24}$ reaction.

Source of error	Magnitude	Error in Q (Mev)
Relative calibration of the analyzers	0.05 percent of T_1 0.02 percent of T_2	0.00059 0.00044
Angle of observation	±3′	0.00032
Location of half-value of reaction edge	±0.00088 Mev	0.00106
Absolute calibration [$Li^7(p,n)Be^7$]	0.1 percent of Q	0.00159
		$(\Sigma e^2)^{\frac{1}{2}}=0.0021$

TABLE III. Comparison with other measurements.

	Present data	Other measurements	Method	Reference
$Na^{23}(p,\alpha)Ne^{20}$	2.379 ±0.003	2.34 ±0.04 2.372 ±0.008	mag. spect. mag. spect.	c d
Ne^{20*}	1.634 ±0.004	1.66 ±0.02 1.63 ±0.02 1.631 ±0.006	photo plate $-F^{20}$ decay $-F^{20}$ decay	e f g
Na^{23*}	0.439 ±0.001	0.45 ±0.01 0.43 ±0.02	gamma-spect. mag. spect.	h i
Mg^{24*}	1.371 ±0.002[a] 1.366 ±0.004[b]	1.3680 ±0.0010 1.3697 ±0.0003	$-Na^{24}$ decay $-Na^{24}$ decay	j k
Al^{27*}	0.843 ±0.002	0.844 ±0.020 0.837 ±0.016	mag. spect. mag. spect.	l m
$Al^{27}(p,\alpha)Mg^{24}$	1.594 ±0.002	1.595 ±0.007 1.585 ±0.015	mag. spect. mag. spect.	d c

[a] From Q of $Mg^{24}(p,p')Mg^{24*}$.
[b] From Q's of $Al^{27}(p,\alpha)Mg^{24}$ and $Al^{27}(p,\alpha)Mg^{24*}$.
[c] J. M. Freeman, Proc. Phys. Soc. (London) **A63**, 668 (1950).
[d] Van Patter, Sperduto, Endt, Buechner, and Enge, Phys. Rev. **85**, 142 (1952).
[e] R. Middleton and C. T. Tai, Proc. Phys. Soc. (London) **A64**, 801 (1951).
[f] J. V. Jelley, Phil. Mag. **41**, 1199 (1950).
[g] D. Alburger, Phys. Rev. **88**, 1257 (1952).
[h] Stelson, Preston, and Goodman, Phys. Rev. **86**, 629 (1952).
[i] Endt, Haffner, and Van Patter, Phys. Rev. **86**, 518 (1952).
[j] A. Hedgran and D. A. Lind, Arkiv Fys. **5**, 177 (1952).
[k] Same as j but recalculated for revised Au^{198} gamma-energy (see reference 10) and making use of Co^{60} to Au^{198} ratio determined by D. A. Lind and A. Hedgran, Arkiv Fysik **5**, 29 (1952).
[l] Reilley, Allen, Arthur, Bender, Ely, and Hausman, Phys. Rev. **86**, 857 (1952).
[m] D. M. Van Patter and W. W. Buechner, Phys. Rev. **87**, 51 (1952).

[5] W. J. Sturm and V. Johnson, Phys. Rev. **83**, 542 (1951).
[6] S. Bashkin and G. Goldhaber, Rev. Sci. Instr. **22**, 112 (1951).

observers within their stated errors. Our values for the excited states are obtained either from inelastic proton scattering or from (p,α) reactions to the ground and first excited states.

Only in the case of the Mg^{24} level at ~1.37 Mev is there an independent measurement which is of higher precision than that here reported. This high precision measurement comes from a Na^{24} gamma-ray energy measurement[7] in terms of the absolutely determined Co^{60} gamma-radiation,[8] or the Au^{198} radiation.

This comparison involves also a comparison of two absolute voltage scales, namely, that of Herb, Snowden, and Sala[9] and that of DuMond's curved crystal gamma-spectrometer.[8] It is of interest that DuMond's recent revision[10] of his Au^{198} gamma-energy significantly improves the agreement of the two scales.

We hope in the near future to obtain higher precision in the measurement of this Mg^{24} level so that a really good consistency check of the two scales will be possible.

[7] A. Hedgran and D. A. Lind, Arkiv Fysik **5**, 177 (1952).
[8] Lind, Brown, and DuMond, Phys. Rev. **76**, 1838 (1949).
[9] Herb, Snowden, and Sala, Phys. Rev. **75**, 246 (1949).
[10] Muller, Hoyt, Klein, and DuMond, Phys. Rev. **88**, 775 (1952).

PHYSICAL REVIEW VOLUME 89, NUMBER 4 FEBRUARY 15, 1953

The Secondaries of Penetrating Showers*

C. C. DAMM†
Brookhaven National Laboratory, Upton, Long Island, New York
(Received September 19, 1952)

The momentum spectrum of penetrating shower secondaries at 11 200 feet altitude has been measured by means of the distribution in projected angle of the multiple Coulomb scattering of those particles in a lead plate of a cloud chamber. The resulting spectrum is compared to that obtained for the meson secondaries of stars in photographic plates exposed at 70 000 feet. For mesons above 500 Mev, the two spectra coincide within the errors. At lower energies, and especially around 100 Mev, a marked difference exists. The respective average energies are also different by a factor of about two. All of these differences appear to to result both from selecting particles emitted in the forward direction, and from higher energies of the particles producing the primary event in the present experiment. The average "primary energy" appears to be less than 8 Bev, which is a lower value than one might deduce from the latitude effect of penetrating showers.

A production of photons in carbon by the penetrating shower secondaries has been observed. Interpreted in terms of π^0 production, this is consistent with the photographic plate work that has suggested inelastic charge exchange scattering.

Three decays of neutral V^0 particles observed show that the cross section for V^0 production by the penetrating shower secondaries is most likely an appreciable fraction of the geometrical cross section.

I. INTRODUCTION

IN recent years a considerable amount of experimental effort has been devoted to the study of penetrating showers (PS). Various assemblies of lead and counters have been used to determine the absorption mean free path of PS producing radiation, as well as to determine the collision cross section of such particles with various nuclei. However, the energy of those particles, or the energy spectrum of the secondaries produced in the penetrating shower, cannot be readily measured because the best experimental methods which can be thought of are hampered by too low a rate of occurrence. Also, one hesitates to build a complex apparatus which yields an answer that is not simply interpretable. With a relatively simple apparatus, some data have been collected on the momentum distribution of the PS secondaries.

On the subject of the spectrum of penetrating secondaries, one recalls immediately the photographic plate work of Camerini *et al.*[1] Their data concern stars detected in photographic emulsions at 70 000 feet altitude. *A priori*, the spectrum of the particles produced in PS, and the spectrum of the shower particles of Camerini *et al.* could be quite different; thus a comparison of the present data and theirs is of interest.

Barker and Butler[2] used a magnetic cloud chamber at sea level to measure the momenta of 135 particles under 25 cm of lead; of these, 85 had momenta >1 Bev/c. Their apparatus required sevenfold coincidences and so selected PS events on a fairly rigid basis.

In the present experiment, performed at 11 200 feet altitude, the momentum spectrum of PS secondaries is measured with a geometry such that the minimum number of particles required to arise from the primary interaction is two, although the average number is

* The present research has been carried out under the auspices of the U. S. Atomic Energy Commission.
† Work performed in partial fulfillment of the requirements of New York University for the degree of Doctor of Philosophy.

[1] Camerini, Fowler, Lock, and Muirhead, Phil. Mag. **41**, 413 (1950).
[2] K. H. Barker and C. C. Butler, Proc. Phys. Soc. (London) **A64**, 4 (1951).

certainly higher. (Prompt coincidences of two or more A counters with one or more B counters triggered the chamber. See Fig. 1.) Also, the total amount of lead has been kept to a minimum without too much danger of confusing soft showers with local penetrating showers, because any soft shower capable of triggering two counters in A and one in B (notice the side shielding) would quite certainly be recognized as an electron shower in the picture. In such electron showers it is known that the density of mesons is only 2 percent of the electron density, so that the contribution of air shower mesons to the particles collected and analyzed to obtain the momentum spectrum must really be inappreciable.

On the other hand, the discrimination against pseudo-PS produced by μ mesons can only depend on the geometry immediately adjacent to tray A. The geometry used here is similar to a geometry[3] for which it was found that 90 percent of the A_2B events were due to particles characterized by an absorption mean free path in air of about 120 g/cm^2. That is, no more than 10 percent of the events can be due to mu-mesons.

As a consequence of the low multiplicity required, and of the relatively small amount of lead absorber, the present apparatus must operate in an energy range which is perhaps as low as possible for an apparatus which detects PS. This can also be seen by making a comparison of approximate rates of occurrence of PS per unit surface for some PS detectors used in the past years to study the nuclear-interacting component of the cosmic rays.

Thus, Tinlot,[4] measuring the altitude dependence of PS events, had a rate of 47 hr.$^{-1}$ with a tray surface of 40 sq. in., at mountain altitudes. Walsh and Piccioni,[5] who measured the altitude and latitude dependence of PS with an apparatus similar to Tinlot's, had a rate of 40 hr^{-1} (computed from higher altitude points). Both of these experiments had a total of about 12 in. lead absorber. With a substantially larger thickness of absorber (24 in.), and requiring a sevenfold coincidence, George and Jason[6] had a rate of 5 hr^{-1} over approximately 100 sq. in. The present arrangement had a rate of 55 hr^{-1}, with a total lead absorber of 5 in., and a surface (tray B) of 50 sq. in. It is thus self-suggestive that the primary energy range characteristic of the present experiment should be close to that of Tinlot's and Walsh's, and appreciably less than that of George and Jason's.

II. APPARATUS

The apparatus was operated at Berthoud Pass, Colorado, at 11 200 ft altitude. The A_2B coincidences were made with a resolving time of 5 microseconds, so that random coincidences were negligible.

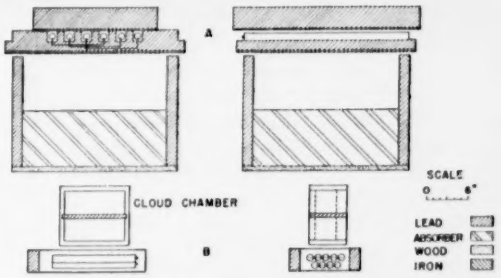

FIG. 1. Apparatus.

The rectangular cloud chamber was kindly made available by Dr. E. C. Fowler at a stage of partial construction. The chamber walls are $\frac{5}{8}$ in. polystyrene with cemented corners, forming a useful, illuminated volume $8\frac{1}{2}\times7\frac{1}{4}\times3$ inches deep. This polystyrene was clamped between a $\frac{1}{4}$-in. glass front plate and an aluminum rear wall. Because of the doubtful strength of this construction, the chamber pressure was restricted to ±5 cm Hg. Consequently, to obtain minimum ionization tracks dense enough for good photography at mountain altitudes, the chamber was filled with krypton. The small chamber size, together with a special filling technique and carefully prolonged operating periods, made this economically feasible.

As compared to argon at the same pressure, one espects an increase in the ionization per cm of about 1.9 for a particle ionizing near minimum in krypton. Indeed, a substantial improvement of this order was observed.

The expansion ratio was pressure controlled, and was varied by adjustment of the regulated air pressure behind the rubber diaphragm. A first-order temperature compensation was achieved by the method of Leighton,[7] although the cloud-chamber room was maintained within ±0.5°C of a set temperature. Altogether, unattended operating periods of 16 hours were the rule, with stable operation over this time.

The fast expansion required 12–14 milliseconds for completion; this time was measured by allowing a collimated light beam to fall on a photocell as the rubber diaphragm completed its last few millimeters of motion. In the compressed position, the rubber blocked the light beam. This simple method was possible because of the transparent (polystyrene) wall construction.

The chamber contained a 0.5-inch lead plate throughout the experiment and was photographed stereoscopically by two cameras.

III. MOMENTUM SPECTRUM

The momentum spectrum of the penetrating secondaries crossing the chamber was determined from the distribution of the projected angle of multiple Coulomb scattering in the 0.5-in. lead plate.

The projected scattering angle was measured in one

[3] O. Piccioni, Phys. Rev. **77**, 1, 6 (1950).
[4] J. Tinlot, Phys. Rev. **73**, 1476 (1948).
[5] T. Walsh and O. Piccioni, Phys. Rev. **80**, 619 (1950).
[6] E. P. George and A. C. Jason, Proc. Phys. Soc. (London) **A63**, 1081 (1950).
[7] R. B. Leighton, Rev. Sci. Instr. **19**, 274 (1948).

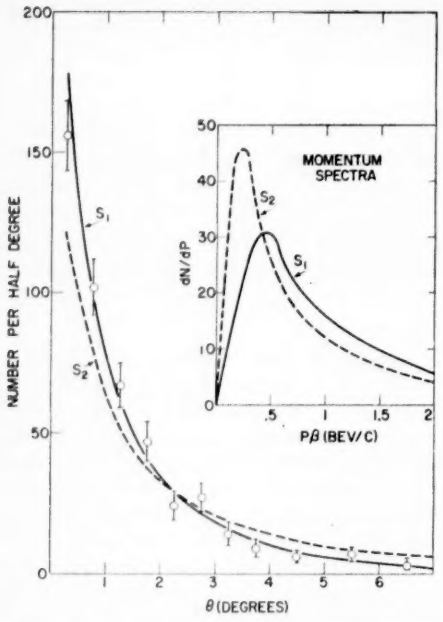

FIG. 2. Distribution of projected angles of scattering in ½-inch Pb, and momentum spectra.

camera view for 507 lightly ionizing (less than ~2 times minimum) penetrating particles whose visible track extended from top to bottom of the chamber. Two absorber arrangements were used, although no distinction is made for the present purposes: (1) 3.2 g/cm² of lead distributed in the absorber volume (Fig. 1); (2) no absorber, with the 1½ inches of lead just below the A counters replaced by 1½ inches of iron.

The bias against observing large angles of scattering has been considered by the method of Crewe and Litherland,[8] and found unimportant for angles below 7 degrees.

The probable error in individual scattering measurements was estimated to be ±0.3 degrees. The results were grouped in 0.5-degree intervals and the experimental points plotted in Fig. 2. There were 28 particles which scattered more than 7 degrees, which, of course, may include some nuclear scatterings.

It is not practically possible to obtain the momentum spectrum directly from the scattering distribution, so a trial and error method was adopted. Momentum spectra were assumed, and the corresponding scattering angle distributions calculated by a numerical synthesis. The fraction of particles in each momentum interval Δp which scatter less than θ is[9]

$$F=\int_0^{\theta}\exp(-\theta^2/2\theta_{\rm rms}^2)d\theta,$$

with $\theta_{\rm rms}^2=(21)^2t/2P^2\beta^2$. t is the plate thickness in radiation lengths (2.4), and P is taken at the mid-point of each Δp. For θ at 0.5-degree values, F is read off directly from tables of the Gauss integral, and the difference between successive F values gives the fraction of particles in Δp per 0.5 degree. After weighting by the number of particles assigned to Δp, a simple synthesis over all momentum intervals gives the scattering angle distribution. In Fig. 2 are plotted two spectra S_1 and S_2 and their scattering distributions so determined. S_1 fits the data better than any of the several spectra tried, while S_2 does not and is included for comparison.

In Fig. 3, the spectra S_1 and S_2 have been converted into energy spectra. Assuming, as an average, that all penetrating showers are produced in the horizontal central plane of the lead above the A counters, the energy spectrum at the point of production has been evaluated, computing the energy loss by ionization along the path from such a production point to the lead inside the cloud chamber (~100 g/cm²). For this correction, it was assumed that all particles observed were mesons. That the dominant portion are mesons is confirmed both by the photographic emulsion work of Camerini *et al.*,[1] who find that ~75 percent of the "shower particles" are mesons, and by the more recent work of Cool and Piccioni[10] who find, in an apparatus similar to the present, that ~80 percent of the penetrating secondaries are mesons.

Above 2 Bev, the differential energy spectrum S_1 decreases as $E^{-2.5}$. The value of the exponent is substantially determined by the *total* number of particles above, say, 2 Bev, and cannot be determined by the shape of the scattering-angle distribution curve at very low angles, because of insufficient accuracy. Although it is difficult to determine the error in this exponent, a value of 2.8 is perhaps compatible with the present data.

The spectrum obtained by Camerini *et al.* for all mesons from stars in emulsions at 73 000 feet is shown on the same plot (Fig. 3). The spectrum S_1 is remarkably different from that obtained in emulsions. The maximum of S_1 is shifted to about 450 Mev, compared to the value of 50 Mev for the Bristol spectrum, while the average total energies are about 2.0 Bev and 800 Mev, respectively. The spectrum S_2 does give a value intermediate between S_1 and Bristol, but appears from Fig. 2 to be inconsistent with the data. On the other hand, it is clear that the spectrum in the present arrangement should be enriched in higher energies because of the triggering requirement, and because only particles projected in the forward direction are accepted.

To examine this explanation in more detail, let us consider the mesons as produced in nucleon-nucleon collisions, including cases where the impinging nucleon is secondary to a previous event in the same nucleus. We may also very reasonably assume that the distribution in angle of the emitted mesons in the c.m.

[8] A. V. Crewe and A. E. Litherland, J. Sci. Instr. **28**, 182 (1951).
[9] B. Rossi and K. Greisen, Revs. Modern Phys. **13**, 240 (1941).
[10] R. L. Cool and O. Piccioni, Phys. Rev. **87**, 531 (1952).

system of the two nucleons is symmetric in the forward and backward hemispheres. The forward hemisphere will project, in the laboratory system, into a solid angle, the semi-aperture of which depends upon the energy of the colliding nucleon (roughly, as the inverse of the square root of the energy). For instance, in the range 2–5-Bev kinetic energy of the colliding nucleon, the semi-aperture in the laboratory system, corresponding to the c.m. forward hemisphere is about 30°. Up to this value of the angle between primary and secondary particles, the requirement that the secondary track cross the cloud chamber cannot introduce much of a bias. If we take into account that the angular distribution in the c.m. system is probably not uniform, we see that the chamber easily receives all of the mesons produced in the forward hemisphere (c.m.), and possibly some of those produced in the backward direction.

Now, the average laboratory energy of the mesons produced in the forward hemisphere (c.m.) is somewhat larger than the average laboratory energy of all mesons. Clearly enough, the ratio of these average energies cannot exceed 2 (given c.m. symmetry). The average total energy in the present experiment is 2050 Mev, while in the experiment of the Bristol group, it is about 800 Mev; the ratio is 2.5. This may be taken as qualitative evidence that the average energy of the PS events is higher than the average energy of the meson-producing stars. The latter energy can be computed from the curves of the Bristol[11] work showing the fraction of stars with meson production *vs* primary energy, and assuming a primary spectrum of $E^{-2.5}dE$. The average value of 4 Bev is the result.

Whether or not secondary collisions taking place in the present experiment, either in the original nucleus of in the absorber below, produce mesons with a degraded spectrum which is added to the meson spectrum of the first collision, the resultant spectrum is still more energetic than the Bristol stars. One concludes that the average energy of the primary particles must be larger than 4 Bev. At the same time, comparing the average energies of the secondaries in the two experiments, the average primary energy in our apparatus appears to be less than, say, twice 4 Bev.

This value is lower than that attributed to the PS detected by Walsh and Piccioni[5] with an apparatus which does not appear to require much more energetic events than the present one. These authors measured a latitude effect of 10 percent and computed the energy of the PS producing particles for two separate assumptions for the behavior of the nucleonic component between the top of the atmosphere and 300 g/cm². The smaller value obtained for the average energy of the registered events was 20 Bev. The value of 8 Bev deduced above indicates that the energy degradation in the 300 g/cm² of atmosphere is even more important than that computed by Walsh and Piccioni, who applied the scheme of Heitler and Janossy, neglecting the contribution of the "cascade" of secondary nucleons.

The fact is also remarkable that the peaks of the two spectra lie at energies which differ by more than a factor of two. In attempting to interpret this on the basis of the angular selection, we note that the angular distribution of shower partices (Bristol paper)[11] about the primary direction is substantially the same for events of different multiplicities, with 16 percent emitted backwards (laboratory system). Unfortunately, no information on the energy spectrum of these particles is available, but even supposing all to be below 350 Mev, the Bristol spectrum contains 62 percent of its particles below this energy, while the spectrum S_1 has only 11 percent in this range. The difference seems too large for the large shift in the spectrum peak to be simply explained by the loss of this backward 16 percent. In order to explain such a large shift again with the forward selection in the present experiment, the assumption that a strong difference in energy exists between backward and forward particles (laboratory system) is not sufficient. One has to assume that a strong difference in energy exists between mesons emitted at angles less than 30° (laboratory), and all of the others. Now, an angular distribution of mesons in the c.m. system which is peaked in the forward and backward directions could give a suitable distribution in angle and energy in the laboratory system. At the same time, this assumption explains the production of so many low energy mesons as found by Camerini *et al.*,[1] whereas the cross section for meson production is only important at energies of the order of a Bev or more. The authors of the Bristol paper[12] prefer to think that the backward emitted mesons (laboratory) are produced in secondary collisions, which process no doubt must have some importance.

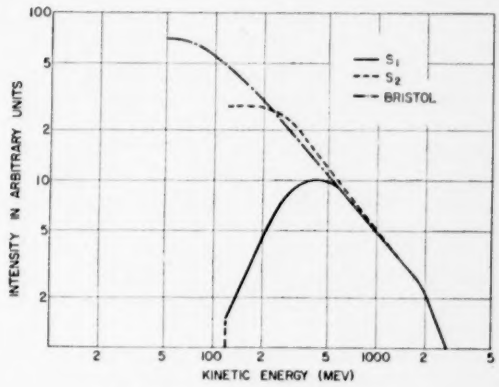

FIG. 3. Energy spectrum at production.

[11] Camerini, Davies, Fowler, Franzinetti, Muirhead, Lock, Perkins, and Yekutieli, Phil. Mag. **42**, 1241 (1951).

[12] Camerini, Davies, Franzinetti, Lock, Perkins, and Yekutieli, Phil. Mag. **42**, 1261 (1951).

As a third possible explanation, if we consider that π-mesons could be absorbed by the same nucleus in which produced, as they are by other nuclei, a plausible interpretation of the backward mesons isotropically distributed would rest on such phenomena as inelastic π-scattering as reported by Lock and Yekutieli[13] and Bernardini *et al.*[14] for "free" mesons. In this case, it would, perhaps, be somewhat easier to understand the difference between the spectrum S_1 of Fig. 3, and the spectrum of Camerini *et al.* on the basis of the triggering requirement and geometrical considerations.

In conclusion, the present experiment shows that, for mesons above 0.5 Bev, the spectrum of the PS secondaries is very similar to the spectrum as determined in photographic plates, and the shape of the spectrum as reported by Camerini *et al.*[1] is supported by the present data. At energies less than 0.5 Bev, a marked difference exists between the two spectra, which appears to result both from selecting forward particles, and from a higher primary energy.

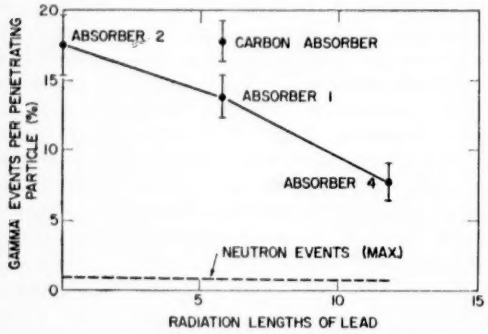

FIG. 4. Gamma-events per penetrating particle for the various absorbers.

IV. GAMMA-EVENTS

A number of events were observed in which two or more lightly ionizing particles emerged below the lead plate of the chamber, with no visible primary particle. That these events are due predominantly to the conversion of photons in the plate can be seen readily from Fig. 4, where is plotted the number of these gamma-events per penetrating particle for each of four absorber arrangements, *viz.*, the two previously mentioned and (3) 34.2 g/cm^2 of carbon in the absorber volume, (4) 36 g/cm^2 of lead distributed in the absorber volume, both (3) and (4) having $1\frac{1}{2}$ inches of lead below the A counters. The abscissa of Fig. 4 is in radiation lengths of lead below the arbitrary zero of the absorber arrangement with iron.

The rapid attenuation of the gamma-events indicates that only a few could be neutron induced events. In fact, for the thickest lead absorber, the neutrons capable of producing such events would have to number as many as all of the penetrating particles observed with this absorber to account for the gamma-events, using an interaction cross section equal to the geometrical one. From the estimate of the number of protons in the beam of penetrating particles (20 percent), one could only hope to account for $\frac{1}{10}$ of the gamma-events by neutrons in this case, since all neutrons would certainly not be energetic enough. Since the maximum absorption cross section is equal to the geometrical, the variation of the number of neutron events with absorber is slight. The dashed line of Fig. 4 indicates the maximum neutron contribution estimated on this basis and its variation with absorber.

Now, the carbon absorber and the 3.2 g/cm^2 of lead arrangement are nearly equivalent thicknesses, measured in radiation lengths. Therefore, at least for the higher energy electronic component, these two absorbers will equally attenuate the gamma-events having their origin in the primary event. The difference between the number of events observed with these two absorbers must be interpreted as a photon production in the carbon (the lead is negligibly thin for nuclear interactions).

Such a production could arise from the decay of neutral pi-mesons generated in the carbon by the PS secondaries. Two mechanisms for π^0 production suggest themselves: (a) production by nucleon secondaries, (b) inelastic charge exchange scattering of π-meson secondaries. Because of the prevalence of events with low multiplicity and wide angles, elastic charge exchange does not appear to be the main source of the gamma-events. The mechanism (a) must certainly be operative to some extent, while the second mechanism (b) is suggested by the experiment of Lock and Yekutieli,[13] using photographic emulsions. These authors estimate from energy balance considerations that the charge exchange process occurs in about half of the π-meson interactions observed.

Without a knowledge of the angular distribution of the emitted π^0 in either of the above processes, it is not possible to determine the production cross section from the present data.

However, Lock and Yekutieli find that scattered charged π mesons are generally strongly reduced in energy with respect to the incident π. It is reasonable to think the same will be true of the π^0, and that furthermore, the angular distribution in such a process will be more or less isotropic.

With this assumption, a cross section can be computed from the net of 3.8 ± 2.3 gamma-events per 100 penetrating particles observed which were evidently produced in the carbon. Assuming that the carbon is effectively concentrated at its horizontal central plane, photons produced at all points in the carbon may be detected, limited only by the illuminated region of the cloud chamber and the B counters. The intensity, $I(\theta)d\theta ds$, of π-mesons incident on the carbon is taken

[13] W. O. Lock and G. Yekutieli, Phil. Mag. **43**, 231 (1952).
[14] Bernardini, Booth, and Lederman, Phys. Rev. **83**, 1075 (1951).

to be a function of zenith angle θ only. The number dn of photons arriving at area $d\sigma$ of the cloud-chamber plate from the area ds of the carbon is

$$dn=(Cp_\gamma/4\pi)[I(\theta)d\theta ds]d\Omega_C,$$

where p_γ is the probability of a π producing a photon in the carbon, $d\Omega_C$ is the differential solid angle of $d\sigma$ seen from ds in the carbon, and C is the factor accounting for the photon loss by conversion in the carbon or lack of conversion in the lead. If $d\Omega_{Pb}$ is the differential solid angle of ds seen from $d\sigma$ in the lead plate, note that $dsd\Omega_C=d\sigma d\Omega_{Pb}$. The number of photons observed is now obtained by integrating all contributions,

$$n=(p_\gamma C/4\pi)\int(I(\theta)d\theta d\sigma)\int d\Omega_{Pb}.$$

The first integral is just the flux n_π of π-mesons through the chamber plate, while the second may be considered an average solid angle $\overline{\Omega}$ of the carbon as seen from the plate. Consequently,

$$p_\gamma=(n/n_\pi)(4\pi/C\overline{\Omega}).$$

From the asymptotic conversion probability of 7/9 per radiation length, C is estimated to be 0.65, while $(\overline{\Omega}/4\pi)$ is estimated at 0.065. The resultant p_γ is therefore 0.90. Accounting for the double photon π^0 decay, the indicated mean free path in carbon for π^0 production by this process is 58 g/cm^2, or approximately geometrical. Thus, the observed production of photons is compatible with a cross section of the order of geometrical for the inelastic charge exchange scattering.

On the other hand, fast nucleons numbering 40 percent (counting neutrons) of the penetrating particles could also account for the observed photon production, although in this case the angular distribution of the π^0 would have to be quite peaked in the forward direction to increase the "detection efficiency" by at least a factor of two over the isotropic case. If, also, only $\frac{1}{3}$ of the mesons produced by nucleons are neutral, it seems improbable that nucleons could account for all the photon production observed.

We must conclude that either of the processes (a) and (b) or a combination of the two, *could* account for the observed production of photons in carbon, although it is unlikely that production by nucleons alone is responsible.

V. NEUTRAL *V* PARTICLES

Three decays of neutral V particles were observed during the experiment. Two of these occurred with carbon as absorber, while the third occurred with the small 3.2 g/cm^2 of lead as absorber. The former two have their apex above the lead plate, while the latter is below the plate. With a mean lifetime of 3×10^{-10} sec, as reported by Leighton,[15] one would expect the V^0 particle to be produced in numbers comparable to the charged penetrating particles (2166) in order to have so many at this distance (68 cm) below the PS production layer. Such a high production in PS has not been observed in other experiments, and a more plausible interpretation is that the first two V^0 particles were produced in the nearby carbon by PS secondaries, while the third V^0 particle actually arrived from the primary event. This view is supported by rather large angular openings of the first two decays (68° and 30°), characteristic of low V^0 energy, and the small angular opening of 3.2° of the third V^0 particle. For the proton-meson decay scheme, the latter angle would indicate a V^0 energy most probably greater than three times the rest energy, so that the relativistic time dilation helps to account for the long path before decay.

This interpretation supports the measurements of Shelton, Wanlass, and Leighton,[16] who find that PS secondaries also produce V^0 particles, and suggest that the majority of V^0 particles are produced by mesons.

An estimate of the cross section for V^0 production by PS secondaries in carbon is simply made on the basis of these two events. With 34.2 g/cm^2 of carbon absorber, 832 penetrating particles were observed in the chamber. If the apparatus detected all V^0 particles produced by these particles, the mean free path is 14 000 g cm^{-2}, or about 230 times the geometrical. However, the detection efficiency certainly is lower than unity because of the decays occurring outside of the chamber. The distance from the center of the carbon to the top of the chamber is 20 cm, or more than twice the mean decay path (at velocity c). A reasonable estimate of the detection efficiency is thus $e^{-2}=0.14$, so that the production cross section becomes 1/30 of the geometrical. Bearing in mind that the low energy secondaries probably do not contribute to this process, it is strongly suggested that energetic π-mesons produce V^0 particles in carbon with a cross section equal to an appreciable fraction of the geometrical cross section.

The author wishes to thank Dr. O. Piccioni for many helpful discussions throughout the course of the work. Dr. R. L. Cool, Dr. W. L. Whittemore, and Dr. E. C. Fowler aided greatly with discussions of cloud-chamber techniques. The Edgerton arcs and the cameras were obtained through the kind cooperation of Dr. R. P. Shutt and his group at Brookhaven National Laboratory. Some of the circuits used had been built by Mr. C. S. Kemic. Thanks are due Dr. T. H. Johnson and Dr. J. C. Boyce for their encouragement and interest throughout the experiment.

[15] R. B. Leighton, Phys. Rev. **87**, 199 (1952).
[16] Shelton, Wanlass, and Leighton, Phys. Rev. **87**, 183 (1952).

The Thermal Expansion of Solids

J. S. DUGDALE* AND D. K. C. MACDONALD
National Research Council, Ottawa, Canada

(Received August 26, 1952)

Under appropriate conditions, the thermal expansion of a solid is closely related to the Grüneisen parameter γ. This in turn may be derived from the variation of the characteristic frequency of the lattice with volume. If, however, this variation is calculated from the usual expressions for the velocity of sound in solids at zero pressure, the γ does not agree with that predicted from lattice theory, and an anomalous thermal expansion is predicted for a solid with a purely harmonic atomic potential.

General expressions for the dependence on volume of the velocity of plane waves in one-, two-, and three-dimensional lattices are obtained, and hence the corresponding Grüneisen γ's. The three-dimensional γ differs by a numerical constant from that used by Slater. All three expressions are now consistent when applied to a body with a purely harmonic atomic potential and predict no thermal expansion.

IF it is possible to express the specific heat at constant volume of a solid as $f(T/\Theta)$, where Θ is a function only of volume, then, as was shown by Grüneisen, the thermal expansion coefficient α is given by

$$\alpha=\gamma C_V\chi/V, \tag{1}$$

where $\gamma=-d\log\Theta/d\log V$ and χ is the compressibility. This is, in fact, equivalent to assuming that the frequency ν_i of each normal mode of vibration of the solid has the same volume dependence, $\nu\sim 1/V^\gamma$.

Although the small vibrations of any lattice may in principle be resolved into its normal modes, such a calculation is in general a cumbersome procedure. In Debye's theory of specific heats these are therefore replaced by the appropriate number of normal modes of a three-dimensional continuum.

For a linear lattice, however, the normal modes and dispersion are well known, and we shall first consider this case. In an infinite linear chain of identical particles of mass m separated by a distance b, in which only nearest neighbor interaction is considered, the velocity of waves of length λ and frequency ν is given by the expression[1]

$$v=\nu\lambda=b\left(\frac{\partial^2 u/\partial r^2}{m}\right)^{\frac{1}{2}}\cdot\frac{\sin(\pi b/\lambda)}{\pi b/\lambda},\quad \text{for}\quad \lambda\geqslant 2b, \tag{2}$$

in which the energy of interaction between two particles, u, depends only on their instantaneous mutual separation, r. There is thus a limiting frequency,

$$\nu_m=\frac{1}{\pi}\left(\frac{\partial^2 u/\partial r^2}{m}\right)^{\frac{1}{2}}, \tag{3}$$

which may be used to characterize the spectrum of frequencies. If, however, more than nearest neighbor interaction is envisaged, it is no longer possible to represent the spectral behavior by a limiting frequency. From Eq. (3),

$$\gamma=-\frac{d\log\nu_m}{d\log l}=-\frac{l}{2}\frac{\partial u''/\partial l}{u''}, \tag{4}$$

where l is the length of the chain, and we have written u'' for $\partial^2 u/\partial r^2$.

For the one-dimensional continuum, moreover, the velocity of longitudinal waves (the only kind of vibration logically possible in one dimension) is

$$v=(E/\rho)^{\frac{1}{2}}, \tag{5}$$

where E is the elastic modulus of the continuum and ρ its mass per unit length. Thus, the frequency corresponding to a wavelength λ is

$$\nu=\lambda^{-1}(E/\rho)^{\frac{1}{2}}, \tag{6}$$

and so

$$\gamma=-\frac{l}{2}\frac{\partial E/\partial l}{E}. \tag{7}$$

This is quite equivalent to Eq. (4) for a linear chain and, in particular, it vanishes if E is strictly constant.

The behavior of a two-dimensional lattice is already too complex to be capable of brief calculation. However, the velocity of propagation of plane waves in, say, a monatomic triangular lattice with nearest neighbor interactions may readily be evaluated for certain particular directions, and the calculation could in principle be extended to any arbitrary direction. The results again indicate that the velocity depends on u'' in the form

$$v=kb\left(\frac{u''}{m}\right)^{\frac{1}{2}}\cdot\frac{\sin\pi b/\lambda}{\pi b/\lambda}, \tag{8}$$

where b is now a lattice parameter dependent on the direction of propagation, and k is a geometrical constant depending on the direction of the wave and its type (i.e., longitudinal or transverse).

This leads directly to a value of γ:

$$\gamma=-\frac{d\log\nu_m}{d\log A}=-\frac{l}{4}\frac{\partial u''/\partial l}{u''}=-\frac{3}{4}-\frac{A}{2}\frac{\partial^2 P/\partial A^2}{\partial P/\partial A}\quad(\text{for } P=0), \tag{9}$$

where l is now a linear dimension of the lattice, P is the force/unit length, and A is the area of the lattice.

* National Research Laboratories Postdoctorate Fellow.

[1] L. Brillouin, *Wave Propagation in Periodic Structures* (McGraw-Hill Book Company, Inc., New York, 1946), Chap. IV.

For the corresponding two-dimensional continuum the formula for the velocity usually quoted in texts is

$$v=\left(\frac{\chi}{\rho(1+\sigma)}\right)^{\frac{1}{2}}, \tag{10}$$

where $\chi=-A\partial P/\partial A$, $\rho=M/A$, and σ is the two-dimensional Poisson's ratio. If this expression is then used to derive γ, one gets

$$\gamma=-\frac{1}{2}-\frac{A}{2}\frac{\partial^2 P/\partial A^2}{\partial P/\partial A}, \tag{11}$$

using the fact that σ (the limiting value of Poisson's ratio for small deformations) in a monatomic lattice does not change with a homogeneous areal change.[2] It will be seen that this does not agree with Eq. (9). Moreover, if the continuum is to correspond to a lattice in which the atoms oscillate purely harmonically [i.e., the atomic potential is the form $u\propto(r-r_0)^2$], then the total internal energy U_0 at absolute zero (Roberts,[3] Slater[4]) must have the form

$$U_0\propto(A^{\frac{1}{2}}-A_0^{\frac{1}{2}})^2;$$

and hence, for $T\to 0$ from Eq. (11),

$$\gamma=-\tfrac{1}{2}+\tfrac{3}{4}=\tfrac{1}{4}.$$

The predicted thermal expansion thus presents a dilemma, since for a purely harmonic atomic potential no atomic mechanism is present to produce such an expansion.

These difficulties persist in the case of a three-dimensional continuum where (see Slater[5]) a value for the Grüneisen parameter,

$$\gamma=-\frac{2}{3}-\frac{V}{2}\frac{\partial^2 p/\partial V^2}{\partial p/\partial V}, \tag{12}$$

is then predicted, and an ideal harmonic body with

$$U_0\propto(V^{\frac{1}{3}}-V_0^{\frac{1}{3}})^2,$$

would then have

$$\gamma=-\tfrac{2}{3}+1=\tfrac{1}{3}.$$

The error arises from the use of formulas for the vibrational velocity which are in fact only valid when $P=0$, and $p=0$ in the two-dimensional and three-dimensional cases, respectively.

The correct expressions follow at once from the fact that the velocity of "plane" waves in a monatomic lattice of any dimensions with nearest-neighbor interaction is always of the form

$$v\propto l(u''/m)^{\frac{1}{2}},$$

where l is the lattice constant and u the interatomic potential.

Alternatively, by extending elasticity theory to the case of small deformations under a finite applied pressure, it is readily shown that for a three-dimensional solid the instantaneous Young's modulus is related to the bulk modulus by

$$E=3(1-2\sigma)\{V\partial p/\partial V+\tfrac{2}{3}p\}. \tag{13}$$

Either mode of attack then yields

$$v\propto l(-\partial F/\partial l)^{\frac{1}{2}}, \tag{14}$$

$$v\propto A(-\partial P/\partial A-P/2A)^{\frac{1}{2}}, \tag{15}$$

$$v\propto V(-\partial p/\partial V-\tfrac{2}{3}p/V)^{\frac{1}{2}}. \tag{16}$$

These expressions evidently reduce to the conventional formulas for the particular case of zero "pressure." However, when differentiated to yield γ, we now have

$$\gamma=-\frac{l}{2}\frac{\partial^2 F/\partial l^2}{\partial F/\partial l}, \tag{17}$$

$$\gamma=-\frac{3}{4}-\frac{A}{2}\left\{\frac{\partial^2 P/\partial A^2-3P/4A^2}{\partial P/\partial A+P/2A}\right\}, \tag{18}$$

$$\gamma=-1-\frac{V}{2}\left\{\frac{\partial^2 p/\partial V^2-10p/9V^2}{\partial p/\partial V+2p/3V}\right\}, \tag{19}$$

which for zero "pressure" reduce to

$$\gamma=-\frac{l}{2}\frac{\partial^2 F/\partial l^2}{\partial F/\partial l}, \tag{20}$$

$$\gamma=-\frac{3}{4}-\frac{A}{2}\left\{\frac{\partial^2 P/\partial A^2}{\partial P/\partial A}\right\}, \quad \text{(see Eq. (9))} \tag{21}$$

$$\gamma=-1-\frac{V}{2}\left\{\frac{\partial^2 p/\partial V^2}{\partial p/\partial V}\right\}, \tag{22}$$

and for a "body" of n dimensions,

$$\gamma=-\frac{3}{2}\left(\frac{n-1}{n}\right)-\frac{\mathcal{U}}{2}\left\{\frac{\partial^2\mathcal{P}/\partial\mathcal{U}^2}{\partial\mathcal{P}/\partial\mathcal{U}}\right\},$$

where $\mathcal{P}$ and $\mathcal{U}$ are the generalized pressure and volume, respectively. If now these expressions are applied to the case of "bodies" with purely harmonic potentials, γ (and hence the expansion coefficient) is *always* zero, as we should expect.

So long as we consider only equations of state at absolute zero, the derivatives $\partial p/\partial V$ and $\partial^2 p/\partial V^2$ are determined without ambiguity, since then the p, V relationships only involve purely mechanical quantities.

[2] Indeed, under these conditions, for any given axis in the lattice, the ratio of the differential orthogonal displacements is a purely geometrical constant dependent on the specific lattice type.

[3] J. K. Roberts, *Heat and Thermodynamics* (Blackie and Son, Ltd., London, 1951), pp. 534–5.

[4] J. C. Slater, *Introduction to Chemical Physics* (McGraw-Hill Book Company, Inc., New York, 1939), p. 212.

[5] See reference 4, p. 239.

In general, however, these derivatives must be evaluated under the physical conditions obtaining when a sound wave is propagated through the body. For example, at low enough temperatures a perfect infinite lattice without impurity will have a thermal conductivity tending to infinity. Consequently, the changes which occur during the propagation of a sound wave will be isothermal, and $(\partial p/\partial V)_T$ is the appropriate derivative. At higher temperatures, however (and this will usually include room temperature),the processes will be practically adiabatic so that $(\partial p/\partial V)_S$ should be employed.

At intermediate temperatures the conditions for the first derivative will be neither isothermal nor adiabatic but lie between. Then within the limitations of the theory $\partial p/\partial V$, and hence the wave velocity and Θ, depend only on the volume. Under these circumstances, the second differentiation with respect to volume presents no ambiguity.

Comparing Eq. (22) with Eq. (12), it follows that Slater's values[6] based on experimental p: V data must be diminished by 0.33. This correction then slightly improves the over-all agreement.

This work forms part of a general investigation of the effects of anharmonicity on the thermodynamic properties of simple solids and the electrical resistance of metals.

[6] See reference 4, pp. 393, 451.

PHYSICAL REVIEW VOLUME 89, NUMBER 4 FEBRUARY 15, 1953

Multiple Scattering Corrections to the Impulse Approximation in the Two-Body System*

K. A. Brueckner
Indiana University, Bloomington, Indiana
(Received November 10, 1952)

Exact solutions for the scattering of a fast particle by two heavy scatterers are obtained and compared with the usual treatment of the impulse approximation in which multiple scattering is neglected. It is found that the multiple scattering qualitatively changes the solution except in the extreme Born approximation limit. The methods developed are applied to the isotopic spin dependent, but spin independent, scattering of mesons in the deuteron. It is found that if high energy scattering is assumed to be in the isotopic spin $\frac{3}{2}$ state, a considerable depression in the total cross section can be expected for phase shifts larger than 45 degrees.

I. INTRODUCTION

THE impulse approximation[1–3] has been developed to deal with the scattering of a fast particle by a system of heavy scatterers where the motion of the scattering centers can be neglected during the scattering process. This approximation leads to simplified theoretical evaluations of many processes and has been applied in particular to a variety of phenomena in deuterium.[4] In these applications, it has been argued that multiple scattering effects can be neglected if the free-particle scattering amplitudes are small compared with the deuteron radius. It will be shown, however, that this criterion is incorrect and that the neglect of multiple scattering is valid only in the limit where the Born approximation is valid for the single scattering center, leading otherwise to qualitatively incorrect results. The exact solutions, in the framework of the impulse approximation, will be discussed first for the simple case of S-state scattering and secondly in the case of P-state meson scattering. In the latter case, spin independent but isotopic spin dependent scattering will be considered.

We shall not discuss the validity of the impulse approximation as such, since this has been discussed in detail particularly by Chew and Wick,[2] and by Chew and Goldberger.[3] We shall also not attempt to consider the effects of scatterings which do not conserve energy since, although such processes undoubtedly give corrections to the impulse approximation, they are distinct from the effect we wish to consider here.

The methods developed here will be applied to the evaluation of spin dependent scattering and to photomesonic phenomena in a forthcoming paper.

II. THE IMPULSE APPROXIMATION FOR S-STATE SCATTERING

We shall consider this very simple case to illustrate the consequences of an exact treatment of the impulse approximation. For the case of S-state scattering from

* This work was done in part while the author was a visiting physicist at Brookhaven National Laboratory during August and September, 1952. The hospitality of this laboratory is gratefully acknowledged. This work was also supported in part by a grant from the National Science Foundation.

[1] G. F. Chew, Phys. Rev. **80**, 196 (1950).
[2] G. F. Chew and G. C. Wick, Phys. Rev. **85**, 636 (1952).
[3] G. F. Chew and M. L. Goldberger, Phys. Rev. **87**, 778 (1952).
[4] Fernbach, Green, and Watson, Phys. Rev. **82**, 980 (1951); B. Segall, Phys. Rev. **83**, 1247 (1951); W. B. Cheston, Phys. Rev. **85**, 952 (1952); Y. Fujimoto and Y. Yamaguchi, Prog. Theoret. Phys. **6**, 166 (1951); G. F. Chew and H. W. Lewis, Phys. Rev. **84**, 779 (1951); Isaacs, Sachs, and Steinberger, Phys. Rev. **85**, 803 (1952).

a two-body system with heavy point scatterers at $\mathbf{r}_A$ and $\mathbf{r}_B$, the wave function for the system is

$$\psi(\mathbf{r})=e^{i\mathbf{k}_0\cdot\mathbf{r}}+\frac{Ae^{ik|\mathbf{r}-\mathbf{r}_A|}}{|\mathbf{r}-\mathbf{r}_A|}+\frac{Be^{ik|\mathbf{r}-\mathbf{r}_B|}}{|\mathbf{r}-\mathbf{r}_B|}, \tag{1}$$

which is the general solution to the wave equation outside the range of the scatterers. The outgoing amplitude A is related to the total wave amplitude at $\mathbf{r}_A$ by the equation

$$A=\eta_A\left(e^{i\mathbf{k}_0\cdot\mathbf{r}_A}+\frac{Be^{ik|\mathbf{r}_A-\mathbf{r}_B|}}{|\mathbf{r}_A-\mathbf{r}_B|}\right), \tag{2}$$

where $k\eta_A=\exp(i\delta_A)\sin\delta_A$, and similarly for B. The resulting equations are easily solved and give for the amplitude of the outgoing wave, where for simplicity we have set $\eta_A=\eta_B=\eta$ and $R=|\mathbf{r}_A-\mathbf{r}_B|$,

$$f(\theta)=\left[\eta(e^{i(\mathbf{k}0-\mathbf{k})\cdot\mathbf{r}A}+e^{i(\mathbf{k}0-\mathbf{k})\cdot\mathbf{r}B})+\eta^2\frac{e^{ikR}}{R}(e^{i(\mathbf{k}_0\cdot\mathbf{r}_A-\mathbf{k}\cdot\mathbf{r}_B)}\right.$$
$$\left.+e^{i(\mathbf{k}_0\cdot\mathbf{r}_B-\mathbf{k}\cdot\mathbf{r}_A)})\right][1-\eta^2(e^{ikR}/R^2)]^{-1}. \tag{3}$$

To obtain the total cross section, we make use of the theorem[5] relating the total cross section to the forward scattering amplitude,

$$\sigma_{\text{total}}=4\pi\lambda Imf(0), \tag{4}$$

and obtain

$$\sigma_{\text{total}}=2\sigma_0[1+\sin x\sin(x+2\delta)/x^2+\sin\delta\sin(2x+\delta)/x^2$$
$$+\sin^2\delta\sin^2x/x^4][(1-\sin^2\delta/x^2)^2$$
$$+4\sin^2\delta\sin^2(x+\delta)/x^2]^{-1}, \tag{5}$$

where we have averaged over the angles of $\mathbf{R}$ and introduced $x=kR$ and $\sigma_0=4\pi\lambda^2\sin^2\delta$. We now note that in the limit $\delta\to0$,

$$\sigma_{\text{total}}=2\sigma_0(1+\sin^2x/x^2), \tag{6}$$

which is the prediction of the impulse approximation if multiple scattering is neglected. This limit is correct, however, only if $\delta\to0$ and not if $R\to\infty$; i.e., even for widely separated scatterers, the neglect of multiple scattering is valid only if the Born approximation is applicable to the free particle case. This is particularly apparent if we take $\delta=90°$ which leads to a cross section less for all values of R than the sum of the free particle cross sections, in striking contrast to the Born approximation result. Another interesting limit is for $R\to0$ where, for arbitrary δ,

$$\sigma_{\text{total}}=8\pi R^2. \tag{7}$$

A plot of the total cross section as a function of x, for various values of δ, is given in Fig. 1. It is apparent that the exact solution deviates rapidly from the Born approximation result even for rather small values of the phase shift. A qualitative feature of importance is that the interference is negative for all values of R for phase shifts somewhat larger than 45°.

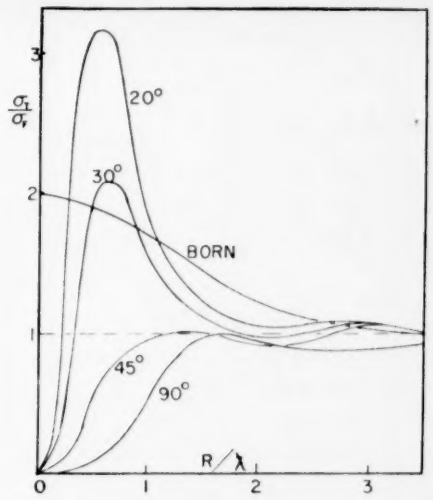

FIG. 1. S-wave scattering by two heavy point scatters, as a function of R/λ; R is the separation of the scatterers, λ the wavelength. The ratio of the cross section to the sum of the free-particle cross sections is given. The phase shifts for the two particles have been assumed to be equal.

III. MESON SCATTERING

We shall restrict ourselves to the consideration of isotopic spin dependent P-state scattering. This is the prediction of pseudoscalar theory with pseudovector coupling and also is in approximate agreement with the experimental results. We shall not, however, consider spin-dependent scattering since the present experiments,[6] while they do not fix the spin dependence unambiquously, suggest that the spin dependence is weak. The spin dependence can be included in a straightforward way, but the resulting equations are considerably more difficult to solve than the simpler case we shall consider. As a consequence of this neglect, our results will not exactly relate to the actual case of meson scattering but will serve to illustrate the effects of interest.

For a single scatterer at $\mathbf{r}_A$, the wave function is

$$\psi=\psi_0-ih\mathbf{\Lambda}\cdot\boldsymbol{\nabla}(e^{ik|\mathbf{r}-\mathbf{r}_A|}/|\mathbf{r}-\mathbf{r}_A|), \tag{8}$$

which is a general solution of the wave equation, outside of the region of interaction, for P-wave scattering alone. The amplitude $\mathbf{A}$ is related to the incoming wave ψ_0 by

$$\mathbf{A}=-ih\lambda^3T_A\boldsymbol{\nabla}\psi_0, \tag{9}$$

where

$$T_A=a\mathbf{U}^*\cdot\mathbf{U}+ab\boldsymbol{\tau}_A\cdot\mathbf{U}^*\times\mathbf{U} \tag{10}$$

[5] B. A. Lippmann and J. Schwinger, Phys. Rev. **79**, 481 (1950).

[6] Anderson, Fermi, Nagle, and Yodh, Phys. Rev. **86**, 793 (1952).

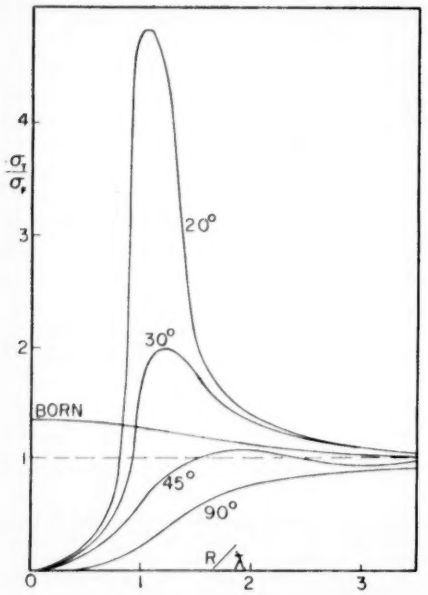

FIG. 2. P-wave isotopic spin $\frac{3}{2}$ scattering of mesons by two heavy point scatterers (neutron and proton).

is the most general isotopic spin dependent operator. The operators U_i^* and U_i create and annihilate the ith component of the meson wave, τ_A is the usual isotopic spin operator. The coefficients a and b are related to the phase shifts for the isotopic spin $\frac{3}{2}$ and $\frac{1}{2}$ states[7] by

$$a=2\eta_{\frac{3}{2}}+\eta_{\frac{1}{2}}, \quad b=-\eta_{\frac{3}{2}}+\eta_{\frac{1}{2}}, \tag{11}$$

where $\eta_t=\exp(i\delta_t)\sin\delta_t$. The asymptotic form of ψ is

$$\psi\sim\psi_0+f(\theta)e^{ikr}/r, \tag{12}$$

where

$$\begin{aligned} f(\theta)&[3\lambda\cos\theta]^{-1} \\ &=\eta_{\frac{3}{2}}, && (P+,P+),(N-,N-) \\ &=(\eta_{\frac{3}{2}}+2\eta_{\frac{1}{2}})/3, && (P-,P-),(N+,N+) \\ &=(2\eta_{\frac{3}{2}}+\eta_{\frac{1}{2}})/3, && (N0,N0),(P0,P0) \\ &=2^{\frac{1}{2}}(\eta_{\frac{3}{2}}-\eta_{\frac{1}{2}})/3, && (N0,P-),(P0,N+). \end{aligned} \tag{13}$$

The notation $(P+, P+)$ means π^+ mesons on protons, etc.

With this as an introduction, we consider next the case of two scatterers at $\mathbf{r}_A$ and $\mathbf{r}_B$, for which the wave function is

$$\begin{aligned}\psi=\psi_0+(h/i)[&\mathbf{A}\cdot\nabla(e^{ik|\mathbf{r}-\mathbf{r}_A|}/|\mathbf{r}-\mathbf{r}_A|) \\ &+\mathbf{B}\cdot\nabla(e^{ik|\mathbf{r}-\mathbf{r}_B|}/|\mathbf{r}-\mathbf{r}_B|)].\end{aligned} \tag{14}$$

ψ_0 describes the initial state of the systems and has the form

$$\psi_0=e^{i\mathbf{k}_0\cdot\mathbf{r}}t_0, \tag{15}$$

[7] For a more detailed development of the theory of the isotopic spin, see W. Heitler, Proc. Roy. Irish Acad. **51**, 33 (1946); K. M. Watson, Phys. Rev. **85**, 892 (1952); and K. A. Brueckner, Phys. Rev. **86**, 106 (1952).

where $\mathbf{k}_0$ is the momentum of the incoming wave and t_0 is an isotopic spin function specifying the initial charge state.

The amplitudes $\mathbf{A}$ and $\mathbf{B}$ are related to the total wave amplitude at $\mathbf{r}_A$ and $\mathbf{r}_B$ by the equations

$$\begin{aligned}\mathbf{A}&=\lambda^3 T_A\frac{h}{i}\nabla\left[\psi_0+\frac{h}{i}\mathbf{B}\cdot\nabla(e^{ik|\mathbf{r}-\mathbf{r}_B|}/|\mathbf{r}-\mathbf{r}_B|)\right]_{r=r_A}, \\ \mathbf{B}&=\lambda^3 T_B\frac{h}{i}\nabla\left[\psi_0+\frac{h}{i}\mathbf{A}\cdot\nabla(e^{ik|\mathbf{r}-\mathbf{r}_A|}/|\mathbf{r}-\mathbf{r}_A|)\right]_{r=r_B}.\end{aligned} \tag{16}$$

The asymptotic form then is

$$\psi(r)=\psi_0+h(\mathbf{A}\cdot\mathbf{k}e^{-i\mathbf{k}\cdot\mathbf{r}_A}+\mathbf{B}\cdot\mathbf{k}e^{-i\mathbf{k}\cdot\mathbf{r}_B})e^{ikr}/r. \tag{17}$$

To obtain the total cross section, we again make use of the theorem relating the cross section to the imaginary part of the forward amplitude. Since only the diagonal part contributes, we need not consider the charge exchange process in the total cross section since it is an off-diagonal process. We cannot, however, neglect the charge exchange processes in computing the values of $\mathbf{A}$ and $\mathbf{B}$, as will be apparent in the following.

TABLE I. Total cross sections for meson-deuteron scattering under the assumption of P-state scattering in the isotopic spin $\frac{3}{2}$ state. The wavelength is given in units of the meson Compton wavelength. The energy is in the laboratory system and is based on the assumption that the system in which the nucleons are assumed to be infinitely heavy is the correct center-of-mass system for the meson and one nucleon. σ_f is the sum of the free-particle cross sections, σ_{Born} is the prediction of the Born approximation calculation (neglecting multiple scattering), σ_{exact} is the result of the exact treatment of the multiple scattering. The cross sections are given in millibarns.

λ	E	$\delta_{3/2}$	σ_f	σ_{Born}	σ_{exact}
1.000	81 Mev	20°	90	113	144
0.833	113 Mev	30°	178	218	153
0.714	150 Mev	45°	261	288	236
0.556	220 Mev	90°	315	340	246

To solve the equations for $\mathbf{A}$ and $\mathbf{B}$, we first write them in the more convenient form,

$$\begin{aligned}\mathbf{A}&=\lambda^3\frac{h}{i}T_A\left[i\mathbf{k}_0\psi_0(r_A)+\mathbf{B}f(R)+\mathbf{B}\cdot\frac{\mathbf{R}}{R^2}\mathbf{R}g(R)\right], \\ \mathbf{B}&=\lambda^3\frac{h}{i}T_B\left[i\mathbf{k}_0\psi_0(r_B)+\mathbf{A}f(R)+\mathbf{A}\cdot\frac{\mathbf{R}}{R^2}\mathbf{R}g(R)\right],\end{aligned} \tag{18}$$

where

$$\lambda^3 f(R)=\frac{1}{x}\frac{d}{dx}\left(\frac{e^{ix}}{x}\right), \quad g(R)=x\frac{df}{dx}. \tag{19}$$

Let us now restrict our attention to the scattering of a π^+ meson by a deuteron. In this case the initial system is an isotopic singlet nucleon state and a π^+ meson: Under the action of the operators T_A and T_B, the system

will undergo transitions to an isotopic triplet state.[8] We can therefore take these two states as the basis vectors for a matrix representation of the operators T_A, T_B. Calling the initial state (1) and the second state (2), we then have

$$T_A=\begin{pmatrix} a & 2^{\frac{1}{2}}b \\ 2^{\frac{1}{2}}b & a+b \end{pmatrix}, \quad T_B=\begin{pmatrix} a & -2^{\frac{1}{2}}b \\ -2^{\frac{1}{2}}b & a+b \end{pmatrix}. \quad (20)$$

The two coupled equations of Eq. (18) can first be solved, after multiplying by $\mathbf{R}$, for the matrix elements of $\mathbf{A}\cdot\mathbf{R}$ and $\mathbf{B}\cdot\mathbf{R}$. These can then be substituted into the vector equations to give a solution for $\mathbf{A}$ and $\mathbf{B}$. In computing the total cross section, as remarked above, we need consider only the elements of A and B corresponding to direct scattering, i.e., A_1 and B_1. Straightforward evaluation leads to the result that

$$\sigma_{\text{total}}=8\pi\lambda\!\!\!^{-2}\, Im\frac{1}{\rho_1}\left\{a+g_1-f(a^2-2b^2+g_2)\frac{\sin x}{x}+\frac{1}{3}\frac{g}{\rho_2}[g_3-\epsilon(a^2-2b^2)-g_4\epsilon]\right\}, \quad (21)$$

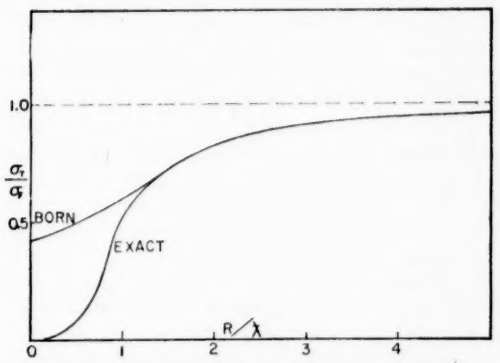

FIG. 3. P-wave scattering by two heavy point scatterers (neutron and proton) with $\delta_{\frac{1}{2}}=10°$, $\delta_{\frac{1}{2}}=-7°$.

where $h=f+g$. The functions f, g, h are now to be considered to be dimensionless functions of $x=r/\lambda\!\!\!^{-}$ alone. The quantities ρ_1, ρ_2, g_1, g_2, g_3, g_4 include the effects of the multiple scattering; they are, in general, extremely complicated function of a, b, f, and h. If the phase shifts go to zero, then the ρ's become equal to one and the g_i's go to zero. For the special case of scattering in the isotopic spin $\frac{3}{2}$ state (with $a=-2b$), they reduce to $\rho_1=1-b^2f^2$, $\rho_2=1-b^2h^2$, $g_1=g_2=0$, $g_3=2b^3(f+h)$, $g_4=(1+b^2fh)2b^2$. In this result, we have averaged over the angles of $\mathbf{R}$ and introduced the symbol

$$\tfrac{1}{3}\epsilon=\tfrac{1}{2}\int_{-1}^{1}\mu^2e^{i\mu x}d\mu. \quad (22)$$

[8] The isotopic spin wave function for this state is

$$2^{\frac{1}{2}}(\omega_1{}^1t_1{}^0-\omega_1{}^0t_1{}^1),$$

where $t_1{}^m$ is the triplet spin function and $\omega_1{}^m$ is the meson wave function.

TABLE II. Total cross sections at 60 Mev. The phase shifts have been taken to be $\delta_{\frac{1}{2}}=10°$, $\delta_{\frac{1}{2}}=-7°$, giving total cross sections for π^+ mesons on protons and neutrons of 32.2 mb and 21.4 mb, respectively. The units are the same as for Table I.

$\lambda\!\!\!^{-}$	E	σ_f	σ_{Born}	σ_{exact}
1.284	60 Mev	53.6	36.7	30.9

Let us first consider this result in the limit $R\to\infty$. We find for the sum of the free particle total cross sections

$$\sigma_f=8\pi\lambda\!\!\!^{-2}Ima=8\pi\lambda\!\!\!^{-2}(2\sin^2\delta_{\frac{1}{2}}+\sin^2\delta_{\frac{1}{2}}), \quad (23)$$

which agrees with the sum as given by Eq. (13).

Next we consider the Born approximation limit. Here we find, as a, $b\to 0$,

$$\sigma_{\text{total}}=8\pi\lambda\!\!\!^{-2}Im[a-(a^2-2b^2)(f\sin x/x+\epsilon g/3)]=\sigma_f\left[1-\frac{(2\sin^2\delta_{\frac{1}{2}}+8\sin\delta_{\frac{1}{2}}\sin\delta_{\frac{1}{2}}-\sin^2\delta_{\frac{1}{2}})}{(2\sin^2\delta_{\frac{1}{2}}+\sin^2\delta_{\frac{1}{2}})}\times Im\left(\frac{f\sin x}{x}+\frac{\epsilon g}{3}\right)\right]. \quad (24)$$

This result is easily shown to be identical with the usual result in which multiple scattering has been neglected. The angular integral encountered in the usual evaluation is

$$\lambda\!\!\!^{-4}\int\frac{d\Omega_k}{4\pi}\int\frac{d\Omega_R}{4\pi}(\mathbf{k}_0\cdot\mathbf{k})^2e^{i(\mathbf{k}_0-\mathbf{k})\cdot R}, \quad (25)$$

which is equal to

$$-Im(f(x)\sin x/x+\epsilon g(x)/3), \quad (26)$$

with f and g defined in Eq. (19). Again it is clear that this limit is valid only in Born approximation and is not approached as a limit for large R when the plane shifts are not small.

These results, of course, break down for small R since the meson-nucleon interaction is of finite extent, modifying the wave function of Eq. (14) for small distances. This is in addition the region where the impulse approximation is particularly bad, since it corresponds to high velocities for the nucleons. The process of meson absorption is also associated with small nucleon separation. These effects all will tend to lead to a finite contribution to the total cross section from the region of small R. Although this region is of small importance for a reasonable choice of the deuteron wave function, the uncertainties in its treatment lead to the largest uncertainties in our results.

IV. EVALUATION OF THE TOTAL CROSS SECTION FOR DEUTERIUM

We consider in detail two cases for which the phase shifts are known or can be deduced with some certainty

from the experimental data. At high energies, it is known[6] that the total cross sections are approximately in the ratio $\sigma(P+,\ P+):\sigma(P-,\ P-):\sigma(N0,\ P-)=9:1:2$. This fixes the scattering predominantly in the isotopic spin $\frac{3}{2}$ state. Accordingly we set $\delta_{\frac{1}{2}}=0$ in Eq. (21). The resulting total cross section is given in Fig. 2 as a function of $x=R/\lambda$ for various values of the phase shift, showing the rapid departure of the cross section from the Born approximation result in which multiple scattering is neglected. It is noteworthy that the net interference effect is negative for phase shifts larger than 45°, in striking contrast with the Born approximation result which gives positive interference for all values of the phase shift.

To evaluate the cross section in deuterium, it is now only necessary to average the cross sections, given in Fig. 2 as a function of R, over the deuteron wave function. For this we assume the Hulthen wave function

$$\psi(r)=\left[\frac{(e^{-\alpha r}-e^{-\beta r})}{r}\right]\left[\frac{\alpha\beta(\alpha+\beta)}{2\pi(\alpha-\beta)^2}\right]^{\frac{1}{2}}. \tag{27}$$

We need also associate a specific wavelength with the various values of the phase shift. We shall assume values which are in approximate agreement with the total cross section measurements of Fermi *et al.*[6] The values of the wavelength, laboratory system energy, phase shift, free particle cross sections, the Born approximation prediction, and the prediction with the multiple scattering properly taken into account, are given in Table I. It is apparent that as the phase shift passes 45°, one can expect a depression of the total cross section in deuterium relative to the free cross section. This is in qualitative agreement with the preliminary experimental results of Fermi.[9]

Another measurement by Isaacs, Sachs, and Steinberger[4] at 60 Mev gives a ratio of the (+, proton) total cross section (28 mb) to the (π^-, proton) total cross section (18 mb) of about 1.6, and a deuterium cross section for π^+ mesons about equal to the proton cross section alone. If we take at this energy phase shifts of 10° and −7° for the isotopic spin $\frac{3}{2}$ and $\frac{1}{2}$ states, respectively, the resulting total deuterium cross section as a function of $x=R/\lambda$ is given in Fig. 3 together with the Born approximation result. The exact and approximate results agree fairly well except at small x where the multiple scattering is important. Averaging these over the deuteron wave function gives us the results tabulated in Table II. The multiple scattering does not charge the result qualitatively; however, it increases the interference from 19 millibarns to 25 millibarns to give a deuterium cross section which is less than the (+, proton) cross section alone.

[9] Anderson, Fermi, Nagle, and Yodh, Phys. Rev. **86**, 413 (1952).

V. CONCLUSIONS

The multiple scattering corrections to the impulse approximation have been evaluated in the case of two heavy scatterers for a simple example of S-wave scattering and for the isotopic-spin dependent P-wave scattering of mesons. The results show that the multiple scattering can be neglected only if the Born approximation is applicable to the free particle cross sections. Evaluation of meson scattering for the deuteron under the assumption of isotopic spin $\frac{3}{2}$ scattering leads to the conclusion that considerable depression of the total cross section relative to the free particle cross sections can be expected for phase shifts larger than 45°. Application to the case of scattering at 60 Mev where the cross sections are small, with the isotopic spin $\frac{3}{2}$ and $\frac{1}{2}$ phase shifts 10° and −7°, respectively, show that the multiple scattering considerably enhances the destructive interference to give a deuterium cross section 58 percent of the sum of the free particle cross sections and less than the (proton, +) cross section alone. The results are approximate principally in that off-the-energy-shell scattering has been neglected, and the impulse approximation assumed.

The author is indebted to Professor L. L. Foldy, who pointed out the simple method for obtaining an exact solution to the two-body scattering problem which is developed here. The author is in addition grateful to Professor Robert Serber, Professor Geoffrey Chew, and Professor Kenneth M. Watson for valuable discussions.

The Coupling of Angular Momenta in Nuclear Reactions*

R. F. CHRISTY
Kellogg Radiation Laboratory, California Institute of Technology, Pasadena 4, California
(Received October 31, 1952)

Seven nuclear reactions have been examined where the angular distribution of reaction products depends on the type of coupling of angular momentum vectors in the nucleus. In six of the seven, the experimental angular distribution is consistent with the assumption of Russell-Saunders coupling in the nucleus. In three of the seven, the experiments are consistent with the assumption that the bombarding particle brings a definite j in the reaction. Neither assumption is sufficient to explain the result in one reaction ($B^{11}+P$).

I. INTRODUCTION

CONSIDERABLE use has been made, in nuclear reactions, of angular distributions and angular correlations to establish the total angular momenta and parities of nuclear states. In some cases, however, such determinations are hampered by the appearance of parameters in the calculated angular distribution which, for definite total angular momentum and parity, lead to a continuous range of possible angular distributions or angular correlations. In fact, such undetermined angular distributions are found whenever three (or more) nonzero angular momenta must be added to give a fourth and the resultant can be reached in more than one way. Geometrically we may think of a four-sided polygon with given lengths for the sides: if the lengths are such that the structure is flexible, then the angular distribution will be incompletely determined by the given angular momenta. In a typical example, the three angular momenta may be the angular momentum of the target nucleus, the intrinsic angular momentum of the bombarding particle, and the orbital angular momentum of the bombarding particle; these must add together to give the angular momentum of the (resonant) compound nucleus.

Where possible, it is customary to combine the several angular momenta in such a way that the result can be expressed as an incoherent mixture (with arbitrary relative weight) of two distribution functions which then represent the extreme possible distributions. Thus, if the arbitrariness arises from nonzero intrinsic angular momenta (J) of bombarding particle and target nucleus and nonzero orbital angular momentum (l) of bombarding particle in the angular distribution of a resonance reaction using unpolarized beam and target, then the intrinsic J's of bombarding particle J_1 and target nucleus J_0 may be added to form a "channel spin" J_c: $\mathbf{J}_0+\mathbf{J}_1=\mathbf{J}_c$, where $|J_0-J_1|\leq J_c\leq J_0+J_1$. The angular distribution will then have an arbitrary parameter if the J of the compound nucleus can be formed by adding l to more than one of the possible values of J_c. The angular distribution can be calculated uniquely for each J_c and the various results combined with arbitrary weight. Since the calculation involves summing the squared amplitudes for the spin states of both particles, one may add the spins first to form the "channel spin" and then sum the squared amplitudes of the states of this quantity with no interference between different channel spins. The same procedure can be used when the residual nucleus and particle have nonzero J and l; a "channel spin" J_c' may be formed out of the J_3 of the residual nucleus and J_2 of the emitted particle and the various distribution functions calculated for each J_c' and combined with arbitrary relative weight.

In the case of electromagnetic radiation, where such ambiguity is also possible, as in cases where both electric quadrupole and magnetic dipole radiation are permitted, it is customary to allow for the arbitrariness by means of a coherent mixture described by an amplitude mixture with an arbitrary complex parameter. In the case of an ambiguous angular correlation arising from emission of particles with intrinsic angular momenta there is no advantage in the channel spin method; it is usually most convenient to add the l and intrinsic angular momentum of the emitted particle to form several j values which must then be combined coherently with arbitrary relative amplitude and phase to describe all possible results.

This arbitrariness in a calculated distribution function is, of course, just a result of our ignorance of the nuclear wave functions. The results would be uniquely determined by complete knowledge of the wave functions involved. It follows that, if we know the J's and l appropriate to a certain reaction, the actual observed angular distribution, if not uniquely calculated, tells us additional facts concerning the nuclear wave functions. The assumption of Russell-Saunders coupling (i.e., that states are describable by L, S, and J, each conserved) is usually sufficient to resolve the ambiguity and give unique predictions of angular distributions for definite L, S, and J. Or, again, the assumption that a bombarding (or emitted) proton or neutron interacts with a single definite j out of the two possible values $l\pm\frac{1}{2}$, instead of a coherent superposition of the two, is sufficient to lead to unique angular distributions. These two assumptions are, of course, closely related to possible nuclear models, i.e., the Russell-Saunders coupling shell model and the $j-j$ coupling shell model. It is thus of interest to examine whether the results of angular distribution and angular correlation experi-

* This work was supported by the joint program of the U. S. Office of Naval Research and the U. S. Atomic Energy Commission.

ments, which are left uncertain by knowledge of the J's involved, agree with either the $L-S$ or the $j-j$ calculations.

II. EXPERIMENTAL EVIDENCE ON ANGULAR DISTRIBUTIONS

A. $T(p,\gamma)He^4$

The radiation is quite accurately $\sin^2\theta$.[1] It is assumed that a single (broad) state of He^{4*} is involved, although examination of the γ-yield itself is not sufficient to establish this fact (examination of the neutron yield lends some support to this view; analysis of the scattering phases should be more decisive). The radiation can be described as due to p-wave protons ($l=1$) forming a $J=1^-$ state in He^4 which radiates by electric dipole to the ground state of He^4.

"Channel spin" calculation

Channel spin J_c	γ-ray angular distribution
0	$\sin^2\theta$
1	$1+\cos^2\theta$

The general distribution is $1+A\cos^2\theta$, where $-1\leq A\leq 1$. The experimental result corresponds to $J_c=0$ with zero admixture of $J_c=1$.

$j-j$ calculation

Incoming proton	γ-ray angular distribution
$p_{\frac{1}{2}}$	spherical—a general result for $j=\frac{1}{2}$
$p_{\frac{3}{2}}$	$1-\frac{1}{3}\cos^2\theta$

$L-S$ calculation

Triton ground state	Compound state	Angular distribution
$^2S_{\frac{1}{2}}$	$^1P_1$	$1-\cos^2\theta$
$^2S_{\frac{1}{2}}$	$^3P_1$	$1+\cos^2\theta$

We see that the observed angular distribution can not be described by the capture of either a $p_{1/2}$ or $p_{3/2}$ proton. On the other hand, if the assumption of resonance is valid, it is consistent with a $L-S$ description where the ground state of T is $^2S_{1/2}$ and the compound state of He^4 is $^1P_1$.

B. $Li^7(p,\gamma)Be^8$—440-Kev Resonance

The requirements of spherical symmetry[2] for the γ-rays, and p-wave protons to explain the scattering,[3] can, as Devons[2] has pointed out, be reconciled with p-wave protons forming a compound state in Be^8 with $J=1^+$ and a certain mixture of channel spins 1 and 2 in the ratio 1 to 5. This mixture of channel spins results in fact in equal population of the magnetic substates of the compound state so that all processes will proceed with spherical symmetry. The question here is, does this spherical symmetry (which appears accidental from the point of view of channel spin) arise naturally in some other description such as $j-j$ or $L-S$. In fact, it does. It is easy to see that the assumption that the proton is $p_{1/2}$ also leads to spherical symmetry since $j=\frac{1}{2}$ cannot lead to any $\cos^2\theta$ terms. On the $L-S$ description, the ground state of Li^7 is $^2P_{3/2}$ so that the compound state could be $^1P_1$, $^3S_1$, $^3P_1$, or $^3D_1$. Of these, the $^3S_1$ again leads to equal population of the substates of the compound state and to spherical symmetry. Thus the observations are consistent either with the assumption that only $p_{1/2}$ protons interact or with an $L-S$ description where the resonance is $^3S_1$.

C. $Li^7(t,\alpha)He^6$—840-Kev Resonance in Be^{10} Observed with 240-Kev Tritons

The α's leaving He^6 in the ground state are distributed as $1-A\cos^2\theta$ with $A\sim 1$, whereas the α's leaving He^6 in its 1.7-Mev excited state are nearly spherical.[4]

It seems reasonable to ascribe this resonance to p-wave tritons on Li^7 forming a compound state of Be^{10} with $J=2$, even, which emits d-wave α's to the ground state of He^6 and (predominantly) s-wave α's to the excited state of He^6, assumed to be $J=2$, even. On this basis we make the following calculations.

The spherical symmetry of the α's to the excited state follows immediately from the s-wave assignment. For the ground-state α's we have the following results:

Channel spin calculation

"Channel spin"	Angular distribution
1	$1+3\cos^2\theta$
2	$1-\cos^2\theta$

The general angular distribution is $1+A\cos^2\theta$, where $-1\leq A\leq 3$.

$L-S$ calculation

We take the ground state of Li^7 as $^2P_{3/2}$ and the triton as $^2S_{1/2}$; then

Compound state	Angular distribution
$^1D_2$	$1+3\cos^2\theta$
$^3D_2$	1
$^3P_2$	$1-6/7\cos^2\theta$

The $j-j$ calculation has no special significance since the triton is not a single particle. It would give the following:

Incoming triton	Angular distribution
$p_{\frac{1}{2}}$	spherical
$p_{\frac{3}{2}}$	spherical

The observations are thus consistent with an $L-S$ description where the compound state is $^3P_2$.

[1] Argo, Gittings, Hemmendinger, Jarvis, Mayer, and Taschek, Phys. Rev. **76**, 182 (1949); Argo, Gittings, Hemmendinger, Jarvis, and Taschek, Phys. Rev. **78**, 691 (1950); J. Perry and S. Bame, private communication.

[2] S. Devons and G. R. Lindsey, Proc. Phys. Soc. (London) **A63**, 1202 (1950); M. B. Sterns and B. D. McDaniel, Phys. Rev. **82**, 450 (1951); Nabholtz, Stoll, and Wäffler, Helv. Phys. Acta **25**, 153 (1952).

[3] Brown, Snyder, Fowler, and Lauritsen, Phys. Rev. **82**, 159 (1951); W. D. Warters and E. A. Milne, Phys. Rev. **85**, 761 (1952); E. R. Cohen, Phys. Rev. **75**, 1463 (1949); Ph.D. thesis, California Institute of Technology, 1949 (unpublished); D. Liberman, private communication.

[4] Pepper, Almqvist, and Lorrain, Phys. Rev. **86**, 630 (1952).

D. $B^{11}(p,\gamma)C^{12}$; $B^{11}(p,\alpha)Be^{8}$—Resonance at 162 Kev

The experimental facts here are not entirely clear. For many years there have existed contradictory statements as to which groups of α's and which γ's were resonant at 162 kev, and as to whether or not they showed a nonspherical distribution. We will assume that the long-range α's leaving Be^{8} in the ground state are resonant and are distributed as $1+0.7\cos^2\theta$.[5] We also assume that the 11-Mev γ-ray leaving C^{12} in its 4-Mev excited state is resonant and is distributed as $1+0.23\cos^2\theta$.[6] It has been shown[6] that the angular correlation of the cascade γ's and the angular distribution of the 11-Mev γ are consistent with the assumption that p-wave protons are responsible for a $J=2$, even, resonance in C^{12} which emits 11-Mev dipole (magnetic) radiation followed by 4-Mev quadrupole (electric) radiation. (However, another γ-ray angular correlation experiment seems inconsistent with the α-particle results.)[7] Unexplained is the angular distribution[5] of the short-range α's to Be^{8} at 3 Mev, which are also resonant.[8] These should be largely spherical since a $J=2$, even, state of Be^{8} could be reached by s-wave α's. Also unexplained is the reported[6] variation with energy of the coefficient of $\cos^2\theta$ for the 11-Mev γ-ray and the apparent absence of the 16-Mev γ-ray at resonance.

Channel spin calculation

Channel spin	11-Mev γ-distribution	Long-range α-distribution
1	$11/4+(7/4)\cos^2\theta$	$1+3\cos^2\theta$
2	$47/12-(21/12)\cos^2\theta$	$3-3\cos^2\theta$
$(1)+(3/7)(2)$	$4.4(1+0.23\cos^2\theta)$	$2.3(1+0.75\cos^2\theta)$.

$j-j$ calculation

Incoming proton	Angular distributions
$p_{\frac{1}{2}}$	spherical
$p_{\frac{3}{2}}$	spherical

$L-S$ calculation

B^{11} ground state	Compound state	Coefficient t of channel spin 2 to add to channel spin 1
$^2P_{\frac{1}{2}}$	$^1D_2$	0
$^2P_{\frac{1}{2}}$	$^3D_2$	1
$^2P_{\frac{3}{2}}$	$^3P_2$	9
$^2D_{\frac{3}{2}}$	$^1D_2$	∞
$^2D_{\frac{3}{2}}$	$^3P_2$	9
$^2D_{\frac{5}{2}}$	$^3D_2$	25/9
$^2D_{\frac{5}{2}}$	$^3F_2$	1/9

None of the above agree with the apparently correct choice of mixing ratio, $\sim 3/7$, of the two channel spins. This may just be normal or it may be associated with the fact that B^{11} lies almost at the middle of the p shell where conflict between the $j-j$ and $L-S$ coupling models can exist.

E. $C^{13}(p,\gamma)N^{14}$—1.76-Mev Resonance

The prominent γ-ray resonance at 1.76 Mev has been shown[9] to decay predominantly by radiation to the ground state of N^{14}. The angular distribution $1-0.48\cos^2\theta$ of these γ-rays is consistent[10] with the assumption of a $J=2$ odd resonance made by d-wave protons and emitting (electric) dipole radiation to the ground state of N^{14}.

Channel spin calculation

Channel spin	Angular distribution
0	$1-0.6\cos^2\theta$
1	$1-\frac{1}{3}\cos^2\theta$

The general angular distribution is $1-A\cos^2\theta$, $\frac{1}{3}\leq A\leq\frac{3}{5}$.

$j-j$ calculation

Incoming proton	Angular distribution
$d_{5/2}$	$1-0.5\cos^2\theta$

$L-S$ calculation

C^{13} ground state	Compound state	Angular distribution
$^2P_{\frac{1}{2}}$	$^3F_2$	$1-0.5\cos^2\theta$

Here the observed angular distribution is consistent with either a $d_{5/2}$ incoming proton or a $^3F_2$ compound state, although the small range allowed to A makes the result rather insensitive.

F. $N^{14}(\alpha,p)O^{17}$

Proton groups leave O^{17} in the ground ($J=5/2$, even) and first excited ($J=1/2$, even) states. It has been reported[11] that at each of two resonances at $E_\alpha=3.6$ and 4.2 Mev the angular distribution of the long-range protons is $\sim 1-\cos^2\theta$, whereas the short-range ones are spherically symmetric. In this case the arbitrariness appears in the decay of the compound nucleus. Unfortunately, no simple choice of angular momentum and parity of the compound state agrees well enough with the reported facts to warrant examination of various coupling schemes.

G. $Li^{7}(d,n)Be^{8*}(\gamma)Be^{8}$

In this reaction, a nonspherical angular correlation of neutron and γ-ray has been reported.[12] Here arbitrariness may appear in the correlation function because of the spin of the neutron. Because of this arbitrariness, the reported assignments of angular momenta in the reaction must be doubted, and there remains insufficient certainty about the various angular momenta to warrant further investigation of coupling schemes.

[5] Haxby, Allen, and Williams, Phys. Rev. **55**, 140 (1939); Thomson, Cohen, French, and Hutchinson, Proc. Phys. Soc. (London) **A65**, 745 (1952). J. R. Oppenheimer and R. Serber, Phys. Rev. **53**, 636 (1938).
[6] Hubbard, Nelson, and Jacobs, Phys. Rev. **87**, 378 (1952).
[7] G. M. Lewis, Phil. Mag. **43**, 690 (1952).
[8] W. Whaling and W. Wenzel (private communication).
[9] Woodbury, Day, and Tollestrup, Phys. Rev. **85**, 760 (1952).
[10] R. B. Day, thesis, California Institute of Technology, 1952 (unpublished).
[11] R. R. Roy, Phys. Rev. **82**, 227 (1951).
[12] J. Thirion, Compt. rend. **233**, 37 (1951).

H. $N^{15}(p,\alpha)C^{12*}(\gamma)C^{12}$

The resonances at $E_p=429$ and 898 kev show[13] angular distributions of γ-rays and α-particles that are consistent with $J_{\text{oxygen}}=2$, odd, formed by d-wave protons emitting p-wave α-particles to an excited state of C^{12} with $J=2$, even, which decays by quadrupole (electric) γ-rays to the ground state of C^{12}.

The angular distributions at $E_p=429$ kev require a mixing ratio of (channel spin 1)$+t\times$(channel spin 0) with $t\approx 5$. The angular distributions at $E_p=898$ kev require $t=3/2$. On $j-j$ coupling we get $t=2/3$ for $d_{3/2}$ protons and $t=3/2$ for $d_{5/2}$ protons. On Russell-Saunders coupling with $^2P_{1/2}$ for N^{15} the various possible compound states of O^{16} give the following mixing ratios: $^3D_2$, $t=6$; $^3F_2$, $t=3/2$; $^3P_2$, $t=2/3$; and $^1D_2$, $t=0$. The 898-kev resonance is consistent with either a $d_{5/2}$ incoming proton or a $^3F_2$ compound state in O^{16}. The 429-kev resonance is consistent only with a $^3D_2$ compound state in O^{16}.

[13] Kraus, French, Fowler, and Lauritsen, Phys. Rev. **89**, 299 (1953). Mr. Kraus has also calculated the angular distributions for the reaction.

III. CONCLUSIONS

These calculations show that in most of the cases which have been examined the observed angular distributions are consistent with the assumption that the states of light nuclei belong predominantly to a definite Russell-Saunders designation. Admixtures of up to 10 percent of other designations could not be excluded in many examples, and even larger admixtures could be allowed if they led to vanishing matrix elements in the examples considered. Thus the examples considered provide no positive proof of the validity of Russell-Saunders coupling. Nevertheless, further evidence of this kind may afford an important guide to the type of coupling prevailing in nuclei.

The agreement of the angular distributions with the demands of $j-j$ coupling are somewhat less satisfactory than with $L-S$ coupling. On the other hand, the restrictions of a literal $j-j$ model are much more severe than those of Russell-Saunders coupling.

PHYSICAL REVIEW VOLUME 89, NUMBER 4 FEBRUARY 15, 1953

Multiple Meson Production by High Energy Nucleon-Nucleon Collisions

H. FUKUDA
Institute for Advanced Study, Princeton, New Jersey
(Received July 1, 1952)

A comparison is made between Fermi's theory and Lewis, Oppenheimer, and Wouthuysen's theory of multiple meson production in high energy nucleon-nucleon collisions, and an analysis is made of some typical examples. The main difference between the two theories concerns the Lorentz covariance of the matrix element which is related, in Fermi's theory, to the Lorentz contraction of the volume in which the thermal equilibrium of virtual mesons is supposed to be established, and to the Lorentz invariant phase volume in L.O.W.'s theory. It is reasonable to take the contracted diameter of the volume in Fermi's theory to be of the order of the wavelength of the emitted meson (not that of the incident nucleon), and as a result both theories can explain to some extent the multiplicity and angular distribution. The main difference lies in the average energy of the emitted mesons in the center-of-mass system as a function of multiplicity.

I. INTRODUCTION

IN recent experiments with photographic emulsions[1] at high altitude, some direct evidence was obtained for multiple meson production by the impact of very high energy nucleons. Most events are nucleon-nucleus collisions which were accompanied not only by shower particles but also by gray and black tracks. In these cases, mesons may be produced not only multiply but also plurally, as the angular distribution of the emitted mesons is sometimes much larger than can be accounted for in a single event. (The half-angle of the emitted mesons in one collision in the laboratory system is proportional to the square root of M/E^*, where E^* and M are the energy and mass, respectively, of the incident nucleon before collision.)

These events often are so complex that it is hard to disentangle from them in any unique way the criteria for truly multiple meson production. There is some direct evidence for multiple meson production by either nucleon-nucleon collision or by the collision of a nucleon at the edge of a nucleus which does not disturb the remaining nucleus. In this paper, we shall analyze the multiplicity and angular distribution and the average energy of the emitted mesons in the center-of-mass system for the latter case. There are two typical treatments of the multiple meson production by high energy nucleon-nucleon collisions. One was proposed by Lewis, Oppenheimer, and Wouthuysen (L.O.W.)[2] using

[1] Camerini, Fowler, Lock, and Muirhead, Phil. Mag. **41**, 413 (1950); Lord, Fainberg, and Schein, Phys. Rev. **80**, 970 (1950); Hopper, Biswas, and Darby, Phys. Rev. **84**, 457 (1951); E. Pickup and L. Voyvodic, Phys. Rev. **84**, 1190 (1951).

[2] Lewis, Oppenheimer, and Wouthuysen, Phys. Rev. **73**, 127 (1948).

the usual weak coupling theory for pseudoscalar mesons with pseudovector coupling which was recalculated elsewhere,[3] using relativistic methods, and considering the conservation of charge. The other was proposed by Fermi,[4] using strong coupling and rather classical methods. Though objections may be raised against both theories, they agree rather well with the very limited experiments.

In the L.O.W. theory, in order to produce mesons multiply, it is necessary to introduce pseudovector coupling between nucleon and pseudoscalar mesons. But in such a coupling, which contains the space-time derivatives of the meson potential, the divergence difficulties of higher order radiative corrections arise because it cannot be renormalized. In other words, the singular nature of the meson cloud around the nucleon, which is favorable to multiple meson production, disturbs the correct treatment of the problem. They therefore made a classical treatment of the problem, and replaced the effect of radiative corrections by assuming that the total cross section was limited by the geometrical cross section. They assumed, first, that only a portion of the energy of the incident nucleons is transferred to the energy of the emitted mesons, i.e., they ignored the effect of the emitted mesons on the nucleon, in particular, the effect of their recoils. Secondly, the velocity of the emitted mesons is smaller than the velocity of the nucleons, i.e., the collision time of nucleons is short compared to the period of the emitted radiation. Thirdly, only those components of the radiation field are considered for which these conditions are satisfied. These assumptions, which are essential in their theory, also simplify the calculations and give a nearly constant matrix element for production, i.e., independent of incident energy and the multiplicity, except for the statistical weight of the mesons. The second assumption is consistent with the calculated results, when the energy of the incident particles is sufficiently high.

It should be noted that, if we consider the higher order corrections, there are some intermediate states which violate the first and second assumptions and complicate the simplicity of calculation, as the matrix element now, besides being divergent, is also a complicated function of the incident energy. But if we could renormalize the high frequencies of the meson field which not only violate the initial assumption but also give the divergent difficulties, it would undoubtedly be found that the low frequency parts are most effective in these phenomena, and the total cross section for inelastic and elastic scattering would have the same magnitude as the cross section for elastic scattering without radiative corrections as in the Bloch-Nordsieck case. If the constancy of the matrix element found valid for low frequencies is extended to high frequencies phenomenologically, it agrees with Glauber's treatment[5] in terms of a direct interaction between a nucleon and many mesons. However, at the present stage the theory cannot be renormalized, and the effect of higher frequencies of virtual mesons is still uncertain.

It is remarkable that these conditions are satisfied in most of the experimental results now existing, and are in rather good agreement with the L.O.W. theory. Of course, we do not know the convergence of the power series expansion in the coupling constant even in quantum electrodynamics, nor what a future theory would give in the high energy region. It is probable, though, that the main contribution comes from the statistical weight (phase volume) of the final state, the pseudoscalar nature of the meson, and the Lorentz invariance requirement of the matrix element. Furthermore, the assumption of constant matrix element, derived under some ambiguous assumptions, may have some more direct physical meaning in a future theory.

In Fermi's theory, it is assumed that there will be established a thermal equilibrium of the virtual mesons in some Lorentz contracted volume. His treatment is more classical and its meaning is not clear. In order to established the thermal equilibrium, the collision time must be longer than the frequency of the emitted mesons, and this condition cannot be satisfied when the energy becomes sufficiently high; moreover, the Lorentz contracted diameter of the volume in which the thermal equilibrium is established is much smaller than the wavelength of the emitted mesons in the high energy region, and thus appears to be inconsistent with the thermal equilibrium assumption. In low energy regions, these conditions are satisfied (i.e., when the velocity of the meson is larger than the incident nucleon's velocity in the center-of-mass system), but the experimental results show that the velocity of the mesons is usually smaller than the nucleon velocity. Otherwise, the results for multiplicity and angular distribution are rather similar to the L.O.W. theory except in some detail points, and again agree fairly well with the experimental examples.

The similarities of both theories come mostly from the statistical weight of the final state and the Lorentz invariant nature of the matrix element; furthermore, the constant matrix element is related to the range of the meson cloud which is of the order of the meson Compton wavelength. The only difference comes from the Lorentz invariant nature of the cross section and is related to the Lorentz invariant phase volume in the L.O.W. theory and to the Lorentz contraction of the volume in which a thermal equilibrium is established, in Fermi's theory. This leads to different results, especially for the average energy of the emitted mesons in the center-of-mass system as a function of multiplicity.

[3] H. Fukuda and G. Takeda, Prog. Theoret. Phys. **5**, 957 (1950); Fujimoto, Fukuda, Hayakawa, and Yamaguchi, Prog. Theoret. Phys. **5**, 669 (1950).

[4] E. Fermi, Prog. Theoret. Phys. **5**, 570 (1950); Phys. Rev. **81**, 683 (1951).

[5] R. J. Glauber, Phys. Rev. **84**, 395 (1951).

II. THE DIFFERENCE BETWEEN FERMI'S METHOD AND THE L.O.W. METHOD

The starting points of these theories are quite different. One is based on weak coupling theory and the other on strong coupling, but both are rather classical treatments, as the L.O.W. method is somewhat similar to the Bloch-Nordsieck treatment.[6] In the L.O.W. theory the matrix element of this process is nearly constant, at high energies, so that the cross section is proportional to the phase volume of the final state. Though the calculation is restricted only to the first order, the results will be true more generally in the case of pseudoscalar mesons because the main contribution for multiple production comes from the statistical weight of the final states. The main difference between these theories stems from the Lorentz contraction of the volume in which the thermal equilibrium of the virtual mesons is established. The Lorentz contracted diameter of this volume (c.m. system) is much smaller than the wavelength of the emitted mesons in Fermi's theory. It is dubious whether the thermal equilibrium of these mesons could be established in such a small domain. For example, in high energy collisions the Lorentz contracted diameter d is given by

$$d=r_0 2Mc^2/W, \quad r_0=\hbar/\mu c^2\sim 1.4\times 10^{-13}\ \text{cm},$$

where W is the total energy of the two colliding nucleons in the center-of-mass system and M, μ are the masses of nucleon and meson, respectively. The average number of mesons produced is about

$$S\sim 1.34(W/Mc^2)^{\frac{1}{4}};$$

hence, the average energy of the emitted pion is proportional to $0.75(W\cdot Mc^2)^{\frac{1}{4}}$. The mean wavelength of the emitted mesons is

$$\lambda=d(2\pi/10)(W/Mc^2)^{\frac{1}{4}},$$

and becomes much larger than the diameter when the total energy (c.m. system) becomes larger than 100 Bev.

It would seem reasonable to assume that the Lorentz contracted diameter of the volume where the thermal equilibrium is established is nearly the same as the wavelength of the emitted mesons. This, then, gives the same results as the L.O.W. theory, and here lies the fundamental difference between the theories.

The matrix elements of the multiple production of n mesons are, according to the L.O.W. theory,

$$M=(2f/\mu)^n(n!)^{-\frac{1}{2}}\phi^n A(\bar{\psi}\psi\bigcup\bar{\psi}\psi),$$

where f is the coupling constant of the pseudovector interaction between nucleons and pseudoscalar mesons, ϕ is the wave function of the emitted mesons, and $\bar{\psi}\psi\bigcup\bar{\psi}\psi$ is the scattering potential between two high energy nucleons which does not depend on n. These matrix elements are nearly the same as the elastic scattering matrix elements in the sense of the Block-Nordsieck treatment. About this part of the matrix elements we have no detailed information either from theory or from experiment. We only assume that this Lorentz invariant part is nearly independent of n and nearly constant. A is the factor such that the total cross section becomes geometrical. The total cross section σ is proportional to

$$\sum \epsilon_i=\gamma W$$

$$\left(\frac{2f}{\mu}\right)^{2n}\frac{1}{n!}\langle\phi^{*n},\phi^n\rangle_0=\left(\frac{2f}{\mu}\right)^{2n}\frac{1}{n!}\frac{1}{(2\pi)^{3n}}\prod_{i=1}^{n}\frac{d\mathbf{q}_i}{2\epsilon_i}, \quad (1)$$

where

$$\langle\phi^*,\phi\rangle_0=\Delta_\mu{}^+(x)=\frac{1}{(2\pi)^3}\int_{q_0>0}dq^4\delta(q^2+\mu^2)$$

$$=\frac{1}{(2\pi)^3}\int\frac{d\mathbf{q}}{2\epsilon}.$$

The quantity $(2\pi)^{-3}\int d\mathbf{q}/2\epsilon$ means the phase volume times the square of the absolute value of the meson wave function, and this expression is Lorentz invariant; γ is the fraction of the energy transferred to the mesons (c.m. system). The cross section in Fermi's theory is

$$\sum \epsilon_i=\gamma W$$

$$\sigma\propto\left(\frac{2Mc^2}{W}\right)^n\frac{1}{n!}\prod_1^n\int\frac{d\mathbf{q}_i}{(2\pi)^3}. \quad (2)$$

The main difference between (1) and (2) is that W enters in Fermi's theory, while the energy of the emitted pions occur in the L.O.W. theory. For intermediate energies this is not so essential for the multiplicity, but we shall show in the next section that there still occurs some difference. We would also like to stress that it is very much more complicated in Fermi's theory to establish a covariant connection between the matrix elements in the c.m. system and the lab. system than is the case for the L.O. W. theory.

III. THE MULTIPLICITY, ANGULAR DISTRIBUTION, AND AVERAGE ENERGY OF THE MESONS

It will be convenient to label the quantities in the laboratory system and the center-of-mass system with and without asterisks, respectively:

c.m. system	lab. system	Interpretation
E	E^*	Energy of the incident nucleon.
$\epsilon_i q_i$	$\epsilon_i{}^* q_i{}^*$	Energy and momentum of the ith emitted meson.
θ_i	$\theta_i{}^*$	Angle between the ith meson and the incident nucleon.

$W=2E$

[6] F. Bloch and H. Nordsieck, Phys. Rev. **52**, 54 (1937).

A.

The multiplicity of mesons in high energy nucleon-nucleon collision which has a total energy W (c.m. system) is given by

$$S\sim(f\gamma W/\pi\mu)^{\frac{1}{2}}\ \text{(L.O.W.)},\quad S\sim 1.34(W/M)^{\frac{1}{4}}\ \text{(Fermi)},\quad (3)$$

where γ is the energy loss of the incident particles (c.m. system). Of course, for the Bloch-Nordsieck approximation to be valid, γ must be much smaller than 1 and we assume $\gamma<\frac{1}{3}$; γ is, of course, different for each event. If we assume equal probability of any value of γ which is smaller than $\frac{1}{3}$, we get a distribution of the multiplicities for given energy as shown in Fig. 1. On the other hand, if we assume an average γ-dependence of $W^{-1/4}$; this gives us the same energy dependence in the L.O.W. theory as in the Fermi theory. The experimental results lie between the two theories so it is not possible to decide which theory fits better. The comparisons with experiment are listed in the next section.

B. The Angular Distribution of Mesons

The angular distribution of the emitted mesons is nearly isotropic in the center-of-mass system in both theories, but is collimated somewhat in the forward and backward direction in Fermi's theory. This is a consequence of the Lorentz contraction of the volume in which the thermal equilibrium is established. There is some evidence for foward-backward collimations of mesons, but symmetrical distributions of mesons have also been found.

In the L.O.W. theory, most of the angular momentum which comes in is carried off by the scattered nucleons, as they do not considerably change their momentum after collision. This gives us a symmetrical distribution of the emitted mesons. But it is probable that the total momentum of the final nucleon is not necessarily zero in the center-of-mass system, i.e., it is smaller than the momentum of each final nucleon, but may be comparable to the energy loss. If we assume further that the final nucleons are preferentially scattered forward and backward (which occurs when the potential between two nucleons is the vector type of interaction, and there is some evidence of forward and backward scattering), the remaining momentum which is directed either forward or backward is shared by the emitted mesons. We have made some rough estimates for the half-angle of the emitted pion and find that it varies between 45° and 135° in the center-of-mass system. Therefore, both theories could explain the experimental angular distribution within the statistical deviations.

Although the velocity of the emitted mesons in the center-of-mass system is much larger in Fermi's theory (see C), the angular distribution in the laboratory system is determined only by the angular distribution in the center-of-mass system, and does not depend on whether their kinetic energy in the c.m. system is larger than or comparable with their rest mass.

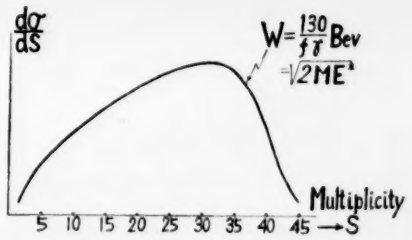

FIG. 1. The distribution of multiplicity of mesons in the L.O.W. theory, assuming equal probable energy transfer to the mesons γ between $0<\gamma<\gamma_{\max}\sim\frac{1}{3}$. E^* is the energy of the incident nucleon in the laboratory system.

By performing a Lorentz transformation we get

$$\sin\theta^*=\frac{Mq\sin\theta}{[(E\epsilon+pq\cos\theta)^2-M^2\mu^2]^{\frac{1}{2}}},\qquad \cos\theta^*=\frac{p\epsilon+Eq\cos\theta}{[(E\epsilon+pq\cos\theta)^2-M^2\mu^2]^{\frac{1}{2}}},\quad (4)$$

where ϵ, q, E, and p are the energy and momentum of the emitted mesons and the initial nucleon (c.m. system), respectively.

When the velocity of the mesons is larger than that of the incident nucleon in the center-of-mass system (Fermi's theory, $E<100$ Bev), the number of mesons which are emitted backward in the laboratory system (the number of particles which deflect more than 90°) is

$$\sim S(M^2q^2-\mu^2p^2)/4(E\epsilon)^2\lesssim SM^2/4E^2\sim\tfrac{1}{2}/4S^3\quad\text{(Fermi)},\quad (5)$$

and can be neglected.

When the meson velocity is smaller than the nucleon velocity ($E>10$ Bev in L.O.W.), the mesons are emitted in a cone in the laboratory system, and the maximum angle $\theta_{\max}{}^*$ (lab. system) is given by

$$\theta_{\max}{}^*=\sin^{-1}\left(\frac{M}{p}\cdot\frac{q}{\mu}\right).\quad (6)$$

The angle $\theta_{\max}$ (c.m. system) which corresponds to $\theta_{\max}{}^*$ (lab. system) is

$$\theta_{\max}=\pi-\sin^{-1}\left\{\frac{\mu}{\epsilon}\left[1-\left(\frac{M}{p}\cdot\frac{q}{\mu}\right)^2\right]^{\frac{1}{2}}\right\},\quad (7)$$

and the number of particles which are emitted between $\theta_{\max}$ and 180 degrees (c.m. system) is

$$s(\mu^2p^2-M\ q^2)/4(E\epsilon)^2\sim 1/36\quad\text{(L.O.W.)},\quad (8)$$

and can be neglected. In both theories, most of the mesons are emitted forward, and the relation between the angle of emission $\theta_i{}^*$, in the laboratory system and the angle θ_i in the center-of-mass system is

$$\sin\theta_i{}^*=\frac{M}{p}\left(\frac{1-\cos\theta_i}{1+\cos\theta_i}\right)^{\frac{1}{2}}.\quad (9)$$

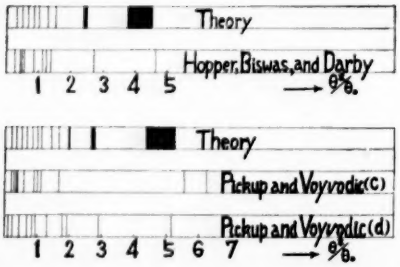

FIG. 2. Experimental results on the angular distribution of mesons and the comparison with the prediction of the theory assuming a spherically symmetric distribution in the center-of-mass system. θ^* is the angle between the emitted mesons and the incident nucleon in the laboratory system, and θ_0 is their half-angle.

When the angular distribution in the center-of-mass system is symmetrical, the angle of the ith particle being counted from the small angle,

$$\sin\theta_i^* \sim \frac{M}{p}\left(\frac{2i}{2(S-i)+1}\right)^{\frac{1}{2}}, \tag{10}$$

and the half-angle in the laboratory system is

$$\sin\bar{\theta}^* = M/p. \tag{11}$$

From this half-angle we can estimate the energy of the incident particle more precisely. It is concluded that the angular distribution in the laboratory system is not affected by the meson energy when the kinetic energy of the meson in the center-of-mass system is comparable with or larger than its rest mass. (This condition is satisfied in both theories.) The angular distribution does not depend essentially on theory within the statistical errors, (see Sec. IV).

C. The Average Pion Energy

The most important difference between both theories concerns the average energy of the mesons as a function of the multiplicity. From Eq. (3), the average energy in the center-of-mass system as a function of multiplicity is given by

$$\bar{\epsilon} \sim (1/2f)\sqrt{S}\ \text{Bev (L.O.W.)}; \quad \bar{\epsilon} \sim 0.6 \times S\ \text{Bev (Fermi)}. \tag{12}$$

It should be noted that it does not depend on the total energy or the energy transfer to the mesons explicitly. This quantity directly reflects the $\frac{2}{3}$-powder dependence (L.O.W) and $\frac{1}{2}$-power dependence (Fermi) in Eq. (3). The deviation from this average energy is of the order of

$$\Delta\epsilon \sim \begin{cases} \bar{\epsilon}/\sqrt{2} & \text{(L.O.W.)} \\ \bar{\epsilon}/\sqrt{3} & \text{(Fermi)}, \end{cases}$$

as the cross section depends sensitively on the phase volume of the final states. The average energy of the mesons in the center-of-mass system is proportional to the multiplicity in Fermi's theory, whereas is varies with the square root of the multiplicity according to L.O.W. (In Heisenberg's theory[7] it is independent of the multiplicity.) The experimental results fit the L.O.W. theory better than the Fermi theory (see Sec. IV).

IV. ANALYSIS OF EXPERIMENTS

There are so few examples of multiple meson production known to be definitely produced in single nucleon-nucleon collisions that it is necessary to include cases that are probably the results of collisions of the incoming nucleon with a nucleus at the edge of a nucleus. It is therefore not possible to get definite conclusions from the experimental results, but it will be interesting at any rate to compare all the cases with the theory. One example of a single nucleon-nucleon col-

TABLE I. Analysis of experimental results for two multiple events, with the help of Lewis, Oppenheimer, and Wouthuysen's theory[a] and Fermi's theory.[b]

Event[c]		$p+p$		
$\sin\bar{\theta}^*$		0.035 ± 0.008		
		Experiment	L.O.W.	Fermi
E(Bev)		22.1	27 ± 5	
S_{charge}		6		
$S_{\text{tot.}}$		9	$(f\gamma\cdot100)^{\frac{1}{2}}$	9
ϵ_i		0.42		
		0.43	$1.5/f$	
(Bev)		0.27		
		0.41		
		0.25		5.0
		0.86		
		0.67		
		0.46	$f=3.3\pm1.0$	
		0.27		
		$\bar{\epsilon}=0.45\pm0.04$		
γ		0.09	0.08	1.00

Event[d]	$p+$nucleus (edge)				
$\sin\bar{\theta}^*$	Narrow cone 0.003		Wider cone 0.13		
	Experiment		L.O.W.		Fermi
E(Bev)			n.c. 330	w.c. 7.7	122
S_{charge}	n.c.[e] $8+$	w.c.[e] 7			
$S_{\text{tot.}}$	$12+11$		$(f\gamma\cdot1320)^{\frac{1}{2}}$	$(f\gamma\cdot31)^{\frac{1}{2}}$	21
	n.c.		n.c.	w.c.	
ϵ_i	$E=122$	$E=330$			
	>0.25	>0.15	$1.73/f$	$1.65/f$	
(Bev)	>1.0	>0.75			
	~1.4	~0.7			
	w.c.				11.7
	$E=122$	$E=7.7$	$f=3\pm2$	$f=3.3\pm1$	
	0.35	0.50			
	0.53	0.34			
	n.c. ~0.01		n.c.	w.c.	
γ	0.10				
	w.c. 0.30		~0.01	0.35	1.00

[a] See reference 2.
[b] See reference 4.
[c] See Hopper, Biswas, and Darby, reference 1.
[d] See Lord, Fainberg, and Schein, reference 1.
[e] n.c.: narrower cone; w.c.: wider cone.

[7] W. Heisenerg, Nature **164**, 65 (1949).

lision, which produced six charged mesons and three neutral mesons, was found by Hopper, Biswas, and Darby. Precise measurements of the angle and energy were made. An example of a nucleon collision with a nucleon at the edge of the nucleus was found by Lord, Fainberg, and Schein,[1] in which 15 mesons were emitted. Fermi concluded that there is forward and backward collimation of the mesons in the center-of-mass system from the result that eight mesons were emitted in a narrow cone (0.003 radian) and seven in a considerably wider cone (0.18 radian). Four examples of both types were found by Pickup and Voyvodic,[1] but, unfortunately, the energy of the meson was not determined.

A. The Multiplicity

The energy of the incident particle can be estimated from Eq. (11), assuming a nearly symmetrical distribution of mesons in the center-of-mass system. Even in Fermi's theory, which implies some forward and backward collimation, the calculated value does not change more than a factor of 4. We assume that there are equal numbers of neutral mesons as positive (or negative) mesons, so the total multiplicity is $\frac{3}{2}$ times the number of charged particles. From Eq. (3) we get the theoretical value of the multiplicity. In the L.O.W. theory we can determine $f\cdot\gamma$ by comparing with the experimental value. The value of ϵ may be determined from an average meson energy in the center-of-mass system, and we can compare γ with the experimental value, which gives rather good agreement.

B. The Angular Distribution

The experimental angular distribution of mesons is nearly symmetrical in the center-of-mass system within the statistical deviation (Fig. 2). One exception is the example of Lord, Fainberg, and Schein, which has a sharp maximum in both the forward and backward direction. But this is not necessarily in contradiction with the L.O.W. theory. It can be interpreted as a cascade process, because this is a nucleon-nucleus collision with too slow protons in the backward direction. The incident nucleon hits a nucleon in the nucleus and produces eight mesons which are emitted in a narrower cone, and one or more of these produced mesons hits another nucleon to produce seven mesons which are emitted in a wider cone. From the angle of each cone, we can estimate the energy of the incident nucleon and the meson which produces secondary mesons, from Eq. (10). (The energy of the meson is larger than the nucleon mass, and the difference of the mass between nucleon and meson does not change the situation. We further assume the multiple production by the meson to be the same as in the case of the nucleon.) The energy of each particle was estimated from the angle of each cone, yielding

$$E_1=330 \text{ Bev}, \quad E_2=7.7 \text{ Bev}, \quad E_2^*=120 \text{ Bev}.$$

The estimated energy E_2^* is of the same order of magnitude of the energy of the primary mesons (>250 Bev, >50 Bev, ~ 86 Bev). In Table I the comparison with theory is made.

C. The Energy of the Mesons

The energy of the mesons in the center-of-mass system can be estimated from the angle and energy of the mesons in the laboratory system, and the energy of the incident nucleon in the center-of-mass system:

$$\epsilon=\frac{1}{2}\left[\frac{\epsilon^*}{E}\left(1+\frac{2}{1+\cos\theta^*}\frac{\sin^2\theta^*}{\sin^2\theta^*}\right)+\left(\frac{\mu}{M}\right)^2\frac{E}{\epsilon^*}\right] \text{ Bev}.$$

These values, in the case where the energy and angle of mesons in the laboratory system are known, are also listed in Table I.

Comparing with the experimental results in the L.O.W. theory we get the value of the coupling constant f:

$$f\sim 3\pm 1.$$

This is of the right order of magnitude to be compatible with the low energy experiments:

$$f^2/4\pi\sim 0.1.$$

On the other hand, in Fermi's theory, it is considerably larger than the experimental values. In Heisenberg's theory, the energy of a meson only increases logarithmically with the multiplicity and somewhat smaller than experiments indicate. From the energy of the emitted π-meson, we can deduce the energy transferred to the meson. It is only a portion of the total energy, while Fermi's theory assigns the total energy available to the mesons.

In conclusion, the author would like to emphasize that in the Fermi theory the Lorentz contracted diameter of the volume in which the thermal equilibrium is established is of the same order of magnitude as the average wavelength of the emitted pions. This is an immediate consequence of calculating the phase volume covariantly, assuming further a constant matrix element.

The author would like to express his sincerest thanks to Professor Oppenheimer, Professor Fermi, and Professor Pais for valuable discussions and for their kind encouragement, and also to Dr. Lewis for a discussion of his investigations on this subject.[8]

[8] H. W. Lewis, Phys. Rev. **86**, 625 (1952).

Combined Pairs of Vacancies in Copper*

J. H. BARTLETT† AND G. J. DIENES
Brookhaven National Laboratory, Upton, Long Island, New York
(Received November 4, 1952)

An approximate theoretical calculation is given of the energy of dissociation of vacancy pairs in copper and of the activation energy required for the motion of associated pairs. If two atoms have been removed from neighboring lattice sites, the resulting double vacancy may be more stable than the configuration consisting of two single vacancies far apart. On the assumption that the lattice energy may be regarded as composed of contributions from pairs of atoms, the energy of dissociation of a double vacancy in copper has been estimated as about 0.6 ev. Furthermore, if the interatomic potential energy be represented by a Morse function, the activation energy for the motion of a double vacancy through any face-centered cubic metal crystal is about one-half that for a single vacancy. Double vacancies are, therefore, expected to be stable and highly mobile in such metals.

I. INTRODUCTION

LATTICE imperfections play an important role in many processes occuring in solids.[1] In this note attention is focused on vacancies and their possible aggregation into pairs and clusters. Studies of ionic crystals have shown that positive and negative vacancies tend to combine into stable pairs whose dissociation energy is about 0.9 ev in NaCl.[2,3] Theory indicates that such pairs are considerably more mobile than single negative vacancies.[4]

Similar studies have not yet been made for metals. Seitz[5] suggests that the energy of dissociation of a pair of vacancies in copper may be quite large and that, analogous to the alkali halides,[4] the pair may be very mobile because the number of repulsive interactions which must be overcome are reduced. Recent experiments on the annealing of lattice disturbances introduced by cold work[6–9] and fast particle irradiation[7,9,10] indicate that an appreciable amount of annealing takes place at quite low temperatures where single vacancies are not mobile enough to anneal out by diffusion out of the sample. Some of the low temperature annealing processes may possibly be attributed to the formation and/or motion of combined pairs of vacancies.[5]

The purpose of the present note is to describe some approximate theoretical calculations carried out in order to investigate the properties of pairs of vacancies. In particular, one wants to answer the following questions:

(a) Do vacancies in metals tend to associate into pairs?
(b) If the pairs are stable, what is their activation energy for migration?

II. THE ENERGY OF DISSOCIATION

The energy required to create isolated vacancies in copper is known theoretically from the work of Huntington and Seitz[11] and Huntington.[12] The energy of formation is about 1.4 ev, which is appreciably less than the cohesive energy, 3.52 ev, because of the rearrangement of the electrons and the atoms around a vacancy. In order to calculate the dissociation energy one has to inquire how much the energy of formation is reduced when a vacancy is created next to an already existing one rather than far away from it. In ionic crystals the major source of the energy of dissociation is the electrostatic attraction between positive and negative vacancies.[2,3] In metals, however, things are more complicated because of the homopolar type of bonding. An accurate calculation would probably use more involved methods than those of Huntington and Seitz, and would therefore be rather long, if indeed possible at present. Accordingly, we have used a fairly crude model, which is based on the assumption that the energy of the lattice can be regarded as composed of terms involving the interaction of pairs of atoms. This is a simple procedure and one which ought to be fairly reliable for obtaining a picture of the general situation.

The formation of a single vacancy requires the breakage of 12 bonds in a face-centered cubic material and the formation of 6 bonds on the surface. The energy of formation may then be expressed as

$$E_f^{(1)} = (12-6)(E_c/6) - W^{(1)}, \qquad (1)$$

where $E_f^{(1)}$ = energy to form an isolated single vacancy, E_c = cohesive energy = 3.52 ev for copper, and $W^{(1)}$

* Under contract with the U. S. Atomic Energy Commission.
† Permanent address: Physics Department, University of Illinois, Urbana, Illinois.
[1] See, for example, the recent review by F. Seitz in *Imperfections in Nearly Perfect Crystals*, edited by W. Shockley (John Wiley and Sons, Inc., New York, 1952), pp. 3–77.
[2] F. Seitz, Revs. Modern Phys. **18**, 384 (1946).
[3] J. R. Reitz and J. L. Gammel, J. Chem. Phys. **19**, 894 (1951).
[4] G. J. Dienes, J. Chem. Phys. **16**, 620 (1948).
[5] F. Seitz, *Advances in Physics* (Supplement to Phil. Mag.) **1**, 43 (1952).
[6] J. Molenaar and W. H. Aarts, Nature **166**, 690 (1950).
[7] Bowen, Eggelston, and Kropschot, J. Appl. Phys. **23**, 630 (1952); also paper given to the Society of Rheology at the Chicago anniversary meeting of the American Institute of Physics, October, 1951 (unpublished).
[8] Blewitt, Taylor, and Coltman, Phys. Rev. **82**, 769 (1951).
[9] For a review and discussion of this topic see G. J. Dienes, *Radiation Effects in Solids*, chapter in Annual Review of Nuclear Science, Vol. II (to be published).
[10] Marx, Cooper, and Henderson, Phys. Rev. **88**, 106 (1952).
[11] H. B. Huntington and F. Seitz, Phys. Rev. **61**, 315 (1942); **76**, 1728 (1949).
[12] H. B. Huntington, Phys. Rev. **61**, 325 (1942).

= energy regained by redistributing the electrons and atoms around the vacancy. From Huntington and Seitz[11,12] it is known that

$$E_f^{(1)} = 1.4 \text{ ev, and therefore } W^{(1)} = 1.7 \text{ ev.}$$

Let now a second atom be removed which is a nearest neighbor of the vacancy. One of the bonds of this atom is already broken, so that only 11 bonds have to be broken in removing it to the surface. Thus,

$$E_f^{(2)} = (11-6)(E_c/6) - W^{(2)}. \quad (2)$$

The dissociation energy ΔE_d, is given by

$$\Delta E_d = E_f^{(1)} - E_f^{(2)} = \tfrac{1}{6}E_c - [W^{(1)} - W^{(2)}]. \quad (3)$$

$W^{(1)}$ and $W^{(2)}$ are expected to be very nearly the same in magnitude. This is the case because the contribution to the dissociation energy arising from a reduction (by the association of two isolated vacancies) in the kinetic energy of the electrons is approximately canceled by the smaller polarization around the pair relative to two single vacancies. Further, simple calculations showed that the difference in repulsive energy arising from the relaxation of the neighbors is very small, of the order of 0.01 ev. On this basis the dissociation energy is estimated to be 0.59 ev. A somewhat lower value is obtained for this energy if $W^{(1)}$ and $W^{(2)}$ are not taken to be equal but are assumed to be distributed among the bonds in the same way as the cohesive energy. In this case the energy of dissociation is equal to $E_f^{(1)}$, which is 0.23 ev. Thus, ΔE_d is expected to be between 0.23 and 0.59 ev and is probably much closer to the 0.59-ev value. Even if the lower figure is the valid one, association is significant.

The relation between the number of combined pairs of vacancies n_2 and the number of isolated vacancies n_1 is given at equilibrium by[2]

$$n_2/n_1 = 12(n_1/N)e^{\Delta E_d/kT}, \quad (4)$$

where N is the density of available sites and the factor 12 enters because the pair can be oriented in 12 different ways in the face-centered cubic lattice. For ΔE_d of 0.59 ev n_2/n_1 is small for a crystal in thermodynamic equilibrium. This is the case because at temperatures where the exponential is large the value of n_1/N is small. However, the fraction of pairs may be made appreciable by freezing in a nonequilibrium number of vacancies.

If thermal equilibrium can be assumed as approximately valid, then Eq. (4) may be applied in different ways to ascertain how vacancies actually tend to associate. If $n_1/N = 10^{-7}$, $n_2 = n_1$, and $\Delta E_d = 0.59$ ev, then the temperature at which the number of pairs equals the number of single vacancies is 502°K. Recent work by Kauffman and Koehler[13] indicates that vacancies in gold may be quenched in to a concentration of the order of 10^{-4}, where the quenching is begun at 900°K and occurs in about 5 milliseconds. The average effective temperature will be lower than 900°K, but this value of T will give a lower limit for n_2/n_1. If $n_1/N = 10^{-4}$, $T = 900$°K, and $\Delta E_d = 0.59$ ev, then Eq. (4) gives $n_2/n_1 = 2.4$. Since this is a lower limit for the ratio of pairs to singles, we suggest that the interpretation of experimental results must allow for the likelihood that vacancies will associate.

Dissociation of the vacancy pair may require not only the dissociation energy of about 0.59 ev but also a further activation energy to permit the pair to diffuse apart. A more careful examination is required for clarification of this point since one would have to determine the detailed form of the interaction potential of two vacancies as a function of their separation.

III. THE ACTIVATION ENERGY FOR THE MIGRATION OF COMBINED PAIRS OF VACANCIES

It was shown in the previous section that combined pairs of vacancies in copper are expected to be quite stable in any crystal in which an appreciable number of vacancies have been frozen in. It is pertinent, therefore, to inquire about the mobility of such pairs. A fairly simple comparative calculation can be carried out based on a Morse potential interaction between neighboring atoms. Such a calculation may be considerably in error as far as absolute magnitude is concerned. However, the comparison of the activation energies for the migration of pairs with that for the migration of single vacancies should be quite reliable when based on the same potential function.

Let the atomic interactions be represented by a Morse potential:

$$U = D[1 - e^{-\alpha(r-r_0)}]^2, \quad (5)$$

where r = interaction distance, r_0 = equilibrium interatomic distance, α = constant, D = dissociation energy per bond (atom-atom interaction), and U = potential energy per atom. In a face-centered cubic lattice,

$$D = \tfrac{1}{6}E_c, \quad (6)$$

where E_c = cohesive energy. In copper $D = 3.52/6$ ev $= 0.59$ ev and a reasonable value for α is[14] 1.4A^{-1}. If a ratio of the two activation energies is taken for comparison, the final results turn out to be independent of the value of D, but are found to depend on the value of α.

Let the coordinates of any point in space be designated, in units of $a/2$ (where a = lattice parameter), by (xyz). These numbers are integers for the lattice points. Let the vacancies be located at (000) and (110). In order that the atomic jump should not dissociate the pair but permit it to move as a unit the moving atom must be a nearest neighbor of both vacant lattice sites. Let the initial position of the moving atom be at (011) and let (xyz) denote its position at any point within the triangle defined by these three lattice points. The total interaction energy was then calculated by means of Eq. (5) as a function of the position of the moving

[13] J. W. Kauffman and J. S. Koehler, Phys. Rev. **88**, 149 (1952).

[14] See, for example, J. C. Slater, *Introduction to Chemical Physics* (McGraw-Hill Book Company, Inc., New York, 1939), pp. 454–455.

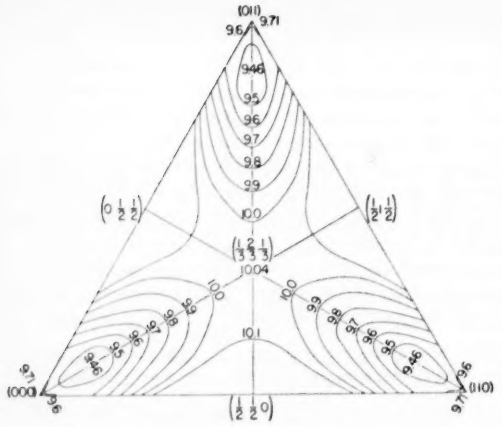

FIG. 1. Potential energy contours for diffusion of a combined pair of vacancy. Moving atom initially at (011), vacancies at (000) and (110).

atom. In this calculation the atom at (xyz) was assumed to interact with all the atoms at lattice points which were nearest neighbors of (000), (110), and (011). The energies were expressed in units of D, and the potential energy contours obtained are plotted in Fig. 1.

It is evident from the geometry of the lattice that the energy contours must be symmetrical with respect to the lines connecting the apex of the triangle to the midway point of the opposite side. As shown in Fig. 1 these lines represent the valleys directed toward the saddle point which was found to be at ($\frac{1}{3}$ $\frac{2}{3}$ $\frac{1}{3}$). Relaxation of the neighbors of the moving atom and of the vacancies was neglected prior to or during diffusion. In a comparative calculation the error introduced is expected to be small. However, because of the relaxation of the atom to be moved from (011) it really starts its climb over the potential barrier from a minimum at (1/12, 11/12, 5/6) which represents its relaxed position. The atom then travels up the valley toward the saddle point. The saddle point is seen to be a rather flat plateau. From the saddle point the atom may move either toward (110) or toward (000). The two paths are entirely equivalent, and the actual course of the particle will be determined by chance fluctuations. The activation energy for this jump, ΔE_2, given by the difference between the maximum and the minimum along the potential barrier, is $0.58D$. Calculations near the minimum and the maximum showed that the jumping atom has no tendency to move out of the plane defined by (000), (011), and (110).

An entirely analogous calculation was carried out for the motion of a single vacancy. In this case there is an atom at (110), the vacancy is at (000) and the atom to be moved is at (011). The motion is, therefore, along the line (011) to (000), and the saddle point is at (0 $\frac{1}{2}$ $\frac{1}{2}$). The minimum in energy was found to be $9.59D$ at (0, 0.91, 0.91) and the maximum $11.135D$, giving an activation energy ΔE_1, of $1.545D$. In this computation the same neighbors were taken into account as in the case of the double vacancy. For reasons of symmetry the noncommon nearest neighbors of (110) should be neglected. These atoms have very little influence on the activation energy, with the revised value being $1.640D$. This activation energy for the jump of a single vacancy is reasonable also in absolute magnitude. With D equal to 0.59 ev the activation energy amounts to 0.97 ev. This value is in good agreement with the estimate of Huntington and Seitz.[11,12]

The sensitivity of the results to variations in the α parameter was also investigated. The energies at the minimal and maximal positions were recalculated for $\alpha=2.8\text{A}^{-1}$ (an extreme value). With this value of α, E_2 and E_1 were found to be $8.75D$ and $12.43D$, respectively. These figures are unreasonably large, of course. The point is that even at this extreme value of α the difference between ΔE_1 and ΔE_2 is significantly large.

The results are summarized in Table I where activation energies, differences, and ratios in activation energies are given for the various cases. The results show very clearly that the combined pairs of vacancies require a considerably lower activation energy for diffusion than the single vacancies. The ratio $\Delta E_2/\Delta E_1$ is probably the most significant quantity since its value

TABLE I. Activation energies for the motion of single and double vacancies in copper.

α in A^{-1}	ΔE_1 in ev (single vacancy)	ΔE_2 in ev (double vacancy)	$\Delta E_1-\Delta E_2$ in ev	$\frac{\Delta E_2}{\Delta E_1}$
1.4	0.97	0.34	0.63	0.354
2.8	7.33	5.16	2.17	0.705

is independent of the value of the bond strength D. The activation energy for the pair is 35 to 70 percent of the value for the simple vacancy, depending on what α is used. As pointed out, the lower α-value is the reasonable one. A conservative estimate for the activation energy for the motion of a pair is, therefore, about one-half of that for the single vacancy. The calculations fully confirm the physical arguments which indicated that a pair should be much more mobile than a single vacancy because of the more open structure of the combined imperfections.

These results are qualitatively valid for any face-centered cubic metal as long as a Morse function is a reasonable approximation to the actual potential function. Quantitatively, the ratio of the activation energies will depend on the value of α and the difference on both parameters, α and D.

The existence of stable pairs of vacancies in simple metals is strongly supported by the theoretical results. Furthermore, these results indicate clearly that pairs are much more mobile than single vacancies.

It is a pleasure to acknowledge the assistance of Miss J. H. Snover in carrying out the detailed calculations. The authors are also grateful to Dr. H. B. Huntington for stimulating discussions.

Periodic Deviations in the Schottky Effect for Molybdenum*

E. G. Brock,† A. L. Houde,‡ and E. A. Coomes
University of Notre Dame, Notre Dame, Indiana
(Received October 2, 1952)

Periodic deviations in the Schottky effect for molybdenum have been measured over a field range of 10^4 to 10^6 volts cm^{-1} in a temperature range of 1400 to 1800°K. The results, interpreted in terms of the two reflection parameters λ and μ, justify the assumption of a mirror image barrier for the emitted electrons.

I. INTRODUCTION

PERIODIC deviations in the Schottky effect have been studied experimentally for tungsten,[1-3] tantalum,[2,4] and for tantalum contaminated with thorium.[4] A quantum-mechanical theory of electron emission[5-7] allows an interpretation of these studies in terms of the field dependence of the electron reflection coefficient for the potential barrier at the emitter surface. This analysis suggests the possibility of using Schottky plots as a tool to investigate some of the surface properties of solids.[8]

Such an investigation was undertaken in the case of tantalum,[4] and now has been continued for molybdenum.

Thermionic emission currents ranging from 10^{-5} to 10^{-9} amp were measured over a temperature interval of 1400 to 1800°K for molybdenum filaments. The periodic deviations in these currents were obtained over a field range of 10^4 to 3×10^5 volts cm^{-1}, and these results are related to the surface potential barrier through the two reflection parameters λ and μ suggested by Herring and Nichols.[8]

II. RESUME OF THEORY

Periodic deviations are related to the field dependent transmission coefficient through the relation[4,6]

$$F_2 = \text{the periodic part of } \log[\bar{D}(E)/\bar{D}(0)], \quad (1)$$

where F_2 is the periodic deviation, $\bar{D}$ is the transmission coefficient averaged over the energy distribution of the emitted electrons, and E the electric field applied to the emitter surface.

Guth and Mullin[7] obtained an expression for F_2 from the straightforward computation of $\bar{D}(E)$ for the one-dimensional box model. This barrier model has been plotted in Fig. 1 for the several applied fields of interest, to illustrate how its shape changes with field. The important mathematical relations derived for this model are listed in Fig. 1, and the general assumptions basic for these relations are: (a) the potential barrier to the left of x_1 is constant, and to the right of x_1 is due to the mirror image and applied fields; and (b) the potential barrier has a discontinuous slope at x_1. As a consequence of these assumptions the location of the barrier maximum, designated as x_0, depends only upon the applied field; theoretically, x_0 moves in toward x_1 from 601 to 19A as the applied field is increased from 10^5 to 10^6 volts cm^{-1}. Simultaneously the barrier half-width is decreased from 5.18×10^5 to 518A, but the barrier height is decreased only by 0.38 volt. The location of x_1 depends upon W_a alone; it is determined therefore for the particular emitter, but not affected by the applied field (see Fig. 1). For this model the Guth-Mullin expression for F_2 has been shown to be equivalent to[4]

$$F_2=\frac{C_2\xi^{\frac{1}{2}}}{T}\left[\frac{1}{f_1}\cos\left(\frac{C_3}{\xi^{\frac{1}{2}}}+C_4\right)+\frac{1}{f_2}\cos\left(\frac{C_3}{\xi^{\frac{1}{2}}}+C_5\right)\right], \quad (2a)$$

where $E^{\frac{1}{2}}$ is designated by the symbol ξ. To a good approximation the C's are constants for a given emitter, and their computation as well as that of the f's involves only natural physical constants [see reference 4, Table I, and Eq. (5)]. The first cosine term results from electron reflections, while the second is due to tun-

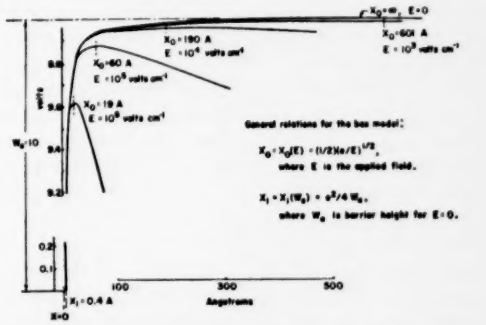

FIG. 1. The box model for an electron emitter with an electric field applied to its surface. $W_a=10$ volts is representative of the highly refractory metals. The periodic deviations in the Schottky effect are due to a large extent to the variations in the position of x_0 with applied field E.

* This research was sponsored by the U. S. Navy Bureau of Ships.
† Now at the General Electric Research Laboratory, Schenectady, New York.
‡ Now at St. John Fisher College, Rochester, New York.
[1] R. L. E. Seifert and T. E. Phipps, Phys. Rev. **53**, 493 (1938); **56**, 652 (1939).
[2] D. Turnbull and T. E. Phipps, Phys. Rev. **56**, 663 (1939).
[3] W. B. Nottingham, Phys. Rev. **57**, 935 (1940).
[4] Munick, LaBerge, and Coomes, Phys. Rev. **80**, 887 (1950).
[5] H. M. Mott-Smith, Phys. Rev. **56**, 668 (1939).
[6] E. Guth and C. J. Mullin, Phys. Rev. **59**, 575 (1941).
[7] E. Guth and C. J. Mullin, Phys. Rev. **61**, 339 (1942).
[8] C. Herring and M. H. Nichols, Revs. Modern Phys. **21**, 185 (1949), Chap. 4.

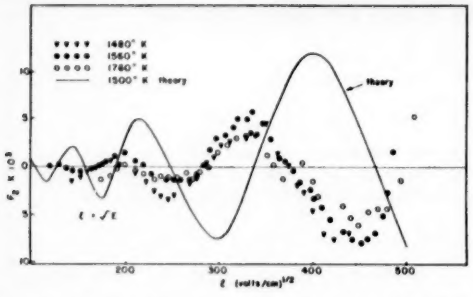

FIG. 2. Periodic deviations F_2 from the Schottky effect for clean molybdenum. The theoretical curve is calculated from the Guth-Mullin theory for $W_a = 10.2$ volts.

neling. Since both cosines have the same period, namely[9] $2\pi/C_3 = 2\pi/357.1$, they may be combined into the single term

$$F_2 = (C\xi^{\frac{1}{2}}/T)\cos[(357.1/\xi^{\frac{1}{2}}) + P], \tag{2b}$$

where C and P are parameters identified as

$$C = C_2[(1/f_1)^2 + (1/f_2)^2 + (2/f_1 f_2)\cos(C_4 - C_5)]^{\frac{1}{2}},$$

$$P = \tan^{-1}\left[\frac{f_2 \sin C_4 + f_1 \sin C_5}{f_2 \cos C_4 + f_1 \cos C_5}\right].$$

The original C's and f's specified in Eq. (2a) were practically functions of W_a alone; this property may be transferred to the C and P of Eq. (2b).

The physical significance of the F_2-dependence on ξ and W_a in Eq. (2b) becomes clear when D is written to show how it includes the effect of interference between electrons reflected in the region x_0 with those reflected near x_1. Because x_0 is field-dependent, while the point x_1, as well as the shape of the potential near this point, are field-independent[9] (see Fig. 1), Herring and Nichols[8] expressed D in terms of two partial reflection coefficients, as follows:

$$D = 1 - [|\mu|^2 + |\lambda|^2 + 2\,\mathrm{Re}(\lambda^*\mu)], \tag{3}$$

where D is the over-all unaveraged transmission coefficient, λ is a complex quantity whose square gives the reflection coefficient for an electron at x_0, and μ is a similar complex quantity for x_1. The quantities D, λ, and μ are therefore functions of the electron energy; λ depends upon the applied field and therefore upon ξ, and μ is essentially independent of the applied field by definition. The periodic part of D comes from the last term on the right of Eq. (3), and F_2 is obtained by averaging this term over all electron energies. When a Maxwellian distribution for emitted electrons is assumed, the averaging introduces the $1/T$ into the final equation (2b), so that $\xi^{\frac{1}{2}}$ in the amplitude and $357.1/\xi^{\frac{1}{2}}$ in the argument of the cosine are introduced by λ, while C and P have their principal contributions from the real and imaginary parts of μ. Therefore, if one could obtain λ and μ separately from experimental data, one would have a description of the barrier at two positions, namely x_0 and x_1. The theory in its present form cannot be used to make a direct separation of λ and μ from experimental data. It is possible, however, to determine whether or not the field dependence introduced by λ is that of a mirror image potential, and whether the μ implied by the data corresponds to the reflections of electrons from the discontinuity at x_1 for the box model.

[9] C_3 as given in reference 4 is slightly different from the value given here. Corrections have been made for more recent values of the physical constants.

III. EXPERIMENTAL METHOD AND DATA

The experimental tube and measurements already have been reported in detail.[4] In the present experiment the test filaments were 0.003-inch molybdenum wire[10]

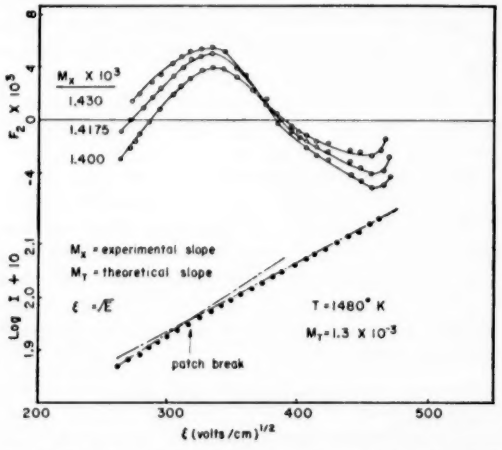

FIG. 3. The effect of choice of slope on the separation of periodic deviations F_2 from the Schottky plot in a patchy region of molybdenum. Note that the amplitude varies with slope, while there is little effect on the phase. The line drawn through the solid circles above the patch break has a slope of 1.4×10^{-3}; this is greater than the theoretical value computed from emitter temperature.

approximately 6.5 inches long. The diameter was determined by weighing and using 10.2 g cm^{-3} for the density.[11]

Prior to each set of emission measurements the molybdenum filament was flashed for two minutes at 2600°K. This seemed sufficient to clean the filament, for it brought the emission current to a value which was stable and reproducible to four significant figures over the two-hour period required in taking data for a precise Schottky plot.

[10] The molybdenum filament was obtained from the Fansteel Metallurgical Corporation, North Chicago, Illinois. Both unpolished and polished specimens of wire were tested, and the periodic deviations had identical patterns for both cases.

[11] *Handbook of Chemistry and Physics* (Chemical Rubber Publishing Company, Cleveland, 1949), thirty-first edition.

The filament temperature determinations were based on temperature-power data supplied by Moore and Allison of Bell Telephone Laboratories.[12] While the absolute temperature determined by these data is estimated to be correct to only $\pm 20°$K, constancy of temperature was checked during the taking of emission data by monitoring the filament heating current and voltage. The variation in temperature during a run was no greater than 1°K.

Precisions realized in the field and emission current measurements in the previous experiment[4] were reproduced here.

The Schottky plots obtained for clean molybdenum exhibited the modifications in slope due to the patch effect;[8] even at the highest fields the experimental slope was always greater than $(1.914/T)$ (cm volt^{-1})$^{\frac{1}{2}}$ predicted by Schottky theory, and in a few instances deviated by as much as 10 percent in the high field region. It was possible, however, as in the case of tantalum to separate each Schottky plot into several regions of constant slope and to obtain F_2-curves for molybdenum in the piecewise fashion previously described for tantalum.[4]

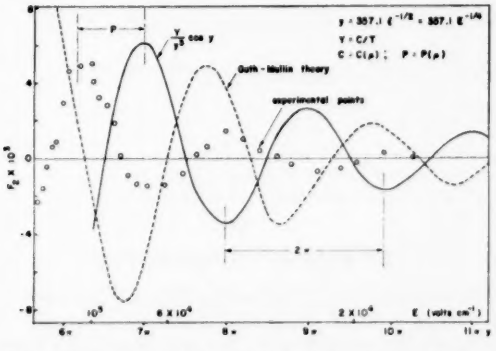

FIG. 4. F_2 *versus* y plot of periodic deviation theory. The curve has a constant period of 2π. A simple normalization to Y and a shift of P to the right should bring experimental points into coincidence with theory for $P=0$, if the emitter surface barrier follows the mirror image law. The Guth-Mullin theory for molybdenum is represented by the dashed curve. The experimental points are for molybdenum at 1480°K.

The experimental F_2-curves given in Fig. 2 are typical for clean molybdenum; here plots are given for temperatures of 1480, 1560, and 1760°K, respectively. An increase in amplitude with decrease in temperature may suggest itself, but the case is not clear as with tantalum.[4] The theoretical prediction that a change in temperature should not cause an appreciable phase change for the F_2 curves is verified. The phases were not appreciably sensitive to patch effects, while the amplitudes were affected to a large extent; Fig. 3 illustrates this (see reference 4, Fig. 4, for similar data in the case of tantalum).

[12] G. E. Moore and H. W. Allison (private communication).

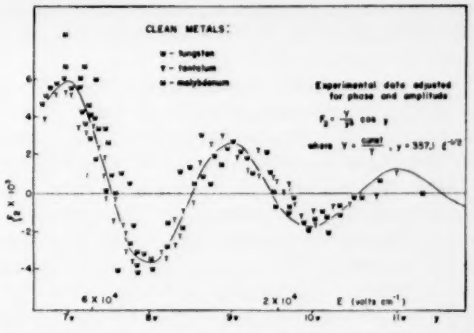

FIG. 5. Composite plot of F_2 *versus* y of periodic deviation data for the clean, highly refractory metals for a temperature range of 1200 to 2300 deg K, indicating that the surface potential barrier is mirror image.

IV. DISCUSSION OF RESULTS

The solid curve in Fig. 2 is a plot of the Guth-Mullin theory in which $W_a = W_i + e\phi = 5.8 + 4.4 = 10.2$ ev has been used for clean molybdenum. The comparison of experiment with theory reveals the same trends observed in all previous data for the clean highly refractory metals. The over-all form of the experimental curves follows the Guth-Mullin theory, with two important differences: (1) the experimental amplitudes are less than the theoretical, and (2) the extrema for the theoretical curves are shifted to larger values of ξ. While these differences may be attributed in a general way to patch effects and to the approximate character of the box model theory, particular and fundamental information seems available when an analysis based on the λ and μ coefficients is pursued.

As a first approximation, all of the field dependence of F_2 can be assumed to be due to λ because it is connected with x_0 alone. Thus, it is the mirror image λ that introduces specific analytic forms $\xi^{\frac{1}{2}}$ into the amplitude and $357.1/\xi^{\frac{1}{2}}$ into the argument of the cosine of Eq. (2) for the box model (the $1/T$ enters from averaging over the energy distribution of emitted electrons). That this field dependence peculiar to the mirror image barrier is verified may be clearly demonstrated if experimental data are compared with Eq. (2) transformed to

$$F_2 = (Y/y^{\frac{3}{2}}) \cos(y+P), \tag{4}$$

by letting $y = 357.1\xi^{-\frac{1}{2}}$, and $Y = (357.1)^{\frac{3}{2}}C/T$. Equation (4) transforms F_2 to an oscillating function with a constant period of 2π. Figure 4 is a graphical illustration of this function; the solid curve is a plot of F_2 *versus* y for $P=0$ and Y arbitrary, while the dashed curve in this figure is a replot of the Guth-Mullin theory represented in Fig. 2 by the solid curve. Typical transformed experimental points (the 1480°K data from Fig. 2) are shown as open circles in Fig. 4. If these data are for a mirror image λ, normalization by a constant amplitude factor and a simple phase shift to the right should

bring coincidence between experiment and the theoretical solid curve for $P=0$. This follows since Y and P are both independent of the field.

These two adjustments, namely the phase shift and the amplitude normalization, have been made for molybdenum, and also for the tungsten and tantalum data previously reported. A composite graphical representation together with the theory is given in Fig. 5. The adjustment factor for the amplitude varied between 1.5 and 2 for the three metals, after taking into account the $1/T$ variation; this range is not beyond the amplitude uncertainty due to the patch effect (see Fig. 3). Figure 5 represents the three highly refractory metals for an over-all temperature range from 1200 to 2300°K. Apparently the mirror image law is justified, and the λ part of the Guth-Mullin theory well verified.

It is apparent in Fig. 4 that the simple phase shift measures P in Eq. (4). In the instances of all data processed for Fig. 5, P had a different value for experiment than for the Guth-Mullin theory, and the deviation from the Guth-Mullin theory in every case was of the order of $\frac{1}{4}$ period. The inference is that the μ of the box model may not be completely justified.

The authors are grateful for the help received through discussions with others. In addition we acknowledge the technical assistance of Mr. Ernest Parsons and Mr. Fay Gifford in carrying out this experiment and in preparing the manuscript.

PHYSICAL REVIEW VOLUME 89, NUMBER 4 FEBRUARY 15, 1953

The Decay of Zn^{69}†

R. B. Duffield* and L. M. Langer‡
University of California, Los Alamos Scientific Laboratory, Los Alamos, New Mexico
(Received November 10, 1952)

The 52-minute ground state of Zn^{69} has been found to decay with a simple beta-spectrum of end point 0.897±0.005 Mev. The 13.8-hour isomer of Zn^{69} decays to the ground state by emission of a gamma-ray of energy 0.436±0.004 Mev. The conversion coefficient of this gamma-ray is 0.06 indicating a $M4$ transition.

INTRODUCTION

THE 52-minute activity of Zn^{69} was first made by Livingood and Seaborg,[1] and absorption techniques showed the radiation to consist of beta-particles of energy 1 Mev[1,2] or subsequently 0.86 Mev.[3] No spectrometer measurements on this activity have been reported.

The 13.8-hour isomer of Zn^{69} has been shown to decay to the ground state by emission of gamma-radiation, the energy of which has been reported to be 0.439 and 0.450 Mev.[4] The internal conversion coefficient has been reported to be between 0.01 and 0.1.

Using a magnetic lens spectrometer we have examined the beta-spectrum of the 52-minute Zn^{69} and have measured the energy and the internal conversion coefficient of the gamma-ray accompanying the 13.8-hour isomeric transition. The beta-spectrum appeared to be simple and to have an end point of 0.897±0.005 Mev. The gamma-ray energy was found to be 0.436 Mev and to have an internal conversion coefficient of 0.06.

EXPERIMENTAL PROCEDURE

The magnetic lens spectrometer used has been described in another paper.[5] A Geiger tube with a 3.6-mg/cm² mica window and a 0.5-inch diameter aperture served as detector. The resolution was 3 percent.

The sources were prepared by neutron irradiation of zinc in the thermal column of the Los Alamos homogeneous reactor. Zinc metal was evaporated in vacuum onto the desired backing material to form a source $\frac{3}{8}$ inches in diameter and perfectly uniform in thickness. This was then irradiated with thermal neutrons to form Zn^{69}. No interfering activities were found.

Data are given below for the beta-spectra from two different sources prepared in the above manner. The first had a thickness of 3.0 mg/cm² and was mounted on 0.00025-inch thick aluminum foil; the second had a thickness of 0.4 mg/cm² and was mounted on zapon of thickness approximately 50 micrograms per cm².

Sources of thicknesses 3 mg/cm² and 1 mg/cm² were used in the spectrometer for examination of the internal conversion electrons from the 13.8-hour isomeric transition.

The unconverted gamma-radiation was observed with a scintillation counter. A thallium-activated sodium iodide crystal 1 inch in diameter and 1 inch thick was used. The pulse-height distribution was

† This work was performed under the auspices of the U. S. Atomic Energy Commission.
* Permanent address: University of Illinois, Urbana, Illinois.
‡ Permanent address: Indiana University, Bloomington, Indiana.
[1] J. J. Livingood and G. T. Seaborg, Phys. Rev. **55**, 457 (1939).
[2] Kennedy, Seaborg, and Segrè, Phys. Rev. **56**, 1095 (1939).
[3] E. Bleuler and W. Zünti, Helv. Phys. Acta **19**, 375 (1946).
[4] See, *Nuclear Data*, National Bureau of Standards Circular No. 499, for a summary.
[5] L. M. Langer, Phys. Rev. **77**, 50 (1950).

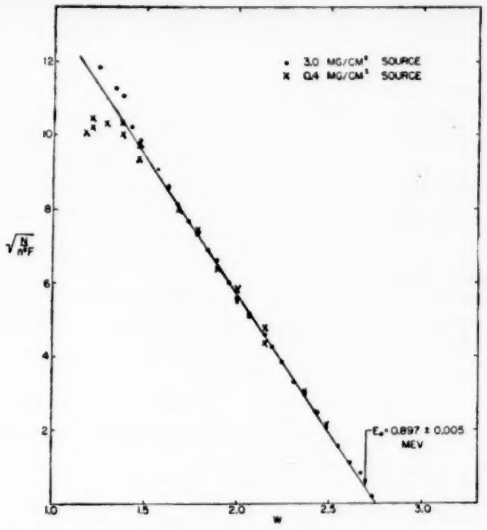

FIG. 1. Fermi plot of the 52-minute Zn^{69} beta-spectrum.

determined with a single channel differential pulse height selector.

RESULTS

52-Minute Zn^{69}

Figure 1 is a Fermi plot of the beta-spectrum of the 52-minute Zn^{69}. Data are plotted for both the 3.0-mg/cm^2 source and the 0.4-mg/cm^2 source. There is evidently only one group of electrons, and the spectrum is of the allowed form. The points for the thinner source lie on a straight line down to approximately 0.250 Mev. The end point is 0.897±0.005 Mev. The log ft is calculated to be 4.17 for this transition.

13.8-Hour Zn^{69} Isomer

An electron line was found at 0.424±0.004 Mev indicating a gamma-ray of 0.434±0.004 Mev. Comparison of the areas under the line and under the beta-spectrum from decay of the 52-minute ground state gave an internal conversion coefficient of 0.06. These data agree well with earlier measurements.[4]

Figure 2 shows the pulse-height distributions obtained in a sodium iodide crystal from the gamma-rays from the 14-hour Zn^{69}, Au^{198} and annihilation radiation from Na^{22}. These data give a gamma-ray energy for Zn^{69} of 0.436±0.004 Mev. No other gamma-rays were found.

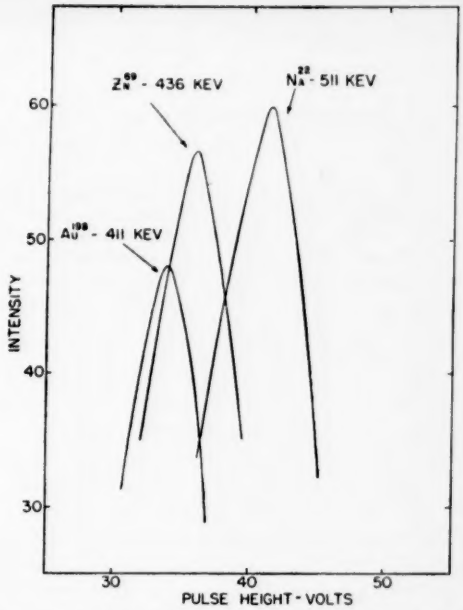

FIG. 2. Pulse-height distribution from sodium iodide scintillation counter excited by gamma-rays from 13.8-hour Zn^{69}, Au^{98}, and annihilation radiation (Na^{22}).

DISCUSSION

These data indicate that the 13.8-hour isomer of Zn^{69} decays entirely by a 0.436-Mev gamma-transition to the 52-minute ground state which then undergoes a simple beta-decay to the ground state of Ga^{69}. The ground state of Ga^{69} is known to have a spin of 3/2,[4] and the nuclear shell model would indicate that this is a $p_{3/2}$ level. Since the beta-transition is certainly allowed, the Zn^{69} ground state is probably $p_{1/2}$. Both lifetime and the conversion coefficient for this isomer indicate that the isomeric transition is an $M4$. The 13.8-hour isomeric level is therefore undoubtedly $g_{9/2}$ in agreement with the shell model predictions.

It would be of some interest to find isomeric levels in Ga^{69} and Ga^{71} so that one could see how the $p_{1/2}$ to $g_{9/2}$ level difference varies with Z in this mass region. A very brief search for these isomers following an $(n,2n)$ reaction in germanium was made but it failed to disclose any new radioactive periods.

We are indebted to B. M. Sorensen, G. W. Knobeloch, J. P. Balagna, R. Prestwood, and M. E. Bunker for the use of apparatus and for assistance with these experiments.

Deviations from *LS* Coupling in the Spheroidal Core Nuclear Model*

J. P. DAVIDSON,† *Washington University, St. Louis, Missouri*

AND

E. FEENBERG,‡ *Washington University, St. Louis, Missouri and Brookhaven National Laboratory, Upton, New York*

(Received November 4, 1952)

Deviations of measured magnetic moments from the Schmidt limits have been interpreted in terms of a failure of *LS* coupling. The model of an odd nucleon coupled to a nonspherical core provides an unforced theoretical basis for this interpretation. Projection operators for pure *LS* coupling states are introduced and applied to compute the statistical weights of the $L=I-\frac{1}{2}$ and $L'=I+\frac{1}{2}$ components in Bohr's strong coupling wave function. The orbital gyromagnetic ratio of each component is also determined.

Numerical results on the energy displacements produced by the coupling of the odd nucleon to the distorted core are generally unfavorable to the strong coupling description. A perturbation method appropriate to a weak coupling description is more likely to provide a satisfactory solution of the dynamical problem.

I. INTRODUCTION

THE theory of a nucleon moving in the field of a spherical core requires two interaction operators: $V_1(r)$, the radial potential function, and $V_2(r)\mathbf{l}\cdot\mathbf{s}$, the spin-orbit coupling potential. Some degree of arbitrariness is involved in any attempt to generalize these operators to a nonspherical core. A simple generalization, possibly inadequate, but suitable for exploratory studies, can be derived from the working hypothesis that V_1 and V_2 are functions of the particle densities $\rho_N(r)$ and $\rho_Z(r)$. To adapt this assumption to a nonspherical core, r is replaced by a new variable,

$$r'=[\lambda(x_1^2+x_2^2)+x_3^2/\lambda^2]^{\frac{1}{2}}, \tag{1a}$$

or

$$r'=r[1-\sum a_\mu^2+\sum a_\mu Y_{2\mu}(\theta'\varphi')]^{-1}, \tag{1b}$$

and the particle densities (and consequently also the potentials) are taken to be the same functions of r' as they were originally of r.

The first r' represents a spheroidal distortion of arbitrary magnitude leaving the volume of the core unchanged. The second is suitable for discussing small deviations from spherical symmetry. Here also the volume is held constant. The angles θ' and φ' are referred to a coordinate system in which the x_3 direction is a principal axis of the distorted core.[1] With this choice of polar axis $a_1=a_{-1}=0$, $a_{-2}=a_2$ and a_0, a_2 are real numbers.

Some information on the eigenvalues and solutions of the Schrödinger equation,

$$\left[-\frac{\hbar^2}{2M}\Delta+V_1(r_1)+\tfrac{1}{2}\mathbf{l}\cdot\mathbf{s}V_2(r')+\tfrac{1}{2}V_2(r')\mathbf{l}\cdot\mathbf{s}\right]\Psi=E\Psi, \tag{2}$$

can be derived from a study of the interaction operators

$${}_1H_{\rm int}=V_1(r')-V_1(r), \tag{3}$$

$${}_2H_{\rm int}=\tfrac{1}{2}[V_2(r')-V_2(r)]\mathbf{l}\cdot\mathbf{s}+\tfrac{1}{2}\mathbf{l}\cdot\mathbf{s}[V_2(r')-V_2(r)], \tag{4}$$

in the limit of small deviations from spherical symmetry. In first order

$${}_1H_{\rm int}=-r(dV_1/dr)\sum a_\mu Y_{2\mu}, \tag{5}$$

$${}_2H_{\rm int}=-\tfrac{1}{2}r(dV_2/dr)\sum a_\mu[\mathbf{l}\cdot\mathbf{s}Y_{2\mu}+Y_{2\mu}l\cdot s]. \tag{6}$$

With a rectangular potential well of constant depth D, Eq. (5) reduces to

$${}_1H_{\rm int}=-\delta(r-R)DR\sum a_\mu Y_{2\mu}, \tag{7}$$

in which R is the nuclear radius and $\delta(r-R)$ is a Dirac delta-function. This is essentially the Rainwater[2–4] interaction operator with corrections for the finite depth of the potential well and the possible absence of symmetry about the body fixed polar axis. The recent study by Bohr[1] of the coupling between the odd nucleon and the surface oscillations of the nonspherical core is based on Eq. (7) and a quadratic approximation for the potential energy of the surface oscillations

$$V_{s0}=\tfrac{1}{2}C\sum a_\mu^2, \quad C=\frac{1}{2\pi}(2E_s-E_c) \tag{8}$$

derived from the theory of nuclear fision.[5] (E_s and E_c are, respectively, surface and Coulomb energies of the spherical core.)

The approximation represented by Eq. (7) is probably adequate on the range $|a_0|<0.2$. This statement is based on explicit numerical calculations for a well of infinite depth and a range of eccentricities[6] and also on comparisons with exact solutions for two analytically simple problems (harmonic oscillator well and well of

* Assisted by the joint program of the U. S. Office of Naval Research and the U. S. Atomic Energy Commission.

† Submitted by J. P. Davidson in partial fulfillment of the requirements for the degree of Doctor of Philosophy at Washington University, St. Louis, Missouri. Now at Pupin Physics Laboratory, Columbia University.

‡ Visiting physicist at Brookhaven National Laboratory, summer, 1952, and visiting lecturer at Princeton University, 1952–1953.

[1] A. Bohr, Kgl. Danske Videnskab. Selskab, Mat.-fys. Medd. **26**, No. 14 (1952).

[2] J. Rainwater, Phys. Rev. **79**, 432 (1950).

[3] E. Feenberg and K. C. Hammack, Phys. Rev. **81**, 285 (1951).

[4] S. Gallone and C. Salvetti, Phys. Rev. **84**, 1064 (1951).

[5] N. Bohr and J. A. Wheeler, Phys. Rev. **56**, 426 (1939).

[6] J. A. Wheeler and D. L. Hill (to be published).

infinite depth in a rectangular region). The present study shows that Eqs. (7) and (8) generally determine deviations from the spherical shape approaching the indicated limits of validity. In some applications a_0 is not small compared to 1, and the theory clearly breaks down. Nevertheless, some interesting conclusions can be derived from the theory based on Eqs. (7) and (8). The need for a critical approach to the theory is indicated by recent work[7] on the quadrupole moment of O^{17}.

The possibilities for the exact solution of Eq. (2) are illustrated by the example of a nonisotropic harmonic oscillator (omitting the spin-orbit interaction):

$$H=-(\hbar^2/2M)\Delta+\tfrac{1}{2}M\omega^2[\lambda(x_1^2+x_2^2)+x_3^2/\lambda^2].$$

The eigenvalues are

$$E=\hbar\omega[\lambda^{\frac{1}{2}}(n_1+n_2+1)+(n_3+\tfrac{1}{2})\lambda], \tag{9}$$

in which the quantum numbers n_1, n_2, n_3 take on all integral values including zero. Minimum energy occurs for

$$\lambda=\left(\frac{2n_3+1}{n_1+n_2+1}\right)^{\frac{1}{2}}. \tag{10}$$

Equations (9) and (10) yield

$$E=\tfrac{3}{2}\hbar\omega(2n_3+1)^{\frac{1}{2}}(n_1+n_2+1)^{\frac{1}{2}}. \tag{11}$$

Numerical results are shown in Table I. The inclusion of the surface energy in the calculation would give qualitatively similar results with somewhat smaller deviations from spherical symmetry and smaller energy displacements.

Of particular interest is the low state in the $n_1+n_2+n_3=2$ function space. This state has $m_l=0$ and, for small deviations from spherical symmetry, contains $l=0$ with statistical weight $\frac{1}{3}$ and $l=2$ with statistical weight $\frac{2}{3}$.

Another example possessing a simple exact solution has a well of infinite depth in a rectangular region with dimensions $L_1=L_2=L/\lambda^{\frac{1}{2}}$, $L_3=\lambda L$. The energy eigenvalue is

$$E=(\hbar^2\pi^2/2ML^2)[\lambda(n_1^2+n_2^2)+n_3^2/\lambda^2],$$

in which the quantum numbers n_1, n_2, n_3 take on all integral values excluding zero.

II. INTERPRETATION OF DEVIATIONS FROM THE SCHMIDT LIMITS

The nuclides $_{15}P_{16}$, $_{48}Cd_{63,65}$, $_{50}Sn_{65,67,69}$, and $_{81}Tl_{122,124}$ have $I=\frac{1}{2}$ and magnetic moments far removed from the Schmidt single particle limits. This group is assigned even parity by the shell model. Other groups with moments departing considerably from the appropriate Schmidt limits occur at $I=\frac{3}{2}$ (odd) and $I=5/2$ (even); $_{33}As_{42}$ is an extreme example in the first category and $_{53}I_{74}$ in the second.

[7] Geschwind, Gunther-Mohr, and Silvey, Phys. Rev. **85**, 474 (1952).

TABLE I. Nonisotropic harmonic oscillator.

n_1	n_2	n_3	m_l	$l(\lambda=1)$	λ	$\epsilon/\hbar\omega$
0	0	0	0	0	1	3/2
1	0	0	±1	1	0.630	2.38
0	1	0		1	0.630	2.38
0	0	1	0	1	2.08	2.16
2	0	0	±2, 0	2 and 0	0.463	3.12
0	2	0				
1	1	0				
1	0	1	±1	2	1.310	3.435
0	1	1				
0	0	2	0	0 and 2	2.93	2.565

These groups present no difficulties from the viewpoint of an extreme single particle model if it is supposed that the effective magnetic moment of the odd nucleon when bound to the core is substantially reduced from the free nucleon values.[8-10] However, as emphasized in recent publications,[11,12] the existence of many closed (±1) shell nuclides with magnetic moments close to the appropriate Schmidt limits[13] is difficult to reconcile with a large systematic modification in the magnetic properties of the bound nucleon.

An alternative working hypothesis puts the major share of the responsibility for the deviations from the Schmidt limits on the failure of LS coupling within the bounds of a pure doublet description.[11,14] The ground state is represented by a linear combination of pure LS coupling components, one with $L=I-\frac{1}{2}$ and the other with $L'=I+\frac{1}{2}$, both components having the same parity:

$$\Psi_M{}^I=\alpha\Psi_M{}^{LI}+(1-\alpha^2)^{\frac{1}{2}}\Psi_M{}^{L'I}. \tag{12}$$

The model of an odd nucleon coupled to a nonspherical core provides an unforced theoretical basis for the failure of LS coupling. Bohr[1] has shown that this model is the dynamical equivalent of Rainwater's[2] spheroidal core considerations. In the present study we investigate the conditions under which the model is likely to produce an extreme failure of LS coupling after first determining the extent to which LS coupling fails when j is treated as a constant of motion.

III. MAGNETIC MOMENTS WHEN j IS A GOOD QUANTUM NUMBER

We consider the case of strong spin-orbit interaction and close coupling between the orbital motion of the odd nucleon and the motion of the deformed core.

[8] F. Bloch, Phys. Rev. **83**, 839 (1951).
[9] H. Mujazawa, Prog. Theoret. Phys. **6**, 263, 801 (1951).
[10] A. de Shalit, Helv. Phys. Acta **24**, 296 (1951).
[11] J. P. Davidson, Phys. Rev. **85**, 432 (1952).
[12] E. Feenberg, Ann. Rev. Nuc. Sci. **I**, 43 (1952).
[13] C^{13}, N^{15}, O^{17}, F^{19}, K^{41}, Y^{89}, and Pb^{207} are mentioned in reference 11. The list should include $_{56}Ba_{81}$, and $_{79}Au_{118}$ (closed $d_{\frac{3}{2}}$ shell at $Z=80$ followed by $s_{\frac{1}{2}}$ shell closing at 82). The magnitude and sign of the quadrupole moment of $_{79}Au_{118}$ [W. von Siemens, Naturwiss. **38**, 455 (1951)] support the single particle interpretation.
[14] G. L. Trigg, Phys. Rev. **86**, 506 (1952).

TABLE II. Magnetic moments for nucleon states with a definite value of j.

l	j	I	Odd proton μ_j	Odd proton $\mu_{cj;I}$	Odd neutron μ_j	Odd neutron $\mu_{cj;I}$
0	1/2	1/2	2.79	2.79	−1.91	−1.91
1	3/2	3/2	3.79	2.52	−1.91	−0.90
2	5/2	5/2	4.79	3.71	−1.91	−1.07
3	7/2	7/2	5.79	4.82	−1.91	−1.17
4	9/2	9/2	6.79	5.89	−1.91	−1.23
1	1/2	1/2	−0.27	−0.27	0.63	0.63
2	3/2	3/2	0.12	0.31	1.14	0.93
3	5/2	5/2	0.87	0.91	1.37	1.27
4	7/2	7/2	1.71	1.65	1.47	1.46
5	9/2	9/2	2.62	2.46	1.56	1.60
2	3/2	1/2	0.12	0.37	1.14	0.03
3	5/2	3/2	0.87	0.56	1.37	0.74
4	7/2	5/2	1.71	1.16	1.47	1.04
5	9/2	7/2	2.62	1.90	1.56	1.25
1	3/2	1/2	3.79	−0.86	−1.91	1.05
2	5/2	3/2	4.79	1.96	−1.91	−0.45
3	7/2	5/2	5.79	3.24	−1.91	−0.68
4	9/2	7/2	6.79	4.42	−1.91	−0.84
5	11/2	9/2	7.79	5.53	−1.91	−0.95

Under these conditions there exist solutions for which the angular momentum components I_3 and j_3 are approximately constants of motion. The product function,

$$\Psi_M{}^I=\varphi[\chi_I{}^i D_{MI}{}^I+(-1)^{I-j}\chi_{-I}{}^i D_{M,-I}{}^I], \quad (13)$$

is a close approximation to such a solution.[1] Here $\chi_{\pm I}{}^i$ is a normalized nucleon wave function with $j_3=\pm I$, $D_{M,\pm I}{}^I$ describes a state of a symmetrical top with total angular momentum I, $I_3=\pm I$, $I_z=M$, and φ embodies the zero-point fluctuations of the surface waves.

The detailed numerical evaluation of the energy matrix in the space of the strong coupling wave functions indicates that strong coupling is an extreme case rather far removed from the actual situation. Nevertheless, the simplicity of the strong coupling model is sufficient justification for a careful examination of all its consequences.[15]

Consider first a nucleon state with a definite value of j. The magnetic moment operator of the compound system has the form

$$\begin{aligned}\mu_{cj}&=g_j\mathbf{j}+g_c(\mathbf{I}-\mathbf{j})\\&=(g_j-g_c)\mathbf{j}+g_c\mathbf{I},\end{aligned} \quad (14)$$

in which $\mu_j=g_j j$ is the magnetic moment of the odd nucleon on a spherical core and $g_c\sim Z/A$ is the gyromagnetic ratio of the core.[16] The magnetic moment computed from Eq. (14) is

$$\mu_{cj;I}=g_c I+(g_j-g_c)\frac{(IM|\mathbf{I}\cdot\mathbf{j}|IM)}{I+1}, \quad (15)$$

in which $(IM|\mathbf{I}\cdot\mathbf{j}|IM)$ is the diagonal matrix element of $\mathbf{I}\cdot\mathbf{j}$ with respect to the wave function of Eq. (13). Straightforward calculations yield

$$\begin{aligned}&I_3 j_3\Psi_M{}^I=I^2\Psi_M{}^I,\\&(I_1 j_1+I_2 j_2)\Psi_M{}^I=\tfrac{1}{2}[2I(j-I+1)(j+I)]^{\frac{1}{2}}\varphi\\&\qquad\cdot[\chi_{I-1}D^I{}_{M,I-1}+(-1)^{I-j}\chi_{-I+1}D^I{}_{M,-I+1}].\end{aligned} \quad (16)$$

In deriving Eq. (16) it must be remembered that the components of $\mathbf{I}$ and $\mathbf{j}$ with respect to the principal axes of the core commute and also that $\mathbf{j}\times\mathbf{j}=i\mathbf{j}$, the normal commutation relations, for both space and body fixed axes, but $\mathbf{I}\times\mathbf{I}=-i\mathbf{I}$ for body fixed axes. Equation (16) implies

$$\begin{aligned}(IM|\mathbf{I}\cdot\mathbf{j}|IM)&=I^2, \quad I>\tfrac{1}{2},\\&=\tfrac{1}{4}[1+(-1)^{I-j}(2j+1)], \quad I=\tfrac{1}{2},\end{aligned} \quad (17)$$

and, consequently,

$$\mu_{cj;I}=\frac{I}{I+1}[g_j I+g_c], \quad I>\tfrac{1}{2}, \quad (18)$$

$$\mu_{cj;\frac{1}{2}}=\tfrac{1}{6}[3g_c+(g_j-g_c)\{1+(-1)^{I-j}(2j+1)\}]. \quad (19)$$

In particular,

$$\mu_{c\frac{1}{2};\frac{1}{2}}=\mu_{\frac{1}{2}}, \quad \mu_{c\frac{3}{2};\frac{1}{2}}=g_c-\tfrac{1}{3}\mu_{\frac{1}{2}}. \quad (20)$$

Equation (18) with $I=j$ is not new,[17] but the important restriction to $I>\frac{1}{2}$ has not been observed in previous applications. Numerical results are listed in Table II.

Excellent agreement of $\mu_{cI;I}$ with the general trend of the experimental moments is found[17] for $I=l+\frac{1}{2}>\frac{1}{2}$. Two examples of extreme departure from the appropriate Schmidt limits may be interpreted in terms of a failure of l and j as good quantum numbers; the moment of ${}_{33}A_{42}$ suggests approximately equal parts of $\mu_{c\frac{3}{2};\frac{1}{2}}$ and $\mu_{c\frac{1}{2};\frac{1}{2}}$ (odd parity) while that of ${}_{53}I_{74}$ can be fitted with two-thirds $\mu_{c\frac{3}{2};\frac{1}{2}}$ and one-third $\mu_{c7/2;\frac{1}{2}}$ (even parity). Close coupling of $f_{\frac{7}{2}}$ and $p_{\frac{3}{2}}$ orbitals through the mediation of the distorted core is a reasonable possibility on the range $29\leqq Z\leqq 38$; similarly an example showing close coupling between $g_{7/2}$ and $d_{\frac{5}{2}}$ is not unexpected on the range $51\leqq Z\leqq 58$.

For $I=l-\frac{1}{2}$, $\mu_{cI;I}$ is generally only slightly better than μ_j leaving a substantial discrepancy between the theory and the general trend of the experimental moments. The possibility of a partial decoupling of $\mathbf{l}$ and $\mathbf{s}$ must be considered here since a state with $I=j=l-\frac{1}{2}$ is coupled through the distorted core to $j'=l+\frac{1}{2}$. One needs the nondiagonal matrix element of the magnetic moment operator

$$\begin{aligned}&(l-\tfrac{1}{2},l-\tfrac{1}{2}|g_s s_3+g_l l_3|l+\tfrac{1}{2},l-\tfrac{1}{2})\\&\quad=(g_s-g_l)(2l)^{\frac{1}{2}}/(2l+1)\\&\quad=4.58(2l)^{\frac{1}{2}}/(2l+1), \text{ odd } Z\\&\quad=-3.82(2l)^{\frac{1}{2}}/(2l+1), \text{ odd } N.\end{aligned} \quad (21)$$

[15] We are indebted to Dr. N. Kroll and Dr. L. Foldy for valuable discussions on the subject of the strong coupling approximation.

[16] H. Margenau and E. P. Wigner, Phys. Rev. **58**, 103 (1939).

[17] A. Bohr, Phys. Rev. **81**, 134 (1951); all the B curves in Figs. 1 and 2 of this reference should coincide with the A curves at $I=\frac{1}{2}$.

If now

$$\Psi_I=(1-\beta^2)^{\frac{1}{2}}\Psi_{cI;I}+\beta\Psi_{cI+1;I}, \tag{22}$$

the correction to the magnetic moment is

$$\mu_I-\mu_{cI;I}\sim\beta(g_s-g_l)(2I+1)^{\frac{1}{2}}/(I+1) \tag{23}$$

for $\beta^2\ll 1$. Rather small values of β^2 are able to account for most of the observed deviations. Thus, at $I=7/2$ and odd Z a correction of 0.8 nuclear magneton requires $\beta^2\sim 0.06$. Both odd N and odd Z require negligible corrections at $I=\frac{1}{2}$ and $\frac{3}{2}$ and the positive sign for β at $I>\frac{3}{2}$.

The remaining important special case is $I=\frac{1}{2}$ (even parity). Here the coupling between $^2s_{\frac{1}{2}}$ and $^2d_{\frac{1}{2}}$ through the distorted core provides a possible explanation of magnetic moments far removed from the $^2s_{\frac{1}{2}}$ Schmidt limit. The calculations are described in a later section.

IV. RESOLUTION INTO *LS* COUPLING COMPONENTS WHEN j IS A GOOD QUANTUM NUMBER

We return to the strong coupling wave function of Eq. (13) under the restriction that l and j are good quantum numbers. The resolution of $\Psi_M{}^I$ into *LS* coupling components is accomplished by the introduction of projection operators

$$\begin{aligned} P_{ljI}{}^{I\pm\frac{1}{2}}&=0, \quad L=I\mp\tfrac{1}{2}\\ &=1, \quad L=I\pm\tfrac{1}{2}. \end{aligned} \tag{24}$$

Explicitly,

$$\begin{aligned} P_{ljI}{}^{I+\frac{1}{2}}&=[(\mathbf{I}-\mathbf{S})^2-(I-\tfrac{1}{2})(I+\tfrac{1}{2})]/(2I+1)\\ &=(I+1-2\mathbf{I}\cdot\mathbf{S})/(2I+1), \end{aligned} \tag{25}$$

$$\begin{aligned} P_{ljI}{}^{I-\frac{1}{2}}&=[(I+\tfrac{1}{2})(I+\tfrac{3}{2})-(\mathbf{I}-\mathbf{S})^2]/(2I+1)\\ &=(I+2\mathbf{I}\cdot\mathbf{S})/(2I+1). \end{aligned} \tag{26}$$

These relations and Eq. (12) yield

$$\alpha^2=(IM|\,P_{ljI}{}^{I-\frac{1}{2}}|\,IM), \tag{27}$$

independent of M.

In the body fixed reference frame, the components of $\mathbf{I}$ and $\mathbf{S}$ commute; this fact and the relations $\mathbf{I}\times\mathbf{I}=-i\mathbf{I}$ and $\mathbf{S}\times\mathbf{S}=i\mathbf{S}$ yield

$$4\mathbf{I}\cdot\mathbf{S}\mathbf{I}\cdot\mathbf{S}=I(I+1)-2\mathbf{I}\cdot\mathbf{S}, \tag{28}$$

in agreement with the idempotence property of the projection operators.

The substitution

$$\begin{aligned} \mathbf{I}\cdot\mathbf{S}&\sim(\mathbf{I}\cdot\mathbf{j})(\mathbf{j}\cdot\mathbf{S})/[j(j+1)]\\ &=(\mathbf{I}\cdot\mathbf{j})(-1)^{l+\frac{1}{2}-j}/(2l+1) \end{aligned} \tag{29}$$

leaves unchanged all matrix elements of $\mathbf{I}\cdot\mathbf{S}$ in the function space defined by $\Psi_{-I}{}^I\cdots\Psi_I{}^I$. Consequently the projection operators can be expressed in the convenient forms:

$$P_{ljI}{}^{I+\frac{1}{2}}=\frac{(I+1)(2l+1)-2\mathbf{I}\cdot\mathbf{j}(-1)^{l+\frac{1}{2}-j}}{(2I+1)(2l+1)}, \tag{30}$$

$$P_{ljI}{}^{I-\frac{1}{2}}=\frac{I(2l+1)+2\mathbf{I}\cdot\mathbf{j}(-1)^{l+\frac{1}{2}-j}}{(2I+1)(2l+1)}. \tag{31}$$

For $I=\frac{1}{2}$ the statistical weight of the $^2S_{\frac{1}{2}}$ component in $\Psi_M{}^{\frac{1}{2}}$ of Eqs. (9) and (13) is

$$\begin{aligned} \alpha^2&=\frac{2l+1+[1+(-1)^{l-\frac{1}{2}}(2j+1)](-1)^{l+\frac{1}{2}-j}}{4(2l+1)}\\ &=1, \quad l=0, \quad j=I=\tfrac{1}{2}\\ &=0, \quad l=1, \quad j=I=\tfrac{1}{2}\\ &=0.4, \quad l=2, \quad j=I+1=\tfrac{3}{2}. \end{aligned} \tag{32}$$

In the same way, the statistical weight of the *LS* coupling component with $L=I-\frac{1}{2}$ in $\Psi_M{}^I$ for $I>\frac{1}{2}$ is

$$\begin{aligned} \alpha^2&=\frac{I(2l+1)+2I^2(-1)^{l+\frac{1}{2}-j}}{(2I+1)(2l+I)}\\ &=\frac{2I}{(2I+1)}, \qquad j=l+\tfrac{1}{2}=I\\ &=\frac{I}{(I+1)(2I+1)}, \quad j=l-\tfrac{1}{2}=I. \end{aligned} \tag{33}$$

Maximum mixing occurs at $I=\frac{3}{2}$ with 75 percent $P_{\frac{1}{2}}$ and 25 percent $D_{\frac{1}{2}}$ from a nucleon in a $p_{\frac{1}{2}}$ state.

The orbital gyromagnetic ratios are quantities of interest in connection with the resolution of $\Psi_M{}^I$ into pure *LS* coupling components. To compute these quantities we start from the operator for the orbital magnetic moment:

$$\begin{aligned} \boldsymbol{\mu}_{\rm orb}&=g_l\mathbf{l}+g_c(\mathbf{I}-\mathbf{j})\\ &=(g_l-g_c)\mathbf{j}-g_l\mathbf{S}+g_c\mathbf{I}. \end{aligned} \tag{34}$$

The easily verified relations,

$$\begin{aligned} [\mathbf{j},\mathbf{I}\cdot\mathbf{S}]&=[\mathbf{S},\mathbf{I}\cdot\mathbf{S}]=[\mathbf{I},\mathbf{I}\cdot\mathbf{S}]\\ &=i\mathbf{I}\times\mathbf{S}, \end{aligned} \tag{35}$$

have the consequence that $\boldsymbol{\mu}_{\rm orb}$ commutes with $\mathbf{I}\cdot\mathbf{S}$ and therefore also with the orbital angular momentum projection operators. This property enables us to write

$$\begin{aligned} \mu_{\rm orb}{}^{I\pm\frac{1}{2}}(II|\,P_{ljI}{}^{I\pm\frac{1}{2}}|\,II)\\ =(II|\,\mathbf{I}\cdot\boldsymbol{\mu}_{\rm orb}P_{ljI}{}^{I\pm\frac{1}{2}}|\,II)/(I+1). \end{aligned} \tag{36}$$

From Eqs. (25), (26), and (34),

$$\begin{aligned} \mathbf{I}\cdot\boldsymbol{\mu}_{\rm orb}P_{ljI}{}^{I+\frac{1}{2}}&=\frac{g_l-g_c}{2I+1}[(I+1)\mathbf{I}\cdot\mathbf{j}-2\mathbf{I}\cdot\mathbf{j}\mathbf{I}\cdot\mathbf{S}]\\ &\quad+I[g_c(I+1)+\tfrac{1}{2}g_l]P_{ljI}{}^{I+\frac{1}{2}}, \end{aligned} \tag{37}$$

$$\begin{aligned} \mathbf{I}\cdot\boldsymbol{\mu}_{\rm orb}P_{ljI}{}^{I-\frac{1}{2}}&=\frac{g_l-g_c}{2I+1}[I(\mathbf{I}\cdot\mathbf{j})+2\mathbf{I}\cdot\mathbf{j}\mathbf{I}\cdot\mathbf{S}]\\ &\quad+(I+1)[g_cI-\tfrac{1}{2}g_l]P_{ljI}{}^{I-\frac{1}{2}}. \end{aligned} \tag{38}$$

Since the operator $\mathbf{I}\cdot\mathbf{j}$ does not mix the two values of j associated with the given l, the substitution

$$\mathbf{I}\cdot\mathbf{j}\mathbf{I}\cdot\mathbf{S}\sim(\mathbf{I}\cdot\mathbf{j})^2(-1)^{l+\frac{1}{2}-j}/(2l+1) \tag{39}$$

TABLE III. Values of $g_{\rm orb}{}^L$.

$I=j$	l	L	$g_{\rm orb}{}^L$ (odd Z)	$g_{\rm orb}{}^L$ (odd N)
1/2	0	0	0	0
		1	—	—
	1	0	—	—
		1	1	0
3/2	1	1	0.760	0.160
		2	0.600	0.267
	2	1	0.280	0.480
		2	0.835	0.110
5/2	2	2	0.829	0.114
		3	0.700	0.200
	3	2	0.571	0.286
		3	0.870	0.086
7/2	3	3	0.867	0.089
		4	0.760	0.160
	4	3	0.689	0.208
		4	0.893	0.071
9/2	4	4	0.891	0.073
		5	0.800	0.133
	5	4	0.755	0.164
		5	0.909	0.061

is permitted in Eqs. (37) and (38). Equations (16) and (17) suggest the procedure followed in computing the diagonal matrix elements of $(\mathbf{I}\cdot\mathbf{j})^2$; these are found to have the values

$$\begin{aligned}&(\tfrac{1}{2}\tfrac{1}{2}|(\mathbf{I}\cdot\mathbf{j})^2|\tfrac{1}{2}\tfrac{1}{2})=\tfrac{1}{16}[1+(-1)^{I-j}(2j+1)]^2,\\&(II|(\mathbf{I}\cdot\mathbf{j})^2|II)=I^2(I^2+1),\quad I=j>\tfrac{1}{2}.\end{aligned}\tag{40}$$

Orbital gyromagnetic ratios g_L for the odd nucleon-distorted core system are defined by the equations

$$\begin{aligned}&\mu_{\rm orb}{}^{I-\frac{1}{2}}=(I-\tfrac{1}{2})g_{\rm orb}{}^{I-\frac{1}{2}},\quad L=I-\tfrac{1}{2};\\&\mu_{\rm orb}{}^{I+\frac{1}{2}}=\frac{I(I+\frac{3}{2})}{I+1}g_{\rm orb}{}^{I+\frac{1}{2}},\quad L=I+\tfrac{1}{2}.\end{aligned}\tag{41}$$

For $I=j=\frac{1}{2}$ and $l=0$, both left- and right-hand members of Eq. (36) vanish. In this case no calculations are needed to establish the absence of an orbital contribution to the magnetic moment. A more interesting check is supplied by $I=j=\frac{1}{2}$, $l=1$ (a pure $^2P_{\frac{1}{2}}$ state). Now

$$\mu_{\rm orb}{}^{I+\frac{1}{2}}=\tfrac{2}{3}g_l\quad\text{and}\quad g_{\rm orb}{}^{I+\frac{1}{2}}=g_l,\tag{42}$$

in agreement with expectations.

General formulas for g_L are listed below

j	L	$g_{\rm orb}{}^L$
$l+\frac{1}{2}$	l	$g_l+(g_c-g_l)/(I+1)$
$l+\frac{1}{2}$	$l+1$	$g_l+2(g_c-g_l)/(I+\frac{3}{2})$
$l-\frac{1}{2}$	l	$g_l+(g_c-g_l)(2I^2+I+1)/(I+\frac{3}{2})(2I^2+2I+1)$
$l-\frac{1}{2}$	$l-1$	$g_l+(g_c-g_l)2I/(I+1)(I-\frac{1}{2})$.

(43)

These formulas with $g_l=1$ (odd proton), $g_l=0$ (odd neutron), and $g_c=0.4$ are used to compute the values of $g_{\rm orb}{}^L$ listed in Table III.

There is little resemblance between these numerical results for $g_{\rm orb}{}^L$ and the values postulated in the $S-MW$ interpolation procedure employed by Trigg[14] and Davidson.[11] Possibly these differences reveal the crudeness of the $S-MW$ interpolation procedure; however, the inadequacy of the distorted core model in regard to magnetic moments for $I=j=l-\frac{1}{2}$ suggests that judgement should be reserved on this question.

Equations (33) and (43) can be used for a simple alternative derivation of the magnetic moment formula of Eq. (18). This procedure is useful in providing a partial check on the formulas for α^2 and $g_{\rm orb}{}^L$.

V. MATRIX ELEMENTS OF $_1H_{\rm int}$

We compute matrix elements of $_1H_{\rm int}$ in the linear approximation of Eq. (7). In the jm_j representation with the axis of quantization along the symmetry axis of the core the diagonal matrix elements are[1]

$$(jm_j|{}_1H_{\rm int}|jm_j)=k_{nl}\left(\frac{5}{4\pi}\right)^{\frac{1}{2}}a_0\frac{3m_j^2-j(j+1)}{4j(j+1)},\tag{44}$$

in which

$$k_{nl}=DR^3R_{nl}{}^2(R),\tag{45}$$

and R_{nl} is the radial function of the state occupied by the odd nucleon. Since this matrix element vanishes at $j=\frac{1}{2}$, there is no direct coupling between a nucleon in a $p_{\frac{1}{2}}$ or $s_{\frac{1}{2}}$ orbital and the surface oscillations of the core.

For each value of $|m_j|$ there exists a low state of the compound system with total angular momentum $I=|m_j|$. The ground state is associated with maximum absolute value of $(jm_j|{}_1H_{\rm int}|jm_j)$, i.e., with

$$(j,\pm j|{}_1H_{\rm int}|j,\pm j)=k_{nl}\left(\frac{5}{4\pi}\right)^{\frac{1}{2}}a_0\frac{2j-1}{4(j+1)},\tag{46}$$

and $I=j$; the next largest absolute value of the matrix element occurs at $I=|m_j|=\frac{1}{2}$ with

$$(j,\pm\tfrac{1}{2}|{}_1H_{\rm int}|j,\pm\tfrac{1}{2})=-k_{nl}\left(\frac{5}{4\pi}\right)^{\frac{1}{2}}a_0\frac{(2j-1)(2j+3)}{16j(j+1)}.\tag{47}$$

One exception must be noted; at $j=\frac{3}{2}$ the absolute value of the matrix element is independent of m_j,

$$\begin{aligned}&(\tfrac{3}{2},\pm\tfrac{3}{2}|{}_1H_{\rm int}|\tfrac{3}{2},\pm\tfrac{3}{2})=k_{nl}\frac{1}{5}\left(\frac{5}{4\pi}\right)^{\frac{1}{2}}a_0,\\&(\tfrac{3}{2},\pm\tfrac{3}{2}|{}_1H_{\rm int}|\tfrac{3}{2},\pm\tfrac{1}{2})=-k_{nl}\frac{1}{5}\left(\frac{5}{4\pi}\right)^{\frac{1}{2}}a_0.\end{aligned}\tag{48}$$

In this case the dynamical theory of the coupling between the odd nucleon and the surface oscillations should yield two closely spaced low levels, one with $I=\frac{3}{2}$ and the other with $I=\frac{1}{2}$, both having the same parity as the odd nucleon state.

Equation (2) clearly implies that l and j are not exact quantum numbers. A number of nondiagonal matrix elements are actually quite large, large enough in some cases to invalidate the usual implicit assumption that l and j are good approximate constants of motion. Elementary calculations yield the following results:

$$({}^2X_{l+\frac{1}{2},\,l-\frac{1}{2}}|\,{}_1H_{\rm int}|\,{}^2X_{l-\frac{1}{2},\,l-\frac{1}{2}}) = -ka_0 3\left(\frac{5}{4\pi}\right)^{\frac{1}{2}}\frac{(2l)^{\frac{1}{2}}}{(2l+1)(2l+3)}, \quad (49)$$

connecting two states with the same l; and

$$({}^2X_{l+\frac{1}{2},\,l+\frac{1}{2}}|\,{}_1H_{\rm int}|\,{}^2X_{l'-\frac{1}{2},\,l+\frac{1}{2}}) = -k'a_0 3\left(\frac{5}{4\pi}\right)^{\frac{1}{2}}\frac{2^{\frac{1}{2}}(l+1)^{\frac{1}{2}}}{(2l+3)(2l+5)}, \quad (50)$$

$$({}^2X_{l+\frac{1}{2},\,l+\frac{1}{2}}|\,{}_1H_{\rm int}|\,{}^2X_{l'+\frac{1}{2},\,l+\frac{1}{2}}) = -k'a_0 3\left(\frac{5}{4\pi}\right)^{\frac{1}{2}}\frac{(l+1)^{\frac{1}{2}}}{(2l+3)^{\frac{1}{2}}(2l+5)}, \quad (51)$$

connecting l and $l'=l+2$. Reversing the sign of $m_I=l\pm\frac{1}{2}$ multiplies the matrix element by the factor $(-1)^{l-l'}$. Here k' denotes the geometric mean of the k's associated with the nl and $n'l'$ states. Extensive calculations[18] of particle densities in oscillator potentials and rectangular wells show that k' and k generally differ by less than 20 percent. In the following we ignore the difference and replace k' by k.

Special cases under Eq. (50) of particular interest are

$$\begin{aligned}
({}^2s_{\frac{1}{2}},\,\pm\tfrac{1}{2}|\,{}_1H_{\rm int}|\,{}^2d_{\frac{1}{2}},\,\pm\tfrac{1}{2}) &= \mp k'a_0/(10\pi)^{\frac{1}{2}},\\
({}^2p_{\frac{3}{2}},\,\pm\tfrac{3}{2}|\,{}_1H_{\rm int}|\,{}^2f_{\frac{5}{2}},\,\pm\tfrac{3}{2}) &= \mp k'a_0 3/7(5\pi)^{\frac{1}{2}},\\
({}^2d_{\frac{5}{2}},\,\pm 5/2|\,{}_1H_{\rm int}|\,{}^2g_{7/2},\,\pm 5/2) &= \mp k'a_0\frac{1}{5}\left(\frac{5}{6\pi}\right)^{\frac{1}{2}}.
\end{aligned} \quad (52)$$

Comparing Eqs. (48) and (52) one sees that the coupling energy between ${}^2s_{\frac{1}{2}}$ and ${}^2d_{\frac{1}{2}}$ through the mediation of the distorted core is indeed quite large; in fact, larger by a factor $2^{\frac{1}{2}}$ than the diagonal matrix elements of $H_{\rm int}$ for the ${}^2d_{\frac{3}{2}}$ state.

VI. COUPLING OF ${}^2s_{\frac{1}{2}}$ AND ${}^2d_{\frac{3}{2}}$ NUCLEON STATES

Consider the group of nuclides with $I=\frac{1}{2}$ and even parity. Experimental evidence locating a state with $I=\frac{3}{2}$ and even parity close to the ground state exists for many of these; for the others the existence of such a low-lying level can be inferred from the shell model. We write

$$\chi_{\pm\frac{1}{2}} = \beta\chi({}^2s_{\frac{1}{2}},\,\pm\tfrac{1}{2}) \pm (1-\beta^2)^{\frac{1}{2}}\chi({}^2d_{\frac{3}{2}},\,\pm\tfrac{1}{2}) \quad (53)$$

in the static approximation for the core, and proceed to compute the energy and the amplitude β from the relations§

$$\begin{aligned}
&\beta[E-\tfrac{1}{2}CA_0^2]+(1-\beta^2)^{\frac{1}{2}}ka_0/(10\pi)^{\frac{1}{2}}=0,\\
&\beta ka_0/(10\pi)^{\frac{1}{2}}+(1-\beta^2)^{\frac{1}{2}}[E-\Delta E+ka_0/(20\pi)^{\frac{1}{2}}\\
&\qquad\qquad -\tfrac{1}{2}Ca_0^2]=0.
\end{aligned} \quad (54)$$

Here ΔE denotes the excitation energy of $d_{\frac{1}{2}}$ relative to $s_{\frac{1}{2}}$ when the core is spherical; negative ΔE means $d_{\frac{1}{2}}$ below $s_{\frac{1}{2}}$.

With the notation

$$\Delta E = nk^2/20\pi C, \quad y=(20\pi)^{\frac{1}{2}}Ca_0/k, \quad (55)$$

the lower of the two eigenvalues determined by Eq. (54) is given by the formula

$$E20\pi C/k^2 = \tfrac{1}{2}[n-y+y^2-\{8y^2+(n-y)^2\}^{\frac{1}{2}}]. \quad (56)$$

The detailed analysis of Eq. (56) yields the result that $\beta^2/(1-\beta^2)$ lies between 2.0 and 0.5 and y between 1.67 and 2.00 on the range $0\leqq n\leqq 3.33$. The corresponding values of μ range from $\frac{2}{3}$ to $\frac{1}{3}$ (approximately) of the Schmidt value.

VII. ROTATIONAL AND ZERO-POINT ENERGIES

Equation (54) represents a static approximation in which the rotational kinetic energy and the zero point vibrational energies are neglected. Bohr's equations (50) and (98) in reference 1 yield the following operator for the rotational kinetic energy:

$$T_{\rm rot} = \frac{\hbar^2}{6Ba_0^2}[I(I+1)+j(j+1)-I_3^2-j_3^2 - 2(I_1j_1+I_2j_2)], \quad (57)$$

subject to the restriction $j_3=I_3=I$. The diagonal matrix elements of $T_{\rm rot}$ can be computed with the help of Eq. (17) and have the values

$$\begin{aligned}
&\frac{\hbar^2}{2Ba_0^2} \quad \text{for} \quad I=j=\tfrac{3}{2},\\
&\frac{\hbar^2}{Ba_0^2} \quad \text{for} \quad I=\tfrac{1}{2}, \quad j=\tfrac{3}{2}.
\end{aligned} \quad (58)$$

Here $B=\frac{1}{2}\rho_0 R^5$, ρ_0 denoting the mean density of nuclear matter. In the absence of coupling to a ${}^2s_{\frac{1}{2}}$ state the energies are given by the minimum values of

$$\begin{aligned}
(20\pi C/k^2)E_{c\frac{3}{2};\frac{1}{2}} &= y+\tfrac{1}{2}y^2+\Gamma/2y^2,\\
(20\pi C/k^2)E_{c\frac{1}{2};\frac{1}{2}} &= -y+\tfrac{1}{2}y^2+\Gamma/y^2,
\end{aligned} \quad (59)$$

with

$$\Gamma = \frac{(20\pi\hbar)^2}{B}\frac{C^3}{k^4}. \quad (60)$$

[18] K. C. Hammack, Doctor's thesis, Washington University (1951) (unpublished).

§ We are indebted to Dr. A. Bohr for calling our attention to an error in a first statement of this problem.

TABLE IV. Values of the physical parameters.

A	C^*	k^*	$k^2/20\pi C^*$	$k/(20\pi)^{\frac{1}{2}}C$	Γ	$\hbar^2/B^*$
31	41.5	40	0.613	0.123	53	0.50
203	63.8	40	0.400	0.080	9.0	0.023

* Energy in Mev units.

Numerical values of the physical parameters are listed in Table IV.

Equation (59) is a special case of the general form

$$(20\pi C/k^2)E_{cj;I}=-\eta y+\tfrac{1}{2}y^2+\eta'\Gamma/2y^2 \qquad (61)$$

in which η and η' are constants determined by j and I. In the extreme case of $\eta'\Gamma\gg1$ the minimum value of $E_{cj;I}$ occurs near

$$\begin{aligned} y&=\tfrac{1}{4}\eta+(\eta'\Gamma)^{\frac{1}{4}}, \quad \eta>0,\\ &=\tfrac{1}{4}\eta-(\eta'\Gamma)^{\frac{1}{4}}, \quad \eta<0, \end{aligned} \qquad (62)$$

and has the value

$$\frac{20\pi C}{k^2}E_{cj;I}=(\eta'\Gamma)^{\frac{1}{2}}-|\eta|(\eta'\Gamma)^{\frac{1}{4}}-\tfrac{1}{8}\eta^2+\cdots. \qquad (63)$$

Equation (62) yields $a_0\cong-0.16$ for $I=j=\frac{3}{2}$, $A=203$. The zero point energies E_β and E_γ of the distorted core [Bohr's equations (108) and (113)] are given by

$$\begin{aligned}(20\pi C/k^2)E_\beta&=2\Gamma/y^2+\tfrac{1}{2}(\Gamma p/C)^{\frac{1}{2}}\\ &=\Gamma^{\frac{1}{2}}\left[1+\frac{2}{\eta'^{\frac{1}{4}}}-\left(\frac{3}{8}+\frac{1}{\eta'^{\frac{1}{4}}}\right)\frac{|y|}{(\eta'\Gamma)^{\frac{1}{4}}}\right.\\ &\quad\left.+\left(\frac{3}{8\eta'^{\frac{1}{2}}}+\frac{21}{128}\right)\frac{\eta^2}{(\eta'\Gamma)^{\frac{1}{2}}}+\cdots\right], \end{aligned} \qquad (64)$$

$$\begin{aligned}(20\pi C/k^2)E_\gamma&=(2\eta')^{\frac{1}{2}}\Gamma/y^2[1+|\eta y^3|/2\eta'\Gamma]^{\frac{1}{2}}\\ &=(2\Gamma)^{\frac{1}{2}}[1-|\eta|/4(\eta'\Gamma)^{\frac{1}{4}}\\ &\quad+(\tfrac{3}{16}-7\eta^2/64)/(\eta'\Gamma)^{\frac{1}{2}}+\cdots]. \end{aligned} \qquad (65)$$

The zero-point energy of the spherical core [Bohr's equation (9)] is

$$\begin{aligned}\frac{20\pi C}{k^2}E_\omega&=\frac{20\pi C}{k^2}\frac{5}{2}\left(\frac{\hbar^2C}{B}\right)^{\frac{1}{2}}\\ &=(5/2)\Gamma^{\frac{1}{2}}. \end{aligned} \qquad (66)$$

A necessary condition for the validity of strong coupling is that the diagonal matrix elements of the energy are lowered by the introduction of the Rainwater interaction. This condition takes the form

$$E_{cj;I}+E_\beta+E_\gamma-E_\omega<0. \qquad (67)$$

It is easily seen that Eq. (67) fails for $\Gamma\gg1$ and $\eta'\Gamma\gg1$. A numerical example will make this clear. At $A=203$, $j=I=\frac{3}{2}$, $\eta=-1$, $\eta'=1$, $\Gamma=9$,

$$\begin{aligned}(20\pi C/k^2)E_{c\frac{3}{2};\frac{3}{2}}&=1.14,\\ (20\pi C/k^2)E_\beta&=7.16,\\ (20\pi C/k^2)E_\gamma&=3.74,\\ (20\pi C/k^2)E_\omega&=7.5,\end{aligned}$$

or

$$(E_{c\frac{3}{2};\frac{3}{2}}+E_\beta+E_\gamma-E_\omega)=1.8 \text{ Mev}.$$

These results show that the numerical values of the physical parameters are inconsistent with the assumption of strong coupling embodied in Eq. (13).[19] An alternative treatment employing the occupation numbers of the surface oscillation states as diagonal variables is indicated.[20]

We turn now to estimate the influence of the rotational kinetic energy on the location of the $I=\frac{1}{2}$ state when $^2s_{\frac{1}{2}}$ and $^2d_{\frac{3}{2}}$ nucleon states are coupled through the distorted core. The energy formula Eq. (56) is replaced by

$$\begin{aligned}(20\pi C/k^2)E_{\frac{1}{2}}=\tfrac{1}{2}[&n-y+y^2+\Gamma/y^2\\ &-\{8y^2+(n-y+\Gamma/y^2)^2\}^{\frac{1}{2}}]. \end{aligned} \qquad (68)$$

Numerical results appear in Table V for a particular value of $\beta/(1-\beta^2)^{\frac{1}{2}}$ corresponding to a moment approximately midway between the Schmidt limits. The example at $A=203$ shows the substantial influence of the rotational kinetic energy on the location and magnitude of the energy minimum under relatively favorable conditions for the validity of the strong coupling approximation. It appears that a perturbation method appropriate to a weak coupling description is more likely to provide a satisfactory solution of the dynamical problem, particularly for small values of the mass number.

One of the authors (JPD) wishes to thank the Central Administration of Washington University for the grant of a University Fellowship under whose tenure this work was done.

TABLE V. Coupling of $^2s_{\frac{1}{2}}$ and $^2d_{\frac{3}{2}}$, $\beta/(1-\beta^2)^{\frac{1}{2}}=1$.

A	Γ	n	y	a_0	$(20\pi C/k^2)E_{\frac{1}{2}}$
90	20.7	0.24	2.83	0.28	0.00
203	9.0	1.06	2.50	0.20	−0.41
∞	0.0	1.91	1.91	...	−0.87

[19] The strong coupling approximation appears to better advantage when two or more equivalent nucleons are coupled to the core (private communication from K. W. Ford).

[20] L. L. Foldy and F. J. Milford, Phys. Rev. **80**, 751 (1950).

APPENDIX A

We evaluate the allowed beta-decay matrix element $|\int\boldsymbol{\sigma}|^2$ for image transitions. Trigg[14] has shown that

$$|\int\boldsymbol{\sigma}|^2=[(I+1)\alpha^2-I(1-\alpha^2)]^2/[I(I+1)]. \quad \text{(A1)}$$

Introducing α^2 from Eq. (33), we get

$$\begin{aligned}|\int\boldsymbol{\sigma}|^2&=I/(I+1), \qquad I=j=l+\tfrac{1}{2}>\tfrac{1}{2},\\ &=[I/(I+1)]^2, \quad I=j=l-\tfrac{1}{2}>\tfrac{1}{2}. \end{aligned}\quad \text{(A2)}$$

Thus, the coupling to the core leaves the ratio for $l+\frac{1}{2}$ and $l-\frac{1}{2}$ unchanged relative to the values for pure *LS* coupling, but reduces both by the factor $I^2/(I+1)^2$. An alternative derivation starts from the equivalence relation,

$$\boldsymbol{\sigma}\sim\mathbf{I}\frac{2I}{I+1}\frac{(-1)^{l+\frac{1}{2}-j}}{2l+1}. \quad \text{(A3)}$$

Then

$$\left|\int\boldsymbol{\sigma}\right|^2=\frac{I^2}{I+1}\frac{1}{(l+\frac{1}{2})^2}, \quad \text{(A4)}$$

in agreement with Eq. (A2).

APPENDIX B

The diagonal matrix elements of $(\mathbf{I}-\mathbf{j})^2$ and $(\mathbf{I}-\mathbf{j})^4$ can be evaluated with the aid of Eqs. (16), (17), and (40). Results are

$$\begin{aligned}&(\tfrac{1}{2}M|(\mathbf{I}-\mathbf{j})^2|\tfrac{1}{2}M)=(j+\tfrac{1}{2})[j+\tfrac{1}{2}-(-1)^{l-\frac{1}{2}}];\\ &(IM|(\mathbf{I}-\mathbf{j})^2|IM)=2I, \quad I>\tfrac{1}{2};\\ &(IM|(\mathbf{I}-\mathbf{j})^4|IM)=2(2I)^2, \quad I>\tfrac{1}{2}.\end{aligned}$$

For $I=\frac{1}{2}$, Eq. (16) shows that $(I-j)^2$ is a constant of motion.

PHYSICAL REVIEW VOLUME 89, NUMBER 4 FEBRUARY 15, 1953

A Third Rydberg Series of N_2

R. EDWIN WORLEY
Department of Physics, University of Nevada, Reno, Nevada
(Received October 31, 1952)

A third series of Rydberg bands, converging to the $^2\Pi$ state of N_2^+, has been identified in the far ultraviolet absorption spectrum of nitrogen. Its interpretation substantiates an assignment of vibrational numbers for the $^2\Pi$ state, and indicates that this state is derived from the o state of N_2.

TWO series of Rydberg terms have previously been identified for N_2, one[1,2] converging to the $X\ ^2\Sigma$ state of N_2^+, the other[3,4] to the excited $B\ ^2\Sigma$ state. I shall refer to these as the $X-X$ and the $B-X$ series, and discuss here a third, or $A-X$, series that converges to the $A\ ^2\Pi$ state, about 1 ev above the ground state. Some years ago Professor Mulliken suggested I examine my spectrograms of the far ultraviolet absorption of N_2, with the object of identifying the corresponding bands and thus locating the $^2\Pi$ state. However, due to overlying absorption on the best plates (nitrogen pressure too high), this proved unfeasible.

The recent identification of $^2\Pi-{}^2\Sigma$ bands of N_2^+ by Meinel,[5] in auroral spectra, affords an approximate value for the limit of the anticipated Rydberg series. I have accordingly re-examined my plates, and have found five distinct bands[6] which fit the following Rydberg formula with residuals of $+1$, -2, $+2$, $+2$, -2 cm^{-1}.

$\nu_m=136\,607-R/(m-0.0441-0.018/m)^2$; $m=2$ to 6, $R=109\,735$ cm^{-1}. The bands are rather narrow, are shaded to longer wavelengths, and show but one head. Starting with the first member, intensities progressively decrease in a normal manner, the values being comparable to those of corresponding $X-X$ bands. The upper term for the first band is the $v=1$ level of state o.

Dalby and Douglas[7] have photographed the $^2\Pi-{}^2\Sigma$ bands of N_2^+ at large dispersion, using a laboratory source. From preliminary results of the analysis, kindly supplied by Dr. Douglas, the empirical series limit, above, is found to correspond to the $v=1$ level of the $^2\Pi$ state, and apparently to its upper component $^2\Pi_{\frac{1}{2}}$. The position of this component, as found by adding $\nu_{00}+\Delta G(\frac{1}{2})+\frac{1}{2}A$ to the limit of the $X-X$ Rydberg series,[2] is 136 597 cm^{-1} above the ground state of N_2. In fact, if the heads of the higher members of the $X-X$ series represent origins—that is, if they are of Q-form as is suggested by the extreme narrowness of the bands—and if a computed origin-to-head interval is added

[1] R. E. Worley and F. A. Jenkins, Phys. Rev. **54**, 305 (1938).
[2] R. E. Worley, Phys. Rev. **64**, 207 (1943).
[3] J. J. Hopfield, Phys. Rev. **36**, 789 (1930). See also Takamine, Suga, and Tanaka, Sci. Pap. Inst. Phys. Chem. Res. Tokyo **34**, 854 (1938).
[4] R. S. Mulliken, Phys. Rev. **46**, 144 (1934).
[5] A. B. Meinel, Astrophys. J. **114**, 431 (1951); **112**, 562 (1950).
[6] Most bands referred to herein are listed in Table I, reference 2. Omitted were the following (cm^{-1}): 123 995* ($m=3$); 124 069* (footnote 8). Recently measured for use in Table I herein were 122 068; 133 995; 135 361 cm^{-1}.
[7] F. W. Dalby and A. E. Douglas, Phys. Rev. **84**, 843 (1951). See also R. Herman, Compt. rend. **233**, 926 (1951); N. D. Sayers, Proc. Phys. Soc. (London) **65**, 152 (1952).

TABLE I. Values of ΔG for the Rydberg terms.

m	$\Delta G(1/2)$	$\Delta G(3/2)$
2	1962	1917
3	(1927)	...
4	...	1863
5	1886	(1860)
6	1883	(1853)
$^2\Pi(N_2^+)$	1872	1843

to the figure just given, the limit predicted for the present series is 136 609 cm^{-1}.

Professor Mulliken (private communication) points out, however, that this feature is readily explained if the upper terms of the $A-X$ absorption bands are $^1\Sigma$, as is suggested by their appearance. $^3\Sigma$ terms of the same electron configuration will then converge to $^2\Pi$, and observable transitions to these terms from $X\,^1\Sigma(N_2)$ are not expected for $m \lesssim 4$. But absorption may become discernible for higher values of m, due to the mixing of wave functions of the singlet and triplet states with change in coupling of the excited electron. Very weak, hence somewhat doubtful, heads are indeed found for $m=5$ and 6, displaced to lower wave numbers by about 110 cm^{-1} and 90 cm^{-1}, respectively. If we accept convergence of this series to $^2\Pi_{\frac{1}{2}}$, no absorption bands converging to the $^2\Pi_{\frac{3}{2}}$ component, which lies about 80 cm^{-1} below $^2\Pi_{\frac{1}{2}}$, were evident.[8]

The $B-X$ and the strongest $X-X$ absorption series of N_2 consist of bands for which $v'=0$. That the $A-X$ bands correspond to $v'=1$ is attributed to a somewhat greater internuclear distance of the excited terms of these bands, as compared to those of the other two series (Franck-Condon principle). A larger internuclear distance is clearly indicated by the low intensity of the $v'=0$ band of the $o-X$ progression. For the higher Rydberg terms, a few heads have been found that correspond to $v'=0$, and it appears that their intensities increase relative to bands with $v'=1$. (A similar trend with increase of m is seen in the $X-X$ bands.) A few possible heads are found also for $v'=2$. The corresponding $\Delta G(\frac{1}{2})$ and $\Delta G(\frac{3}{2})$ values are shown in Table I. Because of overlying diffuse absorption, some of these identifications for $v'=0$ and 2 are questionable, but the more reliable ΔG intervals show a reasonable correlation between the o term of N_2 ($m=2$) and the $^2\Pi$ term of N_2^+.

TABLE II. Data and vibrational analysis, state o of N_2.

Int.	ν_H (cm^{-1})	Vibrational constants (from band heads)
1	105 694.5	$\omega_e = 2020.00 \pm 0.07$ cm^{-1}
6	7657.0	$\omega_e x_e = 32.28 \pm 0.03$ cm^{-1}
5	9574.4	$\omega_e y_e = 2.167 \pm 0.004$ cm^{-1}
3	111 459.8	
$\frac{1}{2}$	3326.1	

In conclusion, this assignment and identification of bands in the absorption spectrum confirms the vibrational numbering for the $^2\Pi$ state of N_2^+ as proposed by Dalby and Douglas,[7] and by Meinel.[5] It also identifies the o state of N_2 as the parent term from which $^2\Pi$ is derived by removal of an electron. Table II lists the intensities and wave numbers of the $o-X$ absorption bands,[9] and gives the vibrational constants of state o, as derived from these data by a least-squares solution.[10]

[8] An alternative interpretation of these details is suggested by the presence of second heads lying 74 cm^{-1} and 70 cm^{-1}, respectively, to *shorter* wavelengths from the bands for $m=3$ and 4. May not the observed series converge to $^2\Pi_{\frac{1}{2}}$, while these other bands converge to $^2\Pi_{\frac{1}{2}}$? The bands for $m=5$ and 6 are unobscured, but no double heads are found here; nor is there a second head for $m=2$ (state o).

[9] The weak head for $v'=4$ is not listed in reference 2, as it was incorrectly attributed to a rotational perturbation in an overlying band. (In Table II, the v' values run from 0 to 4.)

[10] R. T. Birge and J. W. Weinberg, Revs. Modern Phys. **19**, 298 (1947).

Measurement of Magnetostriction in Single Crystals

R. M. Bozorth and R. W. Hamming
Bell Telephone Laboratories, Murray Hill, New Jersey

(Received October 30, 1952)

A simplified procedure is given for determining the 5 magnetostriction constants of a single crystal of a ferromagnetic cubic crystal. The crystal is cut as a disk parallel to a (110) plane, and strain gauges are cemented to the surfaces to measure strains in [001] and [1$\bar{1}$1] directions. A magnetic field sufficient for saturation is oriented in 10° steps at various angles to the [001] direction, and magnetostriction is measured over a 90° range for each gauge. Each of the 18 data is then multiplied by suitable numbers, obtained by inversion of the strain matrix, to give the constants $h_1 \cdots h_5$. The method is applied to a crystal of a 78 percent nickel-iron alloy to determine the magnetostriction associated with spontaneous magnetization in the [111] direction: $\lambda_{111}=2h_2/3+2h_5/9$, a quantity important in the "Permalloy problem." The constants are also determined for a single crystal of nickel.

INTRODUCTION

THE magnetostriction at saturation of single crystals of cubic ferromagnetic materials, such as iron and nickel and their alloys, is often described[1,2] by a 2-constant expression, but is more accurately described by the following expression in 5 constants[3]

$$\begin{aligned}\lambda=&h_1(\alpha_1^2\beta_1^2+\alpha_2^2\beta_2^2+\alpha_3^2\beta_3^2-1/3)\\&+2h_2(\alpha_1\alpha_2\beta_1\beta_2+\alpha_2\alpha_3\beta_2\beta_3+\alpha_3\alpha_1\beta_3\beta_1)+h_3 s\\&+h_4(\alpha_1^4\beta_1^2+\alpha_2^4\beta_2^2+\alpha_3^4\beta_3^2+2s/3-1/3)\\&+2h_5(\alpha_1\alpha_2\alpha_3^2\beta_1\beta_2+\alpha_2\alpha_3\alpha_1^2\beta_2\beta_3+\alpha_3\alpha_1\alpha_2^2\beta_3\beta_1),\end{aligned}\quad(1)$$

where

$$s=\alpha_1^2\alpha_2^2+\alpha_2^2\alpha_3^2+\alpha_3^2\alpha_1^2.$$

Here λ is the fractional change in length measured in the crystallographic direction having the direction cosines β_1, β_2, and β_3 with respect to the crystal axes, when the crystal is magnetically saturated in the direction having direction cosines α_1, α_2, and α_3. This equation gives the change in dimensions of a portion of the crystal, which is originally nonmagnetic, when it is spontaneously magnetized as a single domain in the specified direction. It also represents the changes in dimensions of a crystal composed of many domains, if they are originally oriented so that there are equal numbers in each of the crystallographically equivalent directions of easy magnetization ([111] directions in nickel, [100] in iron).

In previous work the constants have been evaluated only in nickel.[1] The present paper describes a new simplified procedure for determining these constants, and evaluates them for a crystal of nickel, and for a crystal composed of 78 percent nickel and 22 percent iron. This composition was chosen because (1) it is nearly that for the highest magnetic permeability of any of the binary iron-nickel alloys (Permalloys), and (2) the permeability is known to have a close connection to the magnetostriction. More particularly it is known from recent work[4] that the saturation magnetostriction in the [111] direction (λ_{111}) goes through zero at about the composition at which the permeability is a maximum. For a careful test of this coincidence, the composition for $\lambda_{111}=0$ should be known with some accuracy.

In order to determine λ_{111}, it is not sufficient to measure the change in length which occurs when a crystal is magnetized to saturation in the [111] direction, because the result of such a measurement depends on the initial domain distribution. The usual procedure in determining the saturation magnetostriction, so that it is independent of the initial distribution, is to measure the change in length when saturated in that direction (λ_l), and then the change when saturated at right angles to that direction (λ_t), the difference between these changes being independent of the initial domain distribution $\lambda=\frac{3}{2}(\lambda_l-\lambda_t)$. However, λ_{111} cannot be determined accurately in this manner, for evaluation of Eq. (1) shows that, although

$$\lambda_{111}=2h_2/3+2h_5/9,\quad(2)$$

nevertheless the difference in the magnetostrictions measured when a crystal is saturated first in the [111] direction and then in the perpendicular [2$\bar{1}$1] direction is $\lambda_{111}-\lambda_{2\bar{1}1}=h_2+2h_5/9$. Similarly, by saturating first in the [110] direction and then the [1$\bar{1}$0] direction, at right angles, we find that

$$\lambda_{110}-\lambda_{1\bar{1}0}=h_2.$$

However, λ_{111} can be evaluated by measuring the change in length first in the [111] direction and then in the [11$\bar{1}$] direction, in the (1$\bar{1}$0) plane, the difference being $(2h_2/3+h_3/3+2h_5/9)-(-2h_2/9+h_3/3+2h_5/27)=(4/3)(2h_2/3+2h_5/9=(4/3)\lambda_{111}$. In our experiments we have determined the 5 constants in the way to be described and then combined h_2 and h_5 according to Eq. (2).

[1] R. Becker and W. Döring, *Ferromagnetismus* (Julius Springer, Berlin, 1939).
[2] R. M. Bozorth, *Ferromagnetism* (D. Van Nostrand Company, Inc., New York, 1951).
[3] This applies to crystals having [100] as the direction of easy magnetization (e.g., iron). When [111] is the easy direction, the term $h_3/3$ must be subtracted.
[4] R. M. Bozorth and J. G. Walker, Phys. Rev. **88**, 1209 (1952).

TABLE I. Matrix elements for calculation of magnetostriction constants: $h_n=\sum_{i=1}^{18}\delta_{in}\lambda_i$. For data for quenched 78 percent nickel, given in last column, derived h's are given in Table III.

i	θ	Gauge direction	δ_{i1}	δ_{i2}	δ_{i3}	δ_{i4}	δ_{i5}	$\lambda_i(10)^6$
1	10°	[100]	0.3407	0	0	−0.3847	0	−0.48
2	20	[100]	1.1794	0	0	−1.3352	0	−1.83
3	30	[100]	2.0546	0	0	−2.3392	0	−3.58
4	40	[100]	2.4508	0	0	−2.8230	0	−6.10
5	50	[100]	2.0527	0	0	−2.4330	0	−8.92
6	60	[100]	0.9084	0	0	−1.2164	0	−11.50
7	70	[100]	−0.5766	0	0	0.3850	0	−13.28
8	80	[100]	−1.8134	0	0	1.7255	0	−14.35
9	90	[100]	−2.2924	0	0	2.2456	0	−14.47
10	10	[111]	3.9283	2.7614	−3.9283	−5.8924	−2.9159	0.38
11	20	[111]	4.3965	3.1713	−4.3965	−6.5947	−3.3247	0.87
12	30	[111]	2.5990	1.8917	−2.5990	−3.8986	−1.5557	1.24
13	40	[111]	0.3242	0.1363	−0.3242	−0.4863	1.0708	1.50
14	50	[111]	−0.9972	−0.9712	0.9972	1.4958	2.9206	1.59
15	60	[111]	−1.0053	−0.9598	1.0053	1.5080	2.8593	1.57
16	70	[111]	−0.5485	−0.2253	0.5485	0.8227	0.8153	1.40
17	80	[111]	−1.1835	+0.2015	1.1835	1.7752	−2.1742	1.14
18	90	[111]	−4.2853	−0.7800	4.2853	6.4279	−4.4587	0.81

EXPERIMENTAL PROCEDURE

Changes in length caused by magnetization are measured using the strain-gauge method described by Goldman.[5] For our measurements the gauge is cemented to a crystal disk in one position, and the disk is magnetized successively in a number of directions. Thus the β's of Eq. (1) are fixed and the α's varied, measurements of λ being made for a number of α's sufficient to determine the h constants with reasonable accuracy.

The choice of the crystal plane and the gauge position are important. If the crystal is cut parallel to the (100) plane, Eq. (1) shows that some of the terms become zero, so that evaluation of all of the constants is impossible. As a result of calculation it was decided to cut the crystal disk parallel to a (110) plane and place the gauge first parallel to [001], then parallel to $[1\bar{1}1]$ (respectively, 0° and 55° from the [001] direction). A magnetic field, sufficient to saturate the crystal, is applied to the [001] direction and at various angles θ to this direction up to $\theta=90°$ in steps of 10°. The observed values of magnetostriction, measured in the direction of the gauge when the field is reduced to zero, are designated λ_θ. In order to eliminate the effect of initial domain distribution, the data are then given in terms of $\lambda_\theta-\lambda_0$. The h-constants, adjusted for least square fit, are then derived from these 18 data as described in the next section.

It is important to align the gauge accurately so that it will measure the change in length in the specified direction. This is accomplished by observing the directions of the gauge wires under the microscope and aligning them with a scratch on the crystal surface which has previously been drawn parallel to the required crystallographic direction, as determined by x-rays. The accuracy of the gauge placement is estimated to be a few tenths of a degree.

[5] J. E. Goldman, Phys. Rev. **72**, 529 (1947).

THEORY AND RESULTS

Consider a cubic magnetic crystal cut parallel to a (110) plane, and a strain gauge placed on it so that it measures the change in length parallel to the [001] direction. Let a magnetic field, sufficient to produce saturation in the plane of the crystal, be applied at an angle θ from the [001] direction. Let the fractional change in length resulting from application of the field at angle θ be $\Delta l/l=\lambda_\theta$. If we measure λ_θ for each value of θ from $\theta=0$ to $\theta=90°$, in 10° steps and substract from each λ_θ the value of λ_θ for $\theta=0$, we have 9 data which may be represented by $\lambda_i=\lambda_\theta-\lambda_0=\lambda_1, \lambda_2, \cdots, \lambda_9$. According to Eq. (1), we then can write 9 equations ($i=1, \cdots, 9$)

$$\lambda_i=a_{i1}h_1+a_{i2}h_2+\cdots+a_{i5}h_5,$$

the a's being the trigonometric coefficients of the h's.

Because there are experimental errors involved, these equations will not be mutually consistent. If we know the correct values of the h's, the observed value of one

TABLE II. Matrix elements for calculation of magnetostriction as dependent on angle θ. Calculated values of λ_i for quenched 78 percent nickel are compared with observation in Fig. 1.

i	θ	Gauge direction	a_{i1}	a_{i2}	a_{i3}	a_{i4}	a_{i5}
1	10	[100]	−0.03015	0	0.02947	−0.03975	0
2	20	[100]	−0.11698	0	0.10671	−0.14913	0
3	30	[100]	−0.25000	0	0.20312	−0.30208	0
4	40	[100]	−0.41318	0	0.28514	−0.46554	0
5	50	[100]	−0.58682	0	0.32856	−0.61025	0
6	60	[100]	−0.75000	0	0.32812	−0.71875	0
7	70	[100]	−0.88302	0	0.29823	−0.78750	0
8	80	[100]	−0.96985	0	0.26439	−0.82283	0
9	90	[100]	−1.00000	0	0.25000	−0.83333	0
10	10	[111]	0	0.17128	0.02947	0	0.01218
11	20	[111]	0	0.34201	0.10671	0	0.05215
12	30	[111]	0	0.49158	0.20312	0	0.11353
13	40	[111]	0	0.60197	0.28514	0	0.17673
14	50	[111]	0	0.65985	0.32855	0	0.21703
15	60	[111]	0	0.65825	0.32812	0	0.21559
16	70	[111]	0	0.59735	0.29823	0	0.16821
17	80	[111]	0	0.48451	0.26439	0	0.08793
18	90	[111]	0	0.33333	0.25000	0	0

λ_i will differ from the correct value, calculated from the correct values of the h's, by an amount (the "error"),

$$\epsilon_i = a_{i1}h_1 + a_{i1}h_2 + \cdots + h_{i5}h_5 - \lambda_i,$$

and the sum of the squares of the errors in the 9 observations will be a minimum when

$$\frac{\partial}{\partial h_1}\left(\sum_{i=1}^{9}\epsilon_i^2\right) = 0 = 2\sum_{i=1}^{9}(a_{i1}h_1 + a_{i2}h_2 + \cdots + a_{i5}h_5 - \lambda_i)a_{i1},$$

or

$$\sum_{i=1}^{9}(a_{i1}h_1 + \cdots + a_{i5}h_5) = \sum_{i=1}^{9} a_{i1}\lambda_i.$$

Similarly four other equations are obtained by differentiating with respect to $h_2, \cdots h_5$. These 5 equations

TABLE III. Values of the five magnetostriction constants for nickel and for 78 percent nickel crystals. Estimated probable errors are given in parentheses below the values of the constants.

	78 percent Ni-Fe (quenched)	78 percent Ni-Fe (slowly cooled)	Nickel
h_1	13.7×10^{-6} (1.0)	20.9×10^{-6} (0.7)	-68.8×10^{-6} (3.8)
h_2	2.6 (0.5)	2.8 (0.3)	−36.5 (1.9)
h_3	−0.3 (0.8)	1.7 (0.5)	−2.8 (3.1)
h_4	1.1 (1.4)	−1.4 (1.0)	−7.5 (5.2)
h_5	−0.1 (0.8)	−0.2 (0.5)	7.7 (3.1)

are then solved for h_1 to h_5:

$$h_1 = \delta_{11}\lambda_1 + \delta_{12}\lambda_2 + \cdots + \delta_{19}\lambda_9,$$
$$h_2 = \delta_{21}\lambda_1 + \delta_{22}\lambda_2 + \cdots + \delta_{29}\lambda_9,$$
$$\cdots$$
$$h_5 = \delta_{51}\lambda_1 + \delta_{52}\lambda_2 + \cdots + \delta_{59}\lambda_9.$$

For the case considered it is found that these equations are not all independent. Consequently, a second gauge is placed to measure the magnetostriction in the [111] direction, and 9 additional data are recorded in a similar manner, with θ still representing the angle between the [001] direction and the direction of the field, and measured in such a sense that λ is parallel to the field when $\theta \approx 55°$. In practice the second gauge is cemented on the other side of the crystal. This set of data may be represented by $\lambda_{10}, \lambda_{11}, \cdots \lambda_{18}$. The above equations are then changed to

$$h_1 = \delta_{11}\lambda_1 + \delta_{12}\lambda_2 + \cdots + \delta_{1\cdot18}\lambda_{18},$$

and so on.

The values of the δ's, obtained by solving these equations, are given in Table I. The values of h_1 to h_5

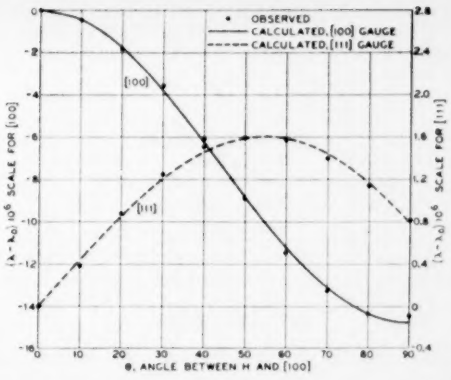

FIG. 1. Comparison of observed values of $\lambda_i = \lambda - \lambda_0$ with those calculated from $h_1, \cdots, h_5$ for least square fit. λ's were measured parallel to [100] and [111] directions.

are evaluated from the data, λ_1 to λ_{18}, and the coefficients, δ_{11} and $\delta_{18.5}$, using the summation

$$h_n = \sum_{i=1}^{18}\delta_{in}\lambda_i.$$

The observed λ_i's for the 78 percent nickel crystal are shown in the last column and the derived values of the h's are given in Table III.

It is desirable to compare the observed values of λ with those calculated from the constants h. The calculated λ's may be obtained from the summation

$$\lambda_i = \sum_{n=1}^{5} a_{in}h_n.$$

Values of the a's are given in Table II. Using the values of the h's given in Table III for quenched 78 percent nickel, we find the agreement between the calculated and observed variation of λ_i with θ as illustrated for this crystal in Fig. 1.

Similar data were taken for a single crystal of nickel, with the results shown in Table III. The results for 78 percent nickel are also repeated here, and the probable errors for all of the constants. The results for nickel diverge widely from those derived by Becker and Döring[1] from the data of Masiyama.[5]

The values of the constant h_3 for the 78 percent nickel alloy and for nickel indicate a small volume contraction associated with domain orientation. These are the first determinations of this kind. However, the values of the constants are small and in most cases do not exceed the experimental error. In slowly cooled 78 percent nickel the error is low enough so that the probability of a finite value of h_3 is 95 percent. In all of the specimens the values of h_4 and h_5 are not certainly different from zero.

[5] Y. Masiyama, Science Repts. Tôhoku Imp. Univ. **17**, 945 (1928).

TABLE IV. Longitudinal and transverse magnetostriction in (100) and (110) planes, as dependent on direction of measurement of change of length as shown in second column.

Plane	Direction	λ_{long}	λ_{trans}	$\lambda_{long}-\lambda_{trans}$
(100)	[001]	$2h_1/3+2h_4/3$	$-h_1/3-h_4/3$	h_1+h_4
	[011]	$h_1/6+h_2/2+h_3/4+h_4/12$	$h_1/6-h_2/2+h_3/4+h_4/12$	h_2
(110)	[001]	$2h_1/3+2h_4/3$	$-h_1/3+h_3/4-h_4/6$	$h_1-h_3/4+5h_4/6$
	$[1\bar{1}0]$	$h_1/6+h_2/2+h_3/4+h_4/12$	$-h_1/3-h_4/3$	$h_1/2+h_2/2+h_3/4+5h_4/12$
	$[1\bar{1}1]$	$2h_2/3+h_3/3+2h_5/9$	$-h_2/3+h_3/4$	$h_2+h_3/12+2h_5/9$
(111)	$[1\bar{1}0]$	$h_1/6+h_2/2+h_3/4+h_4/12$	$-h_1/6-h_2/6+h_3/4-5h_4/36-h_5/9$	$h_1/3+2h_2/3+2h_4/9+h_5/9$
	$[2\bar{1}\bar{1}]$	$h_1/6+h_2/2+h_3/4+5h_4/36+h_5/9$	$-h_1/6-h_2/6+h_3/4-h_4/12$	$h_1/3+2h_2/3+2h_4/9+h_5/9$

SPECIAL CASES

As it is in the experiments described above, the magnetostriction is often measured in a given direction in a plane, when the field giving rise to this magnetostriction is applied in any arbitrary direction in the plane. The magnetostriction then depends on the specified directions in the way described in the Appendix. These expressions were computed because they are important in determining the way in which the various constants enter into the data determined with different crystal and gauge orientations. The expressions in cases 3 and 5 were used in deriving the h's from our data.

Often the saturating field is applied either parallel or perpendicular to the direction of measurement of λ, the effect being then denoted longitudinal (λ_l) or transverse (λ_t). These quantities are shown for some special cases in Table IV.

One case should be mentioned, which at first led to some difficulty in interpreting the results of measurement. It will be noted that λ_l and λ_t for the [011] direction in the (100) plane both contain the terms $h_1/6+h_4/12$. If $h_1+h_4/2$ is large compared with h_2, the longitudinal and transverse effects will both be of the same sign and approximately the same magnitude. In one crystal of Mishima alloy (Fe_2NiAl) this was observed to be the case, as shown in Fig. 2. In all of the other special cases of Table IV, the terms in h_1, h_2, h_4, and h_5 occur with opposite signs in the longitudinal and transverse directions, or one of them is zero.

We are greatly indebted to Miss C. L. Froelich for carrying out the matrix inversions, and to Miss B. B. Cetlin and Miss M. Goertz for checking many of the formulas.

APPENDIX

The dependence of magnetostriction on direction of magnetization to saturation is given below for some of the special cases most frequently used. These are all derived from Eq. (1). Here λ is the fractional change in length in the specified direction, and λ_0 is the same quantity for $\theta=0$, where θ is the angle in the given plane between the direction of the applied field and the [001] direction (except in cases 6 and 7, when it is the $[1\bar{1}0]$ direction). The sense of θ is such that the direction of saturation is parallel to the direction in which λ is measured, when θ has some value $\lesssim 90°$.

(1) Plane (100), $\lambda\|[001]$:

$$\lambda=h_1(1+3\cos2\theta)/6+h_3(1-\cos4\theta)/8+h_4(3+12\cos2\theta+\cos4\theta)/8,$$

$$\lambda_0=2h_1/3+2h_4/3,$$

$$\lambda-\lambda_0=h_1(-1+\cos2\theta)/2+h_3(1-\cos4\theta)/8+h_4(-13+12\cos2\theta+\cos4\theta)/24.$$

(2) Plane (100), $\lambda\|[011]$:

$$\lambda=h_1/6+h_2(\sin2\theta)/2+h_3(1-\cos4\theta)/8+h_4(3+\cos4\theta)/24,$$

$$\lambda_0=h_1/6+h_4/6,$$

$$\lambda-\lambda_0=h_2(\sin2\theta)/2+h_3(1-\cos4\theta)/8+h_4(-1+\cos4\theta)/24.$$

(3) Plane (110), $\lambda\|[001]$:

$$\lambda=h_1(1+3\cos2\theta)/6+h_3(7-4\cos2\theta-3\cos4\theta)/32+h_4(9+20\cos2\theta+3\cos4\theta)/48,$$

$$\lambda_0=2h_1/3+2h_4/3,$$

$$\lambda-\lambda_0=h_1(-1+\cos2\theta)/2+h_3(7-4\cos2\theta-3\cos4\theta)/32+h_4(-23+20\cos2\theta+3\cos4\theta)/48.$$

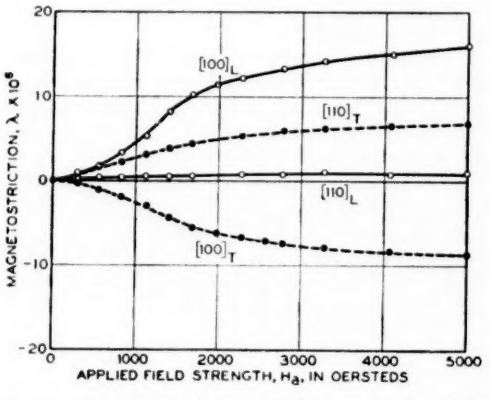

FIG. 2. Magnetostriction *vs* field strength for Fe_2NiAl (Mishima alloy), showing λ_l (longitudinal) with same sign as λ_t (transverse).

(4) Plane (110), $\lambda \| [1\bar{1}0]$:

$$\lambda = h_1(-1-3\cos 2\theta)/12 + h_2(1-\cos 2\theta)/4 + h_3(7-4\cos 2\theta-3\cos 4\theta)/32 + h_4(-9-20\cos 2\theta-3\cos 4\theta)/96 + h_5(1-\cos 4\theta)/16,$$

$$\lambda_0 = -h_1/3 - h_4/3,$$

$$\lambda-\lambda_0 = h_1(1-\cos 2\theta)/4 + h_2(1-\cos 2\theta)/4 + h_3(7-4\cos 2\theta-3\cos 4\theta)/32 + h_4(23-20\cos 2\theta-3\cos 4\theta)/96 + h_5(1-\cos 4\theta)/16.$$

(5) Plane (110), $\lambda \| [111]$:

$$\lambda = h_2(1-\cos 2\theta+2\sqrt{2}\sin 2\theta)/6 + h_3(7-4\cos 2\theta-3\cos 4\theta)/32 + h_5(1+2\sqrt{2}\sin 2\theta-\sqrt{2}\sin 4\theta-\cos 4\theta)/24,$$

$$\lambda_0 = 0,$$

$$\lambda-\lambda_0 = \lambda.$$

(6) Plane (111), $\lambda \| [1\bar{1}0]$:

$$\lambda = h_1(\cos 2\theta)/6 + h_2(1+2\cos 2\theta)/6 + h_3/4 + h_4(4\cos 2\theta-\cos 4\theta)/36 + h_5(\cos 2\theta-\cos 4\theta)/18,$$

$$\lambda_0 = h_1/6 + h_2/2 + h_3/4 + h_4/12,$$

$$\lambda-\lambda_0 = h_1(-1+\cos 2\theta)/6 + h_2(-1+\cos 2\theta)/3 + h_4(-3+4\cos 2\theta-\cos 4\theta)/36 + h_5(\cos 2\theta-\cos 4\theta)/18.$$

(7) Plane (111), $\lambda \| [2\bar{1}\bar{1}]$:

$$\lambda = h_1(\cos 2\theta+\sqrt{3}\sin 2\theta)/12 + h_2(1+\cos 2\theta+\sqrt{3}\sin 2\theta)/6 + h_3/4 + h_4(4\cos 2\theta+4\sqrt{3}\sin 2\theta-\cos 4\theta+\sqrt{3}\sin 4\theta)/72 + h_5(\cos 2\theta+\sqrt{3}\sin 2\theta-\cos 4\theta+\sqrt{3}\sin 4\theta)/36,$$

$$\lambda_0 = h_1/12 + h_2/3 + h_3/4 + h_4/24,$$

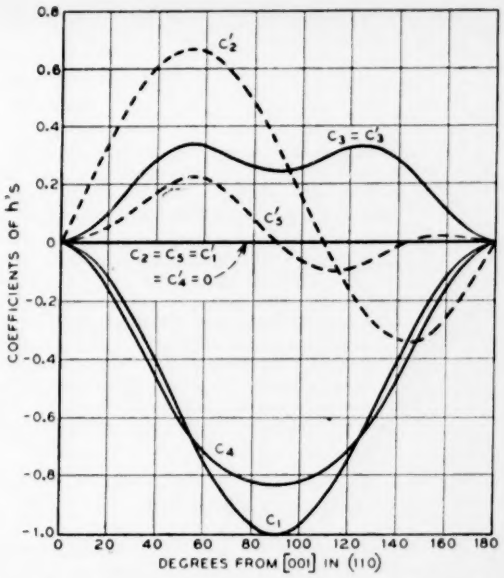

FIG. 3. Coefficients $c_1, c_2, \cdots, c_5$ of the terms in $h_1, \cdots, h_5$ of Eq. (1), for λ measured in (110) plane parallel to [001] (unprimed c's) and to $[1\bar{1}1]$ (primed c's), with magnetization at θ° from [001].

$$\lambda-\lambda_0 = h_1(-1+\cos 2\theta+\sqrt{3}\sin 2\theta)/12 + h_2(-1+\cos 2\theta+\sqrt{3}\sin 2\theta)/6 + h_4(-3+4\cos 2\theta+4\sqrt{3}\sin 2\theta-\cos 4\theta+\sqrt{3}\sin 4\theta)/72 + h_5(\cos 2\theta+\sqrt{3}\sin 2\theta-\cos 4\theta+\sqrt{3}\sin 4\theta)/36.$$

Items (3) and (5) above were used in the computation of the matrix elements of Table I. The way in which the coefficients of the h's vary with θ is shown for these two cases in Fig. 3.

Thermal Conductivity, Electrical Resistivity, and Thermoelectric Power of Graphite

W. W. Tyler and A. C. Wilson, Jr.
Knolls Atomic Power Laboratory, Schenectady, New York*
(Received August 14, 1952)

The thermal conductivity, electrical resistivity, and thermoelectric power have been measured in the temperature range from 20°K to 300°K for samples of artificial extruded graphite, natural molded graphite, and lampblack graphite. Experimental results are presented and discussed briefly in relation to theory.

Due to the very large Wiedemann-Franz ratio and its dependence on temperature and type of graphite, thermal conductivity in graphite is attributed primarily to lattice waves. Scattering of lattice waves from crystallite boundaries limits the conductivity through most of the temperature range investigated. Interpretation of the data in terms of the simple Debye equation for lattice conductivity permits rough estimates of effective crystallite size. At low temperatures, the dependence of conductivity on temperature is more rapid than the dependence of heat capacity, in disagreement with the Debye equation.

The temperature dependence of electrical resistivity is interpreted using a modified Wallace zone theory which permits the Fermi level to differ in position from the zone boundary, owing to an excess or deficit of electrons. Scattering of electrons in the temperature range of interest is attributed to crystallite boundaries or atomic imperfections and assumed temperature independent. The temperature dependence of the Fermi level which gives the best fit to experimental data is not in agreement with theoretical predictions.

I. SAMPLES STUDIED

THE four polycrystalline graphite samples studied were in the form of rods three-eighths inch in diameter and three inches long. Samples *A* and *B* are conventional coke base, pitch bonded, extruded graphite with bulk density of about 1.70 g/cm³. The theoretical single crystal density is 2.25 g/cm³. Sample A is a National Carbon Company grade CS graphite with axis of the sample perpendicular to the preferred c_0 axis orientation. Sample B is a National Carbon Company grade AGOT graphite with the sample axis parallel to preferred c_0 axis orientation. Sample C is natural graphite base, pitch bonded, and molded, with a bulk density of about 1.80 g/cm³ and with the sample axis perpendicular to the preferred c_0 axis orientation. Sample D is a lampblack base, pitch bonded, molded graphite with bulk density of about 1.65 g/cm³. The axis of sample D is parallel to the preferred c_0 axis orientation although because of the small crystallite size, orientation effects are comparatively small for this type of graphite.[1]

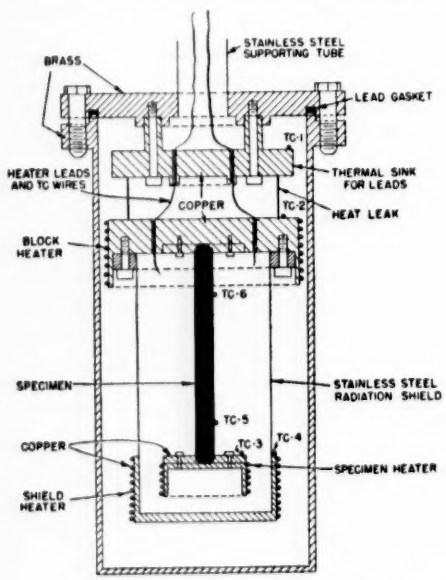

FIG. 1. Diagram of the apparatus.

II. EXPERIMENTAL PROCEDURE

Figure 1 indicates the arrangement used in supporting the specimen and providing suitable thermal conditions during measurements. The container shown is supported in a Dewar containing either liquid hydrogen, liquid nitrogen, solid carbon dioxide and acetone, or ice water, depending on the temperature range desired. The Dewar in turn is contained in a cryostat which may be evacuated to reduce the vapor pressure over the liquid when working with hydrogen or nitrogen. To provide thermal isolation of the sample, the container shown in Fig. 1 is evacuated during measurements to about 5×10^{-6} mm mercury. Alternatively, helium exchange gas may be put in the container to aid thermal equilibration of the specimen and bath.

All heater and thermocouple leads pass through small paraffin filled holes in the copper "thermal sink" and are brought to the bath temperature at this point. Thermocouple leads to the specimen and the specimen heater, and current and potential leads to the specimen heater pass through paraffin filled holes in the "block." Positions of thermocouples are designated by TC in the diagram. TC-5 and TC-6 provide the critical temperature measurements establishing ΔT and the average

* The Knolls Atomic Power Laboratory is operated by the General Electric Company for the U. S. Atomic Energy Commission.

[1] For general information related to the preparation and properties of artificial graphites, see C. L. Mantell, *Industrial Carbon* (D. Van Nostrand Company, Inc., New York, 1946), and the review paper by J. P. Howe, J. Am. Ceram. Soc. **35**, 275 (1952).

temperature of the specimen. For measurements above nitrogen temperature (77°K), TC-3 and TC-4 are held at the same temperature to minimize radiation losses. All of the thermocouples are of copper-constantan, made from stock, samples of which had been calibrated against the Ohio State University temperature scale.[2] The block heater and heat leak perm't measurements in temperature regions between various bath temperatures. This technique has been used extensively by Powers and is described by him[3] in greater detail.

All thermoelectric voltages and potential measurements for power and current calculations are made using a Leeds and Northrup White double potentiometer (0–10,000 microvolts) and high sensitivity galvanometer. The scale sensitivity of this system is 3.5±0.1 cm/microvolt. Use of either the copper or constantan elements of TC-5 and TC-6 as potential leads permits electrical resistivity measurements and thermoelectric power measurements of either copper-graphite or constantan-graphite.

To support the samples in the cryostat, copper disks were soldered to the ends of the specimens after copper plating of the graphite. The copper disks were then fastened to the block and heater by screws. The thermocouples TC-5 and TC-6 were soldered to 0.040-in. copper rods which were pressed snugly into holes in the samples.

III. EXPERIMENTAL RESULTS

Figure 2 shows thermal conductivity data for the four samples. Temperature dependent errors are attributable to power loss in the heater and thermocouple leads, thermal drift, radiation loss, the decrease in sensitivity of thermocouples at low temperatures, and deviations of the individual thermocouples from the standard calibration. Of these, the most important is due to lead losses. As the lengths of the leads and the thermal gradients between the block and the termination of the leads are known (TC-2, TC-3), corrections for lead losses are made using data of Powers[3] for the thermal conductivity of copper and constantan. This correction may be made fairly accurately for data points taken with the specimen near bath temperature, but not for data points in temperature regions such that a large gradient exists between the sink and the block. Under such conditions, failure to attain equilibrium between the leads and the block results in an under estimation of the gradient in the leads. Data points between 35 and 55°K tend to be somewhat high because of this even for the high conductivity specimens. The uncertainty in the magnitude of conductivity data is estimated to be ±5 percent for the highest conductivity points and ±10 percent for the lowest conductivity points.

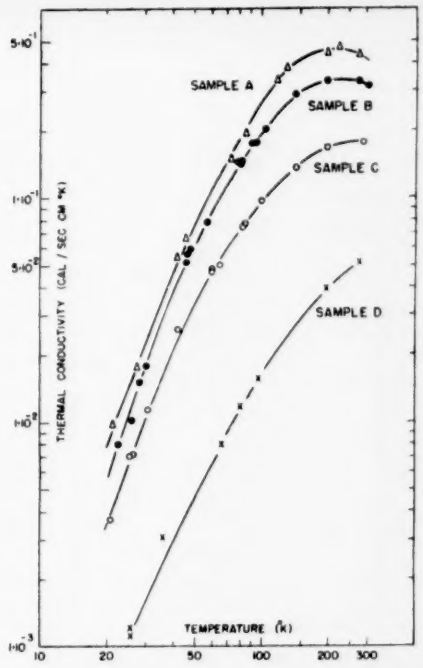

FIG. 2. Thermal conductivity as a function of temperature for the four samples studied.

Our conductivity data for samples A and B agree well with data of Berman[4] and Rasor[5] for samples of extruded graphite which are probably similar to our samples. Our data do not agree with data of Buerschaper[6] which indicate that the conductivity of graphite continues to increase as the temperature decreases down to 90°K.

Figure 3 shows the electrical resistivity data for specimens A, B, and C. Figure 4 compares the higher resistivity lampblack graphite with sample B. The data are probably accurate to ±0.5 percent except for a temperature independent, geometric error of at most 2 percent. The temperature dependence of the resistivity of samples A and B agrees fairly well with work of Goetz and Holser[7] for similar type graphite. The resistivity of the lampblack graphite sample may be represented quite accurately by

$$\rho = A - BT, \tag{1}$$

where A is 7.75×10^{-3} ohm-cm and B is 7.43×10^{-6} ohm-cm/deg. Sample C has a resistivity comparable

[2] Rubin, Johnston, and Altman, J. Am. Chem. Soc. **73**, 3401 (1951). We are indebted to W. DeSorbo for providing us with the thermocouple wire and calibration charts.

[3] Powers, Schwartz, and Johnston (to be published).

[4] R. Berman, Phys. Rev. **76**, 315 (1949); (to be published). We are indebted to Dr. Berman for sending us experimental data prior to publication and for helpful discussion related to the theory of lattice conduction.

[5] N. S. Rasor (unpublished data). We are indebted to W. P. Eatherly for informing us of this recent work at North American Aviation Company.

[6] R. A. Buerschaper, J. Appl. Phys. **15**, 452 (1944).

[7] A. Goetz and A. Holser, Trans. Electrochem. Soc. **82**, 391 (1942).

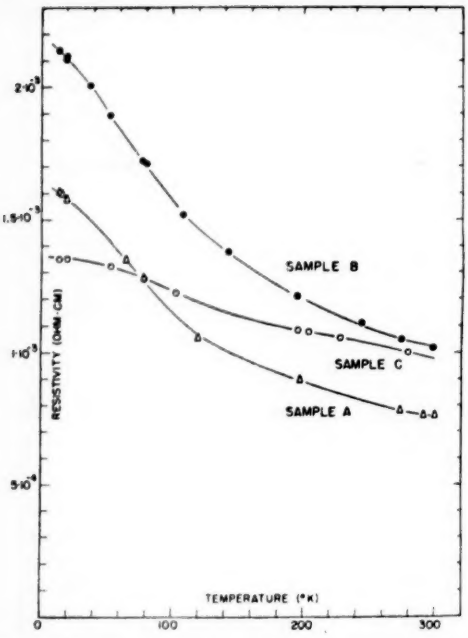

FIG. 3. Electrical resistivity as a function of temperature for samples A, B, and C.

in magnitude to that of A and B but less temperature dependent.

Figure 5 gives Wiedemann-Franz ratios computed from the curves of Figs. 2–4. This ratio is the same for samples A and B within several percent throughout the temperature range, and they are represented by the same curve. Figure 6 shows the absolute thermoelectric power for three samples, calculated from measured values of the thermoelectric power of graphite against constantan. The absolute thermoelectric power of constantan was obtained from the copper-constantan calibration, using data given by Borelius[8] for the absolute thermoelectric power of copper. Thermoelectric power values for the graphite samples were also obtained from graphite-copper data and checked against the values given here. The thermoelectric power data are probably accurate to within 0.5 microvolt.

IV. DISCUSSION AND INTERPRETATION

(a) Thermal Conductivity

The Wiedemann-Franz ratio for extruded graphite at room temperature is about 200 times the free electron theoretical value (2.45×10^{-8} volt^2/deg^2) for a solid in which thermal conductivity is solely by electrons. At 90°K this ratio is about 520 times the theoretical value. As shown in Figure 5, the magnitude of the ratio depends on the temperature and on the type of graphite. At high temperatures[9] and at low temperatures[4] the ratio approaches the theoretical value. Because of the high value of the Wiedemann-Franz ratio and because of its dependence on temperature and type of graphite, it is concluded in agreement with Berman[4] and Mrozowski[10] that the thermal conductivity is due primarily to the transfer of energy by lattice vibrations.

The simple Debye expression for lattice conductivity[11,12] indicates that

$$K=\tfrac{1}{3}c_v\lambda v_g, \tag{2}$$

where K is the thermal conductivity, c_v the specific heat, λ an average mean free path for scattering of lattice waves, and v_g an average group velocity for the waves. For pure, single, nonmetallic crystals, λ dominates in determining the temperature dependence of K except at very low temperatures.[13] At temperatures above the Debye temperature, c_v is constant and λ is inversely proportional to the temperature. At temperatures below the Debye temperature, although c_v is decreasing, K increases exponentially with decreasing temperature due to the very rapid increase of λ. At sufficiently low temperatures λ becomes limited by the scattering of lattice waves from the boundaries of the crystal, and the conductivity reaches a maximum value. For lower temperatures, K decreases, being dominated by c_v.

The temperature dependence of conductivity indicates that boundary scattering in polycrystalline

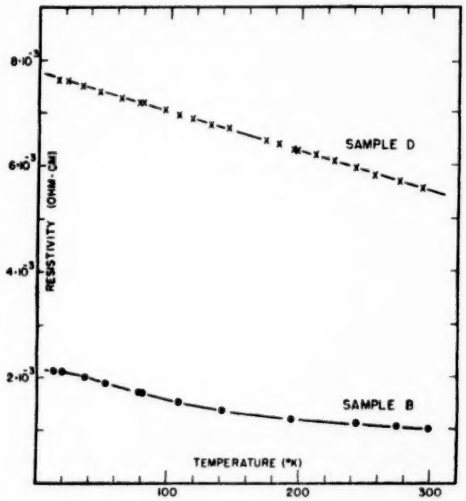

FIG. 4. Electrical resistivity as a function of temperature. Sample B is compared with the higher resistivity lampblack graphite, sample D.

[8] G. Borelius, *Handbuch der Metallphysik* (Akad. verlags. Gesellschaft, Leipzig, 1935), Vol. I, pp. 181–520.

[9] R. W. Powell and F. H. Schofield, Proc. Phys. Soc. (London) **51**, 153 (1939).

[10] S. Mrozowski, Phys. Rev. **86**, 251 (1952).

[11] P. Debye, *Vortraege über die Kinetische Theorie der Materie und der Elektrizität* (B. G. Teubner, Leipzig, 1914).

[12] R. Peierls, Ann. Physik **3**, 1055 (1929).

[13] Berman, Simon, and Wilks, Nature **168**, 277 (1951).

graphite becomes important at relatively high temperatures. For samples A and B the maximum conductivity occurs at about 230°K. The maximum occurs near room temperature for sample C and above room temperature for sample D. Assuming that v_g is about 10^5 cm/sec, substitution of values of K and c_v[14] corresponding to the temperatures of maximum conductivity into Eq. (2), leads to the following approximate values of effective crystallite sizes, λ_{max}.

Sample	λ_{max}
A	6700A
B	5000A
C	1800A
D	<500A

In bounding λ_{max} for Sample D, we assume that c_v increases more rapidly than K from room temperature to the conductivity maximum.

The magnitudes of crystallite sizes deduced in this manner are not inconsistent with x-ray data, which, however, are not capable of distinguishing between the estimated sizes for samples A, B, and C. The difference in the effective crystallite sizes of samples A and B is presumably due to differences in orientation. Sample C is somewhat anomalous as there is no reason to believe that its crystallite size should be smaller than for samples A and B.

According to the interpretation based on Eq. (2), at temperatures considerably below the maximum the thermal conductivity should be proportional to the specific heat. This is not observed, the specific heat of artificial graphite being quite accurately proportional to T^2 in the temperature range from 20°K to 50°K,[14] whereas the thermal conductivity in the same temperature range, for samples A, B, and C is proportional to T^n where n is estimated to be 2.7 ± 0.3. The conductivity of sample D is more nearly proportional to T^2, but the uncertainty in the low conductivity values makes it difficult to assign much quantitative significance to its temperature dependence. The failure of the Debye relationship in explaining the temperature dependence of the conductivity may be related to the large anisotropy of the graphite structure. However, examination of the more detailed expression for the conductivity,[15] which permits λ and v_g to depend on the wave vector, does not suggest an obvious explanation of the discrepancy. The explanation may be related to the temperature dependence of the energy transfer across crystallite boundaries. Densities of the graphites studied are about $\frac{3}{4}$ theoretical density for graphite, and it is easy to believe that the transport phenomena will be affected by temperature dependent interface properties.

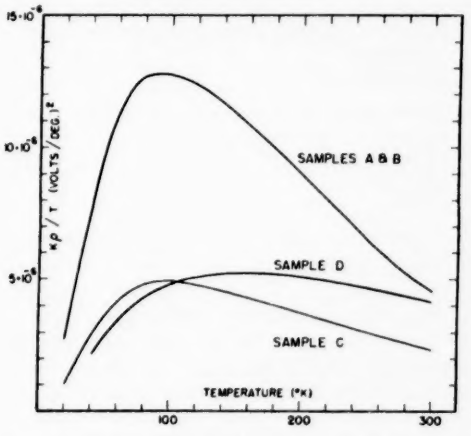

FIG. 5. Wiedemann-Franz ratio as a function of temperature. Values were calculated from the smoothed curves of Figs. 2, 3, and 4.

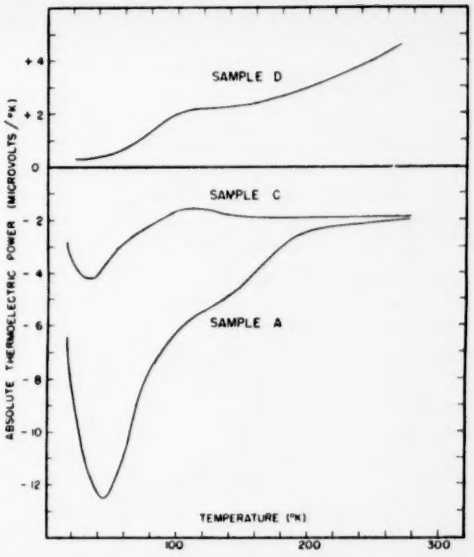

FIG. 6. Absolute thermoelectric power as a function of temperature. Values were obtained from measurements of thermoelectric power of constantan-graphite and copper-graphite couples.

(b) Electrical Resistivity

For a perfect single crystal of graphite, the two-dimensional Wallace theory[16] predicts that

$$\rho = C/(\tau_T 2kT \log 2), \tag{3}$$

where ρ is the resistivity, C a collection of constants and τ_T the mean time for scattering of electrons from lattice vibrations. In order to satisfy the observed positive resistivity *vs* temperature slope for single crystals, Wallace assumes that the temperature dependence of τ_T is given by T^{-n} where n is greater than unity.

For polycrystalline graphite we assume that[17]

$$1/\tau = 1/\tau_T + 1/\tau_0,$$

[14] W. W. Tyler and W. DeSorbo, Phys. Rev. **83**, 878 (1951).

[15] P. G. Klemens, Proc. Roy. Soc. (London) **A208**, 108 (1951).

[16] R. P. Wallace, Phys. Rev. **71**, 622 (1947).

[17] D. Bowen, Phys. Rev. **76**, 1878 (1949).

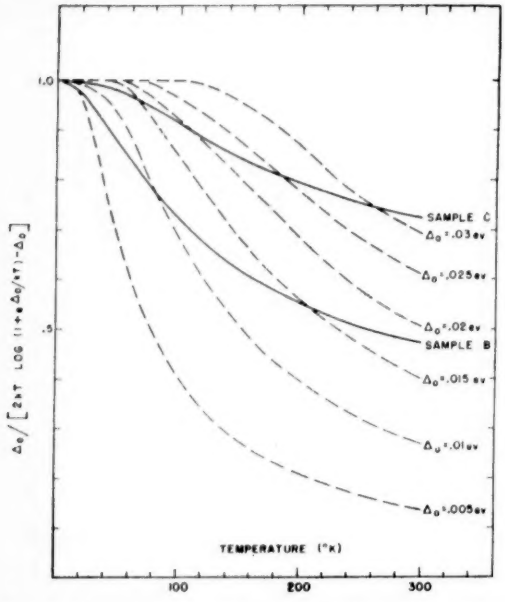

FIG. 7. Comparison of experimental resistivity data with the theoretical expression (6). Experimental and theoretical values are adjusted to a value of unity at absolute zero.

where τ_0 is the mean free time for scattering of electrons from imperfections and crystallite boundaries and is assumed to be independent of temperature. This gives

$$\rho = C'\left(\frac{1}{\tau_T}+\frac{1}{\tau_0}\right)\frac{1}{2kT\log 2}, \tag{4}$$

where C' now contains a geometric factor related to the density and preferred orientation of the crystallites. At sufficiently low temperatures τ_T becomes large compared with τ_0, and

$$\rho = \frac{C'}{\tau_0}\frac{1}{2kT\log 2}. \tag{5}$$

This gives a resistivity *vs* temperature slope which is negative in agreement with experimental results for room temperature and below. However, (5) predicts a hyperbolic dependence of ρ on T which does not agree with experimental results at low temperature. Extrapolation of the curves of Figs. 3 and 4 suggests finite resistivity-temperature slopes at 0°K.

The above expressions are based on the assumption that the Fermi level remains at the Wallace zone boundary. If because of impurity or surface states, the Fermi level is displaced from the zone boundary by an amount Δ, it may be shown[18] that

$$\rho = \frac{C'}{\tau_0[2kT\log(1+e^{\Delta/kT})-\Delta]}, \tag{6}$$

[18] Gerhart Hennig, J. Chem. Phys. **19**, 922 (1951).

where again we assume $\tau_T \gg \tau_0$. For $\Delta=0$, expression (6) reduces to expression (5). For $\Delta \gg kT$, (6) reduces to

$$\rho = C'/\tau_0\Delta. \tag{7}$$

In this case the temperature dependence of ρ is given by the temperature dependence of Δ. For any finite Δ, in the limiting case as $T\to 0$,

$$\rho_0 = C'/\tau_0\Delta_0, \tag{8}$$

where Δ_0 is the deviation of the Fermi level from the zone boundary at absolute zero.

It is of interest to compare the experimental data with Eq. (6) under the assumption that Δ is independent of temperature. Figure 7 shows the function $\Delta_0/[2kt\log(1+e^{\Delta_0/kt})-\Delta_0]$ plotted against temperature for different values of Δ_0 ranging from 0.005 ev to 0.03 ev. The solid curves give relative values of experimental data for samples B and C. Relative resistivity values for sample A are within 5 percent of those for sample B and are not plotted separately. As the experimental data extend down only to about 14°K, it was necessary to extrapolate to absolute zero, and comparison of the behavior of the theoretical and experimental curves in the neighborhood of zero temperature is not too meaningful.

The simplicity of Eq. (8) does permit a direct interpretation of the extrapolated intercept value of resistivity. However, assuming that a reasonable estimate could be given for C', it is still only possible to deduce the value of the product $\tau_0\Delta_0$ from the intercept value. The deviation of the Fermi level from the zone boundary is presumably due to the trapping of electrons at atomic imperfections or crystallite boundaries. As these also contribute to the scattering of electrons, τ_0 and Δ_0 are not independent, although it is not possible to predict their exact relationship except on the basis of rather simple models.

The agreement between the data and Eq. (6) may be improved by allowing the magnitude of Δ to increase with temperature. This is particularly true for sample D for which the resistivity is observed to be a simple function of temperature. Because of the small crystallite size in sample D, it is reasonable to assume that $\Delta \gg kt$ and that Eq. (7) is applicable. If so, the assumption that

$$\Delta = \alpha+\beta T,$$

where βT is small compared with α throughout the temperature range, yields Eq. (1) immediately from Eq. (7). Insertion of a similar temperature dependence of Δ in Eq. (6) gives a better representation of the data for all the samples. It should be noted that as expression (6) is symmetric in the sign of Δ, it is only the temperature dependence of the magnitude of Δ which is important to consider here.

Although a temperature dependence of Δ of the type assumed above gives a better representation of the data, it is not in agreement with the Wallace theory. Hennig[18] has calculated the temperature dependence of

Δ based on the two-dimensional Wallace theory. Because of the nature of the distribution of energy states near the zone boundary, the theory predicts that the magnitude of Δ decreases with increasing temperature. Attempts to fit our data to Eq. (6), assuming that the magnitude of Δ decreases with increasing temperature, result in poorer agreement than that shown in Fig. 7.

In the above discussion, it has been assumed that $\tau \gg \tau_0$ and that τ_0 is independent of temperature. If scattering of electrons by lattice vibrations begins to contribute appreciably below room temperature, the inclusion of this effect in the theoretical expression (6) would give better agreement with the data. Permitting τ_0 to depend on temperature could also result in better agreement. In fact, it is certainly not clear that scattering effects owing to boundaries are temperature independent and that all other boundary effects on the electronic properties may be included in Δ. However, on the basis of the experimental information available, it does not seem fruitful to speculate further on possible temperature dependence of Δ and τ_0 or the possible importance of lattice scattering.

(c) Thermoelectric Power

At present, there is no theory of thermoelectric power in graphite, and we will make no attempt to interpret the temperature dependence of the data. It should be pointed out that the sign of the thermoelectric power in graphite does not necessarily coincide with the sign of the Hall coefficient. Measurements at room temperature indicate that the sign of the Hall coefficient for all four graphite samples studied is negative. Thus, sample D which has a positive thermoelectric power throughout the temperature range studied has a negative Hall coefficient at room temperature. Approximate values of Hall coefficients for the four samples are given below.

Sample	R (emu)
A	−0.66
B	−0.48
C	−0.59
D	−0.37

These values of Hall coefficient are in fair agreement with values quoted by Hennig[18] and Donoghue and Eatherly[19] for well-graphitized material. Studies of the effect of oxidation[18] or degree of graphitization[19] on the Hall coefficient indicate that the sign of the Hall coefficient can be controlled to some extent and that presumably samples with Δ equal to zero could be prepared. The low temperature resistivity of such a sample should be given by Eq. (5). Observation of this would give some evidence for the correctness of the theory.

[19] J. J. Donoghue and W. P. Eatherly, Rev. Sci. Instr. **22**, 513 (1951).

V. CONCLUSION

The results presented indicate the general magnitude and temperature dependence of the properties studied but do not permit entirely satisfactory theoretical interpretation. Refinement of the measurements and their extension to lower temperatures and to a larger variety of graphites may lead to a better understanding of the transport phenomena. However, it seems probable that satisfactory understanding will await measurements on single crystals. Lack of knowledge of the magnitude, temperature dependence, and anisotropy of thermal conductivity in pure single crystals seriously limits efforts to estimate the effects of orientation, crystallite size, and energy transfer across crystallite boundaries on the conductivity of polycrystalline material. Of particular fundamental interest is knowledge of the normal modes which predominate in determining the temperature dependence of the conductivity, the nature of interactions among these modes, and between these modes and free electrons. Interpretation of electrical resistivity and thermoelectric power measurements is also complicated by the polycrystalline nature of the graphites studied and will probably remain uncertain until single crystal experiments test the applicability of the Wallace theory and the effect of the controlled introduction of imperfections.

The work reported was done at the General Electric Company Low Temperature Laboratory and benefited from the cooperation of all members of the Laboratory. W. DeSorbo, M. D. Fiske, and R. W. Powers contributed helpful suggestions concerning experimental techniques. The interpretation of experimental results has been stimulated by discussion with J. P. Howe, J. A. Krumhansl, R. L. Cummerow, and J. B. Sampson of the Knolls Atomic Power Laboratory. Finally, we are indebted to W. C. Dunlap, Jr., and E. M. Pell for measuring Hall coefficients of our samples.

Letters to the Editor

PUBLICATION of brief reports of important discoveries in physics may be secured by addressing them to this department. The closing date for this department is five weeks prior to the date of issue. No proof will be sent to the authors. The Board of Editors does not hold itself responsible for the opinions expressed by the correspondents. Communications should not exceed 600 words in length and should be submitted in duplicate.

Induced Thermoelectric Potential from Radiation Damage*

ALAN ANDREW AND CLIFTON R. DAVIDSON
Atomic Energy Research Department, North American Aviation, Inc., Downey, California
(Received December 22, 1952)

THE effect of radiation damage on the thermoelectric potential of iron and of constantan has been measured in a preliminary experiment. This work is a continuation of a previously reported effort[1] and represents an extension into a region of lower temperatures with a different technique.

The procedure was as follows: A five-mil wire was wound on a mica form measuring approximately one-by-five cm. The central part of the wire was then exposed to a beam of 10-Mev protons from the 60-inch Berkeley cyclotron in Crocker Laboratory. The two end sections of the wire were shielded from the beam and hence gave a length of wire with the central portion irradiated. During the irradiation the wire was maintained below zero degrees centigrade by passing helium, cooled by liquid nitrogen, over the sample.

Following the irradiation the wire was unwound from the mica form and annealed at various temperatures for a period of an hour in a furnace. After each anneal the thermoelectric potential of the irradiated section against the unirradiated section (see Fig. 1) was measured using a L & N Speed-O-Max, coupled with

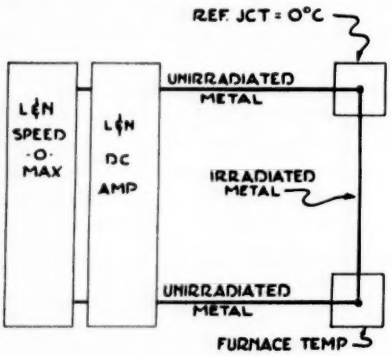

FIG. 1. Schematic diagram of equipment.

a L & N dc amplifier, Model 9835-B. A specially designed furnace was used as the variable temperature source and a standard ice water mixture for the reference temperature source.

The 0.005-inch iron wire was irradiated with the 22 μa hr/cm^2 of 10-Mev protons. The 0.005-inch constantan wire was irradiated with 17 μa hr/cm^2 of 10-Mev protons. Iron was found to be positive with reference to the irradiated iron and constantan negative with reference to the irradiated constantan. The results are given in Figs. 2 and 3. From these curves it is seen that the maximum induced thermoelectric potentials are 0.3 microvolt per degree centigrade for iron and 0.1 microvolt per degree centigrade for constantan, after annealing to about 150 degrees centigrade.

There was a small drift and zero shift in the measurement of the emf of less than ± 1 μv. The variable temperature of the thermocouple loop was measured with another thermocouple, and the estimated variation of the temperature in the special furnace is less than ± 3 percent of the temperature as measured in centigrade units.

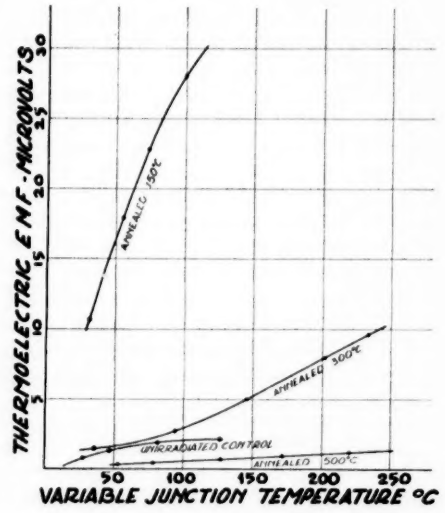

FIG. 2. Emf *vs* temperature for iron—irradiated iron thermocouple. Iron is positive with respect to irradiated iron. Reference junction = 0°C.

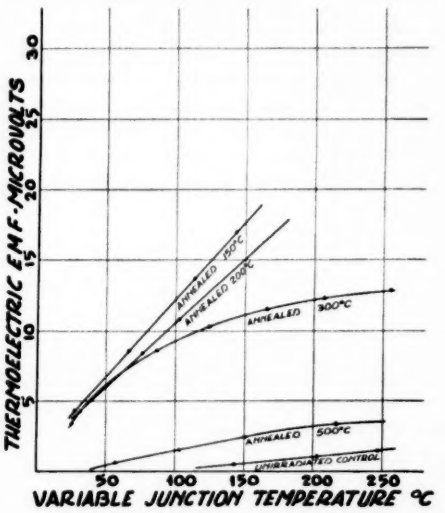

FIG. 3. Emf *vs* temperature for constantan—irradiated constantan thermocouple. Constantan is negative with respect to irradiated constantan. Reference junction = 0°C.

The control specimens were subjected to the same wrapping and twisting as the irradiated wires. They were not annealed before the control measurements were made. In both cases the control and irradiated wires were taken from the same spool, and consequently they should have very nearly the same composition and previous history.

It is a pleasure to acknowledge the interest and cooperation of Dr. J. G. Hamilton and G. B. Rossi of Crocker Laboratory and

the assistance of the members of the Irradiation Physics Group of North American Aviation, Inc., particularly L. E. Glasgow and B. T. Harwick.

* This work was sponsored by the U. S. Atomic Energy Commission.
[1] Andrew, Jeppson, and Yockey, Phys. Rev. **86**, 643 (1952).

Isomeric Branching and Threshold Behavior of the Reaction $Mo^{92}(n,2n)Mo^{91}$†

JOHN E. BROLLEY, JR.
Los Alamos Scientific Laboratories, University of California, Los Alamos, New Mexico
(Received December 31, 1952)

IN a recent paper,[1] we reported an experimental study of the reaction $Mo^{92}(n,2n)Mo^{91}$ employing neutrons in the range from threshold to 27 Mev. A number of investigators have produced Mo^{91} by the (γ,n) process using betatrons. They find, in addition to the 15.5-min Mo^{91}, another Mo^{91} activity of 65.5–75 sec. Katz[2] and collaborators have measured the (γ,n) thresholds of the two activities (15.5 min: 13.1±0.1 Mev, and 65.5 sec: 13.3±0.1 Mev) and the energy dependence of the two photo cross sections. In reference 1, we reported the absence of the shorter half-life, but in view of the recent betatron data, we made another search for it.

Neutrons of various energies were produced by bombarding tritium with deuterons accelerated in a Van de Graaff machine. The geometrical arrangement of foils (normal molybdenum) and tritium target was similar to that employed in the cyclotron experiments.[1] A knowledge of the deuteron energy plus the angular position of the molybdenum foil with respect to the deuteron beam axis makes possible a calculation of the energy of the neutrons passing through the foils. Irradiations of various lengths of time were performed on the foils. They were counted within one minute of bombardment termination on a Geiger counter apparatus adapted for measuring half-lives of the order of one minute. Two- and 15.5-minute bombardments with 14.4-Mev neutrons produced no measureable trace of the short half-life although the 15.5-min activity was abundant. It was interesting to note[2] that 14.5-Mev gamma-rays gave a value of about 0.2 for the ratio of the 65.5-sec to the 15.5-min photo cross sections. Eighteen-Mev neutrons gave a weak 65.5-sec activity. In view of these results, branching will not affect the comparison of the statistical theory to experiment made in reference 1.

We also measured a number of relative cross-section values for the 15.5-min isomer. These values are presented in Fig. 1. The

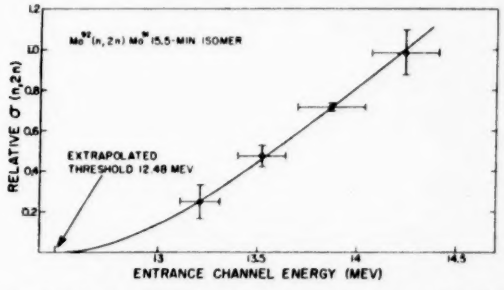

FIG. 1. Relative $\sigma(n,2n)$ as a function of channel energy: curve theoretical, points experimental.

vertical limits are 95 percent confidence intervals. The horizontal limits represent the maximum neutron energy spread intercepted by the foils. The curve drawn through the experimental points was calculated from the statistical theory using the values $a=3.16$ Mev^{-1} and $E_b=12.48$ Mev.

Keith Zeigler performed an iterated least squares calculation to fit the theoretical formula[3] to the data. The above values give the best fit. It is interesting to note that the new value of a is rather close to that obtained in reference 1. However, the threshold energy obtained from these data is in disagreement with betatron measurements. If E_b is varied by 0.1 Mev, the theoretical curve departs markedly from the data. Table I summarizes the results of the least squares calculation.

TABLE I. Comparison of calculated and observed relative cross sections.

Entrance channel energy (Mev)	Observed relative $\sigma(n,2n)$	Calculated relative $\sigma(n,2n)$	Difference
13.21	0.249	0.251	−0.002
13.52	0.474	0.454	0.020
13.87	0.715	0.713	0.002
14.24	0.986	1.005	−0.019

H. C. Martin operated the facilities employed in this experiment which were generously extended by Group P-3. L. K. Schlacks assisted with the computations.

† Work performed under the auspices of the U. S. Atomic Energy Commission.
[1] Brolley, Fowler, and Schlacks, Phys. Rev. **88**, 618 (1952).
[2] L. Katz (private communication).
[3] U. S. Atomic Energy Commission Document NYO 636, p. 153 (unpublished).

Angular Correlation in the Decay of Li^8†

C. M. CLASS* AND S. S. HANNA
Department of Physics, Johns Hopkins University, Baltimore, Maryland
(Received December 24, 1952)

OF the many processes which lead to the formation of the unstable Be^8 nucleus in its first excited state (~3 Mev), the $Li^8(\beta)Be^{8*}(\alpha)He^4$ reaction affords an interesting opportunity for performing a correlation experiment to provide information on this state. The beta-alpha correlation function may also depend on the nature of the Li^8 state and the degree of forbiddenness of the beta-process. Gardner[1] has given a discussion of the correlation functions expected for certain assignments of spin and parity to the participating states.

Li^8 nuclei were produced with the $Li^7(d,p)Li^8$ reaction by bombarding thin lithium targets with a deuteron beam of energy 0.65 Mev. In order to avoid detection of the many products of this bombardment, the beam was pulsed by means of a continuously rotating sector, and the decay products of the Li^8 nuclei were observed only during the period when the beam was interrupted by the sector.

Alpha-particles were detected with a thin, approximately 10-mil, sodium iodide crystal mounted in the vacuum of the target chamber and coupled to a photomultiplier tube through a quartz window. For convenience the alpha-detector was fixed at 90° to the deuteron beam. The target angle was 45°. Hence, the Li^8 nuclei, emitted into a forward 30° cone, were embedded in the target.

Beta-particles were detected with a sodium iodide crystal, 1 in.×1 in.×2 in., and a photomultiplier tube, free to rotate about the source. The cylindrical wall of the aluminum target chamber was about 20 mil thick, allowing beta-particles in the Mev range to pass through with an average loss of 250 kev. A lead collimator was provided between the chamber and the detector.

The pulses from each counter were amplified and passed through a discriminator, giving either a differential or an integral counting rate, and then to the coincidence detector. A switch between each amplifier and discriminator opened and closed the line in synchronization with the pulsing of the beam. The coincidence detector recorded the total number of coincidences, real and accidental, and also the accidental ones separately. The accidental rate was generally less than 10 percent of the real rate.

Differential pulse-height spectra of the alphas and betas are shown at the top of Fig. 1. In the detection of coincidences the

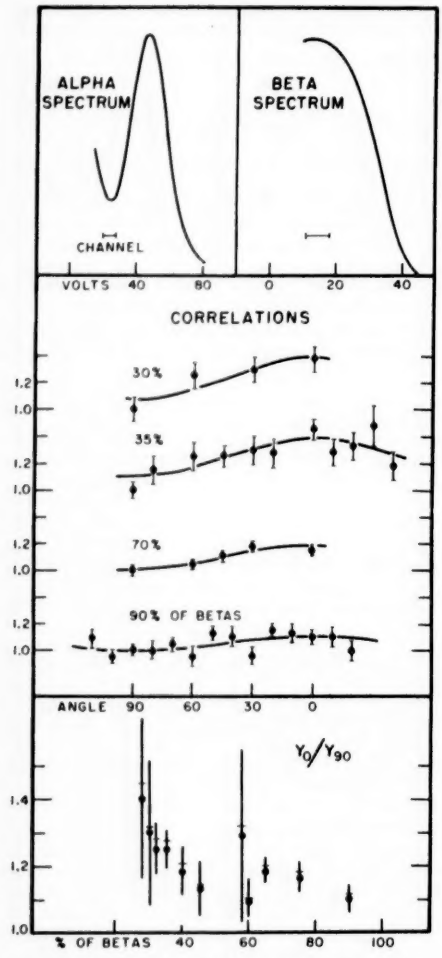

FIG. 1. Top: Differential pulse-height spectra. The prominent alpha-group is the 1.5-Mev group. Middle: Beta-alpha angular correlations for various portions of the upper part of the beta continuum. The 30 percent and 70 percent runs were made with a collimator on the beta-detector. The 35 percent run was with a fairly thick source. The alpha-detector was located at 180°. Bottom: Ratio of yields at 0° and 90° for various portions of the upper part of the beta-spectrum.

integral outputs of the discriminators were used. For the alpha-particles the bias was selected to include the 1.5-Mev group, which predominates (~90 percent).[2] Any higher energy groups were discriminated against in the detection of coincidences, either partially or wholly by the bias setting of the beta-discriminator, which ranged from an electron energy of 2 to 8 Mev. In Fig. 1 these settings are indicated by giving the approximate fraction of the beta-spectrum observed.

The data in Fig. 1 are the number of coincidences per recorded beta-particle. The curves, obtained by least-square analysis, are of the form $1+A_2\cos^2\theta$ and provide a reasonable description of the observations. Additional observations were made of the yields at 0° and at 90°. The ratio $Y_0/Y_{90}=1+A_2$ is plotted as a function of the bias setting of the beta-discriminator, at the bottom of Fig. 1. There is an apparent increase in the value of A_2 with increasing beta-energy, in accordance with the theoretical expectation. Approximate solid angle and scattering corrections have been made, and the corrected ratios are shown by the horizontal lines in the figure.

For the case $0^+-2^+-0^+$ for $Li^8-Be^8-He^4$, discussed by Gardner,[1] a pronounced maximum around 45° ($\sim\cos^2\theta-\cos^4\theta$) is expected. The results, therefore, favor the alternative scheme, $3^--2^+-0^+$, which gives $1+A_2\cos^2\theta$. Other assignments, including the possibility that the Be^8 state is double, have not yet been investigated. Any departure from isotropy rules out the possibility of spin 0 for the Be^8 state and confirms the forbidden character of the beta-process.

We are greatly indebted to Lt. Col. E. C. LaVier, USAF, for generous assistance in performing the experiment.

† Assisted by a contract with the U. S. Atomic Energy Commission.
* Now at Rice Institute, Houston, Texas.
[1] J. W. Gardner, Phys. Rev. **82**, 283 (1951).
[2] W. F. Hornyak and T. Lauritsen, Phys. Rev. **77**, 160 (1950).

Spontaneous Fission Rate of Cf^{246}†

E. K. HULET, S. G. THOMPSON, AND A. GHIORSO
Radiation Laboratory and Department of Chemistry, University of California, Berkeley, California
(Received December 22, 1952)

IN order to obtain further data which may be useful in a study of the spontaneous fission process as, for example, in confirmation of the exponential dependence of the spontaneous fission rate upon Z^2/A of even-even nuclides,[1,2] the spontaneous fission half-life of Cf^{246} has been measured. An extrapolation of previously available data[1,2] indicated that Cf^{246}, for which Z^2/A equals 39.04, should have a spontaneous fission "half-life" of approximately 2000 years. Our measured value is 2100±300 years, which is in excellent agreement with that predicted.

The californium isotope was produced by helium ion bombardment of curium containing all the isotopes ranging from Cm^{242} to Cm^{245}, inclusive.[4] The target technique employed in this work has been previously described.[5] The curium used in this experiment had been produced by a neutron irradiation of long duration of Am^{241} at a position of high flux in the Chalk River pile.[6] After bombarding the curium with 35-Mev helium ions, the californium was separated from other elements, using previously described combinations of precipitation and ion exchange chemical methods.[7] By alpha-pulse analysis at the beginning of the experiment, the californium fraction was observed to contain essentially pure Cf^{246} radioactivity except for a small fraction of Pu^{238} alpha-radioactivity incompletely separated. The amount of Pu^{237}

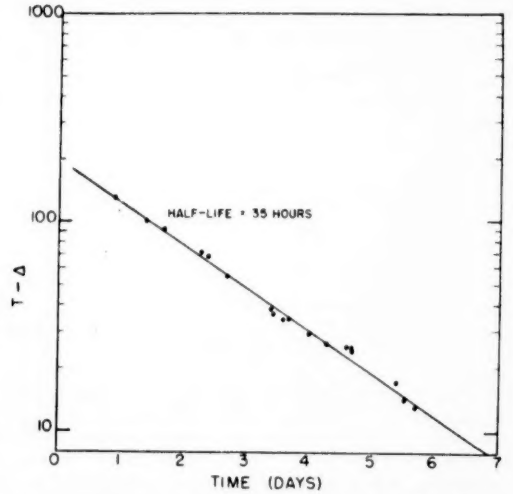

FIG. 1. Decay curve of observed fissions. T = total number of fissions observed and Δ = number of fissions observed to the time t.

present was insufficient to produce any spontaneous fission events in view of its long half-life for this process.[1]

The fission rate was determined by placing a known quantity of Cf^{246} in a thin deposit on one electrode of a parallel plate ionization chamber, filled with a mixture of argon and carbon dioxide. A stylus recorder maintained a record of each fission event and time of occurrence until essentially all of the Cf^{246} had decayed. The fission rate decreased with the same 35-hour half-life as that observed for the alpha-decay of Cf^{246},[4] thus proving that the fissions recorded originated from this isotope. The experimental data are best summarized in Fig. 1. The ratio of the alpha-disintegration rate to the spontaneous fission rate is 5.2×10^5, giving by a simple computation the spontaneous fission half-life of 2100 years. In view of its close agreement with the predicted value, this result might then be considered as evidence that a subshell of 148 neutrons does not exist since, on the basis of the considerations by Seaborg,[1] an abnormally small nuclear radius due to a closed subshell might be expected to result in an increased rate of spontaneous fission.

We are especially indebted to Professor Glenn T. Seaborg for his continued advice and encouragement during the course of this work. We also wish to express our appreciation to Professor J. G. Hamilton, G. B. Rossi, and the operating crew of the 60-inch cyclotron of the Crocker Laboratory for the intensive bombardment of curium, and to Nelson Garden and the Health Chemistry group for providing the excellent protective equipment used in handling the high level alpha-radioactivity. Likewise, the cooperative effort of the Canadian Chalk River Laboratory in handling some difficult problems connected with irradiating and shipping the sample is greatly appreciated.

† This work was performed under the auspices of the U. S. Atomic Energy Commission.

[1] G. T. Seaborg, Phys. Rev. **85**, 157 (1952).
[2] W. J. Whitehouse and W. Galbraith, Nature **169**, 494 (1952).
[3] Ghiorso, Higgins, Larsh, Seaborg, and Thompson, Phys. Rev. **87**, 163 (1952).
[4] Hulet, Thompson, Ghiorso, and Street, Phys. Rev. **84**, 366 (1951).
[5] Thompson, Ghiorso, and Seaborg, Phys. Rev. **80**, 783 (1950).
[6] Reynolds, Hulet, and Street, Phys. Rev. **80**, 467 (1950).
[7] Thompson, Street, Ghiorso, and Seaborg, Phys. Rev. **80**, 790 (1950).

Statistical Fluctuations in Ionization by 31.5-Mev Protons*

G. J. Igo, D. D. Clark,† and R. M. Eisberg
Radiation Laboratory, Department of Physics, University of California, Berkeley, California
(Received December 29, 1952)

USEFUL methods of identifying particles of different mass often involve a measurement of specific ionization and some other parameter such as momentum, energy, or range. These schemes require a counter of small stopping power and good proportionality to measure the ionization. It has often been thought that a gas proportional counter admirably satisfies these requirements, on the assumption that the statistical fluctuations in the energy loss of the particles traversing the counter are governed by the statistical fluctuations in the number of ion pairs, as calculated on the basis of about 25 ev per ion pair. Experiment and the theory of Landau and of Symon indicate, however, that the fluctuations are considerably larger.[1-3]

Protons of 31.5-Mev energy from the Berkeley linear accelerator were scattered elastically from a 0.00025-inch Pb target through a proportional counter and stopped in a NaI counter. The solid angle accepted was defined by a $\frac{1}{4}$-inch hole in a brass plate 10 inches from the target; this hole was centered on the 0.0005-inch thick, $\frac{1}{4}$-inch diameter windows of the proportional counter. The counter telescope and target were in an evacuated scattering chamber. The scattered protons passed through the cylindrical counter perpendicular to its axis and straddling the wire. The counter was $\frac{3}{4}$-inch i.d. and 5 inches long. The 0.003-inch stainless steel wire was accurately centered; the counter was thoroughly outgassed and filled with a mixture of 96 percent A and 4 percent CO_2 and operated at 1700 volts. The elastic protons were separated by means of a single channel pulse-height analyzer fed from the NaI counter, and the output of the analyzer was used to trigger the sweep of an oscilloscope; the proportional counter pulses after amplification and suitable delay were applied to the vertical plates. The oscilloscope screen was photographed on moving film and the film read on a microfilm viewer. The stability and linearity of the system have been shown to be reliably good in previous work.

An estimate of the inherent resolving power of the proportional counter was obtained by a pulse-height analysis of the pulses from collimated 5.5-Mev alpha-particles, which had an energy of 1.6 Mev and a range of about $\frac{3}{4}$ cm after penetrating the counter window. The observed distribution was approximately Gaussian with a full width at half-maximum of 17 percent. Lack of perfect collimation would introduce about 3 percent spread. The effect of fluctuations in energy loss in passing through the window are difficult to estimate; range straggling at this energy is about 2.5

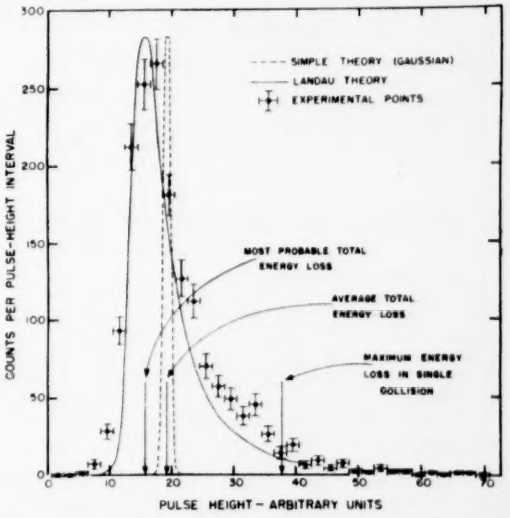

FIG. 1. Frequency distribution of energy losses of 31.5-Mev protons traversing $\frac{1}{4}$-inch proportional counter. Histogram of experimental points shows standard deviations and channel widths. The theoretical Landau distribution is computed from Symon (reference 2). The dashed curve is a Gaussian distribution based on ion pair statistics.

percent and, as the counter sees only the end of the track, this fluctuation is madnified by a factor of four or more. Thus the inherent resolving power of the proportional counter is 12 percent or better and certainly adequate to investigate the observed distribution.

Figure 1 shows the histogram of 1636 pulses read. Amplifier noise limited the accuracy of reading the pulses to within the channel widths chosen. The pulse-height distribution has been observed to be independent of beam intensity, thus indicating that no significant part of it is due to pile-up. A theoretical curve was computed from the formulas and curves of Symon.[2] For comparison with experiment, both the theoretical curve and the experimental points were plotted on log-log graphs; the best fit by eye then gave scaling factors for both coordinates. The solid curve is the resulting theoretical distribution; no additional factors introducing spread have been folded in. The theoretical values of average total energy loss and of maximum energy loss by a 31.5-Mev proton in a single collision with an electron are shown. For comparison there is also shown a Gaussian distribution about the average of the width determined by statistics on the number of ion pairs formed at 25 ev per ion pair. The Gaussian

curve is arbitrarily normalized to the same maximum value as the Landau distribution.

The surprisingly broad distribution with a high energy tail is due to the non-negligible probability of collisions in which the charged particle imparts large kinetic energy to the electron. This reduces radically the number of primary collisions, thus increasing the width of the statistical distribution, and in addition gives rise to the high energy tail. Note in Fig. 1 the maximum allowable energy loss in a single collision is, in this particular case, approximately twice the average total energy loss of the proton in the counter. This is in sharp contrast to the very narrow pulse-height distributions that have been observed in the case in which the charged particle expends its entire track in the counter because, in this case, the statistical fluctuations are due only to the variations in the ratio of energy loss in ionization to energy loss in excitation.

The authors express their appreciation for advice given by Professor L. Alvarez and Professor O. Chamberlain.

* This work was performed under the auspices of the U. S. Atomic Energy Commission.

† U. S. Atomic Energy Commission Predoctoral Fellow.

[1] L. Landau, J. Phys. (U.S.S.R.) **8**, 201 (1944).

[2] K. R. Symon, thesis, Harvard University, 1948 (unpublished). Parts of this work appear in B. Rossi, *High Energy Particles* (Prentice-Hall, Inc., New York, 1952).

[3] N. Bohr also discusses the theory in Phil. Mag. **30**, 581 (1915) and Kgl. Danske Videnskab. Selskab Mat.-fys. Medd. **18**, No. 8 (1942). The Landau effect has also been observed with minimum ionization electrons and mesons. See, for example, Hanson, Goldwasser, and Mills, Phys. Rev. **86**, 617 (1952), and A. Hudson and R. Hofstadter, Phys. Rev. **88**, 589 (1952).

Correlation between Electron and Recoil Nucleus in He^6 Decay*

BRICE M. RUSTAD AND STANLEY L. RUBY
Columbia University, New York, New York, and Brookhaven National Laboratory, Upton, New York
(Received December 31, 1952)

A STUDY of the correlation between the electron and the recoil nucleus in the He^6-Li^6 decay has been made to determine whether the tensor or axial vector interaction should be retained in the formulation of beta-theory. The remaining interactions, scalar, polar vector, and pseudoscalar, are forbidden for this particular transition on the basis of the allowed ft value of 815 ± 70 seconds[1] and the nuclear spin change[2] $\Delta I=1$. A mixture of the Gamow-Teller interactions is not expected, as there is no evidence from the shape of allowed spectra for the existence of the energy dependent, Fierz interference term.[3,4]

The He^6 gas was produced by bombarding $Be(OH)_2$ powder with fast neutrons from the Brookhaven pile. The end-point energy[1] is 3.50 ± 0.05 Mev and the half-life[5] 0.823 sec. A search for γ-emission accompanying the decay was made by the authors, and also independently by Knox,[6] with negative results. Measurements of the β-spectra and the half-life indicate that the contribution to the counting rate at any energy above 0.5 Mev caused by impurities is less than 3 percent.

A schematic diagram of the apparatus is shown in Fig. 1. A semicylindrical source of He^6 gas was defined by a 0.2 mg per cm^2 aluminum foil and a differential pumping diaphragm which also served to collimate a beam of recoil ions from the source region. All structural parts of the source were constructed of polystyrene and evaporated with a thin coating of aluminum to minimize the scattering of electrons and source charging effects. The recoil nuclei were detected by a twelve-stage, Allen-type electron multiplier. The direction and energy of the electrons were determined by a stilbene scintillation spectrometer which could be positioned at any angle between 100 and 180 degrees from the direction of the recoil beam. A coincidence circuit selected those events in which the recoil detector was activated from 0.08 to 1.15 microseconds after the scintillation spectrometer. To prevent gas scattering, the apparatus was continuously evacuated; during each run, pressure measurements were made to insure that the mean free path of the particles was large compared to the geometrical dimensions of the apparatus.

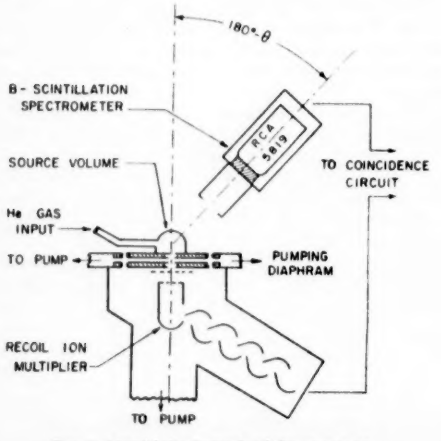

FIG. 1. Simplified schematic of the apparatus.

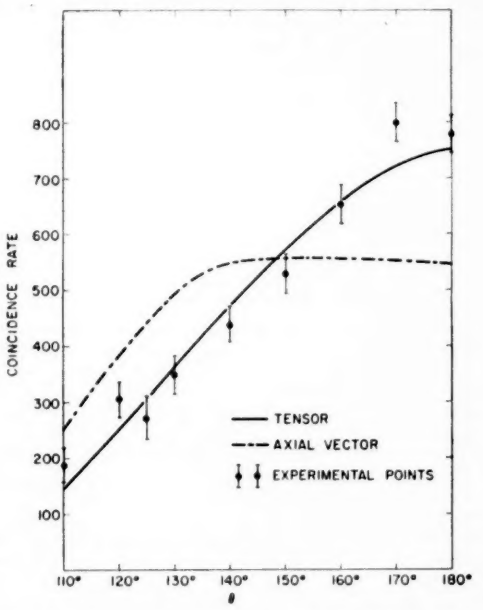

FIG. 2. Coincidence counting rate *versus* angle between electron and recoil nucleus for beta-rays in the range 2.5–4.0 mc^2.

The coincidence rate measured at angles from 110 to 180 degrees between the directions of the electron and the recoil nucleus is shown in Fig. 2. The spectrometer was adjusted to accept electrons only in the energy range between 2.5 and 4.0 mc^2. The experimental points represent the summation of ten individual runs over the angular range.

In Fig. 3, the coincidence counting rate at the angle of 180 degrees between the electron and recoil nucleus is plotted against the energy of the beta-ray. The channel width accepted by the pulse-height analyzer was 1 mc^2.

Curves calculated on the basis of the tensor and the axial vector interactions are presented for comparison with the experimental data. The curves represent the calculated electron-recoil

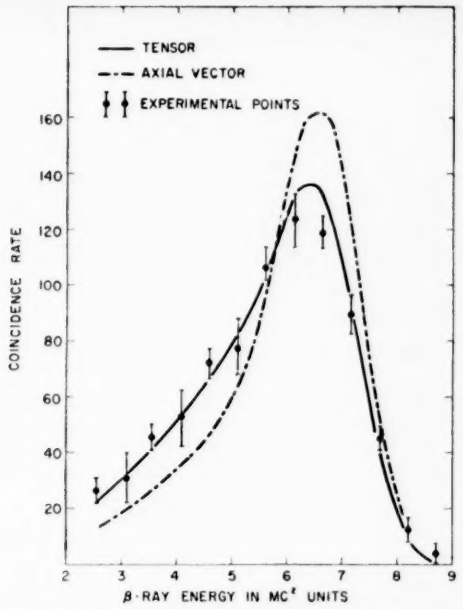

FIG. 3. Coincidence counting rate at 180 degrees between electron and recoil nucleus *versus* energy of beta-ray.

correlation integrated numerically over the solid angles subtended by the detectors and the energy resolution of the scintillation spectrometer. The consistency of both experiments makes it unlikely that instrumental discrimination resulting from the variation of angular position or energy selection systematically affected the data. The agreement between the experimental data and the tensor interaction curves in these experiments indicates that the tensor interaction dominates. This is in agreement with recent data reported by Allen.[7] A complete report covering this work is in preparation.

The authors wish to express their appreciation to Professor J. R. Dunning and Professor E. T. Booth for suggesting this problem, and their gratitude to Professor W. W. Havens, Jr., and Professor C. S. Wu for continual encouragement and many helpful discussions concerning the work.

* Research performed under the auspices of the U. S. Atomic Energy Commission.

[1] Wu, Rustad, Perez-Mendez, and Lidofsky, Phys. Rev. **87**, 1140 (1952).
[2] Hornyak, Lauritsen, Morrison, and Fowler, Revs. Modern Phys. **22**, 291 (1950).
[3] S. R. DeGroot and H. A. Tolhoek, Physica **XVI**, 456 (1950).
[4] C. S. Wu and D. C. Peaslee, private communication.
[5] J. E. R. Holmes, Proc. Phys. Soc. (London) **62**, 293 (1949).
[6] W. J. Knox, Phys. Rev. **74**, 1192 (1948).
[7] J. S. Allen and W. K. Jentschke, Bull. Am. Phys. Soc. **27**, No. 5, p. 17 (1952).

A Test for Charge Independence in High Energy Nucleon-Nucleon Scattering

B. A. JACOBSOHN
Department of Physics, University of Washington, Seattle, Washington
(Received December 8, 1952)

IN a paper on high energy proton-proton scattering, Chamberlain *et al.*[1] mention the inequality,

$$\sigma_{pp}(90°) \lesssim 4\sigma_{np}(90°), \tag{1}$$

as one which must hold if charge independent central forces act between two nucleons. The purpose of this letter is to point out that the inequality (1) holds under much less restrictive conditions and is, in fact, a direct consequence of the assumptions of charge independence and parity conservation for the nucleon-nucleon interaction. In other words, if *np* and *pp* interactions are the same, (1) will be true, no matter what the spin or velocity dependence of the force may be.

Although the proof is easily carried through without it, we shall use the isotopic spin notation. We notice first that, since the wave function must be antisymmetric in all variables, conservation of parity and isotopic spin (T) implies conservation of the magnitude of ordinary spin (S). Then the wave functions in the c.m. frame which represent two nucleons approaching each other along the z axis are

$$\Psi_{ST}{}^{M_S M_T} \to \{[e^{ikz} - (-1)^{S+T} e^{-ikz}]\chi_S{}^{M_S} + (e^{ikr}/r)\Sigma_{M_S'} F_{ST}{}^{M_S M_S'}(\mathbf{n})\chi_S{}^{M_S'}\}\varphi_T{}^{M}. \tag{2}$$

In (2) the χ's are spin functions, the φ's are isotopic-spin functions, and S and T may each be 0 or 1. In the scattering amplitudes F, the quantum number M_T has been omitted, since the scattering is supposed to be independent of orientation in charge-space. Because of the total antisymmetry of the wave function ($\mathbf{n}$ is a unit vector in the scattering direction),

$$F_{ST}(\mathbf{n}) = (-1)^{S+T+1} F_{ST}(-\mathbf{n}). \tag{3}$$

Now all that need be done is to write down the *pp* and *np* cross sections in this notation. Equation (2) yields

$$\sigma_{pp}(\mathbf{n}) = \tfrac{1}{4}[\Sigma_{M_S M_S'} |F_{1,1}{}^{M_S M_S'}(\mathbf{n})|^2 + |F_{0,1}(\mathbf{n})|^2], \tag{4}$$

$$\sigma_{np}(\mathbf{n}) = \tfrac{1}{16}[\Sigma_{M_S M_S'} |F_{1,1}{}^{M_S M_S'}(\mathbf{n}) + F_{1,0}{}^{M_S M_S'}(\mathbf{n})|^2 + |F_{0,1}(\mathbf{n}) + F_{0,0}(\mathbf{n})|^2]. \tag{5}$$

The interference terms spoil any simple comparison of (4) and (5). However, using (3) we can find the following condition necessary for charge-independence:

$$2[\sigma_{np}(\theta) + \sigma_{np}(\pi - \theta)] - \sigma_{pp}(\theta) = \sigma_{T=0}(\theta) \geq 0. \tag{6}$$

The angular distributions for high energy scattering make (6) most restrictive at $\theta = 90°$ (c.m.). In Fig. 1, the relevant high energy data[2] are plotted as functions of the energy. Although the present data satisfy (1) and are therefore consistent with charge independence, the curves show that one would hesitate to predict that (1) will be satisfied for energies greater than about 300 Mev.

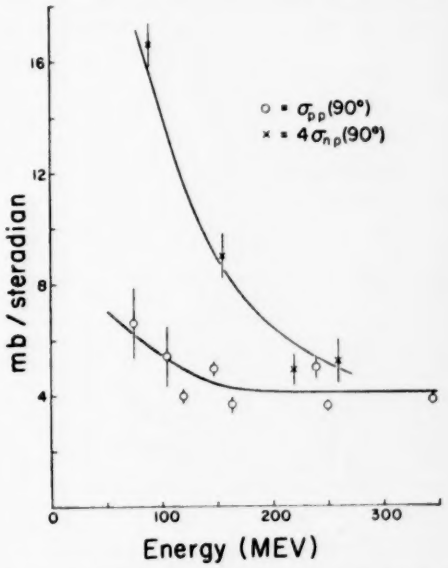

FIG. 1. σ_{pp} and $4\sigma_{np}$ at 90° (c.m.) as functions of the energy. If the scattering is charge independent, the crosses must lie above the circles at all energies.

The fact that (1) is a necessary condition for charge independence, no matter what else is assumed about the nucleon-nucleon interaction, suggests the importance of collecting accurate 90° scattering data at the highest possible energies. However, it should be emphasized that (1) is only a necessary condition; indeed, it is known[3] to be difficult to derive charge independent phase shifts which fit the high energy angular distributions if one uses only the customary velocity independent potentials.

[1] Chamberlain, Segrè, and Wiegand, Phys. Rev. **83**, 923 (1951).
[2] Cassels, Pickavance, and Stafford, Proc. Roy. Soc. (London) **A214**, 262 (1952); Randle, Taylor, and Wood, Proc. Roy. Soc. (London) **A213**, 391 (1952); Guernsey, Mott, and Nelson, Phys. Rev. **88**, 15 (1952). These contain all earlier references.
[3] R. S. Christian and H. P. Noyes, Phys. Rev. **79**, 85 (1950).

Nuclear Stars in Emulsions*

R. W. Waniek† and Taichiro Ohtsuka
Cyclotron Laboratory, Harvard University, Cambridge, Massachusetts
(Received December 29, 1952)

FOR the study of nuclear stars in photographic emulsions, it is highly desirable to have the incoming beam as monoenergetic as possible. In the case of neutrons it is very difficult to meet this requirement. There are a few ways of obtaining neutron beams with a fairly narrow energy spectrum. Namely, degradation of the beam by inserting a hydrogenous absorber or by utilizing the deuteron stripping process. The method we employed in our investigation may be called a "subtraction method." It is based on the following fact: When a beryllium target is bombarded with high energy protons, the emitted neutrons have different spectral distributions at different angles (Fig. 1).[1]

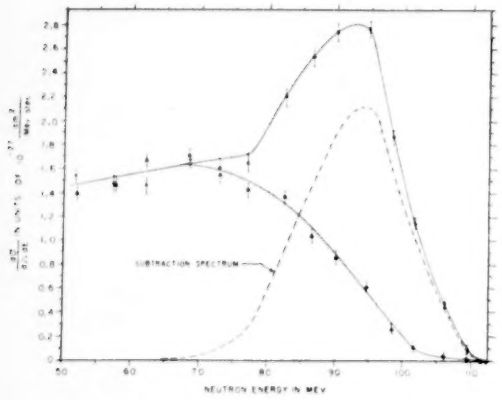

FIG. 1. Neutron spectra from Be. 0°—●; 16°—▲.

From the figure it is evident that the subtraction spectrum exhibits a fairly narrow distribution peaked at about 95 Mev; thus, exposing simultaneously two plates at the two angles, the differences in the results can be attributed to this peak. The experimental set-up was as follows: A $\frac{1}{8}$-inch beryllium target was bombarded with the internal proton beam of the Harvard 95-in. FM-cyclotron. The outgoing neutrons in the 0° and the 14° directions were collimated, and two Ilford Nuclear Plates (G5-200 microns) were exposed simultaneously in "good geometry," subtending the same solid angle at the target. At the same time a three-crystal scintillation counter telescope was set in line with the zero-degree plate to roughly determine the neutron flux (Fig. 2).

About 400 stars were scanned for each plate determining the actual range and the spatial angle for each prong.

Differences in certain features were noticed upon comparison of the results obtained from the two plates. For example, by plotting

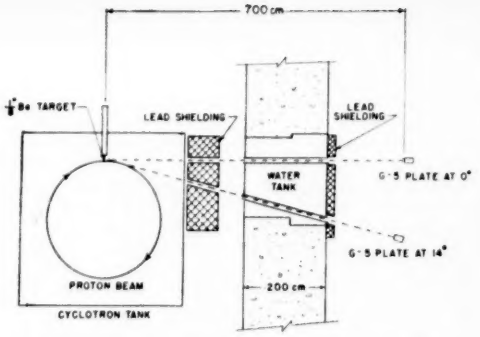

FIG. 2. Exposure of nuclear track plates to neutron beam.

the "asymmetry factor" (ratio of the number of prongs in the forward to the number of prongs in the backward hemisphere) *versus* the star type (indicated by the number of prongs) for each plate one obtains Fig. 3. For isotropic emission the asymmetry

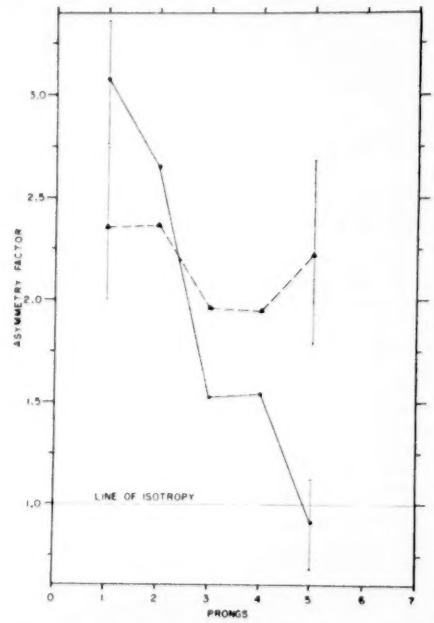

FIG. 3. Asymmetry *vs* prong number. - - - Plate 11, 0°; —— Plate 12, 14°.

factor is equal to 1. One can see from the figure that for the plate exposed at 14°, isotropy is reached much faster than for the plate at 0°. In other words, the larger stars in the 14° plate show practically an isotropic angular distribution, whereas in the 0° plate the prongs are still emitted to an appreciable fraction in the forward direction.

Further differences were detected in the angular distributions and in the number of stars *versus* prong number; thus, the method seems to be discriminative enough to the two different incoming effective neutron energies.

The detailed analysis and discussion for the angular and energy distributions will be published shortly.

* Supported by the joint program of the U. S. Office of Naval Research and the U. S. Atomic Energy Commission.
† Society of Fellows.
[1] K. Strauch and J. A. Hofmann, Phys. Rev. **86**, 563 (1952).

Nuclear Magnetic Resonance of Aligned Radioactive Nuclei*

N. BLOEMBERGEN, *Harvard University, Cambridge, Massachusetts*
AND
G. M. TEMMER, *National Bureau of Standards, Washington, D. C.*
(Received December 23, 1952)

IT occurred to one of us (G.M.T.) that the anisotropy of radiation from radioactive nuclei observed recently[1-4] might be used with advantage for a precise determination of the nuclear gyromagnetic ratio of radioactive isotopes. An experiment is proposed where the minimum number of nuclei necessary to detect magnetic resonance is not determined by the signal-to-noise ratio of radiofrequency equipment, but solely by the statistics of the counters monitoring the radioactive decay. Thus, only minute amounts of the radioactive isotope are needed.[5]

Suppose that in some way a certain alignment of radioactive nuclei in a crystal has been established. When this crystal is subjected to a radiofrequency field of the proper frequency, so that it will induce transitions to levels with other spatial quantization of the radioactive nuclei, the observed radioactive anisotropy will drop or disappear. This effect will occur regardless of the order of magnitude of the spin-spin relaxation time T_2 and the spin-lattice relaxation time[6] T_1. If both T_1 and T_2 are large compared to the inverse of the "nutation frequency" $1/\gamma H_{rf}$, the nuclear spins will oscillate as free spins between the connected spin levels.[7] If $T_2 \ll 1/\gamma H_{rf}$, but $\gamma^2 H_{rf}^2 T_1 T_2 \gg 1$, the nuclear spins will lose their coherence. They will be distributed evenly over the connected spin levels. If finally $\gamma^2 H_{rf}^2 T_1 T_2 \gg 1$, the power absorbed by the radioactive nuclear spins will serve to heat the other degrees of freedom in the crystal. Since a radiofrequency field of a few gauss amplitude will induce transitions at a rate of 10^4 or 10^5 per second, the absorption would be sufficient to increase the entropy of all spins in the crystal in a few seconds, even if the radioactive nuclei occur only in a relative concentration of one part in ten thousand. Spin levels with a much larger splittings, which would require more energy to increase their entropy, need not be considered, since the nuclear alignment will disappear at temperatures, where the contribution to the specific heat of these larger splittings is still negligible. There is absolutely no limitation on the concentration of the radioactive nuclei if $\gamma^2 H_{rf}^2 T_1 T_2 \gg 1$.

Under all circumstances the radioactive anisotropy will be drastically reduced within a few seconds, after the application of a radiofrequency field of sufficient amplitude, at the resonance frequency of the radioactive nuclei. This frequency can thus be determined with the usual precision of the nuclear magnetic resonance in solids. The proposed method, which requires no refined high frequency techniques, is based upon a heating effect, as in Gorter's original proposal of magnetic resonance.[8] The crystal at very low temperatures constitutes a very sensitive calorimeter, the radioactive anisotropy serving as the appropriate thermometer.

If nuclear polarization is obtained for nuclei in nonmagnetic ions, the experiment can be carried out in a known external magnetic field and the nuclear magnetic moment can be measured directly, provided quadrupolar effects can be neglected. So far, nuclear alignment has been obtained only for nuclei in magnetic ions,[1-4] oriented by the strong field from the electron spins. In this case, with zero external field, the magnetic moment can be compared with that of another stable isotope, or the internal field must be calculated from theoretical considerations.[9] The magnetic moment of Co^{60} can be compared with that of Co^{59} in the same salt.[10] The resonance of the Co^{59} nuclei could, of course, also be detected by the heating of the crystal and the disappearance of the radioactive anisotropy of Co^{60}. Bleaney[3] and Gorter[8] have obtained a value of 3.2 ± 0.3 nuclear magnetons for Co^{60} from the observed magnitude of the anisotropy at a known temperature. This approximate value would facilitate the search for the precise magnetic resonance of Co^{60}. A rough calculation indicates that our proposed experiment could be carried out on the samples used by Bleaney and Gorter.

A complication may arise in magnetic salts from nonresonant electronic spin-spin absorption. During the search for the nuclear resonance, the crystal may be warmed up by this spurious absorption. It is true that nuclear alignment is achieved in crystals which are magnetically dilute, so that the nuclear resonance frequency is high compared to the spin-spin frequency. In other words, the hyperfine structure is well resolved. Nevertheless, the absorption in the tail of the spin-spin interaction might still be prohibitively large. If we assume with Broer[11] a Gaussian shape for the spin-spin relaxation, the absorption in the tail will be negligible. It would be interesting in its own right to investigate the nonresonant high frequency absorption in dilute magnetic crystals at very low temperatures. Any of the low temperature thermometers,[12] including the radioactive anisotropy could be used for this purpose.

The experiment is being initiated by the Cryogenics Section of the National Bureau of Standards.

* First reported at the meeting of the American Association for the Advancement of Science, December, 1952, in St. Louis, Missouri.
[1] Daniels, Grace, and Robinson, Nature **168**, 780 (1951).
[2] Gorter, Poppema, Steenland, and Beun, Physica **17**, 1050 (1951).
[3] Bleaney, Daniels, Grace, Halban, Kürti, and Robinson, Phys. Rev. **85**, 688 (1952).
[4] Gorter, Tolhoek, Poppema, Steenland, and Beun, Physica **18**, 135 (1952).
[5] Compare the magnetic resonance in positronium observed by M. Deutsch and S. C. Brown, Phys. Rev. **85**, 1047 (1952).
[6] In order to first establish nuclear alignment, T_1 should not be too long.
[7] See, e.g., N. Bloembergen, thesis, Leiden, 1948 (unpublished).
[8] C. J. Gorter, Physica **3**, 995 (1936).
[9] R. J. Elliott and K. W. H. Stevens, Proc. Phys. Soc. (London) **64**, 205 (1951).
[10] K. D. Bowers (unpublished).
[11] L. J. F. Broer, Physica **10**, 801 (1943).
[12] Steenland, de Klerk, and Gorter, Physica **15**, 711 (1949); D. de Klerk, thesis, Leiden, 1948 (unpublished); M. J. Steenland, thesis, Leiden, 1952 (unpublished).

Exchange Magnetic Moments of Nuclei with Almost Closed Shells of Nucleons

RICHARD W. COLE
Cornell University, Ithaca, New York
(Received December 30, 1952)

THE measured magnetic moments of H^3 and He^3 show that there is an exchange contribution to the magnetic moments of nuclei. Do the measured magnetic moments of heavier nuclei support the same conclusion? Several papers[1] seem to give an affirmative answer. Ross[2] implies that more research is needed before the question can be answered. A detailed study of a few nuclei seems to confirm Ross.

According to the individual-particle model, some nuclei have closed shells of nucleons. Nuclei which have one nucleon outside closed shells or one nucleon missing from a closed shell may be called "closed shell (± 1) nuclei." If the individual particle model were exact and exchange effects contributed nothing, the magnetic moments of closed shell (± 1) nuclei would lie on the Schmidt curves. Feenberg[3] has noted that the measured magnetic moments of closed shell (± 1) nuclei seem to lie nearer to the Schmidt curves than those of other nuclei.

Osborne and Foldy[4] have suggested several operators for the exchange magnetic moment. Some of the operators may be eliminated because they do not have equal and opposite values in H^3 and He^3. An argument about time reversal,[5] which is not conclusive,[6] eliminates other operators. The Osborne-Foldy operators $\mathbf{M}_l$, (c), and (d) remain. The writer has omitted (d) and assumed that the exchange magnetic moment operator is

$$\mathbf{M}_x = \mathbf{M}_l + C \sum_{u,v} f(r_{uv}) \{\boldsymbol{\tau}_u \times \boldsymbol{\tau}_v\}_z \{\boldsymbol{\sigma}_u \times \boldsymbol{\sigma}_v\}$$
$$= \mathbf{M}_l + \mathbf{M}_\sigma.$$

The constant C was adjusted to fit the measured magnetic moments of H^3 and He^3.

In the individual-particle model the expectation value of M_σ in a closed shell (± 1) nucleus is the sum of several terms. Each term is the product of a spatial integral and a matrix element over ordinary and isotopic spin. If the function $f(r_{uv})$ is nowhere negative, the spatial integrals seem to be non-negative. The sign of the integrals has been established for the cases in which $f(r_{uv})$ is a delta-function, a Coulomb potential, or a constant independent of the distance r_{uv} between nucleons u and v. For this reason M_σ tends to put the calculated magnetic moments outside the Schmidt lines; but nearly all the measured magnetic moments are inside. There are at least two ways to reverse such an unwelcome conclusion. Perhaps better wave functions should be used. Perhaps $f(r_{uv})$ is positive when the nucleons are close together and negative when they are far apart, like the nuclear interaction proposed by Lévy.[7] The M_σ exchange moment seems to have the same order of magnitude in light and in heavy nuclei.

The M_σ of four closed shell (± 1) nuclei were calculated. A delta-function was used for $f(r_{uv})$. The radial wave functions $R(r)$ were of the oscillator type

$$R(r) = P(r) \exp(-\tfrac{1}{2}\nu^2 r^2),$$

in which $P(r)$ is a polynomial in r and ν is related to the nuclear radius. The results are listed in Table I. The values of $1/\nu$ are

TABLE I. Calculated and measured magnetic moments.

Nucleus	$1/\nu$	M_σ	M_l	M_x	ΔM
N^{15}	1.5	−0.18	0.1	−0.1	−0.02
O^{17}	1.5	−0.34	?	?	0.02
F^{19}	1.5	0.59	0.0	0.6	−0.16
K^{39}	2.0	−0.20	0.4	0.2	0.27

stated in units of 10^{-13} cm. The $1/\nu$ for H^3 was taken to be 1.6×10^{-13} cm. All magnetic moments are expressed in nuclear magnetons. The ΔM are the deviations of the measured magnetic moments from the Schmidt lines. The ΔM may be compared with the calculated M_x. The values of M_l are those calculated by Spruch.[8]

The preceding results are taken from a doctoral thesis submitted to the Graduate School of Cornell University. Professor Philip Morrison suggested the investigation. Prepublication copies of the papers by Ross and Osborne and Foldy were available.

[1] F. Bloch, Phys. Rev. **83**, 839 (1951); A. deShalit, Helv. Phys. Acta **24**, 296 (1951); H. Miyazawa, Prog. Theoret. Phys. **6**, 263 (1951); A. Russek and L. Spruch, Phys. Rev. **87**, 1111 (1952).
[2] M. Ross, Phys. Rev. **88**, 935 (1952).
[3] E. Feenberg, Phys. Rev. **77**, 771 (1950).
[4] R. K. Osborne and L. L. Foldy, Phys. Rev. **79**, 795 (1950).
[5] G. J. Kynch, Phys. Rev. **81**, 1060 (1951).
[6] E. R. Caianiello, Nuovo cimento **9**, 336 (1952).
[7] M. M. Lévy, Phys. Rev. **88**, 725 (1952).
[8] L. Spruch, Phys. Rev. **80**, 372 (1950).

Superconducting Silicides and Germanides

GEORGE F. HARDY AND JOHN K. HULM
Institute for the Study of Metals, University of Chicago, Chicago, Illinois
(Received January 2, 1953)

WHILE investigating the occurrence of superconductivity among the silicides and germanides of Groups IV, V, and VI transition metals, we have recently observed that the compound V_3Si becomes superconducting at about 17°K, apparently the highest temperature at which the phenomenon has so far been observed.[1] This compound and twenty-nine other silicides and germanides were prepared by sintering compressed pellets consisting of appropriate mixtures of the powdered elements for several hours in an atmosphere of purified helium at 1500°C (silicides) or 1000°C (germanides). Additional specimens which were prepared by melting the compressed pellets in an argon arc furnace gave essentially the same x-ray and superconducting results as those prepared by sintering. The presence of superconductivity was detected by ballistic measurement of the magnetic induction of the specimens in a magnetic field of a few oersteds; the transition temperatures quoted are those for the mid-point of the transition extrapolated to zero field.

The following compounds became superconducting at the temperatures given in parenthesis: V_3Si (17.0°K), V_3Ge (6.0°K), Mo_3Si (1.30°K), Mo_3Ge (1.43°K), $MoSi_{0.7}$ (1.34°K), $MoGe_{0.7}$ (1.20°K), $WSi_{0.7}$ (2.84°K), $ThSi_2$ (3.16°K). On the other hand, compounds which did not show superconductivity at temperatures just below 1.2°K were Ti_5Si_3, Ti_5Ge_3, TiSi, $TiSi_2$, $TiGe_2$, Zr_4Si, Zr_2Si, Zr_3Si_2, Zr_5Si_3, Zr_6Si_5, ZrSi, $ZrSi_2$, VSi_2, $NbSi_{0.6}$, $NbSi_2$, $TaSi_2$, Cr_3Si, Cr_5Si_2, CrSi, $CrSi_2$, WSi_2, $MoSi_2$. It will be noted that in the isomorphous series V_3Si, V_3Ge, Mo_3Si, Mo_3Ge, and Cr_3Si, which have a cubic structure with atomic positions similar to those in β-tungsten, only the chromium compound remained normal down to 1.2°K.

The transition temperature and breadth of transition of V_3Si were found to be rather sensitive to variations in impurity content of the specimens. The purest samples were prepared from vanadium supplied by The Electro Metallurgical Company in which the main impurities were about 0.1 percent of iron and manganese. In these samples, the transition temperatures ranged from about 16.5° to 17°K, the sharpest transition being that of an arc furnace specimen which passed from a completely normal to a completely superconducting state between 17.1° and 16.8°K. On the other hand, both sintered and arc furnace specimens of V_3Si prepared from vanadium containing about 1 percent of iron as its major impurity showed superconducting transitions close to 14.5°K with breadths of more than 1°K. This appreciable drop in transition temperature in the presence of 1 percent Fe suggests that even for our purest samples, containing about 0.1 percent Fe, the transition temperatures probably lie a few tenths of a degree below the correct value for spectroscopically pure V_3Si.

Finally, in an effort to produce superconductivity above 17°K, we replaced a portion of the vanadium or silicon in V_3Si by neighboring elements in the periodic system. The effect of replacing one-tenth of the vanadium by either Ti, Zr, Nb, Mo, Cr, or Ru, or one-tenth of the silicon by either B, C, Al, or Ge, was to depress the transition temperature by amounts ranging from a few tenths to more than ten degrees below that of control specimens of pure V_3Si. Carbon and boron produced the smallest effect, but it must be remarked that although the whole series of specimens was prepared by arc furnace melting, completely homogeneous solid solutions were not formed in all cases.

A detailed account of this work will be published later.

[1] Although Aschermann, Friederich, Justi, and Kramer [Physik. Z. **42**, 349 (1941)], reported superconductivity in niobium nitride at temperatures above 17°K, the more recent work of F. H. Horn and W. T. Ziegler [J. Am. Chem. Soc. **69**, 2762 (1947)] and H. Rögener [Z. Physik **132**, 446 (1952)] indicates that the transition point for this compound is approximately 15°K.

The Tensor Force Interaction between a Shell Closed Except for a Single Vacancy and an External Nucleon

J. HOPE
Department of Mathematics, The University, Southampton, England
(Received December 23, 1952)

THE following results, here quoted without proof, are taken from the author's Ph.D. thesis.[1] They have been derived by an extension of the tensor operator methods introduced by Racah.[2]

General expressions for the tensor force interaction between two separate two-nucleon single-particle configurations have been obtained by L. W. Longdon, of Southampton University, and will soon be published. They are not discussed here. We are concerned with the interaction between two configurations both of which contain a group of $4(2l_1+1)-1$ equivalent nucleons of orbital momentum l_1 (almost closed shell) and both of which

contain an external nucleon, but this is of orbital momentum l_2 in the one configuration and l_2' in the other. The results are given for all of the neutral, symmetric, and charged isotopic spin dependencies.

The direct term is simply related to the corresponding one for the mixing of the two separate two-nucleon configurations l_1l_2 and l_1l_2', obtained from the above by replacing the almost closed shell by a single nucleon of the same orbital momentum, which can be found using Longdon's results. The relationship is as follows: The corresponding direct terms are identical for the neutral isotopic spin dependence and are of opposite sign for the other two cases.

On the other hand, the expression for the exchange term, which as here given is to be added to the direct, reduces to a very simple result. The isotopic spin factors for the three cases are as follows:

neutral	$\delta(T,0)\cdot 2$,
symmetric	$\delta(T,1)\cdot\frac{3}{2}$,
charged	$\delta(T,1)\{\delta(M_T,1)+\delta(M_T,T)\}$,

and the spin, orbit, and radial factor is

$$2\sqrt{5}\delta(S,1)(-1)^{l_1+\frac{1}{2}(l_2+l_2')-J}W(L1L'1,J2)\times\tfrac{1}{2}(2l_1+1)\{(2l_2+1)(2l_2'+1)Cl_1l_2LCl_1l_2'L'\}^{\frac{1}{2}}\times\left[\left\{\frac{C_{LL'2}}{3(2L+1)(2L'+1)}\right\}^{\frac{1}{2}}\{(2L'+1)A^L+(2L+1)B^{L'}\}-\sum_{K=0}^{\infty}\{5(2L+1)(2L'+1)C_{LK1}C_{L'K1}\}^{\frac{1}{2}}W(LL'11,2K)C^K\right].$$

In this expression $W(abcd,ef)$ is a Racah coefficient,[2] and the functions C_{abc} have been tabulated by Shortley and Fried.[3] Also, if one writes the general radial exchange integral,

$$\left.\begin{matrix}A^K\\B^K\\C^K\end{matrix}\right\}=\frac{1}{a_0^6}\int_0^\infty\int_0^\infty u_{n_1l_1}(r_1/a_0)u_{n_2l_2}(r_2/a_0)I^K(r_1,r_2)f(r_1,r_2)\,u_{n_2'l_2'}(r_1/a_0)u_{n_1l_1}(r_2/a_0)r_1^2r_2^2dr_1dr_2,$$

in which $u_{nl}(r/a_0)$ is the general normalized radial wave function (a_0 is the well parameter) and in which $I^K(r_1,r_2)$ is defined in terms of the radial distance dependence $J(r_{12})$ of the tensor force by the expansion

$$J(r_{12})/r_{12}^2=\sum_{K=0}^{\infty}I^K(r_1,r_2)P_K(\cos\theta_{12}),$$

then in the radial integral A^K we have $f(r_1,r_2)=r_1^2$; in B^K it is equal to r_2^2, and in C^K to r_1r_2.

We wish to draw attention to the similarity of these results to those for central forces as derived for the atomic case by Racah. We have also been able to obtain corresponding expressions with a two-particle spin-orbit interaction, but these are more complicated than those for the other forces and will be reported separately. A full account of the derivation of these results is contained in the writer's thesis.

[1] J. Hope, Ph.D. thesis, London University, 1952 (unpublished).
[2] G. Racah, Phys. Rev. **62**, 438 (1942).
[3] G. H. Shortley and B. Fried, Phys. Rev. **54**, 739 (1938).

Approximate Wave Functions for Unbound Relativistic Particles in a Coulomb Field

G. K. Horton and R. T. Sharp
University of Alberta, Edmonton, Alberta, Canada
(Received December 3, 1952)

THE exact relativistic wave functions describing unbound charged particles moving in a Coulomb field are well known.[1] However, they have not proved convenient for actual calculations. This is because they depend on three coordinates; and, in the case of the Dirac equation, the spinor dependence is complicated.[2] For low energy particles, the nonrelativistic Schrödinger equation may be used. As is well known, this equation with a Coulomb potential is separable in parabolic coordinates, and the wave function is fairly simple, depending on only one coordinate. On the other hand, for high energies and low charge, the first Born approximation may be used; in fact, almost all calculations concerning relativistic Coulomb particles have been done in this way. Since the Born approximation is valid only for[3] $|n|\ll 1$, there is a considerable range of charge and energy values not covered by either approximation.

For the Dirac equation, this gap was partially filled by Sommerfeld and Maue.[1] The iterated Dirac equation for a charged particle moving in a Coulomb field is

$$\nabla^2\psi+\left\{\left(E-\frac{zZ}{r}\right)^2-\mu^2\right\}\psi=\left(zZe^2\gamma_4\boldsymbol{\gamma}\cdot\operatorname{grad}\frac{1}{r}\right)\psi,$$

and the solution is[4]

$$\psi(\mathbf{r})=\frac{N}{(2\pi)^{\frac{3}{2}}}e^{i\mathbf{k}\cdot\mathbf{r}}\left\{1-\frac{\gamma_4\beta}{2r}\boldsymbol{\gamma}\cdot\operatorname{grad}_k+O(n^2\beta^2)\right\}L_n(\rho)\Gamma;\qquad(1)$$

also,

$$\varphi(\boldsymbol{\kappa})=-\frac{N}{2\pi^2}\operatorname*{limit}_{\epsilon\to 0}\left[\left\{\frac{\partial}{\partial\epsilon}+\frac{\beta}{2}\gamma_4\boldsymbol{\gamma}\cdot(\operatorname{grad}_k+\operatorname{grad}_\kappa)+O(n^2\beta^2)\right\}\frac{[\kappa^2+(\epsilon-ik)^2]^n}{[\epsilon^2+|\boldsymbol{\kappa}-\mathbf{k}|^2]^{1+n}}\right]\Gamma,\qquad(2)$$

where E, ze, $\mathbf{k}$, μ are, respectively, the energy, charge, momentum, and rest mass of the particle; Ze/r is the Coulomb potential; γ_4, $\boldsymbol{\gamma}$ are the usual Dirac matrices; $N=2\pi in/(1-e^{-2\pi in})$ is a normalizing factor;

$$n=Zze^2/i\beta;\quad\rho=i(kr-\mathbf{k}\cdot\mathbf{r});\quad|\mathbf{k}|=k=\beta E;$$
$$L_n(\rho)=\sum_{j=0}^{\infty}(-)^j\binom{n}{j}\frac{\rho^j}{j!};\qquad(3)$$

Γ is a spinor satisfying $\{i\boldsymbol{\gamma}\cdot\mathbf{k}-\gamma_4E+\mu\}\Gamma=0$; and

$$\phi(\kappa)=(2\pi)^{-\frac{3}{2}}\int d\tau\,\exp(i\boldsymbol{\kappa}\cdot\mathbf{r})\psi(\mathbf{r})$$

is the Fourier transform of $\psi(\mathbf{r})$.

The Sommerfeld-Maue approximation is valid for all energies, and is subject only to the condition $|n^2\beta^2|\ll 1$. This is to be distinguished from the first and second Born approximations, which are subject to the more restrictive conditions $|n|\ll 1$ and $|n^2|\ll 1$, respectively.

The first Born approximation is obtained from (1) and (2) by putting $n=0$. One finds

$$\psi(\mathbf{r})=\frac{1}{(2\pi)^{\frac{3}{2}}}e^{i\mathbf{k}\cdot\mathbf{r}}\Gamma,\quad\varphi(\boldsymbol{\kappa})=-\frac{1}{2\pi^2}\operatorname*{limit}_{\epsilon\to 0}\frac{\partial}{\partial\epsilon}\left\{\frac{1}{\epsilon^2+|\boldsymbol{\kappa}-\mathbf{k}|^2}\right\}\Gamma.\qquad(4)$$

The second Born approximation is obtained from (1) and (2) by expanding to first order in n:

$$\psi(\mathbf{r})=\frac{N}{(2\pi)^{\frac{3}{2}}}e^{i\mathbf{k}\cdot\mathbf{r}}\left(1-\frac{\gamma_4\beta}{2r}\boldsymbol{\gamma}\cdot\operatorname{grad}_k\right)\{1+nf(\rho)\}\Gamma,\qquad(5)$$

where

$$f(\rho)=\operatorname{Ci}|\rho|+i\operatorname{Si}|\rho|-\ln|\rho|-C=\int_0^{|\rho|}\frac{e^{\rho t}-1}{t}dt;\qquad(6)$$

Ci and Si are the cosine- and sine-integral functions, and C is Euler's constant.

The Fourier transform of (5) is

$$\varphi(\boldsymbol{\kappa})=-\frac{N}{2\pi^2}\operatorname*{limit}_{\epsilon\to 0}\left[\left\{\frac{\partial}{\partial\epsilon}-\frac{\beta}{2}\gamma_4\boldsymbol{\gamma}\cdot(\operatorname{grad}_k+\operatorname{grad}_\kappa)\right\}\frac{1}{\epsilon^2+|\boldsymbol{\kappa}-\mathbf{k}|^2}\times\left\{1+n\ln\frac{\kappa^2+(\epsilon-ik)^2}{\epsilon^2+|\boldsymbol{\kappa}-\mathbf{k}|^2}\right\}\right]\Gamma.\qquad(7)$$

For the Klein-Gordon equation with a Coulomb potential,

$$\nabla^2\psi+\left\{\left(E-\frac{zZe^2}{r}\right)^2-\mu^2\right\}\psi=0,\qquad(8)$$

the solution in the Sommerfeld-Maue approximation is

$$\psi(\mathbf{r})=\frac{N}{(2\pi)^{\frac{1}{2}}}e^{i\mathbf{k}\cdot\mathbf{r}}\left\{1+\frac{in\beta^2}{2r}\frac{\partial}{\partial k}+O(n^4\beta^4)\right\}L_n(\rho); \quad (9)$$

also

$$\varphi(\boldsymbol{\kappa})=-\frac{N}{2\pi^2}\lim_{\epsilon\to 0}\left[\frac{\partial}{\partial\epsilon}+\frac{in\beta^2}{2}\left(\frac{\partial}{\partial k}+\frac{\mathbf{k}\cdot\operatorname{grad}_{\boldsymbol{\kappa}}}{k}\right)+O(n^4\beta^4)\right]\frac{[\kappa^2+(\epsilon-ik)^2]^n}{[\beta^2+|\boldsymbol{\kappa}-\mathbf{k}|^2]^{1+n}}. \quad (10)$$

The approximation is definitely better than in the Dirac case, since it is correct to third order in $n\beta$ instead of only to first order. The first Born approximations may be obtained from (9) and (10) by putting $n=0$. The result is

$$\psi(\mathbf{r})=\frac{N}{(2\pi)^{\frac{1}{2}}}e^{i\mathbf{k}\cdot\mathbf{r}},\quad \varphi(\boldsymbol{\kappa})=-\frac{1}{2\pi^2}\lim_{\epsilon\to 0}\frac{\partial}{\partial\epsilon}\frac{1}{\epsilon^2+|\boldsymbol{\kappa}-\mathbf{k}|^2}.$$

The second Born approximation is obtained from (9) and (10) by expanding to first order in n:

$$\psi(\mathbf{r})=\frac{Ne^{i\mathbf{k}\cdot\mathbf{r}}}{(2\pi)^{\frac{1}{2}}}\{1+nf(\rho)\}, \quad (11)$$

$$\varphi(\boldsymbol{\kappa})=-\frac{N}{2\pi^2}\lim_{\epsilon\to 0}\frac{\partial}{\partial\epsilon}\left\{\frac{\left[1+n\ln\frac{\kappa^2+(\epsilon-ik)^2}{\epsilon^2+|\boldsymbol{\kappa}-\mathbf{k}|^2}\right]}{[\epsilon^2+|\boldsymbol{\kappa}-\mathbf{k}|^2]}\right\}. \quad (12)$$

We have derived explicit expressions for the momentum wave functions because they are of considerable interest for various atomic and nuclear problems.[5]

We have applied these approximations to a number of atomic and nuclear processes, and we intend to communicate our results shortly.

[1] See, for example, A. J. W. Sommerfeld, *Atombau und Spektrallinien* (F. Vieweg und Sohn, Braunschweig, 1939). The explicit Coulomb wave functions for unbound particles obeying the Klein-Gordon equation will be given by us in a paper on meson capture processes to be published shortly.

[2] See, for example, J. C. Jaeger and H. R. Hulme, Proc. Roy. Soc. (London) **148**, 708 (1935), where the exact solution of the Dirac equation in the presence of a Coulomb field is applied to the problem of internal pair creation. The authors are forced to resort almost entirely to numerical integrations. Also, Casimir's trick for effecting spin summation cannot be used with these wave functions. It can, however, be used in conjunction with the wave functions discussed here.

[3] n is defined in Eq. (3). We are using natural units, for which $\hbar=c=1$.

[4] We will refer to this as the Sommerfeld-Maue approximation.

[5] See, for example, the remarks of E. Guth and C. J. Mullin, Phys. Rev. **83**, 667 (1951). These authors gave the momentum wave function in the nonrelativistic approximation.

Production of Polarized Particles in Nuclear Reactions

A. Simon and T. A. Welton
Oak Ridge National Laboratory, Oak Ridge, Tennessee
(Received December 29, 1952)

Schwinger[1] has shown that polarized neutrons may be obtained by the elastic scattering of neutrons from He^4. We wish to point out that this result is a special case of a more general theorem to the effect that, under suitable conditions, the products of *any* nuclear reaction will be polarized. As a result it should be possible to use resonant charged particle reactions to obtain directly (rather than by an intervening elastic scattering) high intensity beams of polarized neutrons, with energies variable over a considerable range.

We have obtained a general expression for the polarization resulting from nuclear reactions. The original expression contains a number of sums over magnetic quantum numbers, since we must average over the incident unpolarized beam. However, these sums are essentially geometrical in character and may be reduced to their most elementary form by use of the formalism developed by Racah.[2]

The following general results have been obtained: (1) The polarization is always perpendicular to the plane formed by the directions of the incident and emitted particles. (2) If only S waves are effective in the reaction, for either the incident or the final states, there can be no polarization. (3) If only levels of the compound nucleus having $J=\frac{1}{2}$ (or 0) and a single parity are effective, there will be no polarization. (4) Polarization results from the interference of different subchannels (i.e., partial waves or final channel spins) contributing to the reaction. (The state of the residual nucleus must always be the same, of course.) Hence, if there is only a single incident subchannel leading to a single level and breaking up into a single final subchannel, the polarization will vanish. (5) If there is no spin-orbit coupling, the polarization is zero.

The final result yields the following expression for the dependence of the intensity of polarization upon the angle between the incident and emitted beam:

$$P=\sum_{L=1}^{\infty}A_L P_L^1(\cos\theta), \quad (1)$$

where P_L^1 is the associated Legendre function and A_L is a complicated expression involving several Racah functions and the scattering matrix for the reaction. The results have a formal similarity to the expression previously obtained for the angular dependence of reaction cross sections.[3] In particular, a maximum value of L in Eq. (1) is given by a set of rules which are quite similar to the rules for the limitation of the complexity of angular distributions[4] and which follow from the requirements for the nonvanishing of the Racah coefficients.

It is interesting to note that even a single level of definite $J(\neq\frac{1}{2}$ or 0) and parity will produce polarization if more than one subchannel (1-value or final channel spin) contribute. Several known reactions offer promise. In particular, analyses[5] of the angular distribution of (p,n) neutrons resulting from resonances in C^{13}, B^{11}, Li^7, and H^3 indicate that P waves or higher and opposite parities are interfering. In fact, it seems likely that many neutron sources, hitherto considered unpolarized, may actually exhibit partial polarization.

Details of the above and further calculations will appear in a paper to be submitted to this journal in the near future.

[1] J. Schwinger, Phys. Rev. **69**, 681 (1946).
[2] G. Racah, Phys. Rev. **62**, 438 (1942).
[3] C. N. Yang, Phys. Rev. **74**, 764 (1948).
[4] J. M. Blatt and L. C. Biedenharn, Phys. Rev. **82**, 123 (1951).
[5] H. A. Willard, private communication.

Relativistic Contribution to the Magnetic Moment of $^3S_1$ Helium

William Perl, *New York, New York*
and
Vernon Hughes,* *Columbia University, New York, New York*
(Received October 20, 1952)

The nonquantum electrodynamic contribution of order $\alpha^2\sim(137)^{-2}$ to the magnetic moment of helium in the lowest energy triplet (metastable) state $^3S_1$ has been calculated. This contribution arises because the bound two-electron system has a Dirac type rather than a Schrödinger-Pauli type Hamiltonian. The purpose of the calculation was to isolate to order α^2 the quantum electrodynamic radiative contributions to the magnetic moment of a bound two-electron system, for comparison with experiment.[1]

The method of calculation was to reduce the Dirac sixteen-component form of the matrix of external magnetic interaction energy for two electrons to a four-component form in terms of Pauli-approximation wave functions, which could then be evaluated by use of the angular and spin symmetry properties of the Russell-Saunders coupled $^3S_1$ state. This procedure was practicable because L-S coupling could be shown to yield rigorous results to order $\alpha^2\mu_0 H$. Breit's prescription for treating the Breit interaction was followed.[2]

The result derived was that the nonradiative g value for two electrostatically interacting electrons bound in a $^3S_1$ state is, to order α^2,

$$g=2(1-\tfrac{1}{3}\langle T\rangle), \tag{1}$$

where $\langle T\rangle$ is the expectation value of total kinetic energy in the $^3S_1$ state in units mc^2. This result is similar in form and, to order α^2, of equal exactness to the well-known corresponding result of Breit and of Margenau for one bound electron.[3] Equation (1) shows that nonradiative relativistic contributions to the magnetic moment of two interacting bound electrons are not simply the sum of those for two mutually independent bound electrons, but also contain implicitly a contribution from the electrostatic interaction. The radiative contributions to the g-value of the system are, to order α^2, the sum of those for two mutually independent electrons and an explicit contribution from the Breit interaction, of amount minus one-third the expectation value of electrostatic interaction energy in the $^3S_1$ state, in units mc^2.

Equation (1) can be evaluated exactly for helium. The (now permissible) Schrödinger Hamiltonian and the virial theorem give $\langle T\rangle=-W$, where W is the binding energy of $^3S_1$ helium in units mc^2. Either a theoretical or an experimental spectroscopic value of W then yields for the nonradiative g value in $^3S_1$ helium

$$g=2(1+\tfrac{1}{3}W)=2(1-38.7\times10^{-6}). \tag{2}$$

The contribution from the Breit interaction was calculated to be -2.3×10^{-6}. The total theoretical g value in $^3S_1$ helium, to order α^2, is the sum of (2), the Breit interaction contribution, and the second-[4] and fourth-[5] order radiative corrections to the intrinsic electron magnetic moment, or

$$\begin{aligned}(g_{\mathrm{He}})_{\mathrm{theor}}&=2(1+\alpha/2\pi-2.973\alpha^2/\pi^2-41.0\times10^{-6})\\&=2(1+0.0011614-16.0\times10^{-6}-41.0\times10^{-6})\\&=2(1.001104\pm1\times10^{-6}).\end{aligned} \tag{3}$$

The indicated precision $\pm1\times10^{-6}$ of this number stems from a rough estimate of the first neglected radiative and reduced mass corrections. The first neglected nonradiative correction is of order $\alpha^4Z^4\ll10^{-6}$.

The experimental result[1] is the ratio of g value in $^3S_1$ helium and in $^2S_{\frac{1}{2}}$ hydrogen,

$$(g_{\mathrm{He}}/g_{\mathrm{H}})_{\mathrm{exp}}=1-(12\pm15)\times10^{-6}. \tag{4}$$

This experimental ratio is to be compared with the theoretical ratio

$$(g_{\mathrm{He}}/g_{\mathrm{H}})_{\mathrm{theor}}=1-(23\pm1)\times10^{-6}, \tag{5}$$

in which for hydrogen the same radiative corrections as for helium and a nonradiative correction[3] of $\frac{3}{2}W=-\frac{1}{2}\alpha^2=-17.8\times10^{-6}$ have been used. Alternatively, assuming the theory to have been satisfactorily verified for hydrogen[6] and hence multiplying the experimental ratio (4) by $(g_{\mathrm{H}})_{\mathrm{theor}}$, yields

$$(g_{\mathrm{He}})_{\mathrm{exp}}=2(1.001116\pm15\times10^{-6}), \tag{6}$$

which is to be compared with (3).

The agreement between (4) and (5) and between (3) and (6) is within the assigned theoretical and experimental uncertainties, of which the experimental uncertainty is greater than the theoretical by an order of magnitude. This agreement tends to substantiate the theoretical nonradiative g value correction and the additivity properties of the radiative corrections in hydrogen and in helium. A detailed report of this calculation together with a paper on the experiment[1] will be presented soon to *The Physical Review*.

* Present address is Department of Physics, University of Pennsylvania, Philadelphia, Pennsylvania.

[1] Tucker, Hughes, Rhoderick, and Weinreich, Phys. Rev. **86**, 618 (1952). The latest and hitherto unpublished experimental value is quoted in this letter.

[2] G. Breit, Phys. Rev. **39**, 616 (1932).

[3] G. Breit, Nature **122**, 649 (1928); H. Margenau, Phys. Rev. **57**, 383 (1940).

[4] J. Schwinger, Phys. Rev. **82**, 664 (1951).

[5] R. Karplus and N. M. Kroll, Phys. Rev. **77**, 536 (1950).

[6] Koenig, Prodell, and Kusch, Phys. Rev. **83**, 687 (1951).

Proceedings of the American Physical Society

MINUTES OF THE 1952 THANKSGIVING MEETING HELD AT ST. LOUIS, MISSOURI NOVEMBER 28–29, 1952

(Corresponding to *Bulletin of the American Physical Society*, Volume 27, No. 5)

THE 1952 Thanksgiving meeting of the American Physical Society was held at St. Louis, Missouri, in the buildings of Washington University, on Friday and Saturday, November 28 and 29, 1952. We celebrated two anniversaries: the hundredth of the founding of our host institution, and the tenth of the first achievement of a nuclear chain reaction. This latter event occurred in Chicago on the second of December, 1942; thus we met almost exactly on the anniversary; it was commemorated by a group of four speeches, mainly but not altogether of a historical nature, given by A. H. Compton, Enrico Fermi, E. P. Wigner, and W. H. Zinn. The centennial of Washington University was the theme of some of the after-dinner speeches. There were one hundred and thirty-six contributed papers, and fourteen invited papers in addition to the four just mentioned and the three which constituted the Symposium on Physical Electronics arranged by our Division of Electron Physics. The abstracts of the former and the titles of the latter are reproduced from the *Bulletin* in the following pages. The weather was frigid on the Friday and blizzardy on the Saturday; this did not impair the total registration—507, a figure almost equal to those attained of recent years at the Thanksgiving meetings in Chicago—but may have curtailed the audiences of the Saturday afternoon sessions. The arrangements made by the Local Committee (C. Sharp Cook, Chairman) were excellent, and the Society owes to its members a debt of gratitude.

The banquet of the Society was held on the Friday evening on the Starlight Roof of the Chase Hotel, with an attendance of 176. The after-dinner speakers were A. H. Compton and A. L. Hughes of Washington University, J. B. Macelwane and A. H. Weber of St. Louis University.

The Council met on Friday. It elected 7 candidates to Fellowship and 369 to Membership; their names are appended. Among its other transactions, an item of peculiar interest is the statement appended to these Minutes, which was adopted by the Council and is to be sent to certain high officials of the Federal Government after the change of administration. From the Treasurer's Report it transpired that the financial situation of the Society shows a marked betterment owing to the drastic steps lately taken to increase the revenues of the Society and owing also to the generous grant of the National Science Foundation which has covered a part of the deficit of *The Physical Review*. The thirty-year cumulative index of this journal (1921–1950) is on the verge of appearing, and the prices at which it will be offered to members and to nonmembers of the Society will shortly be determined. S. A. Goudsmit and J. H. Van Vleck are nominated to the Governing Board of the American Institute of Physics for three-year terms commencing in 1953.

Elected to Fellowship: A. L. Bennett, L. T. Bourland, F. E. Fox, E. Gerjuoy, H. F. Olson, M. H. Schrenk, and J. H. Simons.

Elected to Membership: Mercedes M. Agogino, Richard W. Aldrich, George A. Alers, William L. Alford, J. F. Allen, Floyd E. Allison, Joseph R. Altieri, Avraham Amith, Fred J. Anders, Jr., Albert D. Anderson, Carl G. Anderson, Jr., *John S. Arents, Sidney C. Argyle, Ivan M. Aron, Milton Aronoff, Ranga K. Asundi, Toshio Azuma, David R. Bach, Harold J. Babrov, *Duane L. Barney, Robert M. Baum, Alan J. Bearden, *Ralph E. Behrends, *Paul A. Bender, Francis D. Benedict, Robert D. Bent, Forrest R. Biard, George R. Bird, Irving H. Blifford, Jr., Charles L. M. Blocher, Robert C. Block, Alan J. Blotcky, Daniel E. Bloxsom, Jr., Kees Bol, *Edwin Blue, Jacques Bonanomi, *John Boring, Norman Braslau, *Sheila Brenner, *Manuel M. Bretscher, Robert K. Brinton, John W. Brogden, Joseph W. Brouillette, Jr., Norman L. Brown, Floyd E. Bulette, Harold Burris-Meyer, Barney L. Byrum, Jr., Nicolas Cabrera, William Caithness, *Wallace H. Campbell, Tucker Carrington, Arthur B. Carson, *Samuel M. Carter, Joseph W. Chamberlain, Jesse G. Chaney, John E. Chappelear, Bernard Chern, Joseph P. Chernoch, Alexander S. Chodakowski, Jack E. Clair, Abraham Coblenz, Lewis W. Cochran, Irving Cohen, Marshall H. Cohen, *Leon N. Cooper, Raymond D. Cooper, David F. Cope, Robert M. Cotts, Laurence J. Couch, John H. Cover, Jr., Alvin E. Cowan, Samson A. Cox, William W. T. Crane, Warren A. Crapo, Frank S. Crawford, Jr., Alexander Cybriwsky, George F. Dalrymple, Richard F. Daly, Alvin H. Davis, Cecil G. Davis, Jr., Thomas B. Day, Ernest A. DeMetre, Howard C. DeShon, Richard D. Deslattes, David DeWitt, Charles A. Domenicali, Robert E. Donaldson, James R. Donhaiser, Edward Doucette, McLane Downing, James W. Easley, David C. Eckhardt, *David F. Edwards, *Fred H. Eisen, *Maurice Eisenstadt, Robert A. Ellis, Jr., George Frederick Emch, Werner S. Emmerich, Hiroshi Enatsu, Ludwig I. Epstein, William C. Erickson, Fred P. Evans, Arthur A. Evett, William H. Faulkner, Jr., William S. Filler, Reinald G. Finke, David Finkelstein, Vera K. Fischer, Marshall Fixman, Ernest G. Fontheim, Bruce Parks Foster, Kenneth W. Foster, *Peter A. Franken, *Reuben G. Freemantle, Walter R. French, Jr., James P. Friend, Alfred J. Gale, Themistocles E. Ganias, *Donald M. Gardner, William H. Gardner, Jr., Charles A. Gasper, *Ednah H. Geer, Michael J. Geroulo, Robert Pertsch Gilbert, James C. Gilfert, Luc. P. Gillon, Francis N. Glover, S.J., Julien R. Goens,

Alan A. Goerlitz, Robert C. Goettelman, s-Norman Goldberg, s-Walter I. Goldburg, Ralph R. Goodman, Dale Goodson, Daniel I. Gordon, Robert B. Green, Jean L. Groven, s-Martin L. Gursky, G. Richard Hagee, Melvyn L. Halbert, James A. Hall, s-Lynn Hall, William C. Hansen, Robert S. Harding, Edward G. Harris, Richard I. Harrison, William E. Hassinger, Jr., James Forman Hawk, Janet A. Hawkins, Harry G. Heard, Charles B. Hearns, Lawrence A. Heinrich, s-Robert W. Hendricks, William H. Hewitt, Jr., s-Wilson J. Hicks, Gordon L. Hiebert, Merle N. Hirsh, David C. Hiser, Donald F. Holcomb, William C. Holton, s-Richard F. Hood, Fritz G. Houtermans, Vaino T. Hovi, Ronald Huby, s-Lloyd G. Hyman, Ryutaro Ishiwari, Yoshide Ishizaki, Gordon F. Jacobus, Aloysio Janner, Franco P. Jona, Frank C. Jorgensen, George F. Jubber, Ronald E. Kagarise, Bernd Kahn, Paul P. Kallos, Tohru Kamei, Asher D. Kantz, Arno R. Kassander, Jr., Akira Katase, Ludwig Katz, Pieter H. Keesom, Charles Hardy Kelley, William R. Kennedy, John William Kiebler, s-Lawrence E. Killion, Leonard Kings, Toichiro Kinoshita, Jun Kokame, Tadashi Komura, Evani Kondaiah, Charles J. Kriessman, Paul W. Kruse, Jr., Alan B. Kuper, John L. Kuranz, s-Ivan Ladany, Marvin E. Lasser, Eugene Clark LaVier, Alan J. Lazarus, John P. Lazarus, s-Theodore E. Leinhardt, C. W. Li, James P. Lincoln, Cyril T. Linder, Rufus C. Ling, s-Peter B. Linhart, s-Egon E. Loebner, Earle Leonard Lomon, s-Frank J. LoSacco, s-Robert I. Louttit, Jan D. Louw, s-Radon B. Loveland, s-Irving J. Lowe, Oscar T. S. de Lozada, Marvin Lubert, William M. MacDonald, Anthony J. MacKay, Romulo Maciel, Robert A. Mack, Cleon A. Mackliet, William George Maisch, Jerry B. Marion, Hugh J. Martin, Jr., Cecil Bernard Mast, Michael M. May, Malcolm McCaig, David O. McCoy, John T. McLane, James W. Meadows, Jr., David O. Melroy, Andre Mercier, George E Merer, Jean May Meszaros, Frank H. Meyer, Kozo Miyako, James E. Monahan, James A. Moore, Thomas Wendell Morris, Richard G. Morrison, John C. Morrow, III, Frank Moser, Daniel T. Murphy, Charles Muscietta, Jr., Jiro Muto, Jon H. Myer, Sigeru Nagahara, Yoichiro Nambu, Joseph Nemarich, Robert T. Nieset, s-Richard E. Nightingale, Kazuo Niira, Kiyoshi Nishikawa, Keigo Nishimura, Takehiko Oguchi, Kimio Ohno, Albert Okazaki, John F. Ollom, Keith W. Olson, Robert W. Olthuis, s-George T. Orrok, s-Leif Owren, Seiichi Oyama, Joseph M. Palmer, James N. Payne, Maung H. Pe, Lester C. Peach, Cabell A. Pearse, Charles W. Peters, Robert C. Placious, Jack R. Plaster, Hans S. Plendl, Edward Prince, Lyde S. Pruett, John S. Pruitt, Theodore T. Puck, William Knox Pursley, Boris Ragent, s-Stanley W. Rasmussen, Barton J. Raz, Junius B. Reynolds, Charles A. Roberts, Jr., James W. Roberts, Jr., Frederick A. Rojak, Thomas A. Romanowski, s-Robert H. Romer, Frederick Rothwarf, Joseph A. Rudolph, Seymour Sack, Yoshio Saji, Freda Salzman, Raymond I. Schneyer, James Asher Schoke, Efrem S. Schwartz, Gifford G. Scott, Mary J. Scott, Karl William Seemann, Judah Seigel, Robert J. Shalek, Robert B. Shearer, Edwin F. Shelley, Sakae Shimizu, Gen Shirane, Hideo Sibata, Tunshiko Sidei, Samuel D. Siegel, Charles C. Silva, Jr., Searl J. Silverman, Harold Alfred B. Simons, Kundan S. Singwi, Grimes G. Slaughter, James H. Smith, William B. Snow, Billie M. Soileau, Masateru Sonoda, Lewis Van C. Spencer, Joel S. Spira, William Squire, Burton E. Squires, Jr., Harold P. Stephenson, Fred A. Sterzer, s-William L. Stirling, P. H. Stoker, s-Joseph Sucher, Robert E. Swanson, Stanley F. Swiadek, Hisawo Takebe, Hidenkuni Takegoshi, Igal Talmi, Thomas S. Teasdale, James W. Teener, Alfred W. Thiele, Edward C. Thomas, Lewis C. Thompson, Michael Tinkham, Louis F. Torghele, Toshiyuki Toyoda, Frank K. Truby, s-William E. Turchinetz, s-Daniel H. Tycko, Aaron J. Ulrich, Paul M. Uthe, Jr., Edward R. Van Driest, William H. Vaughan, Vendryes Georges, Helene Ven Horst, William Ferdinand Vogelsang, Peter E. Wagner, Thomas E. Wainwright, Joseph F. Walsh, Peter J. Walsh, Shyh Wang, David I. Wanklyn, Robert K. Waring, Jr., s-Marcel Weinrich, Roy M. Weinstein, Frank L. Wellcome, Jr., Robert G. Wheeler, Albert D. Wheelon, s-Eyvind H. Wichmann, Fred Vernon Wilson, Caspar L. Woodbridge, David F. Wright, John J. Yagelowich, Sukeaki Yamashita, Teikichi Yamauchi, Takuji Yanabu, Syukuro Yano, Samuel G. Zizzo, Esther R. Zucker, and Stanley A. Zwick.

s—Student.

KARL K. DARROW, *Secretary*,
American Physical Society,
Columbia University,
New York 27, New York

Statement approved by the Council of the American Physical Society at its meeting in St. Louis, Missouri, November, 1952

In the past few years, the progress of American physics has been impeded by United States visa and passport restrictions. A few American scientists have been denied passports and many distinguished foreign scientists have failed to received United States visas even for short visits to attend scientific meetings. Other foreign scientists fail to come because their visas arrive too late after delays of many months or because they had been irritated by inappropriate questionnaires and inquisitorial personal interrogations. The international notoriety of these difficulties is now such that some international scientific meetings that originally were to be held in the United States are transferred to other countries.

The personal exchange of ideas and the collaboration with foreign scientists are essential sources of information and ideas which cannot be replaced by written correspondence or by the study of foreign publications. The present restrictions of personal contacts are cutting deeply into this important source of our scientific production. This loss of scientific potential may even jeopardize our national security. Had similar regulations been in force prior to 1942, it is questionable if the United States would have developed radar or the atomic bomb during the last war.

This loss to the United States is not compensated by any gain in the security of classified information, since the meetings from which the visitors are

excluded are open scientific meetings on unrestricted subjects. The main reliance for the security of our technical secrets must necessarily be on the very strict guarding of the information by those who have access to it and not on such illusory and ineffective procedures as the exclusion of foreign visitors from open scientific meetings. Furthermore, the interrogations of foreign scientists are chiefly effective in excluding and humiliating scientists who believe in political and intellectual freedom rather than in detecting spies who would be less scrupulous about their answers.

The Council of the American Physical Society is not questioning the propriety of excluding any person who wishes admission to this country with any idea of advancing communism here. However, the Council strongly urges a more realistic approach by the authorities to the problem of travel restrictions so that free scientific interchange will not be impeded.

Errata Pertaining to Papers D10, H10, K3, K9, Q11, X6, X8, X9, and Sp3

D10, by R. H. Sands and G. E. Pake. In lines 12 and 13, "intensity to that of Si^{29} was found to be about 4.3 ± 0.5" should read "intensity to that of Si^{29} was found to be about 2.7 ± 0.5."

H10, by George Antonoff and Raymond Madrazo, Jr. In reference 2 the name "Zakimac" should read "Yakimac."

K3, by W. W. Lindemann and H. J. Hannam. A footnote should be added, reading, "Supported by the Signal Corps." The authors' affiliation is the University of Minnesota.

K9, by Theodore J. Krieger and Hubert M. James. In line 8, "$E(\theta_{ij})=AP_1(\cos\theta_{ij})+BP(\cos\theta_{ij})$" should read "$E(\theta_{ij})=AP_1(\cos\theta_{ij})+BP_2(\cos\theta_{ij})$." In the Author Index, "Kreiger" should read "Krieger."

Q11, by Rolf M. Steffen. Lines 5 and 6 from the end should read "angular correlation: $W(\partial)=1-1.02\cos^2\partial+1.32\cos^4\partial$; $a_2=-1.02\pm0.05$, $a_4=+1.32\pm0.05$, $a_2+a_4=+0.28\pm0.03$."

X6, by D. D. Van Horn. The title should read "Diffusion and the Motion of Phase Boundaries Binary Alloys."

X8, by David B. Langmuir. In line 18 (+) should read (−). In line 19, (−) should read (+). In the last line "negative" should read "positive."

X9, by R. L. Eager and D. B. Langmuir. In line 7, "$2\exp(-110\,000/RT)$" should read "$0.03\exp(-89\,500/RT)$."

SP3, by George Antonoff. In line 13, "comfortable" should read "conformable."

PROGRAMME

FRIDAY MORNING AT 10:00

Brown Hall

(A. L. HUGHES presiding)

Address of Welcome by CHANCELLOR A. H. COMPTON of Washington University
Response by Vice-President ENRICO FERMI of the American Physical Society

Cosmic Rays

Invited Papers

A1. Cosmic-Ray Intensity above the Atmosphere near the Geomagnetic Pole. J. A. VAN ALLEN, *University of Iowa.* (30 min.)

A2. Properties of Cosmic-Ray Intensity Variations. J. A. SIMPSON, *University of Chicago.* (30 min.)

Contributed Papers

A3. Recurring Daily Cycles of Nucleonic Component Intensity.* W. H. FONGER, J. W. FIROR, AND J. A. SIMPSON, *University of Chicago.*—A variation of neutron intensity with a period of one solar day has been found by averaging data over a period of ~65 days. The detectors are lead-paraffin piles containing BF_3 proportional counters to measure the local neutron production from the nucleonic component.[1] Measurements were obtained at geomagnetic latitudes 48°N and 0.5°S at an atmospheric depth of 680 g-cm^{-2}. The mean counting rates at 48°N and 0.5°S were 620 and 380 counts per minute, respectively. After pressure correction the averaged cycles are similar to sine functions with peak to peak amplitude ~1 percent and with maxima near local noon. Using the data at 48°N, significant departures from the *average* cycle have been found for individual days. It has also been found that these departures persist for intervals of 2–3 days and reoccur. The results are insensitive to choice of barometric coefficient.

* Assisted by the Office of Scientific Research, A.R.D.C., U. S. Air Forces.

[1] Simpson, Fonger, and Wilcox, Phys. Rev. **85**, 366 (1952).

A4. Mass Measurements of Heavy Mesons. D. T. KING, NATHAN SEEMAN, AND MAURICE M. SHAPIRO, *Naval Research Laboratory.*—Particles of mass 1400±140 m_e have been observed to originate in apparent nucleon-nucleon interactions of medium energy. The determinations of mass have been derived from measurements of multiple scattering and of grain density on long "gray" tracks associated with collisions of energetic particles with the nuclei of light atoms in photographic emulsions carried high in the atmosphere by free balloons. The accuracy of the mass determinations has been established by corresponding measurements on similar tracks attributable to protons and associated with the disintegration of heavy nuclei in the emulsion. The apparent decay in flight of one of the heavy mesons is described. The relation of the present measurements to those of previous experiments at M.I.T. and Bristol is discussed.

FRIDAY MORNING AT 10:15

Loudermann Hall

(F. B. SHULL presiding)

Reactions of Transmutation

B1. Angular Distribution of (d,t) Reactions.* S. T. BUTLER and E. E. SALPETER, *Cornell University.*—As was recently pointed out,[1] the forward part of angular distributions[2,3] from (d,t) (and also (t,d) (d,He^3) and (He^3,d)) reactions can be analyzed by a method closely analogous to that employed previously[4] for (d,p) reactions. The theoretical distribution is a product of two factors: (1) an oscillating term, identical with that appearing in the (d,p) formula, which depends on the angular momentum transfer; (2) a form factor, directly connected with the momentum space wave function of the triton, which decreases monotonically with angle. An approximate knowledge of the triton wave function is sufficient for determining spin and parities from (d,t) reactions which may be more convenient than the equivalent (p,d) reactions. Further, an accurate determination of (d,t) distributions would furnish direct information on the triton wave function. An analysis of a recent experimental angular distribution[3] for $Be^9(d,t)Be^8$ will be presented. Further possible experiments favorable for investigating the triton wave function will be discussed.

* Supported in part by the ONR.

[1] S. T. Butler and E. E. Salpeter, Phys. Rev. **88**, 133 (1952).
[2] F. A. El Bedewi, Proc. Phys. Soc. (London) **65**, 64 (1952).
[3] H. W. Fulbright *et al.*, private communication.
[4] S. T. Butler, Proc. Roy. Soc. (London) **A208**, 559 (1951).

B2. Angular Distribution and Differential Cross Section of $Li^6(n,\alpha)H^3$.† J. B. WEDDELL AND J. H. ROBERTS, *Northwestern University.*—Photographic plates loaded with enriched

Li^6 were exposed to unidirectional neutrons at energies 1.1, 1.5 Mev.[1] The angular distributions of the tritons of the tritons are plotted as functions of the angle φ_0, in the center-of-mass system, between the triton and neutron, and fitted to expansions of the form $A+B\cos\varphi_0+C\cos^2\varphi_0$. Plates were also exposed to two groups of neutrons, of energy 0.6 Mev and either 1.1 or 1.5 Mev. The total length of the tracks having $\varphi_0<33°$ or $\varphi_0<68°$ was determined, and from comparison of the two resolved groups of tracks we compute the differential cross section, integrated from 0° to 33° or 68°, relative to the values[2] at 0.6 Mev, 33°, 0.17 barn; 0.6 Mev, 68°, 0.27 barn. Preliminary results are 1.1 Mev, 33°, 0.068 barn; 1.5 Mev, 33°, 0.16 barn; 1.5 Mev, 68°, 0.27 barn. Corrections are made for thermal background and for the probability that each track obeys the selection criteria. Work now in progress will extend the results to 2.0 and 2.5 Mev.

† Work performed under AEC Contract.
[1] G. R. Keepin, Jr., and J. H. Roberts, Rev. Sci. Instr. **21**, 163 (1950).
[2] J. M. Blair and R. Holland (private communication).

B3. The Spin of the 7.4-Mev State of Li^7.† W. O. Solano and J. H. Roberts, *Northwestern University*.—We have made a remeasurement of the angular distribution of the tritons from the reaction $Li^6(n, \alpha)$ for 270-kev neutrons. Calculation of the angular distribution $I(\theta)$ assuming spin 5/2 yields a relationship for the ratio R, of the resonance part of the total absorption cross section to the nonresonance part, in terms of the coefficients of the angular distribution.[1] The unpublished absorption cross-section measurements of Blair and Holland show R to be about 3. Fitting the measured angular distribution of tritons in the c.m. system with a function of the form $A+B\cos\theta+C\cos^2\theta$ gives $I(\theta)=0.0556+0.0197\cos\theta+0.0721\cos^2\theta$. Thus $R=3.1$, which is consistent with spin 5/2, as indicated by the total cross section. The measurements were made with Li^6 loaded Ilford *C*-2 nuclear emulsions, exposed to 270-kev neutrons from the Oak Ridge electrostatic generator. Improved techniques permitted a more positive identification of background due to thermal neutrons and a more precise assignment of the probability that a given track may fail to meet geometric selection criteria.

† Work supported by AEC Contract.
[1] M. Peshkin and A. J. F. Siegert, Phys. Rev. **87**, 735 (1952).

B4. Angular Distributions of Protons from the Reaction $F^{19}(d, p)F^{20}$.† H. W. Fulbright, D. A. Bromley, and J. A. Bruner, *University of Rochester*.—A Teflon (CF_2) target was bombarded with 3.6-Mev deuterons from the Rochester 26-inch cyclotron, and the angular distributions of the resulting proton groups were determined using an ionization chamber detector. Table I gives the angular momentum transfer (determined by comparison with the Butler curves) and the cross sections corresponding to the indicated levels in F^{20}. These F^{20} states were found to have even parity, and the ground-state spin was determined to be 1.

TABLE I.

Ground state	$l_n=0$ and 2	$\sigma=0.92\pm0.18$ mb/sterad (at 45°)
0.65-Mev level	$l_n=2$	$\sigma=7.15\pm1.4$ mb/sterad (at 45°)
2.05-Mev level	$l_n=2$	$\sigma<8$ mb/sterad (at 45°)
3.49 and 3.53(ℓ)-Mev level	$l_n=0$	$\sigma=116\pm23$ mb/sterad (at 7°)

† This work was supported in part by the AEC.

B5. Gamma-Rays from Proton Bombardment of Sodium[23].† J. W. Teener, L. W. Seagondollar, and R. W. Krone, *University of Kansas*.—Thick and thin targets of sodium were bombarded with protons at energy intervals of 5 kev over the energy range of 800 to 1700 kev. Thirteen resonances were found at energies in general agreement with earlier work.[1] Each resonance was investigated with the thin target at proton energy intervals of 1 kev. Target thicknesses were calculated by comparison of thick and thin target data by the method of Bernet *et al.*[2] Excitation levels in Mg^{24} were calculated. The energies of the gamma-rays emitted at several resonances were compared by means of a single NaI(Tl) crystal to the energies of gamma-rays from Cs^{137} and Sb^{124} and to the energies of gamma-rays from the bombardment of thick F^{19} and thick Li targets with 1.15-Mev protons. The results of the energy measurements are in disagreement with other recent work.[3]

† Work supported in part by the ONR.
[1] R. L. Burling, Phys. Rev. **60**, 340 (1941).
[2] Bernet, Herb, and Parkinson, Phys. Rev. **54**, 398 (1938).
[3] Stelson, Preston, and Goodman, Phys. Rev. **86**, 629 (A) (1952).

B6. Electrostatic Analysis of Nuclear Reaction Energies.* D. J. Donahue,† K. W. Jones, M. T. McEllistrem, and H. T. Richards, *University of Wisconsin*.—A spherical electrostatic analyzer[1] has been used to measure the reaction energies listed in Table I. The incident particle energy is defined by a cylindrical electrostatic analyzer and the reaction particles are observed at 135° to the incident beam. In addition, the $B^{11}(p, \alpha)Be^8$ reaction has been used as a source of Be^8. Preliminary data indicate that the Be^8 break-up energy is 96 ± 3 kev.

TABLE I.

Reaction	Q (Mev)	Energy of excited state
$Na^{22}(p, \alpha)Ne^{20}$	2.379 ± 0.003	···
$Na^{23}(p, \alpha)Ne^{20*}$	0.745 ± 0.002	1.634 ± 0.004
$Na^{23}(p, p')Na^{23*}$	-0.439 ± 0.001	0.439 ± 0.001
$Mg^{24}(p, p')Mg^{24*}$	-1.371 ± 0.002	1.371 ± 0.002
$Al^{27}(p, p')Al^{27*}$	-0.843 ± 0.002	0.843 ± 0.002
$Al^{27}(p, \alpha)Mg^{24}$	1.594 ± 0.002	···
$Al^{27}(p, \alpha)Mg^{24*}$	0.228 ± 0.003	1.366 ± 0.004

* Work supported in part by the AEC and in part by Wisconsin Alumni Research Foundation.
† Now at General Electric Company, Hanford Works, Richland, Washington.
[1] Browne, Craig, and Williamson, Rev. Sci. Instr. **22**, 952 (1951).

B7. Magnetic Analysis of Protons from $Cr^{52}(d, p)Cr^{53}$ and $Ni^{58}(d, p)Ni^{59}$.* C. E. McFarland, M. M. Bretscher, and F. B. Shull, *Washington University*.—A uniform-field magnetic spectrometer of 42.25-cm mean radius was used to analyze the protons from the $Cr^{52}(d, p)Cr^{53}$ and $Ni^{58}(d, p)Ni^{59}$ reactions. The incident deuteron beam was accelerated by the Washington University cyclotron, and its energy was about 10.2 Mev. The protons were observed at an angle of 90° relative to the deuteron beam and were detected by photographic plates. A series of 12 or more plates exposed at graduated values of magnetic field covered the interesting range of proton momentum thoroughly. The deuteron energy was determined from the same sets of plates by an analysis of the $O^{16}(d, d)O^{16}$ reaction. The targets were isotopically-concentrated Cr_2O_3 and NiO loaned by the Atomic Energy Commission. Eight well-defined proton groups from the chromium target yield Q values of 5.70, 5.16, 4.73, 3.41, 3.04, 2.50, 2.05, and 1.60 Mev. Six well-defined proton groups from the nickel target yield Q values of 6.77, 6.35, 3.69, 2.20, 1.57, and 1.11 Mev, and it seems possible that at least one unresolved group would yield a Q of about 3 Mev.

* Assisted by the joint program of the ONR and AEC.

B8. The Yield of Long-Range α-Particles from $F^{19}(p, \alpha)O^{16}$. E. B. Paul and R. L. Clarke, *Chalk River Laboratories*.—The yield of long-range α-particles from the proton bombardment of fluorine has been studied at 90° to the proton beam using the Chalk River Electrostatic Accelerator. The measurements were made at proton energies which ranged from 0.8

to 2.0 Mev, and evaporated CaF_2 targets less than 30 kev thick were used. The α-particles were analyzed magnetically and detected in a proportional counter. In addition to previously reported[1] resonances, two new resonances in the long-range α-particles yield were observed at proton energies of 1.72 and 1.92 Mev. These occur at the same energies as two of the resonances reported[2] in the yield of pairs from the 6.05-Mev state of O^{16}, and the ratio of the yields at these two resonances in the observed α-particle yield curve is very different from that reported for the pair yield curve.

[1] Chao, Tollestrup, Fowler, and Lauritsen, Phys. Rev. **79**, 108 (1950).
[2] G. C. Phillips and N. P. Heydenberg, Phys. Rev. **83**, 184 (1951).

B9. Energy Distributions of Photoprotons from Heavy Elements.* W. E. STEPHENS, M. E. TOMS, E. E. CARROLL, JR., AND G. ROSENBLUM, *University of Pennsylvania*.—The energy distributions of the photoprotons ejected from indium, cerium, and bismuth by 24-Mev betatron x-rays have been measured and compared with calculated distributions based on Courant's direct photoeffect and Weisskopf's evaporation process. The direct photoprotons can in these cases be partially distinguished from the evaporated protons in the basis of energy distribution. The results of such an analysis give observed yields in particles per mole per roentgen unit and comparable calculated yields as shown in Table I. The agreement

TABLE I.

Observed	Direct protons	Evaporated protons	
Bi	$3.5 \cdot 10^4$	$0.4 \cdot 10^4$	
Ce	$6.6 \cdot 10^4$	$3.8 \cdot 10^4$	
In	$7.5 \cdot 10^4$	$4.5 \cdot 10^4$	
Calculated		$r_0 = 1.5$	$r_0 = 1.3$
Bi	$1.5 \cdot 10^4$	$1.3 \cdot 10^4$	$0.3 \cdot 10^4$
Ce	$0.7 \cdot 10^4$	$0.07 \cdot 10^4$	$0.02 \cdot 10^4$
In	$2 \cdot 10^4$	$1 \cdot 10^4$	$0.5 \cdot 10^4$

seems reasonable except for cerium and indicates the importance of the direct photoeffect for the (γ, p) process in heavy nuclei.

* Assisted by the Air Research and Development Command and by the joint program of the ONR and AEC.

B10. Photoprotons from Mo^{100} and Mo^{92}.* W. A. BUTLER AND G. M. ALMY, *University of Illinois*.—The energy and angular distributions of photon-protons from concentrated isotopes Mo^{100} and Mo^{92}, irradiated with betatron x-rays of 22.5-Mev maximum energy, have been determined from the tracks of the protons caught in nuclear emulsions. For Mo^{100} it had been shown from (γ, p) and (γ, n) induced activities that the binding energy of a proton B_p is 2.4 Mev greater than that of a neutron B_n, and that the ratio $\sigma(\gamma, p)/\sigma(\gamma, n)$ is about 100 times that expected from a statistical model calculation. The latter result was confirmed by a comparison of the directly observed proton spectrum with a calculated spectrum. This implies that the protons are mainly emitted in a direct process without the usual competition with neutron emission. The shape of the observed proton spectrum requires, however, that the directly emitted protons leave the residual nucleus with an exponential energy distribution. In angular distribution most of the protons from 5 Mev to 12 Mev (maximum possible) show marked asymmetry, peaked forward of 90°, similar to the distribution found for the small anisotopic components in Cu and Co. For Mo^{92} B_n exceeds B_p by 5.1 Mev and the proton energy and angular distributions have the same small but definite departures from those predicted from the statistical model which have been found in other nuclei for which $B_n > B_p$.

* Supported by the joint program of ONR and AEC.

B11. Relative Photofission and Photoneutron Cross Sections for U^{238}.* JOHN R. HUIZENGA, *Argonne National Laboratory*, AND ROBERT B. DUFFIELD, *University of Illinois*.—The yields of the two reactions U^{238} (gamma, n) U^{237} and U^{238} (gamma, fission) produced by x-rays from the University of Illinois 22-Mev betatron have been measured as a function of betatron energy. The ratio of the number of fissions to the number of U^{237} atoms was 0.35 at 8 Mev, decreased to 0.25 and 12 Mev, and then increased to 0.42 at 22 Mev. These data are interpreted to show that with betatron energies in excess of 12 Mev, an increasing fraction of the U^{237} atoms formed are left with sufficient excitation energy that they can undergo fission or emit an additional neutron.[1] These secondary processes increase the total fission yield and decrease the U^{237} yield.

* This work supported by the joint program of the AEC and ONR.
[1] J. S. Levinger and H. A. Bethe, Phys. Rev. **85**, 577 (1952).

FRIDAY MORNING AT 10:15

Wilson Hall

(N. S. GINGRICH presiding)

Electron Emission

C1. Use of Ba^{140} in Studies of Oxide Coated Cathodes.* J. H. AFFLECK AND L. V. HOLROYD, *University of Missouri*.—Some experiments on oxide coated cathodes using the radioisotope Ba^{140} as a tracer are presented. An oxide cathode of BaO containing Ba^{140} is used as an evaporator in a tube containing several movable receivers for collecting the evaporated BaO. The activity of the receivers indicates the amount of Ba deposited. An improved tube design permits making the activity measurements through a thin glass bubble window in the side of the tube. The results show that the time rate of deposition is constant for a given temperature. By using a similar tube, one can measure the rate at which "free" Ba, produced at the interface, diffuses to the surface and is evaporated to the anode. The technique of spraying radioactive $BaCO_3$ is introduced in order to introduce cathodes of normal coating weight and density containing appreciable Ba^{140} (0.25 mc/g). These cathodes are operated under quiescent conditions for various periods of time. After life test the activity of the cathode interface is measured. This activity is related to the interface thickness, and its rate of formation can be determined as a function of life.

* Supported in part by the ONR.

C2. Effect of the Evaporation Products from a BaO Coated Cathode on the Secondary Emission of MgO Thin Films.* B. V. HAXBY AND P. WARGO, *University of Minnesota*.—The exposure of a secondary emission surface to the evaporation products of an oxide coated cathode gradually poisons the surface. With the use of a cathode coating including a radioactive tracer of Ba^{140}, this effect has been measured as a function of the number of equivalent atom layers of Ba deposited on the secondary emitter, a thin MgO film on Mg−Ag alloy. The cathode consisted of single BaO coating on a 499-Ni base. The overburden thickness is given as equivalent atom layers of

Ba because the relative concentration of Ba and BaO coming off the cathode is not known. The secondary yield increased initially, reaching a maximum after the deposition of about one equivalent atom layer. At about three layers δ has returned to its initial value. The yield then decreases more or less uniformly until approximately fifteen equivalent layers have been laid down, beyond which little change occurs. These results are independent of the primary electron energy.

* Supported by the U. S. Army Signal Corps.

C3. Rate of Evolution of the Constituents of an Oxide Coated Cathode as a Function of the Molar Composition of the Coating.* R. W. PETERSON, *University of Minnesota.*—Simple planar diodes containing radioactive isotopes of Ba or Sr in cathode coatings having varying molar compositions of Ba and Sr are processed, aged, and run on life test. The cathode based nickel used is No. 499 passive nickel. A removable electrode is provided to shield the anode from the cathode during processing and aging so as to distinguish between cathode products evolved during processing and aging and that evolved during life. Tubes are aged for four hours at cathode brightness temperature of 855°C and run on life for 118 hours at the same temperature. It is found that over a range of molar compositions of Ba from 20 percent to 50 percent the evolution of Ba is essentially independent of molar composition. Results of these experiments will be reported.

* Supported by U. S. Army Signal Corps. This work is an extension of the work reported by W. F. Leverton and W. G. Shepherd, J. Appl. Phys. **22**, 787–793 (1952).

C4. Analysis of the Schottky Deviation for the Highly Refractory Metals.* D. W. JUENKER, G. S. COLLADAY, AND E. A. COOMES, *University of Notre Dame.*—A summary has been made of all the available thermionic Schottky deviation data on the highly refractory metals, tungsten, tantalum, and molybdenum. Comparison with a corrected version of the Guth-Mullin theory[1,2] makes possible the following conclusions: (a) The mirror-image form is the correct one for the surface barrier. (b) The phase of periodic deviations is independent of field, indicating that the image potential is terminated close to the surface. (c) The magnitude of the deviation phase is less than that computed for the "box model" by about a quarter-period for all the metals investigated. This indicates a potential form near the surface somewhat different from the abrupt box model, and a close similarity in this form for the three highly refractory metals. (d) Experimental values for the magnitude of the surface reflection coefficient are not inconsistent with the box model, and suggest that the departure of the real potential shape from this model cannot be extreme.

* This research was sponsored by the U. S. Navy Bureau of Ships.
[1] E. Guth and C. J. Mullin, Phys. Rev. **59**, 575 (1941).
[2] E. Guth and C. J. Mullin, Phys. Rev. **61**, 339 (1942).

C5. The Patch Effect for the Thermionic Emission from Polycrystalline Tantalum.* E. A. COOMES, J. A. DEZOTEUS, AND J. F. WHALEN, *University of Notre Dame.*—The patch modifications in the Schottky effect have been studied for tantalum as a function of thermal aging, and the effect of grain growth has been separated from that of thermal etching. When 3-mil tantalum filaments are heated on either ac or dc, crystal grains several times the wire diameter appear within the first 10 hours. These grains develop on continued thermal aging; associated with this growth, the high-field break in the Schottky plot moves from an $E^{\frac{1}{2}}$ of about 100 (volt/cm)$^{\frac{1}{2}}$ to about 25 (volt/cm)$^{\frac{1}{2}}$ during 26 hours of heating. Within about 15 hours of aging at 2500°K, the characteristic thermal etch appears on some grains of the dc heated filaments, but not on those heated on ac. The Schottky plots for the dc case now show an additional high-field break at about 200 (volt/cm)$^{\frac{1}{2}}$ and a low-field break at about 120 (volt/cm)$^{\frac{1}{2}}$. Herring and Nichols[1] suggest that this anomalous region due to a superstructure on the crystal grains might appear.

* This research was sponsored by the U. S. Navy Bureau of Ships.
[1] C. Herring and M. H. Nichols, Revs. Modern Phys. **21**, 185 (1949), Chapter 2.

C6. A Technique for Secondary Electron Emission Measurements. E. J. SCOTT, *U. S. Naval Ordnance Laboratory.*—A new technique suitable for the study of secondary electron emission from metals and insulating materials is described. The usual methods employ either the pulsed primary beam or the pulsed collection techniques. These fail for very good insulators. The new method employs collection pulses synchronized with two separate primary beam pulses, one of which produces the secondary electrons while the other erases the charge on the emitting surface. In this manner it is possible to control the rate of charging of the surface of the material under investigation.

C7. Secondary Electron Emission of MgO Single Crystals with Excess Oxygen.* K. C. NOMURA, *University of Minnesota.*—The secondary electron yield of MgO single crystals has been measured for several densities of excess oxygen. The measurements of δ were made using a pulse technique. The density of the excess O_2 was determined from optical absorption measurements using Pohl's formula,[1] which has been verified experimentally by Weber[2] for this case. As the oxygen content decreased from 9×10^{17} cm^{-3} to 3×10^{17} cm^{-3} the value of δ_{max} increased from 5.7 to 6.7. The value of the secondary emission coefficient for a stochiometric crystal was found to be 8.

* Work supported by U. S. Army Signal Corps.
[1] R. W. Pohl, *Einführung in die Optik* (Frederick Ungar Publishing Company, 1943), S184, Gl. 204, 205.
[2] H. Weber, Z. Physik **130**, 392–402 (1951).

Post-Deadline Papers, if Any

FRIDAY MORNING AT 10:15

Crow Hall, 101

(G. E. PAKE presiding)

Atomic and Molecular Spectra; Magnetic Resonance

D1. The Hyperfine Structure of the Ground State of Aluminum. HIN LEW AND GÜNTER WESSEL, *National Research Laboratories, Ottawa.*—The measured ratios of the hyperfine structures of the ^3P ground states of Ga, In, and Tl differ from the theoretical ratios for a single p electron. It has been shown[1,2] that this is due to a disturbance by higher configurations, and that the magnetic dipole interaction constant $a(^3P_1)$ is less disturbed than $a(^3P_2)$, while the effect on the quadrupole interaction constant $b(^3P_2)$ is negligible. Consequently, nuclear quadrupole moments should be calculated

with the average value of $1/r^3$ taken from $a(^2P_{\frac{1}{2}})$ rather than $a(^2P_{\frac{3}{2}})$. Since there did not exist a very accurate determination of $a(3p^2P_{\frac{1}{2}})$ of Al^{27}, we undertook to measure it by the atomic beam magnetic resonance method, and have found $\Delta\nu = 3a = 1506.14 \pm 0.05$ Mc/sec. This result, along with the measurements on the $^2P_{\frac{1}{2}}$ state by Lew,[3] shows that the effect of perturbation is small for aluminum. This fits in well with the observed decrease of configuration interaction from Tl to Ga. The influence on the quadrupole moment of Al will be briefly discussed.

[1] E. Fermi and E. Segrè, Rend. reale accad. d'Italia **4**, 18 (1933); Z. Physik **82**, 729 (1933).
[2] G. E. Koster, Phys. Rev. **86**, 148 (1952).
[3] Hin Lew, Phys. Rev. **76**, 1086 (1949).

D2. Hyperfine Structures of the Resonance Lines of Indium 1.* G. V. DEVERALL, K. W. MEISSNER, AND G. J. ZISSIS, *Purdue University.*—In the process of developing an atomic beam light source for use at high oven temperatures, an investigation of the indium resonance lines at 4511A and 4101A was carried out. The employment of a well-collimated atomic beam, excited by electron impact, and of a Perot-Fabry interferometer made it possible to resolve clearly all components of the hyperfine structures of both lines. The complete resolution of the line 4511A has not been accomplished with other light sources.[1-3] The high spectroscopic accuracy led to values of the hyperfine splittings of the $5^2P_{\frac{1}{2},\frac{3}{2}}$ terms which agree within ± 0.0004 cm^{-1} with the values obtained by microwave methods.[4,5] Furthermore, a precise value for the hyperfine splitting of the $6^2S_{\frac{1}{2}}$ term was obtained, namely 0.2814 ± 0.0005 cm^{-1}.

* Supported in part by ONR contract.
[1] H. Schuler and T. Schmidt, Z. Physik **104**, 468 (1937).
[2] D. A. Jackson, Z. Physik **80**, 59 (1933).
[3] J. S. Campbell and R. F. Bacher, Phys. Rev. **38**, 1906 (1931).
[4] A. K. Mann and P. Kusch, Phys. Rev. **77**, 427 (1950).
[5] P. Kusch and H. M. Foley, Phys. Rev. **74**, 250 (1948).

D3. The Molecular Constants of Methyl Alcohol. E. V. IVASH* AND D. M. DENNISON, *University of Michigan.*—Values for the molecular constants of methyl alcohol have been obtained using the observed microwave data. The calculations are based on the theory of Burkhard and Dennison[1] for the asymmetric molecule with hindered rotation, and utilize the measurements of Hughes, Good, and Coles.[2] Values have been obtained for the barrier height, for the moments of inertia, and for the inter-atomic distances giving, on the whole, good agreement with the experimental results. Some of these calculated values are: (1) a barrier height of 374.8 cm^{-1}; (2) 5.333×10^{-40} g cm^2 for the moment of inertia of the methyl group about its symmetry axis; and (3) a displacement of 0.079A of the oxygen atom from the methyl group symmetry axis away from the hydrogen atom.

* Now at the University of Texas, Austin, Texas.
[1] D. G. Burkhard and D. M. Dennison, Phys. Rev. **84**, 408 (1951).
[2] Hughes, Good, and Coles, Phys. Rev. **84**, 418 (1951).

D4. Electronic Spectra of Diatomic Molecules: The Oxygen Molecule. FAUSTO G. FUMI* AND ROBERT G. PARR, *Carnegie Institute of Technology.*—A scheme is proposed for the computation of electronic energy levels of diatomic molecules with fair accuracy and minimum labor. The theoretical LCAO MO method including configuration interaction is employed. However, the energies of the asymptotic dissociation products for the various states are taken from atomic data,[1,2] and the calculation of the interaction energies is simplified by the formal neglect of differential overlap in the electronic repulsion terms.[3] The first application is made to O_2, and the results are in substantial agreement with experiment and with a previously more involved calculation by Moffitt.[3]

* Research Corporation Postdoctoral Fellow.
[1] W. Moffitt, Proc. Roy. Soc. (London) **A210**, 245 (1951).
[2] R. Pariser and R. G. Parr, J. Chem. Phys. (to be published).
[3] W. Moffitt, Proc. Roy. Soc. (London) **A210**, 224 (1951).

D5. Normal Coordinate Analysis of 1, 3, 5-Trifluorobenzene. ELDON E. FERGUSON, *University of Oklahoma.*—A normal coordinate analysis has been carried out for the nonplanar and the totally-symmetric vibrations of the 1,3,5-trifluorobenzene molecule, based on the frequency assignments of Nielsen, Liang and Smith[1] and utilizing results from Crawford and Miller's normal coordinate treatment of benzene.[2,3] The analysis of the nonplanar vibrations has furnished strong support for Nielsen, Liang and Smith's tentative assignment of the lowest A_2'' fundamental and has led to the conclusion that their value for the highest E'' fundamental is too high. The spectral data have been re-examined, and a reasonable new assignment has been given for this E'' fundamental. A plausible reinterpretation of several of the observed combination and overtone bands is given which is consistent with the change in assignment of the E'' fundamental. The analysis of the totally-symmetric planar vibrations has yielded a value of 6.37×10^5 dynes/cm for the CF bond stretching force constant. This is appreciably higher than that found in fluorinated saturated hydrocarbons.

[1] Nielsen, Liang, and Smith, Disc. Faraday Soc. No. 9, p. 177 (1950).
[2] B. L. Crawford, Jr., and F. A. Miller, J. Chem. Phys. **17**, 249 (1949).
[3] F. A. Miller and B. L. Crawford, Jr., J. Chem. Phys. **14**, 282 (1946).

D6. Vibrational Spectra and Calculated Thermodynamic Properties of CCl_3CF_2Cl and CCl_3CFCl_2*. J. RUD NIELSEN AND C. Y. LIANG, *University of Oklahoma,* AND D. C. SMITH AND MORRIS ALPERT, *Naval Research Laboratory.*—The infrared spectra of liquid CCl_3CF_2Cl, and of CCl_3CFCl_2 as glass and in CS_2 solution, have been obtained in the region from 2 to 38μ with the aid of LiF, NaCl, KBr, and KRS-5 prisms. The Raman spectra of these compounds in the liquid state, at 25° and 120°C, respectively, were photographed with a three-prism glass spectrograph of linear dispersion 15A/mm at 4358A. Relative intensities and depolarization ratios were measured for all but the weakest Raman bands. Complete assignments of fundamental vibration frequencies have been made, the spectra have been interpreted in detail, and thermodynamic functions have been calculated.

D7. The High Pressure Inversion Spectrum of ND_3 near 1500 Mc. G. BIRNBAUM AND A. A. MARYOTT, *National Bureau of Standards.*—The absorption of ND_3 associated with the inversion spectrum of the ground vibrational state has been measured at a number of frequencies between 1100 and 2600 Mc and at pressures between 3 and 800 mm Hg. Fine structure appears to be obliterated by pressure broadening even at the lowest pressure. A reasonably good representation of the data for pressures up to 100 mm was obtained with a single Van Vleck-Weisskopf shape factor, provided the line breadth $\Delta\nu$ and the resonance frequency ν_0 were adjusted for each pressure. It was not possible to fit data above 100 mm in this manner. Initially ν_0 has the value 0.0526 cm^{-1} but has shifted noticeably at 10 mm and becomes substantially zero at 80 mm. By comparison with NH_3, this shift occurs at pressures roughly fifteen-fold lower, a result in the direction expected from Margenau's theory.[1] $\Delta\nu/p$ decreases with increasing pressure, the rate of change being considerably greater at the lower pressures. These results will be compared with similar results for NH_3, and their significance will be discussed.

[1] H. Margenau, Phys. Rev. **76**, 1423 (1949).

D8. Variation of Mutual Collision Diameters with Mix Ratio in Binary Mixtures in Microwave Pressure Broadening. L. C. JONES, A. V. BUSHKOVITCH, C. A. POTTER, AND A. G. ROUSE, *Saint Louis University.*—It has been previously found[1] that mutual collision diameters of foreign perturbers determined from pressure broadening of ammonia microwave absorption lines vary with mix ratio. Extensive measurements of the collision diameters of oxygen and helium in binary mixtures with ammonia have now been made using gas

mixtures that were chemically analyzed at various pressures to correct the mix ratio. The variation with mix ratio was again observed. A least squares reduction of the data gave the following results for the variation of collision diameters measured in angstroms: oxygen-ammonia, $b_{12}=4.71-8.52\times10^{-3}$ (percent oxygen); helium-ammonia, $b_{12}=2.47-2.98\times10^{-3}$ (percent helium).

[1] Potter, Bushkovitch, and Rouse, Phys. Rev. **83**, 987 (1951).

D9. The Possible Microwave Absorption in the Molecules Belonging to the Point Groups $D_{2d}=V_d$ and T_d.* VENKATESWARLU PUTCHA† AND MASATAKA MIZUSHIMA, *Duke University.*—It is shown that pure rotational absorption in the molecules belonging to the point group $D_{2d}=V_d$ (allene, etc.) is possible if the molecule is in an excited doubly degenerate vibrational state. The approximate positions of these lines, as calculated from the B value obtained from the infrared data, fall in the microwave region in the case of allene and allene-d_4. The same type of absorption is also possible in the molecules belonging to the point group T_d if they are in the excited triply degenerate (F_2) vibrational states. The matrix element of dipole moment corresponding to our transition is calculated, and it was shown to be proportional to the second derivative of the dipole moment with respect to the corresponding normal coordinate. (The first derivative will also contribute some through the effect of anharmonicity.) It is interesting that the above matrix element of dipole moment is about the same as that of the overtone vibrational bands.

* Work supported by contract with Air Force Cambridge Research Center.
† Also written as Putcha Venkateswarlu.

D10. Anomalous Results in an Attempt to Determine the Spin of Si^{29}.† R. H. SANDS AND G. E. PAKE, *Washington University.*—An attempt has been made to determine the spin of Si^{29} through comparison of its integrated absorption intensity with that of an equal number of I^{127} nuclei. The sample consisted of 0.4295 g of enriched SiO_2 amorphous powder, obtained on loan from Oak Ridge National Laboratory, in a physical mixture with KI powder. The sample was placed in a Pound type spectrometer, and the magnetic field was adjusted so that both resonances could be recorded at the same frequency without any instrumental adjustments. The ratio of the I^{127} integrated intensity to that of Si^{29} was found to be about 4.3 ± 0.5 over a range of experimental conditions. Since the intensity is proportional to $I(I+1)$ and the spin of I^{127} is 5/2, the ratio should be 11.7, 2.3, or 1.0 if the Si^{29} spin were 1/2, 3/2, or 5/2, respectively. Possible systematic errors will be discussed, and a number of silicon-containing materials not yielding a resonance will be listed. Anomalies in Si^{29} resonances have also been found by the Stanford group.[1]

† Assisted by the joint program of the ONR and AEC.
[1] S. Dharmatti (private communication).

D11. Nuclear Magnetic Relaxation in Polytetrafluoroethylene and Polyethylene.* C. W. WILSON, III, AND G. E. PAKE, *Washington University.*—The thermal relaxation time T_1 and the inverse line width parameters T_2 have been measured in the two linear polymers, polyethylene and polytetrafluoroethylene (Teflon), over a temperature range from -180°C to about $+200$°C. The experiments present complexities which can be explained by assuming that each substance possesses two values of T_1 and two values of T_2. A suggested interpretation, based upon the fact that these polymers are stable mixtures of crystalline and amorphous regions, permits one to estimate the degree of crystallinity using the experimental data. The first-order transition[1] at 20°C in Teflon was studied with particular interest. No effect was observed on the resonance attributed to amorphous regions, which can be reasonably well described using the theory of Bloembergen *et al.*[2] for fluids. The resonance from crystalline regions narrows in the neighborhood of the transition. Possible motions of the polymer chains which are consistent with the data will be discussed.

* Assisted by the joint program of the ONR and AEC. The large electromagnet and part of the electronic equipment were provided through a grant from the Research Corporation.
[1] Rigby and Bunn, Nature **164**, 583 (1949).
[2] Bloembergen, Purcell, and Pound, Phys. Rev. **73**, 679 (1948).

D12. Homogeneity Mapping of a Permanent Magnet Field for Chemical Effect Studies in Nuclear Resonance.* C. R. BRUCE (introduced by G. E. Pake), *Washington University.*—The magnetic field in the gap of a permanent magnet has been plotted in considerable detail using the proton resonance from mineral oil samples as small as one cubic millimeter in volume. This has been done for several planes parallel to the pole faces. These contour plots show the field to be quite inhomogeneous and intricate in the planes near the iron of the pole faces. However, the homogeneity improves rapidly, and the detail of the pattern disappears in planes slightly further from the iron. The plots were used to find homogeneous regions suitable for observing the chemical shift of the proton resonances arising from nonequivalent nuclei within the same molecule.[1] Charts of the field contours will be shown with special emphasis placed upon the effect of proximity to the iron.

* Assisted by the joint program of the ONR and AEC.
[1] Arnold, Dharmatti, and Packard, J. Chem. Phys. **19**, 507 (1951).

FRIDAY MORNING AT 10:15

Rebstock Hall

(W. H. ZINN presiding)

Invited Papers

E1. Measurement of Neutron-Capture Gamma-Rays. BERNARD HAMERMESH, *Argonne National Laboratory.* (30 min.)

E2. Accurate Determination of Disintegration-Energies. G. C. PHILLIPS, *Rice Institute.* (30 min.)

Apparatus of Nuclear Physics

E3. Fast Neutron Scintillation Spectrometer. MARSHALL R. CLELAND, *National Bureau of Standards.**—The Monte Carlo sampling procedure has been used to evaluate a proposed spectrometer for neutrons with energies above 1.0 Mev. The efficiency is shown to be about 0.15 percent and the energy resolution about 10 percent for 14.0-Mev neutrons. This instrument employs a cylindrical phosphor, 5 centimeters in diameter and 5 centimeters long, composed of a half-and-half

mixture of phenylcyclohexane and methyl borate activated with 3–5 grams of *p*-terphenyl and 10–15 milligrams of diphenylhexatriene per kilogram of phosphor.[1] Only those events are recorded in which the neutron is first thermalized by elastic collisions and then captured by boron. The capture criterion strongly favors neutrons that lose most of their energy at the first collision, hence the narrow pulse-height distribution. The mean time interval between the recoil proton pulse and the boron capture pulse is shown to be about 2.0 microseconds with 18.8 percent boron-10 and about 0.25 microsecond with 94 percent boron-10. The efficiency and energy resolution are shown to be the same for normal and enriched boron. The delayed pulse distinguishes fast neutrons from most other radiations. Although it does not rule out inelastic scatterings, it assures that the neutron was not absorbed at high energy. The spectrometer is nondirectional.

* Supported by the Office of Basic Instrumentation.
[1] C. O. Muehlhause and G. E. Thomas, Phys. Rev. **85**, 926 (1952).

E4. A Velocity Spectrometer Using a Microsecond Neutron Shutter. F. G. P. SEIDL, D. J. HUGHES, AND H. PALEVSKY, *Brookhaven National Laboratory.**—A neutron shutter (commonly called a "chopper") has been designed and put into operation as part of a time of flight spectrometer, which separates pile neutrons in a collimated beam according to their various times of flight between the chopper and a detector 20 meters away. The chopper action depends upon a fast-spinning rotor which, when spinning at 6000 rpm, periodically produces neutron bursts, each having a full width at half-maximum of one microsecond. Since detector pulses are electronically sorted into various 2 microsecond channels, according to time after each burst, a resolution of 0.2 microsecond/meter results. The open-beam counting rates per channel are never less than 10 counts/minute above background. Curves of neutron transmission *vs* energy will be shown. Since the chopper rotor has been designed to spin at 12,000 rpm, we plan to run at higher resolution in the near future. The spectrometer will be used to study transmission effects for neutrons from 1 ev to 10 kev.

* Work carried out under contract with AEC.

E5. Extrapolated Ionization Ranges for 10- to 250-kv Protons in Various Gases. T. JORGENSEN, E. JONES, AND C. J. COOK. *University of Nebraska.*—An analyzed beam of protons is admitted into a gas filled stopping cell through a differential pumping "window," and the ionization produced along the beam is measured by a double grid ionization chamber. This chamber is so arranged that its transverse dimension may be varied. It has been found that the range is uniquely determined for an effective chamber radius larger than the ionization envelope of the beam in the stopping gas. The results of the measurements are estimated to be known within 2 percent. The range energy curves may be closely approximated by an empirical relationship, $R=kE^n$, $E<E_0$, $n\approx\frac{3}{2}$, $R=C(E+E_1)^{\frac{1}{2}}$, $E>E_0$, where k, C, n, E_0, and E_1 are interrelated constants dependent upon the stopping medium.

E6. An Activity Ratio Method for Measuring the Energy Stability of Betatrons. MILTON BIRNBAUM, ERIC M. HARTH, LEO SEREN, AND RALPH TOBIN. *Naval Research Laboratory.*—For nuclear threshold measurements, betatrons employ a magnetic flux integrator to trigger the expansion circuit at a time in the magnetic cycle which corresponds to the desired peak energy of bremsstrahlung. In practice, betatrons using these magnetic flux integrators exhibit a day to day variation in energy stability of 100 to 200 kilovolts. We have used a method for measuring the stability of the betatron which depends only on nuclear activations, and is therefore independent of the gamma-ray monitor. At a peak bremsstrahlung energy of 11.4 Mev, the radioactivity induced in copper by the reaction $Cu^{63}(\gamma, n)Cu^{62}$ is changing at the rate of 0.8 percent per kilovolt change in peak energy, while the radioactivity induced in silver from the reaction $Ag^{107}(\gamma, n)Ag^{106}$ is changing at the rate of only +0.11 percent per kilovolt. The ratio of the copper activity to the silver activity thus changes by +0.69 percent per kilovolt. We have irradiated copper and silver discs simultaneously and observed the ratio of the induced activities. Using this ratio method, we find the day to day stability of our betatron to be 40 kilovolts at 11 Mev, and the accuracy of the activity ratio method is better than 20 kilovolts.

E7. Measurement of Ionizing Radiation by Frequency Variation. HANS KOHN RICHARDS. *Oak Ridge National Laboratory.*—A method has been developed to measure ionizing radiation by the frequency variation of a rf oscillator operating at a nominal frequency of 2.3 megacycles. An electrometer of variable capacitance is a component of the frequency determining network, the capacitance variation being produced by the movement of a metal vane suspended by means of a quartz fiber between two electrode pairs. The position of the vane between the electrode pairs is determined by an electric charge applied to the vane. Electrostatically, the system represents two capacitances in parallel of the order of 4 to 5 $\mu\mu$f, while the rf capacitance consists of two capacitances in series. Ionizing radiation produces a leakage of the charge from the vane and, therefore, variations in capacitance and frequency. The frequency is measured using a standard quartz crystal oscillator. One mr/hr produces a frequency variation of approximately 20 cycles/minute. Dose rates of gammas, betas, and neutrons have been measured. By connecting the vane through several megohms to different capacitances, the system can measure dose rate of widely different magnitudes. This system makes possible the monitoring of numerous locations from a single remote station.

E8. Evapor-ion Pump.* R. G. HERB, ROBERT H. DAVIS, AJAY S. DIVATIA, AND D. SAXON, *University of Wisconsin.*—A new type of high vacuum pump to replace diffusion pumps and traps has been developed for use on the accelerating tube of a new electrostatic generator now under construction. After initial roughing by a fore pump the system is sealed. Titanium in wire form is evaporated continuously inside a cylindrical metal chamber 7 in. i.d., 24 in. high. The gettering by titanium on the wall of the chamber results in pumping action. In order to pump components that do not respond to gettering action, it is necessary to ionize the gas inside the chamber by electron bombardment and drive the gas ions so formed into the wall by an electric field, where they are buried in fresh layers of evaporated metal. Cylindrical geometry is used for ionization. Qualitative tests indicate that H_2, N_2, O_2, CO_2, SF_6, CCl_2F_2, C_2H_4, NH_3, CH_4 are readily pumped by the gettering action alone; in order to pump the inert gases argon and helium ionization is necessary. On a sealed-off system which had not been baked and which utilized O ring gaskets, a pressure of 5×10^{-7} mm Hg was maintained. Pumping speeds for various gases are being investigated as a function of the temperatures of the gettering surfaces.

* Work supported by the Wisconsin Alumni Research Foundation and the AEC.

FRIDAY AFTERNOON AT 2:00

Brown Hall

(H. D. SMYTH presiding)

Commemoration of the First Functioning of a Nuclear Reactor on December 2, 1942

G1. A. H. COMPTON, *Washington University.*
G2. ENRICO FERMI, *University of Chicago.*
G3. E. P. WIGNER, *Princeton University.*
G4. W. H. ZINN, *Argonne National Laboratory.*

FRIDAY AFTERNOON AT 2:30

Loudermann Hall

(J. B. JOHNSON presiding)

General Physics

H1. Charge States of a Helium Beam in Hydrogen, Helium, Air, and Argon. ELIAS SNITZER, *Department of Physics and Institute for Nuclear Studies, University of Chicago* (introduced by Samuel K. Allison).—Measurements have been made of the fractions of a helium beam in the He^0, He^+, and He^{++} charge states in the energy range of 100 kev to 480 kev for beams which have attained charge equilibrium in hydrogen, helium, air, and argon. For the four gases, the He^0 and He^+ components are equal for helium energies of 148 kev, 145 kev, 98 kev, and 115 kev, respectively. The ratios of the electron loss to electron capture cross sections between He^+ and He^{++} fitted a simple power dependence of $\sigma_l/\sigma_c \alpha V^m$, where V is the velocity of the helium in the beam and m equals 6.1, 5.1, 5.2, and 6.3, respectively, for the four gases studied. For electron capture and electron loss between He^0 and He^+ the exponent m varies from 2.6, 2.0, 2.8, and 3.4 at 100 kev to 4.0, 4.0, 4.3, and 5.1 at 450 kev.

H2. The Separation of Incident and Emitted Radiations in a Solar Furnace by Means of Rotating Sectors. WILLI M. CONN* AND GENE BRAUGHT,† *Rockhurst College.*—A paraboloidal mirror is used for concentrating radiation from the sun in a sample placed near the focal area. The sample is heated to a temperature at which an equilibrium is established between the amount of radiant energy incident on the sample and the losses from it. The temperature is controlled by varying the effective aperture of the mirror by means of a cylindrical shutter traveling along the optical axis of the mirror. The temperature of the sample is measured with an optical pyrometer or a radiation pyrometer equipped with color filters. It was found necessary to shut off the incident radiation from the sample during the measurement of temperature in order to obtain correct data (checked with standard materials). This is accomplished by rotating sectors traveling at 2500 revolutions per minute. One sector of special shape is located near the sample and another sector near the telescopic system. The calibration and use of the sectors in connection with mirrors of maximum apertures 60 in. and 120 in. and focal lengths 25¾ in. and 34 in. is presented.

* Now with the Research Department, Gustin-Bacon Manufacturing Company, Kansas City, Missouri.
† Now with St. Louis University, St. Louis, Missouri.

H3. Contribution of Doppler Effect to Radiation Exchange in the Stratosphere. GILBERT N. PLASS AND DANIEL I. FIVEL, *The Johns Hopkins University.*—The principal contribution to the total line width in the upper stratosphere comes from the Doppler effect. In order to investigate radiative transfer throughout our atmosphere, it is necessary to know the line absorption coefficient $k(\nu)$, when both the Lorentz and Doppler widths ($\Delta\nu_L$ and $\Delta\nu_D$) contribute to the total width. The general term of the expansion of $k(\nu)$ in powers of $\Delta\nu_L/\Delta\nu_D$, as well as the asymptotic expansion in inverse powers of the frequency, has been obtained. From these results the atmospheric transmission functions have been derived for a planetary atmosphere when both $\Delta\nu_L$ and $\Delta\nu_D$ contribute to the line width and when the variation of $\Delta\nu_L$ with pressure is considered. For the earth's atmosphere it is found that the transmission function calculated from the Lorentz shape alone for either strong or weak lines is not changed appreciably by the Doppler effect even at heights where $\Delta\nu_D$ is considerably larger than $\Delta\nu_L$. This is because almost all the radiation transfer takes place in the far wings of a strong line where the Lorentz broadening determines the line shape. For a weak line only the total line strength is of importance. Applications to laboratory absorption measurements will be discussed.

H4. On the Theory of Interstellar Grains. BERTRAM DONN, *Wayne University.*—Interstellar space is known to contain a mixture of atoms (mainly hydrogen) and small solid grains, the whole having an over-all density of approximately 10^{-24} g/cm³.[1] Among the major problems of interstellar matter are those concerned with the origin, evolution, and structure of the grain. This paper discusses one aspect of the general problem, namely, the interaction between the gas and the grains under present conditions. This limited analysis nevertheless requires consideration of a variety of problems associated with surface phenomena, for which no completely satisfactory treatment is available. Among the problems which will be discussed are condensation; evaporation and adsorption for contaminated surfaces; surface mobility; chemical reactions; and heterogeneous catalysis. The application of the limited available results to the case of interstellar matter suggests that the grain will be stable throughout most of space but incapable of further growth. In order to extend the theory and improve the tentative conclusions, further work must be carried out on the basic physical and chemical processes which comprise the gas-grain interaction in space.

[1] See chapter on "Interstellar matter" in *Astrophysics*, edited by Hynek (McGraw-Hill Book Company, Inc., New York, 1951).

H5. The Analysis of a Bridged-T Network by Use of Laplace Transformations. CORRE WILLIAMS, *Consolidated-Vultee Aircraft Corporation*, AND HERBERT D. SCHWETMAN, *Department of Physics, Baylor University.*—The analysis of a simple bridged-T network through the use of Laplace transformations is demonstrated. The resonance frequency, the phase angle, and the output voltage are determined for several values of terminating resistance and network components.

H6. The Entropy of Fusion of Monatomic Liquids. N. K. POPE, *Chalk River Laboratories.*—A relation has been obtained between the entropy of fusion of monatomic liquids and the number of a particular set of neighbors in the liquid. In general, the set of neighbors involved is the nearest set that shows evidence of increase of radial separation on melting. Usually this is not the first, but the second, or even the third set of neighbors. The relationship has been deduced by using a model in which it is assumed that at sufficiently high temperatures one of the neighbors of a given atom in a solid may move outwards to a new equilibrium position. An order-disorder theory of the melting process has been formulated, which identifies the liquid with a state in which every atom has, on the average, one of its neighbors moved out to the new equilibrium position. X-ray and neutron diffraction patterns of liquids give the number and mean positions of the first, second, and third neighbors. In many cases where this information is available, the number of neighbors measured in the liquid state, in the set which is displaced outward on melting, agrees with the number calculated from the measured values of the entropy of fusion.

H7. Respiration of Plant Tissue Cultures as a Function of X-Ray Dose. MARK W. JONES, *University of Florida.*—Tissue cultures of corn root tips, grown in White's culture medium augmented by 10^{-5} mg IAA per liter nutrient, were subjected to x-ray doses of 100, 200, 400, 800, and 1400 roentgens. The mean oxygen uptake of the tissues, measured by standard Warburg techniques, decreased with increasing dose. It ranged from 8.7 to 3.8 $\mu l O_2$/mg/hr for doses from 0 to 1400 roentgens. Analyses of variance and covariance of the respiration *versus* dose of unirradiated tissues and irradiated tissues show the observations to be highly significant. Concomitant observations of dry weights indicate that their use for the arbitrary correction of respiration rates of different weight cultures is not completely justified for the analysis of covariance between different series of observations.

H8. Research on Comfort, Relaxation, and Quality of Sleep. T. SMITH TAYLOR AND L. W. MAX,* *U. S. Testing Company.*—This research was undertaken to determine some methods of measuring the relative comfort experienced by subjects sleeping on different mattresses. The research was directed towards measuring physical properties of the individual during sleep that would give the relative degrees of relaxation and hence the relative comfort experienced. The physical properties measured were heartbeat, muscle tensions, brainwaves, skin temperature, electrical skin resistance, and number of movements. Both men and women have been used as sleeping subjects. By comparing statistically the various values of the various properties measured on one mattress with those while sleeping on another, these were found to be significantly different. The results showed definitely that for a large number of subjects the subjects experienced greater relaxation and hence more comfort on one mattress than they did on others. This paper gives the progress of the research during the last three years. A later paper will give more complete details of the methods and the ultimate findings.

* Head of Department of Physiology, Dental College, New York University, Special Consultant.

H9. Design and Construction of a Universal Test Mattress. NORMAN L. TAYLOR AND T. SMITH TAYLOR, *U. S. Testing Company.*—A Universal Test Mattress has been constructed in which the individual components are rubber bellows instead of springs. Each bellows reacts independently of the others. If a given bellows is compressed, a definite increase in pressure is produced which is measured by a gauge which is proportional to the change in volume. By use of the test mattress, the average distribution of weight in each 3½-in. section of the body has been determined for several individuals. This is the first time that body weight distribution has been determined on live subjects. Since the reaction of each section of the mattress from head to foot can be varied, it is possible to obtained the optimum conditions of pressure variation in the several bellows necessary to give maximum relaxation to the sleeping subject. The mattress is being used in connection with others in an extensive research on mattress comfort.

H10. Angular Points in Densities of Water *vs* Temperature. GEORGE ANTONOFF AND RAYMOND MADRAZO, JR.—The best methods of demonstrating kinks are the following: (I) As was shown elsewhere,[1] kinks are well seen if $d^1(d=d_1-d_v)$ is plotted against T. For kinks in water see Antonoff *et al.*[2] (II) At low T the method (I) becomes less sensitive. Thus we plot X *vs* T with a strongly diminished parameter X, and the kinks appear as the intersection of nearly straight lines. For water the values for X are $X=4$, 8, 16, 32, 64, 128, 256, 512, 1024, 2048, 12,288, 24,576, 75,728, and 147,402 at 4.9°C. (III) The same kinks are easily visible in d_1 and d_v *vs* T curves at high T. The temperatures are counted downwards from an arbitrary zero near the critical point. The equations $d_1=A_1+B_1T-CT^2$ and $d_v=A_2-B_2T+CT^2$, which are valid between two adjacent kinks with given constants, show very good agreement with experimental data. These equations are based on points between two kinks as indicated by method (I). Calculations beyond the two adjacent kinks show a marked departure from continuity. Above $X=64$ the method is not sensitive. Mademoiselle Olivier (Thèse, Strasbourg, 1952) used similar equations starting from low T and failed to reveal kinks. The use of statistical methods is not practicable, because the experimental errors cannot be seen on the graph.

[1] Compt. rend. 3/XII (1951).
[2] Antonoff, Zakimac, Urmanczy, and Madrazo, Phys. Rev. **86**, 586(A) (1952).

FRIDAY AFTERNOON AT 2:30

Rebstock Hall

(V. A. JOHNSON presiding)

Solid-State Physics. I

K1. Shot Noise in Germanium Filaments. R. H. MATTSON AND A. VAN DER ZIEL, *University of Minnesota.*—Herzog and van der Ziel's measurements[1] of the noise ratio n(= total noise power over thermal noise power) of a 10,000-ohm germanium filament have been extended to higher frequencies, and the accuracy of the measurements has been improved considerably.

We find that the formula, $n=1+AI^2/f+BI^2/[1+(f/f_0)^2]$, with $f_0=150$ kc, $AI^2=9.3\times10^8$, $BI^2=54$, can account for all measurements at a dc current of 3 ma. As both electrons and holes are present and as each carrier should show shot effect, it must be concluded that both types of carriers have about the same life time. An application of the theory of shot noise in semiconductors shows that most of the noise comes from the electrons and that the electrons most likely originate from trapping centers located at a depth of about 0.22 ev below the bottom of the conduction band. Similar trapping centers have also been found in other investigations.[2]

[1] G. B. Herzog and A. van der Ziel, Phys. Rev. **84**, 1249 (1951).
[2] R. N. Hall, Phys. Rev. **87**, 387 (1952).

K2. Shot Noise in Semiconductors. A. VAN DER ZIEL, *University of Minnesota.*—The theory of shot noise in semiconductors has been developed for the case that both electrons and holes are present in the semiconductor. If the number N_e of free electrons and the number N_h of free holes in the sample are fluctuating independently, such that $(N_e-\bar{N}_e)^2=\alpha\bar{N}_e$ and $(N_h-\bar{N}_h)^2=\beta\bar{N}_h$, then the noise ratio n_e resulting from shot effect (=shot noise power over thermal noise power) is found to be

$$n_e=(e/kT)(V_0^2/d^2)\left[\frac{\alpha\mu_e\tau_e\sigma_e/(\sigma_e+\sigma_h)}{1+\omega^2\tau_e^2}+\frac{\beta\mu_h\tau_h\sigma_h/(\sigma_e+\sigma_h)}{1+\omega^2\tau_h^2}\right],$$

where d is the length of the sample, V_0 the dc voltage across it, μ_e and μ_h the electron and hole mobility, σ_e and σ_h the electron and hole conductivity, and τ_e and τ_h the electron and hole life time, respectively. This formula will be applied to several cases.

K3. The Flicker Noise Caused by an Interface Layer. W. W. LINDEMANN AND H. J. HANNAM.—When some tube types are aged while only a small current is drawn, a high resistance interface layer develops,[1] the resistance of which increases further with life. If the interface resistance becomes as high as a few hundred ohms, the noise resistance of the tube at low frequencies may have increased by as much as a factor 1000. The noise resistance is proportional to the square of the anode current, which suggests that the phenomenon may be explained by a spontaneous fluctuation in the resistance of the interface layer. Curves showing the increase in noise resistance as a function of time and the dependence of the noise resistance upon cathode temperature will be presented.

[1] A. Eisenstein, *Advances in Electronics* (1948), Vol. I, pp. 1–64.

K4. The Influence of Neutron Bombardment on the Low Temperature Atomic Heat of Silicon.* P. H. KEESOM, K. LARK-HOROVITZ, AND N. PEARLMAN, *Purdue University.*—The heat capacity of B.T.L. silicon below 5°K has been measured before and after fast neutron irradiation in the Oak Ridge reactor. Before bombardment the atomic heat included the lattice contribution and a term linear in temperature due to a degenerate carrier gas. The coefficient γ of the linear term observed for Si V corresponds to the impurity concentration (0.01 percent B by weight) if the effective hole mass is 0.8 the free electron mass. Hall measurements by H. Fritzsche between 4–300°K confirm this concentration. After bombardment the linear term disappeared in Si II and decreased by 75 percent in Si V, owing to carrier trapping by lattice defects produced by neutron irradiation.[1] Annealing ingot Si II at 780°K partly restored the original low temperature atomic heat. The Debye θ decreased after bombardment for both ingots, indicating a decrease in elastic constants[2] larger than expected from theory. See the data compiled in Table I.

TABLE I.

	Si II				Si V	
			Annealed			
	Original	Bombarded	up to 450°C	at 780°C	Original	Bombarded
θ (°K)	658	637	632	642	658	636
γ (joules/mole deg^2)	21.0×10^{-4}	1.55×10^{-4}	1.74×10^{-4}	13.7×10^{-4}	34.6×10^{-4}	9.26×10^{-4}

* Supported by Signal Corps and AEC contracts.
[1] H. M. James and K. Lark-Horovitz, Z. physik. Chem. **198**, 107 (1951).
[2] G. J. Dienes, Phys. Rev. **87**, 666 (1952).

K5. Some Electrical Characteristics of Crystalline Boron. WM. C. SHAW, D. E. HUDSON, AND G. C. DANIELSON, *Iowa State College.*—Micromanipulative techniques for mounting very small crystals with several spring loaded probes have been developed. The method makes use of a modified Chambers micromanipulator, a binocular microscope, and special tools. Crystals 0.01 cm long have been mounted with five spring loaded tungsten probes, allowing electrical conductivity and Hall coefficient measurements to be made over a wide range of temperature. The method has been applied especially to microscopic single crystals of boron. The electrical resistivity varied from about 10^6 ohm/cm at 25°C to less than 1 ohm/cm at 550°C. Preliminary measurements indicate a very small Hall coefficient.

K6. Adsorption of Oxygen on Zinc Oxide.* S. R. MORRISON,† *University of Pennsylvania.*—It has been shown that oxygen is adsorbed on zinc oxide. The total adsorption has not been measured; but it has been shown that when the zinc oxide is heated above 500°C, oxygen previously adsorbed on the sample is desorbed, leaving adsorption sites. The number of these adsorption sites prepared increases rapidly with increasing cleaning temperature. With a constant number of adsorption sites, it has been shown that the amount of oxygen adsorbed is maximum at about 425°C. It has been shown that the number of adsorption sites, if left unoccupied, decreases with time. Postulating that the interstitial zinc in the lattice are the adsorption sites, this effect has been interpreted as being due to the diffusion of the zinc atoms away from the surface. On the basis of this model, the activation energy for the diffusion of interstitial zinc has been calculated to be 1.2 ev.

* Supported by the ONR.
† Now at the University of Illinois.

K7. The Structure of the Surface of Glass and of Bi Films Deposited on Glass. J. J. ANTAL AND A. H. WEBER, *St. Louis University.*—The surface structure of glass has been studied by electron diffraction after deposition of a very thin layer of Bi on the glass to reduce charging. If less than 10A thick, the Bi contributes negligibly to the diffracted intensity or may be eliminated because of its preferred orientation. Radial distribution curves were computed from data obtained from the diffraction patterns by a combination of densitometry and visual examination. The annealed surface of commercially prepared soda-lime-silica glass (72 percent SiO_2, 14 percent Na_2O, 11 percent CaO) was examined. The radial distribution curves indicate that the structure of the glass surface is essentially a random network of Si and O atoms as found for the volume structure of vitreous silica by Warren.[1] Distances to alkali atoms were absent from the radial distribution curves, which indicated an absence of alkali atoms for a depth in the glass equal to the depth of penetration (always less than 10A) of the electrons—although migration of alkali atoms to the surface of a glass is well known. Electron diffraction and electron microscopic examination of the Bi films deposited on glass will also be reviewed.

[1] B. E. Warren, J. Appl. Phys. **8**, 645 (1937).

K8. Rates of Coloration of KCl and KBr During X-Irradiation at 78°K.* WILLIAM H. DUERIG AND JORDAN J. MARKHAM, *Applied Physics Laboratory, The Johns Hopkins University.*—When KCl and KBr crystals are x-rayed at 78°K, several color center bands appear, e.g., the F, F', V_0, V_1, and V_2 bands.

In order to gain further understanding of the nature of the imperfections responsible for these bands, their growth rates during x-raying at 78°K were measured. The rates were obtained under two conditions: (1) when the crystal was in the dark, and (2) when it was exposed to F' light. The results of these experiments will be presented and analyzed.

* This research was supported by the Bureau of Ordnance, United States Navy.

K9. A Theory of Successive Rotational Transitions in Crystals. THEODORE J. KRIEGER AND HUBERT M. JAMES, *Purdue University.*—Some crystals show successive phase transitions attributed to changes in rotational or orientational order, but no detailed calculations have previously been made on crystal models showing more than one orientational transition. A crystal model consisting of classical rotators with next-neighbor interaction energy, $E(\theta_{ij}) = AP_1(\cos\theta_{ij}) + BP(\cos\theta_{ij})$, has been treated in the Bragg-Williams and Bethe approximations. Depending on the magnitude of B/A, it shows a single second-order transition, a single first-order transition, two first-order transitions, or a second-order followed by a first-order transition as T rises. When two transitions occur, the upper transition temperature depends primarily on the value of B, the lower on the values of both A and B. Our results, together with the estimates of dipole and van der Waals forces in hydrogen halides made by Powles, enable one to understand qualitatively the variation of transition temperatures in the hydrogen and deuterium halides.

K10. Approximate Treatment of Order-Disorder Transitions in the Simple Cubic Ising Lattice. L. D. FOSDICK AND H. M. JAMES.—The approximation method previously applied to the square and triangular Ising arrays[1,2] has been applied to the simple cubic lattice. Attention is fixed on a certain site surrounded by six next-neighbors and twelve second-neighbors. Three weighting parameters, characterizing long- and short-range order, are used in computing the configuration probabilities. Three consistency relations determine these parameters as functions of the temperature and coupling energy. This method gives a Curie temperature $kT_c/V = 2.3145$ and a specific heat c, just below the Curie point given by $(c/k)|T_c \cong 2.58$, in close agreement with Kikuchi's results.[3] Correlations (the probability for finding parallel spins minus the probability for finding antiparallel spins) between spin pairs up to fifth neighbors have been computed. The results emphasize that long-range order persists in three-dimensional lattices for higher temperatures and lower short-range order than it does in two-dimensional lattices.

[1] H. M. James and L. D. Fosdick, Phys. Rev. **81**, 312 (1951).
[2] L. D. Fosdick and H. M. James, Phys. Rev. **85**, 714 (1952).
[3] R. Kikuchi, Phys. Rev. **81**, 988 (1951).

K11. A Cellular Calculation of the Band Structure for Barium Oxide. EARL L. STEELE* AND JAMES A. KRUMHANSL, *Cornell University.*—Electronic wave functions and energy levels have been calculated for the barium oxide crystal using methods similar to those developed by Ewing Seitz[1] and Von der Lage and Bethe.[2] The crystal is divided into cells (spheres) surrounding each atom, and a spherically symmetric potential including exchange is developed in each cell. Bloch-type one-electron wave functions were constructed from linear combinations of atomic-like functions, and boundary conditions were imposed where the spheres of neighboring atoms intersected. Energies for particular points in k space for the valence and conduction band were obtained. This calculation gives a minimum band gap of 3.4 ev between $k(000)$ in the conduction band and the $k(110)$ end point in the valence band; however, the minimum gap for optical transitions (constant k) is 7.3 ev for the $k(000)$ point. The self-consistent solution shows that the crystal is highly ionic.

* Now at the General Electric Electronics Laboratory, Syracuse, New York.
[1] D. H. Ewing and F. Seitz, Phys. Rev. **50**, 760 (1936).
[2] F. C. Von der Lage and H. A. Bethe, Phys. Rev. **71**, 612 (1947).

K12. The Calculation of Energy Bands in Crystals. G. PARZEN AND T. WAINWRIGHT, *University of Notre Dame.*—A method has been developed for calculating the energy levels of a crystal which will take into account the actual shape of the atomic polyhedra. The idea behind our approach is to find a variational principle for the energy levels of the crystal which involve only the Wannier functions instead of the usual Bloch wave functions. The hope is that such a variational principle will avoid the difficulties of having to fit the awkward boundary conditions on the surface of the atomic polyhdron and that at the same time the integrals arising will extend over a few cells of the crystal rather than over the entire crystal. The variational principle does not give $E(\mathbf{K})$ directly, but if $E(\mathbf{K})$ for a particular band is expanded in a Fourier series in $\mathbf{K}$, then our variational principle allows us to calculate the Fourier coefficients of $E(\mathbf{K})$ in this expansion. The method has been applied to a one-dimensional problem, and the results seem promising. We are now applying the method to lithium and sodium.

K13. Solids Subjected to a Constant Rate of Generation of Lattice Defects. JEROME ROTHSTEIN, *Signal Corps Engineering Laboratories.*—If a solid is subjected to a constant rate of lattice defect generation (e.g., by photon, electron, or nucleon irradiation), defect concentrations are produced which may exceed those characteristic of thermal equilibrium. At low temperatures, defect destroying mechanisms are largely ineffective; at high temperatures they reduce defect concentrations practically to equilibrium values. A simple kinetic treatment of Frenkel or Schottky thermal defects plus generated defects yields defect density decreasing as temperature rises from low values until a minimum defect density is reached. Thereafter defect density increases, approaching thermal asymptotically. The temperature range below minimum defect density exhibits anomalous dependence of defect concentration on temperature and hence possible anomalies in properties dependent on defects or disorder. Such possibilities include retrograde expansion coefficient, anomalous dip in specific heat, anti-Curie point (temperature below which disordered phase is stable), anomalous temperature dependence of diffusion rate, rate of solid-state chemical reactions, defect-dependent conductivity and photoconductivity in intrinsic semiconductors, density of traps and donors in phosphors and semiconductors, color centers and photoconductivity in alkali halides, internal friction, ultrasonic attenuation, etc. Clear-cut experiments without prohibitive difficulties seem feasible.

FRIDAY EVENING AT 7:00
Starlight Roof, Chase Hotel
(ENRICO FERMI presiding)

Banquet of the American Physical Society

After-dinner speakers: A. H. COMPTON, A. L. HUGHES, and A. H. WEBER

SATURDAY MORNING AT 9:45

Brown Hall

(A. L. HUGHES presiding)

Symposium of the Division of Electron Physics

Physical Electronics

P1. Photoelectric Emission from Solids. L. APKER, *General Electric Research Laboratory.* (40 min.)

P2. Experiments and Thoughts on Secondary Emission. J. B. JOHNSON, *Bell Telephone Laboratories* (now with *Edison Laboratory, Thomas A. Edison, Inc.*) (40 min.)

P3. Researches in Ultra-High Vacuum. D. ALPERT, *Westinghouse Research Laboratories.* (40 min.)

SATURDAY MORNING AT 10:00

Loudermann Hall

(L. M. LANGER presiding)

Beta-Emitters, Helium through Cadmium

Q1. Electron-Neutrino Angular Correlation in the Beta-Decay of He^6.† JAMES S. ALLEN AND W. K. JENTSCHKE, *University of Illinois.*—The energy spectrum of the recoil nuclei emitted during the beta-decay of He^6 has been investigated by means of a time of flight method. The beta-rays were recorded by a scintillation counter having a stilbene crystal, and an electron multiplier tube was used to detect the recoil nuclei. The detection of a beta-ray by the scintillation counter initiated the sweep of an oscilloscope, and the time of flight of the accompanying recoil nucleus was indicated by the position of a pulse on this sweep. In this experiment the angle between the directions of emission of the beta-rays and the recoil nuclei was limited to a range of approximately 100 to 180 degrees. The shape of the time of flight spectrum suggests a $1+(v/3c)\cos\theta$ electron-neutrino angular correlation corresponding to the tensor type of interaction. The experiment is being continued in order to increase the statistical accuracy of the data.

† Assisted by the joint program of the ONR and AEC.

Q2. Spectrometer Measurement on the High Energy Positrons of Sodium 22.* BYRON T. WRIGHT, *University of California at Los Angeles.*—Using a small solenoidal spectrometer,[1] a measurement of the ratio R of the transformation constant of the lower energy spectrum to that of the higher energy spectrum of positrons from Na^{22} was made. By careful attention to the shielding and baffles and by using an end-window Geiger counter seven millimeters in diameter and about 25 millimeters long as the detector, the background counting rate with an 0.3 millicurie source of Na^{22} was reduced to 0.1 counts per second. Momentum plots of the then observed spectra agreed with the expected shapes to a point well below the maximum on each curve (assuming the higher energy spectrum to have an allowed shape; this experiment yields no meaningful data on the details of the shape of the higher energy spectrum). The ratio R was obtained by averaging the ratios of the observed counting rates for four corresponding points near the maxima of the two spectra. The result is $R=1800\pm400$. The transformation constant for the decay of Na^{22} to the ground state of Ne^{22} is $4.7\pm1.0\times10^{-12}$ sec^{-1}, based on a half-life of Na^{22} of 2.60 years.[2]

* Supported in part by the joint program of the ONR and AEC.
[1] Byron T. Wright, Am. J. Phys. 20, 230 (1952).
[2] L. J. Laslett, Phys. Rev. 76, 858 (1949).

Q3. The High Energy Negatron Spectrum of Sc^{46}. J. A. WHALEN, F. T. PORTER, AND C. S. COOK, *Washington University.*—Investigation of the high energy negatron spectrum of Sc^{46} has been continued[1] since sources of higher specific activity have been made available from Oak Ridge. In addition to the internal conversion electrons, a weak continuous negatron spectrum is still observed in the momentum range above 350 kev. It is still not possible to eliminate completely the existence of any Compton electrons produced in the source. However, electrons whose intensity relative to the lower energy beta-spectrum and to the internal conversion lines is constant, independent of source thickness, have been found in the region beyond the highest Compton electron momentum. The energy of this beta-group cannot be greater than 1.2 Mev. The current measurements indicate that less than 0.1 percent of the beta-transitions go through the higher energy group. The total internal conversion coefficients $(K+L+M)$ are, from these measurements, 1.9×10^{-4} for the 0.88-Mev gamma and 8.8×10^{-5} for the 1.11-Mev gamma.

* Assisted by the joint program of the ONR and AEC.
[1] F. T. Porter and C. S. Cook, Phys. Rev. 81, 640 (1951).

Q4. The Beta-Spectrum of S^{35}.* J. P. MIZE AND D. J. ZAFFARANO, *Iowa State College.*—The beta-spectrum of S^{35} [1] has been investigated with a proportional counter spectrometer whose geometric efficiency is ~100 percent. Our data yield a straight Fermi plot from the end point of the spectrum down to 10 kilovolts. The sources consisted of 0.005 microcurie of carrier-free S^{35} mounted on zapon films of 4 ± 2 μg/cm^2 surface density. The source films are supported within the counter volume parallel to and one inch away from the center wire. The cylindrical proportional counter is 24 inches long with an inner diameter of 8.5 inches and is filled with an argon-methane admixture to an absolute pressure of 40 lb/in.^{2}. Data were obtained with a one-channel differential discriminator. The associated electronic equipment was tested for linearity with a mercury relay type of pulse generator. X-rays were fired into the spectrometer through a beryllium window for energy calibration. Calibration and resolution of the spectrometer as well as results obtained with other sources will be discussed.

* This work was performed in the Ames Laboratory of the AEC.
[1] Heller, Sturcken, and Weber, Phys. Rev. 83, 848 (1951). (This contains references to earlier papers.)

Q5. Excited Levels of Ti^{48}. PAUL L. ROGGENKAMP, CHARLES H. PRUETT, AND ROGER G. WILKINSON, *Indiana University.**—The disintegration scheme of the decay of 16-day V^{48} to Ti^{48} has been studied by scintillation counter methods, and spins and parities have been assigned to the levels. The angular correlation of the well-known cascade gamma-ray pair with energies of 0.99 and 1.32 Mev has been measured. The results support the assignment 0–2–4 for the corresponding levels. Interference from the correlation of the annihilation radiation at 180° is eliminated by the use of differential discriminators in each channel. A gamma-ray at 2.20 Mev appears in the scintillation spectrum and is found to be in coincidence with the annihilation radiation, but not with the cascade pair. Further evidence that this gamma-ray is not the crossover of the cascade pair has been obtained from magnetic beta-ray spectrometer studies of the positron spectrum. These measurements suggest positron emission to a level in Ti^{48} 2.20 Mev above the ground state. The positron-group involved in the decay to the 2.31-Mev level of Ti^{48} is found to have an end-point energy of 0.69 Mev. Shell model considerations and the angular-correlation measurements result in consistent assignments of the spins and parities for the ground states of Sc^{48} and V^{48} as well as for the 2.20-Mev level of Ti^{48}.

* Supported by the joint program of the ONR and AEC.

Q6. Atomic Excitation and Ionization Accompanying Orbital Electron Capture by Nuclei. H. PRIMAKOFF AND F. T. PORTER, *Washington University.**—The process of atomic excitation and ionization accompanying orbital electron capture by nuclei is treated on the basis of the general theory of β-decay using a configuration space representation for both nucleons and leptons. Quantitative expressions are obtained (a) for the total number of double holes produced in the K shell due to K capture accompanied by excitation or ejection of the other K electron, and (b) for the total probability of electron ejection in orbital electron capture together with the ejected electron momentum spectrum. A discussion is given of the possibilities of experimental verification of the theory developed.

* Assisted by the joint program of the ONR and AEC.

Q7. An Upper Limit for Atomic Orbital Electron Ejection Accompanying K Capture in Fe^{55}. F. T. PORTER AND H. P. HOTZ, *Washington University.**—An upper limit has been determined for the number of atomic orbital electrons ejected during the decay of Fe^{55} by orbital capture. From cloud-chamber observations it is concluded that less than 0.6×10^{-6} electron are ejected per disintegration with energies in the range 30 kev to 205 kev. The theoretical prediction gives the order of 10^{-6} electron per disintegration for the frequency of the process in the energy range studied.

* Assisted by the joint program of the ONR and AEC.

Q8. Nuclear Spectra of Rb^{82} and Rb^{84}. CHARLES M. HUDDLESTON AND ALLAN C. G. MITCHELL, *Indiana University.**—The nuclear spectra of Rb^{82} (6.3 hr) and Rb^{84} (34 day) have been measured with a magnetic lens spectrometer. Rb^{82} emits two positron groups of energies 0.775 and 0.175 Mev. It also decays by orbital electron capture. A large number of gamma-rays accompanies the disintegration. Reasonable agreement with the gamma-rays emitted by Br^{82} has been obtained. Rb^{84} emits three groups of positrons having end-point energies of 1.629, 0.822, and 0.373 Mev. One gamma-ray whose energy is 0.890 Mev has been found. Level diagrams for these disintegrations will be discussed.

* Supported by the joint program of the ONR and AEC.

Q9. The Isomer Rb^{84m}. R. S. CAIRD AND ALLAN C. G. MITCHELL, *Indiana University.**—With the help of scintillation counters information on the isomer Rb^{84m} has been obtained. The isomer was produced by an $(n, 2n)$ bombardment of ordinary Rb salts. The half-life has been determined as 21 min. Three gamma-rays have been observed at 0.239, 0.463, and 0.890 Mev. The last gamma-ray occurs in the product Kr^{84}. Coincidence measurements show coincidences between the gamma-ray at 0.239 Mev and another of nearly the same energy, while coincidences between the 0.463 and the gamma-rays at 0.239 Mev are essentially negligible. A possible level scheme will be discussed.

* Supported by the joint program of the ONR and AEC.

Q10. The Disintegration of Sr^{91} and Y^{91m}.* D. P. AMES,† M. E. BUNKER, L. M. LANGER,‡ AND B. M. SORENSON, *Los Alamos Scientific Laboratory.*—The radiations from the fission product Sr^{91} (9.67 hr) have been studied using a magnetic lens spectrometer, a high resolution 180-degree focusing spectrometer, and a coincidence arrangement employing scintillation detectors. Five beta-ray groups are observed with end-point energies and relative intensities of 2.665 Mev, 26.1 percent; 2.03 Mev, 4.4 percent; 1.355 Mev, 29.3 percent; 1.093 Mev, 33.1 percent; and 0.62 Mev, 7.1 percent. The 2.665-Mev group has a forbidden shape indicating a spin change of two units and a parity change. Gamma-rays are found with energies of 1.413, 1.025, 0.747, 0.63, and 0.5512 Mev. The 0.5512-Mev gamma-ray has a $K/L+M$ internal conversion ratio of 6.00, which identifies it as an $M4$ isomeric transition. The isomeric state in Y^{91} has a half-life of 50.3 minutes and decays only by gamma-emission to the ground state. A disintegration scheme will be presented.

* Work performed under the auspices of the AEC.
† Now at the University of Kentucky, Lexington, Kentucky.
‡ Indiana University, Bloomington, Indiana.

Q11. Effect of the Chemical Binding and the Phase on Angular Correlations.* ROLF M. STEFFEN, *Purdue University.*—The influence of the chemical state and the phase of In compounds on the angular correlation of the Cd^{111} gamma-rays was investigated. It was found that the phase rather than the chemical structure of a particular In compound is responsible for the differences in the recovery time of the Cd atom, with the exception of the In metal, where the angular correlation depends on the size of the crystallites. Solid In compounds, i.e., dry $InCl_3$, InI_3, $In(NO_3)_3$, In_2O_3, $In(OH)_3$, $In_2(SO_4)_3$, In-8-hydroxyquinolinate, and also quenched In metal, show practically isotropic angular correlation. All liquid samples investigated, i.e., dilute aqueous solutions of $InCl_3$, InI_3, $In_2(SO_4)_3$, $In(NO_3)_3$, In-8-hydroxyquinolinate dissolved in $ChCl_3$, liquid InI_3 and $InCl_3$, and liquid In metal, exhibited the presumably maximum anisotropy $A=-0.19\pm0.02$. Electrodeposited In metal showed an anisotropy of -0.04 to -0.11 depending upon the size of the In crystallites. An attempt to influence the angular correlation of the Pt^{198} gamma-rays by using Au^{198} sources in different chemical states and environments (Au^{198} in Au, Au^{198} in Pt, dry $AuCl_3$, dilute aqueous solution of $AuCl_3$) failed. All Au^{198} sources showed the same angular correlation: $W(\vartheta)=1-1.20\ \cos^2\vartheta+1.12\ \cos^4\vartheta$; $(a_1=-1.20\pm0.05, a_2=+1.12\pm0.05, (a_1+a_2)=-0.08\pm0.03)$. This correlation is characteristic for a $2-Q+D-2-Q-0$ transition, with a 2.7 percent to 5.3 percent dipole admixture in the first transition.

* Supported by the AEC.

Q12. Isomerism for Cd^{117}, In^{117}, and In^{118}.* CHARLES D. CORYELL, PIERRE LÉVÊQUE,† AND HAROLD G. RICHTER,‡ *M.I.T.*—Radiochemical studies on cadmium isotopes formed in fission and their indium daughters, and the products of

Cd(n, γ) and Cd(d, p) reactions, show the known[1] 43d Cd^{115m}, and 2.3d $Cd^{115} \rightarrow 4.5h$ In^{115m}, and new evidence on the following species: 3.0h Cd^{117m}, decaying largely by I.T.; $\sim$50m Cd^{117}, β^- and γ; 70m In^{117m} β^-, weak γ; $\sim$2.5h In^{117} β^-, very weak γ; $\sim$30m Cd^{113} β; and $<$1m In^{113}, 4 Mev β. The $<$1m In^{113} is isomeric with the known[2] 4.5m In^{113} not formed from Cd^{113}. Nishina[3] observed $\sim$50m Cd in fission, assigned[1] to Cd^{111m}. Later workers[1] missed $\sim$30m Cd^{113} and $\sim$50m Cd^{117} by delay in studies. In recent spectrometric work[4] on supposed 1.95h In^{117}, $\sim$2.5h In^{117} was masked by 4.5h In^{115m}. The ratio of 3.0h Cd^{117m} to $\sim$50m Cd^{117} formed in the (d, p) reaction is near to secular equilibrium.

* This work was supported in part by the AEC.
† Research Fellow from the Commissariat à l'Énergie Atomique (Paris) under M.I.T. Foreign Students Summer Project.
‡ Department of Chemistry, University of Oregon, Eugene, Oregon.
[1] C. D. Coryell and N. Sugarman, *Radiochemical Studies: The Fission Products* (McGraw-Hill Book Company, Inc., New York, 1951), Appendix C.
[2] R. B. Duffield and L. M. Lanzer, Phys. Rev. **75**, 1967 (1949).
[3] Nishina, Yasaki, Kimura, and Ikawa, Phys. Rev. **58**, 660 (1940).
[4] J. D. Knight and G. A. Cowan, Los Alamos Scientific Laboratory, private communication

Saturday Morning at 10:00

Wilson Hall

(Eugene Feenberg presiding)

Invited Papers

R1. Photoproduction and Multiple Scattering of Mesons within Atomic Nuclei. K. M. Watson, *Indiana University.* (30 min.)

R2. A New Theoretical Approach to the Pion-Nucleon Interaction. G. F. Chew, *University of Illinois.* (30 min.)

R3. Charge-Independence in Meson Production. R. H. Hildebrand, *University of Chicago.* (30 min.)

R4. Neutron Binding-Energies of Heavy Elements and Some Applications. J. R. Huizenga, *Argonne National Laboratory.* (30 min.)

Saturday Morning at 10:00

Rebstock Hall

(R. D. Sard presiding)

Neutron Physics; General Nuclear Physics

S1. Neutron Resonances in Xenon. S. P. Harris, *Argonne National Laboratory.*—Previous measurements using scattering and boron absorption techniques indicated the existence of resonances in xenon at about 11 ev.[1] Using the high speed neutron velocity selector,[2,3] transmission measurements have been made on xenon gas in the 1.5 ev to a few thousand ev region. Two prominent resonances were found, at 13.9$\pm$0.2 and 9.3$\pm$0.2 ev, with a sample thickness of 0.260 g/cm^2. Calculation of $\sigma_0\Gamma^2$ by the method of Havens and Rainwater[4] for the 13.9-ev resonance gave $\sigma_0\Gamma^2 \sim 1000$ b (ev)^2. The observed cross section at the minimum of the transmission dip was $>$2000 b for this resonance with a resolution of about 1μ sec/meter. Transmission curves will be shown.

[1] S. P. Harris, Phys. Rev. **80**, 20 (1950).
[2] W. Selove, Rev. Sci. Instr. **23**, 350 (1952).
[3] Bollinger, Harris, and Schumann, Phys. Rev. **87**, 184 (1952).
[4] W. W. Havens, Jr., and L. J. Rainwater, Phys. Rev. **83**, 1123 (1951).

S2. Slow Neutron Resonances in Sm and Y.† V. L. Sailor, H. L. Foote, Jr., and H. H. Landon, *Brookhaven National Laboratory.*—The total neutron cross section of Sm and Yb[1] from 0.1 to $\sim$40 ev has been measured with the Brookhaven crystal spectrometer. Resonances in Sm were observed at 0.094, 0.87, 3.43, 4.95, 8.20, 15, and 19 ev. The 0.094-ev resonance was previously reported by Borst[2] and Sturm,[3] and the resonance at 8.20 ev corresponds to the one previously observed by Sturm[3] at about 10 ev. The 8.20-ev resonance is exceptionally strong and, in fact, closely approaches the limiting value $\sigma_0 \approx \pi\lambda_0^2$, which is consistent with the results of Goldhaber.[4] The isotopic assignment of the Sm resonances obtained by using enriched isotopes will be discussed. Resonances in Yb occur at 0.597, 4.55, 8.09, 13.3, 18.2, and $\sim$30 ev.

† Research performed under the auspices of the AEC.
[1] Exceptionally pure samples of Sm and Yb were generously lent to us by Dr. F. H. Spedding of the Ames Laboratory, AEC.
[2] Borst, Ulrich, Osborne, and Hasbrouck, Phys. Rev. **70**, 557 (1946).
[3] W. J. Sturm, Phys. Rev. **71**, 757 (1947).
[4] Goldhaber, Lowry, and Sunyar, Brookhaven National Laboratory Report BNL-C-9, 96 (1949).

S3. Total Cross Sections for Fast Neutrons.* R. L. Becker,† M. Walt,‡ and A. Okazaki, *University of Wisconsin.*—The total neutron cross sections of Co, Ga, Se, Cd, Te, Pt, Au, Hg, and Th were measured as a function of neutron energy, from 0.1 to 3 Mev. Transmission experiments were performed using cylindrical samples of the elements. For energies above 1 Mev, neutrons were produced by bombarding a Zr$-$H^3 target with protons. Below 1 Mev, a lithium target was used. To determine the correction for neutrons scattered into the detector by the sample, the variation of the apparent cross section with diameter of the sample was investigated. Previous data had shown regularities in total fast neutron cross sections,[1] and the present experiment was performed to supplement these data. The results give additional evidence that, aside from resonance structure, curves of total neutron cross

sections *versus* energy have characteristic shapes which vary slowly with atomic weight.

* Work supported by the Wisconsin Alumni Research Foundation and the AEC.
† National Science Foundation Predoctoral Fellow.
‡ AEC Predoctoral Fellow.
[1] H. H. Barschall, Phys. Rev. **86**, 431 (1952).

S4. Gamma-Rays Produced by the Inelastic Scattering of 14-Mev Neutrons.* LEWIS C. THOMPSON, *The Rice Institute* (introduced by J. G. Risser).—A NaI scintillation spectrometer has been used to detect the gamma-rays produced by the inelastic scattering 14-Mev neutrons. Positive results were obtained in the case of iron and lead. In iron, lines were seen corresponding to the 0.845- and 1.24-Mev gamma-rays reported by Elliott and Deutsch[1] from the excited state of Fe^{56}. Above this energy the spectrum appeared to be a continuum which extended to about 8 Mev. The lead spectrum seemed to be a continuum that extended to 3 Mev. This was interpreted to mean that the $(n, 2n\gamma)$ reaction probably predominated in lead, but that the $(n, n\gamma)$ reaction was occurring at least part of the time in iron. The NaI itself showed a possible capture gamma-ray at 5.8 Mev. Its spectrum extended up to 14 Mev.

* Work performed under the auspices of the AEC.
[1] L. G. Elliott and M. Deutsch, Phys. Rev. **63**, 321 (1943).

S5. Measurement of the Energy of Isotropic Fast Neutrons with Li^6 Loaded Emulsions.* J. H. ROBERTS, W. O. SOLANO, D. E. WOOD, AND H. B. BILLINGTON, *Northwestern University*.—One-hundred micron *E*1 and *C*2 Ilford plates loaded with enriched Li^6 were exposed to neutrons produced in electrostatic generators from $Li^7(p, n)Be^7$ and from $H^3(p, n)Ne^3$. The plates, wrapped in cadmium, were rotated so as to mock-up a condition of isotropic neutron incidence. The plates were faded and developed so as to obtain good discrimination in triton-alpha tracks resulting from $Li^6(n, \alpha)H^3$. Neutron energies from the Be^7 ground-state transition were 0.200, 0.600, 1.00, and 1.500 Mev from the $p-t$ reaction. Target thicknesses were usually 25 kev. The plates were treated with glycerine to prevent shrinkage. Measurements of the triton length, alpha-length, and triton-alpha angle gave information to select tracks "favoring"[1] the triton to obtain optimum energy resolution. Peaks having widths from 100 to 300 kev at half-maximum were obtained, depending upon neutron energy and selection criteria. Observer agreement with generally good, but some bad results were obtained. Methods of putting the technique on a more objective basis are being investigated.

* Work supported by an AEC contract.
[1] G. R. Keepin and J. H. Roberts, Rev. Sci. Instr. **21**, 163 (1950).

S6. The Production of Characteristic X-Rays by Proton Bombardment.* B. E. SIMMONS,† H. W. LEWIS, AND E. MERZBACHER,‡ *Duke University*.—Characteristic x-rays produced by 2- to 3-Mev protons on thick targets of Mo, Ag, Ta, Au, and Pb have been investigated with a NaI scintillator. The x-ray energies are such that the *K* series could be studied for the two lightest elements and both *K* and *L* series for the three heavy ones. Lines in the same series could not be resolved, but *K* and *L* series for a given element gave well-separated differential pulse-height peaks. No x-ray continuum is produced by proton bombardment and individual characteristic photons lose their entire energy in the scintillator. Thus, the width of the counting rate peak is due partly to the presence of several lines in a series and partly to crystal and phototube resolution. Variation of the cross section for *K* ionization as a function of target *Z* and proton energy, together with measured absolute cross sections, will be discussed in relation to the theory of Henneberg and to the experimental results of previous workers using ionization chambers and absorbers. Thick target yields were converted to cross sections by numerical integration assuming the fourth power dependence of proton energy derived by Henneberg. The correction for Auger electron emission is less than a factor of two for the lightest element. Results are important in the theory of stopping power for heavy particles.

* This work was supported by the AEC.
† Now at the University of Minnesota.
‡ Now at the University of North Carolina.

S7. X-Rays from the Mesic Carbon Atom.* H. J. SCHULTE, J. B. PLATT, AND M. CAMAC, *University of Rochester*.—We have observed 100-kev quanta in coincidence with the stopping of negative pions in carbon.[1] These quanta are of the correct energy to arise from x-ray transitions of the pion to the *K* shell of the mesic carbon atom. To evaluate the yield of such *K* x-rays we have done the following: (a) measured the spatial distribution and absolute number of pions stopped in the carbon; (b) identified and counted the x-rays by means of a NaI scintillation spectrometer; and (c) calculated the over-all detection efficiency including average solid angle, x-ray filter attenuation and crystal efficiency for the expected energy. The x-ray energies have been measured by two independent methods: (a) the balanced filter method of Ross with x-ray absorbers of Pb and Th; (b) use of an artificial light pulse[1] which had previously been matched to 74-kev NaI response. Our present value for the yield of *K* x-rays from carbon is 0.12 ± 0.02 x-rays per stopped pion.

* Supported jointly by the University of Rochester and the AEC.
[1] Camac, McGuire, Platt, and Schulte, Phys. Rev. **88**, 134 (1952).

S8. *Z* Dependence of Mesic X-Ray Yield.* M. CAMAC, J. B. PLATT, AND H. J. SCHULTE, *University of Rochester*.—Using the experimental arrangement described in the previous paper, x-rays have been observed in coincidence with the stopping of negative pions in Be and H_2O. The energies of these x-rays are in agreement, within experimental error, with the Moseley law predictions for the mesic Be and O atoms. In the case of O the yield of these quanta has been found to be 0.21 ± 0.07 quanta per stopped pion. It is expected that results will also be presented for mesic N and F atoms as well. Simple theoretical arguments[1] indicate that this yield *Y* should be given by $Y = 1/(1+CZ^3)$, where *Z* is the atomic number and *C* is a constant of the order of 0.2. Preliminary work has shown that this formula predicts correctly the yield for the C mesic atom, but the predicted value of 0.06 for O is substantially lower than the observed value. The implications of this disagreement will be discussed.

* Supported jointly by the University of Rochester and the AEC.
[1] A. M. L. Messiah and R. E. Marshak, NYO-3701; Phys. Rev. (to be published).

S9. The Excited Energy Levels of Nuclei as Rational Multiples of the Electron Mass. ENOS E. WITMER, *University of Pennsylvania*.—The writer[1] has recently presented evidence which indicates that the rest mass *m* of the negative electron is the natural unit of mass for nuclei and elementary particles. The mass of any nucleus or elementary particle in any state may be written *Mm*. Then we believe *M* is always a rational number. Consequently, the excited energy levels of nuclei may also be written as *Mm*, because the difference of two rational numbers is another rational number. Now this conclusion can be tested rather precisely in a number of cases. Out of 122 excited energy levels measured with sufficient accuracy for this purpose there were 13 for which *M* was an integer to within ± 0.02. The probability of this occurring by chance is only 8.7×10^{-4}. Also in the same set of energy levels there were 44 for which *q* was 1, 2, 3, or 4, where $M = p/q$, both *p* and *q* being integers. Again the tolerance was ± 0.02. The probability of this occurring by chance is only 9.2×10^{-4}. In the case of one nucleus there were 3 integral values of *M* in 20 energy levels.

[1] Enos E. Witmer, Phys. Rev. **87**, 237 (1952).

SATURDAY MORNING AT 10:00

Crow Hall, 101

(C. F. SQUIRE presiding)

Fluid Dynamics; Cryogenics

T1. On the Fundamentals of the Boundary Layer Theory. M. Z. v. KRZYWOBLOCKI, *University of Illinois* (introduced by F. T. Rogers, Jr.).—The author discusses two fundamental problems in the boundary layer theory, namely, (a) the proof of existence and uniqueness of the solution of the equations governing the motion and energy distribution in the boundary layer and (b) the fundamental differential system of equations governing the distribution of the velocity, density, pressure, and temperature in the boundary layer. A brief discussion on the subject of fundamentals of the boundary layer in hypersonic flow closes the paper.

T2. Streaming Potentials Developed across Porous Diaphragms for Sinusoidal Flow.* R. G. PACKARD, *Baylor University* (introduced by H. D. Schwetman).—Sinusoidal streaming potentials are developed across porous diaphragms of sand, plastic shavings, cellulose, and fritted glass for sinusoidal pressures. The frequency range studied was 20 cps to 350 cps, and the pressure amplitudes ranged from 0 to 20,000 dynes/cm². Distilled water was used throughout the experiments. A specially designed plastic cell in which the samples were retained is described. Frequency response curves and amplitude response curves are given.

* Work done under contract between Defense Reserve Laboratory, the University of Texas, and the U. S. Navy.

T3. Ultrasonic Velocity, Density, and Compressibility of Supercooled H_2O and D_2O. R. T. LAGEMANN AND L. W. GILLEY, *Vanderbilt University*.—Because water can be easily supercooled, it has been possible to measure the velocity of compressional waves in liquid water (H_2O and D_2O) over a range of temperatures extending to some six degrees below the nominal freezing point, using a fixed-frequency (500 kc), variable-path sonic interferometer. It was also possible to determine the density of heavy water in the supercooled state and obtain values of the adiabatic compressibility. The curves representing the variation of density with temperature are symmetrical and congruent for the two isotopic liquids. It is confirmed that the compressibility of D_2O is greater than that of ordinary water, compared either at the same temperature or in corresponding states based on the freezing points. The new measurements on the three properties yield values which fall on smooth extrapolations of the previously known data, indicating that there is not partial ordering of the liquid structure into the solid structure at temperatures below the nominal freezing point, at least none at times removed from the start of observed freezing.

T4. Propagation of Explosive Produced Air Shocks. J. SAVITT, *U. S. Naval Ordnance Laboratory*.—It has been previously reported* that the velocities of ionized air shocks produced by the detonation of highly confined solid explosives depend upon the distance from the explosive air interface, the composition of the explosive, its weight, its geometry, and to some extent for a particular explosive upon its loading density and particle size. These small scale one-dimensional ionized air shock propagation experiments near detonating explosives have been extended to include measurements made in heavy walled tubes varying in internal diameter from 0.100 to 0.300 inch. The velocities of one-dimensional air shocks produced by detonating highly confined TNT and RDX were measured at several distances from the explosive air interface. These velocities were found to depend upon the diameter of the explosive as well as upon the diameter of the shock tube. It was found, in general, that for a fixed shock tube diameter the air shock velocity increased with increasing explosive diameter, while for a fixed explosive diameter it was observed that the air shock velocity increased with decreasing shock tube diameter.

* J. Savitt and R. H. Stresau, Phys. Rev. **85**, 732(A) (1952).

T5. Plane Supersonic Flow Patterns in Ionized Media. W. R. ATKINSON AND R. G. FOWLER, *University of Oklahoma*.—Expansion of spark discharges at low pressure when confined to a cylindrical glass tube can result in plane supersonic flow accompanied by all the normal behavior of such a flow. Shocks and contact surfaces can be observed in their own luminosity, and interactions of these fronts with each other furnish considerable evidence for the supersonic flow interpretation of the Rayleigh phenomenon. Most of the variety of interactions which can be produced are also excellent exemplifications of the theory of plane supersonic flow and will be discussed. New interactions have been observed, however, which are not recognized by this theory and which may reflect the peculiar processes of the highly ionized plasma.

T6. Ion Concentrations in Shock-Type Spark Discharge Tubes. R. G. FOWLER AND H. C. ROSE, *University of Oklahoma*.—Measurements of time-averaged ion concentration at all points along a shock type discharge tube existing as a result of the expansion of gas excited during the discharge of capacitor have shown behavior which can only be accounted for by assuming either that the Holtsmark theory of Stark broadening cannot be applied to this situation, or that excitation continues actively after the cessation of the discharge current. The ion concentration indicated by the Holtsmark theory reaches a maximum during the expansion, and the total intensity of the discharge is a maximum at the same point. The behavior of the post discharge expansion is insensitive to the direction of the original discharge current, so that it is probable that electrical mechanisms are secondary to thermal ones in causing the expansion.

T7. Flow of Helium II through Narrow Slits. RICHARD T. SWIM,* *The Rice Institute*.—Experiments are in progress to measure the volume rate of flow of helium II, under pressure gradients, through slits of width 3.5μ or less. The experimental arrangement is similar to that of Bowers and Mendelssohn[1]; however, the apparatus is such that considerably higher pressure heads can be realized than in previous work of this nature. The measured flow rates at pressure heads of less than 4 cm of helium are in general agreement with the results of other investigators,[1,2] but at higher pressures (extending thus far to 14 cm of helium) the flow rates are no longer adequately described as proportional to a power of the pressure head. In fact, the rate appears to approach a value independent of pressure at the highest pressure heads, the maximum linear velocity being of the order of 30 cm/sec at a temperature of 1.75°K.

* Magnolia Petroleum Company Fellow.

[1] R. Bowers and K. Mendelssohn, Proc. Roy. Soc. (London) **A213**, 158 (1952).

[2] G. K. White, Proc. Phys. Soc. (London) **A64**, 554 (1951).

T8. Frozen Moments in a Superconducting Sphere. TOM S. TEASDALE, *The Rice Institute.*—A series of experiments is being carried out in which the residual magnetic flux of a superconductor is measured. The apparatus consists of a torsion pendulum with which the torque on a superconducting tin sphere is measured as a function of an externally applied magnetic field. If an effective magnetic moment for the sphere is defined by considering the sphere as a magnetic dipole oscillating in a uniform field, then it is found that the moment frozen in at constant temperature is a reproducible function of the critical field for the temperature at which the moment is formed. Preliminary investigations indicate that the moment, when measured at the temperature at which it is formed and calculated using the model indicated above, shows a pronounced minimum when plotted as a function of the critical field at which it is formed. (The moment appears to become large as the zero field transition temperature is approached and as one goes to very low temperatures.)

T9. Current Noise in Partially Superconducting Resistors at Temperatures Down to 2°K. B. KAPLAN AND J. G. DAUNT, *Ohio State University.*—Measurements have been made of the current noise in tantalum and leaded phosphor-bronze in the helium temperature region, the noise power being obtained as a function of the frequency of observation from 200 to 4000 cycles/sec. In the intermediate state the tantalum specimen showed large current noise. A possible explanation is put forward on the basis of temperature fluctuations in the specimen. No current noise was observed in the partially superconducting leaded phosphor-bronze specimen.

SATURDAY AFTERNOON AT 2:00

Loudermann Hall

(J. S. JASTRAM presiding)

Beta-Emitters from Caesium Onward; Nuclear Scattering

V1. Gamma-Radiation from Radioactive Cesium 134.* J. M. LEBLANC, W. H. NESTER, D. W. MARTIN, M. K. BRICE, AND J. M. CORK, *University of Michigan.*—Using photographic magnetic spectrometers the energies of conversion and photoelectrons from specimens of cesium, obtained as a fission product, have been evaluated. The results indicate some needed revision in the previously reported values for seven of the gamma-rays and show the presence of four additional gammas not before observed. The energies of these radiations, believed to be accurate to ±0.2 percent, are 202.5 475.0, 563.0, 569.7, 605.4, 662.7, 796.8, 802.6, 1039, 1168, and 1368 kev. The K/L ratio for the 605.4- and the 796.8-kev gamma-rays are found to be 6.4±0.8 and 7.3±0.8, respectively, and both transitions are believed to be electric quadrupole. From mathematical identities evident in combinations of the gamma-energies it seems quite likely that at least ten of the transitions are associated with beta-emission and not K capture.

* This project received the joint support of the AEC and the ONR.

V2. Radioactivity of Cesium 138.* L. M. LANGER, *Indiana University,* R. B. DUFFIELD, *University of Illinois,* AND C. W. STANLEY, *Los Alamos Scientific Laboratory.*—Cs^{138} was chemically separated from other activities after a delayed collection of gaseous fission products from the "water boiler." Beta- and gamma-activities were found to decay with a single period of 32.0 minutes. The beta-spectrum was studied in a magnetic lens spectrometer. The resulting Fermi plot is concave towards the energy axis with a maximum energy of 3.40 Mev. An internal conversion line corresponding to a 0.463-Mev gamma-ray was also observed. In a ten-channel scintillation spectrometer, gamma-rays of 0.46, 0.98, and 1.44 Mev were observed with relative intensities of 0.33, 0.43, and 1.00, respectively. Beta-gamma coincidence absorption measurements indicate that betas as high as about 3 Mev are followed by one of the harder gamma-rays, probably the 1.44 Mev. Gated gamma-gamma coincidences further suggest that the 1.44-Mev gamma is, surprisingly, in series rather than in parallel with the 0.46- and 0.98-Mev gamma rays. It appears likely then that the 3.40-Mev beta-transition is not to the ground state of Ba^{138} but rather is followed by the 1.44-Mev gamma for a total energy release of 4.8 Mev, in good agreement with the predicted mass difference. It appears somewhat doubtful that the ground state of Cs^{138} has zero spin as suggested by the $(g_{7/2}, f_{7/2})$ assignment of the shell model.

* Research carried out at the Los Alamos Scientific Laboratory of the University of California under contract with the AEC.

V3. The Disintegration of Re^{188m}. J. W. MIHELICH, *Brookhaven National Laboratory.**—Neutron irradiation of Re^{187} produces a 22-minute activity of Re^{188m} which is isomeric with the 16.9-hr ground state. A NaI scintillation spectrometer reveals photopeaks corresponding to photons of ~60 kev and 105 kev. The number of quanta in the "60"-kev peak, consisting of Re $K-X$-rays and 63.5 γ-rays, is at least 10 times as great as the number in the 105-kev peak. The intensity of these photons, as well as that of $L-X$-rays observed with a proportional counter and the photon-photon coincidence rate, decays with a 22-minute half-life. The conversion electron spectrum was investigated with permanent magnet spectrographs. The energies of the conversion lines correspond to atomic electrons ejected by two transitions in Re: 105 kev (K, L_I, M_I) and 63.5 kev (L_I, M_I, N). The 22-minute lifetime cannot yet be definitely ascribed to either transition. Energy-lifetime considerations indicate a transition involving a spin change of 3.

* Research carried out under contract with the AEC.

V4. Isomeric Pt^{193}.* J. B. SWAN, W. M. PORTNOY, AND R. D. HILL, *University of Illinois.*—Iridium was bombarded with 12-Mev deuterons, and the platinum fraction containing radioactive Pt^{191} and Pt^{193} was chemically separated from the target material. The conversion-electron spectrum of the platinum was investigated, using 180° spectrographs. Among a large number of lines present were those of a strong 135-kev transition in platinum, decaying with a half-life ~4 days, and those of 83-, 96-, and 173-kev transitions, probably in iridium, decaying with a half-life ~3 days. The measured K/L ratio of 0.275, the $L_I:L_{II}:L_{III}$ ratios of 1:0:2, and the half-life ~4 days, identify the 135-kev transition as $M4$. Platinum was irradiated with γ-rays from a 22-Mev betatron, and strong lines from the 135-kev transition were observed. This $M4$ isomeric transition is, therefore, in Pt^{193}. The 83-, 96-, and 173-kev transition lines were not observed and are attributed to Pt^{191}. Other transitions of 130 and 76 kev, arising

from Pt^{195m} and Pt^{197}, respectively, were also observed. Neither source gave evidence of the 129- and 42-kev transitions which might be expected to occur following K capture in Pt^{191}.

* Assisted by the joint programs of the AEC and ONR.

V5. Neutron Deficient Isotopes of Hg.† K. GOPALAKRISHNAN AND A. DE-SHALIT, *Princeton University*, AND J. W. MIHELICH, *Brookhaven National Laboratory.*—A study of Hg^{196} and Hg^{193} was undertaken in order to look for a possible "family" of similar decay schemes. The isotopes were prepared by bombarding an Au target with high energy protons (we are indebted to Dr. S. Goldhaber, Dr. W. F. Goodell, and Dr. D. H. Greenberg of Columbia University, New York, for their kind cooperation in carrying out these irradiations at the Nevis Cyclotron Laboratory). The Hg was then separated carrier free and studied in a high resolution double focusing spectrometer at the Palmer Laboratory and in the permanent magnet spectrograph at Brookhaven National Laboratory. An isomeric state in Hg^{195} (38 hr) decays via two gammas (123 and 37 kev) to the ground state of Hg^{195} and also by a K capture to an isomeric state in Au^{195} which decays via two gammas (57 and 262) to the ground state of Au^{195}. The situation in Hg^{193} is similar, the respective gammas being 102 and 39 in Hg (10 hr), 32, 258, and 120 in Au. The half-life of Hg^{193} in the ground state is 27 hr.

† Work supported by the AEC and Higgins Scientific Trust Fund.

V6. Effects of Radioactive Disintegrations on Inner Electrons of the Atom. J. S. LEVINGER, *Louisiana State University.*—The probability that nuclear emission of an alpha-particle causes ionization of a K or L electron of the atom is calculated by time dependent perturbation theory, using Coulomb wave functions. Due to the nuclear recoil, Migdal's results[1] for dipole transitions are multiplied by $(A-2Z)^2/(A-4)^2$, roughly 1/25. Quadrupole transitions are negligible for K electrons, but are the predominant cause of ionization of L electrons. The ionization probabilities per alpha for Po^{210} are 10^{-7} for the K shell and 10^{-4} for the L shell. Relativistic corrections and screening corrections would increase the ionization probability by a factor of about 2 for the K shell and at least 3 for the L shell. This estimate is based on our calculation of the relativistic and screening corrections to the calculation[1] of ionization probability following beta-decay. We will compare our results with recent experiments on characteristic x-rays associated with Po^{210} and with RaE.

[1] A. Migdal, J. Phys. U.S.S.R. **4**, 449 (1941).

V7. A Precise Measurement of the "*F*" Line of Thorium B. D. I. MEYER* AND F. H. SCHMIDT, *University of Washington.*—The internal conversion electrons resulting from the decay of Th B are widely used as calibration standards in beta-ray spectroscopy. Siegbahn, Craig, Lindström,[1] and others have determined the $H\rho$ values of several lines. Lindström's most straightforward method involved the direct measurement of H (in terms of the proton magnetic moment) and of ρ. We have measured the momentum and energy of the "F" line by comparison with electrons accelerated through a measured potential difference. The comparison was made in an iron free high resolution (0.13 percent) solenoid spectrometer. Both components of the earth's field were canceled out. The accelerating potential was measured by a "series-parallel" precision manganin resistor which permitted direct comparison with standard cells. Corrections for the work function of the Wolfram filament of the electron gun were applied. Accelerating potentials up to 20 kv were used corresponding to a momentum of about one-third that of the "F" line. Linearity of the spectrometer was checked over the full range (2–20 kev) of the electron gun and, using published values of electron lines, at intervals up to 2.6 Mev. Our result for the "F" line is 1388.56 ± 0.21 gauss cm, in agreement with Lindström's value.

* Now at the University of Oklahoma.

[1] G. Lindström, Phys. Rev. **83**, 465 (1951).

V8. Proton-Proton Scattering at 5.77 Mev Using Photographic Techniques.* R. O. KERMAN,† W. E. KREGER,‡ AND P. G. KRUGER, *University of Illinois.*—Zimmerman and Kruger's[1] $p-p$ scattering results at 5.86 Mev gave a P-wave phase shift of $-0.36°\pm0.22°$; Rouvina[2] found no p-wave phase shift at 3.4, 6.8, and 7.5 Mev. To check this difference in results, new data have been taken at 5.77 Mev using a modification of the scattering chamber used previously by Rodgers *et al.*[3] The following absolute differential $p-p$ scattering cross sections in millibarns per steradian in the center-of-mass system were obtained (errors are probable errors): 23.00°: 118.0 ± 0.8, 23.87°: 110.0 ± 0.90, 26.00°: 95.91 ± 0.70, 27.85°: 91.73 ± 0.79, 30.00°: 87.30 ± 0.64, 31.84°: 83.53 ± 0.73, 35.00°: 81.98 ± 0.58, 40.00°: 82.82 ± 0.60, 45.00°: 81.12 ± 0.67, 50.00°: 83.28 ± 0.64, 54.76°: 85.00 ± 0.62, 60.00°: 85.70 ± 0.65, 69.70°: 86.86 ± 0.71, 79.68°: 86.73 ± 0.70, 84.73°: 86.51 ± 0.72, 89.68°: 87.18 ± 0.70, 94.71°: 87.28 ± 0.68, 99.68°: 87.87 ± 0.70, 109.69°: 86.01 ± 0.69. These gave an S-wave phase shift of $54.96°\pm0.16°$ and a P-wave phase shift of $-0.08°\pm0.05°$.

* This work has been supported jointly by the ONR and AEC and by a grant from the Research Corporation.
† Now at Kalamazoo College, Kalamazoo, Michigan.
‡ Present address: Code 3941A, U.S.N. Radiological Defense Laboratory, San Francisco 24, California.
[1] E. J. Zimmerman and P. G. Kruger, Phys. Rev. **83**, 218 (1951).
[2] J. Rouvina, Phys. Rev. **81**, 593 (1951).
[3] Rodgers, Leiter, and Kruger, Phys. Rev. **78**, 656 (1950).

V9. Inelastic Scattering of Neutrons. ROBERT B. DAY, *Los Alamos Scientific Laboratory.*—The inelastic scattering of neutrons has been investigated by observing the gamma-rays emitted in the decay of the excited nuclei. The detector was a NaI(Tl) scintillation counter shielded from the neutron source by a tungsten alloy cone and surrounded by a scattering ring of the material to be investigated. By observing the pulse-height spectrum from the scintillation counter it was possible to distinguish the gamma-rays from the scattering ring from the neutron-induced background, and at the same time to measure their energy to an accuracy of 1–2 percent. With a monoenergetic source of 2.5-Mev neutrons the following gamma-rays have been found (energies in Mev): B^{10}: 0.478, 0.717; F^{19}: 0.084, 0.114, 0.199, 1.36; Mg: 1.365; Al^{27}: 0.843, 1.018, 2.20; S: 0.077, 2.23; Fe: 0.850, 1.25, 1.42. With 5.5-Mev neutrons a 4.45-Mev gamma-ray has been found in carbon. These gamma-rays correspond in general to transitions between known levels of the target nuclei. Experiments have shown that the effects due to the cone are negligible except as a shield for the detector. Further work is in progress to measure the cross sections for these reactions.

V10. The Total Neutron-Proton Scattering Cross Section at 2.5 Mev.* R. E. FIELDS, R. L. BECKER,† AND R. K. ADAIR, *University of Wisconsin.*—The total cross section of hydrogen for 2.5-Mev neutrons has been determined by measuring the transmission of samples of 2-2-4 trimethylpentane and graphite. The neutrons were produced by bombarding thin targets of tritium absorbed in zirconium with protons from the electrostatic generator. Proton energy was measured with an electrostatic analyzer. A narrow neutron scattering resonance in carbon at 2078.5-kev neutron energy (measured by comparison with the $Li^7(p,n)Be^7$ threshold) was used as a calibration point. A one-inch diameter hydrogen recoil counter filled to a pressure of 500 pounds per square inch and placed 20 in. from the neutron source, at 0° relative to the proton beam, served as neutron detector. The discriminator was biased to reject pulses from neutrons of less than 1.25-Mev energy, thus reducing the background to about 0.6 percent. The preliminary results of this measurement are $\sigma=2.525\ (\pm0.009)\times10^{-24}$ cm^2

at neutron energy 2.532 (±0.006) Mev. These values together with the values of A_T, A_S, and r_t given by Burgy, Ringo, and Hughes[1] yield a singlet effective range of 2.59 (±0.20)×10^{-13} cm which is not in disagreement with the hypothesis of charge independence of nuclear forces.

* Work supported by the Wisconsin Alumni Research Foundation and AEC.
† National Science Foundation Predoctoral Fellow.
[1] Burgy, Ringo, and Hughes, Phys. Rev. **84**, 1160 (1951).

V11. The Elastic Scattering of Alpha-Particles by O^{16}.† JOHN R. CAMERON,* ROBERT H. DAVIS, AJAY S. DIVATIA, FREDERIC J. EPPLING, AND RICHARD W. HILL, *University of Wisconsin.*—The differential cross section for elastic scattering of alpha-particles by O^{16} was measured in a gas scattering chamber using alpha-particles accelerated in the Wisconsin electrostatic generator. Alpha-particle energies used were between 0.94 and 4.0 Mev. Cross sections were measured at θ(c.m.) = 168.0°; 140.1°; 124.6°; and 90.0°. Because both particles have zero spin, each partial wave except $l=0$ has a zero amplitude at some angular position. The P-wave is zero at 90.0°; the D-wave is zero near 124.6°; and the F-wave is zero at 90.0° and near 140.1°. This permitted the unambiguous assignment of J-values to the resonances from a qualitative observation of the cross section. The resonances were analyzed using the Wigner-Eisenbud one-level approximation to determine the width and resonant energy of each resonance. Five scattering anomalies were observed to which the J-values and resonant energies using the Ne^{20} ground state as the energy zero are the following: S at 6.738 Mev; F at 7.182 Mev; S at 7.218 Mev; D at 7.450 Mev; and D at 7.854 Mev. The parity is odd for odd J and even for even J. The uncertainty in these energies is about 10 kev.

* Work supported by the Wisconsin Alumni Research Foundation and AEC.
† AEC Predoctoral Fellow.

V12. Inelastic Nuclear Scattering of Photons by Rh^{103}.* C. S. DEL RÍO† AND V. L. TELEGDI, *University of Chicago.*—A lower limit to the cross section for inelastic nuclear scattering of photons $\sigma(\gamma, \gamma')$ can be determined by irradiating an element having an isomeric state in its neutron richest isotope with high energy photons and measuring the isomeric activity. Rhodium foils were exposed to the Chicago betatron and the yield of $Rh^{103}(\gamma, \gamma')Rh^{103*}$ was measured as a function of energy. Activities were counted with a windowless 4π-proportional counter and $Ta^{181}(\gamma, n)Ta^{180}$ was used as a monitor above 8 Mev, adopting the improved results of the Saskatchewan group. It was ascertained that the fast neutron contamination of the betatron beam contributed but a small fraction of the Rh^{103*} activity. The cross section is found to go through a peak of the order of 10 mb at about 12.5 Mev and to be appreciable below the $Rh^{102}(\gamma, n)$ threshold, reported at 9.35 Mev. The observed location of the peak is considerably lower than would be expected for $Rh^{103}(\gamma, n)$ from the empirical A-dependence of (γ, n) cross sections and the case of $Au^{197}(\gamma, \gamma')Au^{197*}$, but is theoretically not unreasonable. Similar studies on other elements are in progress.

* Assisted by the joint program of the AEC and ONR.
† From Junta de Energía Nuclear, Madrid.

V13. Multiple Scattering Effects in Pion-Deuteron Scattering. K. A. BRUECKNER, *Indiana University.*—The scattering of pions by deuterons has been considered in the "impulse approximation" in which the motion of the nucleons is neglected during the scattering process. It is then possible to obtain an exact solution to the multiple scattering problem if scatterings which do not conserve energy are neglected. The effects of charge exchange are included, but the scattering has been assumed to be restricted to P-states and to be spin independent. It is found that the scattering is strongly depressed when the nucleons are within a distance roughly equal to the geometric mean of the pion scattering amplitudes from neutron and proton. These results are applied to a consideration of high energy pion scattering, making use of the results of Fermi[1] for the scattering amplitudes. A sizeable depression of the total cross sections relative to the free particle cross sections is found. This is in contrast to the predictions of the theory neglecting multiple scattering which gives a large positive interference effect. A comparison with experiment will be made.

[1] Fermi, Anderson, and Nagle (private communication).

SATURDAY AFTERNOON AT 2:00

Rebstock Hall

(H. L. ANDERSON presiding)

Invited Papers in Nuclear Physics

W1. Recent Research on Mu-Mesons. R. D. SARD, *Washington University.* (30 min.)
W2. Level Classification by Resonance Scattering of Protons and Alphas. H. T. RICHARDS, *University of Wisconsin.* (30 min.)
W3. Atomic Masses of the Light Elements. T. L. COLLINS, *University of Minnesota.* (30 min.)
W4. Coincidence Measurements with Beta-Ray Spectrometers. ERLING JENSEN, *Iowa State College.* (30 min.)

SATURDAY AFTERNOON AT 2:00

Brown Hall

(A. H. WEBER presiding)

Invited Paper

X1. Galvanomagnetic Effects in Semiconductors. VIVIAN A. JOHNSON, *Purdue University.* (30 min.)

Solid-State Physics. II

X2. Energy Loss of Medium-Fast Electrons in Metals.* E. M. BARODY, *Battelle Memorial Institute.*—It has been considered probable that excitation of valence electrons to the next Brillouin zone makes an important contribution to the energy loss in metals of electrons with energy in the range 10^2 to 10^3 ev. According to Wooldridge[1] and Vyatskin,[2] the matrix element for excitations of this type varies inversely as the square of the momentum change of the primary, and the corresponding energy loss per unit primary path is approximately independent of the energy. In the work to be reported, the matrix element is treated by a method somewhat different from that used by Wooldridge and is found to vary more nearly as the inverse *first* power of the momentum change of the primary. This result implies a rate of energy loss which is inversely proportional to the energy and suggests an energy loss curve similar to that for free atoms. Reasons for the discrepancy and the significance of the present result for secondary emission will be discussed.

* Sponsored by the Army Signal Corps and the Air Force.
[1] D. E. Wooldridge, Phys. Rev. **56**, 562 (1939).
[2] A. Ya. Vyatskin, J. Exptl. Theoret. Phys. (U.S.S.R.) **20**, 557 (1950).

X3. On the Transmission of Electrons through Thin Metallic Foils. C. H. CHANG, C. S. COOK, AND H. PRIMAKOFF, *Washington University.**—Experimental studies have been made on the relative transmission of positrons and negatrons through aluminum and platinum windows of an end-window type G-M counter. In qualitative agreement with the theoretical predictions that more scattering takes place in material having higher atomic number, a platinum foil having the same surface density as a corresponding aluminum foil shows lower relative transmission at any given energy, even though the low energy cutoffs of the two windows are just about the same. Also in qualitative agreement with theory a larger percentage of positrons than negatrons are transmitted at any given energy for the same foil. Theoretical transmission curves, with empirically determined constants, have been developed. These curves are in relatively good agreement with the experimental curves.

* Assisted by the joint program of the ONR and AEC.

X4. The Magnetic Structure of Manganese Antimonide. N. S. GINGRICH,* C. G. SHULL, AND M. K. WILKINSON, *Oak Ridge National Laboratory.*—Neutron diffraction data have been obtained for a polycrystalline sample of Mn_2Sb at a series of temperatures ranging from 77°K to 940°K in order to determine the strength and relative orientation of the atomic magnetic moments which are responsible for the observed ferromagnetism of this compound. The room temperature observations (well below the Curie temperature of 275°C) agree reasonably well with Guillaud's model,[1] in which half of the Mn atoms have magnetic moments of three Bohr magnetons parallel to each other and the other half are of five Bohr magnetons directed antiparallel to the first group. At high temperatures above the Curie temperature, however, the observed paramagnetic scattering is only about half that which is calculated for this model. The moments are found to be parallel to the C_0 axis of the tetragonal cell at room temperature and to rotate into the basal plane at low temperature as Guillaud's magnetic measurements have indicated.

* On leave from the University of Missouri during part of 1952.
[1] C. Guillaud, J. phys. et radium **12**, 492 (1951).

X5. Magnetic Inelastic Scattering of Neutrons in Fe. H. PALEVSKY, R. S. CARTER, AND D. J. HUGHES, *Brookhaven National Laboratory.**—The neutron cross section of Fe has been investigated in the 4–14A region with the Brookhaven slow chopper at sample temperatures ranging from 100–1300°K. In the region above 450°K the temperature dependent part of the cross section (presumably inelastic scattering) is found to depart from the values calculated by Kleinman and by Placzek, whereas agreement is found for copper. The calculations are based on the exchange of energy between the neutrons and the lattice vibrations; the principal process for the wavelengths considered here being absorption of phonons by the neutrons. The departure of experiment from theory increases rapidly with temperature, and at the Curie point the inelastic scattering is twice the calculated value. The rate of change of cross section with temperature shows a marked decrease above the Curie point, and at all temperatures it is proportional to wavelength, as expected for inelastic scattering. It is concluded that the excess cross section is magnetic inelastic ("spin wave") scattering. The persistence above the Curie point, however, seems in direct conflict with the supposed paramagnetic nature (uncoupled spins) of iron at high temperature.

* Work carried out under contract with the AEC.

X6. Diffusion and the Motion of Phase in Binary Alloys. D. D. VAN HORN, *Knolls Atomic Power Laboratory.**—In the diffusion interchange between two "adjacent" phases in a binary alloy (for example, diffusion between α- and β-brass) it is generally observed that the position of the phase boundary relative to the initial interface will change with time. For unidirectional diffusion in an infinite specimen, it can be shown that the displacement of the phase boundary is given by $d=K(2t)^{\frac{1}{2}}$. If λ_1 and λ_2, the differences between the initial concentration (c) of each phase and the corresponding solubility limit (c_0) in that phase, and δ, the concentration difference between the two solubility limits ($\delta=c_{20}-c_{10}$) are given, then any two of the three quantities D_1, D_2, and K will determine the third. (D_1 and D_2 are the respective diffusion coefficients in the two phases.) The complete solution of the problem, including the analytical expressions for the concentration curves is determined by the solution of the following equations for β_1 and β_2:

$$\beta_1 D_1^{\frac{1}{2}} = \beta_2 D_2^{\frac{1}{2}} = K/\sqrt{2}, \tag{1}$$

$$\delta\pi^{\frac{1}{2}} = \lambda_2 \exp(-\beta_2^2)/[\beta_2(1+\operatorname{erf}\beta_2)] - \lambda_1 \exp(-\beta_1^2)/[\beta_1(1-\operatorname{erf}\beta_1)]. \tag{2}$$

A nomographic solution of these equations will be given.

* The Knolls Atomic Power Laboratory is operated for the AEC by the General Electric Company.

X7. Diffusion of Sodium in Sodium Tungsten Bronze. J. F. SMITH AND G. C. DANIELSON, *Iowa State College.*—An investigation of the diffusivity of sodium in single crystals of the metal sodium tungsten bronze is in progress. The concentration gradient is established by evaporation of sodium from a sample heated in a vacuum, and the sodium concentration is measured by x-ray determination of the lattice constant which varies linearly with sodium concentration. The diffusivity is evaluated by a method which is based upon Fick's first law rather than his second. The data give a family of curves showing the concentration as a function of depth with time as a parameter. From these curves the mass of sodium transferred through a plane parallel to the surface and at any particular depth may be plotted as a function of time. The slope of this curve divided by the concentration gradient, both evaluated at the same depth and time, is the diffusivity for the corresponding concentration. Preliminary results indicate that the diffusivity decreases with increasing sodium concentration.

X8. Some Observations on the "Direct-Current Etch." DAVID B. LANGMUIR, *Atomic Energy of Canada Limited.*—Tantalum, in common with a number of other metals, develops an etched appearance when heated with direct current in high vacuum at about 2200°K for 50 or more hours. This phenomenon has been investigated by using tantalum strips 0.001–0.005 inch thick in which crystal grains 1 mm or more in diameter have been grown. Goniometer reflections using visible light have been obtained within +5° from the surfaces developed by dc heating, and these surfaces have been identified by comparison with Laue back reflection photographs. In cases observed so far the initial surface of the strip has coincided within a few degrees with either a (110) or (211) plane. In the case of a (211) initial surface with the current flowing parallel to the close packed (111) direction, one face of the crystal grain remains almost smooth, while the opposite face develops a set of ridges running at right angles to the direction of current flow and bounded by (100) surfaces on the (+) side, (110) surfaces at the ends, and a (211) surface on the (−) side. When the close-packed direction makes an oblique angle to the direction of current, a (211) surface usually develops with its normal having a component pointing toward the negative end.

X9. Self-Diffusion of Tantalum. R. L. EAGER* AND D. B. LANGMUIR,† *Atomic Energy of Canada Limited.*—The volume self-diffusion of tantalum has been measured by activating a small volume of a tantalum strip in the thermal column of the NRX pile and heating in vacuum. The volume diffusion coefficient D_v over the range 2100 to 2800°K can be represented by the equation $D_v = 2\exp(-110{,}000/RT)$ cm²/sec. Auto radiographs show that grain boundary diffusion occurs much more rapidly than volume diffusion near 1800°K. Attempts have been made to measure the surface self-diffusion coefficient D_s by evaporating a surface deposit of radiotantalum upon a clean tantalum strip. Using the analysis developed by J. C. Fisher,[1] the results show that $D_s < 10^7 D_v$ at 1800°K.

* Now at the Chemistry Department, University of Saskatchewan, Saskatoon, Saskatchewan.
† USAEC Liaison Officer.
[1] J. C. Fisher, J. Appl. Phys. **22**, 74 (1951).

X10. Improved Techniques in the Aging of Thin Metal Films.* RICHARD B. BELSER, *Georgia Institute of Technology.*—It has been known for over a century that thin metal films change in optical properties, electrical resistivity, and structure with the passage of time or exposure to heat or corrosion. Whereas these properties were known, their exact delineation and quantitative evaluation have awaited improved techniques and instrumentation. Application of improved methods of soldering to thin metal films with the metal indium and its alloys, recognition of the importance of current distribution within the film, and development of a high temperature, infrared-oven, "aging" technique, which may be operated in a vacuum, have resulted in the obtaining of resistivities only slightly above that of the bulk metal for evaporated metal films of about 1000 angstroms thickness. Studies of silver, gold, aluminum, and copper films deposited by vacuum evaporation have been made. Studies of sputtered gold and silver are reported. The resistivity of evaporated films of the metals named deposited at 2×10^{-5} mm of mercury has been found to be about 1.3 bulk resistivity. For sputtered films it is about 1.5–2.0 bulk resistivity, dependent on sputtering rate and conditions. Aging effects are discussed.

* Supported by United States Army Signal Corps.

SATURDAY AFTERNOON AT 2:00

Crow Hall, 101

(R. N. VARNEY presiding)

Invited Paper

Y1. Detection of Weak Electron Paramagnetic Resonance. JONATHAN TOWNSEND, *Washington University.* (30 min.)

Luminescence

Y2. Sensitized Fluorescence Studies using a Photomultiplier Detection Method. ROBERT H. MCFARLAND AND ROBERT E. SWANSON, *Kansas State College.*—Work by Cario and Franck, Loria, Winans, and others has indicated the possibility of collisions of the second kind in which colliding atoms contribute kinetic energy to the excitation energy of the system. In mixtures of mercury and zinc and of mercury and thallium, transfers of 1.05 and 0.67 volts, respectively, have been observed. Experimental evidence has been obtained with mixtures of mercury and thallium to show that this effect is not one of double absorption. Also it is plausible to assume that this is not an effect attributable to collisions of thallium with metastable mercury atoms as postulated by Loria.

Y3. A Study of Intensity Variations in Sensitized Fluorescence. ROBERT E. SWANSON AND ROBERT H. MCFARLAND, *Kansas State College.*—Development of apparatus to make direct readings of low-level light intensities has made an investigation of the mechanisms of sensitized fluorescence possible. Measurements of the intensities of thallium lines emitted from a thallium mercury mixture when irradiated with mercury 2537 show a dependence of intensity on the temperature of both mercury and thallium. With the thallium temperature constant, thallium 3519, 3529 reach their maximum intensity at a lower mercury temperature than does thallium 3776. This may be explained in terms of the partial selection rule $\Delta J = 0$ and metastable mercury states. Thallium 5350, how-

ever, exhibits two maxima under the same conditions. This has been explained only in terms of the possibility of a memory process in the population of the thallium $2S\frac{1}{2}$ level.

Y4. Energy Transfer in Complex Solutions.* MILTON FURST AND HARTMUT KALLMANN, *New York University.*—High energy fluorescence in organic solutions with a single solute is mostly due to transfer of energy from the solvent to the solute molecules. This transfer occurs by some type of collision process. Further experiments adding a second solute (with smaller efficiency and longer wavelengths of fluorescence) gave the possibility of studying energy transfer in more detail. In such complex solutions an additional energy transfer by collision from the first to the second solute occurs. This was shown from the unusual shape of the intensity *vs* concentration curve. This displayed a maximum followed by a minimum and another considerable rise with increasing concentration of both solutes but with the concentration ratio constant. The decrease is caused by an absorption of the light from the first solvent by the second. The second rise occurs by direct energy transfer (without light absorption) from the first to the second solute; its probability increases with concentration even with constant solute ratio. A decrease of lifetime of the excitation energy in the first solute ensues from this energy transfer and reduces the chance of quenching the excitation energy in the first solute. Xylene solutions of *m*-terphenyl, anthracene, xanthone, dihydrocollidine, and fluorene were used.

* Work sponsored by the SCEL, Fort Monmouth, New Jersey.

Y5. A *K*-fluorescence Yield Summary. C. D. BROYLES* AND S. K. HAYNES, *Vanderbilt University.*—An accurate knowledge of the K fluorescence yield as a function of Z is sometimes essential in radioactive decay scheme problems. All previous summaries including recent ones by the authors and by Burhop[1] have not only been incomplete but also have contained several inaccuracies. The theory of K auger yield is also incomplete and approximate.

A brief review of the state of the theory will be presented. A summary of experimental values of the *K*-fluorescence yield will be given which we hope is accurate and complete to July 1, 1952. Copies will be available to those interested. A first summary of experimental values of the ratio of the $K-LL$ to the $K-LM$ plus $K-LN$, etc., yields will also be given. This summary includes previously published values plus that of indium[2] which is as yet unpublished.

* Now at Sandia Corporation, Albuquerque, New Mexico.
[1] E. H. S. Burhop, *The Auger Effect and Other Radiationless Transitions* (Cambridge University Press, Cambridge, 1952), pp. 45, 46.
[2] D. A. Thomas, Ph.D. thesis, Vanderbilt University (1952).

Y6. Cathodoluminescent Studies of (BaSr)O.* HAROLD W. GANDY, *University of Missouri.*—The cathodoluminescent properties of sprayed (BaSr)O samples on electrolytic nickel base metal are being studied as a function of sample temperature and sample thermionic activity. Spectral measurements show three bands to be present in moderately thermionically activated samples. Bands located at 310 mμ and 580 mμ have intensities which decrease with increasing temperature, and a band at 400 mμ has an intensity which increases with increasing temperature. Time decay of the cathodoluminescent intensity of each band is being studied as a function of sample activity and sample temperature. The time rate of decay of the luminescent intensity of each band increases with increasing temperature; however, the rate of decay of the 400-mμ band is less than that of the other two bands. The decay of the 400-mμ band appears to be exponential with time.

The intensity of the 400-mμ and 580-mμ bands seem to increase relative to the intensity of the 310-mμ band with increasing thermionic activity of the sample. The rate of decay of each band does not seem to be influenced by changing sample activity.

* Supported by a grant from the RCA Laboratories Division, Princeton, New Jersey.

Y7. (Abstract withdrawn.)

Y8. Characteristics of Thin Plastic Scintillation Phosphors. G. G. EICHHOLZ, *Department of Mines and Technical Surveys, Ottawa.*—Thin film plastic phosphors have been prepared by a modified pressure moulding technique in a cylindrical mould[1] or by pressing between aluminum sheets on heated platens. Optimum concentrations have been determined using polystyrene solutions of *p*-terphenyl and diphenyl hexatriene or tetraphenyl butadiene. Excellent light collection can be obtained with wedge-shaped phosphors. Results under alpha- and beta-irradiation and relative pulse-height distributions will be discussed. An outline will be given of possible applications in scintillation detectors for use with acid solutions and other cases where large-area detectors are desirable.

[1] G. G. Eichholz and J. L. Horwood, Rev. Sci. Instr. **23**, 305 (1952).

SATURDAY AFTERNOON AT 2:00

Wilson Hall

(HENRY PRIMAKOFF presiding)

Theoretical Physics

Z1. On Approximate Two-body Relativistic Wave Equations. Z. V. CHRAPLYVY, *St. Louis University.*—The Foldy-Wouthuysen method[1] has been extended to the two-body problem. A canonical transformation has been developed which converts any relativistic two-body Hamiltonian into an "even-even" operator, and thus makes it possible to obtain a four-component approximation to the 16-component wave equation with the negative-energy states of both particles excluded. This is especially important in the case of the Breit equation since, as has been pointed out,[2] the difficulties in its applications stem from an admixture of negative-energy states which, of course, are not removed in the large-component approximation usually applied to it.

[1] L. L. Foldy and S. A. Wouthuysen, Phys. Rev. **78**, 29 (1950).
[2] G. E. Brown and D. G. Ravenhall, Proc. Roy. Soc. (London) **208**, 552 (1951).

Z2. An Amplified Dirac Equation and the Lamb-Retherford Shift. W. A. BARKER AND Z. V. CHRAPLYVY, *St. Louis University.*—An amplified Dirac equation containing scalar, vector, tensor, pseudovector, and pseudoscalar interaction terms is converted to an approximately relativistic form by means of the Foldy-Wouthuysen[1] canonical transformation. The resulting relativistic correction terms associated with the five types of interaction are tabulated. Hydrogenic fine structure is discussed as an illustration of the utility of these tables. A relativistic wave equation in which appropriate factors of quantum electrodynamic origin[2] are included phenomenologically is rewritten in an approximately relativistic form. In this new representation one easily sees that the major contributions to the Lamb-Retherford shift are related in a simple way to the Darwin and Thomas corrections to the Balmer energy levels arising from ordinary Dirac theory. This method gives a value of 1062.59 mc/sec for the separation of the $2S$, $2P_{\frac{1}{2}}$ states of hydrogen. This phenomenological treatment, however, fails to yield the 4.00 mc/sec displacement of the $2P_{\frac{1}{2}}$ state.

[1] L. L. Foldy and S. A. Wouthuysen, Phys. Rev. **78**, 29 (1950).
[2] Karplus, Klein, and Schwinger, Phys. Rev. **86**, 288 (1952).

Z3. The Symmetry of the *S* Matrix. F. COESTER, *State University of Iowa.*—It can be shown that any Heisenberg S matrix is symmetric for an appropriate choice of arbitrary phases in a representation in which the square and one component of the total angular momentum are diagonal. The proof combines the theory of time reversal in quantum mechanics given by Wigner[1] with the methods of transformation theory. The consequences of this symmetry for the complex phases of the matrix elements are discussed.

[1] E. P. Wigner, Göttinger Nachr. **31**, 546 (1932).

Z4. The Pairing Property of Nuclear Interactions. G. RACAH, *Hebrew University, Jerusalem,* AND I. TALMI, *Palmer Physical Laboratory, Princeton University.*—Interactions of which the matrix elements have the form

$$(l^n, v, \Gamma | V | l^n, v', \Gamma') = \delta_{vv'}\{(l^v, v, \Gamma | V | l^v, v, \Gamma') + \delta_{\Gamma\Gamma'}(n-v/2)E_0\}$$

are said to possess the pairing property (p.p.). In this formula v is the seniority of the state of the configuration l^n specified by the additional necessary quantum numbers Γ, and E_0 is the energy of $l^2\,{}^1S_0$. In jj coupling the same formula holds in the j^n configuration if we replace l by j; E_0 is then the energy of j^2 $J=0$. This implies in particular that the seniority is a good quantum number. It is found that all the interactions which can be expressed as a sum of products of odd double tensors which operate on the spin and space coordinates of the two interacting nucleons, possess the p.p. in LS coupling as well as in jj coupling. An important central interaction of this kind is $W+2M$ which has the p.p. for any range and form of the potential. In the limit of short range, it goes over into the δ-potential, which is thus shown to possess the p.p. A noncentral interaction of this kind is that of the tensor forces.

Z5. A Lower Limit for the Interaction Time in Photon-Photon Scattering. E. GORA, *Providence College.*—In order to avoid difficulties which are the result of the use of sharp initial conditions in the time dependent perturbation treatment of radiation problems, a switching-on function has been introduced. This leads to the conclusion that the duration of the interaction, the "interaction time," should exceed a well-defined lower limit, or else the well-known formulas of the quantum theory of radiation could not be valid. For scattering of photons by electrons this lower limit turns out to be so small that it is not likely to be observable, but for photon-photon scattering its order of magnitude is $\gamma(\hbar c/e^2)^4(e^2/mc^2)$ $\sim\gamma\times10^{-15}$ sec, where $\gamma=\hbar\omega/mc^2\gg1$. The observed lifetime of a neutral meson decaying into two photons is of the same order of magnitude. This coincidence suggests an investigation of the possibility that the observed lifetime of unstable particles could be in some way linked up with a finite duration of the interaction between the particles which take part in the production and decay processes.

Z6. Photopion Production from a Single Nucleon. F. SALZMAN, *University of Illinois* (introduced by G. F. Chew).—The photopion production from a single nucleon is calculated in the symmetrical pseudo-vector coupling theory with a fixed extended source.[1] Only the free meson current is used in calculating the interaction between the nucleon-meson system and the electromagnetic field.[2]

The photon can be pictured as ejecting a π^+ from a virtual state in the proton cloud into a "real" particle scattering state. The high π^0/π^+ ratio corresponds to the large charge-exchange (π^+, N) scattering cross section. This process is examined in a weak-coupling approximation in which the initial and final wave functions are expanded to order g^3 in the pion-nucleon coupling constant. It is found that the secondary scattering effects are extremely important and dominate the terms of order eg^3. It is known that the perturbation treatment of the pion-nucleon scattering omits large reactive effects, but their inclusion by means of the Dancoff approximation only increases the relative importance of secondary scattering.[1] It is also noted that the terms of order eg^3 cannot be treated phenomenologically as resulting from a static or frequency dependent magnetic moment.

[1] G. F. Chew, Phys. Rev. (to be published).
[2] J. S. Blair and G. F. Chew, Ann. Rev. Nuclear Sci. **2** (1952).

Z7. A Variational Procedure for Electron-Hydrogen Scattering. M. M. GORDON AND J. G. JONES, *University of Florida.*—An improved variational procedure for $e-$H scattering has been developed whereby both the elastic and inelastic scattering amplitudes can be calculated directly. The derivation of this procedure follows from the "spatial-orientation degeneracy" of the wave function and the availability for computations of a complete ortho-normal set of H eigenfunctions.[1] This variational procedure has the following features: (a), it does not involve a partial wave analysis; (b), it includes exchange scattering; (c), it treats elastic and inelastic scattering within the same formalism; and (d), it yields the Born approximation in zero-order. Calculations are now in progress which utilize this procedure to obtain an improvement of the Born approximation for the elastic scattering of 100 to 900 volt electrons. A linear trial wave function of the following form is being used:

$$\Psi=[\{1+(B+Cr_{12})\exp(-r_1/a_0)\}\exp(i\mathbf{k}\mathbf{n}\cdot\mathbf{r}_1) + (A/r_1)\{1-\exp(-r_1/a_0)\}\exp(ikr_1)]\exp(-r_2/a_0),$$

where A, B, C are variational parameters. The preliminary results of this work will be presented.

[1] W. Kohn, Phys. Rev. **74**, 1763 (1948), Sec. III.

Z8. Variation Method in Quantum Statistics.* JOHN M. RICHARDSON AND WILLIAM M. MACDONALD III,† *U. S. Bureau of Mines.*—The statistics of the grand canonical ensemble can be expressed in terms of a variational function Θ which is simply related to the equilibrium pressure, when it is maximized under the constraints of normalization and constancy of temperature and chemical potential. Using the field-theoretic formulation (involving creation and annihilation operators defined in terms of a set of single-particle states) of the Hamiltonian and number of particles, it is possible to expand Θ in a series of terms containing successively higher orders of interaction and correlation. Neglecting all correlations and third- and higher-order interactions, we obtain an approximate Θ in which variations are to be made on the single-particle states and on the quantum distribution

functions concerned with the occupancy of each state. In the case of fermions, we obtain results then reduce to the usual Fermi-Dirac distribution in the limit of vanishing interaction and to Fock's equations in the limit of zero temperature. The boson case is formally similar. We will consider the quantum version of the cell method in the theory of liquids.

* Supported in part by the ONR.
† Now at Princeton University, Princeton, New Jersey.

Z9. Possible Inconsistency in Customary Use of Vectors. J. G. WINANS, *University of Wisconsin*.—For two vectors to be equal they must have the same magnitude, direction, and unit. A cross product or axial vector like area $A = s_1 \times s_2$ has the unit square cm and is perpendicular to s_1 and s_2. In describing vector components by unit vectors i, j, k, it is customary to consider $ij = k$. If $i = 1$ cm, $j = 1$ cm, and $k = 1$ cm, considering $ij = k$ leads to an inconsistency since vector ij has the unit square cm and vector k has the unit cm. A distinction should also be made between square cm, a unit of a vector quantity and cm² a unit of a scalar quantity. For a series representation of $f(x)$, if x is a vector, odd power terms are vectors and even power terms are scalars. To carry out the additions the square of a vector must be considered a dimensionless number and then $f(x) = \text{scalar} + \text{vector} = \text{quaternion}$.

Z10. On the Beta-Decay Interaction. JOHN M. BLATT, *University of Illinois*.—The decays of C^{10} and O^{14} show that there must be an admixture of a Fermi-type interaction. The comparative half-lives (ft-values) of the neutron, H^3, He^6, and O^{14} are used to estimate the relative strengths of the Fermi and Gamow-Teller interactions. Because of the new value of the end-point energy of He^6,[1] the ft-value of this decay does *not* give significant information about the interaction. The matrix element $(f\sigma)^2$ for the H^3 decay is not known very accurately because of the unknown amount of admixture of ^4D and other states to the dominant ^2S state. However, it can be shown that $(f\sigma)^2 \leqslant 3$ as long as the ^2S state is present with at least 25 percent probability. This allows us to put an upper limit on the lifetime of the neutron. An experiment is suggested to determine uniquely the nature of the Fermi-type interaction (scalar or polar vector). The considerations given here do not say anything about the presence or absence of a pseudoscalar component.

[1] Dewan, Pepper, Allen, and Almquist, Phys. Rev. **86**, 416 (1952).

Z11. Special-Relativistic Linear Gravitational Theory. F. J. BELINFANTE, *Purdue University*.—Derive such theory (different from Birkhoff's) from the Lagrangian $\int dt(L_g + L_m)$;

$L_g = -(c^4/16\pi G)\int d^{(3)}\mathbf{x} G^{\alpha\beta}G^{\lambda\mu}G^{\rho\sigma}\{a(\partial_\alpha h_{\lambda\rho})(\partial_\beta h_{\mu\sigma}) + b(\partial_\lambda h_{\mu\alpha})(\partial_\rho h_{\sigma\beta}) + f(\partial_\alpha h_{\lambda\mu})(\partial_\beta h_{\rho\sigma}) + q(\partial_\alpha h_{\lambda\mu})(\partial_\rho h_{\beta\sigma})\}$;

$L_m = \Sigma_i m_i c\{-w_i + Kw_i C^{\alpha\beta}h_{\alpha\beta} + Bh_{\alpha\beta}dx_i{}^\alpha dx_i{}^\beta/2w_i dt^2\}$;

$h_{\lambda\mu} = h_{\mu\lambda}$, $G_{\mu\nu} = G^{\mu\nu} = (1 - 2\delta_{\mu 0})\delta_{\mu\nu}$, $w_i = (-G_{\mu\nu}dx_i{}^\mu dx_i{}^\nu/dt^2)^{\frac{1}{2}}$, $\partial_\alpha = \partial/\partial x^\alpha$, $G = 6.67 \times 10^{-8}$ cm³ g^{-1} sec^{-2}, coefficients a, b, f, q, B, K chosen later. If $(2aq + q^2 - 4bf)/8K = a(b + 2q)/B$ (say $= C$), the gravitational equations around mass M have static spherical solution $h_{\mu\nu} = \{(b+q)G_{\mu\nu} - (b+2q)\delta_{\mu\nu}\}GM/2c^2Cr$. Equations of motion for particles in such field yield Kepler orbits, if $4C = 4Kb - 2Bb - 3Bq$, with perihelion precession $= N\pi MG/c^2a(1-\epsilon^2)$ with $N = -(6Bb + 13Bq + 4Kb)/4C$. First terms in expansion of Einstein's Lagrangian in powers of $h_{\mu\nu} = g_{\mu\nu} - G_{\mu\nu}$ and $k^{\mu\nu} = g^{\mu\nu} - G^{\mu\nu}$ are the above with $B = -4a = 2b = 4f = -2q = 1$ and $K = 0$. This gives $N = 7$. For finding Einstein's $N = 6$, Einstein's theory requires the terms cubic in $h_{\mu\nu}$ and $k^{\mu\nu}$ in L_g (which adds 1 to N) and terms quadratic in $h_{\mu\nu}$ in L_m (which subtracts 2). We adjust N to its experimental value by convenient choice of a, b, f, q, B, K satisfying above conditions. ($B = 0$ won't do.) Energy-momentum 4-vector for particle $p_\mu = mcU^\nu\{G_{\mu\nu} - KG_{\mu\nu}G^{\alpha\beta}h_{\alpha\beta} + Bh_{\mu\nu} + \frac{1}{2}BG_{\mu\nu}h_{\alpha\beta}U^\alpha U^\beta\}$ with $U^\mu = dx^\mu/wdt$ satisfies $dp_\mu/wdt = f_\mu/c \equiv mc\{\frac{1}{2}BU^\alpha U^\beta + KG^{\alpha\beta}\}\partial_\mu h_{\alpha\beta}$. In a static central field p_0 and $\mathbf{r} \times \mathbf{p}$ are conserved.

Z12. The Quadrupole Moment of Li^7. E. G. HARRIS,* *The University of Tennessee*, AND M. A. MELKANOFF, *University of California at Los Angeles* (introduced by R. D. Present).—The quadrupole interaction energy, eqQ, for Li^7 in Li_2 has been reported to be positive.[1] In an attempt to determine $Q(Li^7)$ a calculation of q has been made using two approximate wave functions for Li_2. One of these is a Heitler-London function including inner shells and the other a 12 term variational function[2] which gives a dissociation energy 0.6 ev less than the experimental value. The results of the two calculations differ in sign. The more accurate James function leads to a negative q and consequently a negative value of $Q(Li^7)$. Unfortunately, the electronic and nuclear parts of q are nearly equal in Li_2 so that the magnitude and even the sign are still uncertain.

* AEC Predoctoral Fellow.
[1] Logan, Cote, and Kusch, Phys. Rev. **86**, 280 (1952).
[2] H. M. James, J. Chem. Phys. **2**, 794 (1934).

SUPPLEMENTARY PROGRAMME

SP1. A Technique of Soldering to Thin Metal Films.*† RICHARD B. BELSER, *Georgia Institute of Technology.*—In the past, soldering to thin metal films on glass or quartz substrates has normally been accomplished by suitably reinforcing the film at the soldering point with a thicker underlying film. This performance is necessary in order to prevent tin-lead solders and commonly used fluxes from destroying the film and to give better adhesion to the substrate. It has been found that by using the metal indium and certain of its alloys as a solder, without a flux, adherence to thin metal films may be readily obtained without destruction of the film. Since indium also adheres to glass, quartz, ceramics, and silicious minerals the strength of the joint is not determined by the strength or adherence of the metal film but by the strength of the indium-glass or indium-quartz bond. Thus, films of only a few angstroms in thickness may be soldered without damage, with good mechanical strength and electrical contact. The strength of the bond is usually about 500 pounds per square inch. This technique has been found most useful in studying the resistivities of thin metal films and in the mounting of metal coated piezoelectric crystals. Soldered connections have been made to films of 18 metals including aluminum, titanium, and zirconium.

* Supported by United States Army Signal Corps.
† To be called for at the end of Session X if the Chairman rules that time permits.

SP2. The Frictional Adhesion of Metal to Glass, Quartz, and Ceramic Surfaces.* RICHARD B. BELSER, *Georgia Institute of Technology.*—In 1947, W. A. Wooster and G. L. McDonald[1] reported that titanium by frictional contact would adhere to glass and certain mineral and ceramic surfaces. In order to explore this property further small disks of a number of different metals were mounted separately on one-eighth-inch shafts. These disks, driven by a high speed hand-grinder, were applied to glass, quartz, and ceramic surfaces. By suitably varying the rpm of the motor and the pressure of application, the metal of the disks could be made to adhere securely to such surfaces. At high rpm and moderate pressure, erosion of the glass surfaces usually occurred. Variations of the technique of application allowed the metallic coating or the cutting of glass. The coating method has been found useful for marking glassware, decorative work, metal to nonmetal seals, and for the application of electrically conducting lines to nonmetallic surfaces. Some of the metals tested were titanium, zirconium, aluminum, magnesium, gold, silver, copper, iron, nickel, cobalt, cadmium, zinc, and lead. Titanium and zirconium appeared to be the most active in glass cutting. For decorative and other purposes a number of the metals tested proved useful.

* To be called for at the end of Session X if the Chairman rules that time permits.
[1] W. A. Wooster and G. L. McDonald, Nature **160**, 260 (1947).

SP3. New Theory of Aggregates as Supplement to van't Hoff's Theory of Solutions.* GEORGE ANTONOFF.—This year the centenary of van't Hoff is celebrated. His theory of solutions has one limitation: It is valid only for dilute solutions, because in concentrated ones the van der Waals forces come into play. If supplemented by the new theory of aggragates,[1] it becomes valid at all concentrations. van der Waals theory fails on quantitative side, but he himself changed his views as is seen from his last paper, in which he has made a concession towards recognition of aggregates.[2] According to the new theory of aggregates, $X = d_l/d_v$ is the association factor, where d_l is the density of the liquid and d_v that of vapor. Introduced into the gas equations X makes them comfortable with the laws of thermodynamics: The van der Waals forces are consumed in forming the aggregates and do not make themselves felt. Thus, the gas laws show themselves exact. The concept "activity" introduced by G. N. Lewis as a matter of expediency should be abandoned as having no physical meaning. On the contrary X introduces clarity and simplicity into this theory which shows itself in perfect agreement with experimental evidence.

* To be called for at the end of Session H if the Chairman rules that time permits.
[1] Jerome Alexander, Colloid Chem. **VII**, 83 (1950).
[2] See reference 40 of reference 1.

SP4. Kinks in Vapor Pressure p *vs* Temperature Curves.* GEORGE ANTONOFF.—The p curves show the same kinks as d_v. The values of the National Bureau of Standards are distrusted as being "smoothed," although without justification. They reveal the same law as the 30 liquids of Young. The RP 1229, 1939, gives water values for every 5 degrees. The smoothing could affect only points nearest to the kinks, but it could not mask the law. Paper No. 300 from Massachusetts Institute Technology gives in Table I, pages 154–163, figures *actually* observed mostly for every 10°C. I found the same kinks as in d_v curves. In Table V, page 166, values of p are computed for every degree. All points of Table I found in Table V remained unchanged. The kinks appear as intersections of two curvatures, although not as sharply as in the d^1 method. It is clear that they cannot be the result of "smoothing," which affects only the last figures but not those revealing the law.[1]

* To be called for at the end of Session H if the Chairman rules that time permits.
[1] See Smith, Keyes, and Gerry, Proc. Am. Acad. Arts Sci. **69** (January 1934).

Author Index to Papers Presented at the St. Louis Meeting

Affleck, J. H. and L. V. Holroyd—C1
Allen, James S. and W. K. Jentschke—Q1
Alpert, D.—P3
Ames, D. P., M. E. Bunker, L. M. Langer, and B. M. Sorenson—Q10
Antal, J. J. and A. H. Weber—K7
Antonoff, George—SP3, SP4
——and Raymond Madrazo, Jr.—H10
Apker, L.—P1
Atkinson, W. R. and R. G. Fowler—T5
Barker, W. A. and Z. V. Chraplyvy—Z2
Baroody, E. M.—X2
Becker, R. L., M. Walt, and A. Okazaki—S3
Belinfante, F. J.—Z11
Belser, Richard B.—X10, SP1, SP2
Birnbaum, G. and A. A. Maryott—D7
Birnbaum, Milton, Eric M. Harth, Leo Seren, and Ralph Tobin—E6
Blatt, John M.—Z10
Broyles, C. D. and S. K. Haynes—Y5
Bruce, C. R.—D12
Brueckner, K. A.—V13
Butler, S. T. and E. E. Salpeter—B1
Butler, W. A. and G. M. Almy—B10
Caird, R. S. and Allan C. G. Mitchell—Q9
Camac, M., J. B. Platt, and H. J. Schulte—S8
Cameron, John R., Robert H. Davis, Ajay S. Divatia, Frederic J. Eppling, and Richard W. Hill—V11
Chang, C. H., C. S. Cook, and H. Primakoff—X3
Chew, G. F.—R2
Chraplyvy, Z. V.—Z1
Cleland, Marshall R.—E3
Coester, F.—Z3
Collins, T. L.—W3
Compton, A. H.—G1
Conn, Willi M. and Gene Braught—H2
Coomes, E. A., J. A. Dezoteus, and J. F. Whalen—C5
Coryell, Charles D., Pierre Lévêque, and Harold G. Richter—Q12
Day, Robert B.—V9
del Río, C. S. and V. L. Telegdi—V12
Deverall, G. V., K. W. Meissner, and G. J. Zissis—D2
Donahue, D. J., K. W. Jones, M. T. McEllistrem, and H. T. Richards—B6
Donn, Bertram—H4
Duerig, William H. and Jordan J. Markham—K8
Eager, R. L. and D. B. Langmuir—X9
Eichholz, G. G.—Y8
Ferguson, Eldon E.—D5
Fermi, Enrico—G2
Fields, R. E., R. L. Becker, and R. K. Adair—V10
Fonger, W. H., J. W. Firor, and J. A. Simpson—A3
Fosdick, L. D. and H. M. James—K10
Fowler, R. G. and H. G. Rose—T6
Fulbright, H. W., D. A. Bromley, and J. A. Bruner—B4
Fumi, Fausto G. and Robert G. Parr—D4
Furst, Milton and Hartmut Kallmann—Y4
Gandy, Harold W.—Y6
Gingrich, N. S., C. G. Shull, and M. K. Wilkinson—X4
Gopalakrishnan, K., A. de-Shalit, and J. W. Mihelich—V5
Gora, E.—Z5
Gordon, M. M. and J. G. Jones—Z7
Hamermesh, Bernard—E1
Harris, E. G. and M. A. Melkanoff—Z12
Harris, S. P.—S1
Haxby, B. V. and P. Wargo—C2
Herb, R. G., Robert H. Davis, Ajay S. Divatia, and D. Saxon—E8
Hildebrand, R. H.—R3
Huddleston, Charles M. and Allen C. G. Mitchell—Q8
Huizenga, John R.—R4
——and Robert B. Duffield—B11
Ivash, E. V. and D. M. Dennison—D3
Jensen, Erling—W4
Johnson, J. B.—P2
Johnson, Vivian A.—X1
Jones, L. C., A. V. Bushkovitch, C. A. Potter, and A. G. Rouse—D8
Jones, Mark W.—H7
Jorgensen, T., E. Jones, and C. J. Cook—E5
Juenker, D. W., G. S. Colladay, and E. A. Coomes—C4
Kaplan, B. and J. G. Daunt—T9
Keesom, P. H., K. Lark-Horovitz, and N. Pearlman—K4
Kerman, R. O., W. E. Kreger, and P. G. Kruger—V8
King, D. T., Nathan Seeman, and Maurice M. Shapiro—A4
Kreiger, Theodore J. and Hubert M. James—K9
Lagemann, R. T. and L. W. Gilley—T3
Langer, L. M., R. B. Duffield, and C. W. Stanley—V2
Langmuir, David B.—X8
LeBlanc, J. M., W. H. Nester, D. W. Martin, M. K. Brice, and J. M. Cork—V1
Levinger, J. S.—V6
Lew, Hin and Gunter Wessel—D1
Lindemann, W. W. and H. J. Hannam—K3
McFarland, C. E., M. M. Bretscher, and F. B. Shull—B7
McFarland, Robert H. and Robert E. Swanson—Y2
Mattson, R. H. and A. van der Ziel—K1
Meyer, D. I. and F. H. Schmidt—V7
Mihelich, J. W.—V3
Mize, J. P. and D. J. Zaffarano—Q4
Morrison, S. R.—K6
Nielsen, J. Rud, C. Y. Liang, D. C. Smith, and Morris Alpert—D6
Nomura, K. C.—C7
Packard, R. G.—T2
Palevsky, H., R. S. Carter, and D. J. Hughes—X5
Parzen, G. and T. Wainwright—K12
Paul, E. B. and R. L. Clarke—B8
Peterson, R. W.—C3
Phillips, G. C.—E2
Plass, Gilbert N. and Daniel I. Fivel—H3
Pope, N. K.—H6
Porter, F. T. and H. P. Hotz—Q7
Primakoff, H. and F. T. Porter—Q6
Putcha, Venkateswarlu and Masataka Mizushima—D9
Racah, G. and I. Talmi—Z4
Richards, H. T.—W2
Richards, Hans Kohn—E7
Richardson, John M. and William M. MacDonald III—Z8
Roberts, J. H., W. O. Solano, D. E. Wood, and H. B. Billington—S5
Roggenkamp, Paul L., Charles H. Pruett, and Roger G. Wilkinson—Q5
Rothstein, Jerome—K13
Sailor, V. L., H. L. Foote, Jr., and H. H. Landon—S2
Salzman, F.—Z6
Sands, R. H. and G. E. Pake—D10
Sard, R. D.—W1
Savitt, J.—T4
Schulte, H. J., J. B. Platt, and M. Camac—S7
Scott, E. J.—C6
Seidl, F. G. P., D. J. Hughes, and H. Palevsky—E4
Shaw, Wm. C., D. E. Hudson, and G. C. Danielson—K5
Simmons, B. E., H. W. Lewis, and E. Merzbacher—S6
Simpson, J. A.—A2

Smith, J. F. and G. C. Danielson—X7
Snitzer, Elias—H1
Solano, W. O. and J. H. Roberts—B3
Steele, Earl L. and James A. Krumhansl—K11
Steffen, Rolf M.—Q11
Stephens, W. E., M. E. Toms, E. E. Carroll, Jr., and G. Rosenblum—B9
Swan, J. B., W. M. Portnoy, and R. D. Hill—V4
Swanson, Robert E. and Robert H. McFarland—Y3
Swim, Richard T.—T7
Taylor, Norman L. and T. Smith Taylor—H9
Taylor, T. Smith and L. W. Max—H8
Teasdale, Tom S.—T8
Teener, J. W., L. W. Seagondollar, and R. W. Krone—B5
Thompson, Lewis C.—S4
Townsend, Jonathan—Y1
v. Krzywoblocki, M. Z.—T1
van der Ziel, A.—K2
Van Allen, J. A.—A1
Van Horn, D. D.—X6
Watson, K. M.—R1
Weddell, J. B. and J. H. Roberts—B2
Whalen, J. A., F. T. Porter, and C. S. Cook—Q3
Williams, Corre and Herbert D. Schwetman—H5
Wilson, C. W., III, and G. E. Pake—D11
Wigner, E. P.—G3
Winans, J. G.—Z9
Witmer, Enos E.—S9
Wright, Byron T.—Q2
Zinn, W. H.—G4

THE AMERICAN INSTITUTE OF PHYSICS

INCORPORATED

57 East 55 Street New York 22, N.Y.

MEMBER SOCIETIES:

American Physical Society
KARL K. DARROW, *Secretary*, Columbia University, New York 27, New York.

Optical Society of America
ARTHUR C. HARDY, *Secretary*, Massachusetts Institute of Technology, Cambridge 39, Massachusetts.

Acoustical Society of America
WALLACE WATERFALL, *Secretary*, 57 East 55th Street, New York 22, New York.

Society of Rheology
G. J. DIENES, *Secretary*, Brookhaven National Laboratory, Upton, Long Island, New York.

American Association of Physics Teachers
R. F. PATON, *Secretary*, University of Illinois, Urbana, Illinois.

AFFILIATED SOCIETIES:

American Crystallographic Association
American Society for Metals
Electron Microscope Society of America
Physical Society of Pittsburgh
Physics Club of Chicago
Physics Club of Philadelphia
Cleveland Physics Society
Physics Club of the Lehigh Valley
Sigma Pi Sigma

ASSOCIATES:

Over seventy-five leading industrial enterprises and other institutions which contribute to the support of the Institute.

JOURNALS:

The Physical Review
S. A. GOUDSMIT, *Editor*, Brookhaven National Laboratory, Upton, Long Island, New York.

Reviews of Modern Physics
J. W. BUCHTA, *Editor*, University of Minnesota, Minneapolis, Minnesota.

Journal of the Optical Society of America
WALLACE R. BRODE, *Editor*, National Bureau of Standards, Washington 25, D. C.

The Journal of the Acoustical Society of America
FLOYD A. FIRESTONE, *Editor*, 57 East 55th Street, New York 22, New York.

American Journal of Physics
THOMAS H. OSGOOD, *Editor*, Michigan State College, East Lansing, Michigan.

The Review of Scientific Instruments
GAYLORD P. HARNWELL, *Editor*, Randal Morgan Laboratory of Physics, University of Pennsylvania, Philadelphia, Pennsylvania.

The Journal of Chemical Physics
CLYDE A. HUTCHISON, JR., *Editor*, Institute for Nuclear Studies, University of Chicago, Chicago 37, Illinois.

Journal of Applied Physics
ELMER HUTCHISSON, *Editor*, Case Institute of Technology, Cleveland 6, Ohio.

Physics Today
GAYLORD P. HARNWELL, *Editorial Director*; ROBERT R. DAVIS, *Managing Editor*, American Institute of Physics, 57 East 55 Street, New York 22, New York.

OFFICERS
GEORGE R. HARRISON, *Chairman*
Massachusetts Institute of Technology
GEORGE B. PEGRAM, *Treasurer*
Columbia University

GOVERNING BOARD
KARL K. DARROW
G. J. DIENES
S. A. GOUDSMIT
G. P. HARNWELL
GEORGE R. HARRISON
F. V. HUNT
RUDOLPH KINGSLAKE
HUGH S. KNOWLES
C. C. LAURITSEN
F. W. LOOMIS
WILLIAM F. MEGGERS
GEORGE B. PEGRAM
I. I. RABI
DUANE ROLLER
FREDERICK SEITZ
FRANCIS G. SLACK
JOHN C. STEINBERG
RICHARD M. SUTTON
MARK W. ZEMANSKY

Consultant on Printing
MELVIN LOOS

ADMINISTRATIVE STAFF
HENRY A. BARTON, *Director*
WALLACE WATERFALL, *Executive Secretary*
THEODORE VORBURGER, *Advertising Manager*
RUTH F. BRYANS, *Publication Manager*
BETTY H. GOODFRIEND, *Assistant Secretary*
EILEEN B. NEUBERGER, *Circulation Manager*
KATHRYN SETZE, *Assistant Treasurer*

THE American Institute of Physics was founded in 1931 as a federation of leading societies in the field of Physics. It combines into one operating agency those functions on behalf of physics which can best be done by the Societies jointly. Its purpose is the advancement and diffusion of physics and its applications to human welfare. To this end it publishes for itself or the Societies the nine journals listed on this page; promotes unity and effectiveness of effort among all who are interested in physics; renders numerous direct services to physicists and to the public; and cooperates with government agencies, national associations, educational institutions, technical industries, and others in such manner as to realize the opportunities and fulfill the responsibilities of physics as an important and constructive human activity.

CONTENTS

THE PHYSICAL REVIEW — SECOND SERIES, VOLUME 89, NO. 4 — FEBRUARY 15, 1953

Theory of Electron Diffraction . . . . . ROY GLAUBER AND VERNER SCHOMAKER 667
Experimental Energy and Angular Distribution of Inner Bremsstrahlung . . . . . T. B. NOVEY 672
Continuous Gamma-Ray Spectrum Accompanying Beta-Decay . . P. BOLSIANO, L. MADANSKY, AND F. RASETTI 679
Three-Nucleon Interactions in Yukawa Theory . . . . . G. WENTZEL 684
Paramagnetic Relaxation in Metals . . . . . ALBERT W. OVERHAUSER 689
Induced Conductivity in Luminescent Powders. II. AC Impedance Measurements . . . . . HARTMUT KALLMANN, BERNARD KRAMER, AND ARNOLD PERLMUTTER 700
Drift Velocity of Ions in Oxygen, Nitrogen, and Carbon Monoxide . . . . . ROBERT N. VARNEY 708
Cloud-Chamber Study of the Scattering of Fast Neutrons in Oxygen . . . . . J. P. CONNER 712
Measurement and Interpretation of the *K* Auger Intensities of Sn^{113}, Cs^{137}, and Au^{198} . . . . . C. D. BROYLES, D. A. THOMAS, AND S. K. HAYNES 715
Neutron Energy Distribution from the Proton Bombardment of Li, Be, and C at 378 Mev . . . . . WARREN F. GOODELL, JR., HOWARD H. LOAR, RICHARD P. DUBRIN, AND WILLIAM W. HAVENS, JR. 724
Dynamical Theory of Nuclear Induction . . . . . R. K. WANGSNESS AND F. BLOCH 728
Interpretation of High Energy $p-p$ Scattering . . . . . DON R. SWANSON 740
Polarization Effects in Nucleon-Nucleon Scattering . . . . . DON R. SWANSON 749
Isomeric Transitions in Te^{125} and Te^{127} . . . . . HARRY T. EASTERDAY AND HEINRICH A. MEDICUS 752
Certain Explicit Relationships between Phase Shift and Scattering Potential . . . . . NORMAN LEVINSON 755
Test of the Charge Symmetry Hypothesis: Positive to Negative Pion Production Ratio Obtained in Bombarding Carbon with Alpha-Particles and Protons . . . . . H. W. WILSON AND WALTER H. BARKAS 758
Levels of Al^{28} from the $Mg^{26}(d,n)Al^{28}$ Reaction . . . . . E. GOLDBERG 760
Photoproduction of π^0 Mesons in Hydrogen and Deuterium . . . . . NORMAN C. FRANCIS 766
Average Neutron Total Cross Sections in the 3- to 12-Mev Region . . . . NORRIS NERESON AND SPERRY DARDEN 775
Cross Section for the Reaction $D(d,p)H^3$ . . . . . C. F. COOK AND J. R. SMITH 785
Nuclear Alignment and the Entropy of Liquid He^3 . . . . . BERNARD WEINSTOCK, BERNARD M. ABRAHAM, AND DARRELL W. OSBORNE 787
Electron-Positron Annihilation in Flight . . . . . S. A. COLGATE AND F. C. GILBERT 790
Irreversible Processes with Application to Helium II and the Knudsen Effect in Gases . . . . . O. K. RICE 793
Field Emission: Large Current Densities, Space Charge, and the Vacuum Arc . . W. P. DYKE AND J. K. TROLAN 799
Nuclear Gamma-Rays from Low Energy Proton Bombardment of Sodium, Magnesium, and Aluminum . . . . . HARVEY CARROW 809
Anomalous Critical Current Effect in Superconducting NbN . . . . . FLOYD C. HALEY AND DONALD H. ANDREWS 821
Electrostatic Analysis of Nuclear Reaction Energies. III . . . . . D. J. DONAHUE, K. W. JONES, M. T. MCELLISTREM, AND H. T. RICHARDS 824
Secondaries of Penetrating Showers . . . . . C. C. DAHL 836
Thermal Expansion of Solids . . . . . J. S. DUGDALE AND D. K. C. MACDONALD 832
Multiple Scattering Corrections to the Impulse Approximation in the Two-Body System . . . . K. A. BRUECKNER 836
Coupling of Angular Momenta in Nuclear Reactions . . . . . R. F. CHRISTY 839
Multiple Meson Production by High Energy Nucleon-Nucleon Collisions . . . . . H. FUKUDA 842
Combined Pairs of Vacancies in Copper . . . . . J. H. BARTLETT AND G. J. DIENES 848
Periodic Deviations in the Schottky Effect for Molybdenum . . . E. G. BROCK, A. L. HOUDE, AND E. A. COOMBS 851
Decay of Zn^{69} . . . . . R. B. DUFFIELD AND L. M. LANGER 854
Deviations from *LS* Coupling in the Spheroidal Core Nuclear Model . . . . . J. P. DAVIDSON AND E. FEENBERG 856
Third Rydberg Series of Ni . . . . . R. EDWIN WORLEY 863
Measurement of Magnetostriction in Single Crystals . . . . . R. M. BOZORTH AND R. W. HAMMING 865
Thermal Conductivity, Electrical Resistivity, and Thermoelectric Power of Graphite . . . . . W. W. TYLER AND A. C. WILSON, JR. 870

Letters to the Editor:

Induced Thermoelectric Potential from Radiation Damage . . . . . ALAN ANDREW AND CLIFTON R. DAVIDSON 876
Isomeric Branching and Threshold Behavior of the Reaction $Mo^{98}(n,2n)Mo^{97}$ . . . . . JOHN R. BROLLEY, JR. 877
Angular Correlation in the Decay of Li^8 . . . . . C. M. CLASS AND S. S. HANNA 877
Spontaneous Fission Rate of Cf^{246} . . . . . R. K. HULST, S. G. THOMPSON, AND A. GHIORSO 878
Statistical Fluctuations in Ionization by 31.5-Mev Protons . . . . . G. J. ICO, D. D. CLARK, AND R. M. EISBERG 879
Correlation between Electron and Recoil Nucleus in He^6 Decay . . . . . BRICE M. RUSTAD AND STANLEY L. RUBY 880
Test for Charge Independence in High Energy Nucleon-Nucleon Scattering . . B. A. JACOBSOHN 881
Nuclear Stars in Emulsions . . . . . R. W. WANIEK AND TAIICHIRO OHTSUKA 882
Nuclear Magnetic Resonance of Aligned Radioactive Nuclei . N. BLOEMBERGEN AND G. M. TEMMER 883
Exchange Magnetic Moments of Nuclei with Almost Closed Shells of Nucleons . RICHARD W. COLE 883
Superconducting Silicides and Germanides . . . . . GEORGE F. HARDY AND JOHN K. HULM 884
Tensor Force Interaction between a Shell Closed Except for a Single Vacancy and an External Nucleon . . . . . J. HOPE 884
Approximate Wave Functions for Unbound Relativistic Particles in a Coulomb Field . . . . . G. K. HORTON AND R. T. SHARP 885
Production of Polarized Particles in Nuclear Reactions . . . . . A. SIMON AND T. A. WELTON 886
Nonradiative Relativistic Contribution to the Magnetic Moment of $^1S_0$ Helium . . . . . WILLIAM PERL AND VERNON HUGHES 886

Proceedings of the American Physical Society:

Minutes of the 1952 Thanksgiving Meeting Held at St. Louis, November 28–29, 1952 (Corresponding to *Bulletin of the American Physical Society*, Volume 27, No. 5) 889

LANCASTER PRESS, INC., LANCASTER, PA.